

Ligand Controlled Electronic Structure of Iron and Ruthenium Complexes

Dissertation

zur Erlangung des Grades
„Doktor der Naturwissenschaften“
im Promotionsfach Chemie

am Fachbereich Chemie, Pharmazie,
Geographie und Geowissenschaften
der Johannes Gutenberg-Universität Mainz

vorgelegt von

Johannes Moll

Mainz, Mai 2021



JOHANNES GUTENBERG
UNIVERSITÄT MAINZ

Die vorliegende Arbeit wurde
in der Zeit vom März 2017 bis Mai 2021
im Department Chemie (ehem. Institut für Anorganische Chemie und Analytische Chemie)
der Johannes Gutenberg-Universität Mainz unter Betreuung von Frau Prof. Dr. Katja Heinze
angefertigt.

Ich, Johannes Moll, bestätige hiermit, dass ich diese Arbeit selbstständig verfasst habe und keine weiteren als die angegebene Quellen und Hilfsmittel verwendet habe. Alle Ausführungen, die anderen sinngemäß oder wörtlich entnommen wurden, habe ich kenntlich gemacht.

(Ort, Datum)

(Unterschrift)

Dekan: Prof. Dr. Tobias Reich
Erste Berichterstatterin: Prof. Dr. Katja Heinze
Zweite Berichterstatterin: Prof. Dr. Eva Rentschler

Man sieht nur mit dem Herzen gut.

Das Wesentliche ist für die Augen unsichtbar.

Antoine de Saint-Exupéry („Der Kleine Prinz“)

Wichtig ist, dass man nicht aufhört zu fragen.

Albert Einstein

Kurzzusammenfassung

Ruthenium(II)-komplexe finden breite Anwendung als Photosensibilisatoren. Wegen der geringen Verfügbarkeit von Ruthenium und der damit verbundenen hohen Kosten ist es sinnvoll, Ruthenium(II) durch das leichtere und deutlich häufigere Homolog Eisen(II) zu ersetzen. Allerdings birgt die intrinsisch geringere Ligandenfeldaufspaltung von Eisen(II) die Problematik sehr geringer Lebensdauern der angeregten Zustände, wodurch sich ihre photochemische Anwendung als äußerst herausfordernd gestaltet.

Diese Arbeit beschreibt die Entwicklung von pseudo-oktaedrischen Eisen(II)- und Ruthenium(II)-komplexen, die das Konzept der hohen lokalen Symmetrie mit dem Push-Pull-Liganden-Design verbinden. Ziel ist es, Metall-zu-Ligand-Charge-Transfer (MLCT) angeregte Zustände zu stabilisieren und metallzentrierte Zustände zu destabilisieren, deren Besetzung die Depopulierung von Charge-Transfer angeregten Zuständen fördert. Mit dem neuen Liganden 6,2''-Carboxypyridyl-2,2'-methylaminpyridyl-pyridin (cpmp), der sowohl N-CH₃-Brücken mit σ -Donor-Eigenschaften als auch C=O-Brücken mit π -Akzeptor-Eigenschaften in einem einzelnen Liganden vereint, wurden die homoleptischen Push-pull-komplexe [Ru(cpmp)₂]²⁺ und [Fe(cpmp)₂]²⁺ synthetisiert. Ebenso wurden die heteroleptischen Komplexe [Ru(cpmp)(ddpd)]²⁺ and [Fe(cpmp)(ddpd)]²⁺ mit dem literaturbekannten *N,N*-Dimethyl-*N,N*-dipyridin-2-yl-pyridin-2,6-diamin (ddpd) Liganden mit zwei σ -donierenden N-CH₃-Brücken dargestellt.

Die Ruthenium(II)-komplexe [Ru(cpmp)₂]²⁺ und ([Ru(cpmp)(ddpd)]²⁺ zeigen Phosphoreszenz bei 709 nm bzw. 755 nm mit Quantenausbeuten von 1.3 % bzw. 0.04 %. Die geringere Quantenausbeute des heteroleptischen Komplexes kann durch die flexibleren N-CH₃-Brücken erklärt werden, die eine geringere Aktivierungsbarriere für strahlungslose Relaxation ermöglichen. Gleichwohl fungieren beide Komplexe als Photosensibilisatoren in der durch grünes Licht aktivierten Thiol-En Klick-Reaktion.

Die homologen Eisen(II)-komplexe zeigen energiearme MLCT-Absorptionsbanden bei 610 nm. Allerdings ist die MLCT-Lebensdauer von weniger als 100 fs zu kurz für Phosphoreszenz oder photochemische Anwendungen. Die gemessene Lebensdauer des angeregten Zustandes von 500 ps kann dem ⁵T-Zustand zugeordnet werden. Dynamik-Berechnungen der angeregten Zustände bestätigen die übliche Relaxations-Abfolge ¹MLCT → ³MLCT → ³MC → ⁵MC → ¹A der angeregten Zustände.

Quantenchemische Berechnungen haben die Klasse der [Fe(N[^]N[^]C)(N[^]N[^]N)]⁺-cyclometallierten Eisen(II)-komplexe als gute Kandidaten mit erhöhten Lebensdauern der angeregten Zustände prognostiziert. Daher wurde der Komplex [Fe(pbpy)(tpy)]⁺ (Hpbpy = 6-Phenyl-2,2'-bipyridin und tpy = 2,2':6',2''-Terpyridin) durch Jakob Steube synthetisiert. Die photophysikalischen Eigenschaften sind signifikant besser als die von [Fe(tpy)₃]²⁺. Die ³MLCT-Lebensdauer wurde auf 800 fs gesteigert, verglichen mit 145 fs für [Fe(tpy)₃]²⁺. Sie wurde durch zeitaufgelöste UV/Vis-Spektroskopie durch Ayla Kruse (geb. Pöpcke) bestimmt, die Zuordnung erfolgte über spektroelektrochemische Untersuchungen von Johannes Moll. Allerdings ist diese Lebensdauer zu gering für Phosphoreszenz oder photochemische Anwendungen.

Der Ligand 2,6-Diguanidylpyridin (dgpy) ist ein starker σ -Donor. In Erwartung dadurch stabilerer Charge-Transfer-angeregter Zustände wurde das Verhalten von dgpy in Eisenkomplexen untersucht. Sowohl der homoleptische Eisen(II)- als auch der homoleptische Eisen(III)-komplex zeigen keine Emission. Während der Eisen(III)-komplex im low-spin-Grundzustand vorliegt, zeigt das *meridionale* Isomer des Eisen(II)-komplexes Spin-Crossover-Verhalten, was eine recht geringe Ligandenfeldstärke impliziert. Darüber hinaus liegt in Lösung zusätzlich das *cis*-faciale Isomer vor, das einen high-spin-Grundzustand aufweist.

Abstract

Ruthenium(II) is well applied as photosensitizer. Due to its low abundance and consequently high cost it is worthwhile to replace ruthenium(II) by the more abundant homologue iron(II). The intrinsically lower ligand field splitting makes it challenging to design iron(II) complexes with sufficiently long excited state lifetime for photochemical applications.

This work describes the development of pseudo-octahedral iron(II) and ruthenium(II) complexes combining the concept of high local symmetry with a push-pull ligand design to stabilize metal-to-ligand charge transfer (MLCT) excited states and destabilize quenching metal centered states. Using the novel 6,2''-carboxypyridyl-2,2'-methylaminepyridyl-pyridine (cpmp) ligand combining both, the σ -donating N-CH₃ bridge and one π -accepting C=O bridge in a single ligand, the homoleptic push-pull complexes [Ru(cpmp)₂]²⁺ and [Fe(cpmp)₂]²⁺ were synthesized. Additionally the heteroleptic [Ru(cpmp)(ddpd)]²⁺ and [Fe(cpmp)(ddpd)]²⁺ complexes bearing the literature known *N,N*-dimethyl-*N,N'*-dipyridine-2-yl-pyridine-2,6-diamine (ddpd) ligand with two σ -donating N-CH₃ bridges were synthesized.

The ruthenium(II) complexes [Ru(cpmp)₂]²⁺ and [Ru(cpmp)(ddpd)]²⁺ show phosphorescence at 709 nm and 755 nm, respectively, with quantum yields of 1.3 % and 0.04 %, respectively. The lower quantum yield of the heteroleptic complex can be rationalized with the more flexible N-CH₃ bridges enabling a lower energy barrier for non-radiative relaxation. Nevertheless, both complexes act as photosensitizer in a green-light-sensitized thiol-ene click reaction.

The homologue iron(II) complexes show low-energy MLCT absorption bands around 610 nm. However, the MLCT lifetime below 100 fs is too short for phosphorescence or photochemistry. The measured excited state lifetime of around 500 ps can be assigned to the ⁵T state. Excited state dynamics calculations confirm relaxation occurs along the typical ¹MLCT → ³MLCT → ³MC → ⁵MC excited state relaxation cascade.

As the class of [Fe(N[^]N[^]C)(N[^]N[^]N)]⁺ type cyclometalated iron(II) complexes were predicted by quantum chemical calculations to be good candidates for increased excited state lifetime, the [Fe(pbpy)(tpy)]⁺ (Hpbpy=6-phenyl-2,2'-bipyridine and tpy=2,2':6',2''-terpyridine) complex was synthesized by Jakob Steube. The photophysical properties are significantly improved in comparison to [Fe(tpy)₃]²⁺. The ³MLCT lifetime is increased to 800 fs compared to 145 fs for [Fe(tpy)₃]²⁺. It was estimated by timeresolved UV/Vis spectroscopy, performed by Ayla Kruse (geb. Pöpcke). Spectroelectrochemical investigations by Johannes Moll were used for the assignment. However, this lifetime is too short for phosphorescence or photochemistry.

The 2,6-diguanidylpyridine (dgpy) ligand is a strong σ -donor. Expecting this ligand to stabilize charge transfer excited states, the performance of dgpy in iron complexes was investigated. Both, the homoleptic iron(II) and the homoleptic iron(III) complex are non-emissive. While the iron(III) complex is proved to have a low-spin ground state, the iron(II) complex shows spin crossover behavior in its *meridional* isomer, implying a rather low ligand field strength. Furthermore, the *cis*-facial isomer is present in solution, featuring a high-spin ground state.

Table of content

1. Abbreviations and units	1
Abbreviations	1
Units	3
2. Introduction	5
Ruthenium(II)	5
Iron(II)	9
The spin crossover phenomenon	10
Concepts to increase charge transfer excited state lifetime	14
Influence in SCO behavior	18
Characterization of SCO compounds	19
Excited-State Properties	23
Luminescence spectroscopy	23
Time-resolved UV/Vis and IR spectroscopy	23
Solvatochromic effect	24
Photoinduced electron transfer	24
DFT calculations	27
3. Aim of work	29
4. Literature	31
5. Results and discussion	37
6. Green-Light Activation of Push-Pull Ruthenium(II) Complexes	41
7. Understanding Excited State Kinetics in Asymmetric Iron(II) Push-Pull Complexes	111
8. Excited-State Kinetics of an Air-Stable Cyclometalated Iron(II) Complex	181
9. Panchromatic Absorption and Oxidation of an Iron(II) Spin Crossover Complex	231
10. Curriculum Vitae	301

1. Abbreviations and units

Abbreviations

A_{gr}	absorbance of the ground state species
A_{ox}	absorbance of the oxidized species
A_{red}	absorbance of the reduced species
B	Racah parameter
bpy	2,2'-bipyridine
bpp	2,6-di-pyrazol-2-yl)pyridine
btz	4,4'-bis(1,2,3-tri-azol-5-ylidene)
B3LYP	Becke, 3-parameter, Lee–Yang–Parr
CPCM	conductor-like polarizable continuum model
cpmp	6,2''-carboxylpyridyl-2,2'-methylaminepyridyl-pyridine
CT	charge transfer
dbtpy	6,6''-dibromo-2:2,6':2''-terpyridine
dcpp	2,6-bis(2-carboxypyridyl)pyridine
dctpy	6,6''-dichloro-2:2,6':2''-terpyridine
ddpd	<i>N,N</i> -dimethyl- <i>N,N</i> -dipyridine-2-yl-pyridine-2,6-diamine
DFT	density functional theory
dftpy	6,6''-difluoro-2:2,6':2''-terpyridine
dgpy	2,6-diguanidylpyridine
dpb	1:2',5:2''-dipyridylbenzene
dqp	2,6-di(quinolin-8-yl)pyridine
DSSC	dye sensitized solar cell
D3BJ	Becke-Johnson damping
e.g.	exempli gratia
E	potential energy
E_{ox}	ground state oxidation potential
E_{ox}^*	excited state oxidation potential
E_{P}	spin pairing energy
E_{red}	ground state reduction potential
E_{red}^*	excited state reduction potential
E_{00}	energy of the electronic origin of the excited state
EXAFS	extended X-ray absorption fine structure
f	frequency
FcH	ferrocene
g	Landé factor
g_{hs}	degeneration of the high-spin state
g_{ls}	degeneration of the low-spin state
HERFD	high-energy-resolution fluorescence detected
hs	high-spin
I	integrated emission intensity
IC	internal conversion
i.e.	id est
ILCT	intraligand charge transfer
IR	infra-red
ISC	intersystem crossing
K	equilibrium constant
k_{B}	Boltzmann constant
k_{hl}	hs-ls exchange constant

1. Abbreviations and Units

k_{nr}	rate constant for non-radiative relaxation
k_{obs}	emission decay constant with quechncher
k_q	quechnching constant
k_r	rate constant for radiative relaxation
k_0	emission decay constant without quechncher
L	ligand
LC	ligand centered
LEC	light emitting electrochemical cell
LIESST	light induced excited spin state trapping
LL'CT	ligand-to-ligand charge transfer
LMCT	ligand-to-metal charge transfer
ls	low-spin
M	metal
mbip	2,6-bis(1'-methylimidazol-2'-yl)pyridine
MC	metal centered
MECP	minimum energy crossing point
MLCT	metal-to-ligand charge transfer
N_A	Avogadro number
NHC	<i>N</i> -heterocyclic carbene
NMR	nuclear magnetic resonance
pbpy	6-phenyl-2,2'-bipyridine
PET	photo-induced electron transfer
phen	1,10-phenanthroline
phtmeimb	phenyl(tris(3- methylimidazol-1-ylidene))borate
ptz	1-propyl tetrazole
r	distance
R	ideal gas constant
RIJCOSX	resolution of the identity chain-of-spheres exchange
S	spin quantum number
SCO	spin crossover
SQUID	superconducting quantum interference device
[Sub]	substrate concentration
SVP	split valence polarization
T	temperature
$T_{1/2}$	spin crossover transition temperature
'Bu-bip	2,6-bis(1'-tert-butyl-imidazol-2'-yl)pyridine
TCSPC	time-correlated single photon counting
TD-DFT	time dependent density functional theory
TIESST	thermally induced excited spin state trapping
tpy	2:2',6':2''-terpyridine
TS	transition state
TZVP	valence triple-zeta polarization
UV/Vis	ultraviolet/visible
vs.	versus
XANES	X-ray absorption near edge structure
XAS	X-ray absorption spectroscopy
XES	X-ray emission spectroscopy
XRD	X-ray diffraction
ZORA	zeroth order regular approximation
δ	chemical shift (NMR spectroscopy), isomer shift (Mößbauer spectroscopy)
δ_{hs}	chemical/isomer shift of the high-spin state
δ_s	chemical/isomer shift of the low-spin state

Δ	ligand field splitting
ΔA_{ex}	excited state difference absorbance
ΔE_{hl}	Energy difference between high-spin and low-spin state
ΔE_{Q}	quadrupole splitting
$\Delta E_{\text{Q,hs}}$	quadrupole splitting of the high-spin state
$\Delta E_{\text{Q,ls}}$	quadrupole splitting of the low-spin state
Δf	frequency difference
ΔG	Gibbs free energy change
ΔH	enthalpy change
Δ_{O}	ligand field splitting in octahedral coordination
ΔS	entropy change
ΔS_{el}	electronic entropy change
ΔS_{spin}	spin contribution to electronic entropy change
ΔS_{vib}	vibrational entropy change
Δ_{T}	ligand field splitting in tetrahedral coordination
$\Delta(T)$	line width of NMR resonance
Φ	emission quantum yield
φ_{abs}	number of absorbed photons
φ_{em}	number of emitted photons
χ	magnetic susceptibility
χ_{m}	molar magnetic susceptibility
μ_{B}	Bohr magneton
μ_{eff}	effective magnetic permeability
τ	lifetime

Units

K	Kelvin
eV	electron Volt
meV	millielectron volt
V	Volt
J	Joule
cm^{-1}	reciprocal centimeter
nm	nanometer
Å	Ångström
s	second
μs	microsecond
ps	picosecond
fs	femtosecond
°	degree
%	percent (1/100)

2. Introduction

Ruthenium(II)

Emissive ruthenium(II) complexes like $[\text{Ru}(\text{bpy})_3]^{2+}$ (bpy: 2,2'-bipyridine, Figure 2a) are used as light harvesters in dye sensitized solar cells (DSSC), in light emitting electrochemical cells (LECs), and are also used as photocatalysts.^[1-11] This complex helps to understand the optical properties of d^6 transition metal complexes. The intense high energy absorption band around 285 nm in the UV/Vis spectrum of $[\text{Ru}(\text{bpy})_3]^{2+}$ (Figure 1a) results from the spin allowed ligand centered (LC) $\pi_L\pi_L^*$ excitation (Figure 1b). As this transition does not involve significant charge separation, the geometry remains unchanged upon excitation.^[12,13] Special cases of these ligand centered excitations are intraligand-charge transfer (ILCT) and ligand-to-ligand charge transfer (LL'CT). These processes describe transitions from π_L into π_L^* orbitals as well but attributed with a charge transfer from an electron rich part of a ligand to an electron deficient part of the same ligand (ILCT) or another ligand (LL'CT). The low energy absorption band around 450 nm is attributed to a metal-to-ligand charge transfer ($^1\text{MLCT}$) occurring from a π_{ML} orbital to a π_L^* orbital (Figure 1b). This process represents a formal oxidation of the metal center accompanied by a reduction of a ligand ($[\text{Ru}^{\text{III}}(\text{bpy}^{\cdot-})(\text{bpy})_2]^{2+}$).^[14] No metal based antibonding orbitals are populated and therefore as in the case of a simple LC excitation this excitation has almost no effect on the complex geometry.^[12] Ruthenium(II) complexes usually show phosphorescence from the corresponding triplet states ($^3\text{MLCT}$) that are populated from the (initially) excited $^1\text{MLCT}$ states via intersystem crossing (ISC).^[12,15] For $[\text{Ru}(\text{bpy})_3]^{2+}$ the $^1\text{MLCT}$ absorption band peaks at 452 nm, the resulting $^3\text{MLCT}$ emission band at 615 nm.^[16] The phosphorescence quantum yield equals 6.3 % in water at room temperature^[17] and 38 % in methanol/ethanol at 77 K^[18,19] with $^3\text{MLCT}$ lifetimes of 0.62 μs (H_2O , 298 K)^[18] and 5.21 μs (methanol/ethanol, 77 K)^[18,19], respectively. In d^5 complexes with a higher effective nuclear charge, the charge transfer process occurs in the opposite direction (from σ_{ML} or π_L into π_{ML} or σ_{ML}^*). This ligand-to-metal charge transfer (LMCT) absorption usually shows a lower energy, and a lower extinction coefficient compared to the MLCT absorption of d^6 complexes.

In contrast to CT excitation, the metal centered (MC, dd) $\pi_{\text{ML}}\sigma_{\text{ML}}^*$ excitation in d^6 metal complexes populates metal-ligand antibonding metal centered orbitals leading to an elongation of metal-ligand bonds that depends on the character of the populated antibonding orbital.^[12,20-22] In case of population of the d_{z^2} orbital in the ^3T state which is orientated towards two donor atoms usually two trans-positioned metal-ligand bonds are elongated. The population of the $d_{x^2-y^2}$ orbital leads to an elongation of four metal-ligand bonds in the xy-plane. In the ^5T state all six metal-ligand bonds are elongated. These transitions typically feature low extinction coefficients as they are forbidden by quantum-mechanical selection rules for parity (Laporte's rule) and orbital angular momentum.^[13] The population of metal-ligand antibonding orbitals enables photosubstitution reactions from these states.^[1,13] Moreover, these MC states open an additional pathway to fast non-radiative decay back to the ground state by potential energy surface crossing points and vibrational cooling. Once the metal centered $^3\text{T}_{1g}$ and $^3\text{T}_{2g}$ (^3MC) states are thermally populated from the $^3\text{MLCT}$ state via internal conversion (IC), fast non-radiative relaxation occurs from these states and quenches phosphorescence.^[12,23]

The absorption and excited state properties of $[\text{Ru}(\text{bpy})_3]^{2+}$ type complexes can be tuned by modifying the ligand. However, the Δ/Λ chirality of the ruthenium(II) complexes with differently substituted bidentate ligands enables the formation of diastereomers which complicates the synthesis of pure diastereomers, as well as associated characterization.^[24-31] Another disadvantage of $[\text{Ru}(\text{bpy})_3]^{2+}$ -like ruthenium(II) complexes with bidentate ligands is their relatively low photostability.^[32-35]

2. Introduction

Besides the previously mentioned classical 3T state with the elongation of two trans-positioned Ru-N bonds towards two different bpy ligands, also called $^3T_{\text{trans}}$ state, the $^3T_{\text{cis}}$ state with elongated Ru-N bond towards a single bpy ligand has been found with a similar activation barrier.^[22] While the $^3T_{\text{trans}}$ state is not expected to enable ligand loss, the $^3MC_{\text{cis}}$ state facilitates photodegradation as both Ru-N bonds of the same bpy ligand are elongated. From both 3T states photosolvolytic can occur either by two successive photochemical reactions or concerted via a one-photon mechanism.^[22,36–38] The stepwise mechanism proceeds via bpy dissociation through the formation of a κ^1 -bpy intermediate with one coordinating solvent molecule and photorelease of the κ^1 -bpy ligand by absorption of a second photon, followed by the coordination of a second solvent molecule. In the one-photon mechanism, the initial photoexcitation is followed by dechelation, solvent coordination, and bpy release. All processes occur sequentially within the triplet excited-state manifold.^[22,36–38]

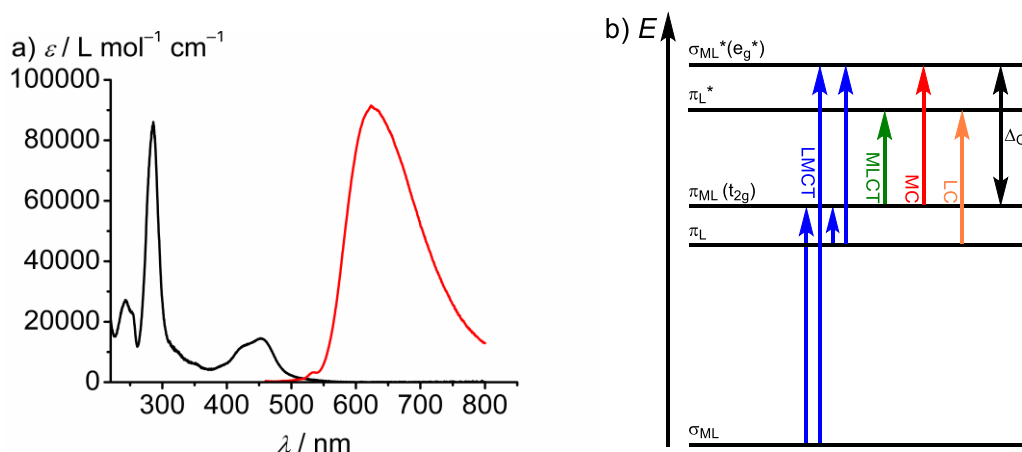


Figure 1: a) UV/Vis (black) and emission (red) spectrum of [Ru(bpy)₃]²⁺ in water;^[18,39–41] b) excitation pathways in octahedral ML₆ complexes.

Higher stability towards photoisomerization can be achieved by using 2:2',6':2''-terpyridine (tpy) instead of bpy.^[42] Modifications of this ligand at the central pyridine do not lead to different isomers, these ligands form meridional isomers exclusively and thus Δ/Λ chirality is avoided facilitating syntheses and isolation.^[43] However, the intraligand N-Ru-N bite angle in [Ru(tpy)₂]²⁺ (Figure 2b, R¹ = R² = H) of 159°^[44] is smaller than that of [Ru(bpy)₃]²⁺ (173°).^[45] This reduces the metal-ligand orbital overlap and thereby the ligand field splitting. This reduction is sufficient to quench phosphorescence at room temperature via thermal population of the 3T state. Therefore, this complex is virtually non-emissive at room temperature in acetonitrile ($\Phi < 5 \times 10^{-4}$ %)^[43] and shows a significantly lower quantum yield in frozen propionitrile/butyronitrile solution at 77 K (4.8 %)^[46,47] compared to [Ru(bpy)₃]²⁺ (38 %).^[18,19] The 3MLCT lifetime is also significantly smaller (0.25 ns in acetonitrile at room temperature,^[48] 11 μs in propionitrile/butyronitrile at 77 K).^[46,47]

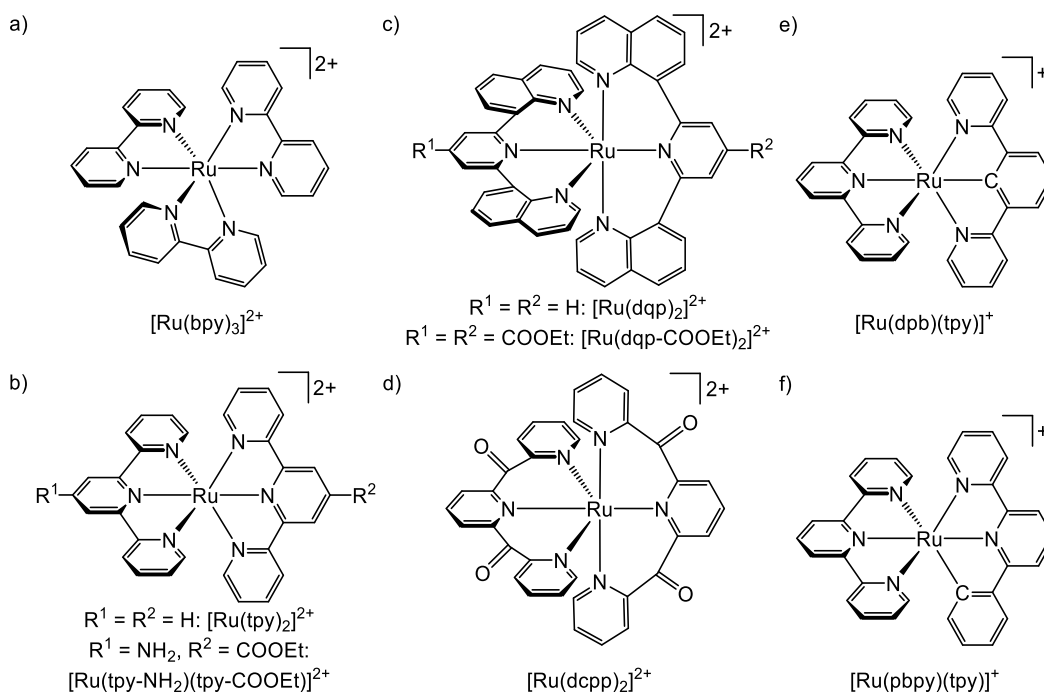


Figure 2: Ruthenium(II) complexes.

To overcome the disadvantage of emission quenching by low lying metal centered states, push-pull complexes like $[Ru(tpy-NH_2)(tpy-COOEt)]^{2+}$ (Figure 2b, $R_1 = NH_2$, $R_2 = COOEt$) with an electron donating and an electron withdrawing ligand were designed. Here, the σ -donating character of the $tpy-NH_2$ ligand increases the energy of the σ_{M-L}^* orbital leading to a destabilization of the 3T state while the π -accepting character of $tpy-COOH$ decreases both the energy of the π_L^* and of the π_{ML} (t_{2g}) orbitals leading to a stabilization of the MLCT states.^[24,43] The quantum yield of 0.18 %, the emission lifetime of 34 ns, and theoretical calculations indicate the success of this concept.^[24,49] The push-pull design in combination with enlargement of the chromophore system can further stabilize the 3MLCT state.^[30,43,49] A stabilization of the MLCT state by introducing an arene spacer between the central pyridine moiety and the carbonyl or amine groups is accompanied with a disruption in the π -conjugation which hinders this desired improvement.^[30,50,51] The improvement of 3MLCT lifetimes and quantum yields is still limited even with a push-pull concept. The push-pull design reduces the HOMO-LUMO gap and thereby the energy gap between the $^1/3MLCT$ states and 1A_g ground state. A decrease in this energy difference leads to more efficient non-radiative relaxation, according to the energy gap law.^[13,52–54]

Six-membered-ring chelate ligands feature 180° bite angles in contrast to five-membered-ring chelate ligands, i.e. 159° for $[Ru(tpy)_2]^{2+}$.^[44,55] The more efficient orbital overlap between the pyridine nitrogen lone pairs and the d orbitals of the central metal with e_g symmetry (approx. 90°) destabilizes the e_g^* orbitals and increases the ligand-field splitting compared to five-membered-ring chelate ligands.^[55] This increased ligand-field splitting leads to a larger energy difference between 3MLCT and 3T states, which hinders non-radiative deactivation via the 3T state.

One approach to form six-membered-ring chelate ligands is the substitution of the terminal pyridine moieties in the tpy ligand by quinoline moieties forming the 2,6-di(quinolin-8-yl)pyridine (dqp) ligand.^[55] The more flexible six-membered-ring chelate ligands additionally induce a helical chirality due to a helical twist of the ligand around the metal center.^[56,57] This helical twist allows a N-Ru-N bite angle in $[Ru(dqp)_2]^{2+}$ (Figure 2c, $R_1 = R_2 = H$) of 178° which enables a better orbital overlap compared to $[Ru(tpy)_2]^{2+}$ and subsequently results in a 3MLCT lifetime of 3.0 μs and a phosphorescence quantum yield of 2 %.^[58] However, the synthesis is

2. Introduction

complicated due to the formation of different isomers, namely *mer*-, *cis-fac* and *trans-fac*, which is a drawback for six-membered-ring chelate ligands because of their higher flexibility compared to five-membered-ring chelate ligands.^[56] The comparably low increase in lifetime to 8.5 μ s at 77 K compared to room temperature indicates the successfully blocked deactivation via ³MC states resulting from the increased ligand field strength.^[55,58] Theoretical investigations on $[\text{Ru}(\text{dqp})_2]^{2+}$ reveal a significantly larger activation barrier for the ³MLCT-³MC transition compared to $[\text{Ru}(\text{tpy})_2]^{2+}$.^[59] While this conversion induces only minor Ru-N bond stretching in $[\text{Ru}(\text{tpy})_2]^{2+}$ the deviation in $[\text{Ru}(\text{dqp})_2]^{2+}$ is larger.

By introducing substituents in the 4-position of the pyridine moieties, the properties of $[\text{Ru}(\text{dqp})_2]^{2+}$ -type complexes can be tuned (Figure 2c, R₁, R₂).^[55] Lifetimes between 0.45 and 5.5 μ s and quantum yields between 0.04 and 7 % were reached with different substituents.^[55,56,58,60] The complex with the best performance (5.5 μ s lifetime and 7 % quantum yield) is $[\text{Ru}(\text{dqp-COOEt})_2]^{2+}$ (Figure 2c, R₁ = R₂ = COOEt).^[60] Using benzoquinone as donor (R₁ in Figure 2c) and phenothiazone as acceptor (R₂ in Figure 2c) attached in the 4-position at the pyridine moieties, a donor-photosensitizer-acceptor triad is formed that is capable of photoinduced charge separation with a lifetime of 200 ns.^[61]

The formal introduction of carbonyl spacers between the pyridine moieties in the tpy ligand gives the six-membered-ring chelate ligand 2,6-bis(2-carboxypyridyl)pyridine (dcp).^[62] In $[\text{Ru}(\text{dcp})_2]^{2+}$ (Figure 2d) the phosphorescence quantum yield was increased to 30 % in acetonitrile at room temperature (43 % in propionitrile/butyronitrile at 77 K, 4.8 % for $[\text{Ru}(\text{tpy})_2]^{2+}$ under same conditions).^[46,47,62]

While the dcp ligand bears electron withdrawing carbonyl bridges, in *N,N*-dimethyl-*N,N*-dipyridine-2-yl-pyridine-2,6-diamine (ddpd), the pyridine moieties are connected via methyl-amine bridges.^[63] This ligand is widely used in transition metal complex chemistry.^[63] A combination of the five-membered-ring chelate ligand tpy-COOEt and the six-membered-ring chelate ligand ddpd was applied to disable isomer formation.^[24,31] However, quantum yield and lifetime were low because of the restrictions associated with five-membered-ring chelates.^[24,31]

Cyclometalating ligands like 1:2',5:2''-dipyridylbenzene (dpb) and 6-phenyl-2,2'-bipyridine (pbpy) are strong σ -donors, and therefore destabilize the quenching metal-centered states resulting in increased luminescence properties for the ruthenium(II) complexes, when compared with $[\text{Ru}(\text{tpy})_2]^{2+}$.^[64] Nevertheless, cyclometalated polypyridine ruthenium(II) complexes like $[\text{Ru}(\text{dpb})(\text{tpy})]^+$ (Figure 2e) and $[\text{Ru}(\text{pbpy})(\text{tpy})]^+$ (Figure 2f) typically exhibit very weak room temperature emission.^[64,65] While in tris(bidentate) $[\text{Ru}(\text{N}^{\wedge}\text{N})_2(\text{N}^{\wedge}\text{C})]^+$ complexes, the predominant relaxation pathway was found to be tunneling into high-energy vibrationally excited singlet states enabling comparably high quantum yields, emission quenching in bis(tridentate) cyclometalated ruthenium(II) complexes occurs via different pathways with lower activation barriers.^[65-67] In $[\text{Ru}(\text{N}^{\wedge}\text{C}^{\wedge}\text{N})(\text{N}^{\wedge}\text{N}^{\wedge}\text{N})]^+$ type complexes, such as $[\text{Ru}(\text{dpb})(\text{tpy})]^+$ (Figure 2e), emission quenching is dominated by two thermally accessible triplet states, that flank the emissive ³MLCT state (³T state and a ³LL'CT state).^[65] The ³LL'CT state is non-emissive because of the orthogonality of both ligands resulting in a symmetry-forbidden radiative process.^[68] Additionally, non-radiative relaxation is possible via a ³MLCT \rightarrow ¹A surface crossing. As a result of the orthogonality of both ligands a stronger push-pull effect introduced by substituents in the ligand backbone does not increase the quantum yields but quenches the emission via the dark ³LL'CT state.^[68] $[\text{Ru}(\text{N}^{\wedge}\text{N}^{\wedge}\text{C})(\text{N}^{\wedge}\text{N}^{\wedge}\text{N})]^+$ type complexes like $[\text{Ru}(\text{pbpy})(\text{tpy})]^+$ (Figure 2f) are supposed to circumvent the low-energy non-emissive ³LL'CT states by lowering the symmetry of the complex. Neither ³T nor ³LL'CT are thermally accessible.^[65] However, the triplet and singlet minimum energy crossing point (MECP) comes close to the relaxed ³MLCT minimum resulting in an efficient non-radiative deactivation channel.^[65]

Iron(II)

A major drawback that must be considered when using ruthenium in photophysical applications is its low abundance and subsequent high cost. The abundance of the 3d homologue iron is more than 7 orders of magnitude higher.^[69] It is therefore a potential candidate to replace ruthenium(II) in these applications. It is important to note that the ligand field splitting of 3d metal complexes is weaker than that of 4d or 5d metal complexes because of the primogenic effect.^[70–72] The absence of nodes in the radial distribution function of the first p, d and f shells (i.e. 2p, 3d, 4f) results in a higher effective nuclear charge and thereby a contraction of the respective orbitals. This contraction of the d orbitals leads to decreased overlap of metal-d and ligand orbitals which implies a smaller ligand field splitting than in higher homologues. A major consequence of the intrinsically smaller ligand field splitting is that the $^5T_{2g}$ (5MC , high-spin) state (red in Figure 3) along with the $^3T_{1g}$ and $^3T_{2g}$ (3MC , blue in Figure 3) states is lower in energy than the 3MLCT state. Moreover, weak ligands like NCS^- lead to a ligand field splitting Δ below the critical ligand field splitting Δ_C resulting in the $^5T_{2g}$ state as ground state (see Tanabe-Sugano diagram, Figure 3a). Therefore, iron(II) complexes mostly have very short MLCT lifetimes and are non-luminescent. The relaxation from the $^1/3MLCT$ states into the 3T states occurs within fs (150 fs for $[Fe(bpy)_3]^{2+}$ ^[73]) as does the following intersystem crossing into the 5T state (70 fs^[73]). The comparably long lived 5T state (676 ps for $[Fe(bpy)_3]^{2+}$ ^[74]) undergoes vibrational cooling into the ground state. This double ISC from a 5T to a 1A state is known as spin crossover (*vide infra*).

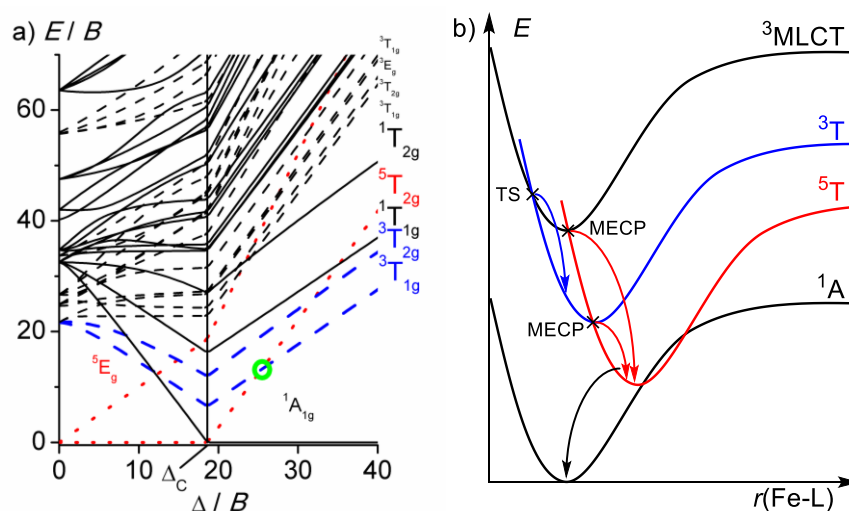


Figure 3: a) Tanabe-Sugano diagram for d^6 complexes, the green circle highlights $^5T_{2g}/^3T_{1g}$ crossing point; b) schematic potential energy diagram for iron(II) complexes (TS = transition state; MECP = minimum energy crossing point).^[75]

2. Introduction

The spin crossover phenomenon

The ground state electronic configuration (as previously described) depends on both the ligand field strength and ligand structure. For example, geometric strain can lead to a ${}^5T_{2g}$ (5MC , high-spin, hs) ground state, instead of 1A_g (low-spin, ls). As antibonding σ_{ML} (e_g^*) orbitals are populated in the ${}^5T_{2g}$ state the metal-ligand bond lengths are elongated by around 0.2 Å compared to the 1A_g state.^[76–81] Therefore, the high-spin state can be stabilized by ligand systems that hinder a shorter metal-ligand bond length in the range usually observed for low-spin complexes. The increased bond lengths in the high-spin state result in a higher vibrational state density and a less steep potential surface as depicted in Figure 4.^[80,81]

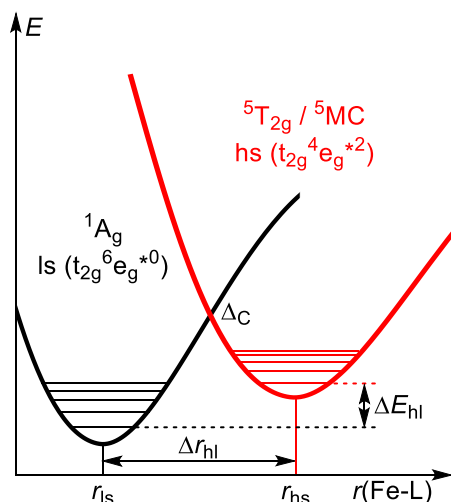


Figure 4: Schematic potential energy diagram of an iron(II) d^6 complex showing high-spin (hs) and low-spin (ls) state on the average metal-ligand bond length ($r(\text{Fe-L})$), Δr_{hl} is the difference in metal-ligand bond length, ΔE_{hl} the energy difference between hs and ls state.

The difference in bond lengths between high and low-spin state is described by Δr_{hl} (as the average Fe-L distance for a specific reaction coordinate). The crossing point between 1A_g and ${}^5T_{2g}$ potentials (Δ_C) indicates the critical ligand field strength, where the ligand field strength (Δ_O) equals the spin pairing energy (E_P). Spin crossover (SCO) can occur when Δ_O is in close to Δ_C .^[80–82] Typical values for Δ_O for hs, ls and SCO complexes are given in Table 1. Thermal SCO can occur when the energy difference between hs and ls state (ΔE_{hl}) is lower than the thermal energy ($k_b T \approx 200 \text{ cm}^{-1}$).

Table 1: Typical values for Δ_O in cm^{-1} for hs, ls and SCO complexes.^[82]

	no SCO	SCO
hs	< 11 000	11 500 – 12 500
ls	> 21 500	19 000 – 21 000

SCO can generally occur in 3d metal complexes with the electron configuration of d^4 – d^7 . SCO can be induced by thermal energy, light irradiation or pressure.^[81] The switching between two different states occurs with a concomitant change of the structural, optical, chemical and magnetic characteristics.^[81] These property changes makes SCO compounds promising candidates for application in data storage devices,^[83,84] displays,^[82] actuators^[85] or sensors.^[86] However, the thermal accessibility of the 5T state results in an insufficient charge transfer excited state lifetime for photochemical applications while the 5T state is usually redox-inactive.

The occurrence of SCO depends on the ratio between the ligand field strength (Δ_O) and spin pairing energy (E_P). The electronic ground state is either a 1A state ($\Delta_O > E_P$) or a ${}^5T_{2g}$ state ($\Delta_O < E_P$).^[81] SCO can only be observed if Δ_O and E_P are of similar magnitude. Although spin

crossover is generally possible for all transition metal complexes with a d^4 – d^7 electron configuration, ligand field theory can help to predict whether SCO is likely to occur or not. While the spin pairing energy E_p is not significantly influenced by increasing the nuclear charge, the ligand field strength Δ_o increases. Therefore, only 3d metals show SCO, while complexes of heavier homologues feature solely the *ls* ground state configuration, and no SCO behavior. Oxidation of a complex (without changes in coordination sphere), can also increase the ligand field strength.^[87] Thus, oxidation of a SCO complex usually results in the loss of the SCO characteristics. Furthermore, SCO behavior cannot occur in tetrahedral complexes because the small tetrahedral ligand field strength $\Delta_T \approx 4/9 \Delta_o$, results in the exclusive formation of *hs* complexes.^[87] The majority of examples in the literature refers to Fe^{II} (d^6), Fe^{III} (d^5) and Co^{II} (d^7) as a result of matching Δ_o and E_p .^[88,89] Fewer examples are known for Co^{III} (d^6), Mn^{II} (d^5), Mn^{III} (d^4) and Cr^{II} (d^4) complexes.^[90] Changes can be made to the ligand geometry, and its electronic structure, and thus Δ_o can be tuned to facilitate SCO behavior.

The spin crossover phenomenon was first discovered in 1930s by Cambi et al. as temperature dependent change in the magnetic behavior of $[Fe^{III}(R_2NCS)_2)_3]$ (R: alkyl), it was at the time inaccurately reported as two different isomers.^[91–93] A correct description of this phenomenon followed 30 years later^[94–96] and has resulted in numerous reviews.^[97–103]

The thermodynamics of the SCO process is described by the Gibbs-Helmholtz equation:^[104]

$$\Delta G = \Delta H - T\Delta S \quad \text{equation 1}$$

where ΔG is the difference in Gibbs free energy, ΔH the difference in enthalpy, T the temperature and ΔS the difference in entropy. During the spin transition, ΔG is zero at the transition temperature $T_{1/2}$.

With the definition of the Gibbs free energy^[104]

$$\Delta G = -RT\ln(K) \quad \text{equation 2}$$

depending on the ideal gas constant R , the temperature T and the equilibrium constant K (*hs* and *ls* as product and educt of the spin transition), ΔH and ΔS can be estimated from any spectroscopic data that give access to the *hs/ls* ratio using equation 3:

$$K = \frac{hs}{ls} = \exp\left(-\frac{\Delta H - T\Delta S}{RT}\right) \quad \text{equation 3}$$

Typical values of ΔH and ΔS for iron(II) complexes are 10–20 kJ mol⁻¹ and 50–80 J K⁻¹ mol⁻¹, respectively.^[82,105] The difference in entropy between *hs* and *ls* state is a consequence of electronic (ΔS_{el}) and vibrational (ΔS_{vib}) entropy changes. ΔS_{el} is composed of spin (ΔS_{spin}) and orbit contributions and a result of the *hs* degeneracy (5 fold for the spin contribution and 3 fold for the orbit contribution) of the *hs* ($^5T_{2g}$) state, while the *ls* ($^1A_{1g}$) state is non-degenerate. By taking the different degrees of degeneracy of *hs* (g_{hs}) and *ls* (g_{ls}) states for ideal octahedral complexes with T states into account, ΔS_{el} can be estimated, using (equation 4):^[82,105,106]

$$\Delta S_{el} = R\ln\left(\frac{g_{hs}}{g_{ls}}\right) = R\ln\left(\frac{15}{1}\right) = 22.5 \text{ J mol}^{-1} \text{ K}^{-1} \quad \text{equation 4}$$

As the orbit contribution is often quenched by symmetry usually it can be ignored resulting in:

$$\Delta S_{el} \approx \Delta S_{spin} = R\ln\left(\frac{g_{hs}}{g_{ls}}\right) = R\ln\left(\frac{5}{1}\right) = 13.4 \text{ J mol}^{-1} \text{ K}^{-1} \quad \text{equation 5}$$

The electronic contribution to ΔS is about 30 % while the remaining 70 % are attributed to ΔS_{vib} resulting from intramolecular stretching and vibrational deformation modes, due to elongation of metal-ligand bonds.^[82,105,106]

Considering the characteristics of the SCO process as transitions between two states, the change in structural, magnetic and optical properties can be gradual or abrupt. Cooperative effects between several switchable spin centers influence the behavior of thermal spin

2. Introduction

transition.^[82] The different spin transition curves in Figure 5 represent the influence of intermolecular cooperativity.^[82] Weak intermolecular interactions result in a gradual SCO over a wide temperature range (Figure 5a), which is usually the case in solution. Independent spin centers follow Boltzmann statistics.^[107,108] In the solid state a gradual SCO is related to propagation of structural changes through the solid.^[82] A higher level of cooperativity leads to an abrupt spin transition (Figure 5b) where the SCO occurs “simultaneously” for all spin centers within a few Kelvin. Thermal hysteresis (Figure 5c) can occur because of structural phase changes allowing two different electronic states in the same system within a specific temperature range (bistability). This type of hysteresis is a requirement for storage and memory applications.^[83,107,108] Incomplete spin transitions in a material are the result of defects in a crystal lattice. The corresponding spin transition curve is similar to Figure 5a but the low temperature hs/lS ratio does not reach zero as a significant amount of spin centers remains in the hs state or the high temperature hs/lS ratio does not reach the maximum as not all spin centers switch to hs state at high temperature.^[81,109] Incomplete transitions can also be explained by a kinetic effect related to rapid freezing, known as “Thermally Induced Excited Spin State Trapping” (TIESST).^[110–113]

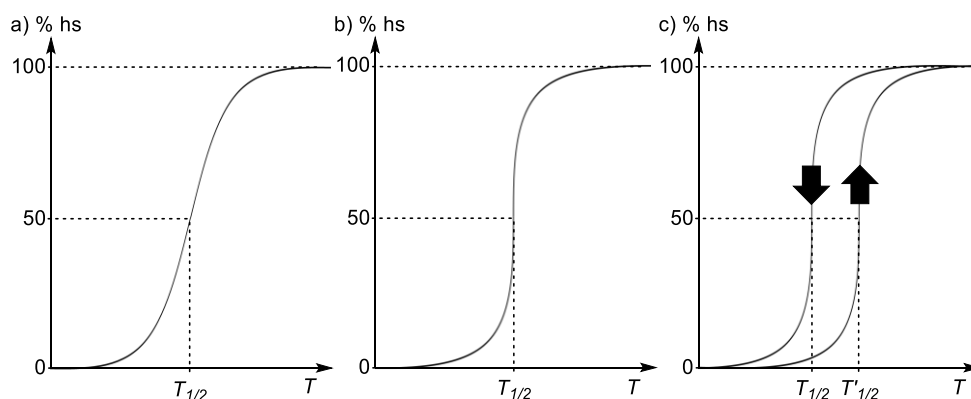


Figure 5: Schematic representation of possible spin transitions plotted as hs molar ratio vs. temperature: a) gradual, b) abrupt, c) abrupt with hysteresis.

Light induced excited spin state trapping (LIESST) is the process of light induced SCO. This effect can be observed for the complex $[\text{Fe}(\text{ptz})_6]^{2+}$ (ptz: 1-propyl tetrazole, Figure 6a).^[114,115] Irradiation with green light ($\lambda = 515 \text{ nm}$) at low temperature populates the ligand field states $^1\text{T}_{1g}$ and $^1\text{T}_{2g}$, from the $^1\text{A}_{1g}$ ground state (black arrows in Figure 6b).^[114,115] Relaxation via the triplet states $^3\text{T}_{2g}$ and $^3\text{T}_{1g}$, results in repopulation of the $^1\text{A}_{1g}$ state, or population of the metastable $^5\text{T}_{2g}$ state. Under prolonged irradiation at low temperature a complete conversion to the $^5\text{T}_{2g}$ state is possible. At low temperature the system is trapped in this state as thermal energy is required for relaxation into the $^1\text{A}_{1g}$ ground state. The LIESST effect can also occur in iron(II) complexes coupled with suitable ligands from $^1\text{MLCT}$ excited states. Subsequent ISC into the triplet states enables population of the $^5\text{T}_{2g}$ state. Besides thermally induced relaxation from the metastable $^5\text{T}_{2g}$ state into the $^1\text{A}_{1g}$ ground state, light induced depopulation of the $^5\text{T}_{2g}$ state is possible (reverse-LIESST effect, red arrow in Figure 6b). In this case, optical excitation of the $^5\text{T}_{2g}$ state leads to population of the $^5\text{E}_g$ state and subsequent repopulation of the $^5\text{T}_{2g}$ state or population of the $^1\text{A}_{1g}$ ground state.^[90] Under continuous irradiation at 753 nm at low temperature a complete recovery of the $^1\text{A}_{1g}$ ground state is observed for the $[\text{Fe}(\text{ptz})_6]^{2+}$ complex.^[116]

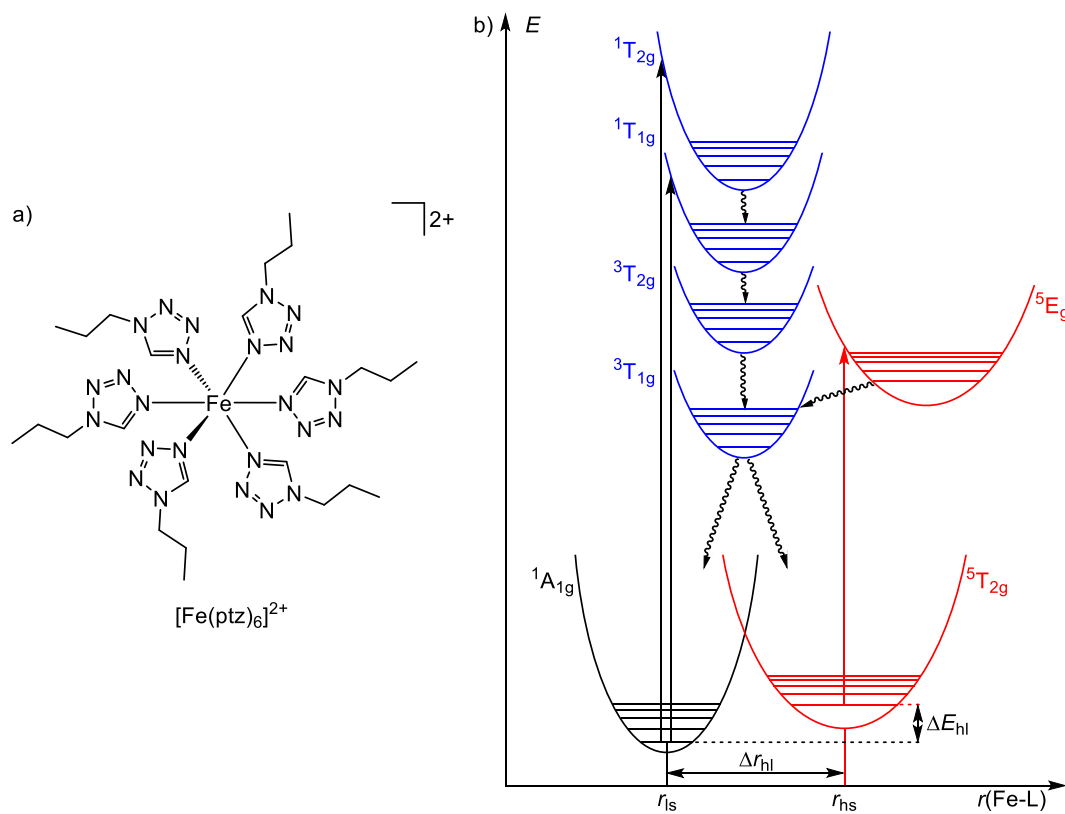


Figure 6: a) $[\text{Fe}(\text{ptz})_6]^{2+}$; b) schematic representation of states involved in the LIESST process.

2. Introduction

Concepts to increase charge transfer excited state lifetime

For photochemical applications thermal population of the 5T state must be avoided. Moreover, the charge transfer excited state has to be stabilized to extend its lifetime and potentially achieve luminescent iron(II) complexes.

This solution is not without challenges, the MLCT energy lowering is limited by the energy gap law, and small energy differences between the 1A and the 3MLCT state can lead to direct non-emissive relaxation to the ground state.^[54] The Tanabe-Sugano diagram of d^6 complexes (Figure 3) shows the consequence of an increase of the ligand field splitting.^[117] The energies of the lowest energy metal centered states $^3T_{1g}$, $^3T_{2g}$ (blue) and $^5T_{2g}$ (red) increase with Δ/B . While the ligand field splitting (Δ) is dependent on metal-ligand orbital overlap, the Racah-parameter (B) depends on the covalent character of the metal-ligand bond.^[118]

The population of a metal centered excited state is not only dependent on the relative energies, but also on the respective activation barrier. This refers to the 3MLCT - 3T transition state (TS) in the case of the 3T state which is shown in Figure 7a.^[65] In the case of the 5T state it is related to the 3T / 3MLCT - 5T MECP. The higher the 5T energies are, compared to the 3MLCT state, the higher are the TS and the MECP. A larger MECP energy can also be achieved by strong distortion between two states leading to a horizontal displacement of the metal centered states in the energy diagram.

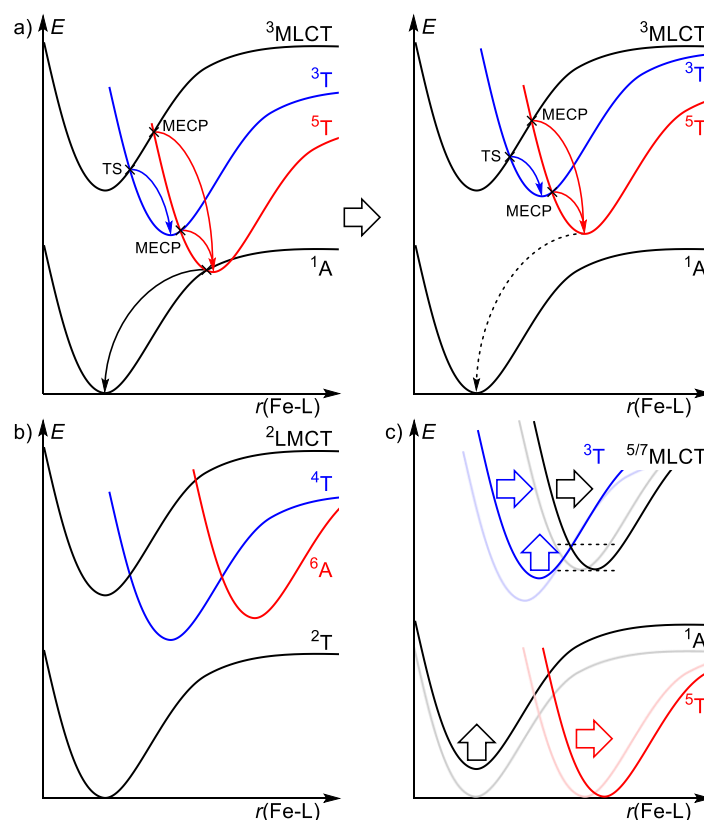


Figure 7: Potential energy diagrams illustrating the influence of the different concepts on the excited state energies for a) iron(II) with high symmetry, push-pull systems, NHC and mesoionic carbene ligands and cyclometalating ligands; b) iron(III) complexes and c) iron(II) complexes with 5T ground state resulting from high strain.

To achieve a MLCT stabilization and MC destabilization, there are few concepts that must be discussed in detail.^[119] The influence on the potential energy surfaces of the respective states is illustrated in Figure 7 where the same anharmonicity for all potentials is assumed and the x-axis represents the totally symmetric distortion (A_{1g}) although other nuclear coordinates can be relevant as well.^[76]

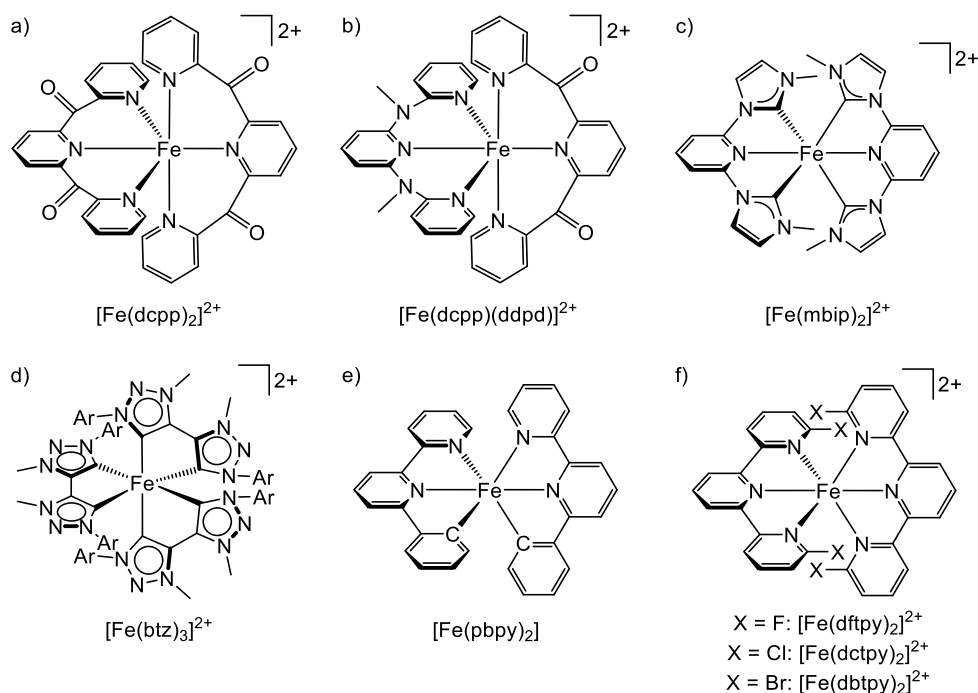


Figure 8: Iron(II) complexes as prototypes for the different concepts towards luminescent iron(II) complexes.

A high local $[\text{FeN}_6]$ symmetry enabled by six-membered-ring chelate ligands results in a better orbital overlap, and consequently higher ligand field splitting. These ligands enable N-Fe-N bite angles close to 180° , and a nearly ideal octahedral coordination geometry. This increased six-membered-ring chelate ligand concept was tested using the $[\text{Ru}(\text{dcpp})_2]^{2+}$ iron homologue (Figure 8a).^[79] The N-Fe-N bite angle of 178° is significantly closer to the ideal value of 180° than for $[\text{Fe}(\text{tpy})_2]^{2+}$ (161°).^[79,120] The dcpp ligand is highly symmetric, and contains two carbonyl groups making it a highly electron withdrawing ligand. The low energy π^* orbitals make it a good π -acceptor while the pyridine moiety acts as σ -donor. Comparing the cyclic voltammogram and UV/Vis absorption data to those of $[\text{Fe}(\text{tpy})_2]^{2+}$ reveals stabilization of the π_{ML} (t_{2g}) orbitals and, concomitantly, a stabilization of the MLCT state as illustrated in Figure 7a.^[79,121,122] Nevertheless, the complex follows the classical excited state deactivation pathway $^1\text{MLCT} \rightarrow ^3\text{MLCT} \rightarrow ^3\text{T} \rightarrow ^5\text{T} \rightarrow ^1\text{A}$ and is non-luminescent.^[78,79,122] A different explanation for the comparably short excited state lifetime of 280 ps ($[\text{Fe}(\text{tpy})_2]^{2+}$: 960 ps) is based on the assumption of the ^3T state as lowest excited state corresponding to a ligand field strength higher than the $^5\text{T}_{2g}/^3\text{T}_{1g}$ crossing point in the Tanabe-Sugano diagram (O in Figure 3a). A direct $^3\text{T} \rightarrow ^1\text{A}$ relaxation would occur instead of a ^5T population. This explanation was ruled out on the basis of ultrafast time resolved X-ray spectroscopy.^[78,79] The shorter excited state lifetime could have been explained by a stronger electron coupling between the ^3T and the ground state and a lower reorganization energy, resulting from a single spin transition compared to a double in a $^5\text{T} \rightarrow ^1\text{A}$ relaxation.^[79,119] Instead the short excited state lifetime results from a significantly lower $^5\text{T} \rightarrow ^1\text{A}$ reorganization energy for $[\text{Fe}(\text{dcpp})_2]^{2+}$ compared to $[\text{Fe}(\text{tpy})_2]^{2+}$.^[78,79]

A combination of the dcpp ligand with the electron-rich ddpd ligand leads to the push-pull complex $[\text{Fe}(\text{dcpp})(\text{ddpd})]^{2+}$ (Figure 8b).^[122] Here the push-pull effect does not result from different substituents but from σ -electron donating methylamine and π -electron withdrawing carbonyl bridges between the pyridine moieties. A MLCT state stabilization accompanied by a destabilization of the MC states was expected (Figure 7a). Yet, the $^1/3\text{MLCT}$ lifetime is below 100 fs and the complex is non-luminescent as well.^[122] The MLCT energy is comparable to that of $[\text{Fe}(\text{dcpp})_2]^{2+}$, the ligand field strength is 45 meV smaller and the excited state lifetime of 548 ps (attributed to the ^5T state) is between the values for $[\text{Fe}(\text{dcpp})_2]^{2+}$ and $[\text{Fe}(\text{tpy})_2]^{2+}$.^[79,122]

2. Introduction

The $[\text{Fe}(\text{dcp})(\text{ddpd})]^{2+}$ complex underlines that not only the excited state energies but also the energy of transition states and MECPs need to be taken into account as the population of the ^3T and ^5T states is not solely dependent on the relative energy minima of the respective states.

While the highly symmetric and π -accepting ligands stabilize the t_{2g} orbitals, a different approach to increase the ligand field splitting is the destabilization of the e_g^* orbitals using strongly σ -donating *N*-heterocyclic carbene (NHC) ligands.^[123,124] One of the first iron(II) NHC complexes is $[\text{Fe}(\text{mbip})_2]^{2+}$ (mbip: 2,6-bis(1'-methylimidazol-2'-yl)pyridine, Figure 8c).^[125] The $^3\text{MLCT}$ lifetime of 9 ps can be extended to 16 ps by replacing the imidazolylidene moiety with benzimidazolylidene or using carboxyl groups in the 4-position of the pyridine moieties, and extended to 26 ps with a combination of both.^[125–127] However, their σ -donation capabilities do not sufficiently destabilize the detrimental MC states and hence, the achieved MLCT lifetimes are too low. Therefore, the introduction of a π -accepting moiety is necessary to further increase the ligandfield splitting and the MLCT lifetimes.

Based on this concept, the first phosphorescent iron(II) complex was designed. The π -system in FeNHCPZn (Figure 9a) was expanded by a zinc(II)-porphyrin.^[128] The $^3\text{MLCT}$ state shows a lifetime of 160 ps (estimated by a pump-probe experiment; phosphorescence lifetime was 175 ps).^[128] The $^1\text{MLCT}$ state is comparably long lived as well, with a lifetime of 0.3 ps.^[128] The significant polarization of the MLCT to the zinc-porphyrin minimizes the wave function overlap between MLCT and MC states resulting in an extended MLCT lifetime.

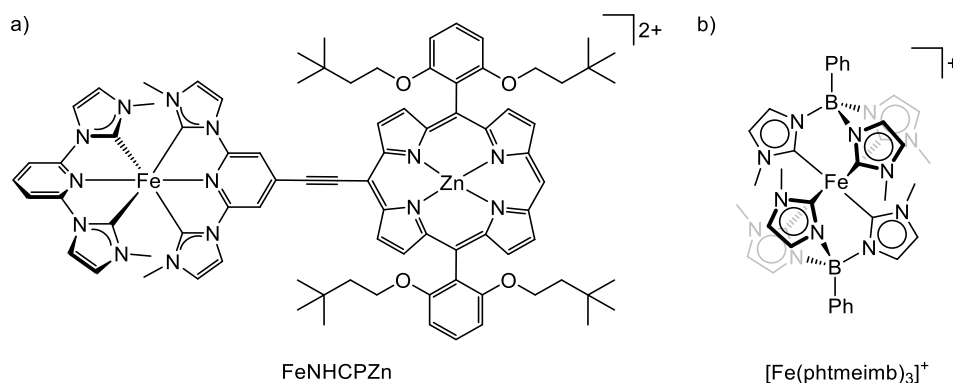


Figure 9: First luminescent iron complexes.

Another important aspect that affects the MLCT lifetime of iron(II) complexes with NHC ligands is the *N*-substituent. To illustrate this $[\text{Fe}(\text{mbip})_2]^{2+}$ (Figure 8c) is compared with its *tert*-butyl derivative $[\text{Fe}(\text{^tBu-bip})_2]^{2+}$ (^tBu-bip: 2,6-bis(1'-*tert*-butyl-imidazol-2'-yl)pyridine). The distortion in the ^5T state relative to the ^1A state is stronger for $[\text{Fe}(\text{mbip})_2]^{2+}$ than for $[\text{Fe}(\text{^tBu-bip})_2]^{2+}$. This results in a stronger destabilization of the ^5T state in $[\text{Fe}(\text{mbip})_2]^{2+}$ compared to $[\text{Fe}(\text{^tBu-bip})_2]^{2+}$.^[129,130] Therefore, the highly distorted ^5T state is not populated in $[\text{Fe}(\text{mbip})_2]^{2+}$ while the $[\text{Fe}(\text{^tBu-bip})_2]^{2+}$ complex follows the typical $^3\text{MLCT} \rightarrow ^3\text{T} \rightarrow ^5\text{T} \rightarrow ^1\text{A}$ relaxation cascade.^[125,130]

To overcome the relatively weak π -accepting character of NHC ligands, mesoionic carbene ligands like 4,4'-bis(1,2,3-tri-azol-5-ylidene) (btz) can be used that feature stronger σ -donor and π -acceptor properties.^[131] The strong σ -donor ability can be explained by the formal negative charge on the carbene C-atom, seen in the resonance structures of btz, while the π^* orbital is lowered by additional N-atoms, increasing the π -accepting ability.^[131,132] The homoleptic $[\text{Fe}(\text{btz})_3]^{2+}$ complex (Figure 8d) shows a record $^3\text{MLCT}$ lifetime of 528 ps. This is primarily due to destabilized metal centered states.^[133] However, no phosphorescence has been reported.

The high σ -donating character of the btz ligand results in a low oxidation potential of -0.58 V vs. FcH/FcH⁺.^[134] The oxidation product $[\text{Fe}(\text{btz})_3]^{3+}$, a low-spin $3d^5$ complex, exhibits

fluorescence from a $^2\text{LMCT}$ state of 100 ps lifetime with 0.03 % quantum yield at room temperature.^[134] For low-spin iron(III) complexes, the ground state is a ^2T state. The initial photoexcited state is a $^2\text{LMCT}$ state. ISC into the lower lying ^4T and ^6A states is comparable to the processes in iron(II) complexes as well as the geometric distortion in these states (Figure 7b). The main difference when compared with iron(II) complexes is the spin-allowed emission process. While phosphorescence from a $^3\text{MLCT}$ state is spin-forbidden, the $^2\text{LMCT}$ fluorescence is spin-allowed. As the rate constant for the fluorescence is competitive to the rate constant of the non-radiative $^2\text{LMCT} \rightarrow ^4\text{T}$ relaxation, $^2\text{LMCT}$ fluorescence occurs at shorter lifetimes (than that required for phosphorescence from $^3\text{MLCT}$ states of d^6 complexes).

A higher fluorescence lifetime (2.2 ns) and quantum yield (2%) was achieved with the $[\text{Fe}(\text{phtmeimb})_2]^+$ (phtmeimb: phenyl(tris(3-methylimidazol-1-ylidene))borate) complex (Figure 9b).^[135] This facially coordinating ligand enables a rigid, nearly ideal octahedral coordination sphere. Together with the anionic scorpionate-like structure, this leads to further destabilization of metal centered states in this complex compared to $[\text{Fe}(\text{btz})_3]^{3+}$.^[134,135] In both complexes the $^4\text{T}/^6\text{A}$ states are lower in energy than the $^2\text{LMCT}$ state. However, the activation barrier is sufficiently high to oppress their MC state population and, as a result, (spin-allowed) $^2\text{LMCT}$ fluorescence is enabled.^[134,135]

Cyclometalating σ - and π -donating ligands have been successfully applied to ruthenium(II) although the limit of this concept has been shown.^[55,56,65] So the effect on iron(II) was investigated by means of quantum chemical calculations. Derivatives of the iron(II) complex $[\text{Fe}(\text{tpy})_2]^{2+}$ with one or two pbpy (6-phenyl-2,2'-bipyridine) or dpb (1:2,5:2'-dipyridylbenzene) ligands, where pyridine units are replaced by phenyl moieties at different positions e.g. $[\text{Fe}(\text{pbpy})_2]$ (Figure 8e) were compared to the parent complex $[\text{Fe}(\text{tpy})_2]^{2+}$.^[136,137] The MLCT states are strongly stabilized by ~ 1 eV due to the stronger π -donor capabilities which decrease the energy of π_{L}^* orbitals.^[137] The destabilizing effect on the σ_{ML}^* orbitals due to the strong σ -donation is reduced by the π -donation capability of cyclometalating ligands that destabilizes the π_{ML} orbitals resulting small changes (± 0.2 eV) of the ^3T state energy.^[136,137] When using dpb ligand (where the central N-atom is replaced by carbon) the ^3T state is stabilized, while it is destabilized using pbpy (where a N-atom in the peripheral pyridine ring is replaced by a carbon atom). Calculations were carried out on $[\text{Fe}(\text{dpb})(\text{pbpy})]$ and it was found to be promising because of hindered $^3\text{MLCT} \rightarrow ^3\text{T}$ conversion.^[137,138] However, a general slowdown of this process is predicted by DFT calculations as a result of cyclometalating ligands.^[137-139] These calculations were also carried out on a cyclometalated iron complex featuring more than two phenyl moieties and predicted an oxidation to iron(III).^[138] Although the results of these calculations were promising, the experimental access to these complexes is more complicated and furthermore for corresponding ruthenium(II) complexes, a low photoluminescence was observed (*vide supra*).^[65,68]

A fundamentally different approach to increase the MLCT lifetime is the use of highly strained iron(II) complexes to force the complex to adopt a ^5T ground state by interligand steric repulsion. From this ^5T ground state the initially photoexcited state is a $^5\text{MLCT}$ state. Intersystem crossing can lead to a $^7\text{MLCT}$ state as shown in Figure 7c. The steric strain hinders the population of the ^1A state that requires comparably short metal-ligand bond lengths. Besides the potential luminescent relaxation into the ^5T ground state, non-radiative relaxation via the ^3T state is possible.

In the series of the homoleptic iron(II) complexes (Figure 8f) with 6- and 6'-fluorine, chlorine and bromine substituted tpy ligands (dftpy (6,6''-difluoro-2:2,6':2''-terpyridine), dctpy (6,6''-dichloro-2:2,6':2''-terpyridine), and dbtpy (6,6''-dibromo-2:2,6':2''-terpyridine) the MLCT lifetime increases from 14.0 to 16.0 and 17.4 ps.^[140,141] Here, an increasing MLCT lifetime corresponds to an increased activation barrier to the ^3T state, a direct result of the destabilization of the ^3T state (Figure 7c). Therefore, the energy of the ^3T state strongly

2. Introduction

depends on the size of the halogen substituent; this is because of the higher metal-ligand bonding character of the 3T state compared with the $^{5/7}MLCT$ or 5T state. The reorganization energy related to this $^{5/7}MLCT$ - 3T ISC also increases in this series, because of an increased geometric strain.^[140] However, all three complexes are non-luminescent.

Influence in SCO behavior

Besides the concepts to stabilize charge transfer excited states there are concepts to facilitate SCO behavior. For example, the formation of the 1A_g state in $[Fe(dftpy)_2]^{2+}$, $[Fe(dctpy)_2]^{2+}$ and $[Fe(dbtpy)_2]^{2+}$ (Figure 8f) is hindered by halide substituents. In case of fluorine substituents thermal SCO occurs. The sterically more demanding chlorine and bromine substituents lead to the exclusive formation of high-spin complexes.^[140]

The effect of bulky substituents next to the coordinating position can be comprised by the example $[Fe(phen)_3]^{2+}$ (Figure 10a).^[142,143] Methyl groups in 2-position of the 1,10-phenanthroline ligand cause an extension of the Fe-N bond, and subsequent a stabilization of the hs state at room temperature; the low-spin state is accessible at low temperatures. This steric effect dominates over the ligand's σ -donation resulting from the positive inductive effect of the methyl groups. A similar trend was observed in comparable systems.^[98,144,145] Geometric strain that reduces ligand field strength can also be induced by five-membered-ring chelate ligands instead of six-membered-ring chelate ligands.^[81]

Another derivative of $[Fe(phen)_3]^{2+}$ that has been investigated comprehensively is $[Fe^II(phen)_2(NCS)_2]$ (phen: 1,10-phenanthroline, Figure 10b).^[146-148] This complex represents the approach to shift the ligand field strength towards Δ_c by replacing one chelate ligand with weaker ligands, effectively reducing Δ_o .^[149] $[Fe(phen)_3]^{2+}$ (Figure 10a) in fact features a low-spin ground state without SCO while $[Fe(phen)_2(NCS)_2]$ (Figure 10b) shows thermally induced SCO.^[146] Unfortunately, to date, there is no reasonable approach to predict the occurrence of SCO, as this effect is not only dependent on the ligand strength.^[81,107]

The transition temperature depends on ligand field strength of the coordinating monodentate ligands as shown for $[Fe(L)_2(X)_2]$ (L: 4-*p*-tolyl-3-(2-pyrazinyl)-5-(2-pyridyl)-1,2,4-triazole, X^- : NCS^- , $NCSe^-$, $NCBH_3^-$, Figure 10c). Increasing ligand field strength of X^- ($NCS^- < NCSe^- < NCBH_3^-$) according to the spectrochemical series results in an increased SCO temperature.^[150-153] This effect is well established in literature.^[111,154-160]

Facilitation of SCO by tuning the electronic structure of the ligand was demonstrated by the example of $[Fe(bpp)_2]^{2+}$ (bpp: 2,6-di-pyrazol-2-yl)pyridine, Figure 10d).^[161,162] In the 4-position of the pyridine ring (X) and the 4-position of the pyrazole moiety (Y), different substituents were surveyed. It was found that electron withdrawing groups at the pyridine moiety and electron donating groups at the pyrazole moiety stabilize the low-spin state. However, since the relationship between spin state and ligand design is a fine balance between σ - and π -donating and accepting effects, no general concept was put forward.^[161,163]

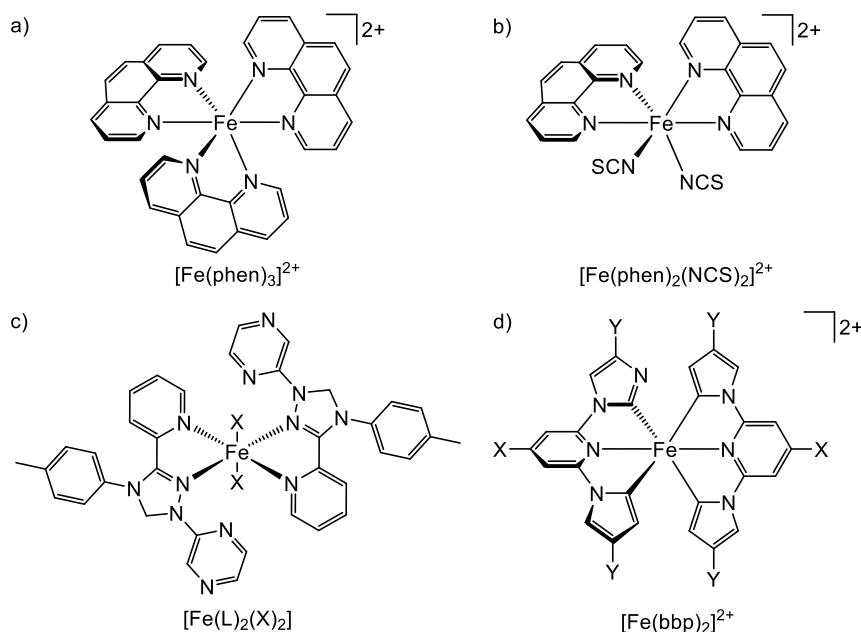


Figure 10: Iron(II) SCO complexes.

Characterization of SCO compounds

The SCO characteristics can be explored using methods such as magnetic susceptibility measurements, NMR spectroscopy, Mößbauer spectroscopy, optical, IR and X-ray spectroscopy as well as X-ray diffraction.

The most common technique for temperature dependent magnetic susceptibility measurements (in the solid state) is SQUID (Superconducting Quantum Interference Device) magnetometry. This method is highly sensitive to changes in the (molar) magnetic susceptibility (χ_m). As SCO occurs with a change in the number of unpaired electrons, in iron(II) complexes the diamagnetic low-spin state ($S = 0$) and the strongly paramagnetic high-spin state ($S = 2$) are well distinguishable. A plot of $\chi_m T$ versus the temperature for typical iron(II) SCO complexes, is directly comparable to Figure 5 as it represents the h_s/l_s ratio.^[81,82,107,109]

Using the spin-only formalism (equation 6):^[104,149]

$$\mu_{\text{eff}} = g\sqrt{S(S+1)}\mu_B \quad \text{equation 6}$$

with the Landé factor $g = 2.0023$, the total spin S , and the Bohr magneton μ_B the effective magnetic moment μ_{eff} can be estimated.

Using the second definition of μ_{eff} :^[149]

$$\mu_{\text{eff}} = \sqrt{\frac{3k_B}{N_A\mu_B^2}} \cdot \sqrt{\chi_m T} = 2.828\sqrt{\chi_m T} \quad \text{equation 7}$$

χ_m can be predicted for iron(II) high-spin systems:^[149]

$$\chi_m T = \left(\frac{\mu_{\text{eff}}}{2.828}\right)^2 = \left(\frac{g\sqrt{S(S+1)}}{2.828}\right)^2 = \left(\frac{2.0023\sqrt{2(2+1)}}{2.828}\right)^2 = 3.008 \text{ cm}^3 \text{ K mol}^{-1} \quad \text{equation 8}$$

The experimentally determined data are usually slightly higher than the calculated ones for iron(II) in the high-spin state because the orbit contribution to the magnetic moment is not taken into account, see equation 8.

To estimate χT in solution, the Evans NMR method can be used.^[164] The chemical shift (δ) of NMR resonances is influenced by the magnetic environment. While $\chi_m T$ is changing with increasing temperature, the ^1H NMR resonance of the solvent is shifting as well. By measuring

2. Introduction

the dissolved sample together with an external standard in a closed capillary (inside the same NMR tube) a temperature dependent shift between the signal of the solvent (containing the SCO compound) and the signal of the standard can be observed. If the standard is the same solvent as used for the sample, the molar magnetic susceptibility χ_m can be calculated by equation 9:^[164–166]

$$\chi_m = \frac{3}{4\pi c} \frac{\Delta f}{f} \quad \text{equation 9}$$

where c is the sample concentration in mol cm^{-3} , Δf the frequency difference between the two solvent signals and f the spectrometer frequency.

From NMR spectroscopy the hs-ls exchange rate constant k_{hl} can be calculated using equation 10:^[167]

$$k_{hl}(T) = \frac{\pi}{2} \left(\frac{(\delta_{hs} - \delta_{ls})^2}{\Delta(T)} \right) \quad \text{equation 10}$$

where δ_{hs} and δ_{ls} are the chemical shifts of the same resonance for high-spin state and low-spin state, respectively, and $\Delta(T)$ is the line width of the respective resonance.

To gain information about the electronic structure in the solid state, ^{57}Fe Mößbauer spectroscopy is an established method for iron SCO complexes, as it can distinguish the oxidation and spin state of iron complexes.^[81,107,109,168] The isomer shift δ provides information regarding the oxidation and spin state, while the quadrupole splitting ΔE_Q gives information regarding the electronic environment of the Mößbauer active core. Values of $\delta_s \leq 0.5 \text{ mm s}^{-1}$ and $\Delta E_{Q,ls} \leq 1 \text{ mm s}^{-1}$ are typically observed for ls-iron(II).^[81] A higher anisotropy in the hs state leads to higher values of $\delta_{hs} \approx 1 \text{ mm s}^{-1}$ and $\Delta E_{Q,hs} \approx 2\text{--}3 \text{ mm s}^{-1}$.^[81] If the spin transition is slower than the Mößbauer time scale (10^{-7} s for ^{57}Fe), the two overlapping subspectra can be distinguished using Lorentzian deconvolution.

The different spin states also have different electronic absorption energies. Therefore, temperature dependent optical spectroscopy can also be used to obtain the spin transition.^[81] In transition metal complexes where the color solely originates from Laporte forbidden π_{ML} to σ_{ML}^* (dd) transitions without CT transitions in the visible spectral region, the ls state is usually intensively colored while the hs state is colorless.

The Tanabe-Sugano diagram (Figure 3a) reveals two spin-allowed transitions in the ls state ($^1A_{1g} \rightarrow ^1T_{1g}$ and $^1A_{1g} \rightarrow ^1T_{2g}$) and one in the hs state ($^5T_{2g} \rightarrow ^5E_g$). For $[\text{Fe}(\text{ptz})_6]^{2+}$, the ls absorption bands are in the visible region while the hs absorption band is in the near infra-red region.^[81] However, these transitions are Laporte-forbidden and usually only detectable by solid state absorption measurements.^[81] For complexes with well resolved dd-bands and complexes with charge transfer excited states, temperature dependent spectral changes in solution are observable. Upon cooling, the spectral features/bands of the hs state are weakened while the ones of the ls species gain intensity.^[81,82,109,114] Similar spectral changes are observable for charge transfer bands.

The difference in structure between hs and ls can also be observed using X-ray diffraction (XRD). In the hs state, the iron-ligand bond lengths are about 0.2 \AA elongated compared to the ls state due to the occupation of anti-bonding σ_{ML} (e_g^*) orbitals.^[76–81] However, XRD is typically inappropriate for time-resolved experiments.

Coordination geometry and electronic structure of the metal center can be probed using X-ray absorption spectroscopy (XAS) and X-ray emission spectroscopy (XES).^[169,170] The extended X-ray absorption fine structure (EXAFS) in XAS spectra gives information about the local structure around the X-ray absorbing core.^[169] The X-ray absorption near edge structure (XANES) in XAS spectra provides information about the LUMO since the pre-edge region is caused by $1s \rightarrow 3d$ transitions.^[170–173] It allows deduction to the electronic state (oxidation and

spin state) and the coordination geometry. To overcome the line broadening caused by low core-hole lifetime high-energy-resolution fluorescence detected (HERFD) XANES can be used.^[174,175] The electronic structure of coordinating ligands can be probed using valence-to-core X-ray emission spectroscopy (XES).^[175,176] The radiative HOMO→1s relaxation induced by non-resonant excitation of an 1s electron into the continuum is highly sensitive to the ligand because the character of the valence orbitals changes the most for different chemical species.^[170] For the interpretation of the spectra theoretical modeling is necessary. The simplest model is comparison to similar complexes with known spectra and slight differences in structure.^[170,177] By ultrafast X-ray spectroscopy, including EXAFS, a spin transition including structural changes in iron(II) complexes can be observed.^[78]

2. Introduction

Excited-State Properties

Luminescence spectroscopy

The excited state lifetime τ is defined as the reciprocal of the sum over the deactivation rate constants for radiative (k_r , i.e. ${}^3\text{MLCT} \rightarrow {}^1\text{A}$) and usually multiple non-radiative (k_{nr}), i.e. ${}^3\text{T} \rightarrow {}^1\text{A}$, ${}^5\text{T} \rightarrow {}^1\text{A}$) pathways:^[178]

$$\tau = \frac{1}{k_r + \sum k_{nr}} \quad \text{equation 11}$$

The estimation of luminescence lifetimes using a luminescence spectrometer presumes a sufficient quantum yield and a detectable long lifetime. As these requirements are often not met time-correlated single photon counting (TCSPC) can be used instead. It allows measurements in the ps range. For this technique, the time between the excitation laser pulse and the first emitted photon is measured.^[179] A laser with a high-repetition rate but a low light intensity is used. This results in a negligible probability to emit more than one photon by a single laser pulse. Therefore, the time measurement can end after the first emitted photon. A histogram of several repetitions reveals the expected exponential decay of the number of emitted photons.^[179]

The luminescence quantum yield ϕ is the ratio between the radiative decay constant k_r and the sum over all decay constants:^[180]

$$\phi = \frac{k_r}{k_r + \sum k_{nr}} = k_r \tau \quad \text{equation 12}$$

ϕ is also defined as the ratio of the numbers of emitted φ_{em} and absorbed φ_{abs} photons:^[180]

$$\phi = \frac{\varphi_{em}}{\varphi_{abs}} \quad \text{equation 13}$$

Using equation 13, the absolute luminescence quantum yield ϕ can be estimated with a setup to measure all emitted photons.^[181–183] A relative determination of ϕ can be performed with a standard sample with known ϕ_0 . For irradiation at the wavelength where the absorption profiles of both compounds cross each other, ϕ is defined by equation 14:^[180]

$$\phi = \frac{I}{I_0} \phi_0 \quad \text{equation 14}$$

where I is the integrated emission intensity of the sample and I_0 the integrated emission intensity of the standard.

Time-resolved UV/Vis and IR spectroscopy

To gain insight into the lifetime of dark excited states, time-resolved pump-probe spectroscopy is useful.^[180] After excitation with a fs-laser pulse (pump), the time-resolved absorption spectra (probe) are measured. Usually difference spectra are plotted resulting from subtraction of the ground state spectrum. From characteristic excited state absorption bands and their time traces, the lifetime of these states can be estimated. In case of d^6 transition metal complexes, the characteristic bands are related to a LMCT absorption at lower energy and to the ligand radical e.g. $\text{bpy}^{\cdot-}$ at higher energy.^[180] A second excitation into the initially populated MLCT state ($[\text{M}^{\text{III}}\text{LL}^{\cdot-}]^{2+}$) results in a charge transfer back from the ligand to the metal.^[180]

To assign the excited state absorption bands, the MLCT excited state absorption spectra can be simulated using spectroelectrochemical methods. As the MLCT state can be understood as a formal oxidation of the metal center accompanied by a reduction of the ligand, for the simulation both electron transfer processes can be investigated separately by electrochemical oxidation and reduction by absorption spectroscopy.^[180,184] From both subspectra, the excited state difference absorbances ΔA_{ex} can be determined using equation 15:^[184]

2. Introduction

$$\Delta A_{\text{ex}} = (A_{\text{ox}} + A_{\text{red}})\eta - 2A_{\text{gs}}(1 - \eta) \quad \text{equation 15}$$

where A_{ox} , A_{red} and A_{gs} are the absorbances of the oxidized, reduced and ground state species, respectively, and η is a scaling factor.

The overall excited state lifetime is defined as ground state recovery time. Directly after the excitation, the first spectral change is the ground state bleach. The excitation is accompanied by a depopulation of the ground state resulting in a bleaching of the respective bands. The rate constant for the recovery of these bands is the ground state recovery time.

A carbonyl group present in the complex can act as probe for timeresolved IR spectroscopy. The formal oxidation of the metal center in the MLCT excited state results in a strengthened σ -bond and a weakened π -back bond. The increased C=O bond strength leads to a shift of the stretching vibration to higher energies. The simulation of the excited state IR spectra is carried out in a similar fashion using IR spectroelectrochemical techniques.

Solvatochromic effect

The solvatochromic effect is the dependence of absorption and emission wavelength on the solvent. For d^6 complexes, the 1A ground state is less polar compared to the $^1/3MLCT$ state. Therefore, the latter state is stabilized in polar solvents. As a result of this stabilization, the 1A - 1MLCT excitation energy is lower compared to nonpolar solvents, the absorption band is bathochromically shifted.^[185,186] The 3MLCT - 1A emission energy is bathochromically shifted as well. In case of a polar ground state and a less polar excited state, a hypsochromic shift occurs.

Photoinduced electron transfer

For luminescent complexes, the excited state reactivity can be probed via Stern-Volmer analysis.^[187,188] By measuring the decay constant of emission with (k_{obs}) and without (k_0) substrate, or the respective quantum yields Φ_{obs} and Φ_0 , depending on the substrate concentration [Sub], (see equation 16) the quenching constant k_q can be determined.^[187,188]

$$\frac{k_{\text{obs}}}{k_0} = \frac{\Phi_0}{\Phi_{\text{obs}}} = \frac{k_0 + k_q[\text{Sub}]}{k_0} = 1 + \frac{k_q[\text{Sub}]}{k_0} \quad \text{equation 16}$$

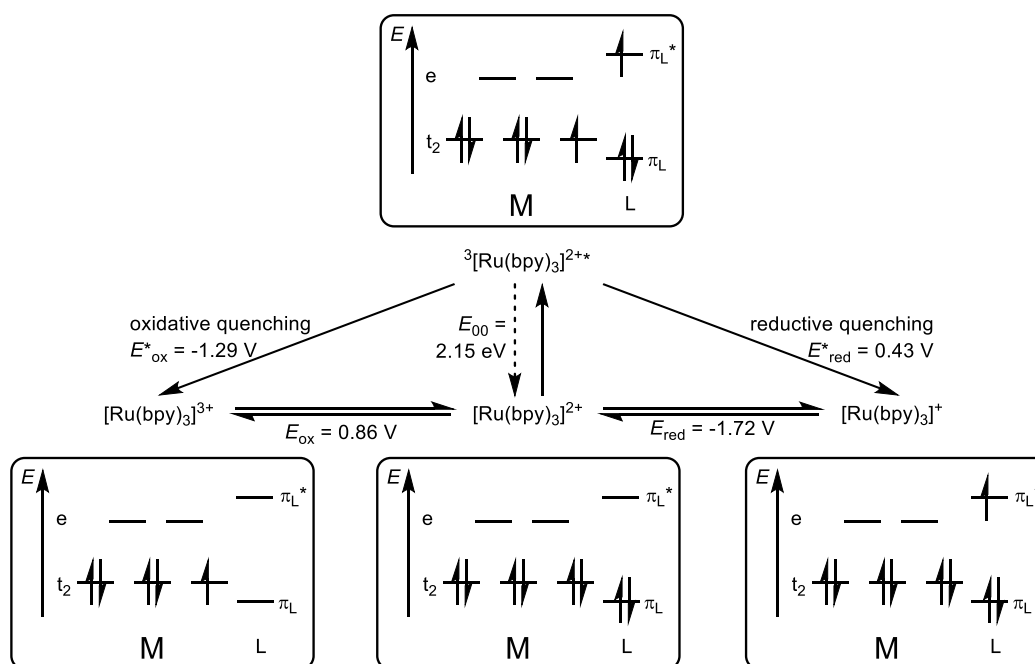
A distinction between dynamic (bimolecular, diffusion controlled) and static (pre-association) processes is possible by comparison of Stern-Volmer data extracted from steady-state with time-resolved emission experiments.^[180]

A possible application for complexes with long-living photoexcited states is photocatalysis.^[189] The key step of photoredox catalysis is the photo-induced electron transfer (PET). Whether PET is possible or not, is controlled by the excited state redox potentials. They are significantly different from ground state redox potentials.^[190] This notion can be explained using the complex $[\text{Ru}(\text{bpy})_3]^{2+}$ (Figure 2a) as an example. The MLCT excited state is a formal oxidation of the ruthenium(II) center, along with reduction of one bpy ligand. In the MLCT excited state, the metal is easier to reduce and the ligand easier to oxidize than in the ground state.^[191] The resulting excited state redox potentials are given by the Rehm-Weller equations (equations 17a and 17b).^[192,193]

$$E_{\text{ox}}^* = E_{\text{ox}} - E_{00} \quad \text{equation 17a}$$

$$E_{\text{red}}^* = E_{\text{red}} + E_{00} \quad \text{equation 17b}$$

The relation between the ground state oxidation (E_{ox}), reduction (E_{red}) potentials, and the excited state potentials E_{ox}^* , E_{red}^* and E_{00} (energy of the electronic origin for the excited state, the energy difference between 0th vibrational levels of ground and excited states) relevant for oxidative and reductive PET is illustrated in Figure 11.

Figure 11: Oxidative and reductive quenching pathways.^[194–196]

The energy E_{00} , is accessible by a single modular fit of the emission spectrum as described by Claude and Meyer.^[180,197,198] Some less accurate approximations are also used (especially for non-luminescent complexes). They include a high-energy onset of emission bands at low temperature, the intersection between normalized absorption and emission bands, the low-energy onset of an absorption band, and the HOMO-LUMO gap calculated from the difference between oxidation and reduction potential for CT excited states. A larger excited state energy E_{00} leads to an increased photocatalytic power (stronger oxidant and stronger reductant), but also increases the energy needed for photoexcitation.^[189]

To be used in such PET processes, photosensitizer should show a broad absorption profile in the visible region (where most substrates are transparent), high photostability, reversible redox behavior, sufficient excited state lifetime (ns needed for diffusion controlled reaction), excited state character suitable for ET, and an excited state redox potential suitable for the desired redox process.^[180,189]

2. Introduction

DFT calculations

To predict the ground and excited state properties, density functional theory (DFT) calculations are a powerful theoretical tool. As for all theoretical methods, the right model is essential. DFT is based on a combination of functional and basis set.^[199] The functional describes the position dependent electron density for a given system. All properties can be deduced from this electron density. The commonly used B3LYP (Becke, 3-parameter, Lee-Yang-Parr) functional admixes electron exchange correlation from Hartree-Fock methods that is poorly described by pure DFT methods.^[200–202] The smallest basis set applies a single basis function for each included atom orbital including unoccupied orbitals for the highest principal quantum number of the respective atom. On the other hand a complete basis set would be composed of an infinite number of basis functions. Split-valence basis sets use more than one function to describe the valence orbitals. For example the TZVP (triple-zeta valence polarization) basis set uses three basis functions for each valence orbital while the SVP (split valence polarization) basis set uses two.^[203,204] Both include valence polarization.

A well-established program for DFT calculations is the ORCA program package.^[205,206] To accelerate hybrid DFT calculations, the resolution of the identity chain-of-spheres exchange (RIJCOSX) Coulomb approximation, an approximation to the Hartree-Fock exchange term, can be used.^[207,208] Relativistic effects were calculated at the zeroth order regular approximation (ZORA) level.^[209] To take van der Waals interactions into account, atom-pairwise dispersion correction can be performed with the Becke-Johnson damping scheme (D3BJ).^[210,211] As geometry and energy of charge-transfer states are dependent on the environment of the complex, a calculation in the gas phase would lead to unreliable results. Although no discrete counter ions and/or solvent molecules were taken into account, the conductor-like polarizable continuum model (CPCM) leads to more reliable results.^[212,213] Obviously this model is insufficient for investigations of bimolecular reactivity.

For a given charge and multiplicity, the geometry at the potential energy minimum can be calculated. As a geometry optimization for the multiplicity of 3 starting from the 1A ground state geometry usually results in the 3MCLT geometry, the access to 3T states is more complicated. By optimizing structures using geometry constraints for certain metal ligand bonds and subsequent unconstrained optimizations, different 3T states can be found with different elongation axis. As the optimized geometry not necessarily corresponds to an energy minimum the presence of the minimum can be checked by (numerical) frequency calculations. These calculations also reveal the Gibbs free enthalpy of the system and simulate the vibrational spectra.^[214] A potential energy surface map can be calculated by geometry optimization along a certain coordinate (often the A_{1g} stretching vibration of ML_6) set to fixed values above and below the relaxed distances for all states followed by numerical frequency calculations.

To simulate the UV/Vis spectra, time dependent (TD) DFT calculations can be performed. They predict spin-allowed transitions together with the corresponding oscillator strength.^[214,215] The character (LC, ILCT, LL'CT, MLCT, LMCT, MC) can be predicted by charge transfer number analyses by partitioning the complex into suitable fragments e.g. M and L, using TheoDORE 2.2.^[216,217]

3. Aim of work

Ruthenium(II) complexes are already well investigated and used in photochemical applications. The major drawback for a wider application is their low abundance and subsequent high cost. The higher abundance makes the 3d homologue iron(II) a potential candidate to replace ruthenium(II) in these applications. Thus, the aim of this work is to design, synthesize and characterize novel iron(II) complexes. It will focus on octahedral complexes with six-membered-ring chelate ligands because this concept promises a high ligand field splitting and hopefully enables extended excited state lifetimes. This concept of high local $[\text{FeN}_6]$ symmetry will be combined with a push-pull design of the ligands induced by different bridges between the pyridine moieties of polypyridine ligands as shown in Figure 12a.

Therefore, the novel 6,2''-carboxypyridyl-2,2'-methylaminepyridyl-pyridine (cpmp) ligand bearing a σ -donating N-CH₃ bridge and a π -accepting C=O bridge will be synthesized. For heteroleptic complexes in combination with the literature known *N,N*-dimethyl-*N,N*-dipyridin-2-ylpyridine-2,6-diamine (ddpd) ligand an increased push-pull effect can be expected.^[31,63] The higher σ -donor ability of the ddpd ligand results from two N-CH₃ bridges. The homoleptic $[\text{Fe}(\text{cpmp})_2]^{2+}$ and heteroleptic $[\text{Fe}(\text{cpmp})(\text{ddpd})]^{2+}$ complexes will be synthesized and characterized as well as the analogous ruthenium(II) complexes $[\text{Ru}(\text{cpmp})_2]^{2+}$ and $[\text{Ru}(\text{cpmp})(\text{ddpd})]^{2+}$ for comparison (Figure 12b).

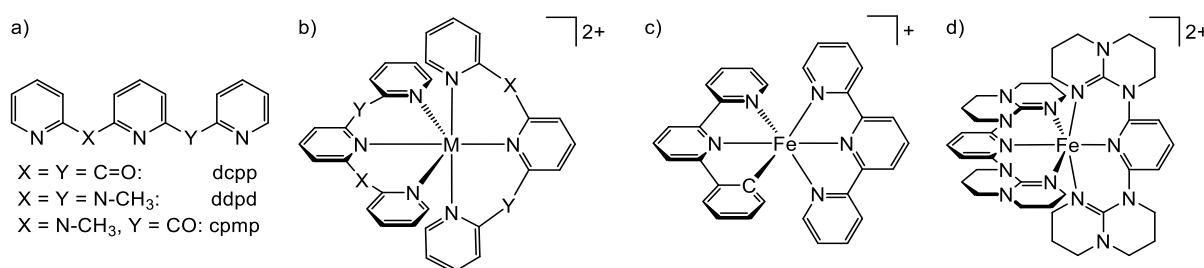


Figure 12: a) polypyridine ligands used in this work; b) general structure for octahedral polypyridine transition metal complexes; c) structure of $[\text{Fe}(\text{pbpy})(\text{tpy})]^+$; d) structure of $\text{mer-}[\text{Fe}(\text{dgpy})_2]^{2+}$.

The photophysical and electrochemical properties of the first cyclometalated iron(II) complex with five-membered-ring chelate ligands $[\text{Fe}(\text{pbpy})(\text{tpy})]^+$ (Figure 12c), synthesized by Jakob Steube from the group of Prof. Dr. Matthias Bauer at the University of Paderborn, will be discussed.

Furthermore, the stronger σ -donor 2,6-diguanyldipyridine (dgpy) ligand will be applied in the homoleptic iron(II) complex $[\text{Fe}(\text{dgpy})_2]^{2+}$ (Figure 12d) to examine its influence on the ligand field splitting.^[218]

The structures of the resulting complexes will be investigated by single crystal X-ray diffraction, ¹H and ¹³C NMR, IR spectroscopy and mass spectrometry to verify the proposed structure geometry. Their photophysical and photochemical properties will be studied employing spectroscopic (steady state and time resolved UV-VIS, IR and emission spectroscopy) and theoretical (DFT and TD-DFT) methods, to examine the excited state landscape and thus understand their excited state dynamics. Electrochemical investigations will be carried out using cyclic voltammetry, square-wave voltammetry and UV/Vis and IR spectroelectrochemistry. If the complexes exhibit reasonable MLCT lifetimes, first applications of the complexes as photocatalysts should be explored.

4. Literature

- [1] B. Durham, J. V. Caspar, J. K. Nagle, T. J. Meyer, *J. Am. Chem. Soc.* **1982**, *104*, 4803–4810.
- [2] B. O'Regan, M. Grätzel, *Nature* **1991**, *353*, 737–740.
- [3] J.-F. Yin, M. Velayudham, D. Bhattacharya, H.-C. Lin, K.-L. Lu, *Coord. Chem. Rev.* **2012**, *256*, 3008–3035.
- [4] P. G. Bomben, K. C. D. Robson, B. D. Koivisto, C. P. Berlinguette, *Coord. Chem. Rev.* **2012**, *256*, 1438–1450.
- [5] R. D. Costa, E. Ortí, H. J. Bolink, F. Monti, G. Accorsi, N. Armaroli, *Angew. Chem. Int. Ed.* **2012**, *51*, 8178–8211.
- [6] P. Dreyse, B. Loeb, M. Soto-Arriaza, D. Tordera, E. Ortí, J. J. Serrano-Pérez, H. J. Bolink, *Dalton Trans.* **2013**, *42*, 15502–15513.
- [7] H. J. Bolink, L. Cappelli, E. Coronado, P. Gaviña, *Inorg. Chem.* **2005**, *44*, 5966–5968.
- [8] H. J. Bolink, E. Coronado, R. D. Costa, P. Gaviña, E. Ortí, S. Tatay, *Inorg. Chem.* **2009**, *48*, 3907–3909.
- [9] K. M. Maness, R. H. Terrill, T. J. Meyer, R. W. Murray, R. M. Wightman, *J. Am. Chem. Soc.* **1996**, *118*, 10609–10616.
- [10] A. Inagaki, M. Akita, *Coord. Chem. Rev.* **2010**, *254*, 1220–1239.
- [11] C. K. Prier, D. A. Rankic, D. W. C. MacMillan, *Chem. Rev.* **2013**, *113*, 5322–5363.
- [12] S. Campagna, F. Puntoriero, F. Nastasi, G. Bergamini, V. Balzani, *Top. Curr. Chem.* **2007**, *280*, 117–214.
- [13] T. J. Meyer, *Pure Appl. Chem.* **1986**, *58*, 1193–1206.
- [14] E. M. Kober, B. P. Sullivan, T. J. Meyer, *Inorg. Chem.* **1984**, *23*, 2098–2104.
- [15] J.-P. Sauvage, J.-P. Collin, J. C. Chambron, S. Guillerez, C. Coudret, V. Balzani, F. Barigelletti, L. de Cola, L. Flamigni, *Chem. Rev.* **1994**, *94*, 993–1019.
- [16] A. Juris, V. Balzani, P. Belser, A. von Zelewsky, *Helv. Chim. Acta* **1981**, *64*, 2175–2182.
- [17] K. Suzuki, A. Kobayashi, S. Kaneko, K. Takehira, T. Yoshihara, H. Ishida, Y. Shiina, S. Oishi, S. Tobita, *Phys. Chem. Chem. Phys.* **2009**, *11*, 9850–9860.
- [18] K. Kalyanasundaram, *Coord. Chem. Rev.* **1982**, *46*, 159–244.
- [19] Crosby, G. A., Demas, J. N., *J. Am. Chem. Soc.* **1971**, *93*, 2841–2847.
- [20] V. M. Miskowski, H. B. Gray, R. B. Wilson, E. I. Solomon, *Inorg. Chem.* **1979**, *18*, 1410–1412.
- [21] R. B. Wilson, E. I. Solomon, *J. Am. Chem. Soc.* **1980**, *102*, 4085–4095.
- [22] A. Soupart, F. Alary, J.-L. Heully, P. I. P. Elliott, I. M. Dixon, *Inorg. Chem.* **2018**, *57*, 3192–3196.
- [23] P. D. Fleischauer, P. Fleischauer, *Chem. Rev.* **1970**, *70*, 199–230.
- [24] A. Breivogel, M. Meister, C. Förster, F. Laquai, K. Heinze, *Chem. Eur. J.* **2013**, *19*, 13745–13760.
- [25] L. Gong, S. P. Mulcahy, D. Devarajan, K. Harms, G. Frenking, E. Meggers, *Inorg. Chem.* **2010**, *49*, 7692–7699.
- [26] A. Reynal, E. Palomares, *Eur. J. Inorg. Chem.* **2011**, *2011*, 4509–4526.
- [27] C. Fu, M. Wenzel, E. Treutlein, K. Harms, E. Meggers, *Inorg. Chem.* **2012**, *51*, 10004–10011.
- [28] E. Meggers, *Chem. Eur. J.* **2010**, *16*, 752–758.
- [29] E. Meggers, *Eur. J. Inorg. Chem.* **2011**, *2011*, 2911–2926.
- [30] A. Breivogel, C. Kreitner, K. Heinze, *Eur. J. Inorg. Chem.* **2014**, *2014*, 5468–5490.
- [31] A. Breivogel, C. Förster, K. Heinze, *Inorg. Chem.* **2010**, *49*, 7052–7056.
- [32] A. Soupart, F. Alary, J.-L. Heully, P. I. P. Elliott, I. M. Dixon, *Inorg. Chem.* **2018**, *57*, 3192–3196.
- [33] B. Durham, J. L. Walsh, C. L. Carter, T. J. Meyer, *Inorg. Chem.* **1980**, *19*, 860–865.
- [34] M. Gleria, F. Minto, G. Beggiano, P. Bortolus, *J. Chem. Soc., Chem. Commun.* **1978**, *0*, 285.
- [35] L. Feng, Y. Wang, *Inorg. Chem.* **2018**, *57*, 8994–9001.
- [36] A. Soupart, F. Alary, J.-L. Heully, P. I. P. Elliott, I. M. Dixon, *Coord. Chem. Rev.* **2020**, *408*, 213184.
- [37] A. Soupart, F. Alary, J.-L. Heully, I. M. Dixon, *Inorganics* **2020**, *8*, 15.
- [38] A. Soupart, F. Alary, J.-L. Heully, P. I. P. Elliott, I. M. Dixon, *Inorg. Chem.* **2020**, *59*, 14679–14695.
- [39] J. M. Dixon, M. Taniguchi, J. S. Lindsey, *Photochem. Photobiol.* **2005**, *81*, 212–213.
- [40] H. Du, R.-C. A. Fuh, J. Li, L. A. Corkan, J. S. Lindsey, *Photochem. Photobiol.* **1998**, *68*, 141–142.
- [41] J. van Houten, R. J. Watts, *J. Am. Chem. Soc.* **1976**, *98*, 4853–4858.
- [42] R. Hogg, R. G. Wilkins, *J. Chem. Soc.* **1962**, *0*, 341–350.
- [43] M. Maestri, N. Armaroli, V. Balzani, E. C. Constable, Cargill Thompson, Alexander M. W., *Inorg. Chem.* **1995**, *34*, 2759–2767.
- [44] K. Lashgari, M. Kritikos, R. Norrestam, T. Norrby, *CCDC 130924: Experimental Crystal Structure Determination*, Cambridge Crystallographic Data Centre, **1999**.
- [45] M. Biner, H. B. Bürgi, Ludi, A., C. Röhr, *J. Am. Chem. Soc.* **1992**, *114*, 5197–5203.
- [46] J.-P. Collin, M. Beley, J.-P. Sauvage, *Inorg. Chim. Act.* **1991**, *186*, 91–93.
- [47] M. L. Stone, G. A. Crosby, *Chem. Phys. Lett.* **1981**, *79*, 169–173.
- [48] J. R. Winkler, T. L. Netzel, C. Creutz, N. Sutin, *J. Am. Chem. Soc.* **1987**, *109*, 2381–2392.
- [49] K. Heinze, K. Hempel, A. Breivogel, *Z. Anorg. Allg. Chem.* **2009**, *635*, 2541–2549.
- [50] Y.-Q. Fang, N. J. Taylor, G. S. Hanan, F. Loiseau, R. Passalacqua, S. Campagna, H. Nierengarten, A. van Dorsselaer, *J. Am. Chem. Soc.* **2002**, *124*, 7912–7913.

4. Literature

- [51] Y.-Q. Fang, N. J. Taylor, F. Laverdière, G. S. Hanan, F. Loiseau, F. Nastasi, S. Campagna, H. Nierengarten, E. Leize-Wagner, A. van Dorsselaer, *Inorg. Chem.* **2007**, *46*, 2854–2863.
- [52] J. V. Caspar, T. J. Meyer, *J. Am. Chem. Soc.* **1983**, *105*, 5583–5590.
- [53] J. V. Caspar, E. M. Kober, B. P. Sullivan, T. J. Meyer, *J. Am. Chem. Soc.* **1982**, *104*, 630–632.
- [54] J. V. Caspar, T. J. Meyer, *J. Phys. Chem.* **1983**, *87*, 952–957.
- [55] L. Hammarström, O. Johansson, *Coord. Chem. Rev.* **2010**, *254*, 2546–2559.
- [56] M. Jäger, R. J. Kumar, H. Gorls, J. Bergquist, O. Johansson, *Inorg. Chem.* **2009**, *48*, 3228–3238.
- [57] G. A. Parada, L. A. Fredin, M.-P. Santoni, M. Jäger, R. Lomoth, L. Hammarström, O. Johansson, P. Persson, S. Ott, *Inorg. Chem.* **2013**, *52*, 5128–5137.
- [58] M. Abrahamsson, M. Jäger, T. Österman, L. Eriksson, P. Persson, H.-C. Becker, O. Johansson, L. Hammarström, *J. Am. Chem. Soc.* **2006**, *128*, 12616–12617.
- [59] T. Österman, M. Abrahamsson, H.-C. Becker, L. Hammarström, P. Persson, *J. Phys. Chem. A* **2012**, *116*, 1041–1050.
- [60] M. Abrahamsson, M. Jäger, R. J. Kumar, T. Österman, P. Persson, H.-C. Becker, O. Johansson, L. Hammarström, *J. Am. Chem. Soc.* **2008**, *130*, 15533–15542.
- [61] R. J. Kumar, S. Karlsson, D. Streich, A. Rolandini Jensen, M. Jäger, H.-C. Becker, J. Bergquist, O. Johansson, L. Hammarström, *Chem. Eur. J.* **2010**, *16*, 2830–2842.
- [62] F. Schramm, V. Meded, H. Fliegl, K. Fink, O. Fuhr, Z. Qu, W. Klopfer, S. Finn, T. E. Keyes, M. Ruben, *Inorg. Chem.* **2009**, *48*, 5677–5684.
- [63] C. Förster, M. Dorn, T. Reuter, S. Otto, G. Davarci, T. Reich, L. M. Carrella, E. Rentschler, K. Heinze, *Inorganics* **2018**, *6*, 86.
- [64] S. H. Wadman, M. Lutz, D. M. Tooke, A. L. Spek, F. Hartl, R. W. A. Havenith, G. P. M. van Klink, G. van Koten, *Inorg. Chem.* **2009**, *48*, 1887–1900.
- [65] C. Kreitner, K. Heinze, *Dalton Trans.* **2016**, *45*, 13631–13647.
- [66] E. C. Constable, J. M. Holmes, *J. Organomet. Chem.* **1986**, *301*, 203–208.
- [67] M. L. Muro-Small, J. E. Yarnell, C. E. McCusker, F. N. Castellano, *Eur. J. Inorg. Chem.* **2012**, *2012*, 4004–4011.
- [68] C. Kreitner, E. Erdmann, W. W. Seidel, K. Heinze, *Inorg. Chem.* **2015**, *54*, 11088–11104.
- [69] D. L. Anderson, *Theory of the earth*, Blackwell Scientific Publ., Boston, **1991**.
- [70] J. K. McCusker, *Science* **2019**, *363*, 484–488.
- [71] P. Pyykkö, *Chem. Rev.* **1988**, *88*, 563–594.
- [72] M. Kaupp, *J. Comput. Chem.* **2006**, *28*, 320–325.
- [73] W. Zhang, R. Alonso-Mori, U. Bergmann, C. Bressler, M. Chollet, A. Galler, W. Gawelda, R. G. Hadt, R. W. Hartsock, T. Kroll, K. S. Kjær, K. Kubiček, H. T. Lemke, H. W. Liang, D. A. Meyer, M. M. Nielsen, C. Purser, J. S. Robinson, E. I. Solomon, Z. Sun, D. Sokaras, T. B. van Driel, G. Vankó, T.-C. Weng, D. Zhu, K. J. Gaffney, *Nature* **2014**, *509*, 345–348.
- [74] J. K. McCusker, K. N. Walda, R. C. Dunn, J. D. Simon, D. Magde, D. N. Hendrickson, *J. Am. Chem. Soc.* **1993**, *115*, 298–307.
- [75] R. J. Lancashire, *Tanabe-Sugano diagrams via spreadsheets*, Department of Chemistry, University of the West Indies, Jamaica, <http://wwwchem.uwimona.edu.jm/courses/Tanabe-Sugano/TSSpread.html>, **1999**.
- [76] M. C. Carey, S. L. Adelman, J. K. McCusker, *Chem. Sci.* **2019**, *10*, 134–144.
- [77] S. E. Canton, X. Zhang, L. M. Lawson Daku, A. L. Smeigh, J. Zhang, Y. Liu, C.-J. Wallentin, K. Attenkofer, G. Jennings, C. A. Kurtz, D. Gosztola, K. Wärmmark, A. W. Hauser, V. Sundström, *J. Phys. Chem. C* **2014**, *118*, 4536–4545.
- [78] A. Britz, W. Gawelda, T. A. Assefa, L. L. Jamula, J. T. Yarranton, A. Galler, D. Khakhulin, M. Diez, M. Harder, G. Doumy, A. M. March, É. Bajnóczi, Z. Németh, M. Pápai, E. Rozsályi, D. Sárosiné Szemes, H. Cho, S. Mukherjee, C. Liu, T. K. Kim, R. W. Schoenlein, S. H. Southworth, L. Young, E. Jakubikova, N. Huse, G. Vankó, C. Bressler, J. K. McCusker, *Inorg. Chem.* **2019**, *58*, 9341–9350.
- [79] L. L. Jamula, A. M. Brown, D. Guo, J. K. McCusker, *Inorg. Chem.* **2014**, *53*, 15–17.
- [80] A. W. Hauser in *Top. Curr. Chem.*, Vol. 233 (Eds.: P. Gütllich, H. A. Goodwin), Springer, Berlin/Heidelberg, **2004**.
- [81] P. Gütllich, Y. Garcia, H. A. Goodwin, *Chem. Soc. Rev.* **2000**, *29*, 419–427.
- [82] P. Gütllich, A. W. Hauser, H. Spiering, *Angew. Chem. Int. Ed. Engl.* **1994**, *33*, 2024–2054.
- [83] O. Kahn, C. J. Martinez, *Science* **1998**, *279*, 44–48.
- [84] S. Brooker, *Chem. Soc. Rev.* **2015**, *44*, 2880–2892.
- [85] M. D. Manrique-Juárez, S. Rat, L. Salmon, G. Molnár, C. M. Quintero, L. Nicu, H. J. Shepherd, A. Bousseksou, *Coord. Chem. Rev.* **2016**, *308*, 395–408.
- [86] J. Linares, E. Codjovi, Y. Garcia, *Sensors* **2012**, *12*, 4479–4492.
- [87] C. E. Housecroft, A. G. Sharpe, A. Rompel, *Anorganische Chemie*, 2. Aufl., Pearson Studium, München, **2008**.
- [88] P. Gütllich, *Eur. J. Inorg. Chem.* **2013**, *2013*, 581–591.
- [89] J. S. Griffith, L. E. Orgel, *Q. Rev. Chem. Soc.* **1957**, *11*, 381–393.
- [90] Y. Garcia, P. Gütllich in *Top. Curr. Chem.*, Vol. 234 (Eds.: P. Gütllich, H. A. Goodwin), Springer, Berlin/Heidelberg, **2004**.

- [91] L. Cambi, L. Szegő, *Ber. Dtsch. Chem. Ges.* **1931**, *64*, 2591-2598.
- [92] L. Cambi, L. Szegő, *Ber. Dtsch. Chem. Ges.* **1933**, *66*, 656-661.
- [93] L. Cambi, L. Malatesta, *Ber. Dtsch. Chem. Ges.* **1937**, *70*, 2067-2078.
- [94] A. H. White, R. Roper, E. Kokot, H. Waterman, R. L. Martin, *Austr. J. Chem.* **1964**, *17*, 294.
- [95] A. H. Ewald, R. L. Martin, I. G. Ross, A. H. White, *Proc. R. Soc. Lond. A* **1964**, *280*, 235-257.
- [96] B. N. Figgis, G. E. Toogood, *J. Chem. Soc., Dalton Trans.* **1972**, *1972*, 2177-2182.
- [97] E. König, *Coord. Chem. Rev.* **1968**, *3*, 471-495.
- [98] H. A. Goodwin, *Coord. Chem. Rev.* **1976**, *18*, 293-325.
- [99] P. Gütllich in *Metal Complexes. Structure and Bonding* (Eds.: R. Bau, P. Gütllich, R. G. Teller), Springer, Berlin, Heidelberg, **1981**.
- [100] P. Gütllich, H. A. Goodwin (Hrsg.) *Top. Curr. Chem.*, Vol. 233, Springer, Berlin/Heidelberg, **2004**.
- [101] P. Gütllich, H. A. Goodwin (Hrsg.) *Top. Curr. Chem.*, Vol. 234, Springer, Berlin/Heidelberg, **2004**.
- [102] P. Gütllich, H. A. Goodwin (Hrsg.) *Top. Curr. Chem.*, Vol. 235, Springer, Berlin/Heidelberg, **2004**.
- [103] M. A. Halcrow (Hrsg.) *Spin-Crossover Materials*, John Wiley & Sons Ltd, Oxford, UK, **2013**.
- [104] P. W. Atkins, J. de Paula, *Physikalische Chemie*, 4. Aufl., Wiley-VCH, Weinheim, **2006**.
- [105] E. König in *Structure and Bonding*, Vol. 76, Springer, Berlin/Heidelberg, **1991**.
- [106] E. König, G. Ritter, S. K. Kulshreshtha, *Chem. Rev.* **1985**, *85*, 219-234.
- [107] P. Gütllich, H. A. Goodwin in *Top. Curr. Chem.*, Vol. 233 (Eds.: P. Gütllich, H. A. Goodwin), Springer, Berlin/Heidelberg, **2004**.
- [108] M. P. Shores, C. M. Klug, S. R. Fiedler in *Spin-Crossover Materials* (Eds.: M. A. Halcrow), John Wiley & Sons Ltd, Oxford, UK, **2013**.
- [109] P. Gütllich, A. B. Gaspar, Y. Garcia, *Beilstein J. Org. Chem.* **2013**, *9*, 342-391.
- [110] T. Buchen, P. Gütllich, H. A. Goodwin, *Inorg. Chem.* **1994**, *33*, 4573-4576.
- [111] N. Moliner, A. B. Gaspar, M. C. Muñoz, V. Niel, J. Cano, J. A. Real, *Inorg. Chem.* **2001**, *40*, 3986-3991.
- [112] M. Marchivie, P. Guionneau, J.-F. Létard, D. Chasseau, J.A.K. Howard, *J. Phys. Chem. Solids* **2004**, *65*, 17-23.
- [113] V. Gómez, C. Sáenz de Pipaón, P. Maldonado-Illescas, J. C. Waerenborgh, E. Martin, J. Benet-Buchholz, J. R. Galán-Mascarós, *J. Am. Chem. Soc.* **2015**, *137*, 11924-11927.
- [114] S. Decurtins, P. Gütllich, K. M. Hasselbach, A. W. Hauser, H. Spiering, *Inorg. Chem.* **1985**, *24*, 2174-2178.
- [115] S. Decurtins, P. Gütllich, C. P. Köhler, H. Spiering, A. W. Hauser, *Chem. Phys. Lett.* **1984**, *105*, 1-4.
- [116] A. W. Hauser, *Chem. Phys. Lett.* **1986**, *124*, 543-548.
- [117] Y. Tanabe, S. Sugano, *J. Phys. Soc. Jpn.* **1954**, *9*, 766-779.
- [118] C. K. Jørgensen, *Discuss. Faraday Soc.* **1958**, *26*, 110-115.
- [119] O. S. Wenger, *Chem. Eur. J.* **2019**, *25*, 6043-6052.
- [120] A. T. Baker, H. A. Goodwin, *Austr. J. Chem.* **1985**, *38*, 207-214.
- [121] T. Duchanois, T. Etienne, M. Beley, X. Assfeld, E. A. Perpète, A. Monari, P. C. Gros, *Eur. J. Inorg. Chem.* **2014**, *2014*, 3747-3753.
- [122] A. K. C. Mengel, C. Förster, A. Breivogel, K. Mack, J. R. Ochsmann, F. Laquai, V. Ksenofontov, K. Heinze, *Chem. Eur. J.* **2015**, *21*, 704-714.
- [123] Y. Liu, P. Persson, V. Sundström, K. Wärnmark, *Acc. Chem. Res.* **2016**, *49*, 1477-1485.
- [124] T. Duchanois, L. Liu, M. Pastore, A. Monari, C. Cebrián, Y. Trolez, M. Darari, K. Magra, A. Francés-Monerris, E. Domenichini, M. Beley, X. Assfeld, S. Haacke, P. C. Gros, *Inorganics* **2018**, *6*, 63.
- [125] Y. Liu, T. C. B. Harlang, S. E. Canton, P. Chábera, K. Suarez-Alcantara, A. Fleckhaus, D. A. Vithanage, E. Goransson, A. Corani, R. Lomoth, V. Sundström, K. Wärnmark, *Chem. Commun.* **2013**, *49*, 6412-6414.
- [126] L. Liu, T. Duchanois, T. Etienne, A. Monari, M. Beley, X. Assfeld, S. Haacke, P. C. Gros, *Phys. Chem. Chem. Phys.* **2016**, *18*, 12550-12556.
- [127] T. Duchanois, T. Etienne, C. Cebrián, L. Liu, A. Monari, M. Beley, X. Assfeld, S. Haacke, P. C. Gros, *Eur. J. Inorg. Chem.* **2015**, *2015*, 2469-2477.
- [128] T. Jiang, Y. Bai, P. Zhang, Q. Han, D. B. Mitzi, M. J. Therien, *Proc. Natl. Acad. Sci. USA* **2020**, *15*.
- [129] D. Leshchev, T. C. B. Harlang, L. A. Fredin, D. Khakhulin, Y. Liu, E. Biasin, M. G. Laursen, G. E. Newby, K. Haldrup, M. M. Nielsen, K. Wärnmark, V. Sundström, P. Persson, K. S. Kjær, M. Wulff, *Chem. Sci.* **2018**, *9*, 405-414.
- [130] L. A. Fredin, M. Pápai, E. Rozsályi, G. Vankó, K. Wärnmark, V. Sundström, P. Persson, *J. Phys. Chem. Lett.* **2014**, *5*, 2066-2071.
- [131] Y. Liu, K. S. Kjær, L. A. Fredin, P. Chábera, T. C. B. Harlang, S. E. Canton, S. Lidin, J. Zhang, R. Lomoth, K.-E. Bergquist, P. Persson, K. Wärnmark, V. Sundström, *Chem. Eur. J.* **2015**, *21*, 3628-3639.
- [132] S. Hohloch, L. Suntrup, B. Sarkar, *Organometallics* **2013**, *32*, 7376-7385.
- [133] P. Chábera, K. S. Kjær, O. Prakash, A. Honarfar, Y. Liu, L. A. Fredin, T. C. B. Harlang, S. Lidin, J. Uhlig, V. Sundström, R. Lomoth, P. Persson, K. Wärnmark, *J. Phys. Chem. Lett.* **2018**, *9*, 459-463.
- [134] P. Chábera, Y. Liu, O. Prakash, E. Thyraug, A. E. Nahhas, A. Honarfar, S. Essen, L. A. Fredin, T. C. B. Harlang, K. S. Kjær, K. Handrup, F. Ericson, H. Tatsuno, K. Morgan, J. Schnadt, L. Haggstrom, T. Ericsson, A. Sobkowiak, S. Lidin, P. Huang, S. Styring, J. Uhlig, J. Bendix, R. Lomoth, V. Sundström, P. Persson, K. Wärnmark, *Nature* **2017**, *543*, 695-699.

4. Literature

- [135] K. S. Kjær, N. Kaul, O. Prakash, P. Chábera, N. W. Rosemann, A. Honarfar, O. Gordivska, L. A. Fredin, K.-E. Bergquist, L. Häggström, T. Ericsson, L. Lindh, A. Yartsev, S. Styring, P. Huang, J. Uhlig, J. Bendix, D. Strand, V. Sundström, P. Persson, R. Lomoth, K. Wärnmark, *Science* **2019**, *363*, 249–253.
- [136] I. M. Dixon, F. Alary, M. Boggio-Pasqua, J.-L. Heully, *Inorg. Chem.* **2013**, *52*, 13369–13374.
- [137] I. M. Dixon, F. Alary, M. Boggio-Pasqua, J.-L. Heully, *Dalton Trans.* **2015**, *44*, 13498–13503.
- [138] I. M. Dixon, S. Khan, F. Alary, M. Boggio-Pasqua, J.-L. Heully, *Dalton Trans.* **2014**, *43*, 15898–15905.
- [139] S. Mukherjee, D. N. Bowman, E. Jakubikova, *Inorg. Chem.* **2015**, *54*, 560–569.
- [140] S. M. Fatur, S. G. Shepard, R. F. Higgins, M. P. Shores, N. H. Damrauer, *J. Am. Chem. Soc.* **2017**, *139*, 4493–4505.
- [141] S. G. Shepard, S. M. Fatur, A. K. Rappé, N. H. Damrauer, *J. Am. Chem. Soc.* **2016**, *138*, 2949–2952.
- [142] H. A. Goodwin, R. N. Sylva, *Austr. J. Chem.* **1968**, *21*, 83.
- [143] H. A. Goodwin, E. S. Kucharski, A. H. White, *Austr. J. Chem.* **1983**, *36*, 1115–1124.
- [144] J. Elhaik, D. J. Evans, C. A. Kilner, M. A. Halcrow, *Dalton Trans.* **2005**, 1693–1700.
- [145] E. C. Constable, G. Baum, E. Bill, R. Dyson, R. van Eldik, D. Fenske, S. Kaderli, D. Morris, A. Neubrand, M. Neuburger, D. R. Smith, K. Wieghardt, M. Zehnder, A. D. Zuberbühler, *Chem. Eur. J.* **1999**, *5*, 498–508.
- [146] Baker, W. A., Jr., H. M. Bobonich, *Inorg. Chem.* **1964**, *3*, 1184–1188.
- [147] E. König, K. Madeja, *Chem. Commun.* **1966**, 61–62.
- [148] E. König, K. Madeja, *Inorg. Chem.* **1967**, *6*, 48–55.
- [149] L. H. Gade, *Koordinationschemie*, 2. Aufl., Wiley-VCH, Weinheim, **2004**.
- [150] R. W. Hogue, R. G. Miller, N. G. White, H. L. C. Feltham, G. N. L. Jameson, S. Brooker, *Chem. Commun.* **2014**, *50*, 1435–1437.
- [151] T. Ryutaro, *Bull. Chem. Soc. Jpn.* **1938**, *13*, 388–400.
- [152] T. Ryutaro, *Bull. Chem. Soc. Jpn.* **1938**, *13*, 436–450.
- [153] A. F. Holleman, E. Wiberg, N. Wiberg, *Lehrbuch der anorganischen Chemie*, 101. Aufl., De Gruyter, Berlin, **1995**.
- [154] M. Sorai, S. Seki, *J. Phys. Chem. Solids* **1974**, *35*, 555–570.
- [155] J. Klingele, D. Kaase, M. Schmucker, Y. Lan, G. Chastanet, J.-F. Létard, *Inorg. Chem.* **2013**, *52*, 6000–6010.
- [156] N. Moliner, M. C. Muñoz, S. Létard, J.-F. Létard, X. Solans, R. Burriel, M. Castro, O. Kahn, J. A. Real, *Inorg. Chim. Act.* **1999**, *291*, 279–288.
- [157] J. Klingele, D. Kaase, M. H. Klingele, J. Lach, *Dalton Trans.* **2012**, *41*, 1397–1406.
- [158] H. S. Scott, T. M. Ross, N. F. Chilton, I. A. Gass, B. Moubaraki, G. Chastanet, N. Paradis, J.-F. Létard, K. R. Vignesh, G. Rajaraman, S. R. Batten, K. S. Murray, *Dalton Trans.* **2013**, *42*, 16494–16509.
- [159] S. Zheng, M. A. Siegler, O. Roubeau, S. Bonnet, *Inorg. Chem.* **2014**, *53*, 13162–13173.
- [160] X.-R. Wu, H.-Y. Shi, R.-J. Wei, J. Li, L.-S. Zheng, J. Tao, *Inorg. Chem.* **2015**, *54*, 3773–3780.
- [161] L. J. K. Cook, R. Mohammed, G. Sherborne, T. D. Roberts, S. Alvarez, M. A. Halcrow, *Coord. Chem. Rev.* **2015**, *289–290*, 2–12.
- [162] C. Hansch, A. Leo, R. W. Taft, *Chem. Rev.* **1991**, *91*, 165–195.
- [163] M. A. Halcrow, *Chem. Soc. Rev.* **2011**, *40*, 4119–4142.
- [164] D. J. Evans, *J. Chem. Soc.* **1959**, 2003–2005.
- [165] E. M. Schubert, *J. Chem. Educ.* **1992**, *69*, 62.
- [166] C. Piguet, *J. Chem. Educ.* **1997**, *74*, 815–816.
- [167] R. Graf, *1H Solid-State NMR Investigation of Structure and Dynamics in Anhydrous Proton Conducting Polymers*, Salerno, Italy, **2009**.
- [168] P. Gütlich, *Z. Anorg. Allg. Chem.* **2012**, *638*, 15–43.
- [169] M. Bauer, H. Bertagnolli in *Methods in physical chemistry* (Eds.: R. Schäfer), Wiley-VCH, Weinheim, **2012**.
- [170] M. Bauer, *Phys. Chem. Chem. Phys.* **2014**, *16*, 13827–13837.
- [171] M. Bauer, C. Gastl, *Phys. Chem. Chem. Phys.* **2010**, *12*, 5502.
- [172] M. Bauer, T. Kauf, J. Christoffers, H. Bertagnolli, *Phys. Chem. Chem. Phys.* **2005**, *7*, 2664–2670.
- [173] F. Farges, Y. Lefrère, S. Rossano, A. Berthureau, G. Calas, G. E. Brown, *J. Non-Cryst. Solids* **2004**, *344*, 176–188.
- [174] O. V. Safonova, M. Tromp, J. A. van Bokhoven, F. M. F. de Groot, J. Evans, P. Glatzel, *J. Phys. Chem. B* **2006**, *110*, 16162–16164.
- [175] P. Glatzel, M. Sikora, G. Smolentsev, M. Fernández-García, *Catal. Today* **2009**, *145*, 294–299.
- [176] M. Rovezzi, P. Glatzel, *Semicond. Sci. Technol.* **2014**, *29*, 23002.
- [177] M. U. Delgado-Jaime, S. DeBeer, M. Bauer, *Chem. Eur. J.* **2013**, *19*, 15888–15897.
- [178] V. Balzani, S. Campagna, *Top. Curr. Chem.* **2007**, *280*.
- [179] W. Becker, *The bh TCSPC Handbook. Time-Correlated Single Photon Counting Modules*, 8. Aufl., Berlin, **2019**.
- [180] D. M. Arias-Rotondo, J. K. McCusker, *Chem. Soc. Rev.* **2016**, *45*, 5803–5820.
- [181] C. Würth, D. Geißler, T. Behnke, M. Kaiser, U. Resch-Genger, *Anal. Bioanal. Chem.* **2015**, *407*, 59–78.
- [182] C. Würth, M. G. González, R. Niessner, U. Panne, C. Haisch, U. R. Genger, *Talanta* **2012**, *90*, 30–37.
- [183] C. Würth, J. Pauli, C. Lochmann, M. Spieles, U. Resch-Genger, *Anal. Chem.* **2012**, *84*, 1345–1352.
- [184] A. M. Brown, C. E. McCusker, J. K. McCusker, *Dalton Trans.* **2014**, *43*, 17635–17646.

- [185] M. J. Kamlet, J. L. Abboud, R. W. Taft, *J. Am. Chem. Soc.* **1977**, *99*, 6027–6038.
- [186] K. Dimroth, C. Reichardt, T. Siepmann, F. Bohlmann, *Liebigs Ann. Chem.* **1963**, *661*, 1–37.
- [187] O. Stern, M. Volmer, *Physik. Z.* **1919**, *20*, 183–188.
- [188] A. Y. Moon, D. C. Poland, H. A. Scheraga, *J. Phys. Chem.* **1965**, *69*, 2960–2966.
- [189] B. M. Hockin, C. Li, N. Robertson, E. Zysman-Colman, *Catal. Sci. Technol.* **2019**, *9*, 889–915.
- [190] A. Juris, V. Balzani, F. Barigelletti, S. Campagna, P. Belser, A. von Zelewsky, *Coord. Chem. Rev.* **1988**, *84*, 85–277.
- [191] C. B. Larsen, O. S. Wenger, *Chem. Eur. J.* **2018**, *24*, 2039–2058.
- [192] D. Rehm, A. Weller, *Isr. J. Chem.* **1970**, *8*, 259–271.
- [193] S. E. Braslavsky, *Pure Appl. Chem.* **2007**, *79*, 293–465.
- [194] D. A. Bohling, J. F. Evans, K. R. Mann, *Inorg. Chem.* **1982**, *21*, 3546–3551.
- [195] B. J. Coe, D. W. Thompson, C. T. Culbertson, J. R. Schoonover, T. J. Meyer, *Inorg. Chem.* **1995**, *34*, 3385–3395.
- [196] H. B. Ross, M. Boldaji, D. P. Rillema, C. B. Blanton, R. P. White, *Inorg. Chem.* **1989**, *28*, 1013–1321.
- [197] S. Otto, M. Grabolle, C. Förster, C. Kreitner, U. Resch-Genger, K. Heinze, *Angew. Chem. Int. Ed.* **2015**, *54*, 11572–11576.
- [198] S. Treiling, C. Wang, C. Förster, F. Reichenauer, J. Kalmbach, P. Boden, J. P. Harris, L. M. Carrella, E. Rentschler, U. Resch-Genger, C. Reber, M. Seitz, M. Gerhards, K. Heinze, *Angew. Chem. Int. Ed.* **2019**, *58*, 18075–18085.
- [199] P. Hohenberg, W. Kohn, *Phys. Rev. B* **136**, 1964, 864–871.
- [200] A. D. Becke, *J. Chem. Phys.* **1993**, *98*, 5648–5652.
- [201] Chengteh Lee, Weitao Yang, R. G. Parr, *Phys. Rev. B* **1988**, *37*, 785–789.
- [202] B. Miehlisch, A. Savin, H. Stoll, H. Preuss, *Chem. Phys. Lett.* **1989**, *157*, 200–206.
- [203] A. Schäfer, H. Horn, R. Ahlrichs, *J. Chem. Phys.* **1992**, *97*, 2571–2577.
- [204] A. Schäfer, C. Huber, R. Ahlrichs, *J. Chem. Phys.* **1994**, *100*, 5829–5835.
- [205] F. Neese, *Comput. Mol. Sci.* **2012**, *2*, 73–78.
- [206] F. Neese, *WIREs Comput. Mol. Sci.* **2018**, *8*, e1327.
- [207] F. Neese, F. Wennmohs, A. Hansen, U. Becker, *Chem. Phys.* **2009**, *356*, 98–109.
- [208] R. Izsák, F. Neese, *J. Chem. Phys.* **2011**, *135*, 144105-1–11.
- [209] D. A. Pantazis, X.-Y. Chen, C. R. Landis, F. Neese, *J. Chem. Theory Comput.* **2008**, *4*, 908–919.
- [210] S. Grimme, J. Antony, S. Ehrlich, H. Krieg, *J. Chem. Phys.* **2010**, *132*, 154104 1-19.
- [211] S. Grimme, S. Ehrlich, L. Goerigk, *J. Comput. Chem.* **2011**, *32*, 1456–1465.
- [212] S. Miertus, E. Scrocco, J. Tomasi, *Chem. Phys.* **1981**, *55*, 117–129.
- [213] V. Barone, M. Cossi, *J. Phys. Chem. A* **1998**, *102*, 1995–2001.
- [214] F. Neese, *Coord. Chem. Rev.* **2009**, *253*, 526–563.
- [215] F. Neese, *J. Biol. Inorg. Chem.* **2006**, *11*, 702–711.
- [216] F. Plasser, *TheoDORE. A package for theoretical density, orbital relaxation and exciton analysis*, <http://theodore-qc.sourceforge.net>.
- [217] F. Plasser, *J. Chem. Phys.* **2020**, *152*, 84108.
- [218] A. K. Pal, N. Zaccheroni, S. Campagna, G. S. Hanan, *Chem. Commun.* **2014**, *50*, 6846–6849.
- [219] A. K. Pal, C. Li, G. S. Hanan, E. Zysman-Colman, *Angew. Chem. Int. Ed.* **2018**, *57*, 8027–8031.

5. Results and discussion

All findings of this dissertation have been published/submitted as scientific articles in/to peer-reviewed chemistry journals or are in preparation for submission. These articles will be reprinted in the following with permission of the respective publishers.

Both the 2,6-bis(2-carboxypyridyl)pyridine (dcpp, Figure 12a, X = Y = C=O) ligand and the *N,N*-dimethyl-*N,N*-dipyridine-2-yl-pyridine-2,6-diamine (ddpd, ligand, Figure 12a, X = Y = N-CH₃) support the concept of high local symmetry. The bridges between the pyridine moieties enable a nearly 180° N-Ru-N bite angle that increases the ligand field splitting and destabilizes metal centered states. While in dcpp carbonyl bridges act as strong π -acceptors that stabilize the metal-to-ligand charge transfer MLCT excited states, in ddpd σ -donating methylamine bridges destabilize the metal centered states. The novel 6,2''-carboxylpyridyl-2,2'-methylaminepyridyl-pyridine (cpmp, Figure 12a, X = N-CH₃, Y = C=O) ligand combines both types of bridges in a single ligand. Complexes bearing this ligand are capable of an intraligand push-pull effect. Besides the increased stabilization of the MLCT state in respect of the ³T state additional ILCT and LL'CT excitations are expected to be available.

The ruthenium(II) push-pull complexes [Ru(cpmp)₂]²⁺ and [Ru(cpmp)(ddpd)]²⁺ that are presented in section 6 "Green-Light Activation of Push-Pull Ruthenium(II) Complexes" (pp. 41) show phosphorescence upon green light irradiation. The differences between the homoleptic complex bearing two carbonyl groups and two methylamine groups and the heteroleptic complex bearing a single carbonyl group and three methylamine groups are evident by comparing the optical and electrochemical properties. The presence of two π -accepting carbonyl groups in [Ru(cpmp)₂]²⁺ leads to a red-shift of the MLCT absorption maximum and higher Ru(III/II) oxidation potential compared to [Ru(cpmp)(ddpd)]²⁺ which indicates a more stabilized MLCT state. For the homoleptic complex two ligand centered reduction waves were observed while the heteroleptic complex shows a single reduction wave due to the lack of a second carbonyl group. Based on TD-DFT calculations the low-energy absorption bands of both complexes were assigned to MLCT transitions which rules out the presence of low lying ILCT or LL'CT states.

IR-spectroelectrochemical oxidation leads to a 20 cm⁻¹ high energy shift which indicates a weaker π -back-bonding in the oxidized complex. Reduction results in a complete bleach of the C=O band for the heteroleptic complex and a decrease to half intensity for the homoleptic complex as a result of the presence of a second carbonyl group. This finding proves the ligand centered character of the reduction. The phosphorescence quantum yield was determined to be 1.3 % for [Ru(cpmp)₂]²⁺ and 0.04% for [Ru(cpmp)(ddpd)]²⁺, respectively. The 33-fold higher quantum yield for the homoleptic complex corresponds to the MLCT excited state lifetime of 477 ns for [Ru(cpmp)₂]²⁺ and 56 ns for [Ru(cpmp)(ddpd)]²⁺, respectively, that have been estimated by Vis-pump-Vis-probe spectroscopy. This trend also fits to the even higher MLCT lifetime and quantum yield of [Ru(dcpp)₂]²⁺.^[62] Because the local symmetry is independent of the type of bridging group, the ligand field splitting is expected to solely depend on the electronic structure of the ligands. The different excited state lifetimes and quantum yields result from different energy barriers for relaxation pathways. DFT calculations reveal a lower ³MLCT-³MC energy difference in [Ru(cpmp)₂]²⁺ which would imply facilitated relaxation in this complex that is not observed. The difference is the location of distortion axis in the ³T state. In [Ru(cpmp)₂]²⁺ the less flexible cpmp ligand is necessarily involved leading to a stronger distortion of the carbonyl group in this complex. In contrast the distortion in [Ru(cpmp)(ddpd)]²⁺ occurs within the ddpd ligand rather symmetrically distributed over both terminal pyridine moieties inducing less distortion. This results in a steeper potential energy well along the distortion axis for [Ru(cpmp)₂]²⁺ than for [Ru(cpmp)(ddpd)]²⁺. The ³T minima are isoenergetic,

5. Results and Discussion

while the crossing point of the 3T state with the 1A ground state is higher $[\text{Ru}(\text{cpmp})_2]^{2+}$ than for $[\text{Ru}(\text{cpmp})(\text{ddpd})]^{2+}$, explaining the different excited state lifetimes.

Nevertheless, $[\text{Ru}(\text{cpmp})_2]^{2+}$ and $[\text{Ru}(\text{cpmp})(\text{ddpd})]^{2+}$ have been successfully applied as photoredox catalysts for a thiol-ene click reaction between allyl alcohol as olefin component and *N*-Boc cysteine methyl ester as thiol component using *p*-toluidine as redox mediator. The yields of 56 % and 18 %, respectively, after 3 hours again correspond to the lower excited state lifetime of $[\text{Ru}(\text{cpmp})(\text{ddpd})]^{2+}$. The yield using $[\text{Ru}(\text{bpy})_3]^{2+}$ as catalyst under the same conditions is 20 %.

Following the same concept of push-pull systems bearing the asymmetric cpmp ligand, the homologue iron(II) complexes $[\text{Fe}(\text{cpmp})_2]^{2+}$ and $[\text{Fe}(\text{cpmp})(\text{ddpd})]^{2+}$ are presented in section 7 "Understanding Excited State Kinetics in Asymmetric Iron(II) Push-Pull Complexes" (pp. 111).

According to the primogenic effect the ligand field splitting of iron(II) complexes is lower than that of ruthenium(II) complexes making it more challenging to design iron complexes with sufficient excited state lifetime for emission. As for the homologue ruthenium(II) complexes, the Fe(III/II) oxidation potential is higher for the homoleptic complex and the homoleptic complex shows two ligand centered reduction waves while the heteroleptic complex shows a single reduction wave due to the lack of a second carbonyl group. The assignment was proved by IR spectroelectrochemistry showing a shift of the C=O stretching vibration to higher energy due to the weakened π -back bonding upon oxidation and a partial bleach of the band upon reduction resulting from decrease of bond order in one carbonyl group.

The spin state of the ground state was proved to be low-spin by EPR, NMR and X-ray absorption spectroscopy for $[\text{Fe}(\text{cpmp})_2]^{2+}$ and by NMR spectroscopy for $[\text{Fe}(\text{cpmp})(\text{ddpd})]^{2+}$. Unfortunately, the ligand field strength of the used ligand is too weak to destabilize the metal centered states enough to prevent their population. Therefore, both complexes are non-luminescent. Moreover, the heteroleptic complex undergoes fast ligand exchange in solution forming a mixture of $[\text{Fe}(\text{cpmp})_2]^{2+}$, $[\text{Fe}(\text{cpmp})(\text{ddpd})]^{2+}$, and $[\text{Fe}(\text{ddpd})_2]^{2+}$. This ligand exchange makes it challenging to isolate the complex and perform spectroscopy. For this reason time-consuming methods are carried out solely on the more stable homoleptic complex.

The red-shift of the MLCT absorption bands indicates a stabilization of the MLCT states compared to the symmetric push-pull complex $[\text{Fe}(\text{dcpp})(\text{ddpd})]^{2+}$. The excited state lifetime of the homoleptic complex $[\text{Fe}(\text{cpmp})_2]^{2+}$ was estimated by Vis-pump-Vis-probe and Vis-pump-IR-probe spectroscopy to be around 500 ps. For both spectroscopic methods the characteristic MLCT excited state absorption properties have been simulated using UV/Vis and IR spectroelectrochemistry. The lack of these characteristic bands in the transient spectra indicated a MLCT lifetime below the detection time resolution of 100 fs.

To gain deeper insight into the excited state ordering, DFT, TD-DFT and molecular dynamic calculations have been conducted on $[\text{Fe}(\text{cpmp})_2]^{2+}$. Like for the ruthenium(II) complexes the $^1\text{ILCT}$ or $^1\text{LL}'\text{CT}$ transitions appear at higher energy than the MLCT transitions. Again the corresponding triplet states $^3\text{ILCT}$ and $^3\text{LL}'\text{CT}$ are too high-energetic to be populated. DFT calculations predict the 5T state as lowest excited state and the 3T state between the $^3\text{MLCT}$ and 5T state. According to molecular dynamics calculations the 3T state is populated from the $^1\text{MLCT}$ and the $^3\text{MLCT}$ states within 80 fs and 390 fs, respectively. No direct $^3T \rightarrow ^1A$ relaxation was found in the dynamics calculations. The $^3T \rightarrow ^5T$ ISC was not included in these calculations. The system follows the usual excited state deactivation cascade: $^3\text{MLCT} \rightarrow ^3T \rightarrow ^5T \rightarrow ^1A$ with time constants of 390 fs for the $^3\text{MLCT} \rightarrow ^3T$ relaxation and around 500 ps for the 5T state.

The iron(III) complex $[\text{Fe}(\text{cpmp})_2]^{3+}$ has been prepared electrochemically as well as by chemical oxidation with $[\text{NH}_4]_2[\text{Ce}(\text{NO}_3)_6]$. It shows a low-energy absorption band at 962 nm. Its low-spin ground state is proved by EPR and X-ray spectroscopy. In spite of the high ligand

field strength of both, the cpmp and the ddpd ligand, and the increased push-pull effect no emission was observed for neither the iron(II) complexes $[\text{Fe}(\text{cpmp})_2]^{2+}$ and $[\text{Fe}(\text{cpmp})(\text{ddpd})]^{2+}$, nor the iron(III) complex $[\text{Fe}(\text{cpmp})_2]^{2+}$ at room temperature and in frozen solution at 77 K.

As cyclometalation was predicted to stabilize the MLCT state and enable an increased excited MLCT lifetime, probably sufficiently long for photochemical applications,^[136–139] $[\text{Fe}(\text{pbpy})(\text{tpy})]^+$ (Figure 12c) was synthesized as first cyclometallated iron(II) complex by Jakob Steube from the group of Prof. Dr. Matthias Bauer at the University of Paderborn. Section 8 “Excited-State Kinetics of an Air-Stable Cyclometalated Iron(II) Complex” (pp. 181) describes the ground and excited state characteristics of this complex.

The characteristic MLCT excited state absorption properties have been simulated using UV/Vis spectroelectrochemistry to interpret the Vis-pump-Vis-probe spectroscopy. From this timeresolved method a $^3\text{MLCT}$ lifetime of 800 fs was found which is a factor of 5.5 higher compared to $[\text{Fe}(\text{tpy})_2]^{2+}$ (145 fs). This increased lifetime shows the success of the concept of strongly σ -donating cyclometalating ligands. The excited state deactivation cascade follows a $^1\text{MLCT} \rightarrow ^3\text{MLCT} \rightarrow ^3\text{MC} \rightarrow ^1\text{A}$ scheme without population of the ^5T state. The respective time constants are 800 fs for the $^3\text{MLCT} \rightarrow ^3\text{MC}$ IC and 12 ps for the $^3\text{MC} \rightarrow ^1\text{A}$ relaxation. As this complex is non-emissive, too, one cyclometalating position in a five-membered-ring chelate ligand is insufficient for a stabilization of the MLCT state below the metal centered states.

Inspired by one of the first phosphorescent $3d^6$ metal complexes $[\text{Co}(\text{dgpy})_2]^{3+}$ ^[219] (dgpy: 2,6-diguanidylpyridine), $[\text{Fe}(\text{dgpy})_2]^{2+}$ (Figure 12d) was synthesized to investigate the ligand field strength of the dgpy ligand. The results are presented in section 9 “Panchromatic Absorption and Oxidation of an Iron(II) Spin Crossover Complex” (pp. 231).

A complex bearing two tridentate six-membered-ring chelate ligands can generally perform *mer*, *cis-fac* and *trans-fac* isomers. The high flexibility of dgpy allows for $[\text{Fe}(\text{dgpy})_2]^{2+}$ the presence of the *mer* and the *cis-fac* isomer in solution while the *trans-fac* isomer is absent. While the *cis-fac* isomer has a high-spin ground state according to DFT calculations because of reduced bite angles in this coordination mode, the *meridional* isomer features a low-spin ground state. The comparably weak ligand field strength of dgpy results in a ligand field splitting for *mer*- $[\text{Fe}(\text{dgpy})_2]^{2+}$ in the vicinity to Δ_{c} and spin crossover behavior for this isomer. The thermodynamics have been investigated in solution by temperature dependent UV/Vis and ^1H NMR spectroscopy as well as in the solid state by temperature dependent SQUID and Mößbauer measurements. The optical changes can be observed by UV/Vis spectroscopy. The increase of the MLCT band at 582 nm during cooling is well reproduced by TD-DFT calculations. From the temperature dependent ^1H NMR data a high-spin/low-spin exchange constant k_{hl} was estimated around $(7.2\text{--}30) \times 10^5 \text{ s}^{-1}$, a range typically observed for SCO complexes. Taking the different spin states of the *meridional* isomer into account the *hs-mer*:*ls-mer*:*hs-cis-fac* ratio in solution at room temperature is estimated to be 61:20:19 from temperature dependent ^1H NMR spectroscopy. In solution and in the solid state the enthalpy change is estimated to be around 30 kJ mol^{-1} while the entropy change is around $110 \text{ J K}^{-1} \text{ mol}^{-1}$ in solution and around $80 \text{ J K}^{-1} \text{ mol}^{-1}$ in the solid state, respectively. This difference in entropy change can be explained by less degrees of freedom in the solid state and becomes manifest in the spin-transition temperature $T_{1/2}$ of 270 K in solution and 295 K in the solid state, respectively.

The different isomers of $[\text{Fe}(\text{dgpy})_2]^{2+}$ are observable by cyclic voltammetry, too. Two reversible Fe(III/II) oxidation waves appear at -0.65 V and -0.37 V vs. FcH/FcH^+ in a 8:2 ratio that can be assigned to the *meridional* and the *cis-facial* isomer, respectively. The comparably low oxidation potential results from the high σ -donating ability of the dgpy ligand. Therefore, the complex can be oxidized using ferrocene. The oxidation is accompanied by a blue shift of

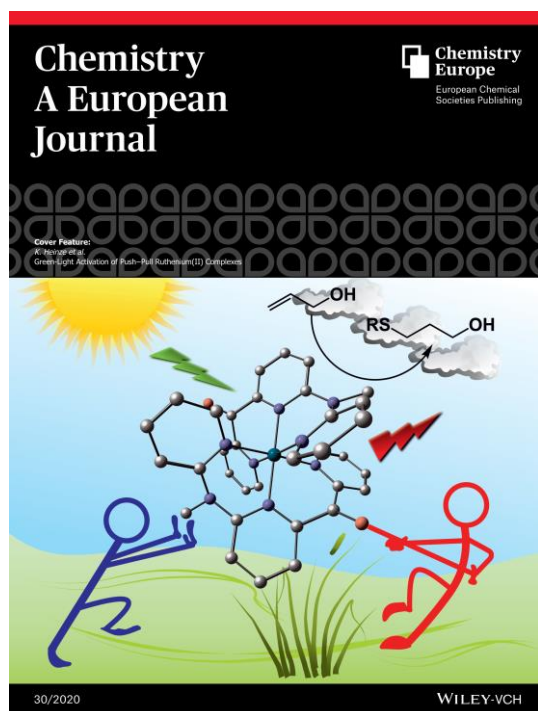
5. Results and Discussion

the LMCT absorption compared to the MLCT bands of $[\text{Fe}(\text{dgpy})_2]^{2+}$. The $[\text{Fe}(\text{dgpy})_2]^{3+}$ complex is confirmed to be a low-spin complex state without SCO behavior by NMR and EPR spectroscopy. The simultaneous observation of ^1H NMR resonances for the iron(II) and iron(III) complexes after addition of 0.5 equivalents of ferrocene indicates a rather slow electron self-exchange.

The room temperature solution containing high-spin *mer*- $[\text{Fe}(\text{dgpy})_2]^{2+}$, low-spin *mer*- $[\text{Fe}(\text{dgpy})_2]^{2+}$ and high-spin *cis-fac*- $[\text{Fe}(\text{dgpy})_2]^{2+}$ exhibits panchromatic $^1\text{MLCT}/^5\text{MLCT}$ absorption bands in the visible spectral region. As a result of high-energy MLCT states and a comparably low ligand field strength in the *meridional* coordination mode, MC excited states are lower in energy than the $^1/3\text{MLCT}$ states preventing luminescence. The ligand field strength in the oxidized complex is higher which becomes manifest in the exclusively observation of the low-spin *mer*- $[\text{Fe}(\text{dgpy})_2]^{3+}$ complex. However, the MC excited states of *mer*- $[\text{Fe}(\text{dgpy})_2]^{3+}$ are still lower in energy than the CT states preventing fluorescence from the $^2\text{LMCT}$ states. Although the dgpy ligand leads to amazing $^2\text{LMCT}$ fluorescence in the *mer*- $[\text{Co}(\text{dgpy})_2]^{3+}$ complex its ligand field strength is insufficient for a comparable performance in iron(II) and iron(III) complexes. Moreover, its high flexibility enables different isomers making it challenging to isolate a single isomer.

6. Green-Light Activation of Push-Pull Ruthenium(II) Complexes

Johannes Moll, Cui Wang, Ayla Pöpcke, Christoph Förster, Ute Resch-Genger, Stefan Lochbrunner and Katja Heinze



Chem. Eur. J. **2020**, *26*, 6820–6832.

The push-pull ruthenium(II) complexes $[\text{Ru}(\text{cpmp})_2]^{2+}$ (cpmp: 6,2''-carboxylpyridyl-2,2'-methylaminepyridyl-pyridine) and $[\text{Ru}(\text{cpmp})(\text{ddpd})]^{2+}$ (ddpd: *N,N*-dimethyl-*N,N*-dipyridin-2-ylpyridine-2,6-diamine) bearing the asymmetric six-membered ring chelate ligand cpmp were synthesized. The phosphorescence quantum yield of 1.3 % and 0.04 %, respectively, and the $^3\text{MLCT}$ lifetime of 477 and 56 ns, respectively, is related to the number of carbonyl groups in the complex. Both complexes were successfully applied in a photocatalytic radical thiol-ene click reaction.

Author Contributions

Johannes Moll synthesized and characterized the cpmp ligand and the ruthenium complexes presented in this manuscript, conducted NMR, UV-VIS, IR and emission spectroscopic experiments and carried out the electrochemical and spectroelectrochemical experiments and performed all DFT calculations. Ayla Kruse (geb. Pöpcke) and Prof. Stefan Lochbrunner from the University of Rostock performed UV/Vis pump-probe spectroscopy. Cui Wang and Dr. Ute Resch-Genger from the Federal Institute for Materials Research and Testing (BAM) in Berlin determined the emission quantum yields and excited state lifetimes. The crystal structure was solved and refined by Dr. Christoph Förster from the Johannes Gutenberg University in Mainz. The manuscript was written by Johannes Moll and Prof. Katja Heinze.

Supporting Information for this article is found at pp. 57.

"Moll, J.; Wang, C.; Pöpcke, A.; Förster, C.; Resch-Genger, U.; Lochbrunner, S.; Heinze, K. *Chem. Eur. J.* **2020**, *26*, 6820–6832." Open Access publication.

6. Green-Light Activation of Push–Pull Ruthenium(II) Complexes


 Photochemistry | *Very Important Paper*

 Green-Light Activation of Push–Pull Ruthenium(II) Complexes

 Johannes Moll,^[a] Cui Wang,^[b, c] Ayla Pöpcke,^[d] Christoph Förster,^[a] Ute Resch-Genger,^[b] Stefan Lochbrunner,^[d] and Katja Heinze^{*[a]}


Abstract: Synthesis, characterization, electrochemistry, and photophysics of homo- and heteroleptic ruthenium(II) complexes $[\text{Ru}(\text{cpmp})_2]^{2+}$ (2^{2+}) and $[\text{Ru}(\text{cpmp})(\text{ddpd})]^{2+}$ (3^{2+}) bearing the tridentate ligands 6,2'-carboxypyridyl-2,2'-methylamine-pyridyl-pyridine (cpmp) and *N,N'*-dimethyl-*N,N'*-dipyridin-2-ylpyridine-2,6-diamine (ddpd) are reported. The complexes possess one (3^{2+}) or two (2^{2+}) electron-deficient dipyridyl ketone fragments as electron-accepting sites enabling intraligand charge transfer (ILCT), ligand-to-ligand charge transfer (LL'CT) and low-energy metal-to-ligand charge transfer (MLCT) absorptions. The latter peak around 544 nm (green light). Complex 2^{2+} shows $^3\text{MLCT}$ phosphor-

escence in the red to near-infrared spectral region at room temperature in deaerated acetonitrile solution with an emission quantum yield of 1.3% and a $^3\text{MLCT}$ lifetime of 477 ns, whereas 3^{2+} is much less luminescent. This different behavior is ascribed to the energy gap law and the shape of the parasitic excited ^3MC state potential energy surface. This study highlights the importance of the excited-state energies and geometries for the actual excited-state dynamics. Aromatic and aliphatic amines reductively quench the excited state of 2^{2+} paving the way to photocatalytic applications using low-energy green light as exemplified with the green-light-sensitized thiol–ene click reaction.

Introduction

Polypyridyl ruthenium(II) complexes (low spin d^6 electron configuration)^[1–6] often display phosphorescence from triplet metal-to-ligand charge transfer ($^3\text{MLCT}$) states. Due to the comparably high ligand field splitting imposed by the metal ion and the ligands, non-radiative relaxation via thermal population of metal-centered states (^3MC) can be retarded.^[2] The prototypical complex $[\text{Ru}(\text{bpy})_3]^{2+}$ (bpy = 2,2'-bipyridine; Scheme 1) and its photophysical properties have been thoroughly investigated experimentally and theoretically.^[2–14]

$[\text{Ru}(\text{bpy})_3]^{2+}$ shows high phosphorescence quantum yields of 6.3% (H_2O),^[15] 9.5% (CH_3CN) at 298 K^[15,16] and 38% (methanol/ethanol glass) at 77 K,^[5,9,17] respectively. The favorable photophysical properties (such as high absorbance in the visible spectral region, high $^3\text{MLCT}$ lifetimes of 620 ns (H_2O)^[5,18] and 850–1100 ns (CH_3CN)^[9,18] at 298 K, and high quantum yields)

[a] J. Moll, Dr. C. Förster, Prof. Dr. K. Heinze
Department of Chemistry, Johannes Gutenberg University of Mainz
Duesbergweg 10–14, 55128 Mainz (Germany)
E-mail: katja.heinze@uni-mainz.de
Homepage: www.ak-heinze.chemie.uni-mainz.de

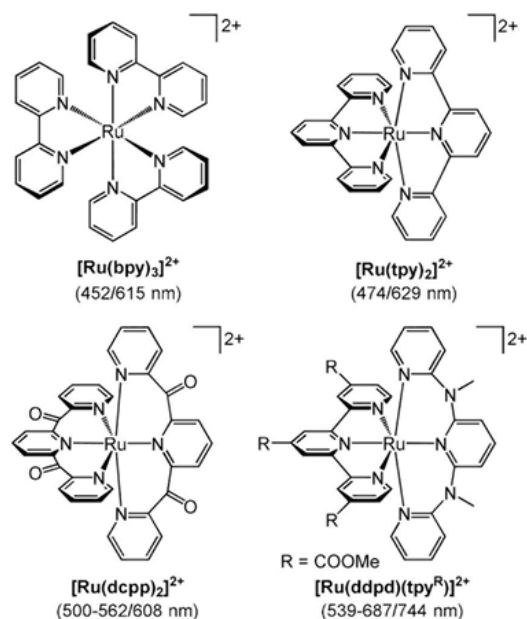
[b] C. Wang, Dr. U. Resch-Genger
Division 1.2 Biophotonics
Federal Institute for Materials Research and Testing (BAM)
Richard Willstätter-Straße 11, 12489 Berlin (Germany)

[c] C. Wang
Institut für Chemie und Biochemie, Freie Universität Berlin
Arnimallee 22, 14195 Berlin (Germany)

[d] A. Pöpcke, Prof. Dr. S. Lochbrunner
Institute for Physics and Department of Life, Light and Matter,
University of Rostock, 18051 Rostock (Germany)

Supporting information and the ORCID identification number(s) for the author(s) of this article can be found under:
<https://doi.org/10.1002/chem.202000871>.

© 2020 The Authors. Published by Wiley-VCH Verlag GmbH & Co. KGaA.
This is an open access article under the terms of the Creative Commons Attribution License, which permits use, distribution and reproduction in any medium, provided the original work is properly cited.



Scheme 1. Benchmark ruthenium(II) complexes and their absorption/ emission band maxima.

enable the application of $[\text{Ru}(\text{bpy})_3]^{2+}$ and its analogues as chromophores in dye sensitized solar cells, in light emitting electrochemical cells and as photosensitizers.^[19–29] In fact, the majority of photosensitized redox reactions is still performed using $[\text{Ru}(\text{bpy})_3]^{2+}$, which is further enabled by its favorable redox properties and its redox stability.

Despite the favorable quantum yields and lifetimes, blue light is required for efficient excitation. Further challenges of $[\text{Ru}(\text{bpy})_3]^{2+}$ originate from the bidentate nature of the bpy ligands. The Δ/Λ chirality of the complex^[30–37] can lead to diastereomeric di- or multinuclear complexes with sites of varying stereochemistry. Two differently substituted bpy ligands can form diastereomers even for mononuclear complexes $[\text{Ru}(\text{bpy})(\text{bpy}^R)(\text{bpy}^R)]^{2+}$. Finally, bidentate ligands are comparably photolabile enabling photoisomerization of the complex or photosubstitution of the ligands.^[14a,38–40] Replacing bpy by the tridentate ligand 2,2':6'2''-terpyridine (tpy) yields achiral, comparably photostable $[\text{Ru}(\text{tpy})_2]^{2+}$ complexes (Scheme 1).^[41] However, $[\text{Ru}(\text{tpy})_2]^{2+}$ is essentially non-phosphorescent at room temperature. This is due to the much lower ligand field splitting of this complex. The weaker ligand field splitting imposed by the tpy ligands significantly lowers the energy of ^3MC states leading to efficient non-radiative relaxation via these distorted ^3MC states.^[1,2,30,37,42–45]

Eliminating thermal deactivation via the classical Jahn–Teller type and other distorted ^3MC states is a key to higher phosphorescence quantum yields and longer excited-state lifetimes.^[14] Complementary concepts to increase the energy gap between the emissive $^3\text{MLCT}$ and the deactivating ^3MC state have been devised, namely i) shifting the ^3MC states to higher energy by an increase of the ligand field splitting with six-membered ring chelate ligands allowing 180° N–Ru–N bond angles and hence optimal Ru–N orbital overlap and with strong σ -donating/ π -accepting ligands and ii) lowering the energy of the $^3\text{MLCT}$ state with electron-deficient pyridine ligands. Examples successfully employing these concepts are $[\text{Ru}(\text{dcpp})_2]^{2+}$ (dcpp = 2,6-bis(2-carboxypyridyl)pyridine)^[46] and the heteroleptic complex $[\text{Ru}(\text{ddpd})(\text{tpy}^R)]^{2+}$ (ddpd = *N,N'*-dimethyl-*N,N'*-dipyridin-2-ylpyridine-2,6-diamine) (Scheme 1).^[30,37] $[\text{Ru}(\text{dcpp})_2]^{2+}$ with accepting dipyrindyl ketone moieties and six-membered chelate rings shows a very high phosphorescence quantum yield of 30% in CH_3CN at 298 K.^[46] $[\text{Ru}(\text{ddpd})(\text{tpy}^R)]^{2+}$ with an electron-donating ddpd ligand with six-membered chelate rings and an electron-deficient ester substituted tpy^R ligand has a phosphorescence quantum yield of 1.1% in CH_3CN .^[30,37] On the other hand, cyclometalating tridentate ligands $\text{N}^A\text{C}^A\text{N}$ or $\text{C}^A\text{N}^A\text{N}$ in ruthenium(II) complexes with five-membered chelate rings were unsuccessful in improving quantum yield and lifetime. This is due to an unfavorable distortion of their excited $^3\text{MLCT}$ states and the presence of low-energy $^3\text{LL}'\text{CT}$ states composed of orthogonal tridentate L and L' ligands resulting in symmetry-forbidden and hence inefficient radiative transitions.^[47–52]

A further strategy to increase the $^3\text{MLCT}$ lifetime beyond expanding the ^3MC – $^3\text{MLCT}$ gap and increasing the barrier is to retard the ^3MC to ground state (^1GS) decay by increasing the energy of the $^3\text{MC}/^1\text{GS}$ crossing point.^[14b] Although the ^3MC

state can be still thermally populated in this scenario, this would not contribute to the decay to the ground state provided that the crossing point is at high enough energy.^[9] Yet, such effects arising from the energies of surface crossing points are difficult to design as the shapes of potential energy surfaces have to be known and modified in addition to the minimum energies. Clearly, the rigidity of the ligands plays a significant role in the excited-state distortions.

Herein, we introduce a novel tridentate mixed donor/acceptor ligand cpmp (cpmp = 6,2''-carboxypyridyl-2,2'-methylamine-pyridyl-pyridine). This ligand enables six-membered chelate rings combining the concepts of increasing the ^3MC energy via a strong ligand field and of lowering the $^3\text{MLCT}$ energy based on the electron-deficient dipyrindyl ketone fragment. In addition to the low-energy MLCT states, the push–pull ligand cpmp can provide intra-ligand transitions ($^1,^3\text{ILCT}$), which might have a low energy as well. Furthermore, in contrast to complexes with merely five-membered chelate rings of tridentate ligands (tpy type) and hence planar ligands with orthogonal orientation, the ligand cpmp can enable symmetry-allowed transitions *between* the non-orthogonal twisted tridentate ligands ($^1,^3\text{LL}'\text{CT}$). This can in principle lead to emission from $^3\text{LL}'\text{CT}$ states depending on their energy relative to the $^3\text{MLCT}$ energy. In fact, the angle between planes of the central pyridines is only around 10 – 20° in $[\text{M}(\text{dcpp})_2]^{2+}$, $[\text{M}(\text{dcpp})(\text{ddpd})]^{2+}$ and $[\text{M}(\text{ddpd})_2]^{2+}$ complexes,^[46,53–56] instead of the approximate 90° angle in $[\text{M}(\text{tpy})_2]^{2+}$ -type complexes.

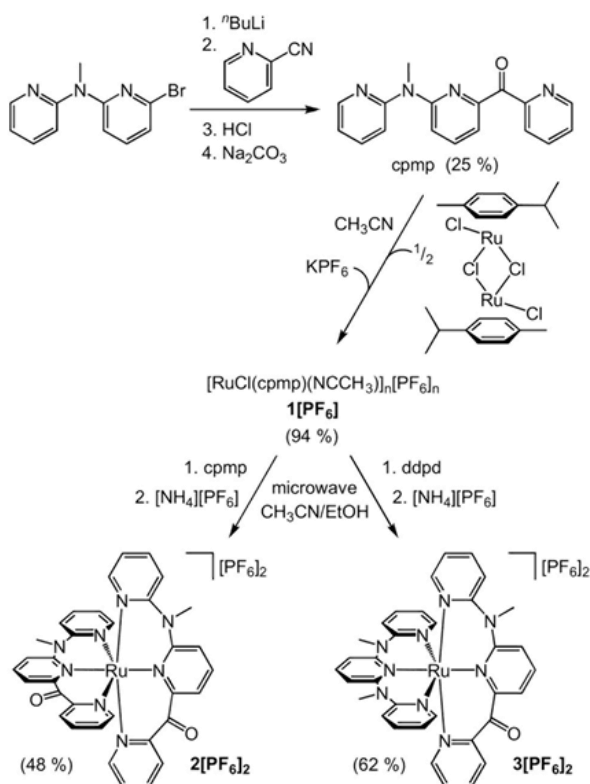
We report the syntheses, structure, electrochemical as well as steady-state and time-resolved photophysical properties of the novel homoleptic $[\text{Ru}(\text{cpmp})_2][\text{PF}_6]_2$ (**2** $[\text{PF}_6]_2$) and heteroleptic ruthenium(II) complex $[\text{Ru}(\text{cpmp})(\text{ddpd})][\text{PF}_6]_2$ (**3** $[\text{PF}_6]_2$). We discuss the effects of ligand symmetry on the excited-state types, their energies, their geometries and finally their excited-state dynamics. The relevant excited states will be characterized by DFT and time-dependent (TD-) DFT calculations to gain a deeper understanding of the excited-state dynamics. The new ruthenium(II) complexes **2** $[\text{PF}_6]_2$ and **3** $[\text{PF}_6]_2$ are applied in a light-sensitized thiol–ene click reaction using low-energy green light for excitation.

Results and Discussion

Synthesis and ground-state structures

The push–pull ligand cpmp is prepared by lithiating 6-bromo-*N*-methyl-*N*-(pyridin-2-yl)pyridyl-2-amine^[57] with *n*BuLi and quenching with 2-cyanopyridine in moderate yields as yellow oil (Scheme 2; Supporting Information, Figures S1–S10).

Thermal ligand exchange with $[(\text{RuCl}(\text{p-cymene}))_2(\mu\text{-Cl})_2]^{58}$ and counter ion exchange with KPF_6 in acetonitrile gives the red-purple cpmp complex $[\text{RuCl}(\text{cpmp})(\text{NCCCH}_3)]_n[\text{PF}_6]_n$ **1** $[\text{PF}_6]$ in very good yields (Supporting Information, Figures S11–S19). The coordinated CH_3CN ligand in **1** $[\text{PF}_6]$ displays a broad band for the CN stretching vibration at 2275 cm^{-1} in the IR spectrum (KBr disk). ^1H and ^{13}C NMR resonances for the CH_3 groups of the CH_3CN ligands in the NMR spectra agree with a single CH_3CN ligand coordinated to ruthenium. During the NMR ex-



Scheme 2. Synthesis of the ligand cpmp and its ruthenium(II) complexes **1**[PF₆]₂, **2**[PF₆]₂ and **3**[PF₆]₂.

periments, the coordinated CH₃CN ligand does not exchange with the solvent CD₃CN (Supporting Information, Figures S11–S15). The chlorido ligand is observed in the electrospray ionization (ESI) mass spectrum and the [PF₆][−] counter ion in the ³¹P NMR and IR spectra. The combined data are compatible with a dimeric arrangement (*n* = 2) with bridging chlorido ligands.

Replacing the chlorido and acetonitrile ligands in **1**[PF₆]₂ by a further tridentate cpmp or ddpd ligand requires activation by microwave irradiation. Using cpmp and ddpd, the respective homo- and heteroleptic complexes **2**²⁺ and **3**²⁺ form. After counter ion exchange with [NH₄][PF₆], **2**[PF₆]₂ and **3**[PF₆]₂ are obtained as purple crystals in good to moderate yields (Supporting Information, Figures S20–S28, S29–S38). Obviously, **1**[PF₆]₂ is a convenient precursor for homo- and heteroleptic cpmp ruthenium(II) complexes. Further heteroleptic ruthenium(II) complexes with cpmp should be accessible via this general route as well employing other tridentate ligands such as tpy, H₂-tpda,^[55,59] R₂-tpda,^[55] ddpd-NH₂^[30] or dcpp.^[46,54,60]

The compositions of **2**[PF₆]₂ and **3**[PF₆]₂ are confirmed by (high-resolution) ESI mass spectrometry (Supporting Information, Figures S26, S36) and elemental analyses. Multinuclear and correlation NMR spectroscopic data suggest a single isomer being present in solution as only a single set of ¹H and ¹³C NMR resonances is observed for both cations (Supporting Information, Figures S20–S24, S29–S34). Although the flexible ddpd ligand can enable a facial coordination,^[53] dcpp and

cpmp ligands are quite rigid at the dipyrindyl ketone units and consequently a meridional coordination of the tridentate ligands is very likely in both cases. This is also consistent with the NMR data.

The geometric structure of **3**²⁺ with meridional coordination was experimentally confirmed by X-ray diffraction analysis of a single crystal of **3**[PF₆]₂ (Figure 1). The unit cell of **3**[PF₆]₂ contains two independent cations **3A**²⁺ and **3B**²⁺ (Table 1). Furthermore, the geometries of both dications **2**²⁺ and **3**²⁺ were calculated by DFT methods (Figure 1, Table 1; CPCMC(acetonitrile)-B3LYP-D3BJ-ZORA/old-TZVP). In all cases, a nearly perfect [RuN₆] octahedral coordination geometry is found with Ru–N bond lengths of 2.05 to 2.08 Å for the terminal pyridine rings of each ligand and slightly shorter Ru–N bonds for the central pyridine N atoms of each ligand (Table 1) as typically observed for [M(ddpd)₂]²⁺, [M(dcpp)₂]²⁺ or [M(dcpp)(ddpd)]²⁺ complexes.^[46,53–56] The N–Ru–N bond angles are very close to 90° for the dipyrindyl ketone moieties and slightly smaller for the

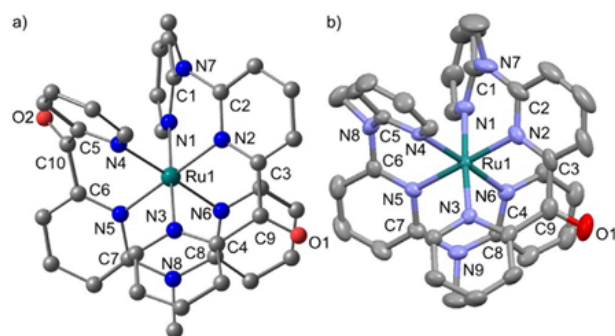


Figure 1. a) Molecular structure of **2**²⁺ determined by DFT geometry optimization and b) **3A**²⁺ determined by single crystal XRD, ellipsoids set at 50% probability. Hydrogen atoms are omitted for clarity.

Table 1. Selected bond lengths [Å], angles [°], planarization PL [%] and continuous shape parameter *S*(OC-6)^[61] of **2**²⁺ and **3**²⁺ from XRD analysis (as PF₆[−] salt) and by DFT calculations.

	2 ²⁺ (DFT)	3 ²⁺ (DFT)	3A ²⁺ (XRD)	3B ²⁺ (XRD)
Ru1–N1	2.080	2.081	2.085(3)	2.069(4)
Ru1–N2	2.048	2.047	2.023(3)	2.040(4)
Ru1–N3	2.072	2.071	2.045(3)	2.064(3)
Ru1–N4	2.081	2.077	2.061(3)	2.077(3)
Ru1–N5	2.049	2.054	2.044(3)	2.036(3)
Ru1–N6	2.072	2.076	2.062(3)	2.063(3)
N1–Ru1–N2	87.73	87.69	87.06(13)	87.54(15)
N2–Ru1–N3	90.23	90.26	90.16(13)	89.75(14)
N4–Ru1–N5	90.22	88.42	87.94(13)	87.62(14)
N5–Ru1–N6	87.74	88.39	87.91(14)	88.66(13)
PL(N7)	87.4	87.3	88.9	86.7
PL(N8)	87.3	86.8	87.0	84.1
PL(N9)		86.8	88.9	87.6
PL(C9)	97.8	97.7	97.8	97.5
PL(C10)	97.8			
<i>S</i> (OC-6)	0.04	0.09	0.06	0.08
Ru1...F1			4.176	4.270
Ru1...F2			4.322	–
Ru1...N1 (CH ₃ CN)			5.267	5.137
Ru1...O1 (neighboring molecule)			4.655	4.822

more flexible dipyridyl methyl amine moieties of the cpmp and ddpd ligands. The shape parameter $S(\text{OC-6})^{[61]}$ quantifying the deviation from an ideal octahedron is close to zero, corroborating the high local $[\text{RuN}_6]$ symmetry in all cases (Table 1) as expected for a metal ion with low-spin d^6 electron configuration. The steric strain, as measured from the pyramidalization of the bridging nitrogen atoms, inversely correlates to the degree of planarization $\text{PL}\% = 100 \times [\Sigma(X-N-Y) - 3 \times 109.5^\circ] / [3 \times 120.0^\circ - 3 \times 109.5^\circ]$. Expectedly, the carbonyl carbon atom is coordinated in an essentially planar fashion while the bridging nitrogen atom is more pyramidalized (Table 1).

In the solid state, the second coordination sphere of 3A^{2+} and 3B^{2+} is composed of hexafluorophosphate ions, co-crystallized acetonitrile and the carbonyl group of a neighboring complex with closest contacts of $\text{Ru} \cdots [\text{F}(\text{PF}_5)]^-$, $\text{Ru} \cdots \text{N}(\text{CCH}_3)$ and $\text{Ru} \cdots \text{O}$ ranging from 4.18 to 5.27 Å (3A^{2+}) and 4.27 to 5.14 Å (3B^{2+}) (Table 1).

In the IR spectra of $2[\text{PF}_6]_2$ and $3[\text{PF}_6]_2$ (Supporting Information, Figures S27, S37), the characteristic PF stretching vibrations indicate the successful counter ion exchange. This is also consistent with the ^{31}P NMR spectra of $1[\text{PF}_6]$, $2[\text{PF}_6]_2$ and $3[\text{PF}_6]_2$ which show the typical resonance of $[\text{PF}_6]^-$ (Supporting Information, Figures S16, S25, S35).

In the solid state, the IR absorption band of the C=O stretching vibration of the cpmp ligand is found at 1679 cm^{-1} and that of 1^+ at 1672 cm^{-1} (Supporting Information, Figures S8, S18). On the other hand, the dicationic complexes 2^{2+} and 3^{2+} show the CO band at lower energy (Supporting Information, Figures S27, S37; 1664 and 1666 cm^{-1} , respectively), suggesting π back-donation of ruthenium(II) into the $\pi^*(\text{CO})$ orbitals. As the homoleptic complex 2^{2+} merely displays a single IR band for the two CO groups, these two oscillators are decoupled.

Electrochemistry

Both complexes 2^{2+} and 3^{2+} are reversibly oxidized in their cyclic and square wave voltammograms at $+0.92\text{ V}$ and $+0.67\text{ V}$ vs. ferrocene, respectively (Figure 2a; Supporting Information, Figures S39, S40). The oxidation processes are metal-centered as confirmed by the DFT calculations on the trications 2^{3+} and 3^{3+} (Figure 2b). The oxidation potential of $2^{2+}/2^{3+}$ is higher than that of $3^{2+}/3^{3+}$ by 0.25 V due to the electron withdrawing effect of two CO groups in 2^{2+} instead of merely a single one in 3^{2+} . The even higher oxidation potential of the $[\text{Ru}(\text{dcp})_2]^{2+}/[\text{Ru}(\text{dcp})_2]^{3+}$ couple ($+1.10\text{ V}$ vs. ferrocene) with four CO groups is consistent with this trend.^[46] The $\text{Ru}^{\text{II}}/\text{Ru}^{\text{III}}$ oxidations of 2^{2+} and 3^{2+} are perfectly reversible on the time scale of IR spectroelectrochemistry in acetonitrile (Supporting Information, Figures S41, S42). Relative to the parent ruthenium(II) complexes, the bands of the CO stretching vibrations of the ruthenium(III) complexes 2^{3+} and 3^{3+} shift to higher energy by 19 and 21 cm^{-1} , respectively, implying weaker π back-bonding in the ruthenium(III) complexes.

The bis(cpmp) complex 2^{2+} exhibits two reversible reduction waves at -1.29 V and -1.46 V (Figure 2a). These processes are assigned to the reduction of the individual cpmp ligands (Figure 2b). The reduction wave of the single cpmp ligand in 3^{2+}

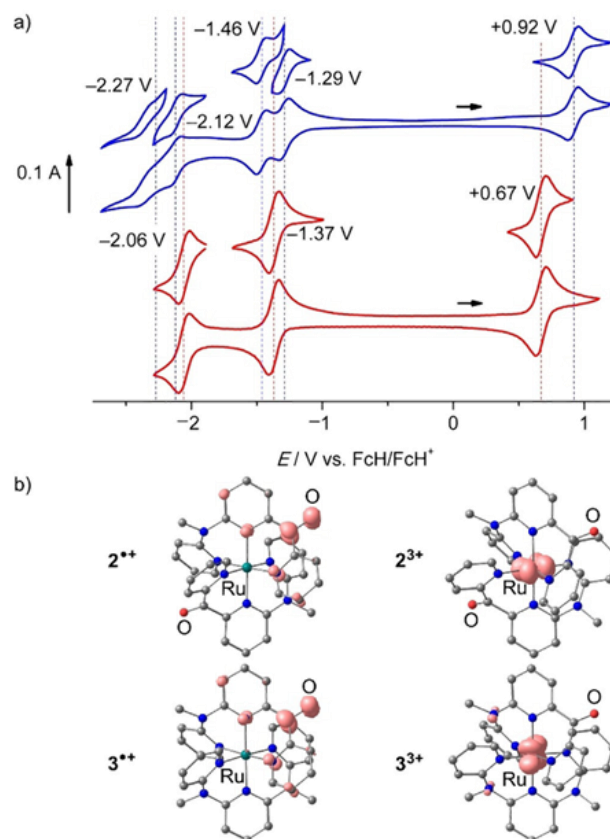


Figure 2. a) Cyclic voltammograms of $2[\text{PF}_6]_2$ (blue) and $3[\text{PF}_6]_2$ (red), 1 mM in acetonitrile, 0.1 M $[\text{nBu}_4\text{N}][\text{PF}_6]$ and b) DFT optimized geometries and spin densities (isosurface at 0.01 a. u.) of the radical cations 2^{2+} and 3^{2+} and the ruthenium(III) complexes 2^{3+} and 3^{3+} .

appears at -1.37 V (Figure 2a). The first two reductions of $[\text{Ru}(\text{dcp})_2]^{2+}$ are very similar to those of 2^{2+} (Table 2).^[46] The reduction waves of 2^{2+} and 3^{2+} below -2 V are assigned to a second reduction of the CO groups in the cpmp ligands. Reduction of cpmp itself to $\text{cpmp}^{\cdot-}$ at -1.99 V is only quasireversible (Supporting Information, Figure S10) likely due to subsequent pinacol coupling reactions.^[62,63] Obviously, the cationic nature of 2^{2+} and 3^{2+} and steric hindrance prevent an analogous coupling reaction, at least on the time scale of the electrochemical experiments. Chemical reduction of $2^{2+}/3^{2+}$ to $2^{\cdot+}/3^{\cdot+}$ by one equivalent decamethylcobaltocene decreases

Table 2. Electrochemical properties of cpmp, $[\text{Ru}(\text{bpy})_3][\text{PF}_6]_2$, $[\text{Ru}(\text{dcp})_2][\text{PF}_6]_2$, $2[\text{PF}_6]_2$ and $3[\text{PF}_6]_2$. $E_{1/2}$ in V vs. ferrocene/ferrocenium.

	Reductions			Oxidation
cpmp			$-1.99^{\text{[a]}}$	$+0.97^{\text{[a]}}$
$[\text{Ru}(\text{bpy})_3]^{2+}$ ^[64]	-2.20	-1.93	-1.74	$+0.84$
$[\text{Ru}(\text{dcp})_2]^{2+}$ ^[46]	-2.09	-1.84	-1.51	$+1.10$
2^{2+}	-2.27	-2.12	-1.46	$+0.92$
3^{2+}		-2.06	-1.37	$+0.67$

[a] Irreversible, E_p given.

the intensity of the CO stretching modes in the IR spectra partially ($2^{2+}/2^{3+}$) and nearly completely ($3^{2+}/3^{3+}$), respectively, reflecting the number of CO groups in the complexes (Figure 2b; Supporting Information, Figures S43, S44). The band of the CO stretching vibration of the reduced cpmp in the radical cations 2^{2+} and 3^{3+} disappears due to a large shift to lower energy into the fingerprint region (which is obscured by solvent absorptions). This is consistent with the additional electron being localized on a CO group of a cpmp ligand. DFT calculations on 2^{2+} and 3^{3+} support this view as the spin density is essentially localized on the CO group (Figure 2b). Furthermore, the calculated C–O bond length increases from 1.217 to 1.274 Å and from 1.218 to 1.277 Å on the reduced ligand for $2^{2+}/2^{3+}$ and $3^{2+}/3^{3+}$, respectively (Figure 2b).

Oxidative UV/Vis/NIR spectroelectrochemical experiments of 3^{2+} in CH_3CN containing 0.1 M $[\text{nBu}_4\text{N}][\text{PF}_6]$ confirm the reversibility of the oxidation (Figure 3a). The MLCT band of 3^{2+} bleaches, while a ligand-to-metal charge transfer (LMCT) band at 882 nm concomitantly appears resulting in an isosbestic point at 661 nm. On the other hand, spectroelectrochemical reduction of 3^{2+} is not fully reversible on the time scale of spectroelectrochemistry (Figure 3b). Apart from the MLCT bleach, no prominent spectral changes in the visible spectral region evolve during reduction of 3^{2+} (Figure 3b). Spectroelectrochemical oxidation of 2^{2+} to 2^{3+} leads to the bleaching of the MLCT band at 549 nm and an increase of the LMCT band of 2^{3+} at 1039 nm, while reduction of 2^{2+} is not fully reversible as well on this time scale (Supporting Information, Figure S45).

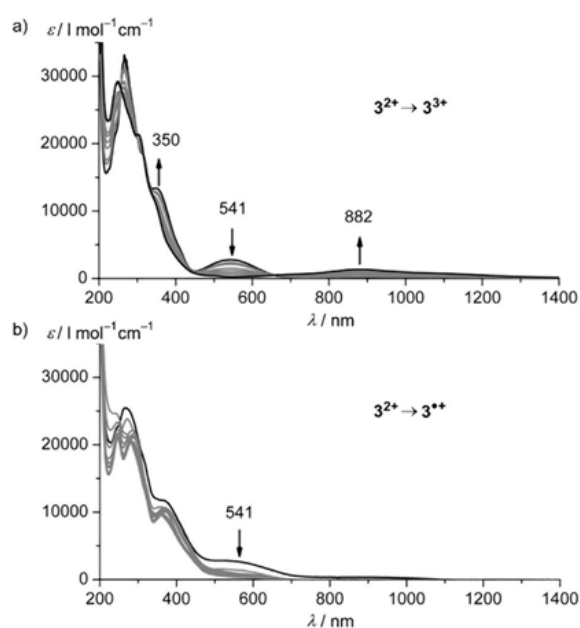


Figure 3. UV/Vis/NIR absorption spectra of $3[\text{PF}_6]_2$ in acetonitrile with 0.1 M $[\text{nBu}_4\text{N}][\text{PF}_6]$ at 298 K collected during a) electrochemical oxidation and b) electrochemical reduction.

Photophysical properties

The cpmp ligand possesses several $\pi\pi^*$ absorption bands and bands with ILCT character, namely CT from the electron-rich pyridyl methyl amine to the electron-poor dipyridyl ketone moiety according to TD-DFT calculations (distal and proximal ILCT; Supporting Information, Figure S9). Irradiating into the (proximal) ILCT band at 354 nm leads to fluorescence at 455 nm (Supporting Information, Figure S9).

UV/Vis/NIR absorption spectra of $2[\text{PF}_6]_2$ and $3[\text{PF}_6]_2$ recorded in acetonitrile at room temperature are depicted in Figure 4 (Supporting Information, Figures S28, S38 for complete spectra). According to TD-DFT calculations and derived charge transfer numbers for the transitions (Supporting Information,

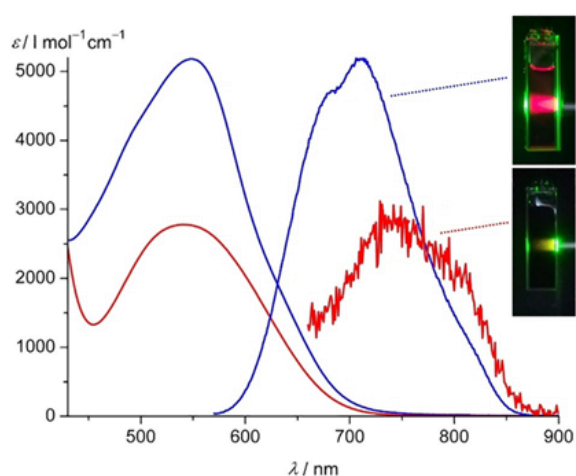


Figure 4. UV/Vis/NIR absorption and emission spectra (scaled to the respective MLCT absorption band) of $2[\text{PF}_6]_2$ (blue) and $3[\text{PF}_6]_2$ (red) in acetonitrile at 298 K ($\lambda_{\text{exc}} = 544$ nm). The photos display cuvettes of acetonitrile solutions of $2[\text{PF}_6]_2$ and $3[\text{PF}_6]_2$ under irradiation with green light (560 nm).

Figures S28, S38), absorption bands at 342 nm (2^{2+}) and 350 nm (3^{2+}) are mainly composed of MLCT transitions and weaker ILCT transitions at the lower energy side (≈ 390 –400 nm). Weak LL'CT transitions are calculated at 402 nm for 2^{2+} and at lower energy (497 nm) for 3^{2+} . According to TD-DFT calculations, the characteristic absorption bands of 2^{2+} and 3^{2+} at 549 and 541 nm are composed of six and three transitions with MLCT character, respectively (Table 3, Supporting Information, Figures S28, S38). The intensity of the MLCT band of 2^{2+} is significantly higher due to the larger number of acceptor sites, namely the dipyridyl ketones of the two cpmp ligands and consequently more MLCT transitions (Figure 4). Although the MLCT band of 3^{2+} overlaps with the low-energy LL'CT transition calculated at 497 nm, all ILCT and LL'CT bands are higher in energy than the low-energy MLCT transitions. Hence, the MLCT states should dominate the excited-state dynamics of the complexes when excited with low energy light.

Upon excitation at 544 nm, both complexes are phosphorescent in acetonitrile at room temperature with broad emission bands peaking at 709 nm and 755 nm, respectively (Figure 4).

Table 3. Absorption and emission wavelengths, E_{00} calculated from low temperature emission spectra and excited-state lifetimes of $2[\text{PF}_6]_2$, $3[\text{PF}_6]_2$ and benchmark complexes in deaerated acetonitrile at 298 K and in butyronitrile at 77 K (if not stated otherwise), respectively.

	λ_{abs} [nm] (298 K)	ϵ [$\text{M}^{-1} \text{cm}^{-1}$] (298 K)	λ_{em} [nm] (298 K)	Φ [%] (298 K)	λ_{em} [nm] (77 K)	E_{00} [eV]	τ [ns] (298 K)
2^{2+}	549	5200	709	1.3	693	1.79	477
3^{2+}	541	2800	755	0.04	740	1.68	56
$[\text{Ru}(\text{bpy})_3]^{2+}$	452 ^[a,9]	13 000 ^[9]	615 ^[a,9]	9.5 ^[15,16]	582 ^[b,9]	2.15 ^[c,66]	1100 ^[a]
$[\text{Ru}(\text{tpy})_2]^{2+}$	474 ^[41]	10 400 ^[41]	629 ^[41]	$< 5 \times 10^{-4}$ ^[41]	598 ^[41]	2.09 ^[c,66]	0.25
$[\text{Ru}(\text{ddpd})(\text{tpy}^{\text{R}})]^{2+}$ R = COOMe	539, 603, 687 ^[30]	6360, 3100 (sh), 800 (sh) ^[30]	744 ^[30]	1.1 ^[d,30]	728 ^[30]	1.70 ^[30]	841
$[\text{Ru}(\text{dcpq})_2]^{2+}$	500, 522, 562 ^[46]	5428, 6425, 2604 ^[46]	608 ^[46]	30 ^[46]	613 ^[46]	2.02 ^[46]	3300

[a] 293 K. [b] in MeOH/EtOH 4:1. [c] in EtOH/MeOH 4:1. [d] 295 K.

The excitation spectrum of 2^{2+} matches the absorption spectrum (Supporting Information, Figure S28a), confirming that the emission originates from 2^{2+} . The luminescence quantum yield of $\Phi = 1.3\%$ measured with an integrating sphere in deaerated acetonitrile drops to 0.88% under aerated conditions suggesting quenching of the excited triplet state by triplet oxygen (68% quenching). Concomitantly, the excited-state lifetime decreases from $\tau = 477$ ns to $\tau = 237$ ns under ambient conditions (acetonitrile, $\lambda_{\text{exc}} = 544$ nm, Supporting Information, Figure S46a) confirming the triplet character of the excited state.

The phosphorescence quantum yield of 3^{2+} of $\Phi = 0.04\%$, measured relative to that of 2^{2+} in acetonitrile at 298 K, is 33 times lower. The excitation spectrum of 3^{2+} only fits to the low-energy $^1\text{MLCT}$ band, while the higher energy transitions around 267 and 350 nm do not significantly evolve to the emissive $^3\text{MLCT}$ state (Supporting Information, Figure S38a). Obviously, the $^3\text{MLCT}$ state of 3^{2+} is only populated efficiently via the low-energy $^1\text{MLCT}$ states but not from the high-energy $^1\text{MLCT}/^1\text{LL'CT}$ states suggesting an alternate excited-state decay behavior from these higher energy states as compared to 2^{2+} . This alternate decay path is possibly enabled by the higher flexibility of the ddpd ligand. The $^3\text{MLCT}$ excited-state lifetime of 3^{2+} was determined using the lifetime spectrometer ($\tau = 45$ ns, Supporting Information, Figure S46b) and confirmed by streak camera measurements ($\tau = 56$ ns) at room temperature in CH_3CN (Supporting Information, Figure S47). In both experiments, a second component with higher lifetime (lifetime spectrometer: 294 ns; by streak camera: 468 ns) was present. We ascribe the second component to some trace impurity, possibly traces of 2^{2+} below the NMR detection limit.

Transient absorption spectroscopy was used to explore the initial dynamics of 2^{2+} and 3^{2+} after the excitation pulse (540 nm; Figure 5 a, Supporting information, Figures S48–S50). For 2^{2+} , a ground-state bleach at 535 nm is observed together with excited-state absorptions around 400 nm and above 600 nm. This fits to MLCT states with the MLCT band of the ground-state bleached and the LMCT band of the excited state appearing as suggested by the estimated difference spectrum derived from the absorption spectra of 2^{2+} , 2^{1+} and 2^{3+} (Figure 5 b),^[67] prepared by electrochemical oxidation and reduction (Supporting Information, Figure S45). Intersystem crossing from the $^1\text{MLCT}$ to the $^3\text{MLCT}$ state occurs within the time resolution of the instrument (100 fs). The populated $^3\text{MLCT}$ state

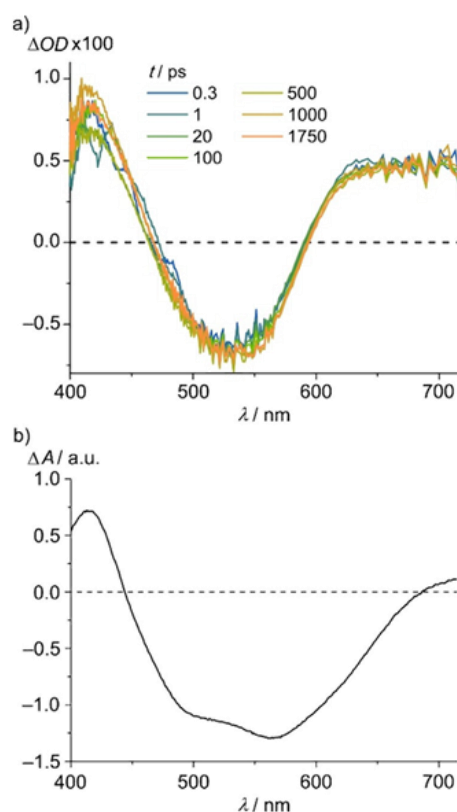


Figure 5. a) fs-Transient absorption spectra of $2[\text{PF}_6]_2$ in acetonitrile at different delay times after excitation at 540 nm at 293 K and b) estimated difference spectrum^[67] derived from absorption spectra of 2^{2+} , 2^{3+} and 2^{1+} , prepared electrochemically in acetonitrile with 0.1 M $[\text{nBu}_4\text{N}][\text{PF}_6]$ at 298 K by "scaled $[1/2(2^{3+} + 2^{1+}) - 2^{2+}]$ ".

features a lifetime in the nanosecond range. This fits to the TCSPC and streak camera measurements (Supporting Information, Figures S46a, S47a). The heteroleptic complex 3^{2+} displays an analogous behavior, yet superimposed by the spectral characteristics of trace impurities of 2^{2+} (Supporting Information, Figure S48).

In frozen butyronitrile solution at 77 K, the emission bands of 2^{2+} and 3^{2+} at 693 and 740 nm, respectively, are sharper with less vibrational broadening (Supporting Information, Figure S51; Table 3). From these data, the triplet excited-state energies are calculated as 1.79 and 1.68 eV, respectively. The

lower $^3\text{MLCT}$ energy of the latter might also contribute to the low quantum yield of 3^{2+} due to its higher non-radiative decay rate constants according to the energy gap law.^[68,69]

Compared to $[\text{Ru}(\text{tpy})_2]^{2+}$,^[36,41] the emission quantum yields of 2^{2+} and 3^{2+} are significantly higher in spite of the lower $^3\text{MLCT}$ energy and hence potentially increased non-radiative relaxation (based on the energy gap law), demonstrating the usefulness of the “large ligand field” concept. The emission quantum yield of the push–pull complex 2^{2+} is similar to that of the heteroleptic donor–acceptor complex $[\text{Ru}(\text{ddpd})(\text{tpy})]^{2+}$ bearing only a single tridentate ligand with large bite angles (Scheme 1). In the complex series 3^{2+} , 2^{2+} , $[\text{Ru}(\text{dcp})]^{2+}$ with exclusively six-membered chelate rings, but an increasing number of dipyridyl ketone units, quantum yields increase by factors of 35 and 23, and the lifetimes by 8.5 and 6.9, respectively. The enhancement in quantum yield in this series parallels the increasing $^3\text{MLCT}$ energies (Table 3) in accordance with the energy gap law.^[68,69] This again demonstrates that merely lowering the $^3\text{MLCT}$ energies to increase the ^3MC – $^3\text{MLCT}$ gap is counterproductive. However, the $^3\text{MLCT}$ energies of 2^{2+} and 3^{2+} differ only by 0.11 eV and hence further aspects must be additionally relevant for the excited-state dynamics of 2^{2+} and 3^{2+} .

To gain a deeper insight in the excited-state landscape, geometry optimizations based on DFT calculations on the singlet ground states (^1GS), the $^3\text{MLCT}$ and ^3MC states of 2^{2+} and 3^{2+} were performed on the CPCM(acetonitrile)-B3LYP-D3BJ-ZORA/old-TZVP level of theory. The calculated $^3\text{MLCT}$ energies are slightly lower than the experimental ones. Yet, the calculations correctly reproduce the order of the $^3\text{MLCT}$ energies with that of 2^{2+} being higher by 0.16 eV than that of 3^{2+} . On the other hand, the calculated ^3MC state minima of 2^{2+} and 3^{2+} are very similar in energy. This leads to a larger ^3MC – $^3\text{MLCT}$ energy difference for 3^{2+} (0.77 eV) than for 2^{2+} (0.57 eV), which would imply a facilitated non-radiative decay via the ^3MC state in 2^{2+} , which is not observed.

The difference between the ^3MC states of 2^{2+} and 3^{2+} is the location of the Jahn–Teller distortion. In 2^{2+} , a cmp ligand is necessarily involved with large changes in Ru–N4 and Ru–N6 distances and a high torsional distortion involving the CO–py unit (Figure 6a). On the other hand, the ddpd ligand in 3^{2+} enables a Jahn–Teller distortion, which is rather symmetrically distributed over the Ru–N4 and Ru–N6 bonds (Figure 6b). The ancillary tridentate ligands are barely distorted relative to the ground-state geometry. Obviously, the π -accepting CO–py unit experiences a stronger distortion than the more electron-rich NMe–py units. This might be ascribed to the loss of π -backbonding in the ^3MC state due to the electron depletion in the metal π orbitals. For a more detailed view, the geometries of ^1GS , $^3\text{MLCT}$ and ^3MC states were optimized along the Jahn–Teller type axis of the distorted ^3MC states (projected onto the two averaged elongated Ru–N bond lengths, Figure 7). The potential energy well of the ^3MC state along the Jahn–Teller mode is steeper for 2^{2+} than for 3^{2+} . The optimized ^3MC geometries of 3^{2+} with Ru–N distances of ≈ 2.3 and 2.6 Å along the Jahn–Teller axis are essentially isoenergetic (Figures 6b and 7b). Consequently, the crossing point of the ^3MC state with

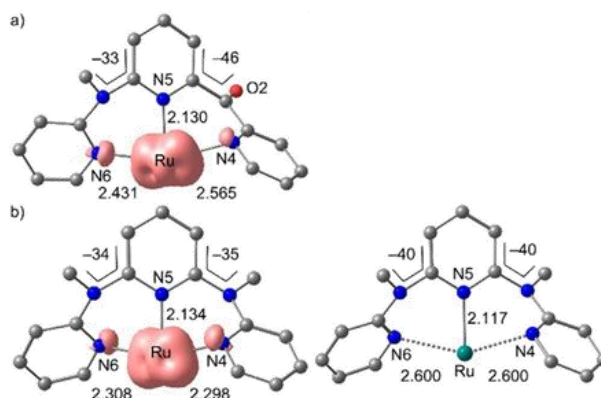


Figure 6. DFT-optimized geometries of the ^3MC states of a) 2^{2+} and b) 3^{2+} showing the relevant distances and angles of the tridentate ligand involved in the Jahn–Teller distortion (spin density plotted with an isosurface value of 0.01 a.u.). The essentially unaffected ancillary ccmp ligand is not shown for clarity. The two displayed geometries of 3^{2+} are nearly isoenergetic.

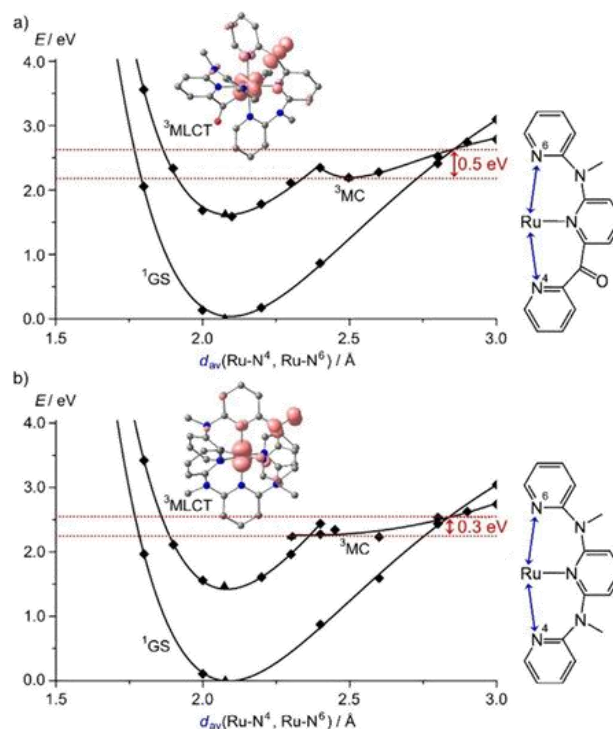


Figure 7. Calculated potential energy diagrams of a) 2^{2+} and b) 3^{2+} with averaged Ru–N bond lengths along the respective Jahn–Teller axis as simplified reaction coordinate. DFT optimized geometries and spin densities of the $^3\text{MLCT}$ states of 2^{2+} and b) 3^{2+} (isosurface value at 0.01 a. u.).

the singlet ground state at around 2.6–2.7 Å is higher in energy by ca. 0.2 eV for 2^{2+} than for 3^{2+} with respect to the energy minimum of the respective ^3MC states. Stronger Ru–N bonds and a more rigid ligand backbone may account for the steeper ^3MC potential well of 2^{2+} as compared to 3^{2+} . Consequently, the type of the bridging units between the coordinating pyridines modifies the excited-state potential steepness,

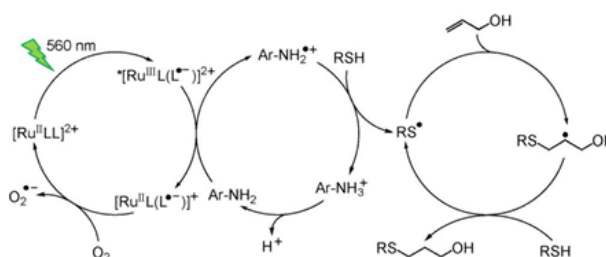
which in turn affects the excited-state dynamics. Obviously, CO linkers are better than NMe linkers in this respect. This also fits to the excellent performance of $[\text{Ru}(\text{dcp})_2]^{2+}$, which exclusively possesses CO bridging moieties in the six-membered chelate rings.^[46]

Reductive quenching of the $^3\text{MLCT}$ state

The intense absorption band at 549 nm with a molar extinction coefficient of $5200 \text{ M}^{-1} \text{ cm}^{-1}$, the 477 ns $^3\text{MLCT}$ state lifetime, the sufficient redox stability and the $^3\text{MLCT}$ energy of 2^{2+} (1.79 eV) should enable excited-state quenching by suitable redox partners. The excited-state redox potential of 2^{2+} $E_{1/2}(*2^{2+}/2^{2+}) = +0.50 \text{ V}$ vs. ferrocene is somewhat higher than that of $*[\text{Ru}(\text{bpy})_3]^{2+}/[\text{Ru}(\text{bpy})_3]^+$ ($E_{1/2} = +0.41 \text{ V}$ vs. ferrocene). Furthermore, green light (560 nm) can be used to excite 2^{2+} , while the molar extinction coefficient of $[\text{Ru}(\text{bpy})_3]^{2+}$ at 560 nm ($\epsilon = 250 \text{ M}^{-1} \text{ cm}^{-1}$) is ca. 21 times smaller. Hence, using $[\text{Ru}(\text{bpy})_3]^{2+}$ as photosensitizer typically requires the use of blue light matching its MLCT maximum at 452 nm. Consequently, we were interested in the reductive quenching of the $^3\text{MLCT}$ state of 2^{2+} using low-energy green light.

Gratifyingly, aliphatic and aromatic amines such as *N,N*-diisopropylethylamine (DIPEA), *p*-toluidine and *N,N,N',N'*-tetramethyl-1,4-phenylenediamine (TMPA) quench the $^3\text{MLCT}$ emission of 2^{2+} . Stern–Volmer analyses yield the Stern–Volmer constants $K_{\text{SV}} = 2.2$ (DMF, $\lambda_{\text{exc}} = 555 \text{ nm}$), 93 (CH_3CN , $\lambda_{\text{exc}} = 546 \text{ nm}$) and 2819 M^{-1} (DMF, $\lambda_{\text{exc}} = 555 \text{ nm}$), respectively (Supporting Information, Figures S52–S54). For the aromatic amines, the higher K_{SV} of TMPA correlates to its lower TMPA/TMPA⁺ redox potential ($-0.27 \text{ V}^{[70]}$ vs. ferrocene) than that of *p*-toluidine ($+0.34 \text{ V}$ vs. ferrocene^[71]). With the excited-state lifetime of 477 ns of 2^{2+} , the quenching rate constants of the amines amount to $k_{\text{q}} = 0.005 \times 10^9$, 0.19×10^9 and $5.91 \times 10^9 \text{ M}^{-1} \text{ s}^{-1}$ for DIPEA, *p*-toluidine and TMPA, respectively.

Encouraged by these initial quenching results and the recorded reduction potential of 2^{2+} ($E_{1/2}(2^{2+}/2^{2+}) = -1.29 \text{ V}$), which could be sufficient for re-oxidation by oxygen, a visible light induced radical thiol–ene click reaction^[71–73] was attempted using $2[\text{PF}_6]_2$, $3[\text{PF}_6]_2$ and $[\text{Ru}(\text{bpy})_3][\text{PF}_6]_2$ (2.2–2.5 mol-%) as sensitizer, allyl alcohol (2.5 equiv) as olefin component, *N*-Boc cysteine methyl ester (1.0 equiv) as thiol component and *p*-toluidine (0.46 equiv) as redox mediator as developed by Yoon et al. (Scheme 3).^[71] The thiol quenches the emission of $2[\text{PF}_6]_2$ only very moderately ($K_{\text{SV}} = 0.60 \text{ M}^{-1}$, CH_3CN , $\lambda_{\text{exc}} = 546 \text{ nm}$; $k_{\text{q}} = 0.0013 \times 10^9 \text{ M}^{-1} \text{ s}^{-1}$; (Supporting Information, Figure S55). Consequently, the observed photoreactivity occurs via quenching of the excited ruthenium(II) complex by the amine as suggested by Yoon for $[\text{Ru}(\text{bpy})_3]^{2+}$.^[71] In contrast to the reported conditions, which relied on blue light (450 nm), we employed green light ($560 \pm 5 \text{ nm}$ by bandpass filters; Supporting Information, Figure S56). After 3 h of irradiation, 56, 18 and 20% of the thiol–ene product were observed for $2[\text{PF}_6]_2$, $3[\text{PF}_6]_2$ and $[\text{Ru}(\text{bpy})_3][\text{PF}_6]_2$, respectively (Supporting Information, Figure S57). The smaller molar extinction coefficient at 560 nm (Figure 4), a lower excited-state energy (Supporting Information, Figure S51) and a significantly smaller $^3\text{MLCT}$ lifetime ac-



Scheme 3. Photocatalytic radical thiol–ene click reaction utilizing the (green) light-induced reductive quenching pathway of $[\text{RuL}(\text{L}')_2]^{2+} = 2^{2+}$, 3^{2+} and $[\text{Ru}(\text{bpy})_3]^{2+}$ mediated by *p*-toluidine ($\text{Ar} = p\text{-C}_6\text{H}_4\text{-CH}_3$) according to ref. [71] ($\text{R} = \text{CH}_2\text{-CHNH}_2\text{Boc-COOCH}_3$).

count for the poorer performance of $3[\text{PF}_6]_2$ (vide supra). The lower yields and slow conversion obtained with $[\text{Ru}(\text{bpy})_3][\text{PF}_6]_2$ are ascribed to its significantly lower molar extinction coefficient at 560 nm. Hence, with respect to employing green instead of blue light, $2[\text{PF}_6]_2$ outperforms the standard sensitizer $[\text{Ru}(\text{bpy})_3][\text{PF}_6]_2$ in this exemplary photosensitized reaction.

Conclusions

With the aim to lower MLCT and increase ^3MC energies and possibly to induce further luminescent states of $^3\text{ILCT}$ or $^3\text{LL'CT}$ character in ruthenium(II) complexes, we prepared the donor–acceptor ligand cpmp and its homo- and heteroleptic ruthenium(II) complexes 2^{2+} and 3^{2+} (with ddpd as ancillary tridentate ligand). The cpmp and ddpd ligands form six-membered chelate rings which increases the ligand field splitting and hence the ^3MC energies. The electron accepting py_2CO and electron donating py_2NMe units within the same cpmp ligand lead to ILCT/LLCT transitions in the complexes. However, these are found at too high energy to enable emission from these states and to play a significant role in the excited-state decay when excited at lower energy. The $^3\text{MLCT}$ states are emissive at room temperature in solution. The homoleptic complex 2^{2+} emits at 709 nm with a luminescence quantum yield of 1.3% and a 477 ns excited-state lifetime, while the heteroleptic complex 3^{2+} featuring an additional ddpd ligand with only py_2NMe units is less emissive (755 nm, 0.037%, 56 ns). This difference is ascribed to the energy gap law and furthermore to a higher flexibility of the coordinated ddpd ligand in 3^{2+} facilitating non-radiative decay to the ground state. These results highlight the importance of the excited-state geometries in addition to the excited-state energies for the actual excited-state dynamics. The complexes are active in photoinduced electron transfer reactions with *p*-toluidine as redox mediator using green light as excitation source. Due to its more favorable optical properties, 2^{2+} is a more potent photosensitizer than 3^{2+} .

Experimental Section

General procedures

CH_3CN and diethyl ether were distilled under argon atmosphere from CaH_2 and sodium, respectively. All other solvents and re-

agents were used as received from commercial suppliers (Acros, Alfa Aesar, Fischer and Sigma–Aldrich). Microwave heating was performed in a Discover Benchmate Plus (CEM Synthesis) single-mode microwave cavity, producing continuous irradiation at 2.455 GHz with 150 W. Reaction mixtures were stirred with a magnetic stir bar during irradiation. Temperature and irradiation power were monitored during the course of the reaction. NMR spectra were recorded on a Bruker Avance DRX 400 spectrometer at 400.31 MHz (^1H), 100.05 MHz ($^{13}\text{C}\{^1\text{H}\}$), and 162.05 MHz ($^{31}\text{P}\{^1\text{H}\}$). All resonances are reported in ppm versus the solvent signal as an internal standard [CD_3CN (^1H , $\delta = 1.94$; ^{13}C , $\delta = 1.24$ ppm)]^[74] or versus external H_3PO_4 (85%) (^{31}P : $\delta = 0$ ppm); (s) = singlet, (d) = doublet, (t) = triplet, (sept) = septet, (m) = multiplet. Atom numbering is shown in the Supporting Information at the respective NMR spectra. IR spectra were recorded with a Bruker ALPHA II FT-IR spectrometer with a platinum Di-ATR module (cpmp) and BioRad Excalibur FTS 3100 spectrometer using KBr disks (**1**[PF₆]₂, **2**[PF₆]₂, **3**[PF₆]₂). Electrochemical experiments were carried out on a BioLogic SP-50 voltammetric analyzer using platinum wires as counter and working electrodes and 0.01 M Ag/AgNO₃ as the reference electrode. The measurements were carried out at a scan rate of 100 mV s⁻¹ for cyclic voltammetry experiments and at 50 mV s⁻¹ for square-wave voltammetry experiments using 0.1 M [*n*Bu₄N][PF₆] as the supporting electrolyte in CH₃CN. Potentials are referenced to the ferrocene/ferrocenium couple. UV/Vis/NIR spectroelectrochemical experiments were performed using a BioLogic SP-50 voltammetric analyzer and a Specac omni-cell liquid transmission cell with CaF₂ windows equipped with a Pt-gauze working electrode, a Pt-gauze counter electrode and a Ag wire as pseudo reference electrode, melt-sealed in a polyethylene spacer (approximate path length 1 mm) in CH₃CN (0.3 mm and 0.9 mm for oxidation and reduction, respectively) containing 0.1 M [*n*Bu₄N][PF₆].^[75] IR spectroelectrochemical experiments were performed using a BioLogic SP-200 voltammetric analyzer and using the same cell, electrodes and electrolyte as above (12 mm). UV/Vis/NIR spectra were recorded on a Varian Cary 5000 spectrometer using 1.00 cm cells. Emission spectra were recorded on a Varian Cary Eclipse spectrometer. For low temperature photoluminescence measurements, a solution of the complex in butyronitrile freshly filtered over alumina was filled into a quartz cuvette in an argon filled glovebox and the cuvette was sealed and transferred to an Oxford cryostat (Oxford instruments Optistat^{DN}). Measurements were conducted at 295 K and 77 K. Fluorescence decays were recorded with an Edinburgh Instruments lifetime spectrometer (FLS 920) equipped with a microchannel plate photomultiplier tube (MCP-PMT; Hamamatsu R3809U-50) using a 330 nm ps laser diode (EPLD, Edinburgh Instruments) as excitation light source. All measurements were performed under magic-angle conditions (polarizers in the excitation and emission channel set to 0° and 54.7°, respectively). Transient absorption spectra were recorded with a time resolution of ca. 100 fs by a pump-probe setup based on a Ti:sapphire laser system (CPA 2001, Clark MXR, Inc.) operating at a center wavelength of 775 nm and at a repetition rate of 1 kHz. Applying a noncollinear optical parametric amplifier (NOPA), excitation pulses with a center wavelength of 540 nm were generated whose dispersion was controlled by a prism compressor. As probe, a white light continuum was used which was generated in a CaF₂ crystal. The polarizations of pump and probe were set to magic angle and the beams were focused into the sample to overlapping spots with diameters of 330 μm for the pump and 90 μm for the probe. After the sample, the probe was dispersed by a prism and transmission changes were spectrally resolved recorded by a CCD array detector. The sample compounds were dissolved in CH₃CN and the solutions were filled into a 1 mm thick fused silica cuvette. Time-resolved luminescence was mea-

sured by a streak camera system (C10627, Hamamatsu Photonics) using again excitation pulses at 540 nm generated by a NOPA. For the measurements with the streak camera, the samples dissolved in CH₃CN were filled into a 1 cm thick fused silica cuvette. All samples were deaerated with argon prior the spectroscopic measurements. The luminescence quantum yield of **2**[PF₆]₂ was determined with an Ulbricht integrating sphere (Quantaurus-QY C11347-11, Hamamatsu).^[76–77] The luminescence quantum yield of **3**[PF₆]₂ was determined by comparing the areas under the emission spectra on an energy scale cm⁻¹ recorded for optically matched solutions of the sample and the reference { Φ (**2**[PF₆]₂) = 0.0088 in aerated CH₃CN}. ESI mass spectra were recorded on an Agilent 6545 QTOF-MS spectrometer (cpmp) and a Micromass Q-TOF-Ultima spectrometer (**1**[PF₆]₂, **2**[PF₆]₂, **3**[PF₆]₂). Elemental analyses were performed by the microanalytical laboratory of the department of chemistry of the University of Mainz. The catalysis experiments were carried out using an Asahi Spectra Max-303 Xenon Light Source (300 W), together with 560 nm ± 5 nm filters (Supporting Information, Figure S56).

Crystal structure determination

Intensity data were collected with a Bruker AXS Smart1000 CCD diffractometer with an APEX II detector and an Oxford cooling system and corrected for absorption and other effects using Mo_{K α} radiation ($\lambda = 0.71073$ Å). The diffraction frames were integrated using the Bruker SMART software package,^[78] and most were corrected for absorption with MULABS^[79a] of the PLATON software package.^[79b] The structures were solved by direct methods and refined by the full-matrix method based on F^2 using the SHELX software package^[80] using the ShelXle graphical interface.^[81] Non-hydrogen atoms were refined anisotropically, while the positions of all hydrogen atoms were generated with appropriate geometric constraints and allowed to ride on their respective parent carbon atoms with fixed isotropic thermal parameters. CCDC 1852838 (**3**[PF₆]₂) contains the supplementary crystallographic data for this paper. These data are provided free of charge by The Cambridge Crystallographic Data Centre.

Density functional theoretical calculations

DFT calculations were carried out using the ORCA program package (version 4.0.1).^[82,83] All calculations were performed using the B3LYP functional^[84–86] and employ the RIJCOSX approximation.^[87,88] Relativistic effects were calculated at the zeroth order regular approximation (ZORA) level.^[89] The ZORA keyword automatically invokes relativistically adjusted basis sets. To account for solvent effects, a conductor-like screening model (CPCM) modeling acetonitrile was used in all calculations.^[90,91] Geometry optimizations were performed using Ahlrichs polarized valence triple-zeta basis set (old-TZVP equivalent to def2-TZVP from ORCA 3.0) together with a segmented all electron relativistically contracted (SARC) auxiliary basis set.^[89,92] Atom-pairwise dispersion correction was performed with the Becke–Johnson damping scheme (D3BJ).^[93,94] The presence of energy minima was checked by numerical frequency calculations. Explicit counterions and/or solvent molecules were not taken into account. The ³MC structures were found by constraining certain Ru–N bonds to longer distances and re-optimizing the thus obtained structure without geometry constraints. All optimized geometries were ascertained as minima by numerical frequency analysis. For the potential diagrams, the two Ru–N bonds that are elongated in the ³MC states were constrained to the respective averaged elongated values. The assignment of the state characters has been done dividing the molecule into three fragments (metal

center and two ligands) and calculating charge transfer numbers, as implemented in the TheoDore software package.^[95,96]

Synthesis of cpmp (6,2''-carboxypyridyl-2,2'-methylamine-pyridyl-pyridine)

6-Bromo-*N*-methyl-*N*-(pyridin-2-yl)pyridyl-2-amine^[57] (3.06 g, 16 mmol, 1.0 equiv.) was dissolved in dry diethyl ether (100 mL) under argon. At -78°C , *n*-butyl lithium (2.5 M in hexane, 7.0 mL, 18 mmol, 1.1 equiv.) was added dropwise. After stirring for 1 h at -78°C , 2-cyanopyridine (1.67 g, 16 mmol, 1.0 equiv.) dissolved in dry diethyl ether (20 mL) was added dropwise, keeping the temperature below -70°C . After 30 minutes stirring below -70°C , the solution was allowed to warm to room temperature. The dark brown solution was poured over ice (500 g) to yield an orange solution, which was acidified with hydrochloric acid (1 M, 150 mL). The separated organic layer was extracted with hydrochloric acid (1 M, 3×150 mL). The combined aqueous phases were neutralized with saturated aqueous sodium carbonate solution. The aqueous solution was extracted with methylene chloride (3×150 mL). The combined organic phases were dried over magnesium sulfate and the solvent was removed under reduced pressure. The crude product was purified by column chromatography (silica gel, petroleum ether/ethyl acetate 1:1) to yield a yellow oil (25%, 1.29 g, 4.44 mmol). R_f (SiO₂, petroleum ether/ethyl acetate 1:1)=0.30. Elem. anal. calcd for C₁₇H₁₄N₄O \times 0.1 H₂O: C, 69.90; H, 4.90; N, 19.18. Found: C, 69.91; H, 5.17; N, 19.08. ¹H NMR (CD₃CN): δ =8.70 (dt, J =4.8, 1.4 Hz, 1H, H¹⁶), 8.30–8.24 (m, 2H, H¹), 7.94–7.89 (m, 2H, H¹⁴, H¹⁵), 7.79 (dd, J =8.5, 7.4 Hz, 1H, H⁹), 7.58–7.50 (m, 3H, H³, H¹⁰, H¹⁷), 7.39 (d, J =8.5 Hz, 1H, H⁸), 7.32 (d, J =8.4 Hz, 1H, H⁴), 6.91 (ddd, J =7.4, 5.1, 0.9 Hz, 1H, H²), 3.48 (s, 3H, H⁶). ¹³C{¹H} NMR (CD₃CN): δ =192.8 (C¹²), 156.2 (C⁵), 155.7 (C⁷), 154.3 (C¹³), 151.7 (C¹¹), 148.1 (C¹⁶), 146.9 (C¹), 137.1 (C⁹), 136.4 (C¹⁰), 135.8 (C¹⁴), 125.3 (C¹⁷), 123.5 (C¹⁵), 116.8 (C³), 116.2 (C⁸), 115.6 (C²), 114.5 (C⁴), 34.5 (C⁶). MS (ESI⁺): m/z =291.1 (100%, [M+H]⁺). MS(HR-ESI⁺): calcd for C₁₇H₁₅N₄O⁺: m/z =291.1240. Found: m/z =291.1234. IR (ATR): $\tilde{\nu}$ =3052 (vw, CH), 3003 (vw, CH), 2958 (vw, CH), 2910 (vw, CH), 2816 (vw, CH), 1679 (m, C=O), 1578 (s), 1565 (m), 1429 (vs.), 1348 (s), 1320 (m), 1267 (m), 1241 (w), 1185 (vw), 1141 (w), 1115 (w), 1081 (w), 1046 (vw), 973 (m), 891 (w), 826 (w), 776 (m), 737 (s), 698 (m), 655 (w), 614 (m), 559 (vw), 432 (vw), 403 (w) cm⁻¹. CV (CH₃CN, vs. FcH/FcH⁺): $E_{1/2}$ =-1.99 (irrev.), +0.97 (irrev.) V. UV/Vis (CH₃CN): λ_{max} (ϵ)=231 (13000), 267 (9790), 305 (12800), 354 nm (sh, 1970 m⁻¹ cm⁻¹). Emission (CH₃CN, 295 K, λ_{exc} =354 nm): λ_{em} =455 nm.

Synthesis of 1[PF₆][RuCl(cpmp)(NCCH₃)₂][PF₆]_{*n*} (*n*=2)

Di- μ -chlorido-bis[chlorido(η^5 -1-isopropyl-4-methylbenzene)ruthenium(II)]^[58] (1.06 g, 1.72 mmol, 1.0 equiv.), cpmp (1.00 g, 3.45 mmol, 2.0 equiv.) and KPF₆ (1.06 g, 5.74 mmol, 3.3 equiv.) were dissolved in acetonitrile (150 mL). The solution was heated to reflux for 6 h to yield a red-purple solution. After filtration over alumina, the solvent was removed under reduced pressure. The solid was dissolved in acetonitrile (5 mL) and precipitated by addition of diethyl ether (100 mL). The red-purple solid was washed with diethyl ether (250 mL). The red-purple micro crystals were dried under reduced pressure. Yield 1.99 g (3.25 mmol, 94%). ¹H NMR (CD₃CN) δ =8.89 (d, J =5.3 Hz, 1H, H¹⁷), 8.85 (dd, J =5.9, 1.9 Hz, 1H, H¹), 8.19 (dd, J =7.0, 1.0 Hz, 1H, H¹⁴), 8.11 (dd, J =7.8, 1.3 Hz, 1H, H¹⁵), 8.00 (dd, J =7.4, 7.4 Hz, 1H, H⁹), 7.94 (ddd, J =8.8, 7.4, 1.8 Hz, 1H, H³), 7.87 (dd, J =7.3 Hz, 1H, H¹⁰), 7.62 (ddd, J =7.4, 5.7, 1.7 Hz, 1H, H¹⁶), 7.51 (dd, J =8.3, 1.3 Hz, 1H, H⁸), 7.38 (dd, J =8.3, 1.0 Hz, 1H, H²), 7.21 (ddd, J =7.2, 5.8, 1.2 Hz, 1H, H⁴), 3.63 (s, 3H, H⁶), 2.59 (s, 3H, H¹⁹).

¹³C{¹H} NMR (CD₃CN): δ =182.4 (C¹²), 157.6 (C²), 156.7 (C⁵), 156.6 (C¹³), 155.6 (C¹¹), 155.1 (C¹⁷), 153.9 (C¹), 137.8 (C³), 137.1 (C⁹), 136.5 (C¹⁵), 126.1 (C¹⁴), 126.0 (C¹⁶), 125.6 (C¹⁸), 122.7 (C¹⁰), 118.7 (C⁴), 116.8 (C⁸), 113.0 (C²), 38.9 (C⁶), 2.9 (C¹⁹). ³¹P{¹H} NMR (CD₃CN): δ =-144.6 (sept, ¹ J_{PF} =700 Hz). MS (ESI⁺): m/z =426.9 (63%, [RuCl(cpmp)]⁺), 467.9 (100%, [RuCl(cpmp)(NCCH₃)₂]⁺), 485.9 (34%, [RuCl(cpmp)(H₂O)(NCCH₃)₂]⁺), 508.96 (24%, [RuCl(cpmp)(NCCH₃)₂]⁺). MS (HR-ESI⁺): calcd for C₂₁H₂₀ClRuN₆O⁺: m/z =509.0425. Found: m/z =509.0421. IR (KBr): $\tilde{\nu}$ =3091 (vw, CH), 2966 (vw, CH), 2933 (vw, CH), 2275 (vw, C \equiv N), 1672 (s, C=O), 1590 (s), 1483 (s), 1455 (s), 1437 (s) 1353 (s), 1314 (w), 1290 (vw), 1266 (w), 1247 (m), 1172 (vw), 1151 (w), 1091 (vw), 1063 (vw), 1030 (w), 972 (w), 843 (vs., PF), 757 (s), 717 (w), 704 (w), 675 (vw), 582 (w), 559 (vs., PF₂, def), 519 (vw) cm⁻¹. UV/Vis (CH₃CN): λ_{max} (ϵ)=276 (19100), 341 (10500), 494 nm (3150 m⁻¹ cm⁻¹). [RuCl(cpmp)(NCCH₃)₂][PF₆] was used directly without further purification.

Synthesis of 2[PF₆]₂[(Ru(cpmp))₂][PF₆]₂

[RuCl(cpmp)(NCCH₃)][PF₆] (1[PF₆]) (100 mg, 0.16 mmol, 1.0 equiv.) and cpmp (77 mg, 0.27 mmol, 1.6 equiv.) were dissolved in a mixture of acetonitrile (1 mL) and ethanol (6 mL). The solution was heated to reflux in a laboratory microwave oven for 20 h (100 W, 90°C). The solvents were removed under reduced pressure. The solid was dissolved in acetonitrile (1 mL) and precipitated by addition of diethyl ether (100 mL). The precipitate was washed with diethyl ether (100 mL) to remove excess ligand. The dark red product was dissolved in acetonitrile (1 mL). Addition of an aqueous solution of [NH₄][PF₆] (1 g, 6 mmol, 37 equiv. in 100 mL H₂O) resulted in the precipitation of a purple solid, which was collected by filtration and purified by diffusion of diethyl ether into a solution of 2[PF₆]₂ in acetonitrile. The purple crystals were dried under reduced pressure. Yield: 76 mg (0.08 mmol, 48%). ¹H NMR (CD₃CN): δ =8.21 (dd, ³ J =8.0, 8.0 Hz, 2H, H⁹), 8.11–8.01 (m, 4H, H¹⁶, H¹⁷), 7.92 (d, ³ J =7.8 Hz, 2H, H¹⁰), 7.88 (ddd, ³ J =7.9, 7.9 Hz, ⁴ J =1.8 Hz, 2H, H³), 7.61 (d, ³ J =8.4 Hz, 2H, H⁸), 7.57 (d, ³ J =5.7 Hz, 2H, H¹⁴), 7.35 (ddd, ³ J =7.6 Hz, ³ J =5.7 Hz, ⁴ J =2.3 Hz, 2H, H¹⁵), 7.21 (d, ³ J =8.6 Hz, 2H, H⁴), 7.03 (dd, ³ J =5.9 Hz, ⁴ J =1.8 Hz, 2H, H¹), 6.80 (dd, ³ J =6.6 Hz, ³ J =6.6 Hz, 2H, H²), 2.88 (s, 6H, H⁶). ¹³C{¹H} NMR (CD₃CN): δ =183.3 (C¹²), 156.6 (C⁵), 155.8 (C⁷), 154.5 (C¹⁴), 153.7 (C¹¹), 153.6 (C¹³), 152.2 (C¹), 139.6 (C⁹), 139.0 (C³), 137.7 (C¹⁶), 127.7 (C¹⁵), 126.8 (C¹⁷), 123.8 (C¹⁰), 120.4 (C²), 119.2 (C⁸), 113.8 (C⁴), 38.2 (C⁶). ³¹P{¹H} NMR (CD₃CN): δ =-145.5 (sept, ¹ J_{PF} =700 Hz). MS (ESI⁺): m/z =341.1 (64%, [Ru(cpmp)₂]²⁺), 827.1 (100%, [Ru(cpmp)₂][PF₆]⁺). MS (HR-ESI⁺): calcd for C₃₄H₂₈F₆RuN₈O₂P⁺: m/z =827.1021. Found: m/z =827.1003. Elem. anal. calcd for C₃₄H₂₈F₁₂RuN₈O₂P₂: C, 42.03; H, 2.90; N, 11.53. Found: C, 41.88; H, 3.04; N, 11.86. IR (ATR): $\tilde{\nu}$ =3110 (vw, CH), 3092 (vw, CH), 1664 (w, CO), 1587 (w), 1486 (vw), 1455 (w), 1437 (w), 1354 (w), 1318 (vw), 1292 (vw), 1265 (vw), 1244 (vw), 1176 (vw), 1149 (w), 1141 (vw), 1125 (vw), 1105 (vw), 1089 (vw), 1064 (vw), 1021 (vw), 973 (vw), 871 (vw), 833 (vs., PF), 794 (w), 777 (m), 758 (m), 710 (w), 668 (vw), 651 (vw), 634 (vw), 612 (vw), 578 (vw), 555 (vs., PF₂), 515 (vw) cm⁻¹. IR (KBr): $\tilde{\nu}$ =3127 (vw, CH), 3103 (vw, CH), 3040 (vw, CH), 3015 (v), 2985 (vw), 2916 (vw), 2835 (vw), 2249 (vw), 1666 (vs., CO), 1591 (s), 1572 (w), 1480 (s), 1469 (m), 1411 (w), 1379 (w), 1352 (s), 1314 (m), 1291 (w), 1251 (m), 1194 (vw), 1174 (w), 1148 (w), 1137 (w), 1118 (vw), 1100 (vw), 1087 (vw), 1064 (vw), 1025 (w), 972 (w), 921 (vw), 879 (s), 846 (vs., PF), 793 (m), 757 (s), 714 (w), 675 (vw), 653 (vw), 633 (vw), 615 (vw), 577 (w), 558 (vs., PF₂), 519 (vw), 469 (vw), 449 (vw), 430 (vw), 414 (vw), 398 (vw) cm⁻¹. CV (CH₃CN, vs. FcH/FcH⁺): $E_{1/2}$ =-2.27 (irrev.), -2.12 (irrev.), -1.46 (rev.), -1.29 (rev.), +0.92 (rev.) V. UV/Vis (CH₃CN): λ_{max} (ϵ)=269 (40800), 342 (20600), 549 nm (5200 m⁻¹ cm⁻¹). Emission (CH₃CN, 298 K): λ_{em} =709 nm (λ_{exc} =554 nm), τ =477 ns (deaerated),

237 ns (aerated) ($\lambda_{\text{exc}} = 544$ nm), Φ ($\lambda_{\text{exc}} = 544$ nm) = 1.3% (deaerated), 0.88% (aerated). Emission ($^{\text{a}}\text{PrCN}$, 77 K, $\lambda_{\text{exc}} = 549$ nm): $\lambda_{\text{em}} = 693$ nm.

Synthesis of 3[PF₆]₂ ([Ru(cpmp)(ddpd)][PF₆]₂)

[RuCl(cpmp)(NCCH₃)PF₆] (1[PF₆]) (100 mg, 0.16 mmol, 1.0 equiv.) and ddpd^[84] (71 mg, 0.25 mmol, 1.5 equiv.) were dissolved in a mixture of acetonitrile (1 mL) and ethanol (6 mL). The solution was heated to reflux in a laboratory microwave oven for 8 h (100 W, 90 °C). The solvents were removed under reduced pressure. The dark red solid was dissolved in acetonitrile (1 mL) and precipitated by addition of diethyl ether (100 mL). The precipitate was washed with diethyl ether (100 mL) to remove excess ligand. The product was collected by filtration and dissolved in acetonitrile (1 mL). Addition of an aqueous solution of [NH₄][PF₆] (1 mg, 6 mmol, 37 equiv. in 100 mL of H₂O) resulted in the precipitation of a purple solid, which was collected by filtration and purified by slow diffusion of diethyl ether into a solution of 3[PF₆]₂ in acetonitrile to yield crystals suitable for single-crystal X-ray diffraction. The purple crystals were dried under reduced pressure. Yield: 98 mg (0.10 mmol, 62%). ¹H NMR (CD₃CN): $\delta = 8.12$ (dd, ³J = 8.0, 8.0 Hz, 1H), 8.03 (dd, ³J = 8.1, 8.1 Hz, 1H), 8.01–7.97 (m, 2H), 7.87–7.79 (m, 4H), 7.55 (dd, ³J = 8.4 Hz, ⁴J = 1.2 Hz, 1H), 7.42 (d, ³J = 5.8 Hz, 1H), 7.30–7.20 (m, 6H), 7.18 (dd, ³J = 8.1, 8.1 Hz, 2H), 6.92–6.84 (m, 2H), 6.81 (ddd, ³J = 6.6, 5.9 Hz, ⁴J = 1.2 Hz, 1H), 6.76 (ddd, ³J = 6.6, 5.9 Hz, ⁴J = 1.2 Hz, 1H), 3.02 (s, 3H, CH₃), 3.01 (s, 3H, CH₃), 2.81 (s, 3H, CH₃). ¹³C{¹H} NMR (CD₃CN): $\delta = 185.0$ (C¹), 159.8, 158.9, 158.3, 157.9, 156.9, 156.3, 156.2, 155.9, 154.4, 154.1, 153.5, 152.7, 141.2, 140.6, 140.2, 140.0, 139.7, 138.7, 128.8, 128.4, 125.4, 121.9, 121.7, 121.4, 119.9, 115.7, 115.6, 115.2, 113.7, 113.4, 40.8, 40.7, 40.0. The nuclei of the two ligands feature too similar chemical shifts to allow a detailed assignment. However, the number of ¹H and ¹³C NMR resonances, their intensity and multiplicity fit to the proposed structure. ³¹P{¹H} NMR (CD₃CN): $\delta = -144.7$ (sept, ¹J_{PF} = 700 Hz). MS (ESI⁺): $m/z = 341.6$ (48%, [Ru(cpmp)(ddpd)]²⁺), 828.2 (100%, [Ru(cpmp)(ddpd)][PF₆]⁺). MS (HR-ESI⁺): calcd for C₃₄H₃₁F₆RuN₉OP⁺: $m/z = 828.1337$. Found: 828.1320. Elem. anal. calcd for C₃₄H₃₁F₁₂RuN₉OP₂: C, 41.98; H, 3.21; N, 12.96. Found: C, 41.72; H, 3.34; N, 12.84. IR (ATR): $\tilde{\nu} = 3096$ (vw, CH), 2976 (vw, CH), 2905 (vw, CH), 2829 (vw, CH), 1666 (vw, CO), 1592 (vw), 1576 (vw), 1486 (w), 1450 (w), 1434 (w), 1351 (vw), 1335 (vw), 1314 (vw), 1246 (vw), 1236 (vw), 1196 (vw), 1170 (vw), 1136 (vw), 1096 (vw), 1064 (vw), 1024 (vw), 972 (vw), 947 (vw), 877 (vw), 829 (vs., PF), 774 (m), 746 (m), 713 (w), 673 (vw), 647 (vw), 633 (vw), 589 (vw), 581 (vw), 555 (s, PF₂), 521 (vw), 467 (vw), 448 (vw), 437 (vw), 412 (vw) cm⁻¹. IR (KBr): $\tilde{\nu} = 3111$ (vw, CH), 2970 (vw, CH), 2913 (vw, CH), 2833 (vw, CH), 1668 (w, CO), 1597 (w), 1578 (w), 1489 (m), 1451 (m), 1436 (m), 1352 (w), 1337 (w), 1316 (vw), 1249 (w), 1171 (vw), 1140 (w), 1097 (vw), 1082 (vw), 1065 (vw), 1024 (vw), 973 (vw), 950 (vw), 842 (vs., PF), 799 (w), 778 (w), 753 (w), 715 (vw), 673 (vw), 664 (vw), 649 (vw), 633 (vw), 611 (vw), 591 (vw), 581 (vw), 557 (s, PF₂), 528 (vw), 514 (vw), 496 (vw), 494 (vw), 463 (vw), 449 (vw), 438 (vw), 420 (vw), 410 (vw) cm⁻¹. CV (CH₃CN, vs. FcH/FcH⁺): $E_{1/2} = -2.06$ (rev.), -1.37 (rev.), $+0.67$ (rev.) V. UV/Vis (CH₃CN): λ_{max} (ϵ) = 267 (33 200), 350 (14 200), 541 nm (2800 m⁻¹ cm⁻¹). Emission (CH₃CN, 298 K): $\lambda_{\text{em}} = 755$ nm ($\lambda_{\text{exc}} = 544$ nm), $\tau = 56$ ns ($\lambda_{\text{exc}} = 540$ nm, streak camera), Φ ($\lambda_{\text{exc}} = 545$ nm, comparative method) = 0.04% (deaerated), 0.028% (aerated). Emission ($^{\text{a}}\text{PrCN}$, 77 K, $\lambda_{\text{exc}} = 541$ nm): $\lambda_{\text{em}} = 740$ nm.

Reduction of 2[PF₆]₂ and 3[PF₆]₂ using decamethylcobaltocene

The respective ruthenium(II) complex 2[PF₆]₂ or 3[PF₆]₂ (0.80 mg) was dissolved in CH₃CN (0.5 mL). CoCp*₂ was added (0.27 mg) and the IR spectrum was recorded immediately.

Catalysis experiments

To an oven-dried NMR tube were added the olefin (0.157 mmol; dried over molecular sieves), the thiol (0.063 mmol), the sensitizer (2[PF₆]₂: 1.4 μ mol, 2.2 mol-%; 3[PF₆]₂: 1.4 μ mol, 2.2 mol-%; [Ru(bpy)₃][PF₆]₂: 1.6 μ mol, 2.5 mol-%), *p*-toluidine (0.029 mmol) and CD₃CN (0.5 mL). The tube was sealed with a Teflon cap and irradiated with the green light source. Yields were determined by ¹H NMR spectroscopy using 1,4-bis(trimethylsilyl)benzene as internal standard.

Acknowledgements

Financial support from the Deutsche Forschungsgemeinschaft [DFG, Priority Program SPP 2102 "Light-controlled reactivity of metal complexes" (HE 2778/14-1; LO 714/11-1)] and RE 1203/23-1 is gratefully acknowledged. Parts of this research were conducted using the supercomputer Mogon and advisory services offered by Johannes Gutenberg University Mainz (www.hpc.uni-mainz.de), which is a member of the AHRP and the Gauss Alliance e.V. We thank Regine Jung-Pothmann for collection of the diffraction data.

Conflict of interest

The authors declare no conflict of interest.

Keywords: luminescence · photocatalysis · photochemistry · photophysics · ruthenium

- [1] J. P. Sauvage, J. P. Collin, J. C. Chambrion, S. Guillerez, C. Coudret, V. Balzani, F. Barigelletti, L. de Cola, L. Flamigni, *Chem. Rev.* **1994**, *94*, 993–1019.
- [2] S. Campagna, F. Puntoriero, F. Nastasi, G. Bergamini, V. Balzani, *Top. Curr. Chem.* **2007**, *280*, 117–214.
- [3] G. A. Crosby, *Acc. Chem. Res.* **1975**, *8*, 231–238.
- [4] V. Balzani, F. Boletta, M. T. Gandolfi, M. Maestri, *Top. Curr. Chem.* **1978**, *75*, 1–64.
- [5] K. Kalyanasundaram, *Coord. Chem. Rev.* **1982**, *46*, 159–244.
- [6] D. W. Thompson, A. Ito, T. J. Meyer, *Pure Appl. Chem.* **2013**, *85*, 1257–1305.
- [7] P. Müller, K. Brettel, *Photochem. Photobiol. Sci.* **2012**, *11*, 632–636.
- [8] O. Bräm, F. Messina, A. M. El-Zohry, A. Cannizzo, M. Chergui, *Chem. Phys.* **2012**, *393*, 51–57.
- [9] a) A. Juris, V. Balzani, F. Barigelletti, S. Campagna, P. Belser, A. von Zelewsky, *Coord. Chem. Rev.* **1988**, *84*, 85–277; b) A. Juris, V. Balzani, P. Belser, A. von Zelewsky, *Helv. Chim. Acta* **1981**, *64*, 2175–2182.
- [10] A. Cannizzo, F. van Mourik, W. Gawelda, G. Zgrablic, C. Bressler, M. Chergui, *Angew. Chem. Int. Ed.* **2006**, *45*, 3174–3176; *Angew. Chem.* **2006**, *118*, 3246–3248.
- [11] N. H. Damrauer, G. Cerullo, A. Yeh, T. R. Bousie, C. V. Shank, J. K. McCusker, *Science* **1997**, *275*, 54–57.
- [12] A. T. Yeh, C. V. Shank, J. K. McCusker, *Science* **2000**, *289*, 935–938.
- [13] A. J. Atkins, L. González, *J. Phys. Chem. Lett.* **2017**, *8*, 3840–3845.

- [14] a) A. Soupart, F. Alary, J.-L. Heully, P. I. P. Elliott, I. M. Dixon, *Inorg. Chem.* **2018**, *57*, 3192–3196; b) A. Soupart, I. M. Dixon, F. Alary, J.-L. Heully, *Theor. Chem. Acc.* **2018**, *137*, 37.
- [15] K. Suzuki, A. Kobayashi, S. Kaneko, K. Takehira, T. Yoshihara, H. Ishida, Y. Shiina, S. Oishi, S. Tobita, *Phys. Chem. Chem. Phys.* **2009**, *11*, 9850–9860.
- [16] H. Ishida, S. Tobita, Y. Hasegawa, R. Katoh, K. Nozaki, *Coord. Chem. Rev.* **2010**, *254*, 2449–2458.
- [17] G. A. Crosby, J. N. Demas, *J. Am. Chem. Soc.* **1971**, *93*, 2841–2847.
- [18] R. C. Young, T. J. Meyer, D. G. Whitten, *J. Am. Chem. Soc.* **1976**, *98*, 286–287.
- [19] B. Durham, J. V. Caspar, J. K. Nagle, T. J. Meyer, *J. Am. Chem. Soc.* **1982**, *104*, 4803–4810.
- [20] B. O'Regan, M. Grätzel, *Nature* **1991**, *353*, 737–740.
- [21] J.-F. Yin, M. Velayudham, D. Bhattacharya, H.-C. Lin, K.-L. Lu, *Coord. Chem. Rev.* **2012**, *256*, 3008–3035.
- [22] P. G. Bomben, K. C. D. Robson, B. D. Koivisto, C. P. Berlinguette, *Coord. Chem. Rev.* **2012**, *256*, 1438–1450.
- [23] R. D. Costa, E. Ortí, H. J. Bolink, F. Monti, G. Accorsi, N. Armadori, *Angew. Chem. Int. Ed.* **2012**, *51*, 8178–8211; *Angew. Chem.* **2012**, *124*, 8300–8334.
- [24] P. Dreyse, B. Loeb, M. Soto-Arriaza, D. Tordera, E. Ortí, J. J. Serrano-Pérez, H. J. Bolink, *Dalton Trans.* **2013**, *42*, 15502–15513.
- [25] H. J. Bolink, L. Cappelli, E. Coronado, P. Gaviña, *Inorg. Chem.* **2005**, *44*, 5966–5968.
- [26] H. J. Bolink, E. Coronado, R. D. Costa, P. Gaviña, E. Ortí, S. Tatay, *Inorg. Chem.* **2009**, *48*, 3907–3909.
- [27] K. M. Maness, R. H. Terrill, T. J. Meyer, R. W. Murray, R. M. Wightman, *J. Am. Chem. Soc.* **1996**, *118*, 10609–10616.
- [28] A. Inagaki, M. Akita, *Coord. Chem. Rev.* **2010**, *254*, 1220–1239.
- [29] C. K. Prier, D. A. Rankic, D. W. C. MacMillan, *Chem. Rev.* **2013**, *113*, 5322–5363.
- [30] A. Breivogel, M. Meister, C. Förster, F. Laquai, K. Heinze, *Chem. Eur. J.* **2013**, *19*, 13745–13760.
- [31] L. Gong, S. P. Mulcahy, D. Devarajan, K. Harms, G. Frenking, E. Meggers, *Inorg. Chem.* **2010**, *49*, 7692–7699.
- [32] A. Reynal, E. Palomares, *Eur. J. Inorg. Chem.* **2011**, 4509–4526.
- [33] C. Fu, M. Wenzel, E. Treutlein, K. Harms, E. Meggers, *Inorg. Chem.* **2012**, *51*, 10004–10011.
- [34] E. Meggers, *Chem. Eur. J.* **2010**, *16*, 752–758.
- [35] E. Meggers, *Eur. J. Inorg. Chem.* **2011**, 2911–2926.
- [36] A. Breivogel, C. Kreitner, K. Heinze, *Eur. J. Inorg. Chem.* **2014**, 5468–5490.
- [37] A. Breivogel, C. Förster, K. Heinze, *Inorg. Chem.* **2010**, *49*, 7052–7056.
- [38] B. Durham, J. L. Walsh, C. L. Carter, T. J. Meyer, *Inorg. Chem.* **1980**, *19*, 860–865.
- [39] M. Gleria, F. Minto, G. Beggiato, P. Bortolus, *J. Chem. Soc. Chem. Commun.* **1978**, 285a.
- [40] L. Feng, Y. Wang, *Inorg. Chem.* **2018**, *57*, 8994–9001.
- [41] M. Maestri, N. Armadori, V. Balzani, E. C. Constable, A. M. W. Cargill Thompson, *Inorg. Chem.* **1995**, *34*, 2759–2767.
- [42] J. R. Winkler, T. L. Netzel, C. Creutz, N. Sutin, *J. Am. Chem. Soc.* **1987**, *109*, 2381–2392.
- [43] Y. Liu, R. Hammit, D. A. Lutterman, R. P. Thummel, C. Turro, *Inorg. Chem.* **2007**, *46*, 6011–6021.
- [44] L. Hammarström, O. Johansson, *Coord. Chem. Rev.* **2010**, *254*, 2546–2559.
- [45] P. D. Fleischauer, P. Fleischauer, *Chem. Rev.* **1970**, *70*, 199–230.
- [46] F. Schramm, V. Meded, H. Fliegl, K. Fink, O. Fuhr, Z. Qu, W. Klopfer, S. Finn, T. E. Keyes, M. Ruben, *Inorg. Chem.* **2009**, *48*, 5677–5684.
- [47] C. Kreitner, K. Heinze, *Dalton Trans.* **2016**, *45*, 13631–13647.
- [48] C. Kreitner, E. Erdmann, W. W. Seidel, K. Heinze, *Inorg. Chem.* **2015**, *54*, 11088–11104.
- [49] C. Kreitner, K. Heinze, *Dalton Trans.* **2016**, *45*, 5640–5658.
- [50] S. H. Wadman, M. Lutz, D. M. Tooke, A. L. Spek, F. Hartl, R. W. A. Havenith, G. P. M. van Klink, G. van Koten, *Inorg. Chem.* **2009**, *48*, 1887–1900.
- [51] P. G. Bomben, K. C. D. Robson, P. A. Sedach, C. P. Berlinguette, *Inorg. Chem.* **2009**, *48*, 9631–9643.
- [52] S. H. Wadman, J. M. Kroon, K. Bakker, R. W. A. Havenith, G. P. M. van Klink, G. van Koten, *Organometallics* **2010**, *29*, 1569–1579.
- [53] C. Förster, M. Dorn, T. Reuter, S. Otto, G. Davarci, T. Reich, L. Carrella, E. Rentschler, K. Heinze, *Inorganics* **2018**, *6*, 86.
- [54] A. K. C. Mengel, C. Förster, A. Breivogel, K. Mack, J. R. Ochsmann, F. Laquai, V. Ksenofontov, K. Heinze, *Chem. Eur. J.* **2015**, *21*, 704–714.
- [55] A. K. C. Mengel, C. Bissinger, M. Dorn, O. Back, C. Förster, K. Heinze, *Chem. Eur. J.* **2017**, *23*, 7920–7931.
- [56] L. L. Jamula, A. M. Brown, D. Guo, J. K. McCusker, *Inorg. Chem.* **2014**, *53*, 15–17.
- [57] J. L. Bolliger, M. Oberholzer, C. M. Frech, *Adv. Synth. Catal.* **2011**, *353*, 945–954.
- [58] M. A. Bennett, T. N. Huang, T. W. Matheson, A. K. Smith, S. Ittel, W. Nickerson, *Inorg. Synth.* **1982**, *21*, 74–78.
- [59] K.-Y. Ho, W.-Y. Yu, K.-K. Cheung, C.-M. Che, *J. Chem. Soc. Dalton Trans.* **1999**, 1581–1586.
- [60] C. R. Goldsmith, T. D. P. Stack, *Inorg. Chem.* **2006**, *45*, 6048–6055.
- [61] P. Alemany, D. Casanova, S. Alvarez, C. Dryzun, D. Avnir, *Continuous Symmetry Measures: A New Tool in Quantum Chemistry, Reviews in Computational Chemistry* (Eds.: A. L. Parrill, K. B. Lipkowitz), Vol. 30, Wiley, Hoboken, **2017**, pp. 289–352.
- [62] H. Kronenwetter, J. Husek, B. Etz, A. Jones, R. Manchanayakage, *Green Chem.* **2014**, *16*, 1489–1495.
- [63] T. Tsuritani, S. Ito, H. Shinokubo, K. Oshima, *J. Org. Chem.* **2000**, *65*, 5066–5068.
- [64] H. B. Ross, M. Boldaji, D. P. Rillema, C. B. Blanton, R. P. White, *Inorg. Chem.* **1989**, *28*, 1013–1021.
- [65] D. P. Rillema, C. B. Blanton, R. J. Shaver, D. C. Jackman, M. Boldaji, S. Bundy, L. A. Worl, T. J. Meyer, *Inorg. Chem.* **1992**, *31*, 1600–1606.
- [66] B. J. Coe, D. W. Thompson, C. T. Culbertson, J. R. Schoonover, T. J. Meyer, *Inorg. Chem.* **1995**, *34*, 3385–3395.
- [67] A. M. Brown, C. E. McCusker, J. K. McCusker, *Dalton Trans.* **2014**, *43*, 17635–17646.
- [68] J. V. Caspar, E. M. Kober, B. P. Sullivan, T. J. Meyer, *J. Am. Chem. Soc.* **1982**, *104*, 630–632.
- [69] J. V. Caspar, T. J. Meyer, *J. Phys. Chem.* **1983**, *87*, 952–957.
- [70] S. J. L. Lauw, X. Xu, R. D. Webster, *ChemPlusChem* **2015**, *80*, 1288–1297.
- [71] E. L. Tyson, Z. L. Niemeyer, T. P. Yoon, *J. Org. Chem.* **2014**, *79*, 1427–1436.
- [72] E. L. Tyson, M. S. Ament, T. P. Yoon, *J. Org. Chem.* **2013**, *78*, 2046–2050.
- [73] C. E. Hoyle, A. B. Lowe, C. N. Bowman, *Chem. Soc. Rev.* **2010**, *39*, 1355–1387.
- [74] G. R. Fulmer, A. J. M. Miller, N. H. Sherden, H. E. Gottlieb, A. Nudelman, B. M. Stoltz, J. E. Bercaw, K. I. Goldberg, *Organometallics* **2010**, *29*, 2176–2179.
- [75] M. Krejčík, M. Daněk, F. Hartl, *J. Electroanal. Chem.* **1991**, *317*, 179–187.
- [76] a) C. Würth, D. Geißler, T. Behnke, M. Kaiser, U. Resch-Genger, *Anal. Bioanal. Chem.* **2015**, *407*, 59–78; b) C. Würth, M. G. González, R. Niessner, U. Panne, C. Haisch, U. Resch-Genger, *Talanta* **2012**, *90*, 30–37.
- [77] C. Würth, J. Pauli, C. Lochmann, M. Spieles, U. Resch-Genger, *Anal. Chem.* **2012**, *84*, 1345–1352.
- [78] SMART Data Collection and SAINT-Plus Data Processing Software for the SMART System (various versions), Bruker Analytical X-Ray Instruments, Inc.: Madison, WI **2000**.
- [79] a) R. H. Blessing, *Acta Crystallogr. Sect. A* **1995**, *51*, 33–38; b) A. L. Spek, *Acta Crystallogr. Sect. D* **2009**, *65*, 148–155.
- [80] a) G. M. Sheldrick, *Acta Crystallogr. Sect. C* **2015**, *71*, 3–8; b) G. M. Sheldrick, *SHELXL-2014/7*, University of Göttingen, Göttingen, Germany, **2014**.
- [81] C. B. Hübschle, G. M. Sheldrick, B. Dittrich, *J. Appl. Crystallogr.* **2011**, *44*, 1281–1284.
- [82] F. Neese, *WIREs Comput. Mol. Sci.* **2012**, *2*, 73–78.
- [83] F. Neese, *WIREs Comput. Mol. Sci.* **2018**, *8*, e1327.
- [84] A. D. Becke, *J. Chem. Phys.* **1993**, *98*, 5648–5652.
- [85] C. Lee, W. Yang, R. G. Parr, *Phys. Rev. B* **1988**, *37*, 785–789.
- [86] B. Miehlich, A. Savin, H. Stoll, H. Preuss, *Chem. Phys. Lett.* **1989**, *157*, 200–206.
- [87] F. Neese, F. Wennmohs, A. Hansen, U. Becker, *Chem. Phys.* **2009**, *356*, 98–109.
- [88] R. Izsák, F. Neese, *J. Chem. Phys.* **2011**, *135*, 144105.
- [89] D. A. Pantazis, X.-Y. Chen, C. R. Landis, F. Neese, *J. Chem. Theory Comput.* **2008**, *4*, 908–919.
- [90] S. Miertuš, E. Scrocco, J. Tomasi, *Chem. Phys.* **1981**, *55*, 117–129.
- [91] V. Barone, M. Cossi, *J. Phys. Chem. A* **1998**, *102*, 1995–2001.
- [92] F. Weigend, R. Ahlrichs, *Phys. Chem. Chem. Phys.* **2005**, *7*, 3297–3305.

- [93] S. Grimme, J. Antony, S. Ehrlich, H. Krieg, *J. Chem. Phys.* **2010**, *132*, 154104.
- [94] S. Grimme, S. Ehrlich, L. Goerigk, *J. Comput. Chem.* **2011**, *32*, 1456–1465.
- [95] S. Mai, F. Plasser, J. Dorn, M. Fumanal, C. Daniel, L. González, *Coord. Chem. Rev.* **2018**, *361*, 74–97.

- [96] F. Plasser, Theodore 2.0, <http://theodore-qc.sourceforge.net>.

Manuscript received: February 18, 2020

Revised manuscript received: March 9, 2020

Accepted manuscript online: March 11, 2020

Version of record online: April 30, 2020

6. Green-Light Activation of Push–Pull Ruthenium(II) Complexes

6. Green-Light Activation of Push–Pull Ruthenium(II) Complexes

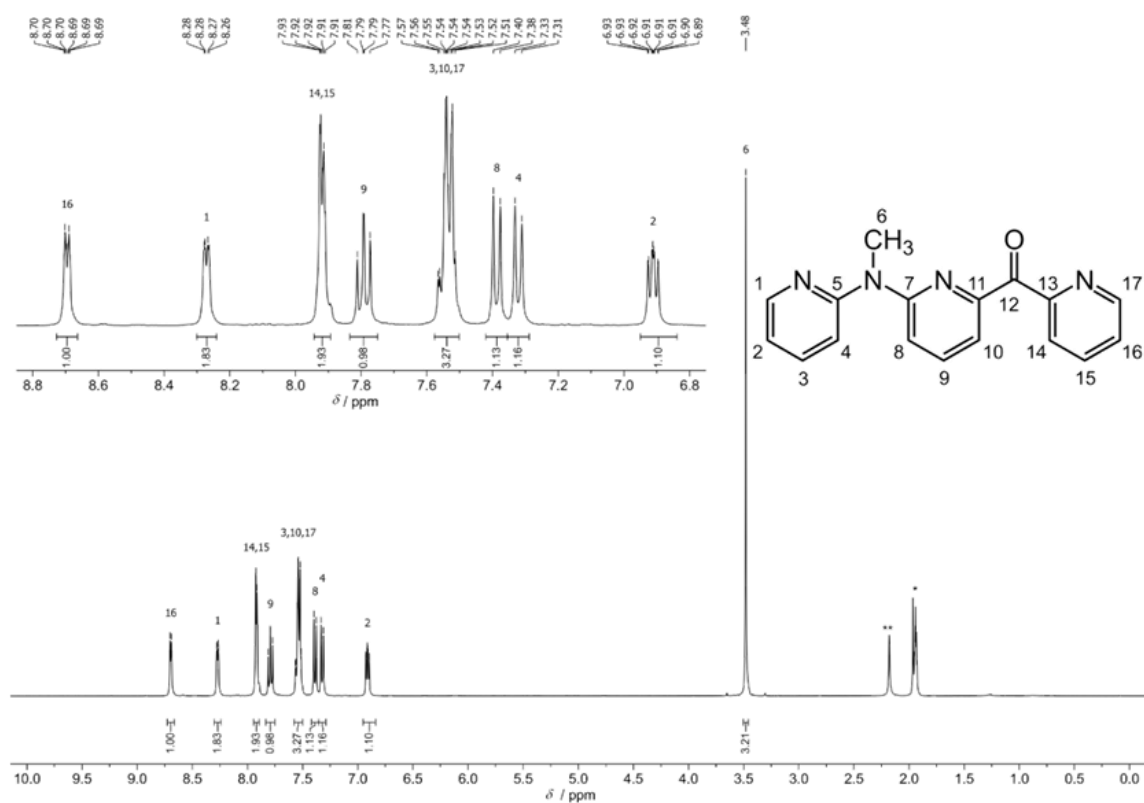


Figure S1. ^1H NMR spectrum of cpmp in CD_3CN at 293 K. * denotes solvent resonance; ** denotes water resonance.

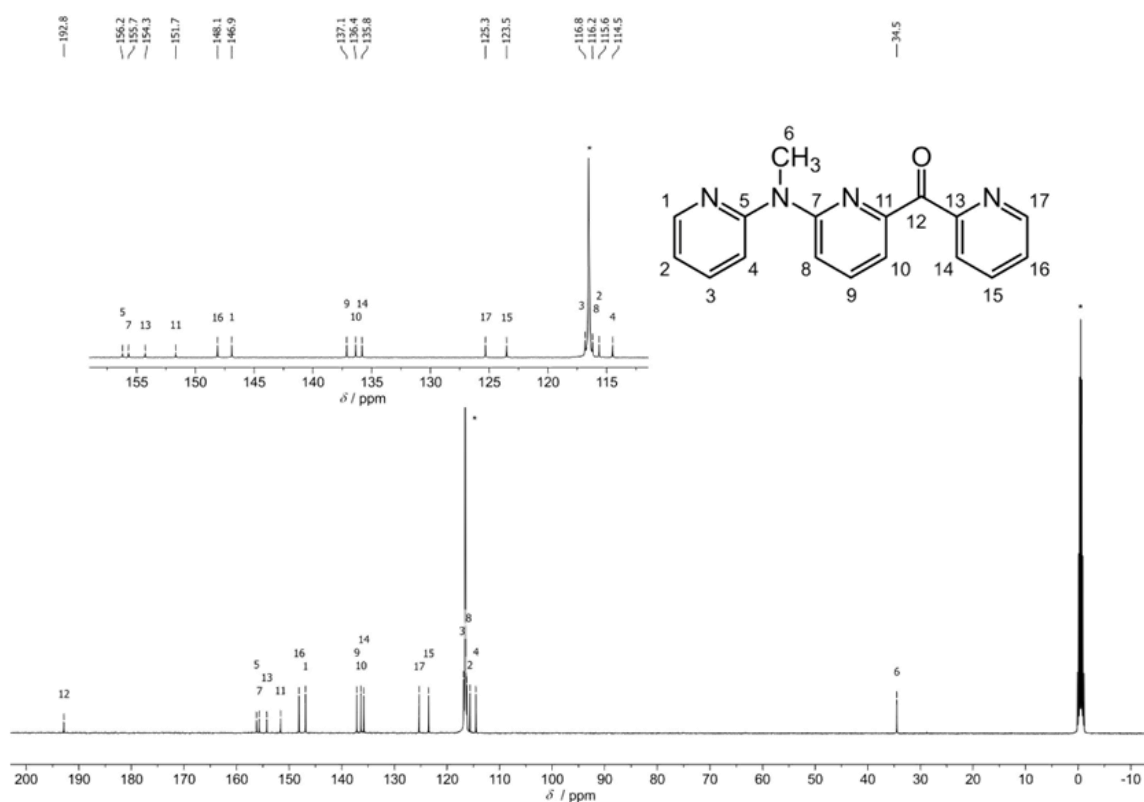


Figure S2. $^{13}\text{C}\{^1\text{H}\}$ NMR spectrum of cpmp in CD_3CN at 293 K. * denote solvent resonances.

6. Green-Light Activation of Push–Pull Ruthenium(II) Complexes

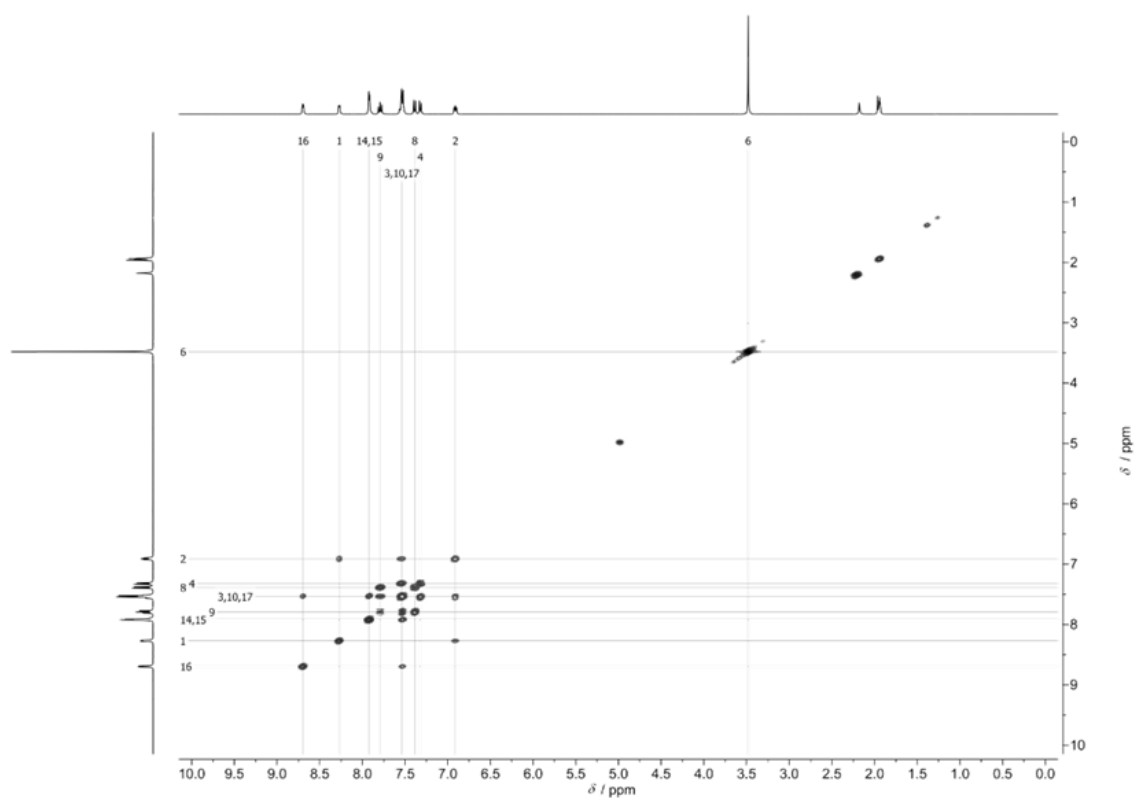


Figure S3. ^1H - ^1H COSY of cpm in CD_3CN at 293 K.

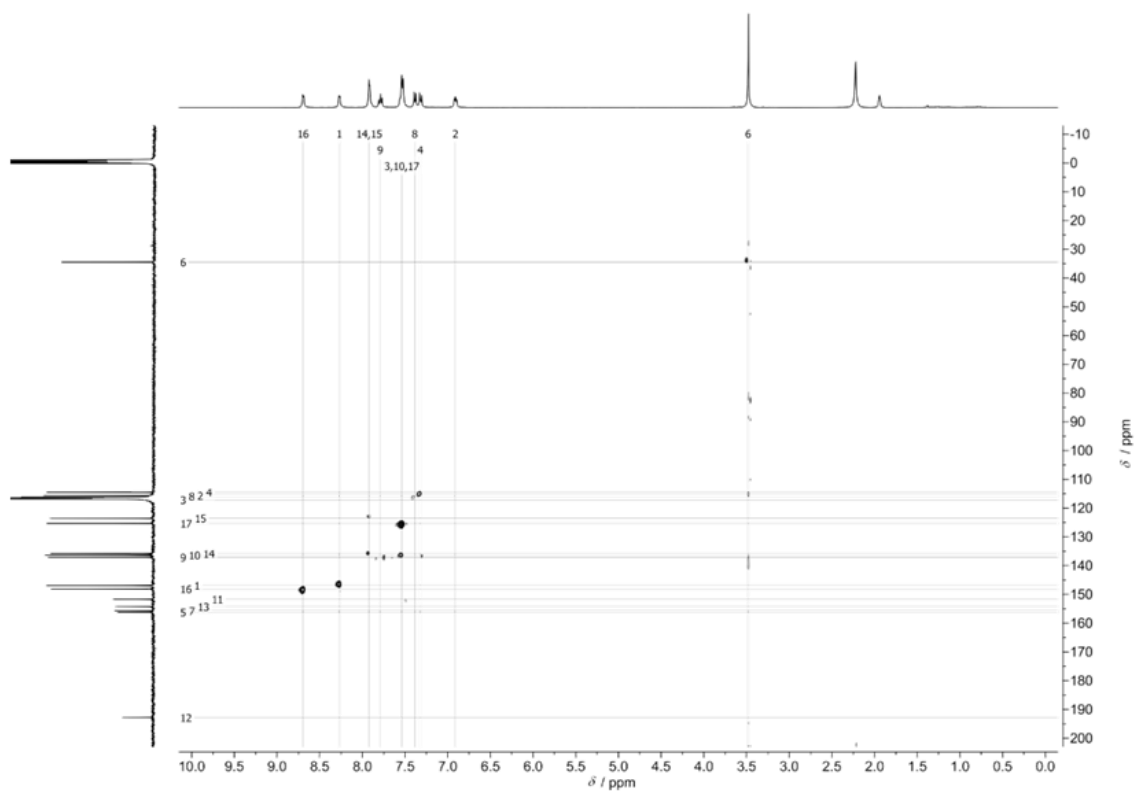


Figure S4. ^1H - ^{13}C HSQC of cpm in CD_3CN at 293 K.

6. Green-Light Activation of Push–Pull Ruthenium(II) Complexes

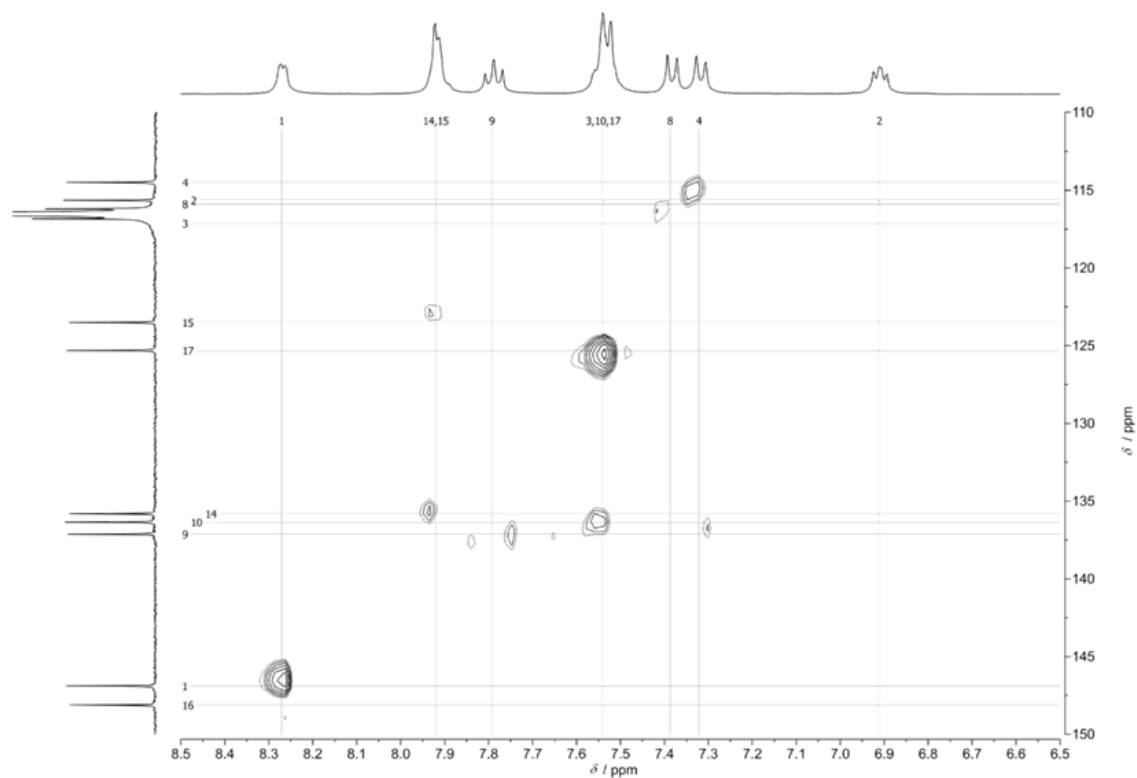


Figure S5. ^1H - ^{13}C HSQC of cpmp in CD_3CN at 293 K (zoom into aromatic region).

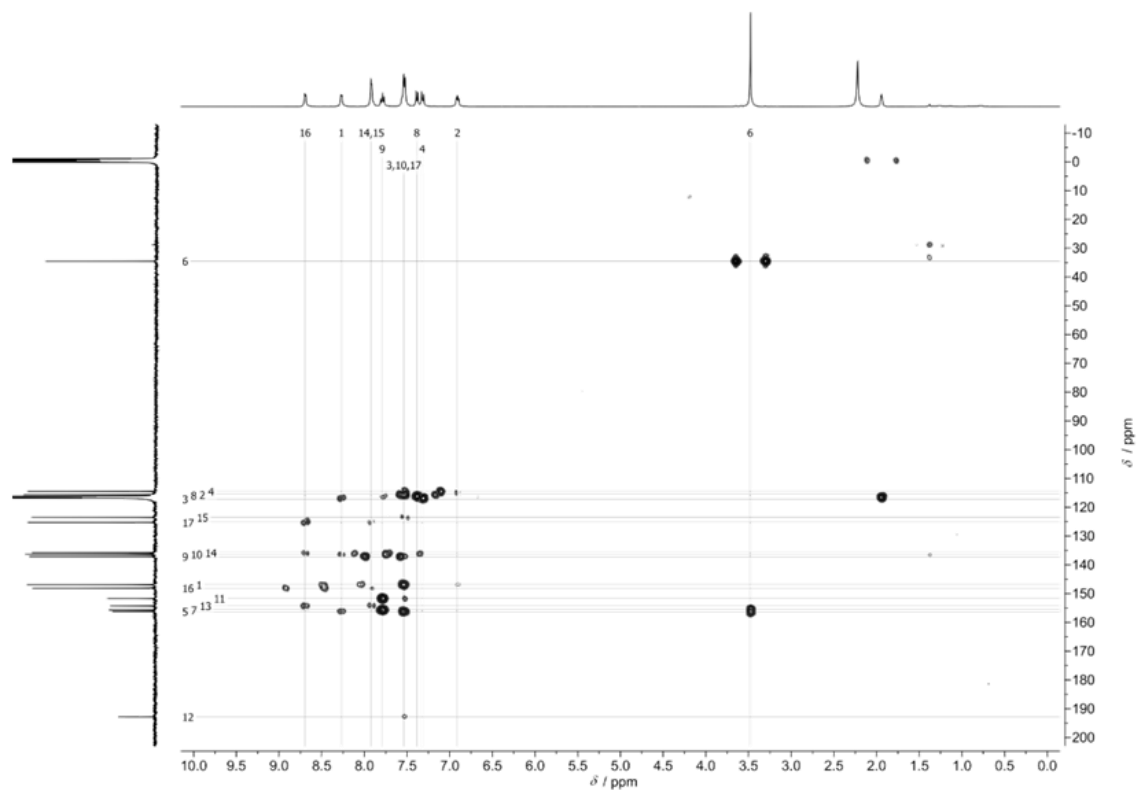


Figure S6. ^1H - ^{13}C HMBC of cpmp in CD_3CN at 293 K.

6. Green-Light Activation of Push–Pull Ruthenium(II) Complexes

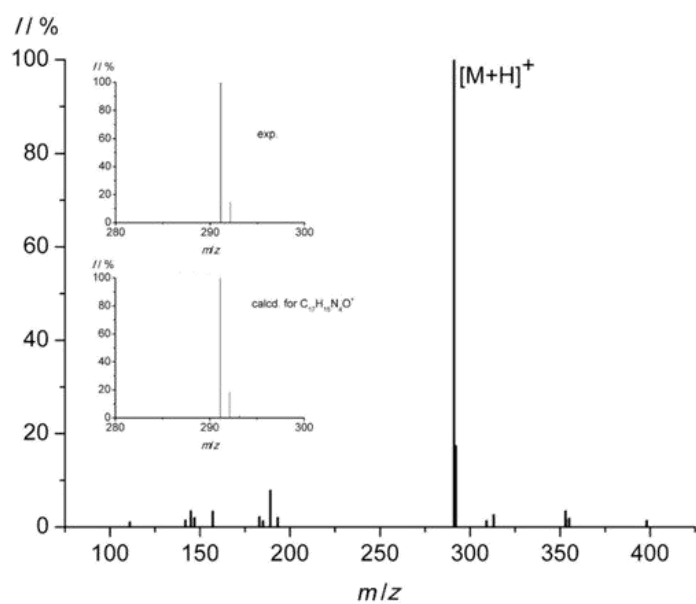


Figure S7. ESI⁺ mass spectrum of cpm in acetonitrile.

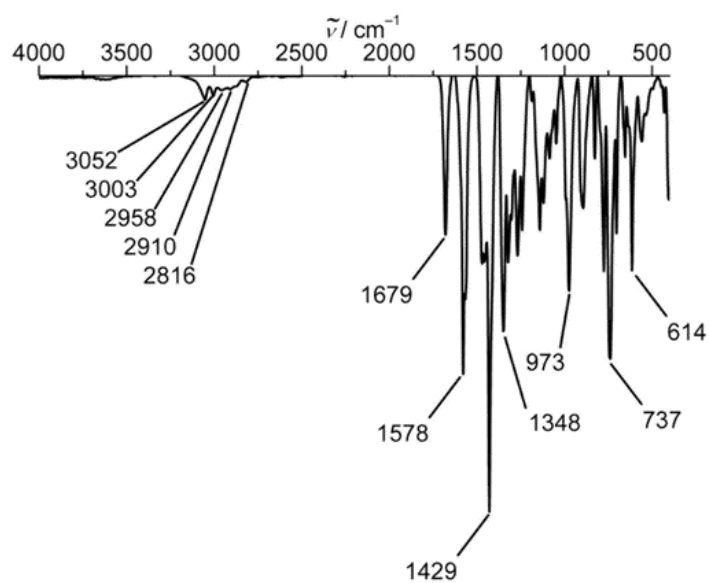


Figure S8. ATR-IR spectrum of cpm.

6. Green-Light Activation of Push–Pull Ruthenium(II) Complexes

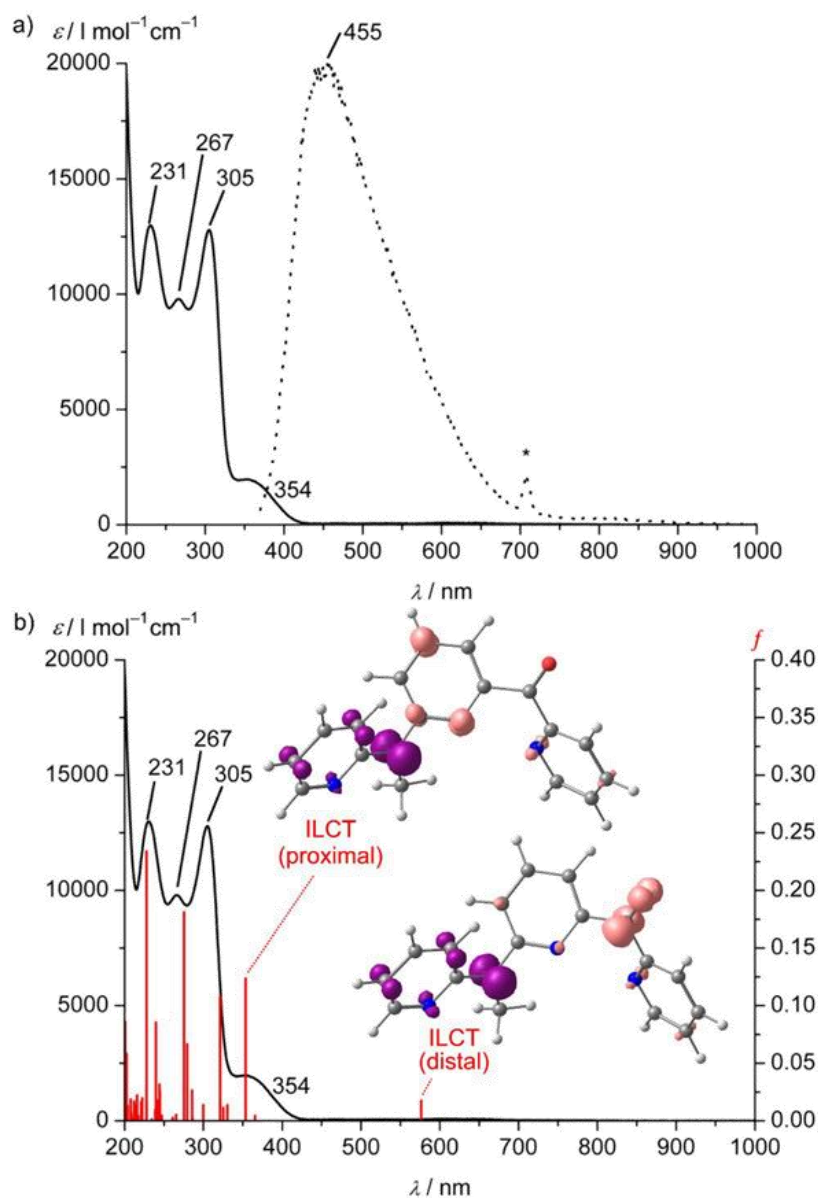


Figure S9. a) UV/Vis/NIR absorption and emission spectrum of cpmp in acetonitrile at 298 K ($\lambda_{\text{exc}} = 354$ nm, $\lambda_{\text{em}} = 2\lambda_{\text{exc}}$) and b) UV/Vis/NIR absorption spectrum (black line) and TD-DFT calculated oscillator strengths (red stick spectrum) of cpmp. Difference densities of the most intense low-energy ILCT transitions (TD-DFT, contour value of 0.01; purple = electron depletion; orange = electron gain). Possibly, the distal ILCT is very weak in solution due to the flexibility of cpmp, which is not reflected in the TD-DFT calculation of the static molecule.

6. Green-Light Activation of Push–Pull Ruthenium(II) Complexes

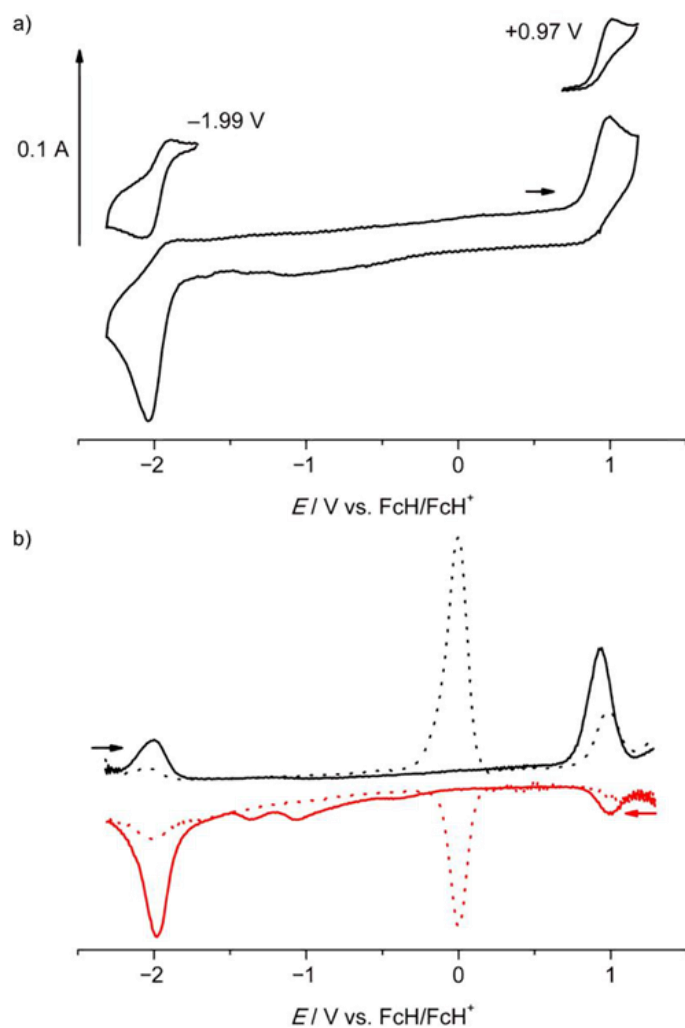


Figure S10. a) Cyclic voltammogram and b) square wave voltammogram of cpmp without (solid) and with (dotted) added ferrocene, 1 mM in acetonitrile, 0.1 M [$n\text{Bu}_4\text{N}$][PF₆].

6. Green-Light Activation of Push–Pull Ruthenium(II) Complexes

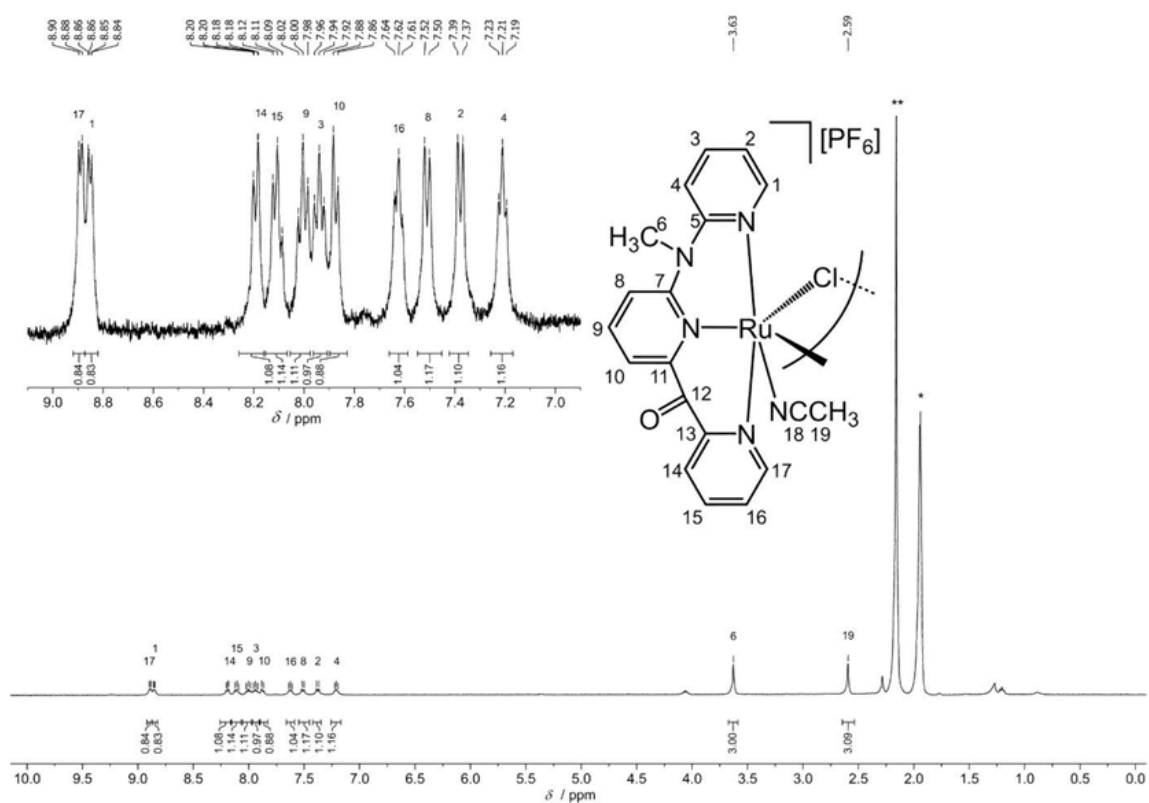


Figure S11. ^1H NMR spectrum of **1** $[\text{PF}_6]$ in CD_3CN at 293 K. * denotes solvent resonance; ** denotes water resonance.

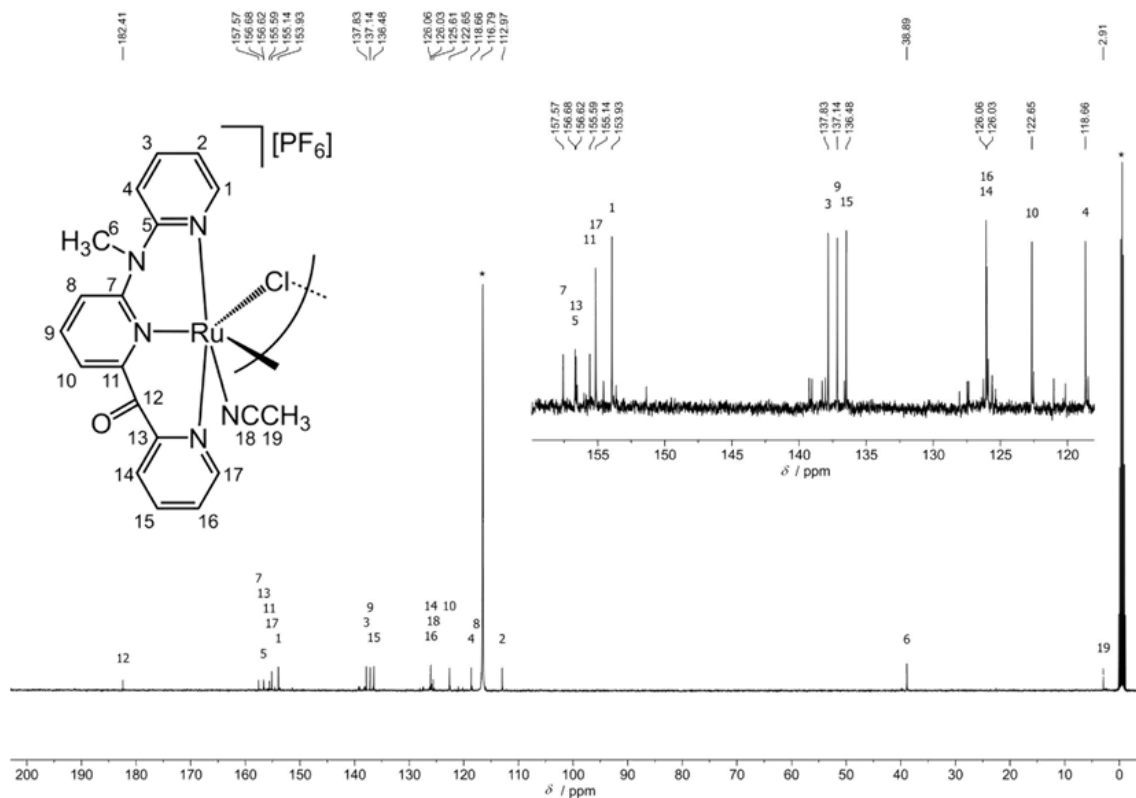


Figure S12. $^{13}\text{C}\{^1\text{H}\}$ NMR spectrum of **1** $[\text{PF}_6]$ in CD_3CN at 293 K. * denote solvent resonances.

6. Green-Light Activation of Push–Pull Ruthenium(II) Complexes

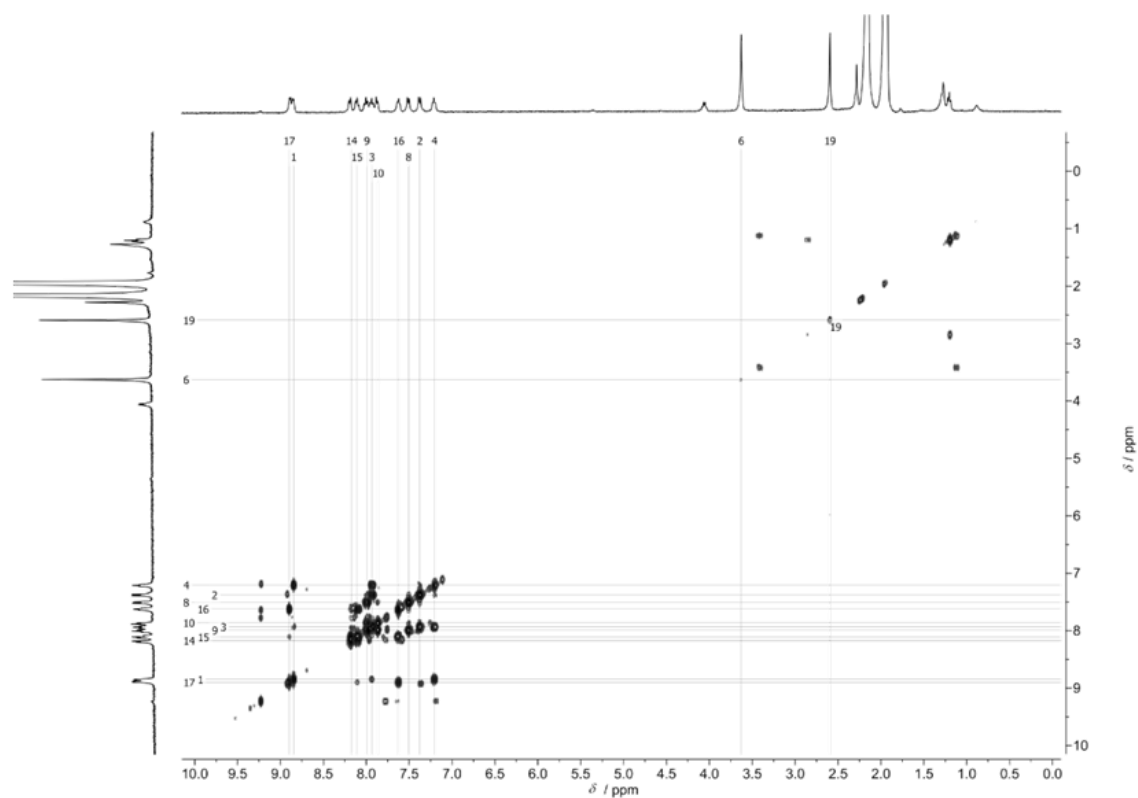


Figure S13. ^1H - ^1H COSY of $1[\text{PF}_6]$ in CD_3CN at 293 K.

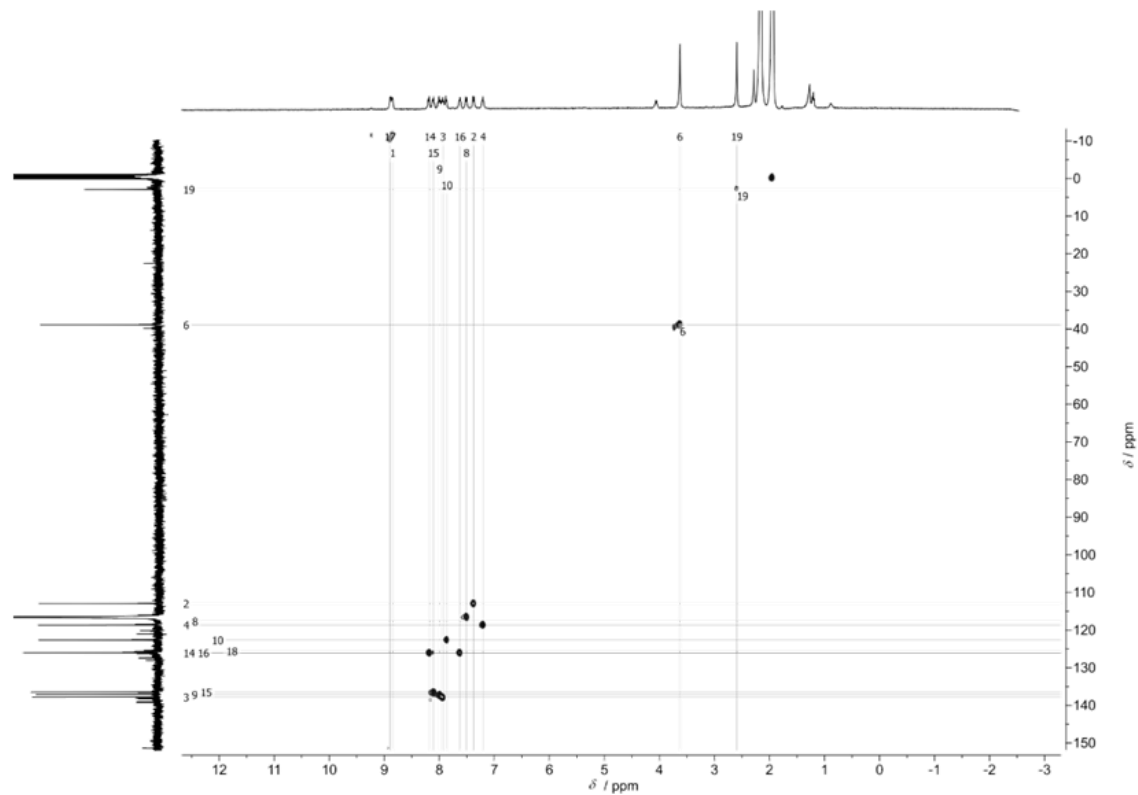


Figure S14. ^1H - ^{13}C HSQC of $1[\text{PF}_6]$ in CD_3CN at 293 K.

6. Green-Light Activation of Push–Pull Ruthenium(II) Complexes

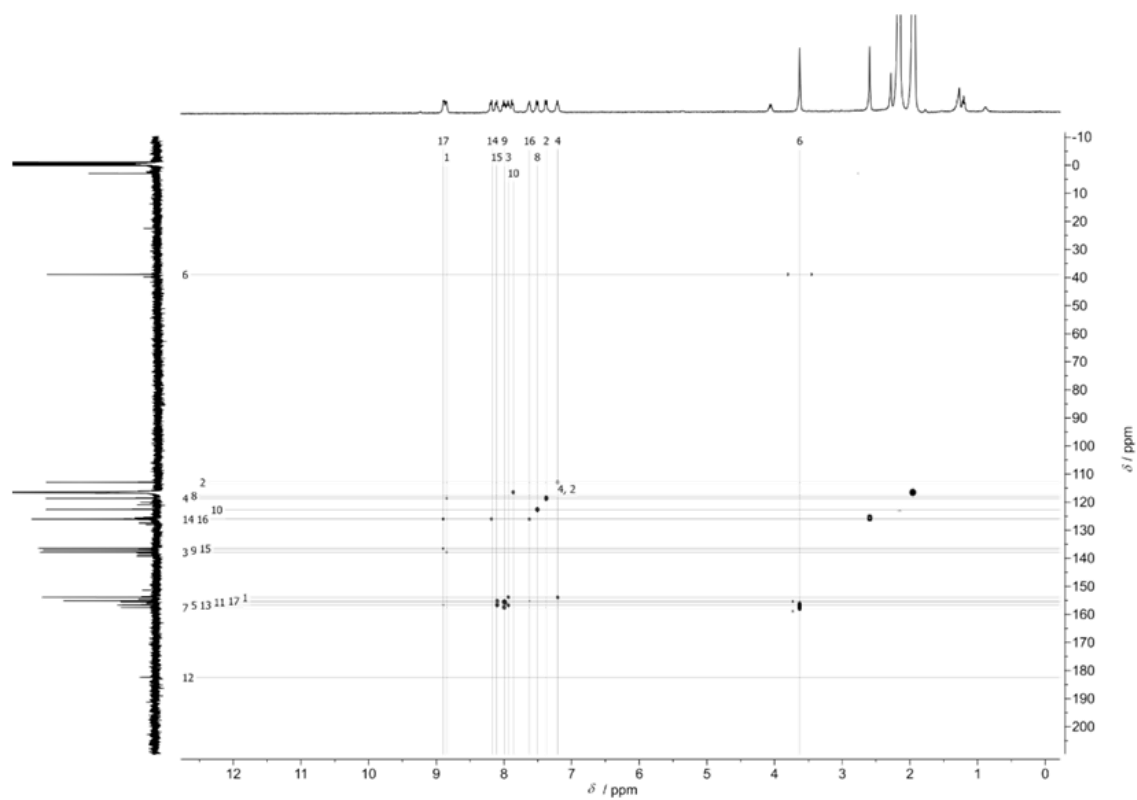


Figure S15. ¹H-¹³C HMBC of **1**[PF₆] in CD₃CN at 293 K.

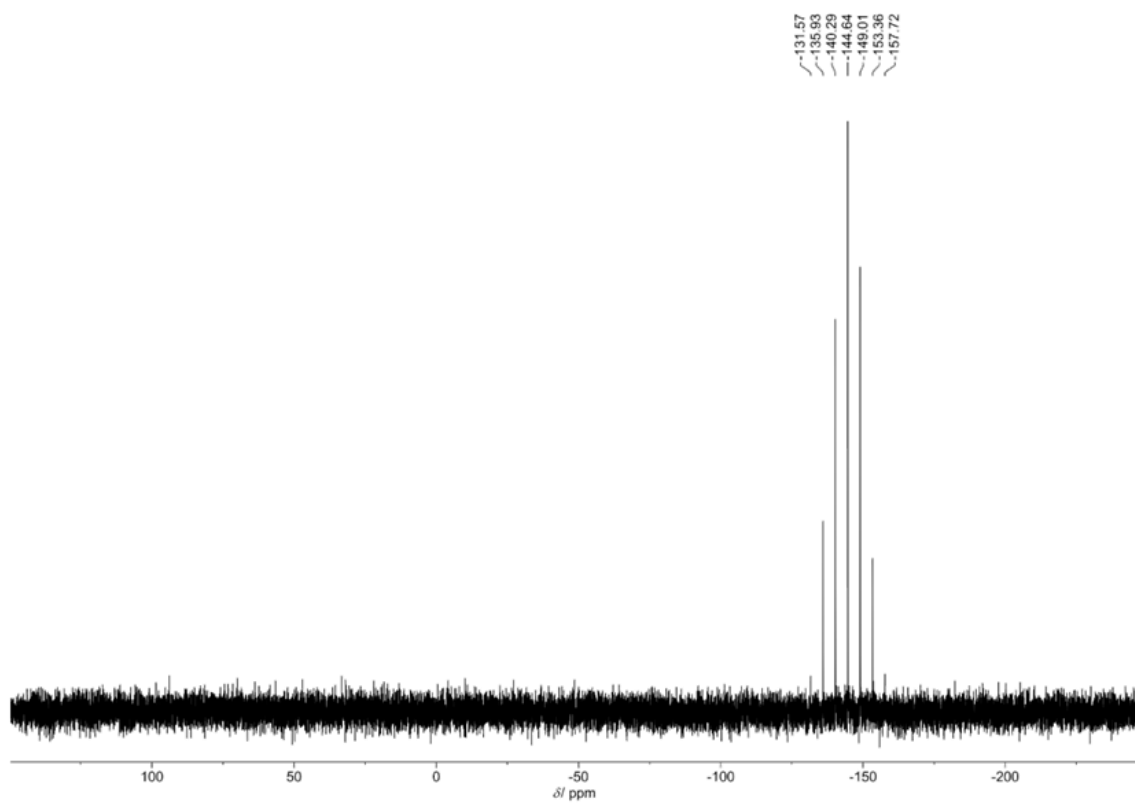


Figure S16. ³¹P{¹H} NMR spectrum of **1**[PF₆] in CD₃CN at 293 K.

6. Green-Light Activation of Push–Pull Ruthenium(II) Complexes

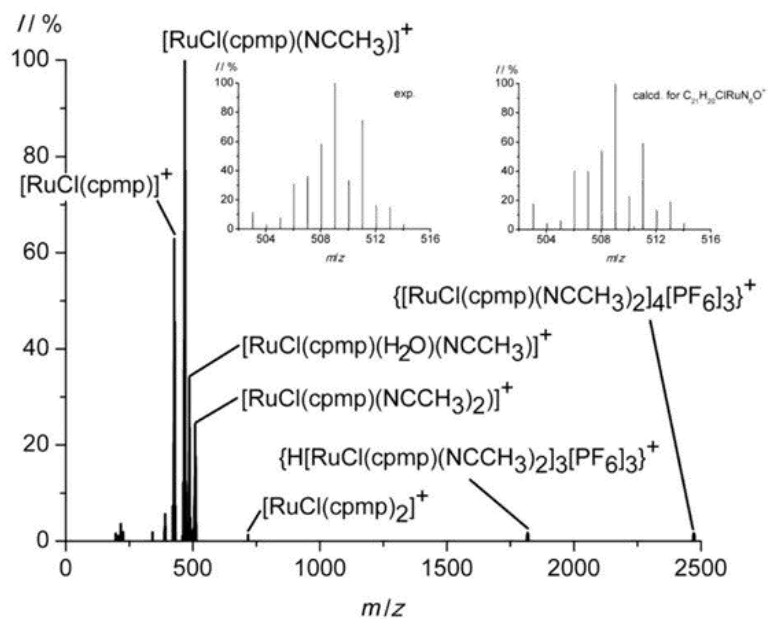


Figure S17. ESI⁺ mass spectrum of **1**[PF₆] in acetonitrile.

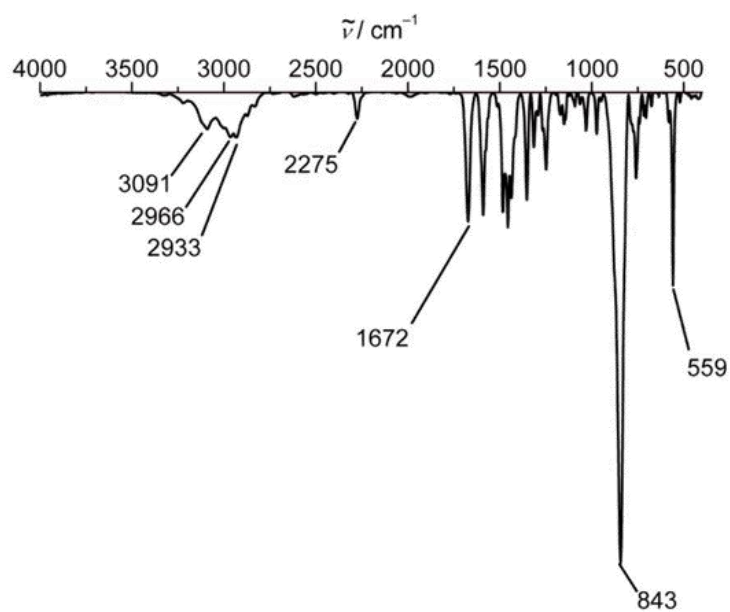


Figure S18. IR spectrum of **1**[PF₆] in KBr.

6. Green-Light Activation of Push–Pull Ruthenium(II) Complexes

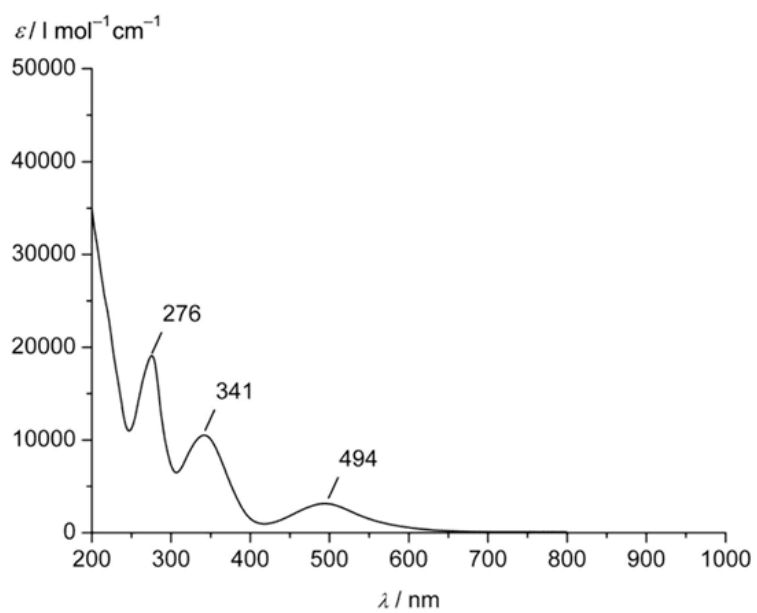


Figure S19. UV/Vis/NIR absorption spectrum of **1[PF₆]** in acetonitrile at 298 K.

6. Green-Light Activation of Push–Pull Ruthenium(II) Complexes

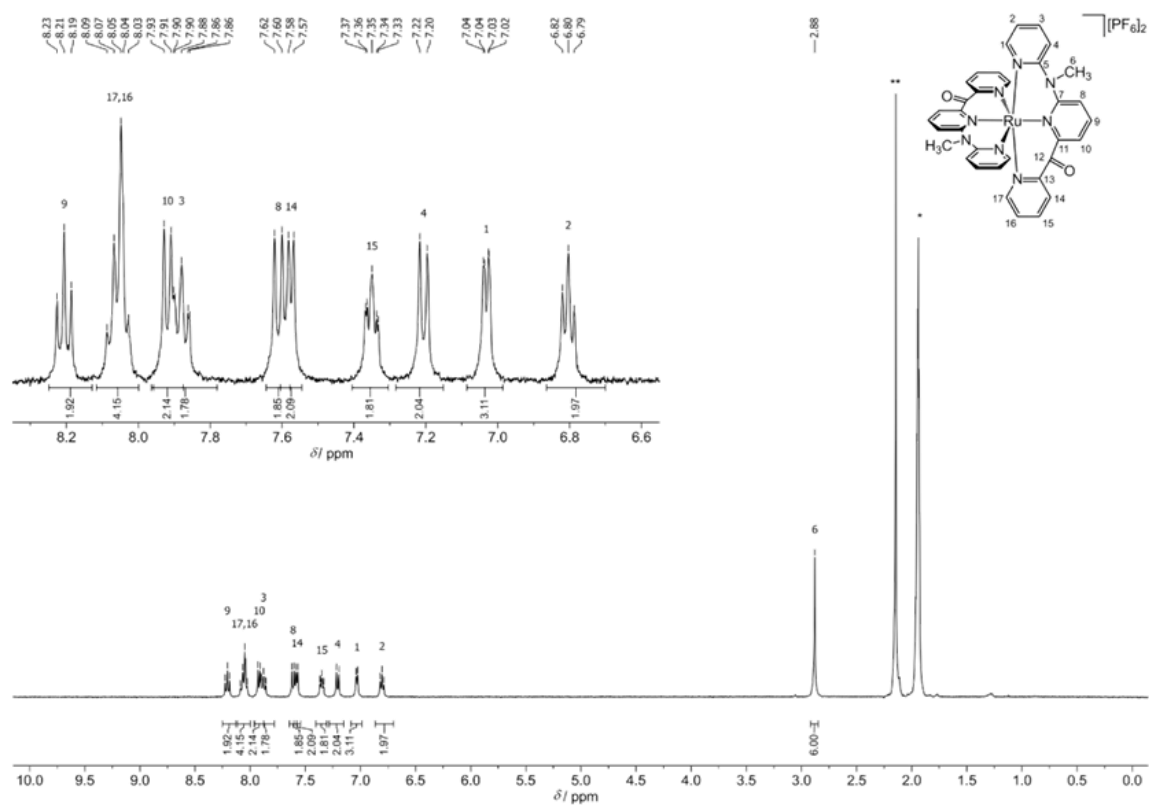


Figure S20. ^1H NMR spectrum of $2[\text{PF}_6]_2$ in CD_3CN at 293 K. * denotes solvent resonance; ** denotes water resonance.

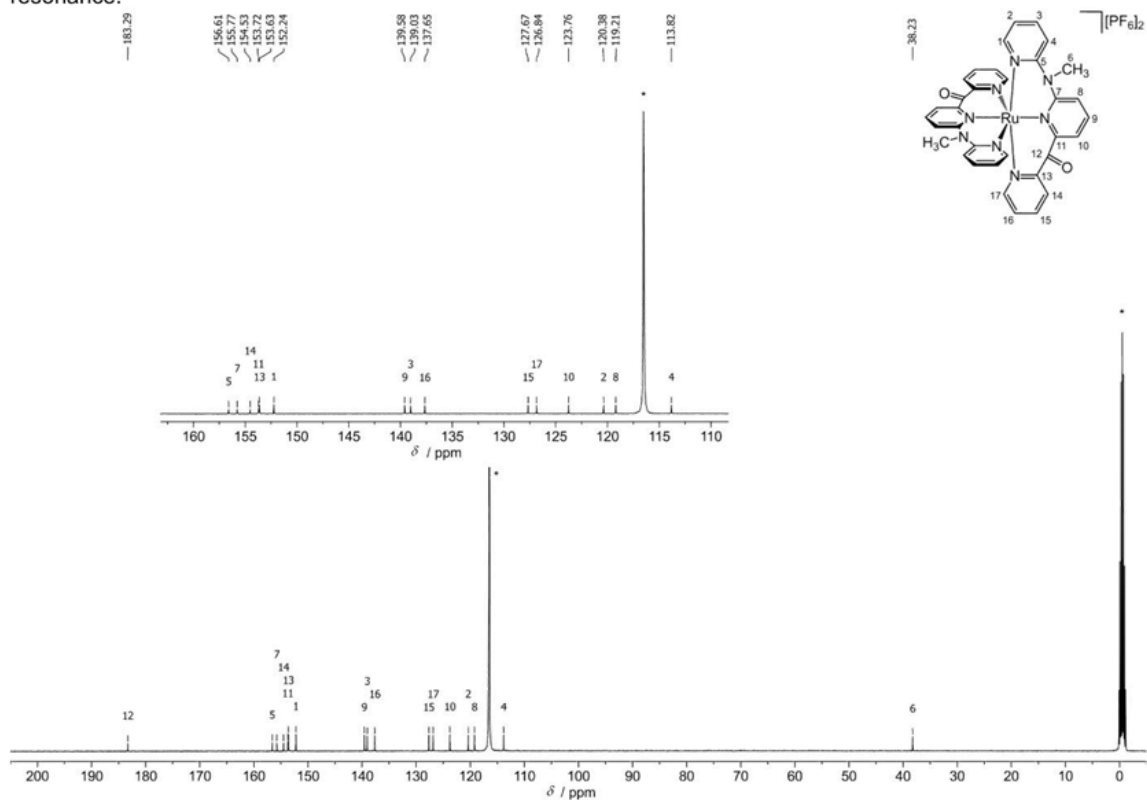


Figure S21. $^{13}\text{C}\{^1\text{H}\}$ NMR spectrum of $2[\text{PF}_6]_2$ in CD_3CN at 293 K. * denote solvent resonances.

6. Green-Light Activation of Push–Pull Ruthenium(II) Complexes

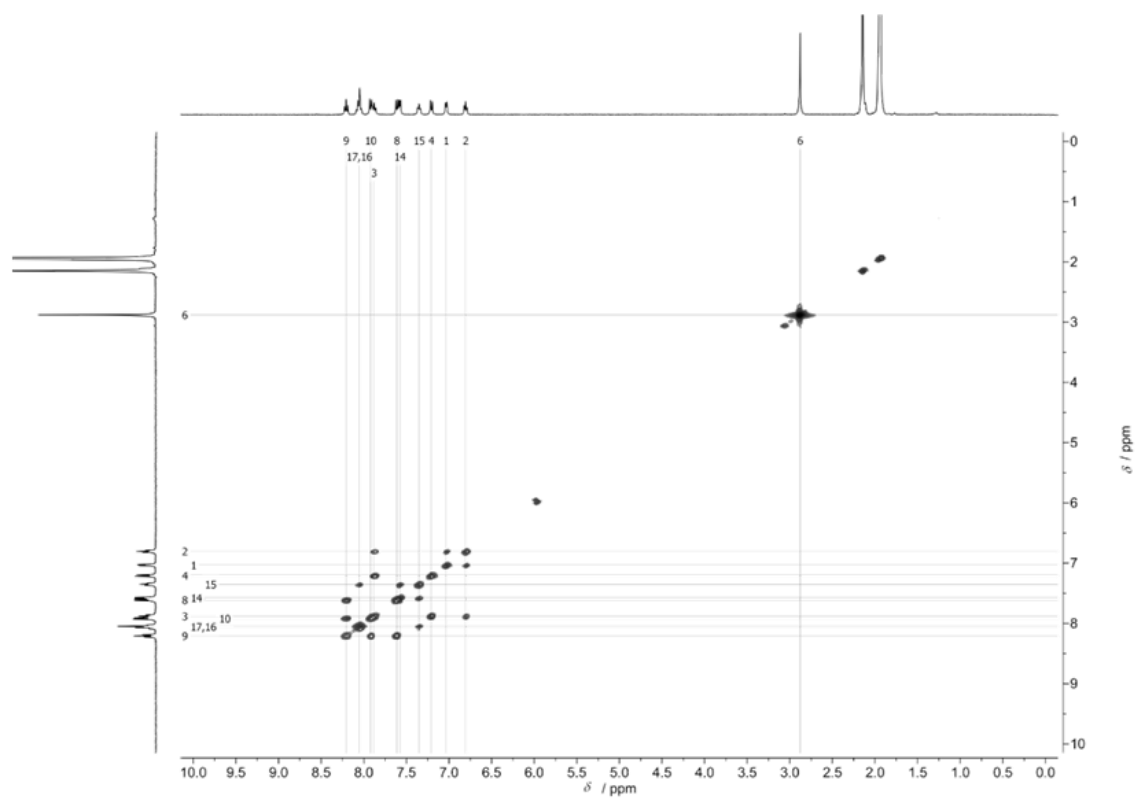


Figure S22. ^1H - ^1H COSY of $2[\text{PF}_6]_2$ in CD_3CN at 293 K.

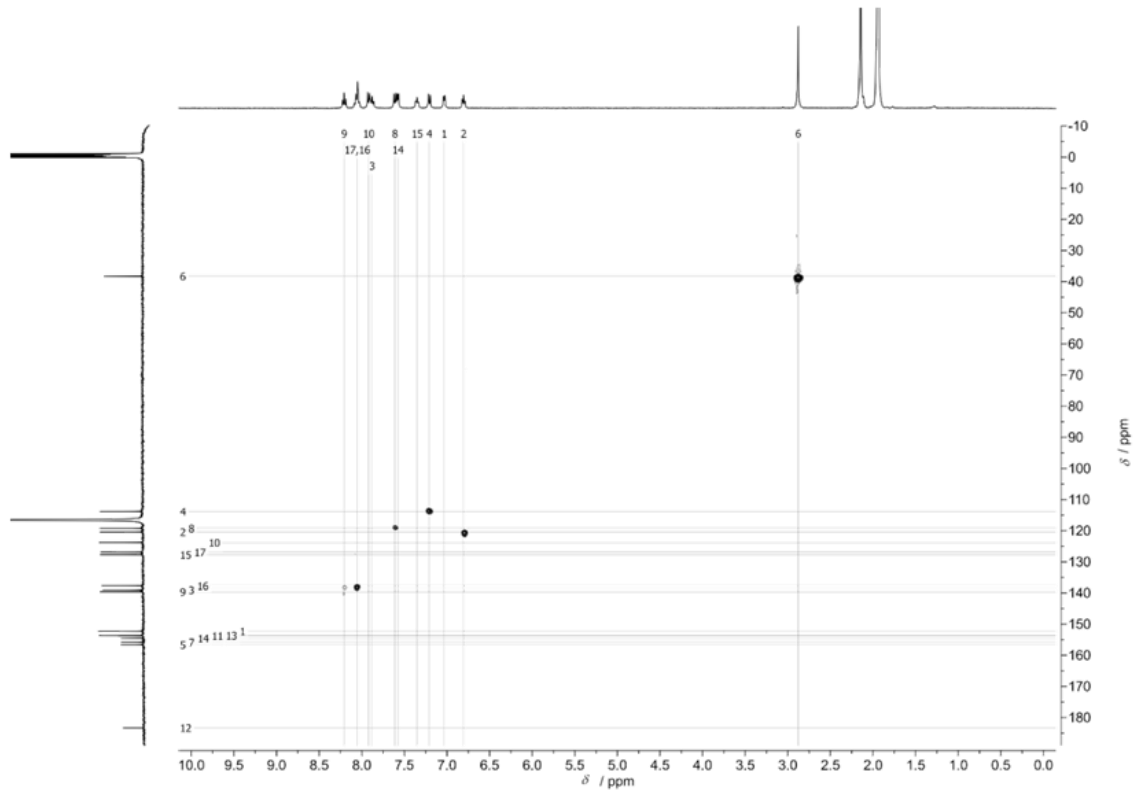


Figure S23. ^1H - ^{13}C HSQC of $2[\text{PF}_6]_2$ in CD_3CN at 293 K.

6. Green-Light Activation of Push–Pull Ruthenium(II) Complexes

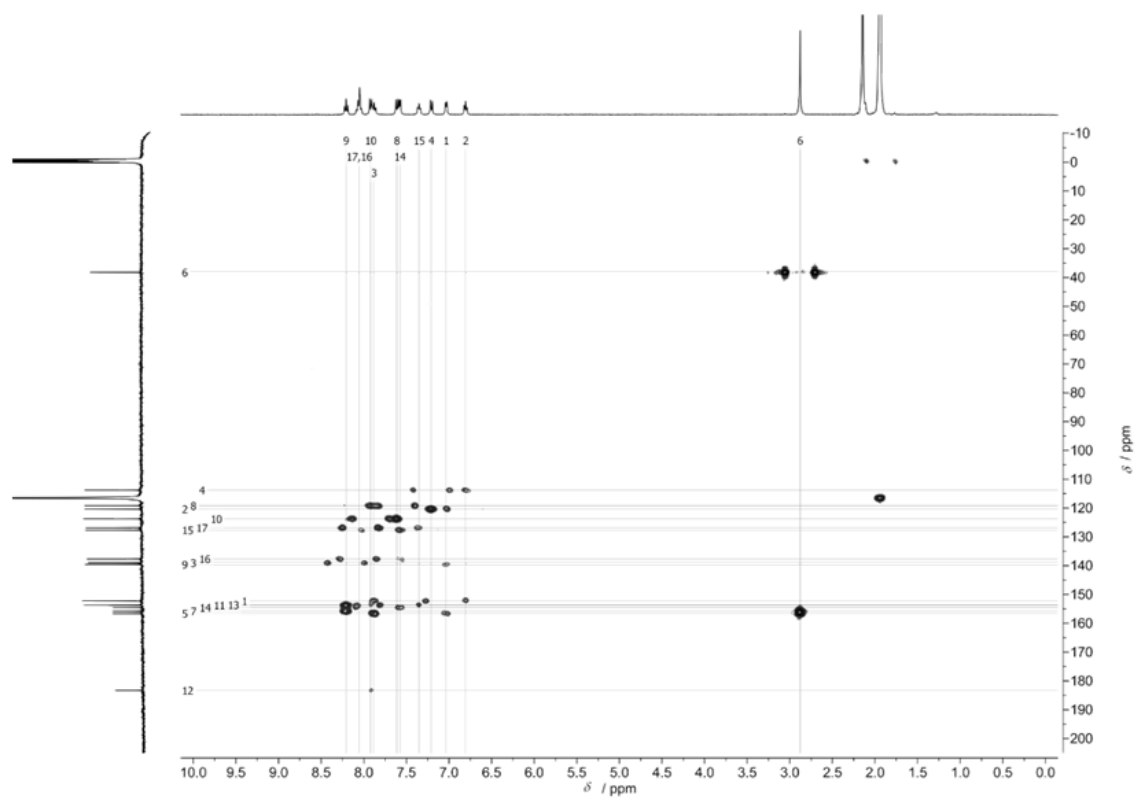


Figure S24. ^1H - ^{13}C HMBC of $2[\text{PF}_6]_2$ in CD_3CN at 293 K.

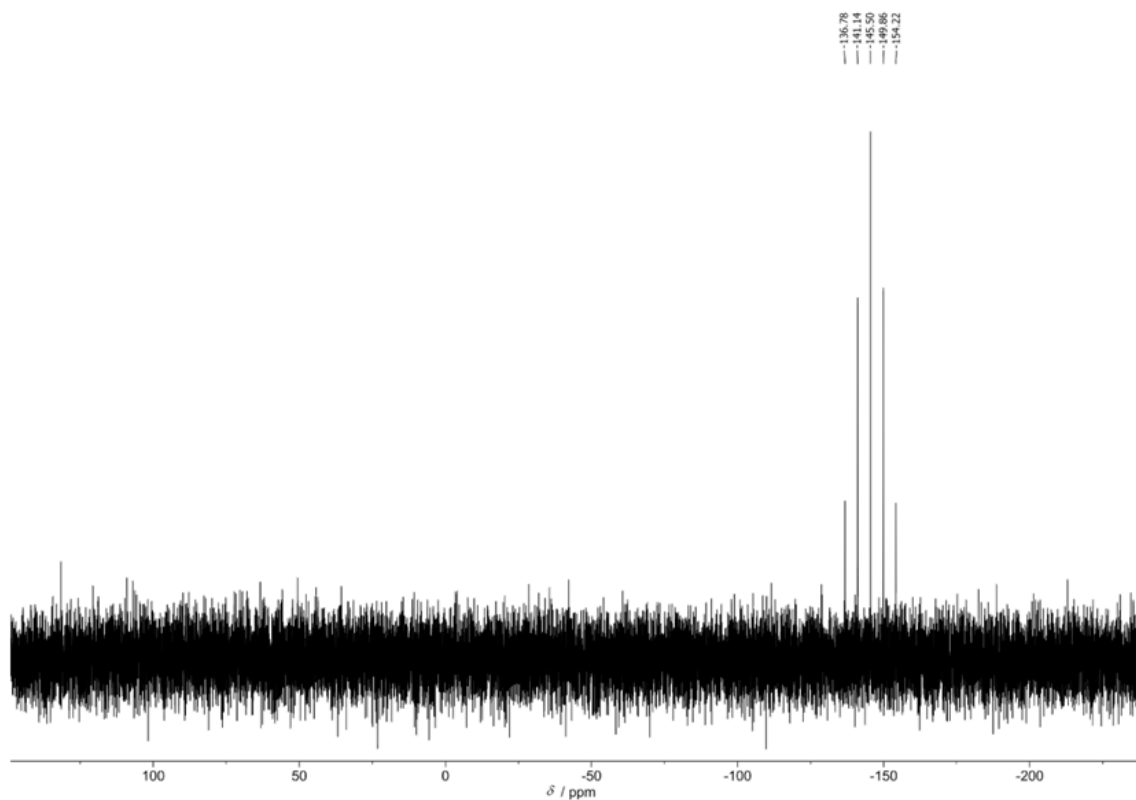


Figure S25. $^{31}\text{P}\{^1\text{H}\}$ NMR spectrum of $2[\text{PF}_6]_2$ in CD_3CN at 293 K.

6. Green-Light Activation of Push–Pull Ruthenium(II) Complexes

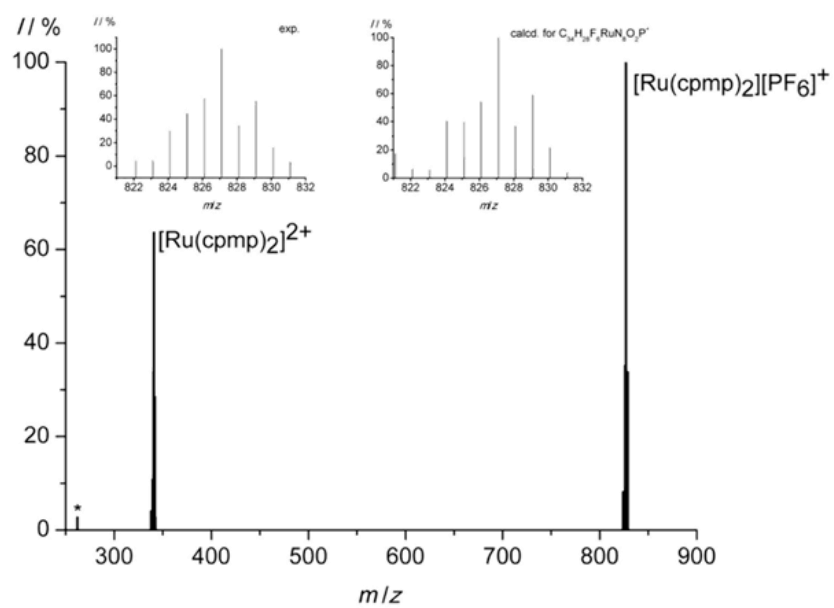


Figure S26. ESI⁺ mass spectrum of $2[\text{PF}_6]_2$ in acetonitrile. * denotes an impurity in the ESI spectrometer.

6. Green-Light Activation of Push–Pull Ruthenium(II) Complexes

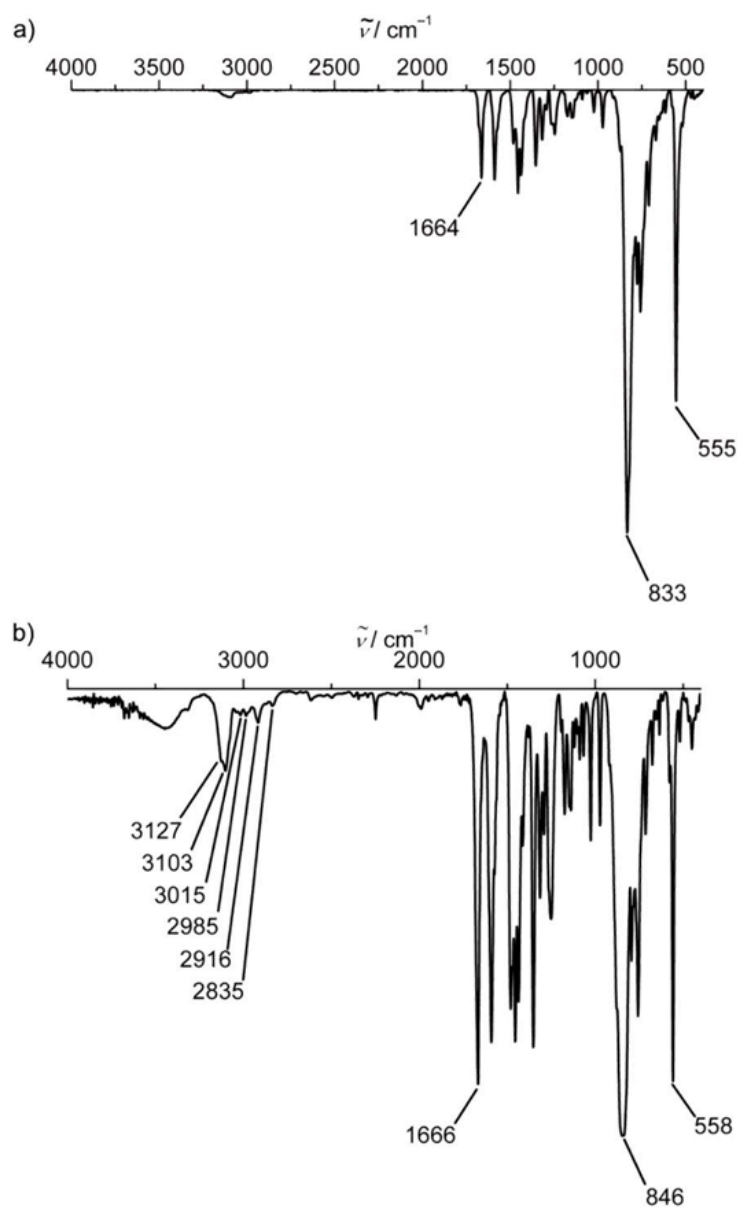


Figure S27. a) ATR-IR spectrum of $2[\text{PF}_6]_2$ and b) IR spectrum of $2[\text{PF}_6]_2$ in KBr.

6. Green-Light Activation of Push–Pull Ruthenium(II) Complexes

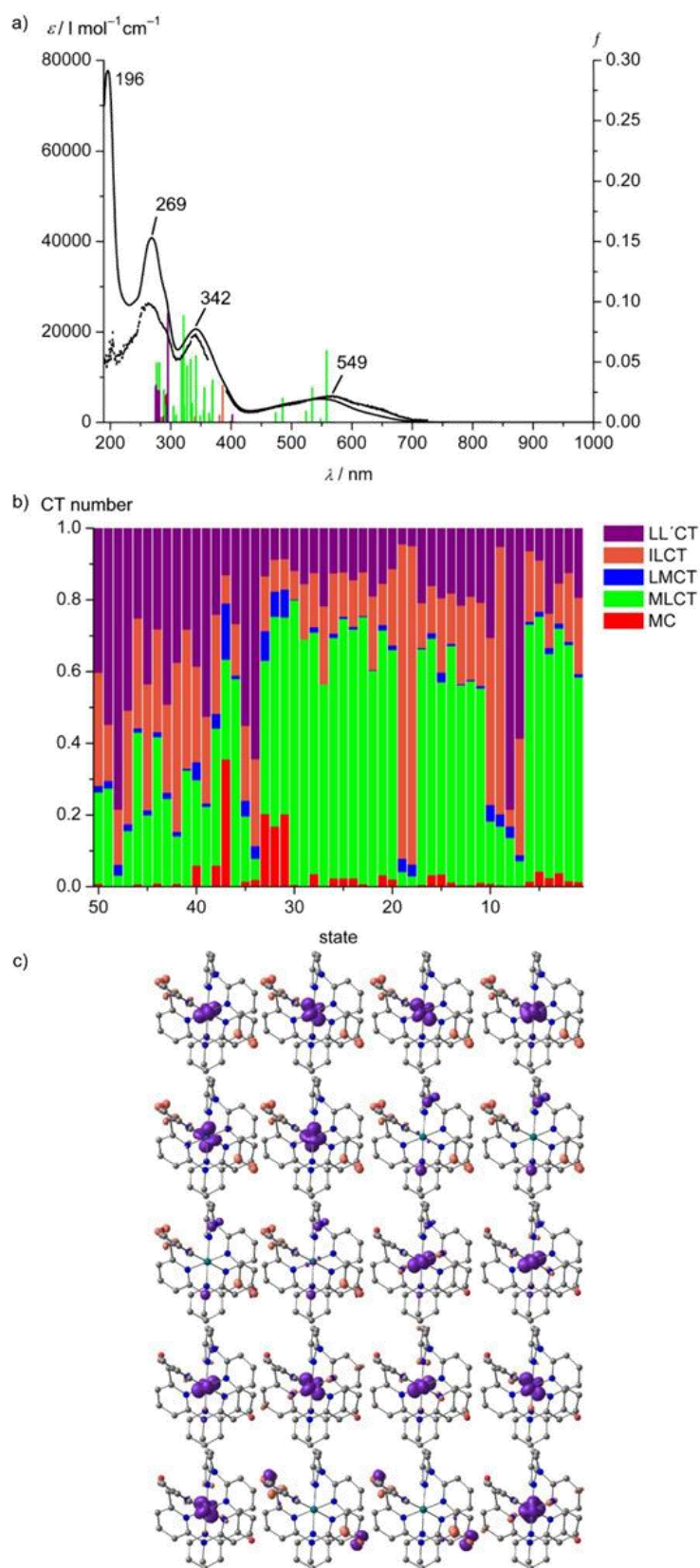


Figure S28. a) UV/Vis/NIR absorption (black solid) and excitation spectrum (black dotted, $\lambda_{em} = 709 \text{ nm}$) of $2[\text{PF}_6]_2$ in acetonitrile at 298 K and TD-DFT calculated oscillator strengths of 2^{2+} (stick spectrum, color code according to charge transfer (CT) numbers); b) TD-DFT CT numbers from 0 to 1 of the 50 lowest lying singlets and c) difference densities of 20 lowest energy transitions (TD-DFT, contour value of 0.01; purple = electron depletion; orange = electron gain).

6. Green-Light Activation of Push–Pull Ruthenium(II) Complexes

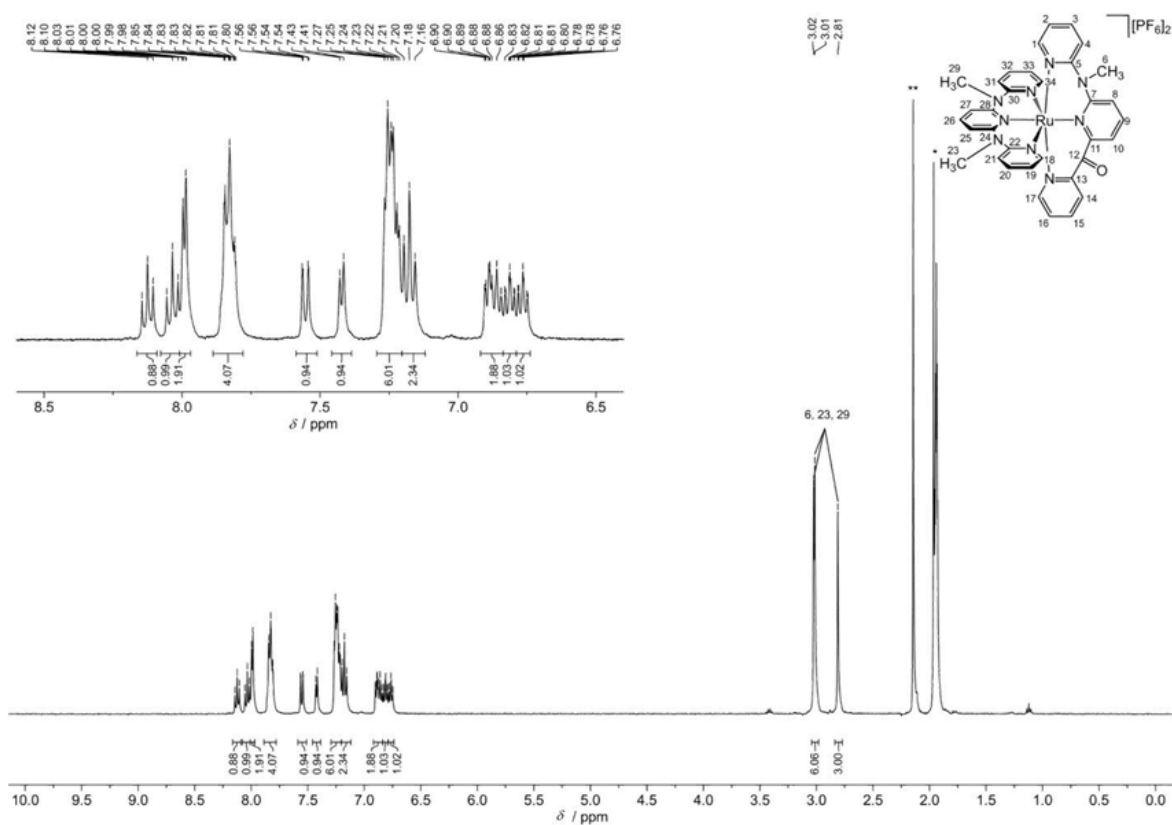


Figure S29. ^1H NMR spectrum of $3[\text{PF}_6]_2$ in CD_3CN at 293 K. * denotes solvent resonance; ** denotes water resonance.

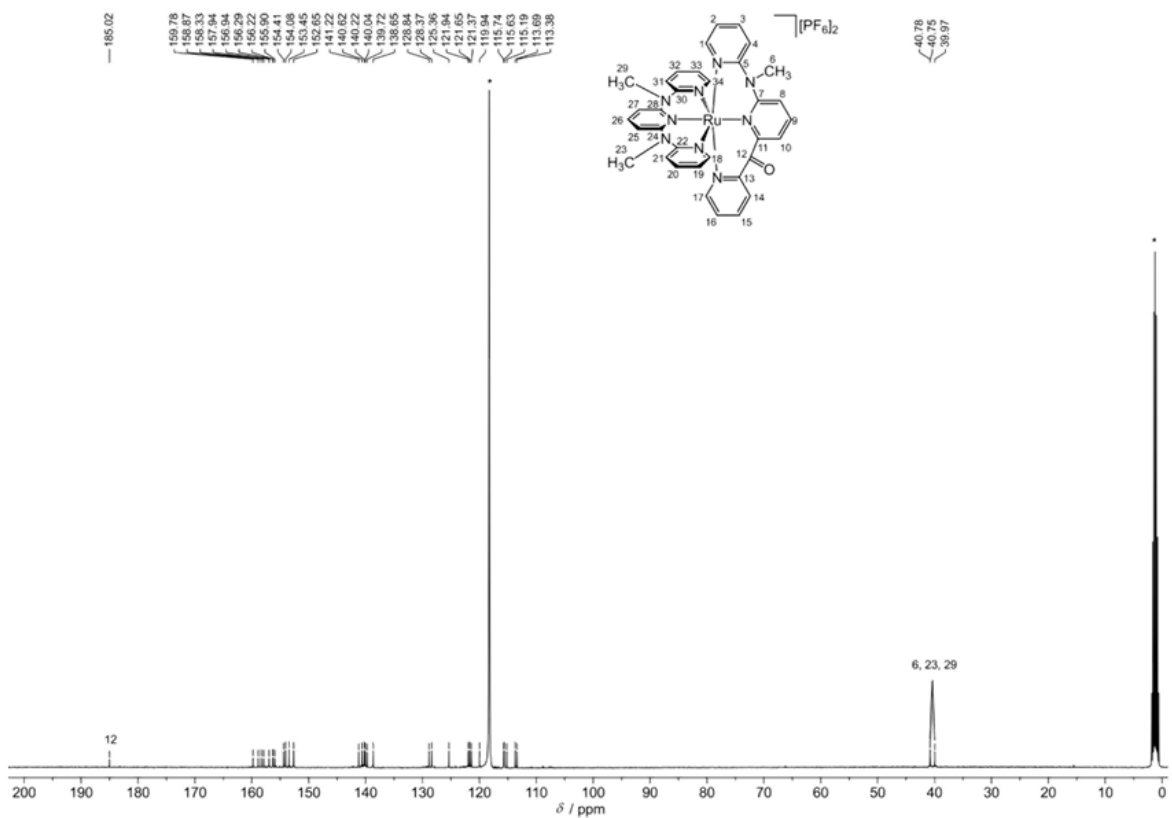


Figure S30. $^{13}\text{C}\{^1\text{H}\}$ NMR spectrum of $3[\text{PF}_6]_2$ in CD_3CN at 293 K. * denote solvent resonances.

6. Green-Light Activation of Push–Pull Ruthenium(II) Complexes

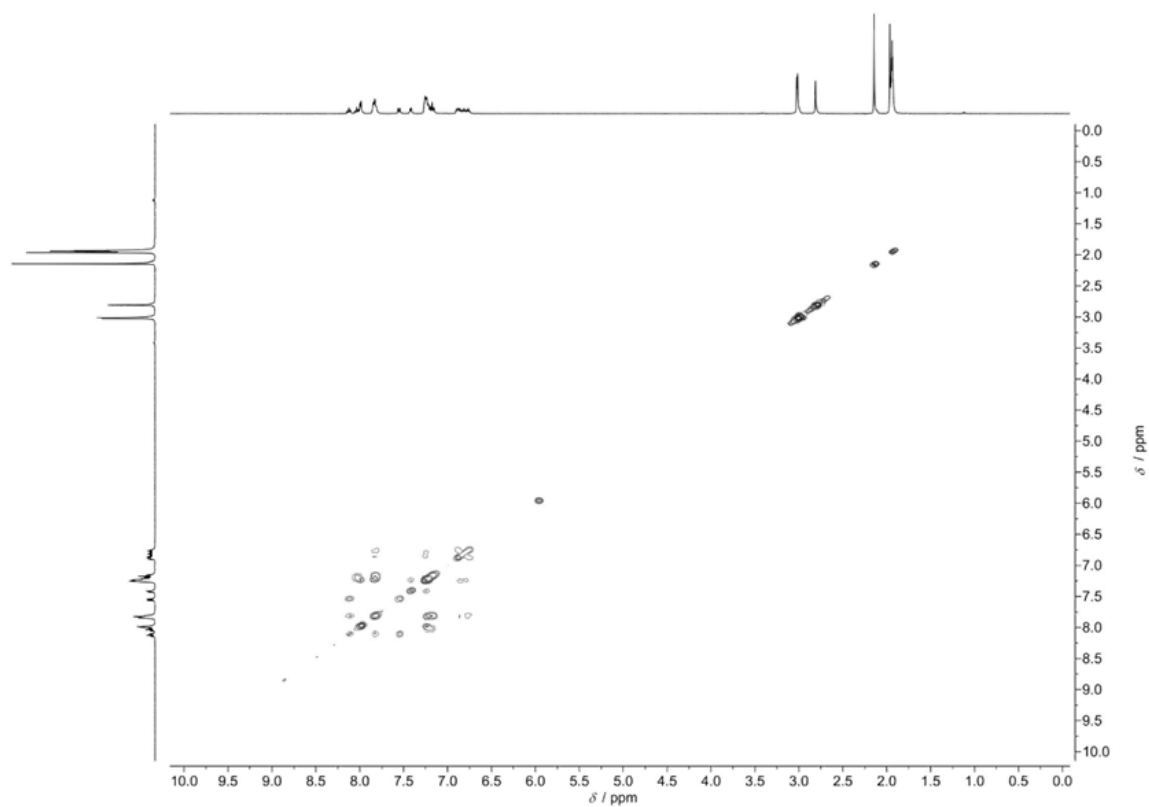


Figure S31. ¹H-¹H-COSY of **3**[PF₆]₂ in CD₃CN at 293 K.

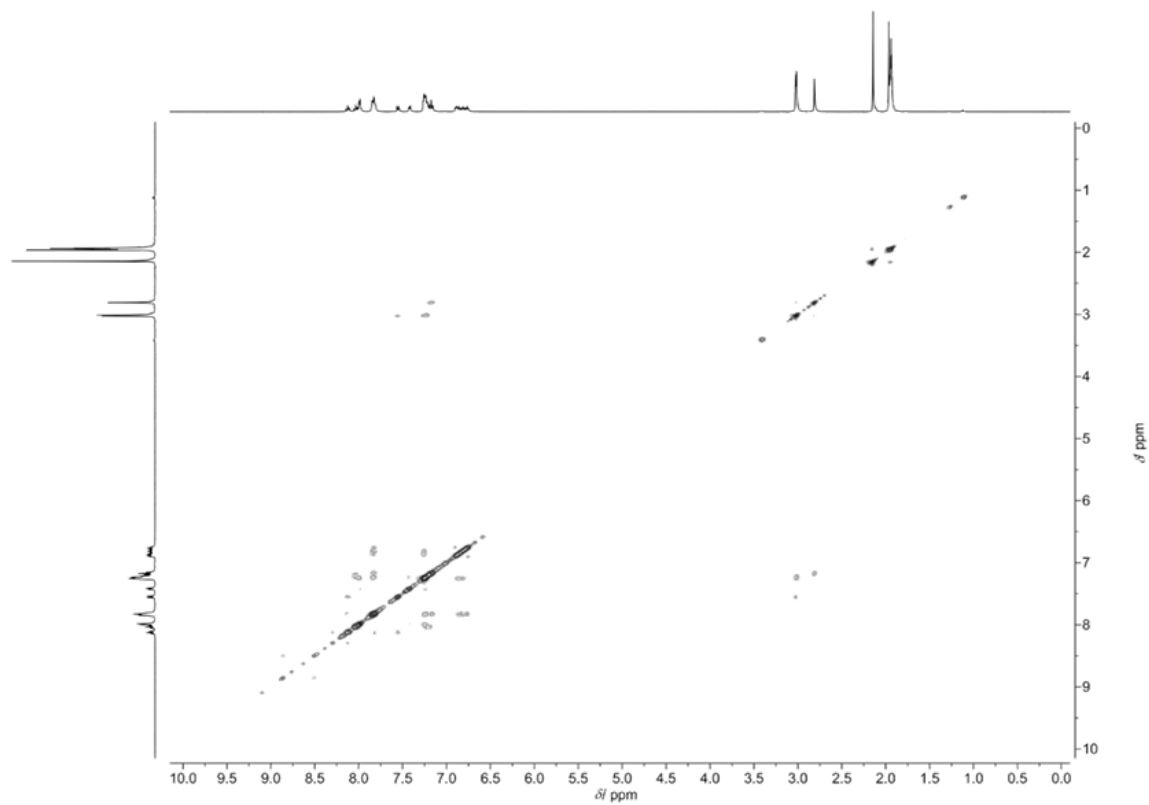


Figure S32. ¹H-¹H-NOESY of **3**[PF₆]₂ in CD₃CN at 293 K (*t*_{mix} = 1 s).

6. Green-Light Activation of Push–Pull Ruthenium(II) Complexes

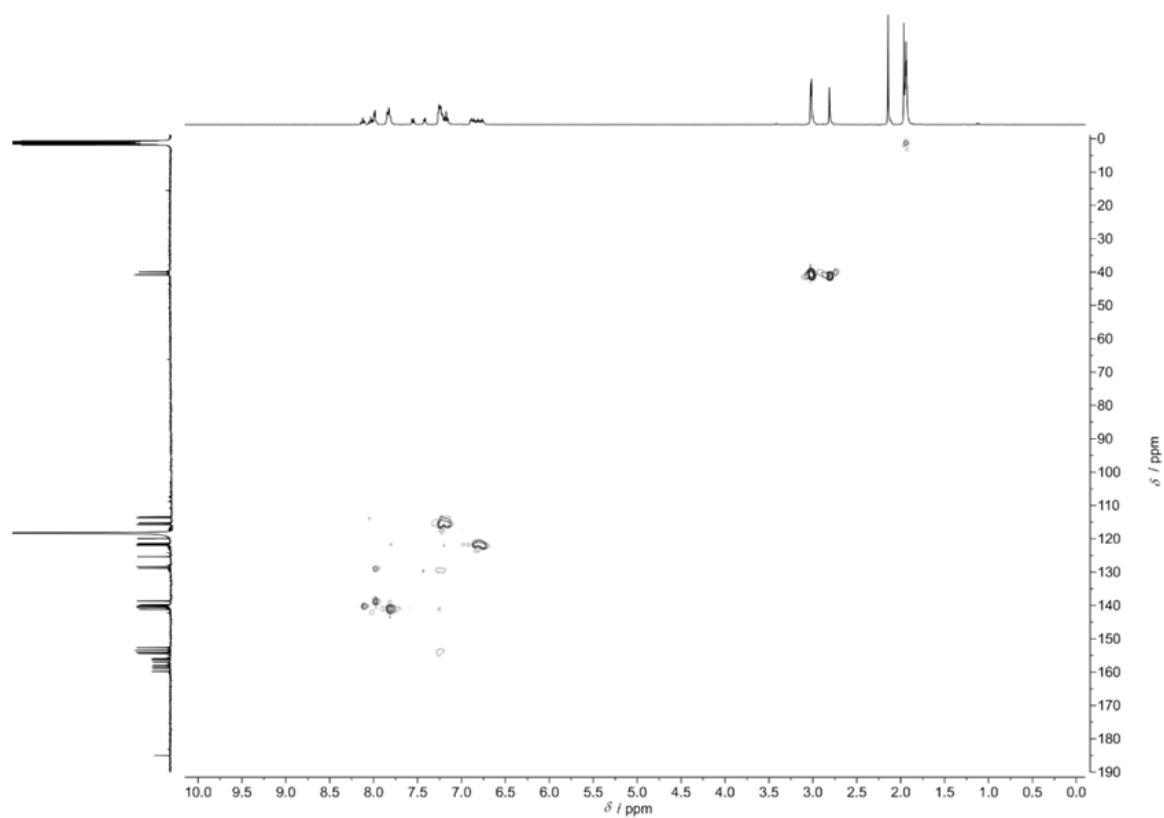


Figure S33. ^1H - ^{13}C HSQC of $3[\text{PF}_6]_2$ in CD_3CN at 293 K.

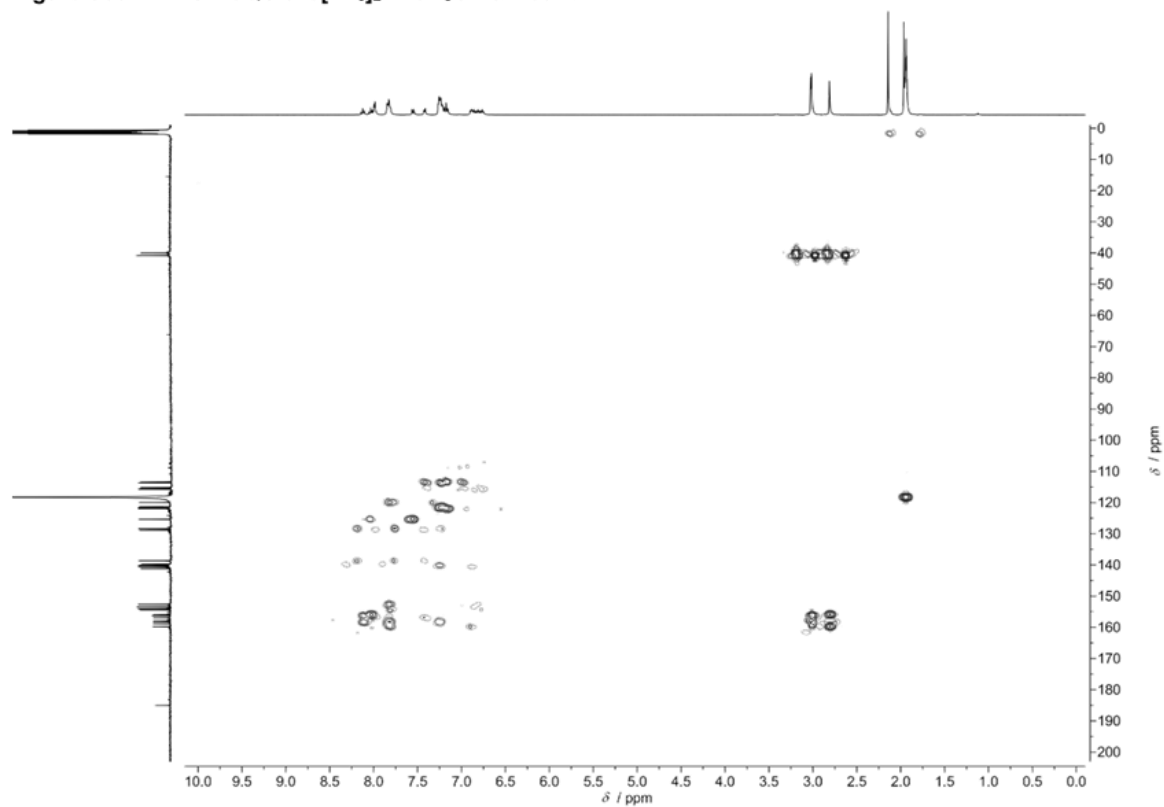


Figure S34. ^1H - ^{13}C -HMBC of $3[\text{PF}_6]_2$ in CD_3CN at 293 K.

6. Green-Light Activation of Push–Pull Ruthenium(II) Complexes

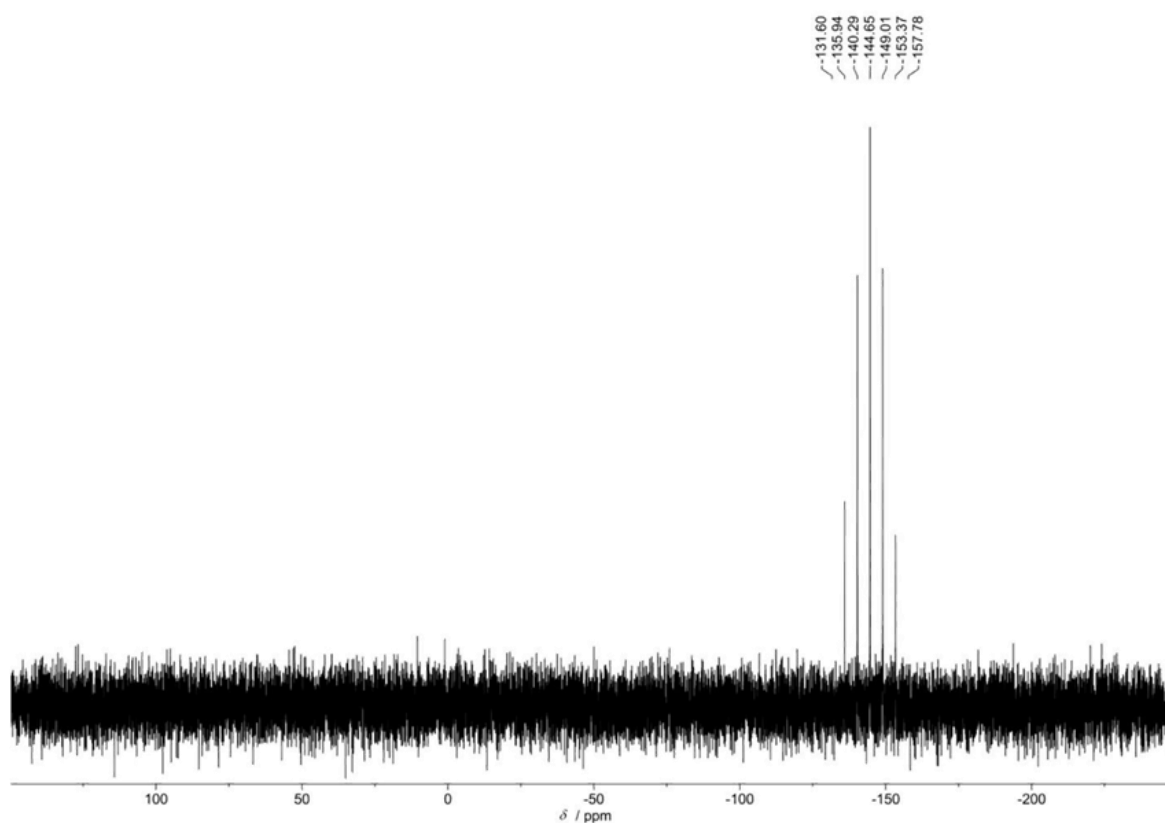


Figure S35. $^{31}\text{P}\{^1\text{H}\}$ NMR spectrum of $3[\text{PF}_6]_2$ in CD_3CN at 293 K.

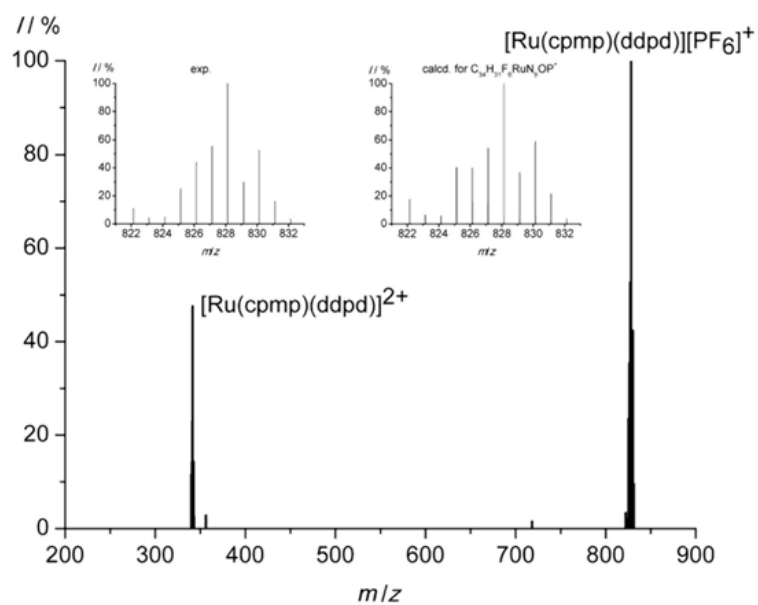


Figure S36. ESI $^+$ mass spectrum of $3[\text{PF}_6]_2$ in acetonitrile.

6. Green-Light Activation of Push–Pull Ruthenium(II) Complexes

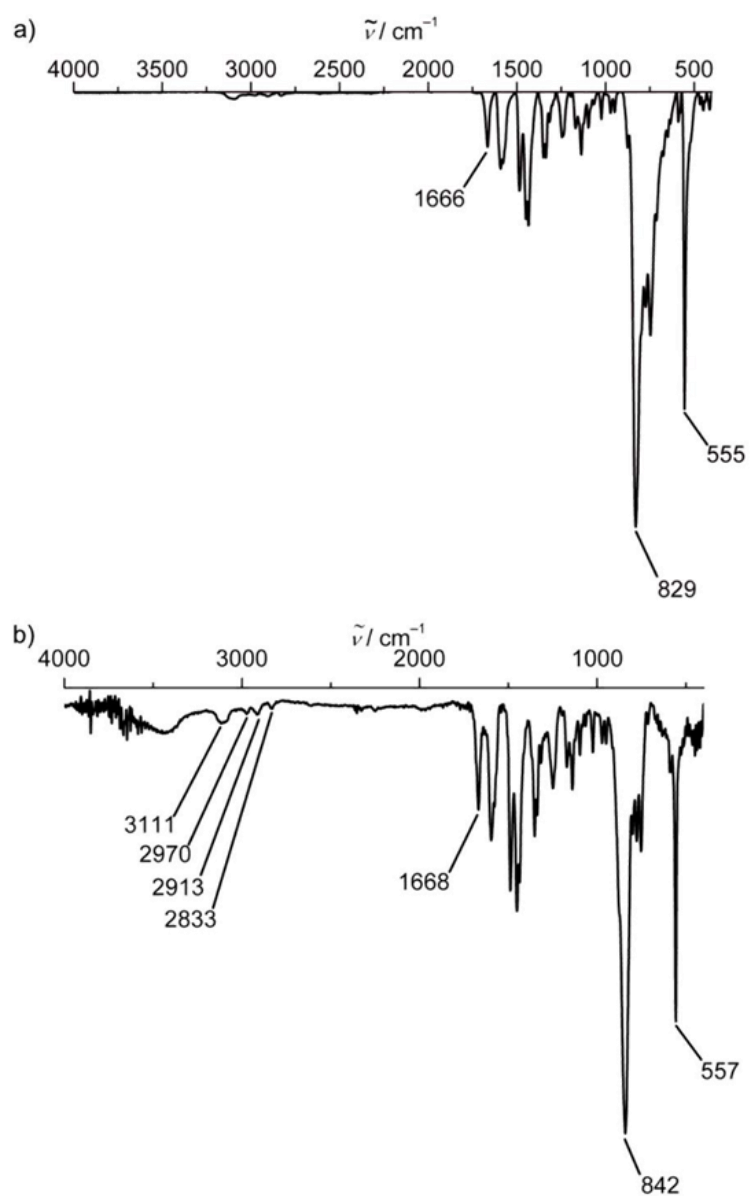


Figure S37. a) ATR-IR spectrum of $3[\text{PF}_6]_2$ and b) IR spectrum of $3[\text{PF}_6]_2$ in KBr.

6. Green-Light Activation of Push–Pull Ruthenium(II) Complexes

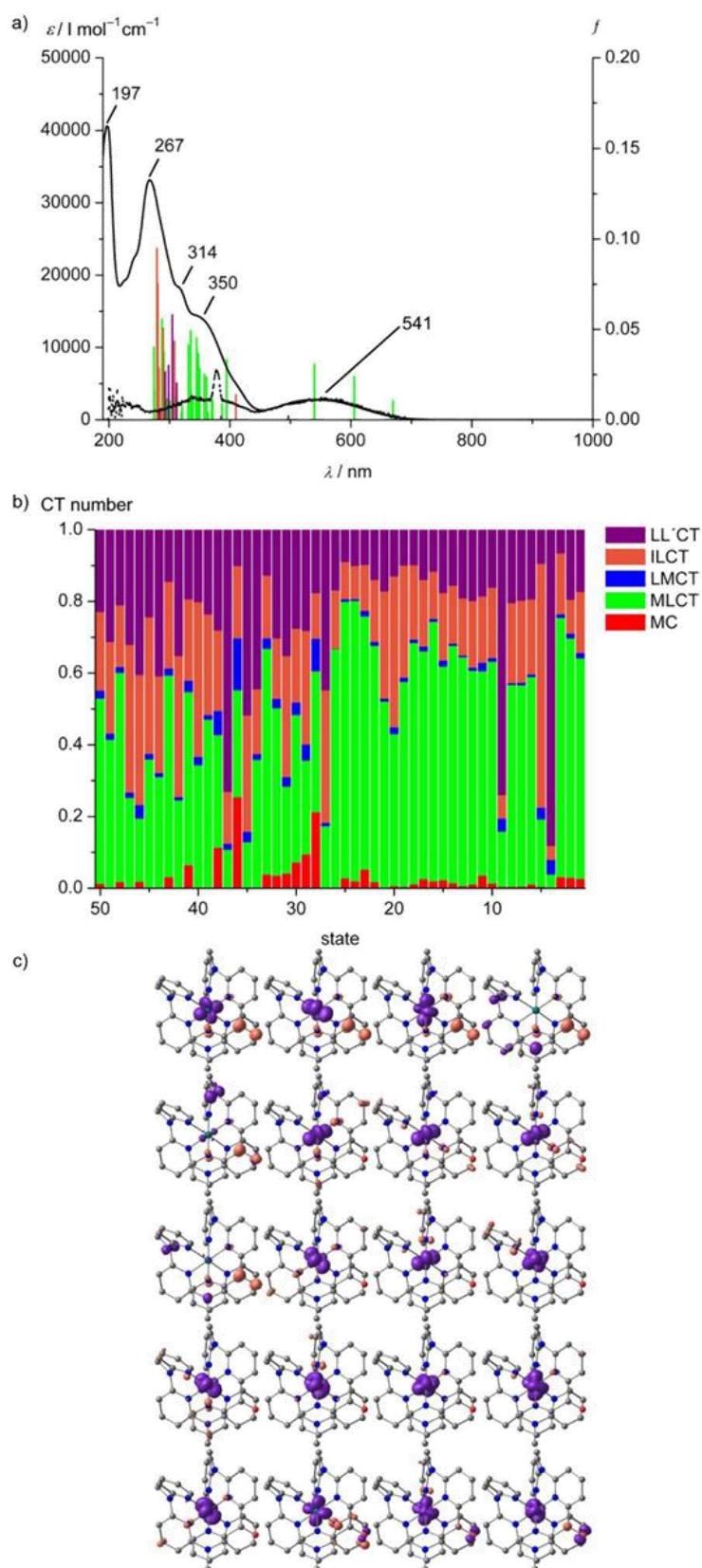


Figure S38. a) UV/Vis/NIR absorption (black solid) and excitation spectrum (black dotted, $\lambda_{em} = 755 \text{ nm}$) of $3[\text{PF}_6]_2$ in acetonitrile at 298 K and TD-DFT calculated oscillator strengths of 3^{2+} (stick spectrum, color code according to charge transfer (CT) numbers); b) TD-DFT CT numbers from 0 to 1 of the 50 lowest lying singlets and c) difference densities of 20 lowest energy transitions (TD-DFT, contour value of 0.01; purple = electron depletion; orange = electron gain).

6. Green-Light Activation of Push–Pull Ruthenium(II) Complexes

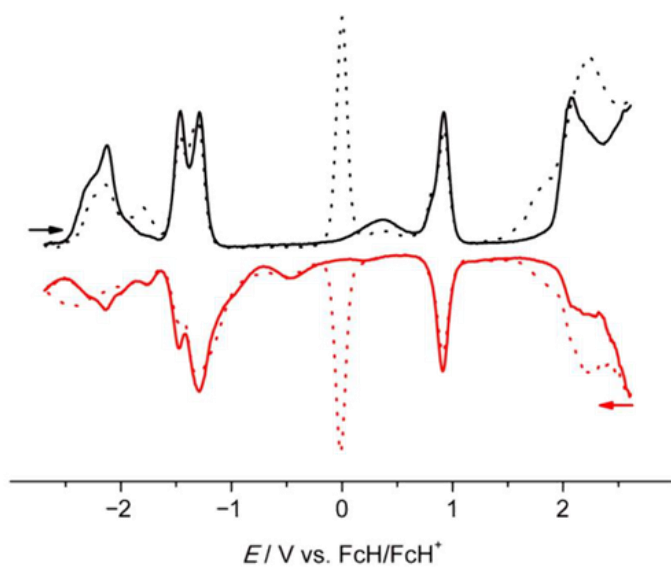


Figure S39. Square wave voltammogram of **2**[PF₆]₂ without (solid) and with (dotted) added ferrocene, 1 mM in acetonitrile, 0.1 M [ⁿBu₄N][PF₆].

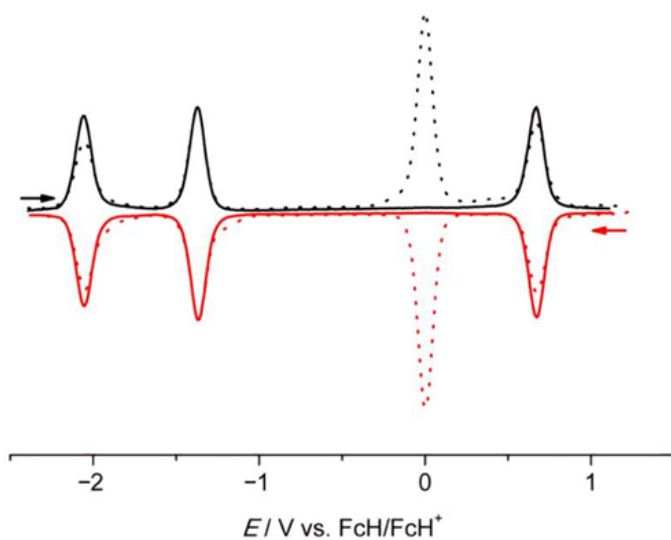


Figure S40. Square wave voltammogram of **3**[PF₆]₂ without (solid) and with (dotted) added ferrocene, 1 mM in acetonitrile, 0.1 M [ⁿBu₄N][PF₆].

6. Green-Light Activation of Push–Pull Ruthenium(II) Complexes

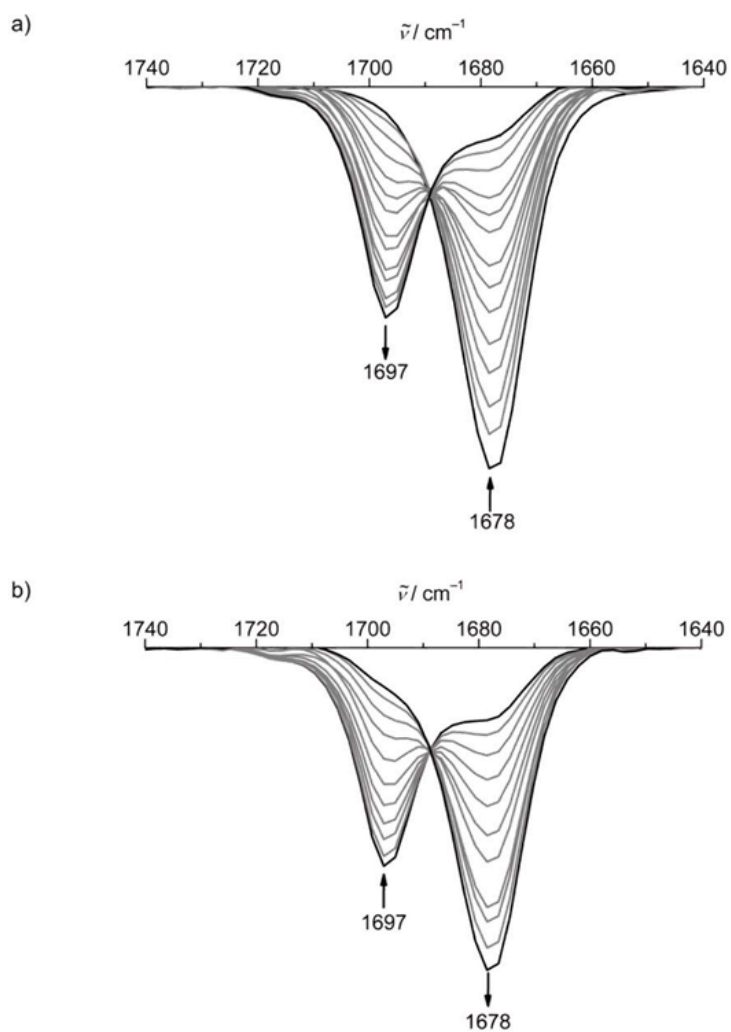


Figure S41. IR spectra (CO region) of $2[\text{PF}_6]_2$ in acetonitrile, 0.1 M $[\text{nBu}_4\text{N}][\text{PF}_6]$ a) during oxidation $2^{2+} \rightarrow 2^{3+}$ and b) during re-reduction $2^{3+} \rightarrow 2^{2+}$.

6. Green-Light Activation of Push–Pull Ruthenium(II) Complexes

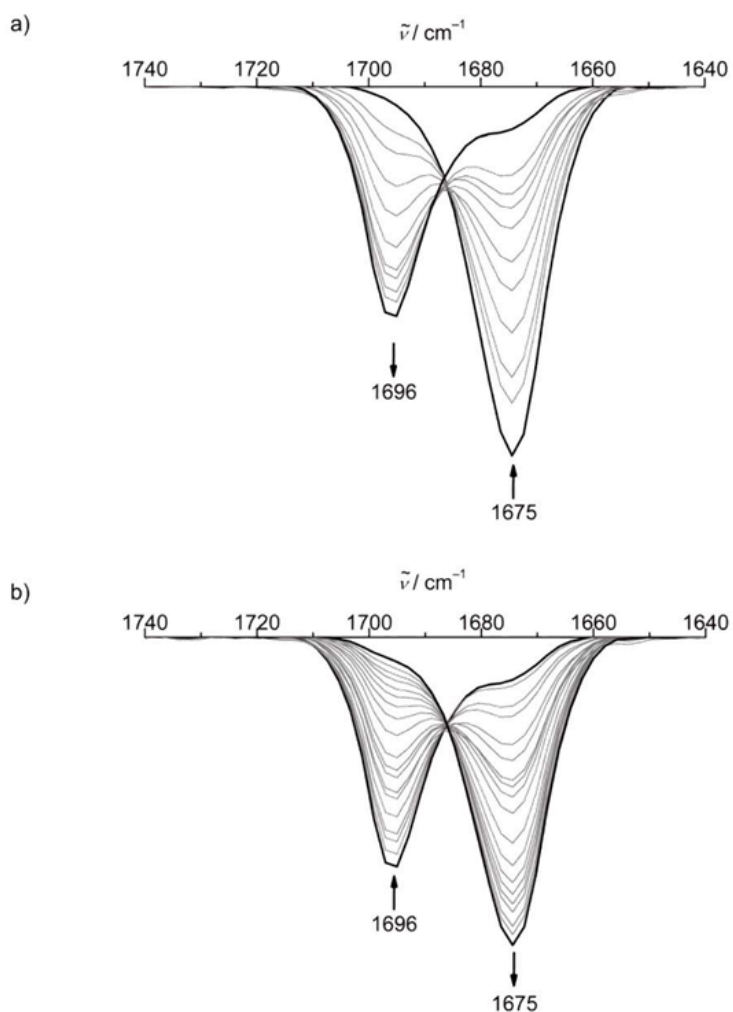


Figure S42. IR spectra (CO region) of $3[\text{PF}_6]_2$ in acetonitrile, 0.1 M $[\text{nBu}_4\text{N}][\text{PF}_6]$ a) during oxidation $3^{2+} \rightarrow 3^{3+}$ and b) during re-reduction $3^{3+} \rightarrow 3^{2+}$.

6. Green-Light Activation of Push–Pull Ruthenium(II) Complexes

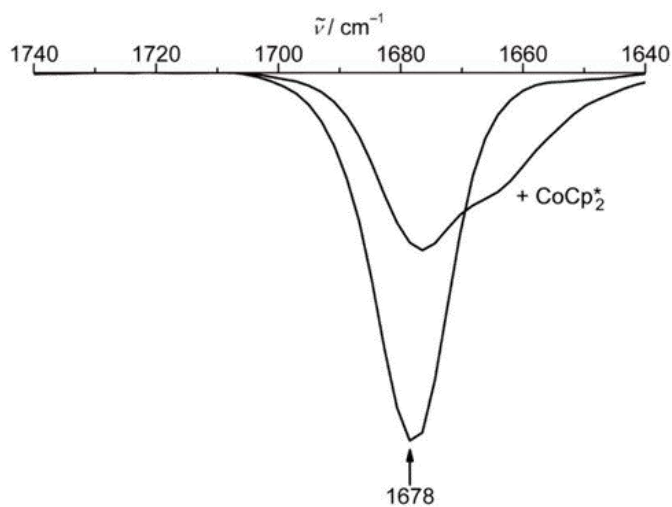


Figure S43. IR spectra (CO region) of **2**[PF₆]₂ in acetonitrile before and after reduction $2^{2+} \rightarrow 2^+$ with 1 eq. of decamethylcobaltocene.

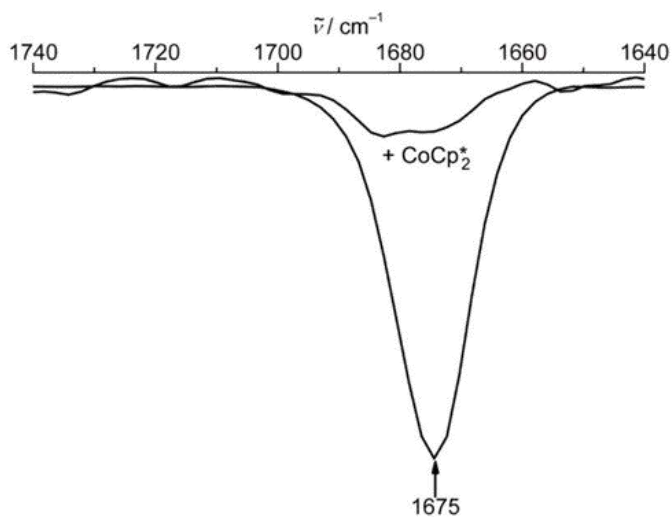


Figure S44. IR spectra (CO region) of **3**[PF₆]₂ in acetonitrile before and after reduction $3^{2+} \rightarrow 3^+$ with 1 eq. of decamethylcobaltocene.

6. Green-Light Activation of Push–Pull Ruthenium(II) Complexes

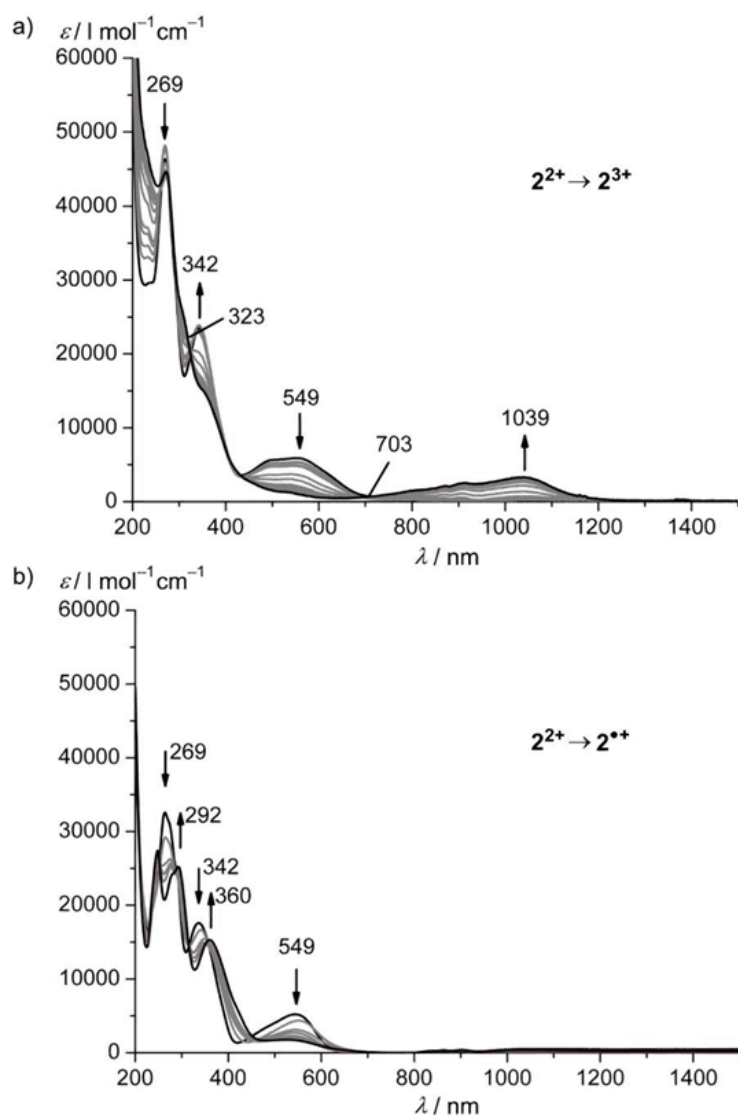


Figure S45. UV/Vis/NIR spectra of $2[PF_6]_2$ in acetonitrile with $0.1 \text{ M } [nBu_4N][PF_6]$ at 298 K collected during a) electrochemical oxidation and b) electrochemical reduction.

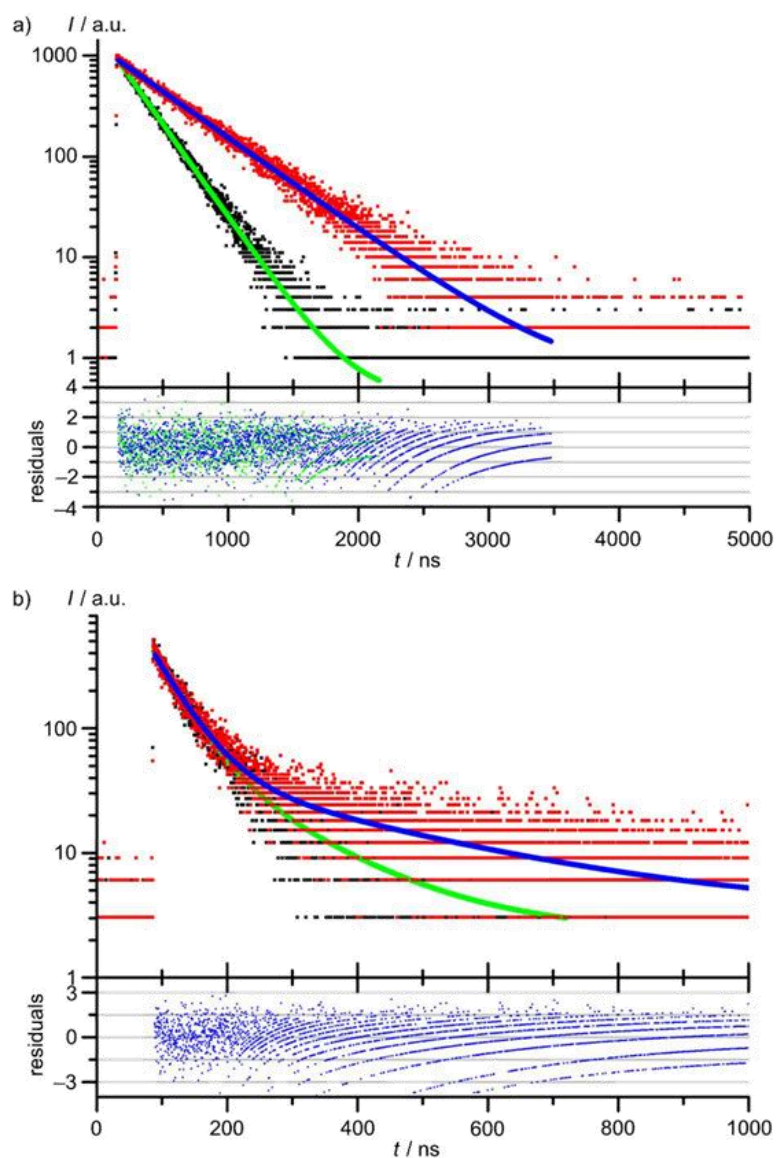


Figure S46. a) Luminescence decay of $2[\text{PF}_6]_2$ in acetonitrile ($\lambda_{\text{exc}} = 544$ nm, $\lambda_{\text{em}} = 709$ nm) under argon (red) and air-saturated (black) with monoexponential fit functions (blue: $\tau = 477$ ns; green: $\tau = 237$ ns) and b) luminescence decay of $3[\text{PF}_6]_2$ in acetonitrile ($\lambda_{\text{exc}} = 542$ nm, $\lambda_{\text{em}} = 755$ nm) under argon (red) and air-saturated (black) with biexponential fit functions (blue: $\tau_1 = 45$ ns and $\tau_2 = 294$ ns; green: $\tau_1 = 41$ ns and $\tau_2 = 137$ ns).

6. Green-Light Activation of Push–Pull Ruthenium(II) Complexes

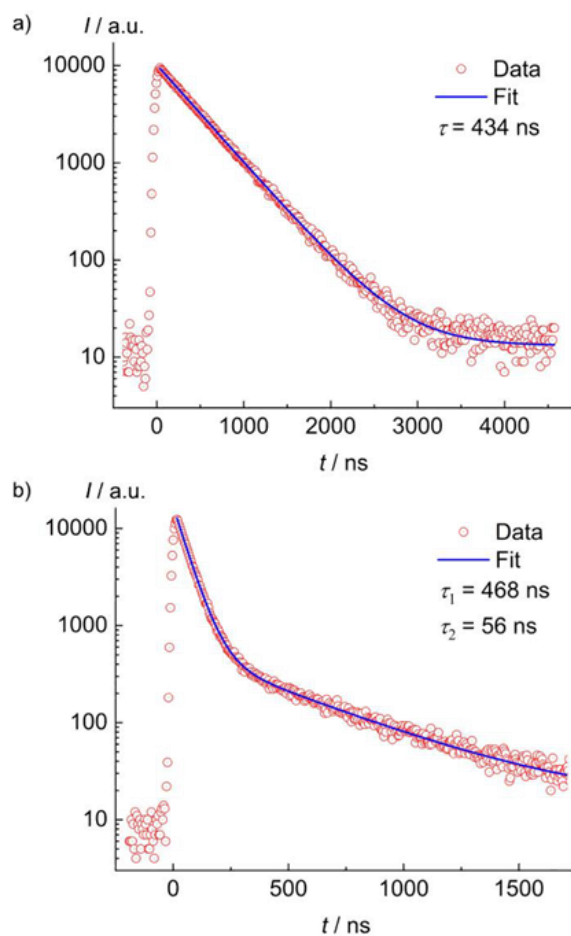


Figure S47. a) Streak camera measurement of **2**[PF₆]₂ in acetonitrile ($\lambda_{\text{exc}} = 540$ nm), emission data integrated from 590 – 900 nm; monoexponential fit function with $\tau = 434$ ns (blue) and b) streak camera measurement of **3**[PF₆]₂ in acetonitrile ($\lambda_{\text{exc}} = 540$ nm), emission data integrated from 620 – 930 nm; biexponential fit function with $\tau_1 = 468$ ns and $\tau_2 = 56$ ns (blue).

6. Green-Light Activation of Push–Pull Ruthenium(II) Complexes

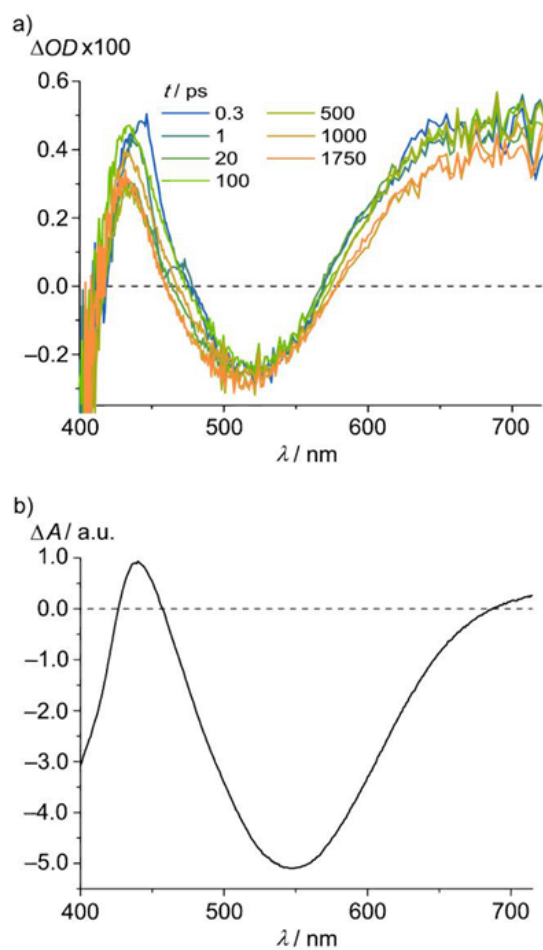


Figure S48. fs-Transient absorption spectra of $3[PF_6]_2$ in acetonitrile at different delay times after excitation at 540 nm at 293 K (magic angle) and b) estimated difference spectrum derived from absorption spectra of 3^{2+} , 3^{3+} and 3^{*+} , prepared electrochemically in acetonitrile with 0.1 M $[n\text{Bu}_4\text{N}][PF_6]$ at 298 K by "scaled $[\frac{1}{2}(3^{3+} + 3^{*+}) - 3^{2+}]$ ".

6. Green-Light Activation of Push–Pull Ruthenium(II) Complexes

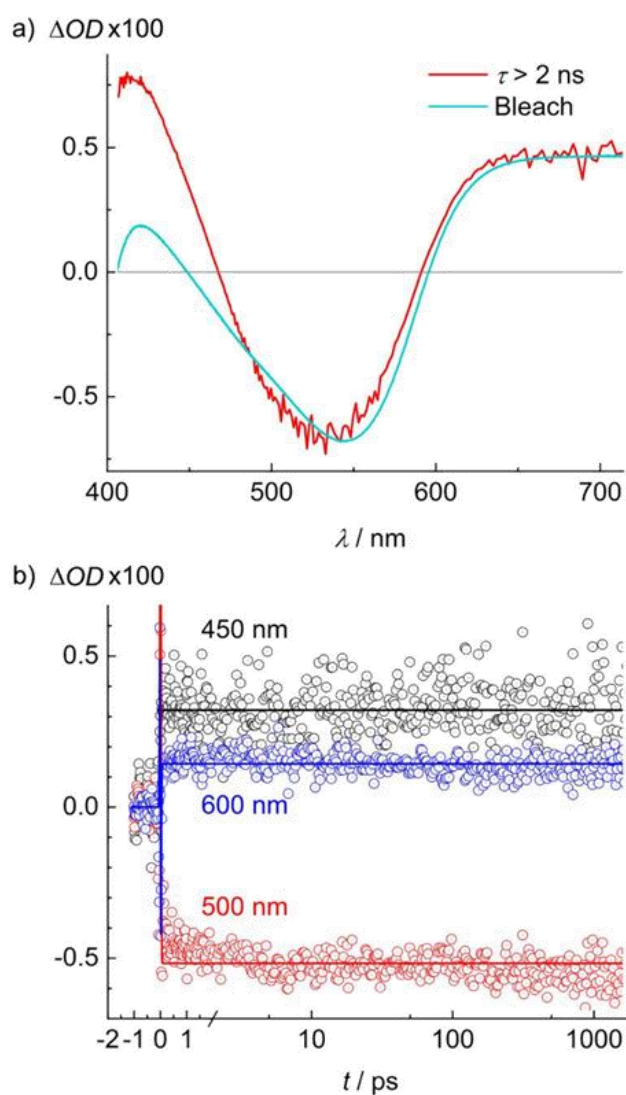


Figure S49. a) Amplitude spectrum (red) for $2[\text{PF}_6]_2$ in acetonitrile obtained by a global fit of a long living component to the transient absorption data and compared to the bleach (cyan, scaled and vertically shifted negative ground state absorption). b) Time traces of the transient absorption of $2[\text{PF}_6]_2$ at the detection wavelengths 450 nm (black), 500 nm (red), and 600 nm (blue) together with the time curves resulting from the global fit.

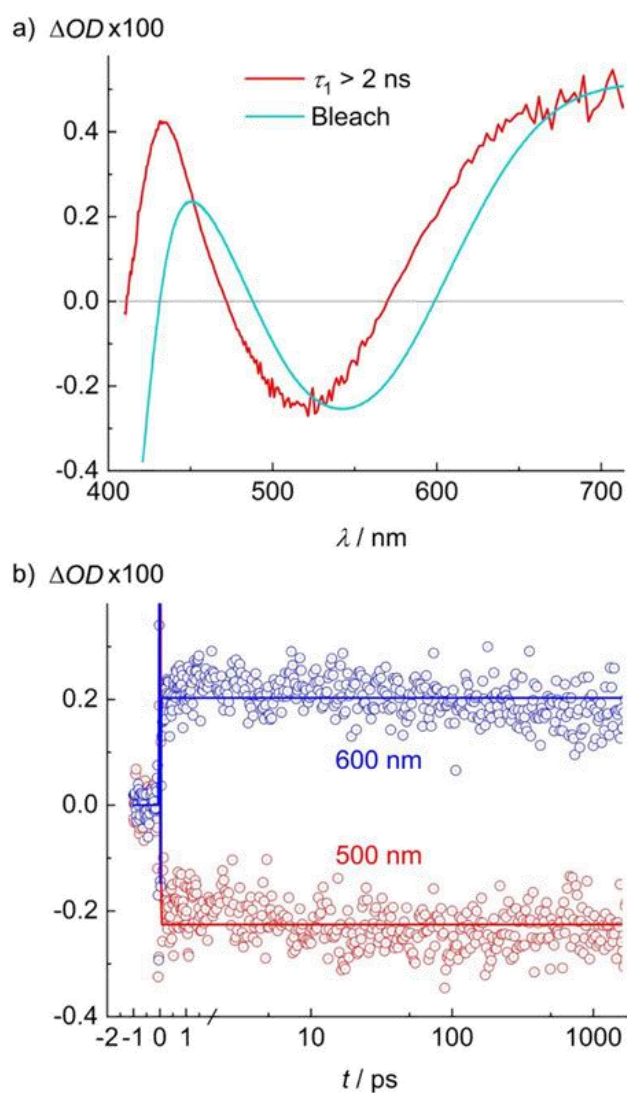


Figure S50. a) Amplitude spectrum (red) for $3[\text{PF}_6]_2$ in acetonitrile obtained by a global fit of a long living component to the transient absorption data and compared to the bleach (cyan, scaled and vertically shifted negative ground state absorption). b) Time traces of the transient absorption of $3[\text{PF}_6]_2$ at the detection wavelengths 500 nm (red) and 600 nm (blue) together with the time curves resulting from the global fit.

6. Green-Light Activation of Push–Pull Ruthenium(II) Complexes

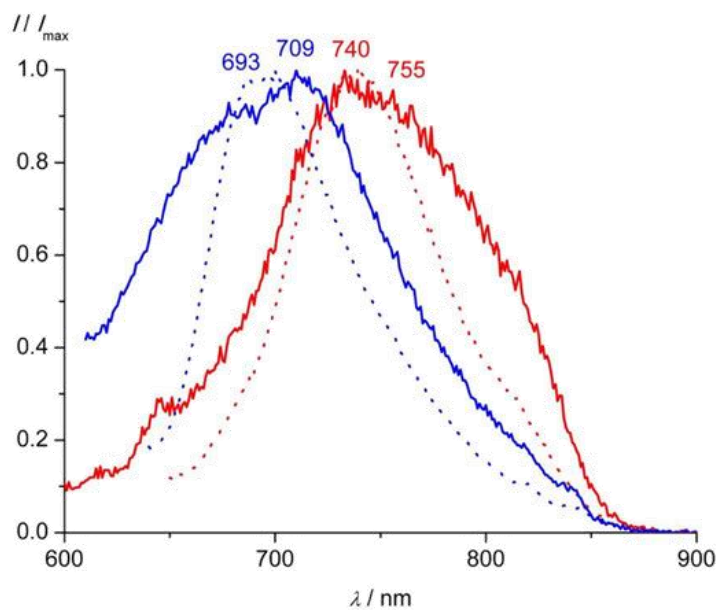


Figure S51. Normalized emission spectra of **2**[PF₆]₂ (blue; $\lambda_{\text{exc}} = 549$ nm) and **3**[PF₆]₂ (red; $\lambda_{\text{exc}} = 541$ nm) in butyronitrile at 298 K (solid lines) and at 77 K (dotted lines).

6. Green-Light Activation of Push–Pull Ruthenium(II) Complexes

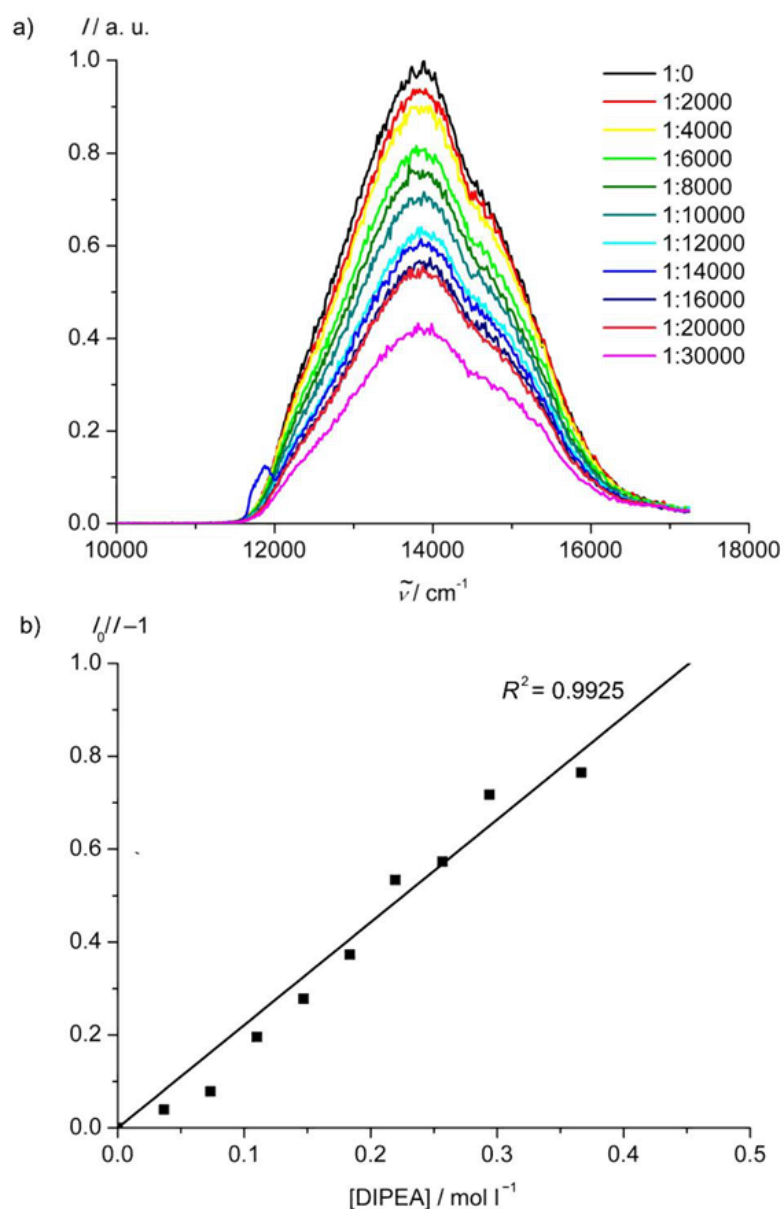


Figure S52. a) Emission spectra of $2[\text{PF}_6]_2$ with increasing concentration of DIPEA in dry and deaerated DMF at 298 K ($\lambda_{\text{exc}} = 555 \text{ nm}$) and b) Stern-Volmer plot for phosphorescence quenching of $2[\text{PF}_6]_2$ with DIPEA in dry and deaerated DMF at 298 K ($K_{\text{SV}} = 2.2 \text{ M}^{-1}$).

6. Green-Light Activation of Push–Pull Ruthenium(II) Complexes

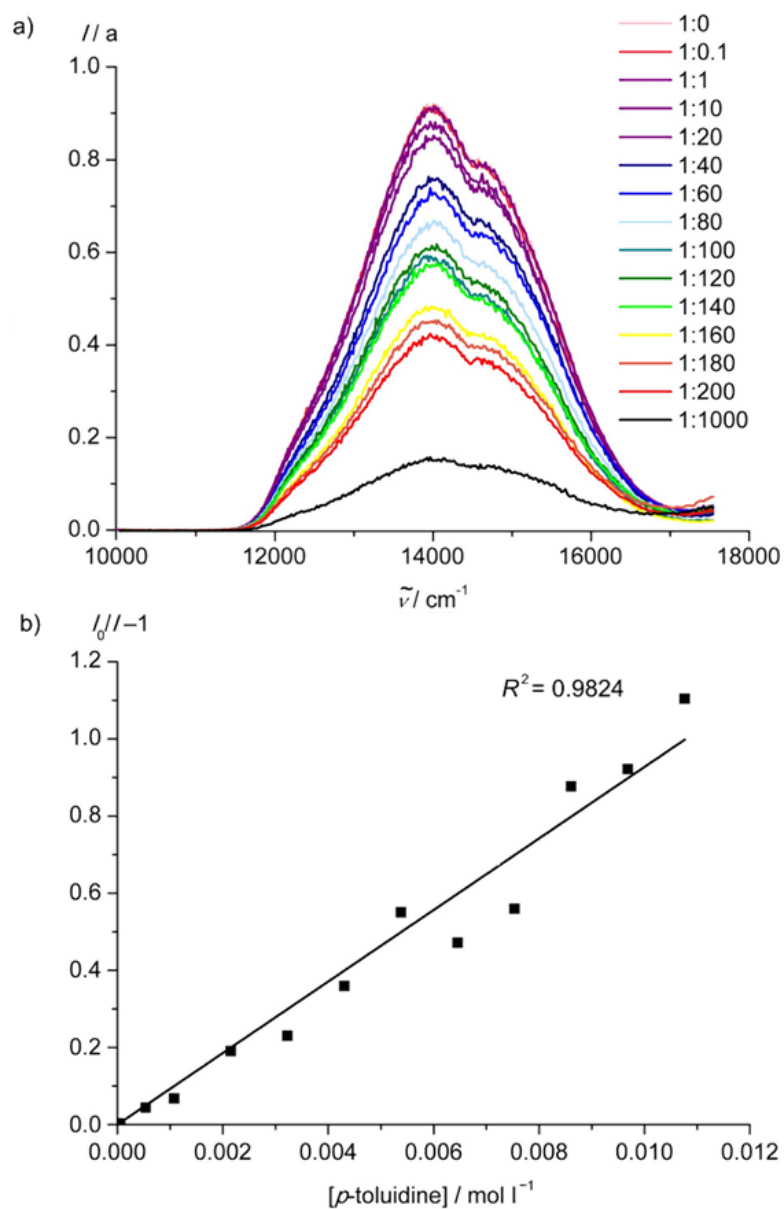


Figure S53. a) Emission spectra of $2[\text{PF}_6]_2$ with increasing concentration of *p*-toluidine in dry and deaerated CH_3CN at 298 K ($\lambda_{\text{exc}} = 546 \text{ nm}$) and b) Stern-Volmer plot for phosphorescence quenching of $2[\text{PF}_6]_2$ with *p*-toluidine in dry and deaerated CH_3CN at 298 K ($K_{\text{SV}} = 93 \text{ M}^{-1}$).

6. Green-Light Activation of Push–Pull Ruthenium(II) Complexes

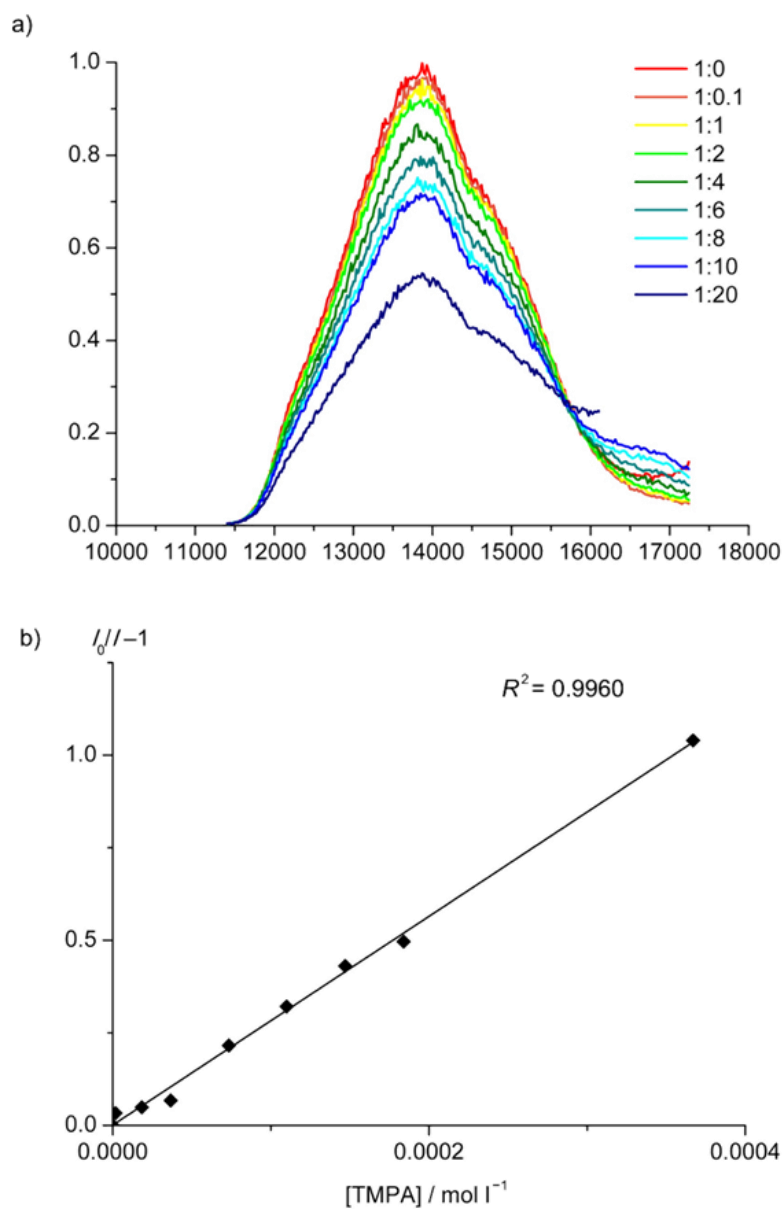


Figure S54. a) Emission spectra of of $2[\text{PF}_6]_2$ with increasing concentration of TPA in in dry and deaerated DMF at 298 K ($\lambda_{\text{exc}} = 555 \text{ nm}$) and b) Stern-Volmer plot for phosphorescence quenching of $2[\text{PF}_6]_2$ with TPA in in dry and deaerated DMF at 298 K ($K_{\text{SV}} = 2819 \text{ M}^{-1}$).

6. Green-Light Activation of Push–Pull Ruthenium(II) Complexes

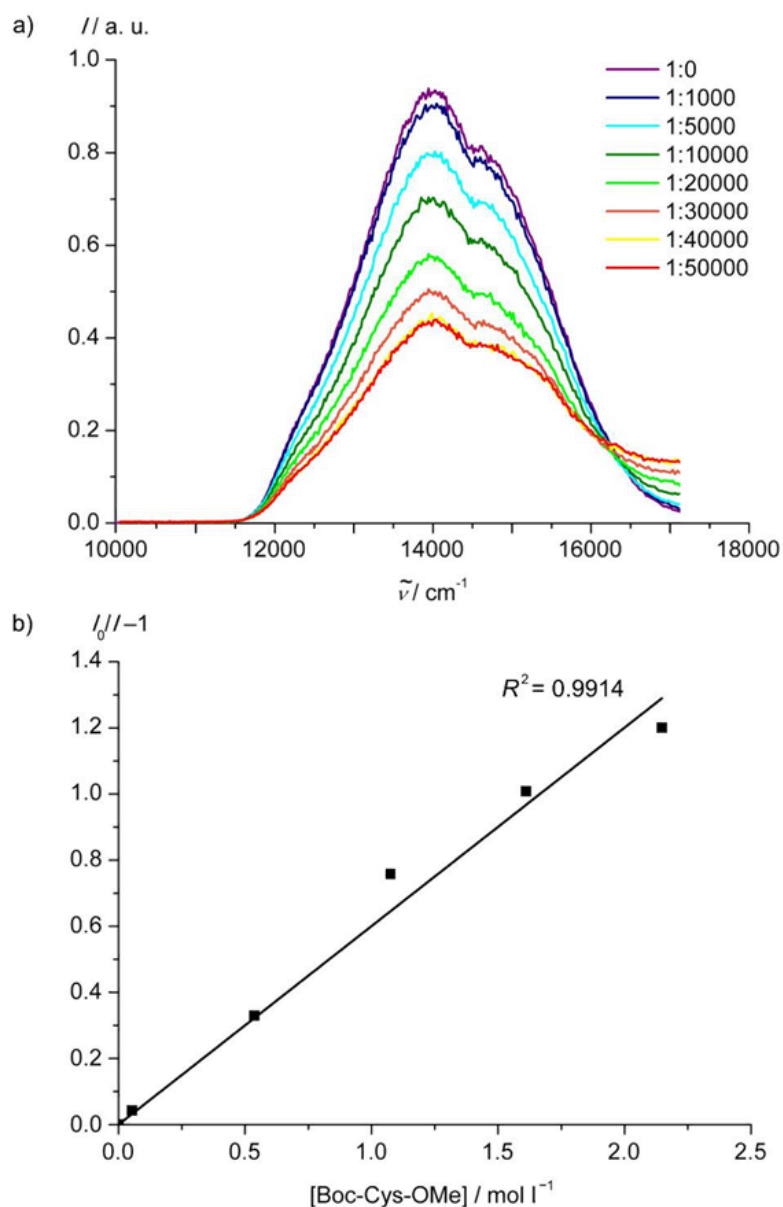


Figure S55. a) Emission spectra of $2[PF_6]_2$ with increasing concentration of N -Boc-cysteine methyl ester in dry and deaerated CH_3CN at 298 K ($\lambda_{exc} = 546\text{ nm}$) and b) Stern-Volmer plot for phosphorescence quenching of $2[PF_6]_2$ with N -Boc-cysteine methyl ester in dry and deaerated CH_3CN at 298 K ($K_{SV} = 0.60\text{ M}^{-1}$).

6. Green-Light Activation of Push–Pull Ruthenium(II) Complexes

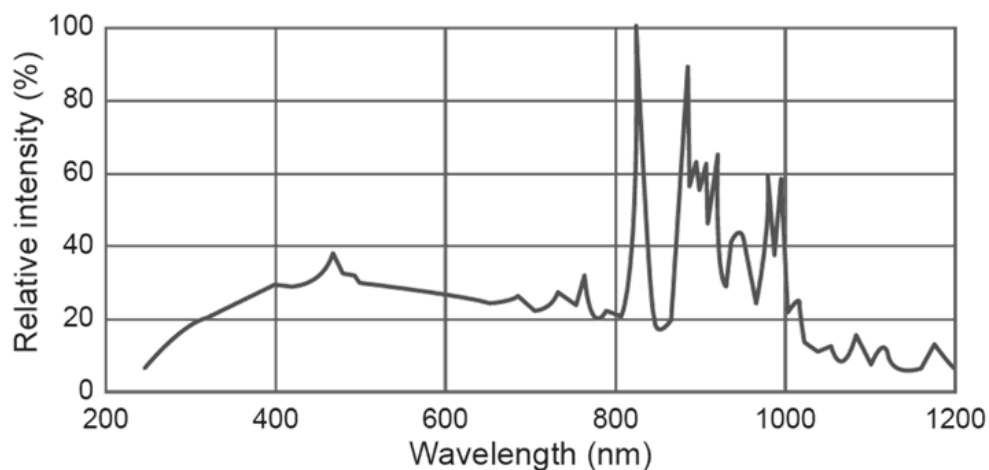


Figure S56. Spectral irradiance of the employed light source Asahi Spectra Max-303 Xenon Light Source (300 W).

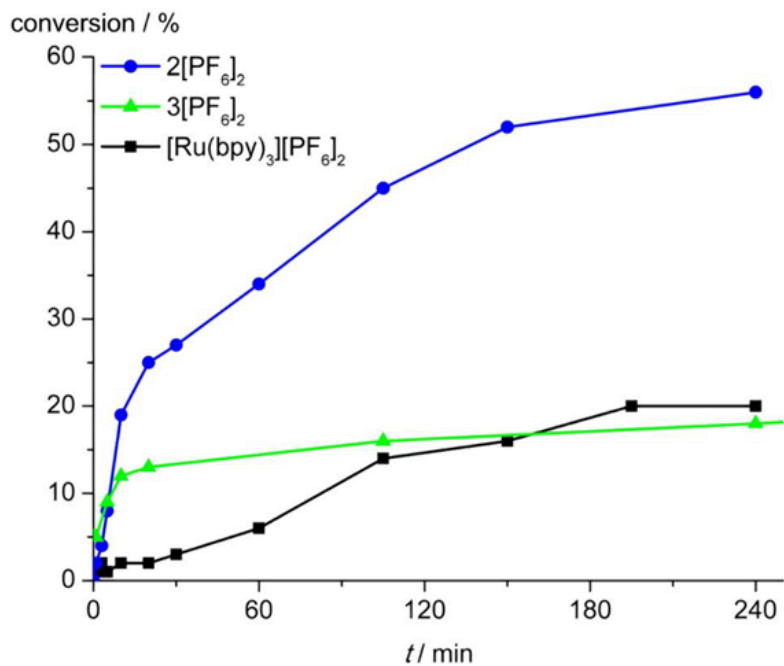


Figure S57. Conversion vs. time traces of the sensitized thiol-ene reaction between *N*-Boc cysteine methyl ester and allyl alcohol using **2**[PF₆]₂ (blue), **3**[PF₆]₂ (green) and [Ru(bpy)₃][PF₆]₂ (black) as sensitizer and *p*-toluidine as mediator in acetonitrile ($\lambda_{\text{exc}} = 560 \pm 5$ nm).

6. Green-Light Activation of Push–Pull Ruthenium(II) Complexes

Table S1. Cartesian coordinates of DFT optimized geometry of cpm (1GS)

6	-2.129222000	3.161485000	-4.261733000
6	-2.912723000	4.023627000	-3.513729000
6	-3.417422000	3.584081000	-2.284910000
7	-3.220491000	2.350701000	-1.827717000
6	-2.470421000	1.519610000	-2.564419000
6	-1.884834000	1.882677000	-3.772799000
1	-1.725574000	3.475095000	-5.215567000
1	-3.146396000	5.019005000	-3.865845000
1	-1.269668000	1.176165000	-4.311869000
7	-4.199518000	4.449003000	-1.485082000
8	-1.090023000	-0.356982000	-2.194675000
6	-1.948588000	7.269119000	-0.779719000
6	-2.893001000	8.193492000	-0.323763000
6	-4.214145000	7.784916000	-0.277227000
7	-4.640466000	6.574772000	-0.667715000
6	-3.732602000	5.698076000	-1.120966000
6	-2.356226000	6.012146000	-1.172674000
1	-0.897263000	7.528409000	-0.815412000
1	-2.605801000	9.184478000	-0.000472000
1	-4.984036000	8.455871000	0.088657000
1	-1.633125000	5.278350000	-1.496487000
6	-5.593802000	4.083633000	-1.238704000
1	-6.268909000	4.667796000	-1.868109000
1	-5.707340000	3.027733000	-1.472215000
1	-5.858320000	4.259107000	-0.196729000
6	-3.219470000	-0.534500000	-1.181538000
7	-4.502612000	-0.309573000	-1.498917000
6	-2.820647000	-1.425339000	-0.185140000
1	-1.769095000	-1.575699000	0.018199000
6	-5.432005000	-0.977784000	-0.815842000
6	-3.800075000	-2.100256000	0.531440000
1	-6.462053000	-0.791423000	-1.099464000
1	-3.527513000	-2.789199000	1.320802000
6	-5.132607000	-1.873553000	0.209999000
1	-5.930491000	-2.376937000	0.739164000
6	-2.177199000	0.164633000	-1.995820000

6. Green-Light Activation of Push–Pull Ruthenium(II) Complexes

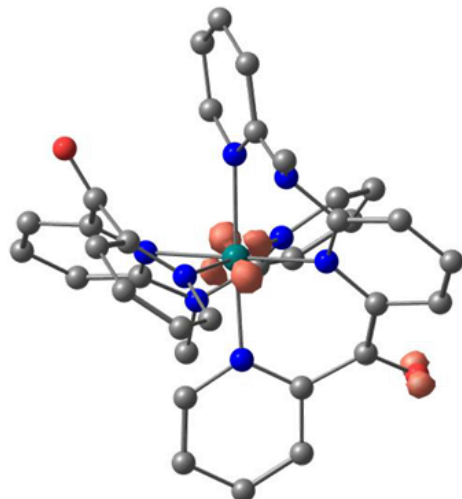
Table S2. Cartesian coordinates of DFT optimized geometry of 2^{2*} (1GS).

6	1.570086000	-2.602123000	-0.160146000
6	1.748467000	-3.988079000	-0.146245000
6	0.656832000	-4.815102000	0.036276000
6	-0.604198000	-4.252699000	0.197025000
6	-0.714196000	-2.873414000	0.211790000
7	0.352813000	-2.056759000	0.051062000
1	2.728531000	-4.407224000	-0.312402000
1	-1.485715000	-4.861440000	0.331306000
6	1.511101000	0.995841000	-2.389047000
6	2.507249000	1.164453000	-3.323336000
6	3.635008000	0.352067000	-3.239724000
6	3.693494000	-0.622600000	-2.260925000
6	2.639823000	-0.749330000	-1.351778000
7	1.582312000	0.086117000	-1.391641000
1	4.445939000	0.455606000	-3.948881000
1	0.621680000	1.605874000	-2.409249000
1	2.404798000	1.921169000	-4.088100000
1	4.536123000	-1.294384000	-2.210655000
6	-2.253814000	-1.195970000	1.465738000
6	-3.336529000	-1.272076000	2.336672000
6	-3.463639000	-0.326924000	3.343387000
6	-2.491945000	0.659836000	3.453669000
6	-1.458176000	0.693476000	2.535121000
7	-1.342301000	-0.204377000	1.540256000
1	-4.293404000	-0.369190000	4.036162000
1	-4.049573000	-2.075768000	2.223680000
1	-2.533109000	1.408607000	4.232728000
1	-0.699928000	1.459852000	2.584296000
6	0.944139000	2.827463000	0.271426000
6	0.834125000	4.206947000	0.273267000
6	-0.423298000	4.771740000	0.093399000
6	-1.510522000	3.947100000	-0.122672000
6	-1.331872000	2.561584000	-0.148949000
7	-0.118970000	2.013006000	0.077848000
1	1.712342000	4.813676000	0.435597000
1	-2.486936000	4.368395000	-0.304676000
6	1.641565000	-0.775711000	2.555537000
6	2.652795000	-0.753153000	3.499065000
6	3.622993000	0.238742000	3.427670000
6	3.517401000	1.197942000	2.431909000
6	2.456330000	1.131703000	1.533918000
7	1.546250000	0.137154000	1.572122000
1	4.435488000	0.273277000	4.141118000
1	0.884077000	-1.544128000	2.574809000
1	2.677521000	-1.513594000	4.267428000
1	4.230315000	2.005412000	2.348569000
6	-2.382464000	0.726387000	-1.383320000
6	-3.422156000	0.612891000	-2.310193000
6	-3.348061000	-0.347381000	-3.301936000
6	-2.218687000	-1.158150000	-3.379788000
6	-1.237072000	-1.003170000	-2.427897000
7	-1.323998000	-0.108161000	-1.418589000
1	-4.147897000	-0.440748000	-4.025022000
1	-4.265788000	1.283736000	-2.263177000
1	-2.103565000	-1.903114000	-4.154215000
1	-0.347243000	-1.612711000	-2.443510000
7	2.664695000	-1.751075000	-0.371646000
6	-2.081492000	-2.295408000	0.463466000
8	-3.057378000	-2.841872000	-0.016714000
1	0.782759000	-5.889546000	0.031497000
1	-0.549309000	5.846154000	0.100409000
44	0.116566000	-0.022191000	0.080374000
7	-2.422810000	1.713471000	-0.389391000
6	2.305404000	2.245262000	0.544336000
8	3.291908000	2.797696000	0.093598000
6	-3.748437000	2.188850000	0.029192000
1	-4.191343000	2.902908000	-0.668207000
1	-4.404452000	1.326806000	0.123103000

6. Green-Light Activation of Push–Pull Ruthenium(II) Complexes

1	-3.655202000	2.657245000	1.006084000
6	3.983792000	-2.232818000	0.060636000
1	3.874696000	-2.715190000	1.028985000
1	4.436941000	-2.936820000	-0.640571000
1	4.638048000	-1.372244000	0.178141000

Table S3. Cartesian coordinates of DFT optimized geometry of 2^{2*} ($^3\text{MLCT}$; spin density at 0.05 a.u.).

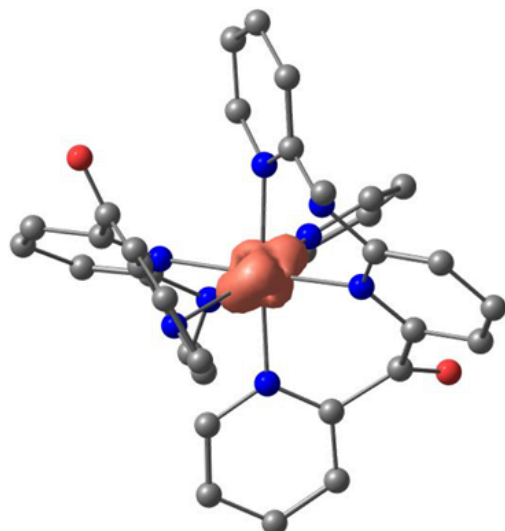


6	1.586066000	-2.583220000	-0.135360000
6	1.762784000	-3.972682000	-0.058389000
6	0.667589000	-4.786758000	0.114456000
6	-0.604749000	-4.220958000	0.219264000
6	-0.717076000	-2.850132000	0.188725000
7	0.359845000	-2.036752000	0.031963000
1	2.745301000	-4.398750000	-0.183041000
1	-1.486632000	-4.830119000	0.348254000
6	1.519044000	1.007270000	-2.369363000
6	2.528303000	1.196359000	-3.281183000
6	3.669306000	0.402097000	-3.179918000
6	3.731114000	-0.574587000	-2.206358000
6	2.659719000	-0.729364000	-1.321390000
7	1.592375000	0.088179000	-1.378734000
1	4.490000000	0.523097000	-3.874661000
1	0.622662000	1.605126000	-2.396697000
1	2.428865000	1.956921000	-4.042152000
1	4.584428000	-1.230956000	-2.146082000
6	-2.285901000	-1.185215000	1.413596000
6	-3.381771000	-1.259654000	2.263168000
6	-3.516708000	-0.317116000	3.273800000
6	-2.539950000	0.658837000	3.411536000
6	-1.487222000	0.690706000	2.513349000
7	-1.370197000	-0.202919000	1.517365000
1	-4.359484000	-0.356456000	3.950624000
1	-4.098400000	-2.057581000	2.133934000
1	-2.587473000	1.400548000	4.196520000
1	-0.721517000	1.448021000	2.580833000
6	0.979748000	2.842279000	0.279410000
6	0.830212000	4.230498000	0.178066000
6	-0.414971000	4.776048000	-0.046806000
6	-1.521047000	3.942249000	-0.206666000
6	-1.331774000	2.571534000	-0.167523000
7	-0.109276000	2.025773000	0.075881000
1	1.702339000	4.848099000	0.325302000
1	-2.495610000	4.352787000	-0.415752000
6	1.622601000	-0.776016000	2.524833000
6	2.683533000	-0.857738000	3.393172000
6	3.716512000	0.083187000	3.269177000
6	3.602832000	1.088027000	2.336591000
6	2.468310000	1.163358000	1.503094000
7	1.531264000	0.173999000	1.566957000

6. Green-Light Activation of Push–Pull Ruthenium(II) Complexes

1	4.582234000	0.033628000	3.917170000
1	0.817306000	-1.493762000	2.569765000
1	2.712910000	-1.643840000	4.134136000
1	4.355394000	1.855751000	2.237398000
6	-2.405291000	0.731978000	-1.365534000
6	-3.465897000	0.584708000	-2.264950000
6	-3.372913000	-0.354624000	-3.272723000
6	-2.212624000	-1.117869000	-3.395116000
6	-1.217946000	-0.944254000	-2.463475000
7	-1.325283000	-0.069061000	-1.437160000
1	-4.185119000	-0.470093000	-3.978408000
1	-4.334495000	1.219201000	-2.188079000
1	-2.087988000	-1.844498000	-4.184902000
1	-0.309575000	-1.524628000	-2.503961000
7	2.680233000	-1.760030000	-0.373529000
6	-2.094280000	-2.272571000	0.400680000
8	-3.052656000	-2.806891000	-0.117289000
1	0.790554000	-5.861094000	0.142692000
1	-0.538802000	5.849597000	-0.107349000
44	0.119044000	0.001700000	0.077920000
7	-2.429200000	1.712575000	-0.374643000
6	2.304306000	2.335869000	0.649501000
8	3.312352000	3.070617000	0.417922000
6	-3.749690000	2.201102000	0.050451000
1	-4.198535000	2.895764000	-0.661599000
1	-4.405465000	1.342836000	0.176798000
1	-3.639410000	2.697250000	1.010795000
6	4.003691000	-2.245932000	0.057854000
1	3.891858000	-2.744244000	1.016374000
1	4.455020000	-2.931476000	-0.660255000
1	4.648964000	-1.382508000	0.195258000

Table S4. Cartesian coordinates of DFT optimized geometry of 2^{2+} (3MC ; spin density at 0.05 a.u.).



6	1.591740000	-2.648073000	-0.202235000
6	1.770057000	-4.035664000	-0.168134000
6	0.703019000	-4.862297000	0.109305000
6	-0.545738000	-4.296286000	0.338071000
6	-0.667719000	-2.920017000	0.308842000
7	0.381519000	-2.096282000	0.053265000
1	2.739575000	-4.454625000	-0.386567000
1	-1.412275000	-4.904636000	0.550457000
6	1.818895000	0.872235000	-2.619616000
6	2.879632000	0.979032000	-3.497454000
6	3.946039000	0.096699000	-3.338360000
6	3.905979000	-0.859960000	-2.337186000
6	2.794197000	-0.897959000	-1.487030000
7	1.794243000	-0.027030000	-1.626817000
1	4.798788000	0.141584000	-4.003656000

6. Green-Light Activation of Push–Pull Ruthenium(II) Complexes

1	0.964594000	1.535480000	-2.682507000
1	2.874414000	1.731361000	-4.273730000
1	4.712467000	-1.568922000	-2.227982000
6	-2.343557000	-1.340959000	1.574750000
6	-3.656778000	-1.028715000	1.915527000
6	-3.876232000	-0.058173000	2.885832000
6	-2.783028000	0.568845000	3.473523000
6	-1.505455000	0.206594000	3.064491000
7	-1.287606000	-0.731651000	2.140242000
1	-4.883240000	0.214241000	3.173516000
1	-4.475616000	-1.535668000	1.425680000
1	-2.912825000	1.330908000	4.229858000
1	-0.628495000	0.688533000	3.478377000
6	0.847664000	2.906372000	0.331025000
6	0.695047000	4.276840000	0.385814000
6	-0.590698000	4.801208000	0.291587000
6	-1.660166000	3.950427000	0.100154000
6	-1.438746000	2.572543000	0.004835000
7	-0.196758000	2.062437000	0.158560000
1	1.559871000	4.909486000	0.518035000
1	-2.655051000	4.349044000	-0.016321000
6	1.878403000	-0.710476000	2.490572000
6	2.947203000	-0.644411000	3.367155000
6	3.848761000	0.406429000	3.256969000
6	3.626591000	1.373571000	2.287391000
6	2.512836000	1.258768000	1.462671000
7	1.664472000	0.215515000	1.539816000
1	4.701791000	0.477576000	3.918299000
1	1.162793000	-1.516941000	2.540542000
1	3.065419000	-1.414067000	4.117408000
1	4.287325000	2.220158000	2.170922000
6	-2.477513000	0.743107000	-1.257026000
6	-3.545737000	0.624432000	-2.149718000
6	-3.479429000	-0.310712000	-3.165860000
6	-2.339537000	-1.100290000	-3.298014000
6	-1.330316000	-0.943438000	-2.377565000
7	-1.403453000	-0.066439000	-1.351338000
1	-4.299503000	-0.403118000	-3.866083000
1	-4.402300000	1.273856000	-2.064201000
1	-2.237059000	-1.826472000	-4.091574000
1	-0.426876000	-1.530651000	-2.427849000
7	2.716180000	-1.834123000	-0.436791000
6	-2.068903000	-2.388030000	0.545478000
8	-2.985397000	-2.916601000	-0.057088000
1	0.833236000	-5.936233000	0.126803000
1	-0.752331000	5.869701000	0.342769000
44	0.103536000	0.014811000	0.119251000
7	-2.512826000	1.697291000	-0.223494000
6	2.244138000	2.358599000	0.481599000
8	3.166194000	2.925305000	-0.069833000
6	-3.846018000	2.170793000	0.183360000
1	-4.274432000	2.891353000	-0.515784000
1	-4.503163000	1.309686000	0.259291000
1	-3.766988000	2.625173000	1.166872000
6	3.997838000	-2.334470000	0.084527000
1	3.825960000	-2.778294000	1.061649000
1	4.471054000	-3.074243000	-0.564420000
1	4.668832000	-1.486549000	0.204843000

6. Green-Light Activation of Push–Pull Ruthenium(II) Complexes

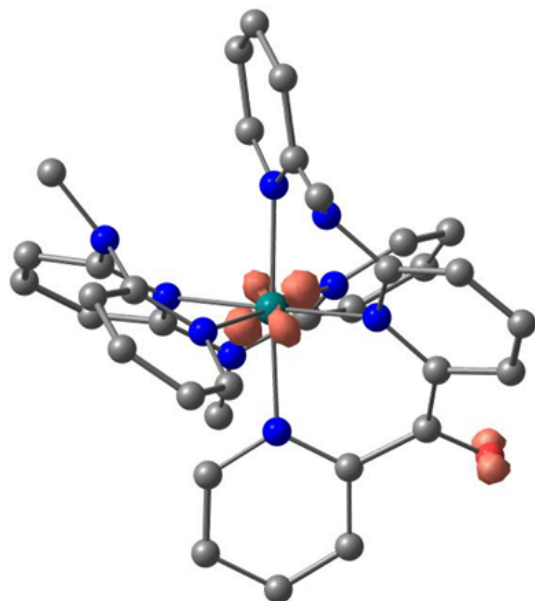
Table S5. Cartesian coordinates of DFT optimized geometry of 3^{2+} (1GS).

6	1.424306000	-2.566881000	-0.261222000
6	1.597366000	-3.946103000	-0.290281000
6	0.499131000	-4.761837000	-0.076064000
6	-0.741614000	-4.198499000	0.172246000
6	-0.855880000	-2.812237000	0.202292000
7	0.212398000	-2.011350000	-0.021505000
1	2.564780000	-4.370318000	-0.507019000
1	-1.599460000	-4.820830000	0.371259000
6	1.408078000	1.057944000	-2.457486000
6	2.407828000	1.226626000	-3.388035000
6	3.528694000	0.403929000	-3.308585000
6	3.575040000	-0.580816000	-2.339364000
6	2.517114000	-0.707546000	-1.433599000
7	1.468016000	0.139520000	-1.467183000
1	4.342970000	0.507558000	-4.014015000
1	0.523349000	1.674843000	-2.474852000
1	2.314315000	1.991399000	-4.146034000
1	4.412176000	-1.259867000	-2.293153000
6	-2.279155000	-1.243155000	1.446676000
6	-3.316682000	-1.364011000	2.377280000
6	-3.474038000	-0.397042000	3.352987000
6	-2.572580000	0.662315000	3.410944000
6	-1.572838000	0.719329000	2.465358000
7	-1.440544000	-0.189839000	1.476818000
1	-4.273871000	-0.485094000	4.076757000
1	-3.979169000	-2.214716000	2.344002000
1	-2.642254000	1.430165000	4.168621000
1	-0.846918000	1.518008000	2.472593000
6	0.874439000	2.867585000	0.214827000
6	0.784838000	4.249782000	0.226739000
6	-0.461977000	4.835118000	0.045957000
6	-1.559828000	4.026739000	-0.182983000
6	-1.402613000	2.639169000	-0.216050000
7	-0.199170000	2.068660000	0.013418000
1	1.671844000	4.841396000	0.397108000
1	-2.529011000	4.463134000	-0.368809000
6	1.521800000	-0.757305000	2.477189000
6	2.538168000	-0.758636000	3.415034000
6	3.526033000	0.216393000	3.345112000
6	3.431025000	1.183104000	2.356148000
6	2.364071000	1.141151000	1.462592000
7	1.437561000	0.161314000	1.497242000
1	4.342786000	0.231829000	4.054410000
1	0.751879000	-1.512784000	2.495020000
1	2.553132000	-1.524197000	4.178696000
1	4.156506000	1.979508000	2.274190000
6	-2.472969000	0.827330000	-1.466215000
6	-3.511704000	0.734212000	-2.397502000
6	-3.454380000	-0.230436000	-3.386975000
6	-2.343124000	-1.065954000	-3.454589000
6	-1.359653000	-0.924031000	-2.500568000
7	-1.430206000	-0.022662000	-1.499492000
1	-4.253245000	-0.309908000	-4.112915000
1	-4.341646000	1.422486000	-2.354400000
1	-2.241314000	-1.818237000	-4.224034000
1	-0.482097000	-1.551540000	-2.509052000
7	2.527591000	-1.716862000	-0.463731000
7	-2.104173000	-2.213841000	0.447455000
6	3.841093000	-2.220071000	-0.040530000
1	4.287181000	-2.918506000	-0.752189000
1	4.506624000	-1.369833000	0.090701000
1	3.726206000	-2.717906000	0.919168000
6	-3.296670000	-2.964161000	0.036095000
1	-3.583782000	-3.745251000	0.743896000
1	-4.120412000	-2.261761000	-0.072694000
1	-3.100375000	-3.417799000	-0.932336000
1	0.610018000	-5.837996000	-0.101477000
1	-0.572343000	5.911200000	0.061445000

6. Green-Light Activation of Push–Pull Ruthenium(II) Complexes

44	0.006865000	0.032135000	0.004820000
7	-2.504681000	1.808712000	-0.464012000
6	2.226994000	2.266625000	0.485821000
8	3.221807000	2.816060000	0.046854000
6	-3.823881000	2.298991000	-0.047630000
1	-4.257262000	3.021713000	-0.742901000
1	-4.491627000	1.445043000	0.041316000
1	-3.727968000	2.762193000	0.931542000

Table S6. Cartesian coordinates of DFT optimized geometry of 3^{2+} ($^3\text{MLCT}$; spin density at 0.05 a.u.).

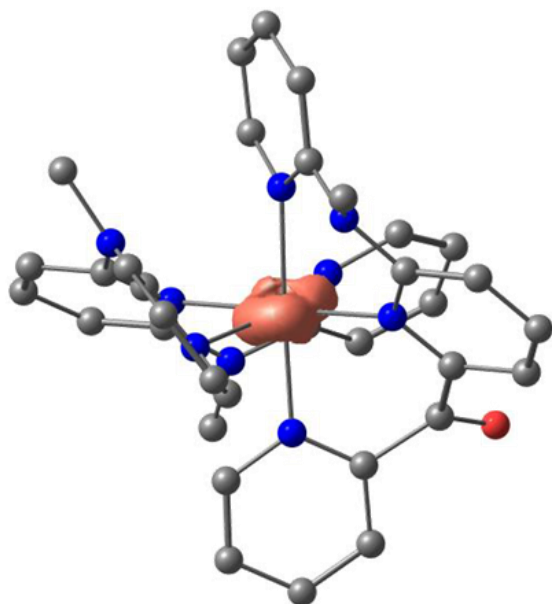


6	1.421907000	-2.567610000	-0.253335000
6	1.567575000	-3.948041000	-0.271957000
6	0.450071000	-4.742923000	-0.080445000
6	-0.788723000	-4.164867000	0.139259000
6	-0.883900000	-2.779790000	0.177445000
7	0.207898000	-1.993877000	-0.025722000
1	2.529530000	-4.391284000	-0.472832000
1	-1.657122000	-4.776779000	0.321326000
6	1.447501000	1.061622000	-2.424863000
6	2.460288000	1.238014000	-3.337310000
6	3.579484000	0.413119000	-3.249140000
6	3.616350000	-0.579353000	-2.288898000
6	2.544630000	-0.715553000	-1.400912000
7	1.500572000	0.130027000	-1.447059000
1	4.402822000	0.523456000	-3.942729000
1	0.565042000	1.681115000	-2.443316000
1	2.378976000	2.011120000	-4.087849000
1	4.453552000	-1.257152000	-2.236712000
6	-2.311070000	-1.192517000	1.394055000
6	-3.403639000	-1.248096000	2.267555000
6	-3.532411000	-0.286553000	3.250379000
6	-2.554566000	0.698961000	3.382389000
6	-1.513182000	0.706633000	2.486995000
7	-1.417114000	-0.189534000	1.477931000
1	-4.370465000	-0.325811000	3.933683000
1	-4.122657000	-2.047962000	2.192125000
1	-2.603825000	1.449986000	4.157712000
1	-0.730879000	1.447382000	2.540169000
6	0.883190000	2.887730000	0.240548000
6	0.725670000	4.277272000	0.154128000
6	-0.523412000	4.820063000	-0.051701000
6	-1.627796000	3.983116000	-0.209361000
6	-1.430397000	2.612330000	-0.191122000
7	-0.204188000	2.067093000	0.033973000
1	1.596768000	4.896729000	0.299265000

6. Green-Light Activation of Push–Pull Ruthenium(II) Complexes

1	-2.605847000	4.391533000	-0.405720000
6	1.581611000	-0.757672000	2.435559000
6	2.641053000	-0.827562000	3.309489000
6	3.650750000	0.137930000	3.206428000
6	3.517369000	1.149510000	2.283705000
6	2.386537000	1.206440000	1.442967000
7	1.469255000	0.202359000	1.493189000
1	4.513600000	0.101594000	3.859205000
1	0.795472000	-1.496770000	2.466324000
1	2.683856000	-1.624365000	4.038527000
1	4.251625000	1.936119000	2.196497000
6	-2.508386000	0.773334000	-1.389681000
6	-3.590217000	0.601183000	-2.262422000
6	-3.503520000	-0.339555000	-3.268476000
6	-2.331661000	-1.082374000	-3.416299000
6	-1.318177000	-0.885531000	-2.510434000
7	-1.416102000	-0.007893000	-1.486328000
1	-4.329584000	-0.472467000	-3.954795000
1	-4.467902000	1.220791000	-2.168644000
1	-2.213657000	-1.809437000	-4.206783000
1	-0.399432000	-1.447243000	-2.570167000
7	2.534752000	-1.743341000	-0.450686000
7	-2.126535000	-2.173742000	0.414621000
6	3.841805000	-2.272269000	-0.028561000
1	4.281870000	-2.953588000	-0.759080000
1	4.511687000	-1.431051000	0.132115000
1	3.712007000	-2.792446000	0.916226000
6	-3.322728000	-2.916766000	-0.015467000
1	-3.626380000	-3.682810000	0.699743000
1	-4.134196000	-2.205552000	-0.149028000
1	-3.109624000	-3.382531000	-0.973563000
1	0.544928000	-5.820563000	-0.102221000
1	-0.652507000	5.893704000	-0.099516000
44	0.020893000	0.042497000	0.016594000
7	-2.528977000	1.757654000	-0.406379000
6	2.210723000	2.386872000	0.597578000
8	3.212482000	3.134472000	0.377117000
6	-3.846813000	2.235256000	0.038111000
1	-4.311838000	2.923956000	-0.669346000
1	-4.493266000	1.371812000	0.176771000
1	-3.725715000	2.732740000	0.996030000

Table S7. Cartesian coordinates of DFT optimized geometry of 3^{2+} (3MC ; spin density at 0.05 a.u.).



6	1.427243000	-2.642312000	-0.289440000
6	1.586899000	-4.024572000	-0.311301000

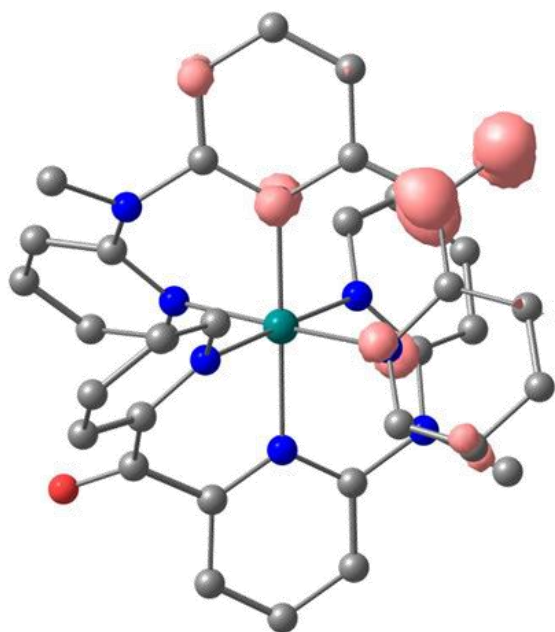
6. Green-Light Activation of Push–Pull Ruthenium(II) Complexes

6	0.499151000	-4.834717000	-0.041099000
6	-0.726092000	-4.258606000	0.240474000
6	-0.839045000	-2.871095000	0.244292000
7	0.225437000	-2.070305000	-0.019066000
1	2.544646000	-4.454311000	-0.559586000
1	-1.580854000	-4.869417000	0.485527000
6	1.484947000	0.768527000	-2.685281000
6	2.636064000	1.214668000	-3.298189000
6	3.841956000	0.621495000	-2.925204000
6	3.850015000	-0.401882000	-1.993500000
6	2.634425000	-0.806230000	-1.423795000
7	1.487095000	-0.190826000	-1.742129000
1	4.773397000	0.947398000	-3.369335000
1	0.518938000	1.199915000	-2.915963000
1	2.593052000	2.003570000	-4.035683000
1	4.776474000	-0.888525000	-1.736001000
6	-2.362059000	-1.303535000	1.396411000
6	-3.650728000	-1.053387000	1.891318000
6	-3.821436000	-0.039001000	2.819275000
6	-2.721601000	0.699203000	3.257383000
6	-1.490199000	0.398102000	2.717319000
7	-1.316983000	-0.556830000	1.785350000
1	-4.810017000	0.172896000	3.205558000
1	-4.495719000	-1.646419000	1.582164000
1	-2.821020000	1.486376000	3.991563000
1	-0.600583000	0.946634000	2.999715000
6	0.831408000	2.904462000	0.161692000
6	0.723976000	4.280302000	0.178938000
6	-0.547557000	4.842546000	0.111030000
6	-1.650289000	4.023889000	-0.023104000
6	-1.476070000	2.636331000	-0.095405000
7	-0.246209000	2.094232000	0.041048000
1	1.611354000	4.888741000	0.265686000
1	-2.635100000	4.452535000	-0.118567000
6	1.760004000	-0.704309000	2.349155000
6	2.864617000	-0.690499000	3.182266000
6	3.824583000	0.300830000	3.020028000
6	3.618140000	1.270054000	2.049683000
6	2.467605000	1.209898000	1.269274000
7	1.568436000	0.214064000	1.386173000
1	4.707349000	0.326482000	3.644624000
1	1.001228000	-1.466405000	2.437249000
1	2.965873000	-1.455113000	3.940207000
1	4.319074000	2.077950000	1.897917000
6	-2.598308000	0.807981000	-1.279433000
6	-3.700586000	0.692066000	-2.132250000
6	-3.695479000	-0.277014000	-3.118849000
6	-2.579466000	-1.096869000	-3.261675000
6	-1.532099000	-0.930288000	-2.384642000
7	-1.549201000	-0.025986000	-1.382383000
1	-4.543225000	-0.374386000	-3.784515000
1	-4.536736000	1.366855000	-2.038147000
1	-2.521105000	-1.852134000	-4.032643000
1	-0.641845000	-1.535349000	-2.451687000
7	2.567338000	-1.838838000	-0.491317000
7	-2.110138000	-2.309428000	0.468425000
6	3.837581000	-2.352890000	0.037504000
1	4.378556000	-2.962904000	-0.689179000
1	4.461303000	-1.510869000	0.330225000
1	3.633258000	-2.946257000	0.923118000
6	-3.264861000	-3.030129000	-0.083773000
1	-3.719945000	-3.707053000	0.642836000
1	-4.007529000	-2.304437000	-0.410451000
1	-2.941838000	-3.596478000	-0.950938000
1	0.606028000	-5.911539000	-0.048868000
1	-0.672648000	5.916933000	0.138713000
44	0.004882000	0.052101000	0.010403000
7	-2.578462000	1.793512000	-0.273676000
6	2.214198000	2.319764000	0.298227000
8	3.143583000	2.871421000	-0.258892000

6. Green-Light Activation of Push–Pull Ruthenium(II) Complexes

6	-3.882408000	2.307395000	0.171826000
1	-4.323799000	3.018405000	-0.529398000
1	-4.552960000	1.462579000	0.299946000
1	-3.752808000	2.785723000	1.138404000

Table S8. Cartesian coordinates of DFT optimized geometry of **2**** (²GS; spin density at 0.01 a.u.).

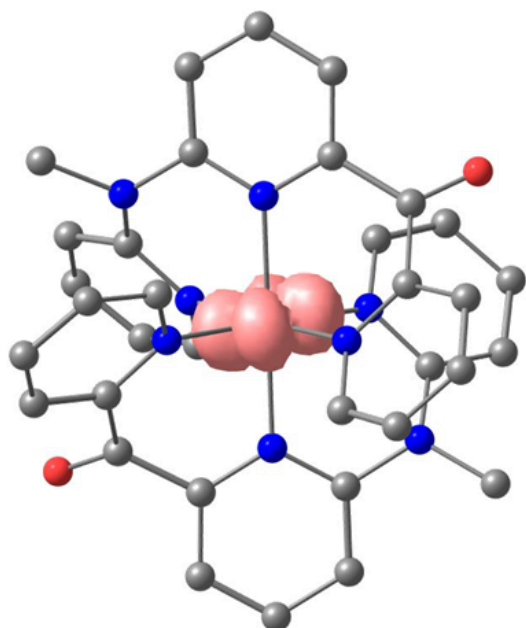


6	1.555283685	-2.597543257	-0.184758003
6	1.721079680	-3.983554254	-0.201013270
6	0.624599020	-4.807558373	-0.017739609
6	-0.627163413	-4.237347133	0.168925549
6	-0.727062552	-2.854867866	0.210328906
7	0.344446763	-2.042041028	0.050099327
6	1.518272499	1.038990844	-2.349169682
6	2.503424850	1.206281765	-3.297564323
6	3.615759661	0.371015694	-3.248940342
6	3.670805737	-0.619710480	-2.284989478
6	2.630270754	-0.737990591	-1.358753605
7	1.585572204	0.111369056	-1.371378716
6	-2.242793413	-1.176450455	1.493319146
6	-3.319353196	-1.244350247	2.375088255
6	-3.433596214	-0.297295483	3.380196409
6	-2.454654287	0.685350685	3.479769575
6	-1.427866800	0.710916825	2.554527497
7	-1.326930473	-0.188149500	1.557418386
6	0.956608530	2.857034317	0.319479651
6	0.810668324	4.246615673	0.146239720
6	-0.418428918	4.778082672	-0.165697039
6	-1.513511492	3.928138283	-0.331652845
6	-1.317955098	2.561396747	-0.204993741
7	-0.113545033	2.027519875	0.099077327
6	1.655991937	-0.819281742	2.532655014
6	2.673028804	-0.864443845	3.461350502
6	3.639657835	0.147660561	3.431852046
6	3.506079739	1.167435921	2.517839109
6	2.418137882	1.189242786	1.617095822
7	1.537910796	0.150292689	1.604253748
6	-2.392246298	0.696717941	-1.366225059
6	-3.448598918	0.541473741	-2.271331942
6	-3.361062418	-0.418418334	-3.261844859
6	-2.205000103	-1.189763497	-3.361521214
6	-1.214304621	-1.003076643	-2.424087422

6. Green-Light Activation of Push–Pull Ruthenium(II) Complexes

7	-1.312452713	-0.111661162	-1.413399094
7	2.655586593	-1.753054686	-0.391208569
6	-2.085992373	-2.277720699	0.493576320
8	-3.074672220	-2.833106510	0.041966931
44	0.119181300	-0.010054897	0.101373956
7	-2.420288459	1.686544515	-0.386368714
6	2.262561888	2.373641484	0.769278196
8	3.269244873	3.140560608	0.621285841
6	-3.735289689	2.180575927	0.032332730
6	3.972082220	-2.248055023	0.025151795

Table S9. Cartesian coordinates of DFT optimized geometry of 2^{3+} (2GS ; spin density at 0.01 a.u.).

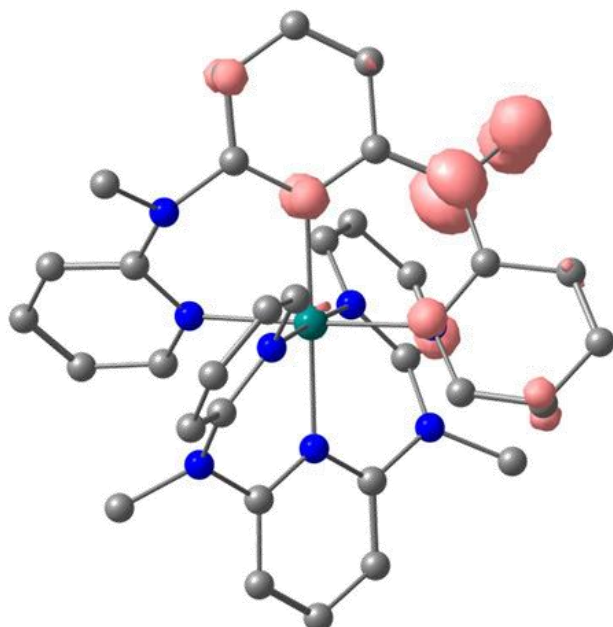


6	1.557544860	-2.620600039	-0.181142135
6	1.729238006	-4.007899053	-0.171583077
6	0.634777215	-4.826180121	0.015661001
6	-0.623176062	-4.257983458	0.193377771
6	-0.724905096	-2.881424097	0.213192813
7	0.347147155	-2.074058897	0.037228149
6	1.504495899	1.012692852	-2.373608146
6	2.509577065	1.200987875	-3.284511108
6	3.648202460	0.398220168	-3.189295187
6	3.707565034	-0.590250124	-2.228834247
6	2.637219380	-0.761293970	-1.346108915
7	1.571228325	0.075272818	-1.392088068
6	-2.242034044	-1.188855958	1.487294992
6	-3.309528491	-1.257161099	2.371132126
6	-3.431507022	-0.291241166	3.361574132
6	-2.478159283	0.714784052	3.439059440
6	-1.461244126	0.748337065	2.503199950
7	-1.345617309	-0.181017778	1.538491304
6	0.935862136	2.839447112	0.263463064
6	0.826452094	4.215761464	0.258155946
6	-0.431245061	4.779489225	0.064055848
6	-1.517802061	3.957503387	-0.151566948
6	-1.337890263	2.571641089	-0.172420765
7	-0.128018031	2.028540129	0.058504249
6	1.650966341	-0.821225939	2.517781958
6	2.648518373	-0.792560937	3.474457165
6	3.593295029	0.223466260	3.431636142
6	3.483748459	1.201496944	2.451808372
6	2.435576389	1.136551020	1.544946208

6. Green-Light Activation of Push–Pull Ruthenium(II) Complexes

7	1.546291906	0.121319176	1.564545875
6	-2.389323123	0.724784973	-1.379234352
6	-3.443468016	0.565811132	-2.283068035
6	-3.360526361	-0.401703212	-3.262361336
6	-2.217465932	-1.199143163	-3.350164012
6	-1.230642968	-1.026174171	-2.416365138
7	-1.319147863	-0.106473108	-1.419963009
7	2.659174415	-1.779078036	-0.397489903
6	-2.085529343	-2.297133037	0.485623845
8	-3.068699396	-2.826253135	0.012993947
44	0.112776139	-0.022877920	0.059257798
7	-2.430984189	1.725989387	-0.414148932
6	2.293243055	2.257345258	0.555326014
8	3.283606215	2.796830351	0.110242967
6	-3.760578540	2.211678320	-0.001714005
6	3.979994478	-2.283450101	0.021922755

Table S10. Cartesian coordinates of DFT optimized geometry of **3**** (²GS; spin density at 0.01 a.u.).

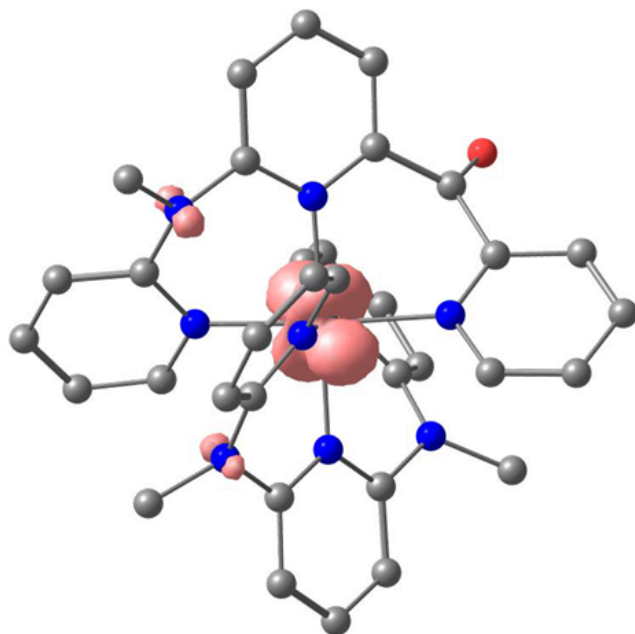


6	1.415226872	-2.562458277	-0.278060948
6	1.582390261	-3.943093361	-0.321765168
6	0.484462301	-4.758448608	-0.103660002
6	-0.751403118	-4.191107096	0.159786129
6	-0.859800315	-2.803813374	0.199562266
7	0.207923795	-2.002654365	-0.024745916
6	1.415851301	1.101464981	-2.416929241
6	2.404787269	1.267373161	-3.361939264
6	3.509393447	0.421419827	-3.317617495
6	3.551096318	-0.578001788	-2.361779976
6	2.506932237	-0.694728235	-1.438533955
7	1.470127953	0.165804991	-1.444954992
6	-2.269257038	-1.239014023	1.469146330
6	-3.292398495	-1.369957346	2.414371199
6	-3.443724137	-0.404928018	3.393947080
6	-2.549488142	0.661040282	3.438640332
6	-1.561841250	0.725264937	2.479712418
7	-1.436169062	-0.182029036	1.489167222
6	0.883106868	2.896160096	0.265505159
6	0.758385083	4.290382335	0.112089267
6	-0.461850028	4.845415185	-0.194792791
6	-1.567470108	4.013350108	-0.376854107
6	-1.392528872	2.641020989	-0.266767247

6. Green-Light Activation of Push–Pull Ruthenium(II) Complexes

7	-0.198901853	2.084811250	0.036161856
6	1.529197364	-0.797890810	2.457649960
6	2.552652093	-0.867839046	3.378489283
6	3.542549047	0.121727172	3.341051051
6	3.422648066	1.146943003	2.431335034
6	2.325217003	1.196997350	1.541669013
7	1.423736042	0.174446984	1.531121981
6	-2.481354455	0.806027969	-1.459662944
6	-3.531958094	0.680478021	-2.376388443
6	-3.459478273	-0.279803000	-3.369343512
6	-2.323222005	-1.080081987	-3.456064022
6	-1.334278099	-0.914097076	-2.510372418
7	-1.417948960	-0.020867046	-1.503354993
7	2.520638457	-1.718027386	-0.480890883
7	-2.105387249	-2.204560357	0.461716146
6	3.833020260	-2.222035906	-0.063980175
6	-3.303144497	-2.948345969	0.059547787
44	0.005142015	0.042663857	0.022040232
7	-2.505333063	1.784393092	-0.464401191
6	2.184136232	2.387690082	0.703805212
8	3.203239007	3.142419079	0.554941831
6	-3.815925189	2.289874313	-0.051585257

Table S11. Cartesian coordinates of DFT optimized geometry of 3^{3+} (2GS ; spin density at 0.01 a.u.).



6	1.428239341	-2.570933050	-0.245554119
6	1.577469971	-3.948640197	-0.261169081
6	0.460231274	-4.747075531	-0.074483815
6	-0.781214848	-4.173256360	0.136376915
6	-0.881078003	-2.788728118	0.173589188
7	0.210543223	-2.000159294	-0.023835202
6	1.436163241	1.018506922	-2.471161972
6	2.450310271	1.185468165	-3.382509442
6	3.579003539	0.375965089	-3.270455102
6	3.623510520	-0.597793017	-2.291282983
6	2.549783952	-0.730439232	-1.407250054
7	1.498242082	0.108403018	-1.471124923
6	-2.316916329	-1.194033957	1.366238288
6	-3.428225065	-1.225504128	2.218068135
6	-3.558175122	-0.259433909	3.194696499
6	-2.565081408	0.710162218	3.344378517
6	-1.508966918	0.700097796	2.468947365

6. Green-Light Activation of Push–Pull Ruthenium(II) Complexes

7	-1.409068307	-0.200340156	1.461129294
6	0.860034211	2.867977174	0.211421128
6	0.738862146	4.236036361	0.288295236
6	-0.535046883	4.799078308	0.187924071
6	-1.623869290	3.985915443	-0.027008148
6	-1.437885184	2.602231239	-0.149647093
7	-0.210427862	2.055060376	0.013701987
6	1.600965970	-0.727138224	2.451354338
6	2.639478967	-0.714704147	3.366120294
6	3.615676051	0.266385181	3.266425417
6	3.495156462	1.229604193	2.273871993
6	2.412560354	1.173189136	1.406094860
7	1.494583880	0.189383012	1.475032897
6	-2.488758174	0.785121234	-1.410487032
6	-3.552940501	0.644543181	-2.306866195
6	-3.473744363	-0.303242906	-3.306891072
6	-2.323510407	-1.083661871	-3.423344463
6	-1.321449255	-0.910789189	-2.501471128
7	-1.412649250	-0.021969852	-1.483781256
7	2.538408229	-1.736747031	-0.435528222
7	-2.126072258	-2.185567127	0.403484952
6	3.845338448	-2.258726940	-0.000665176
6	-3.318924033	-2.935353080	-0.030138232
44	0.022920783	0.024588221	-0.001209170
7	-2.52553455	1.780007271	-0.428353108
6	2.235221416	2.285172044	0.418289215
8	3.198036137	2.829064125	-0.079306207
6	-3.857108408	2.245341931	0.003446002

7. Understanding Excited State Kinetics in Asymmetric Iron(II) Push-Pull Complexes

Johannes Moll, Lukas Sorge, Christoph Förster, Niklas Gessner, Patrick Nürnberger, ██████████, ██████████, Matthias Bauer, Ayla Kruse, Stefan Lochbrunner, Olga Bokareva, Sergey Bokarev, Oliver Kühn, Omar Baig, Leticia González and Katja Heinze

The push-pull iron(II) complexes $[\text{Fe}(\text{cpmp})_2]^{2+}$ (cpmp: 6,2''-carboxylpyridyl-2,2'-methylaminepyridyl-pyridine) and $[\text{Fe}(\text{cpmp})(\text{ddpd})]^{2+}$ (ddpd: *N,N*-dimethyl-*N,N*-dipyridin-2-ylpyridine-2,6-diamine) bearing the asymmetric cpmp ligand were synthesized. As a result of the asymmetric push-pull design the MLCT states are stabilized compared to $[\text{Fe}(\text{dcpp})(\text{ddpd})]^{2+}$. However this stabilization is too weak to enable sufficiently long-living MLCT states for photochemical applications.

Author Contributions

Johannes Moll synthesized and characterized the iron complexes presented in this manuscript, conducted NMR, EPR, UV-VIS and IR spectroscopic experiments and carried out the electrochemical and spectroelectrochemical experiments as well. Ayla Kruse and Prof. Stefan Lochbrunner from the University of Rostock performed Vis-pump-Vis-probe spectroscopy, Niklas Gessner and Prof. Patrick Nürnberger from the University of Regensburg conducted Vis-pump-IR-probe spectroscopy. ██████████ and Prof. Matthias Bauer from the University of Paderborn performed the X-Ray absorption and emission experiments. The crystal structures were solved and refined by Dr. Christoph Förster from the Johannes Gutenberg University in Mainz. EPR simulation was conducted by Lukas Sorge from the Johannes Gutenberg University in Mainz. Johannes Moll, Dr. Olga Bokareva, Dr. Sergey Bokarev and Prof. Oliver Kühn from the University of Rostock performed DFT and TD-DFT calculations. Molecular dynamics calculations using a LVC model were conducted by Omar Baig and Prof. Leticia González from the University of Vienna. The manuscript was written by Johannes Moll and Prof. Katja Heinze.

Supporting Information for this article is found at pp. 135.

"Moll, J.; Sorge, L.; Förster, C.; Gessner, N.; Nürnberger, P.; ██████████; Bauer, M.; Kruse, A.; Lochbrunner, S.; Bokareva, O.; Bokarev, S.; Kühn, O.; Baig, B.; González, L.; Heinze, K. Manuscript in preparation."

7. Understanding Excited State Kinetics in Asymmetric Iron(II) Push-Pull Complexes

Understanding Excited State Kinetics in Asymmetric Iron(II) Push-Pull Complexes

Johannes Moll,^[a] Lukas Sorge,^[a] Christoph Förster,^[a] Niklas Gessner,^[b] Patrick Nürnberger,^[b] XXXXXXXXXX^[c] Matthias Bauer,^[c] Ayla Pöpcke,^[d] Stefan Lochbrunner,^[d] Olga Bokareva,^[d] Sergey Bokarev,^[d] Oliver Kühn,^[d] Omar Baig,^[e] Leticia González^[e] and Katja Heinze^{[a]*}

[a] Department of Chemistry, Johannes Gutenberg University, Mainz, Germany; [b] Department of Chemistry and Pharmacy, University of Regensburg, Germany; [c] Institute of Chemistry, University of Paderborn, Germany; [d] Institute for Physics and Department of Life, Light and Matter, University of Rostock, Germany; [e] Institute of theoretical chemistry, University of Vienna, Austria.

Abstract

Synthesis, characterization, electrochemistry, and photophysics of homo- and heteroleptic iron(II) complexes $[\text{Fe}(\text{cpmp})_2]^{2+}$ (**1²⁺**) and $[\text{Fe}(\text{cpmp})(\text{ddpd})]^{2+}$ (**2²⁺**) bearing the tridentate ligands 6,2''-carboxypyridyl-2,2'-methylamine-pyridyl-pyridine (cpmp) and *N,N'*-dimethyl-*N,N'*-di-pyridin-2-ylpyridine-2,6-diamine (ddpd) are reported. The complexes possess one (**2²⁺**) or two (**1²⁺**) electron-deficient dipyridyl ketone fragments as electron-accepting sites enabling intraligand charge transfer (ILCT), ligand-to-ligand charge transfer (LL'CT) and low-energy metal-to-ligand charge transfer (MLCT) absorptions. The latter peak around 610 nm. This study highlights the influence of the excited-state energies and geometries for the actual excited-state dynamics including theoretical investigations using Surface Hopping including Arbitrary Couplings (SHARC).

7. Understanding Excited State Kinetics in Asymmetric Iron(II) Push-Pull Complexes

Introduction

Emissive ruthenium(II) complexes like $[\text{Ru}(\text{bpy})_3]^{2+}$ (bpy: 2,2'-bipyridine) are used as light harvesters in dye sensitized solar cells (DSSC), in light emitting electrochemical cells (LECs) and as photo catalysts.^[1-11] It would be favorable to replace the expensive ruthenium by the earth abundant homologue iron. Unfortunately, the ligand field splitting in 3d metals like iron is generally significantly smaller than in homologous 4d metals. While ruthenium(II) complexes usually show phosphorescence from triplet metal-to-ligand charge transfer states ($^3\text{MLCT}$), in iron(II) complexes non-emissive metal centered states ($^3/5\text{MC}$) are the lowest excited states.^[12] This results in ultrafast inner conversion from $^3\text{MLCT}$ to ^3MC state followed by intersystem crossing to ^5MC state and relaxation to the ground state which inhibits luminescence.^[13,14] To increase the MLCT lifetime there are several concepts.^[15] Wärnmark et al. used a σ -donating bidentate five-membered ring chelate NHC ligand to yield a $^3\text{MLCT}$ lifetime of 528 ps.^[16] For ruthenium(II) complexes cyclometallation has been successfully used to increase the quantum yield ($9.4 \cdot 10^{-6}$ for $[\text{Ru}(\text{dpb})(\text{tpy})]^+$ (dpb: 1,2',5,2''-dipyridylbenzene) and $1.4 \cdot 10^{-5}$ for the cyclometallated push-pull complex $[\text{Ru}(\text{dpb-COOEt})(\text{tpy-NHCOMe})]^+$, compared to $<5 \cdot 10^{-6}$ for $[\text{Ru}(\text{tpy})_2]^{2+}$, all measured in acetonitrile at 298 K).^[17-19] The same strategy has been tried for the iron(II) complex $[\text{Fe}(\text{pbp})(\text{tpy})]^+$ (pbp: 6-phenyl-2,2'-bipyridine), resulting in a non-emissive iron(II) complex.^[20-22]

Another strategy is to use highly symmetric complexes with a coordination of the iron center close to ideal octahedral geometry, i.e. N-Fe-N trans angles next to 180° . Here the ligand field splitting is maximized.^[23,24] For example $[\text{Fe}(\text{dcpp})_2]^{2+}$ (dcpp: 2,6-bis(2-carboxypyridyl)pyridine) with carbonyl bridged pyridine rings shows a N-Fe-N trans angle of 178.3° compared to 161.1° in $[\text{Fe}(\text{tpy})_2]^{2+}$.^[25,26] This concept can be combined with push-pull systems like i.e. $[\text{Fe}(\text{dcpp})(\text{ddpd})]^{2+}$ where the electron rich ddpd ligand (ddpd: *N,N'*-dimethyl-*N,N'*-dipyridin-2-ylpyridine-2,6-diamine) destabilizes metal centered states while the π -acceptor dcpp stabilizes charge transfer states.^[27] Yet, To the best of our knowledge there is up to now no emissive mononuclear iron(II) complex known.

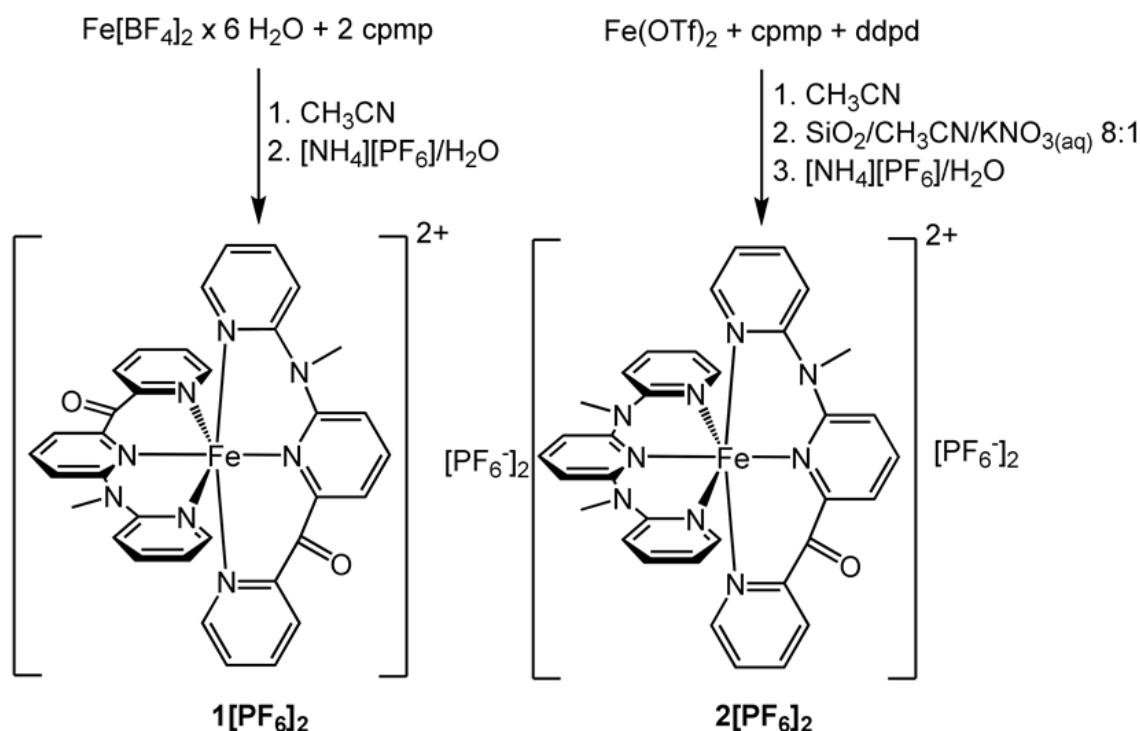
The tridentate ligand 6,2''-carboxypyridyl-2,2'-methylamine-pyridyl-pyridine (cpmp) combines the concept of larger biting angles with a donor-acceptor-system.^[28] The push-pull effect will be further increased by the combination of ddpd as donor and cpmp ligand with one single acceptor site. These systems offer not only MLCT transitions but also the possibility of ligand-to-ligand charge transfer (LL'CT) and intra-ligand charge transfer (ILCT) excited states. Such LL'CT states have been also found in cyclometallated ruthenium(II) complexes where the quantum yield is reduced by forbidden LL'CT transitions due to the orthogonality of L and L'.^[29,30] The angle between the central pyridine rings of tridentate six-membered ring chelate ligands is about 30° for iron(II) complexes^[31] in principle allowing LL'CT transitions on symmetry arguments in contrast to five-membered ring chelate complexes.

We report the synthesis, structure, electrochemical and photophysical properties of the novel homoleptic $[\text{Fe}(\text{cpmp})_2][\text{PF}_6]_2$ (**1** $[\text{PF}_6]_2$) and heteroleptic iron(II) complex $[\text{Fe}(\text{cpmp})(\text{ddpd})][\text{PF}_6]_2$ (**2** $[\text{PF}_6]_2$). The optical properties are supported by DFT- and TDDFT-calculations as well as molecular dynamics calculations.

Results and Discussion

Syntheses and geometrical structure

While the homoleptic complex $[\text{Fe}(\text{cpmp})_2]^{2+}$ ($\mathbf{1}^{2+}$) is the only product of the reaction of $\text{Fe}[\text{BF}_4]_2 \times 6 \text{H}_2\text{O}$ with the ligand cpmp and can be purified by crystallization, the heteroleptic complex $[\text{Fe}(\text{cpmp})(\text{ddpd})]^{2+}$ ($\mathbf{2}^{2+}$) is not the only product of the reaction of $\text{Fe}[\text{OTf}]_2$ with one equivalent of each ligand. The green complex is formed within seconds in acetonitrile. Yet, the yellow homoleptic complex $[\text{Fe}(\text{ddpd})_2]^{2+}$ formed, too. It can be removed by column chromatography. Because of fast ligand exchange resulting in formation of significant amounts of both homoleptic complexes, time consuming analytic in solution is not possible for $\mathbf{2}^{2+}$.



Scheme 1: Synthesis scheme for the synthesis of $\mathbf{1}[\text{PF}_6]$ and $\mathbf{2}[\text{PF}_6]_2$.

The compositions of $\mathbf{1}[\text{PF}_6]_2$ and $\mathbf{2}[\text{PF}_6]_2$ are confirmed by high resolution ESI mass spectrometry (Supporting Information Fig. S14 and S15) and elemental analysis as well as multinuclear and correlation NMR spectroscopy, showing only a single set of ^1H and ^{13}C NMR resonances (Supporting Information Fig. S1–S13).

The sharp NMR resonances indicate low-spin d^6 electron configuration. The meridional coordination is confirmed by single crystal X-ray diffraction (Fig. 1 and Fig. 2). The unit cell of each complex contains two independent dications $\mathbf{1A}^{2+}$, $\mathbf{1B}^{2+}$ and $\mathbf{2A}^{2+}$, $\mathbf{2B}^{2+}$, respectively (Table 1). Additionally, the geometries were calculated by DFT methods (CPCM(acetonitrile)-B3LYP-D3BJ-ZORA/def2-TZVP). The coordination geometry is nearly perfect octahedral for both complexes. The Fe-N bond lengths for the central pyridine rings of 1.95 to 1.96 Å for $\mathbf{1}^{2+}$ and 1.95 to 1.97 Å for $\mathbf{2}^{2+}$ are slightly shorter than for the terminal pyridine rings of 1.98 to 2.02 Å and 1.98 to 2.00 Å, respectively, as typically observed for $[\text{M}(\text{ddpd})_2]^{2+}$, $[\text{M}(\text{dcp})_2]^{2+}$ or $[\text{M}(\text{dcp})(\text{ddpd})]^{2+}$ complexes.^[25,27,31–33]

The N-Fe-N bond angles are very close to 90° for the dipyridyl ketone moieties and slightly smaller for the methylamine moieties of the cpmp and ddpd ligands. The high local $[\text{FeN}_6]$ symmetry is confirmed by the shape parameter $S(\text{OC-6})$ ^[34] quantifying the deviation from an ideal octahedron close to zero (Table 1) as expected for a metal ion with low-spin d^6 electron configuration. The degree of planarization $\text{PL} = 100 \times (\sum(\text{X-N-Y}) - 3 \times 109.5^\circ) / [3 \times 109.5^\circ]$ of 96 to

7. Understanding Excited State Kinetics in Asymmetric Iron(II) Push-Pull Complexes

98 % for the dipyridyl ketone moieties and 87 to 92 % for the methyl amine moieties correlates inversely to the steric strain of bridging groups.

In the solid state, the second coordination sphere of both complexes is formed by hexafluorophosphate ions, co-crystallized acetonitrile and the carbonyl group of a neighboring complex with closest contacts of $\text{Fe}\cdots[\text{F}(\text{PF}_5)]$, $\text{Fe}\cdots\text{N}(\text{CCH}_3)$ and $\text{Fe}\cdots\text{O}$ ranging from 4.33 to 5.00 Å ($\mathbf{1A}^{2+}$), 4.56 to 4.87 Å ($\mathbf{1B}^{2+}$) and 4.37 to 6.05 Å ($\mathbf{2A}^{2+}$), 4.24 to 5.29 Å ($\mathbf{2B}^{2+}$).

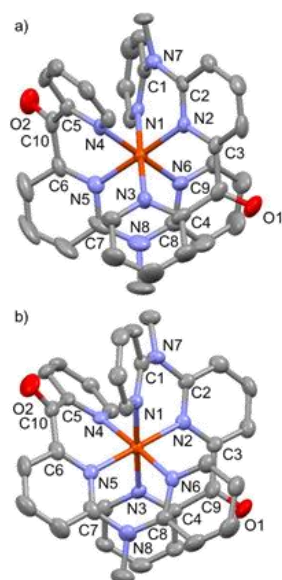


Figure 1: Molecular structure of a) $\mathbf{1A}^{2+}$ and b) $\mathbf{1B}^{2+}$ (determined by XRD, at 50 % probability ellipsoids. Hydrogen atoms omitted for clarity).

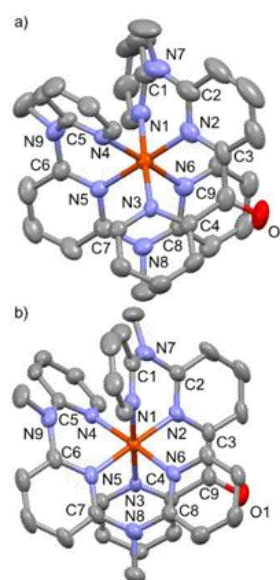


Figure 2: Molecular structure of a) $\mathbf{2A}^{2+}$ and b) $\mathbf{2B}^{2+}$ (determined by XRD, at 50 % probability ellipsoids. Hydrogen atoms omitted for clarity).

Table 1: Fe-N Bond lengths (Å), angles ($^\circ$), planarization values (PL),^[a] shape parameters (S(OC-6))^[b] and distance between iron center and second coordination sphere of $\mathbf{1}^{2+}$ and $\mathbf{2}^{2+}$. DFT: Orca 4.1: CPCM(acetonitrile)-RIJCOSX-B3LYP-D3BJ-ZORA/def2-TZVP.

	$\mathbf{1}^{2+}$ (DFT)	$\mathbf{1A}^{2+}$	$\mathbf{1B}^{2+}$	$\mathbf{2}^{2+}$ (DFT)	$\mathbf{2A}^{2+}$ (Fe2)	$\mathbf{2B}^{2+}$ (Fe1)
Fe1-N1	2.00877	2.001(6)	1.979(5)	2.0118	1.993(4)	1.995(4)
Fe1-N2	1.97822	1.959(6)	1.947(6)	1.97231	1.955(4)	1.949(4)
Fe1-N3	1.99704	1.998(6)	1.975(6)	2.00214	1.982(4)	1.966(4)
Fe1-N4	2.00449	1.971(6)	1.982(6)	2.00331	1.983(4)	1.978(4)
Fe1-N5	1.97612	1.950(6)	1.952(6)	1.97996	1.953(4)	1.967(4)
Fe1-N6	2.00153	1.981(6)	2.015(6)	2.00165	1.988(4)	1.984(4)
N1-Fe1-N2	87.882	88.2(2)	87.6(2)	87.627	88.21(18)	87.92(16)
N2-Fe1-N3	90.523	90.2(2)	90.8(2)	90.852	90.33(17)	90.49(15)
N4-Fe1-N5	90.38	89.9(2)	90.5(2)	88.835	88.20(16)	88.74(16)
N5-Fe1-N6	87.62	89.3(3)	87.9(2)	88.784	89.05(16)	88.31(16)
PL(N7) ^[a]	87.8	90.2	88.9	91.0	88.3	91.7
PL(C9) ^[a]	98.0	95.9	98.4	97.9	95.6	97.5
PL(C10) ^[a]	97.7	97.1	97.1	-	-	-
PL(N8) ^[a]	90.3	87.3	88.9	87.8	88.3	89.2
PL(N9) ^[a]	-	-	-	87.8	88.6	89.2
S(OC-6) ^[b]	0.04241	0.04489	0.04302	0.05584	0.05214	0.05694
Fe1 \cdots F1	-	4.33	4.83	-	4.368	4.414
Fe1 \cdots F2	-	4.73	4.87	-	6.047	4.243
Fe1 \cdots N1 _(CH3CN)	-	5.00	-	-	5.079	5.288
Fe1 \cdots O1 _(neighboring molecule)	-	4.759	4.583	-	4.784	4.617
Fe1 \cdots O2 _(neighboring molecule)	-	-	5.56	-	-	-

[a] PL = PL/% = $100 \times \{[\Sigma (X - N - Y)] - 3 \times 109.5^\circ\} / [3 \times 120.0^\circ - 3 \times 109.5^\circ]$ [b] Continuous shape measure^[34]

The characteristic PF stretching vibration around 830 cm^{-1} in the IR spectra of $\mathbf{1}[\text{PF}_6]_2$ and $\mathbf{2}[\text{PF}_6]_2$ (Supporting Information, Fig. S16 and S17) indicates the successful counter ion

7. Understanding Excited State Kinetics in Asymmetric Iron(II) Push-Pull Complexes

exchange which is also consistent with the ^{31}P NMR spectra of $\mathbf{1}[\text{PF}_6]_2$ and $\mathbf{2}[\text{PF}_6]_2$ showing the typical septet of $[\text{PF}_6]^-$ (Supporting Information, Fig. S6 and S13).

The IR absorption band of the C=O stretching vibration of the cpmp ligand is slightly shifted to lower energies (1669 and 1672 cm^{-1} , respectively) in the dicationic complexes compared to the free ligand (1679 cm^{-1}) suggesting π back-donation of iron(II) into the $\pi^*(\text{CO})$ orbitals. The homoleptic complex $\mathbf{1}^{2+}$ shows only a single CO stretching vibration indicating no coupling of the two CO oscillators.

Table 2: IR bands of the C=O, P-F and PF_2 vibrations of cpmp, $\mathbf{1}^{2+}$ and $\mathbf{2}^{2+}$ in the solid state (KBr).

	$\tilde{\nu} / \text{cm}^{-1}$			
	C=O	P-F	PF_2	N-O
cpmp ^[28]	1679	-	-	-
$\mathbf{1}^{2+}$	1669	833	559	-
$\mathbf{1}^{3+}$	1694	-	-	816, 834, 1427
$\mathbf{2}^{2+}$	1672	831	555	-

Electrochemistry

Both complexes $\mathbf{1}[\text{PF}_6]_2$ and $\mathbf{2}[\text{PF}_6]_2$ are reversibly oxidized at +0.79 and +0.55 V vs. ferrocene, respectively, in their cyclic voltammograms (Fig. 3). The oxidation potential of $\mathbf{1}^{2+}$ is higher by 0.23 V due to the electron withdrawing effect of two carbonyl groups instead of a single one in $\mathbf{2}^{2+}$. The even higher oxidation potential of $[\text{Fe}(\text{dcp})_2]^{2+}$ (+1.29 V vs. ferrocene) with four CO groups is consistent with this trend.^[25,33] The $\text{Fe}^{\text{II/III}}$ oxidation of $\mathbf{1}^{2+}$ is perfectly reversible on the timescale of IR spectroelectrochemistry (Supporting Information Fig. S33). The CO stretching band of the Fe^{III} complex is shifted to higher energy by 18 cm^{-1} , suggesting a much weaker π backbonding in the iron(III) complex than in the dication.

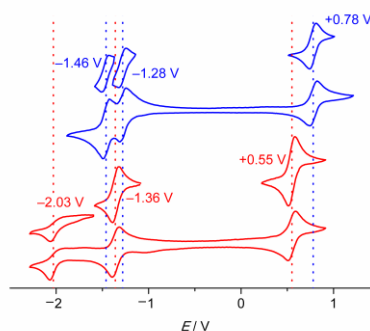


Figure 3: Cyclic voltammograms of $\mathbf{1}[\text{PF}_6]_2$ (blue) and $\mathbf{2}[\text{PF}_6]_2$ (green), 1 mM in acetonitrile, 0.1 M $[\text{nBu}_4\text{N}][\text{PF}_6]$.

The homoleptic complex $\mathbf{1}^{2+}$ exhibits two reversible reduction waves at -1.28 and -1.46 V that are assigned to the reduction of the individual cpmp ligands. The reduction wave of the single cpmp ligand in $\mathbf{2}^{2+}$ appears at -1.36 V. The second reduction of the same carbonyl group appears at -2.03 V. The $\mathbf{1}^{2+}/\mathbf{2}^{2+}$ to $\mathbf{1}^{+}/\mathbf{2}^{+}$ reduction is reversible, at least on the timescale of the CV experiments. Spectroelectrochemical reduction of $\mathbf{1}^{2+}$ shows a partial decrease of the CO stretching mode due to the reduction of a single CO group (Supporting Information, Fig. S34). This band for the monocation is likely shifted to the fingerprint region due to the additional electron localized on the CO group. The increase of the calculated C-O bond length from 1.215 to 1.271 Å on the respective reduced ligand due to reduction supports this.

7. Understanding Excited State Kinetics in Asymmetric Iron(II) Push-Pull Complexes

Table 3: Electrochemical properties of **cpmp**, **2[PF₆]₂** and **3[PF₆]₂**. $E_{1/2}$ in V vs. FcH/FcH⁺.

	reduction			oxidation	
cpmp ^[28]			-1.99	-1.99	+0.97
1²⁺			-1.46	-1.28	+0.78
2²⁺			-2.03	-1.36	+0.55
[Fe(bpy)₃]²⁺ ^[25]				-1.78	+0.66
[Fe(tpy)₂]²⁺ ^[25]				-1.68	+0.71
[Fe(dcpp)₂]²⁺ ^[33]	-1.81	-1.53	-1.21	-0.81	+1.29
[Fe(ddpd)₂]²⁺ ^[33]				-2.33	+0.33
[Fe(dcpp)(ddpd)]²⁺ ^[33]		-2.22	-1.60	-1.21	+0.84
					+1.63

Photophysical properties

UV/Vis/NIR absorption spectra of **1[PF₆]₂** and **2[PF₆]₂** measured in acetonitrile at room temperature are shown in Fig. 4 (Supporting Information, Fig. S20 for complete spectra). The band at 270 nm with a shoulder at 300 nm in the absorption spectrum of **1[PF₆]₂** is mainly assigned to ligand centered $\pi\pi^*$ transitions according to TD-DFT calculations. For **2[PF₆]₂** these bands occur at 276 and 325 nm, respectively, and can be assigned to ligand centered $\pi\pi^*$ and LL'CT transitions according to TD-DFT calculations.

The 350 nm band for **1[PF₆]₂** can be mainly assigned to MLCT transitions while the shoulder at 410 nm is caused by ILCT/LC and LL'CT transitions with MLCT contribution. **2[PF₆]₂** shows this MLCT band with ILCT/LC and LL'CT admixes at 365 nm with a MLCT shoulder at 420 nm. The characteristic low-energy ¹MLCT band of **1[PF₆]₂** and **2[PF₆]₂** appears at 609 and 616 nm, respectively. The extinction coefficient of **1²⁺** is nearly twice intense as for **2²⁺** due to two acceptor sites instead of one, namely the carbonyl groups of the cpmp ligands. The even higher extinction coefficient of **[Fe(dcpp)₂]²⁺** fits to this trend as well as the lower absorption energy with 606 nm due to the lack of donor groups.^[25,33]

Table 4: Absorption data of **1[PF₆]₂**, **2[PF₆]₂** and similar complexes in acetonitrile at 298 K.

complex	$\lambda_{\text{abs}} \text{ (MLCT) / nm } (\epsilon) /$ $\text{L mol}^{-1} \text{ cm}^{-1}$
1[PF₆]₂	609 (3960)
2[PF₆]₂	616 (2249)
[Fe(bpy)₃]²⁺	520 ^[14,35]
[Fe(tpy)₂]²⁺	560 ^[14]
[Fe(dcpp)₂]²⁺	606 (7380) ^[33]
[Fe(ddpd)₂]²⁺	395 (4570) ^[33]
[Fe(dcpp)(ddpd)]²⁺	592 (4035) ^[33]

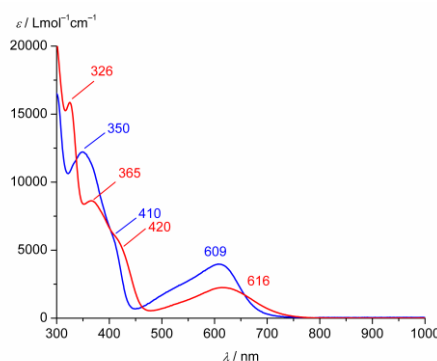


Figure 4: UV/Vis spectra of **1²⁺** (blue) and **2²⁺** (red) in acetonitrile at 298 K.

Oxidative UV/Vis spectroelectrochemical investigations of **1²⁺** in acetonitrile containing 0.1 M [ⁿNBu₄][PF₆] confirm the reversibility of the Fe^{II/III} oxidation on this longer time scale (Fig. 5a). The MLCT band bleaches while a LMCT band at 962 nm arises resulting in an isosbestic point at 710 nm. The spectroelectrochemical reduction is not reversible on this time scale. Apart

7. Understanding Excited State Kinetics in Asymmetric Iron(II) Push-Pull Complexes

from the MLCT bleach, no spectral changes in the visible spectral region occur (Fig. 5b). Chemical oxidation with $[\text{NH}_4]_2[\text{Ce}(\text{NO}_3)_6]$ yields an orange solid. Its absorption spectrum in acetonitrile fits to the spectrum of the electrochemically oxidized complex (Fig. 5a). During these time consuming experiments the ligand exchange processes in the solution of 2^{2+} would lead to changing sample compositions. Therefore these and the following methods are mainly focused on 1^{2+} .

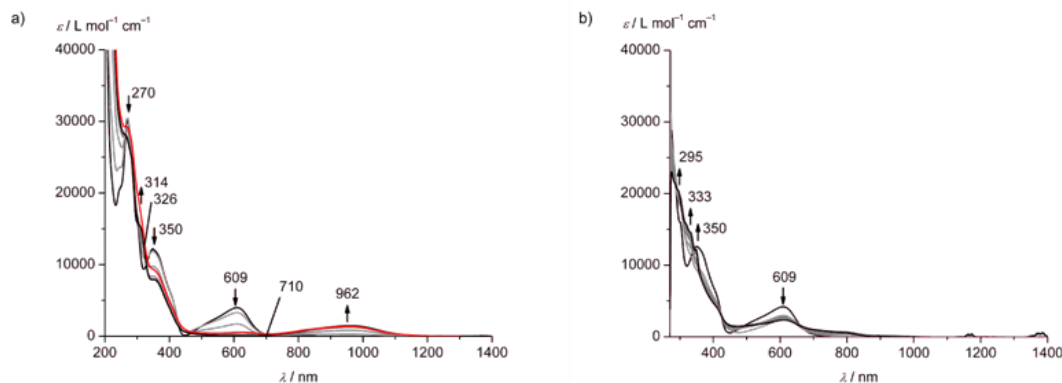


Figure 5: UV/Vis/NIR spectra during electrochemical oxidation of 1^{2+} to 1^{3+} in acetonitrile with 0.1 M $[\text{t}^{\text{r}}\text{NBu}_4][\text{PF}_6]$ at 298 K; red spectrum corresponding to chemically oxidized complex using $[\text{NH}_4]_2[\text{Ce}(\text{NO}_3)_6]$ b) corresponding spectra during the electrochemical reduction of 1^{2+} to 1^{1+} .

The EPR spectrum (X-band, 77 K, PrCN glass, Fig. 6) of this chemically oxidized complex 1^{3+} confirms the low-spin configurations of the iron(III) center. Two independent species are visible that could be assigned to the two isomers with identical structure and a switch in CO and N-Me bridges, resulting in two sets of g values $g_{1,1} = 2.74530$, $g_{2,1} = 2.66579$, $g_{1,2} = 2.23901$, $g_{2,2} = 2.23892$, $g_{3,1} = 1.67583$, $g_{3,2} = 1.60628$ that cannot be assigned to the different species due to the lack of resolved hyperfine coupling. The anisotropy therefor is in a range from 0.98996 to 1.13902. The nearly identical g_2 values indicate a difference of anisotropy in only two directions which is in agreement with the four bridging groups that cannot evolve a three dimensional anisotropy. Both anisotropy values are higher than for $[\text{Fe}(\text{ddpd})_2]^{3+}$ ($\Delta g = g_1 - g_3 = 0.675$ ($g_1 = 2.490$, $g_2 = 2.296$, $g_3 = 1.815$)) but lower than for $[\text{Fe}(\text{dcpp})(\text{ddpd})]^{3+}$ ($\Delta g = g_1 - g_3 = 1.26$ ($g_1 = 2.821$, $g_2 = 2.247$, $g_3 = 1.561$)).^[33] This indicates a higher symmetry for a complex containing two asymmetric cpm ligands compared to $[\text{Fe}(\text{dcpp})(\text{ddpd})]^{3+}$ with two different symmetric ligands, which is also represented by the space groups of the respective iron(II) complexes, Ia for 1^{2+} and $Pbca$ for $[\text{Fe}(\text{dcpp})(\text{ddpd})]^{2+}$.^[33]

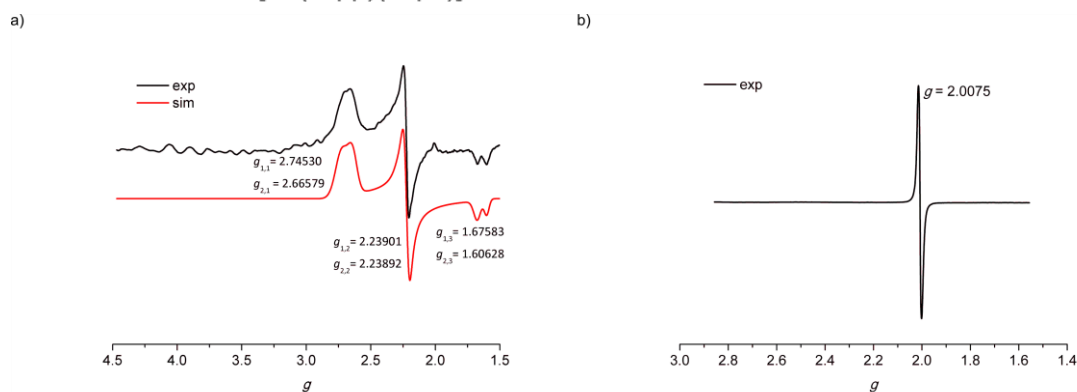


Figure 6: EPR spectrum of a) 1^{3+} oxidized with ammonium ceric(IV) nitrate in frozen butyronitrile at 77 K (black) and simulation (red) and b) 1^{1+} reduced by decamethylcobaltocenium in frozen acetonitrile at 77 K.

The ligand centered reduction is further confirmed by the EPR spectrum of 1^{1+} in frozen acetonitrile showing a g value of 2.0075 indicating no interaction to a metal.

7. Understanding Excited State Kinetics in Asymmetric Iron(II) Push-Pull Complexes

CtC X-ray emission spectroscopy shows the mainline maximum of 1^{2+} at 7057.9 eV, blue shifted in the oxidized complex 1^{3+} to 7058.1 eV. The low-energy satellite is not separated from the mainline. The intensity ratio between satellite and mainline is small for both complexes. Therefore, CtC-XES clearly confirms a low-spin ground state for both investigated complexes $1[\text{PF}_6]_2$ ($M_S = 1$) and $1[\text{NO}_3]_3$ ($M_S = 3$). HERFD-XANES shows the edge-position of 1^{3+} blue shifted by about 1.3 eV in relation to 1^{2+} , due to the decreasing Fe 3d occupation of 1^{3+} ($3d^5$) in relation to 1^{2+} ($3d^6$). The pre-edge of 1^{2+} exhibits two features, a low-energy shoulder around 7113.3 eV and a main feature around 7114.8 eV. While the Fe^{III} complex 1^{3+} exhibits overall four pre-edge features, two weak low-energy peaks at 7111.9 eV and 7113.7 eV and a broad intense peak at 7116.8 eV with a low-energy shoulder around 7115.4 eV.

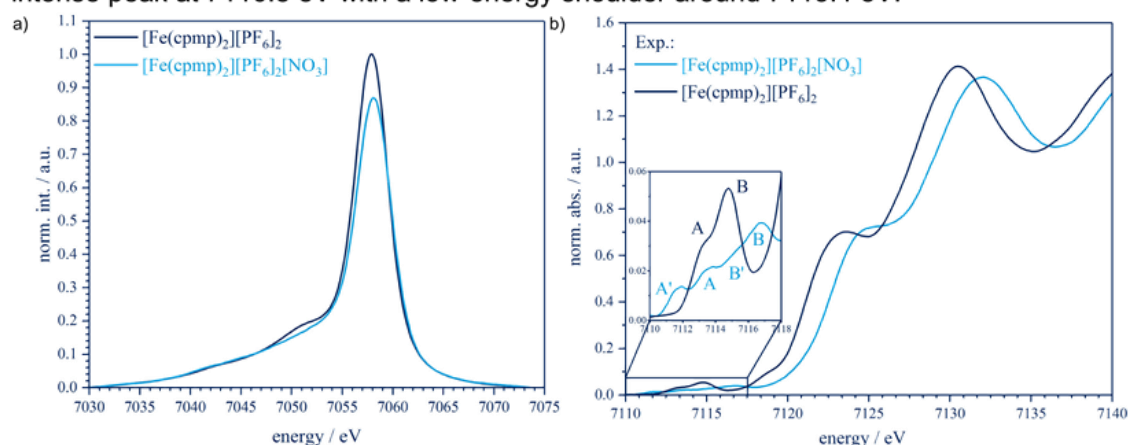


Figure 7: a) Experimental CtC-XES spectra of $1[\text{PF}_6]_2$ and $2[\text{PF}_6]_2[\text{NO}_3]$. b) experimental HERFD-XANES spectra of $1[\text{PF}_6]_2$ and $2[\text{NO}_3]_3$.

To understand the quantum mechanical origin of experimental observed HERFD-XANES features, TD-DFT XANES calculations applying the TPSSh functional with an adjusted Hartree-Fock exchange of 12.5 % were performed.^[36] Theoretical spectra are compared to the experimental, an excellent agreement between experiment and theory is obtained and therefore further information of underlying transitions will be extracted. The low energy shoulder A of 1^{2+} is caused by a superposition of Fe $1s \rightarrow e_g^*$ (low-energy slope) and Fe $1s \rightarrow \text{LUMO} / \text{LUMO}+1$ (high energy slope) transitions (predominant acceptor orbitals are shown in Fig. 9a), while feature B is solely evoked by Fe $1s \rightarrow \text{ligand } \pi^*$ transitions. In the oxidized complex 1^{3+} , an additional low-energy feature A' appears which is caused by a single transition of the Fe $1s$ to the singly occupied Fe $3d_{yz}$ orbital (predominant acceptor orbitals are shown in Fig. 9b). The second pre-edge feature A of 1^{3+} is caused by Fe $1s \rightarrow e_g^*$ transitions, while main feature B is caused by Fe $1s \rightarrow \text{ligand } \pi^*$ transitions. Low-energy shoulder B' is evoked by Fe $1s \rightarrow \text{LUMO} / \text{LUMO}+1$ (α, β) transitions.

7. Understanding Excited State Kinetics in Asymmetric Iron(II) Push-Pull Complexes

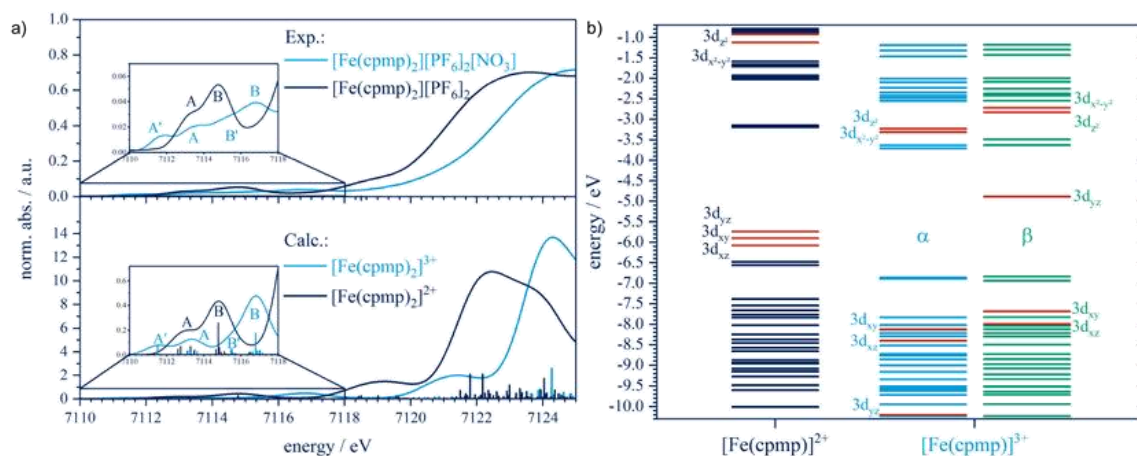


Figure 8: a) Experimental Fe K-edge HERFD-XANES spectra of **1**[PF₆]₂ and **1**[NO₃]₃ in comparison to theoretical Fe K-edge XANES spectra (bottom); b) Molecular levels of **1**²⁺ and **1**³⁺.

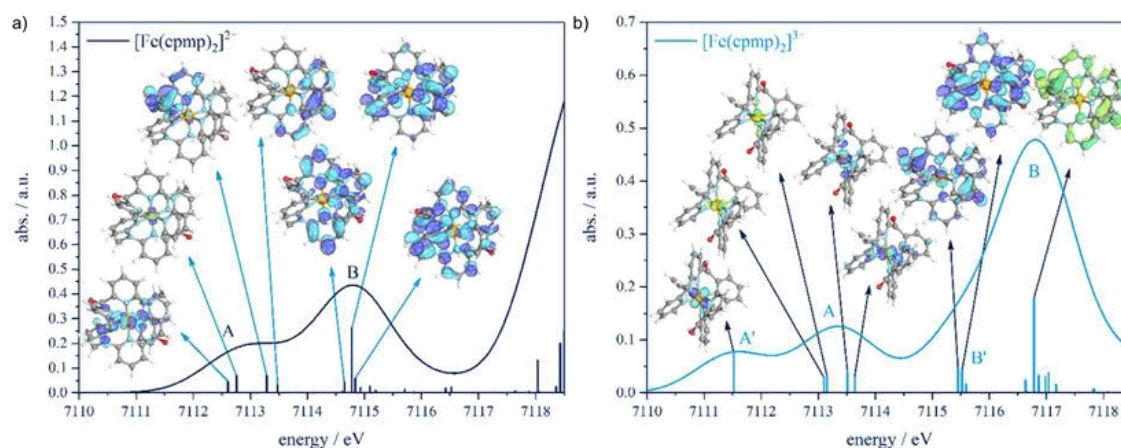


Figure 9: Comparison of theoretical Fe K-edge XANES spectra of a) **1**²⁺ and b) **1**³⁺ (predominant acceptor orbitals are shown).

Both iron(II) complexes are non-emissive in acetonitrile at room temperature and in frozen butyronitrile solution at 77 K, as well as **1**³⁺.

The excited state lifetime of **1**²⁺ was estimated by UV/Vis transient absorption spectroscopy upon MLCT excitation (620 nm, Fig. 10). Apart from the ground state bleach there is no band arising. A single exponential ground state recovery was found to occur with a time constant of 548 ps. Since metal centered states show no characteristic excited state absorption bands this lifetime can be assigned to either the ³MC or ⁵MC state. A similar time constant for a single-exponential decay of 495 ps was estimated via IR transient spectroscopy upon excitation at 610 nm (Fig. S18). These findings mean that the intersystem crossing from ¹MLCT to ³MLCT and relaxation into the ^{3/5}MC state occur within less 50 fs. The time constant for ground state recovery is similar to the excited state lifetime found for $[\text{Fe}(\text{dcp})_2(\text{ddpd})]^{2+}$ (548 ps) and $[\text{Fe}(\text{dcp})_2]^{2+}$ (280 ps).^[25,33] For the latter an excited state decay following the ¹MLCT → ³MLCT → ³MC → ⁵MC → ¹GS scheme was found by ultra-fast time resolved spectroscopy as known for than for $[\text{Fe}(\text{bpy})_3]^{2+}$ and $[\text{Fe}(\text{tpy})_2]^{2+}$.^[37]

7. Understanding Excited State Kinetics in Asymmetric Iron(II) Push-Pull Complexes

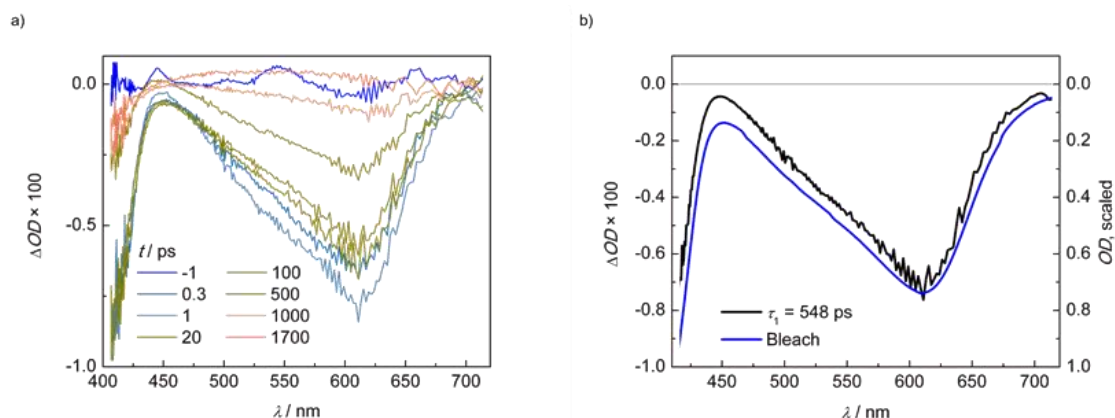


Figure 10: a) UV/Vis transient absorption spectra of **1**[PF₆]₂ in CH₃CN after optical excitation at 620 nm at the specified delay times and b) amplitude spectrum **1**[PF₆]₂ compared to the scaled bleach (negative ground state absorptions spectrum).

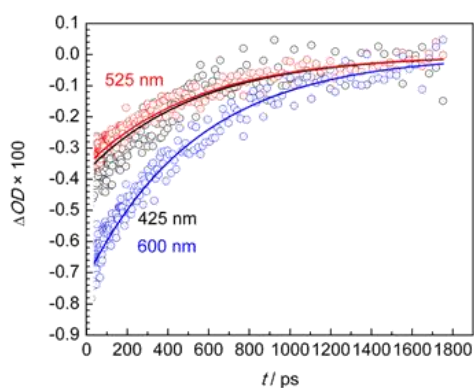


Figure 11: Time traces of transient absorption of **1**[PF₆]₂ for 425 nm (black), 525 nm (red) and 600 nm (blue) detection wavelength.

The calculated energy diagrams with ground and excited state parabola (calculated with average of the six Fe-N bond lengths as reaction coordinate, Fig. 12) reveal the ⁵MC state as lowest excited state for both, **1**²⁺ and **2**²⁺ supporting a relaxation pathway including this state. In this two-dimensional representation of the involved potentials a direct ³MC → ¹GS relaxation seems likely. However this needs a minimum energy crossing point in the multidimensional reality that could not be found.

7. Understanding Excited State Kinetics in Asymmetric Iron(II) Push-Pull Complexes

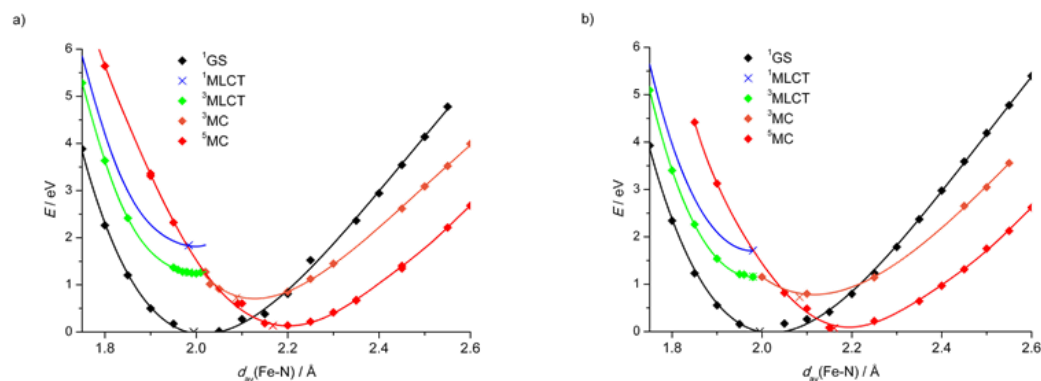


Figure 12: Calculated energy scheme of a) 12^+ and b) 22^+ with average Fe-N bond length (black: $1GS$, blue: $1MLCT$ (calculated from absorption data), green: $3MLCT$, orange: $3MC$, red: $5MC$; crosses for fully optimized minimum energies, filled diamonds for energies at different fixed Fe-N distances; Orca 4.1: CPCM(acetonitrile)-RIJCOSX-B3LYP-D3BJ-ZORA/def2-TZVP).

To simulate the excited state dynamics a linear vibronic coupling model was parametrized and used for surface hopping molecular dynamics. This allows for efficient treatment of large transition metal complexes.^[38,39] Single-point TDDFT calculations (Fig. S22 and S25) showed a considerably better description of the absorption spectrum with the tuned LC-BLYP ($\alpha = 0$, $\omega = 0.14$) functional compared to B3LYP. Because the calculated LC-BLYP absorption spectrum did not drastically depend on CPCM(acetonitrile) solvation, calculations in gas phase were practicable.

The excited states were characterized by wave function analysis. The system was split into metal center, ligand 1 and ligand 2, as customary for metal complexes. The CT characters for first 10 Singlet and 20 Triplet states can be seen in Fig. 13. These states describe a bit more than the lowest-energy band of the absorption spectrum. The analysis of the diabatic populations in the molecular dynamics is based on this characterization. Every excited state is named and assigned a character based on the Franck Condon geometry characterization. Therefore, it is important to note that further designations of the excited states, e.g. "T1", designate the excited state in the ground state geometry. It does not necessarily mean that the "T1" state is actually the energetically lowest Triplet state throughout the dynamics.

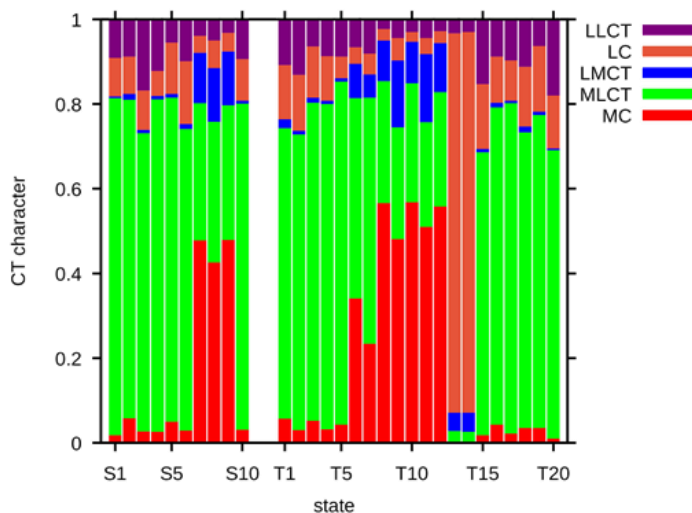


Figure 13: Charge transfer characterisation of the excited states of 12^+ , ORCA 4.1: RIJCOSX-LC-BLYP ($\alpha = 0$; $\omega = 0.14$)-D3BJ-ZORA/def2-TZVP. MC (red), MLCT (green), LMCT (blue), LC (orange), average LLCT (purple).

7. Understanding Excited State Kinetics in Asymmetric Iron(II) Push-Pull Complexes

Fig. 14 shows the evolution of the diabatic populations after 1500 fs. It can be seen that there is fast population transfer from the initial Singlet states to Triplet states. No relaxation back to the ground state happens in any of the trajectories. Therefore, the ground state has been omitted from all figures. A simple kinetic model was used to fit a time constant for the ISC. It allows for return from the Triplet states back to the Singlet states initially, but assumes that the population is finally transferred into “cold” Triplet states: $S \leftrightarrow T_{\text{hot}} \rightarrow T_{\text{cold}}$. The calculated time constant for the Singlet to Triplet ISC is 67 ± 8 fs. Return to the Singlets from the Triplets is much slower at 595 ± 151 fs. The time constant for further relaxation to “cold” Triplet states, that are not available for ISC, was calculated to be significantly larger than the simulation time. After 300 fs most of population transferred to more than 60% $^3\text{MLCT}$ states, approximately 20% ^3MC and less than 10% ^3LC excited states.

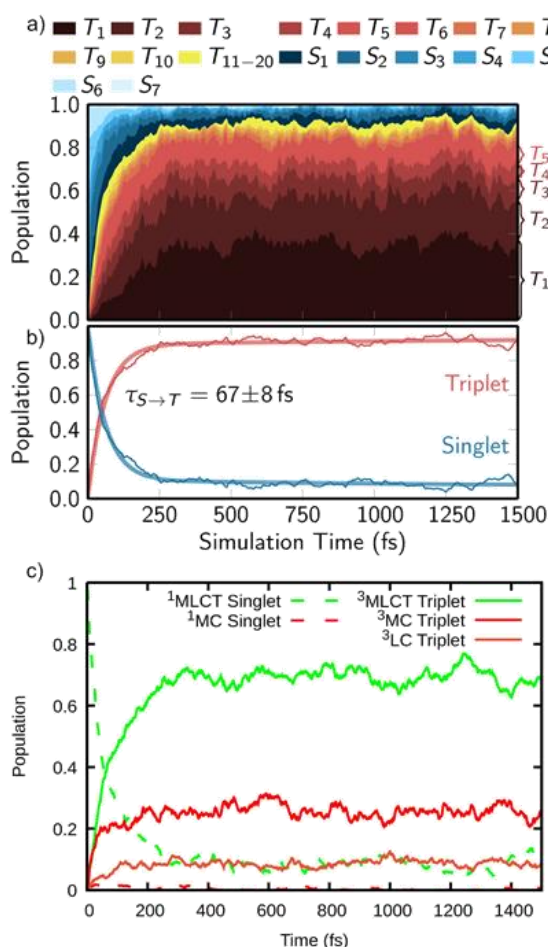


Figure 14: a) Evolution of the diabatic populations over simulation time. b) Evolution of the summed up Singlet and Triplet diabatic populations over simulation time. A time constant for the Singlet to Triplet ISC was fitted. c) Evolution of the diabatic populations over simulation time summed up by characterisation.

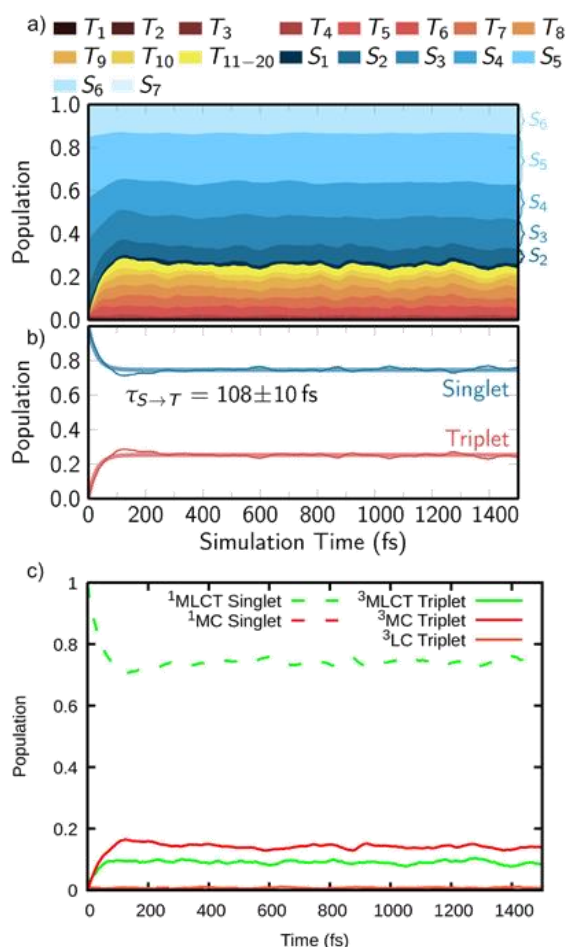


Figure 15: a) Evolution of the diabatic populations over simulation time with frozen nuclei. b) Evolution of the summed up Singlet and Triplet diabatic populations over simulation time with frozen nuclei. A time constant for the Singlet to Triplet ISC was fitted. c) Evolution of the diabatic populations with frozen nuclei over simulation time summed up by characterisation.

Based on the hops performed during the calculation another fitting was done. For this model the Singlet data was summed up as above, because the only non-MLCT state, S_7 , is negligible. The excited states T_1 to T_5 were collected as $^3\text{MLCT}$ and T_6 to T_{12} as ^3MC . T_{13} to T_{20} were neglected because of their small role in the overall dynamics, as can be seen in Fig. 14 a) in yellow. The time constant resulting from this model are $\tau(^1\text{MLCT} \rightarrow ^3\text{MLCT}) = 160 \pm 3$ fs for the

7. Understanding Excited State Kinetics in Asymmetric Iron(II) Push-Pull Complexes

ISC to the $^3\text{MLCT}$ states, $\tau(^1\text{MLCT} \rightarrow ^3\text{MC}) = 80 \pm 1$ fs for ISC to ^3MC states and $\tau(^3\text{MC} \rightarrow ^1\text{MLCT}) = 68 \pm 1$ fs for the return to the Singlets, $\tau(^3\text{MC} \rightarrow ^3\text{MLCT}) = 81 \pm 2$ fs for population transfer from ^3MC to $^3\text{MLCT}$ and $\tau(^3\text{MLCT} \rightarrow ^3\text{MC}) = 390 \pm 6$ fs for transfer from $^3\text{MLCT}$ to ^3MC .

A second set of trajectories was calculated using exactly the same starting conditions as above, but with the nuclei “frozen” in place. The diabatic populations for these “frozen core dynamics” can be seen in Fig. 15. They reveal that without nuclear motion most trajectories stay in Singlet states. The time constant for population transfer to the Triplets was obtained with the simple kinetic model mentioned previously. It is slightly larger than for the normal dynamics. Around 75% of the population stay in the Singlets, while 10% populate the $^3\text{MLCT}$ states and around 15% ^3MC states. The latter population transfer is notable, because it is only slightly smaller than in the normal dynamics. This indicates that ISC to $^3\text{MLCT}$ states is considerably more dependent on molecular motion. Meanwhile ^3MC states can be quickly populated from the initial conditions through a purely electronic process.

Conclusion

Two novel iron(II) complexes bearing the asymmetric push-pull ligand cpmp could be synthesized. The absorption spectra show promising low energy charge transfer bands. The ligand field strength of the cpmp ligand is generally high enough to stabilize the low-spin ground state in both, the iron(II) and iron(III) oxidation state, as proven by XAS, NMR and EPR spectroscopy. However, the iron(II) complexes are non-emissive, as well as the oxidized complex $\mathbf{1}^{3+}$. Femtosecond pump-probe spectroscopy revealed single exponential excited state decay with a time constant of 0.5 ns (548 ps from Vis-pump-Vis-probe, 495 ps from Vis-pump-IR-probe spectroscopy). According to DFT calculations the ^5MC state is the lowest excited state. Therefore, the $^1\text{MLCT} \rightarrow ^3\text{MLCT} \rightarrow ^3\text{MC} \rightarrow ^5\text{MC} \rightarrow ^1\text{GS}$ relaxation cascade seems likely although a direct $^3\text{MC} \rightarrow ^1\text{GS}$ is generally conceivable. Performing excited state dynamics simulation using a linear vibronic coupling model ruled out the latter possibility. No relaxation to the ground state was found including singlet and triplet excited states. As only possible relaxation pathway a population of the ^5MC remains. Interestingly besides the $^1\text{MLCT} \rightarrow ^3\text{MLCT} \rightarrow ^3\text{MC}$ pathway a direct $^1\text{MLCT} \rightarrow ^3\text{MC}$ intersystem crossing was found. The short $^3\text{MLCT}$ lifetime and the latter process circumventing the $^3\text{MLCT}$ state explain the non-emissive nature of the complexes.

7. Understanding Excited State Kinetics in Asymmetric Iron(II) Push-Pull Complexes

Experimental

General Procedures

CH₃CN and diethyl ether were distilled from CaH₂ and sodium, respectively. The ligands **cpmp** and **ddpd** were synthesized according to literature.^[28,40] All reagents were used as received from commercial suppliers (Acros Organics, Alfa Aesar, Fischer and Sigma-Aldrich). NMR spectra were recorded on a *Bruker Avance DRX 400* spectrometer (**1**[PF₆]₂ and ¹H, ¹³C, ¹H-¹H NOESY and ³¹P NMR spectra of **2**[PF₆]₂) at 400.31 MHz (¹H), 100.05 MHz (¹³C{¹H}), and 162.04 MHz (³¹P{¹H}) and on a *Bruker Avance III HD 400* spectrometer (¹H-¹H COSY, ¹H-¹³C-HSQC and ¹H-¹³C HMBC NMR spectra of **2**[PF₆]₂) at 400.42 MHz (¹H) and 100.7 MHz (¹³C{¹H}), respectively. All resonances are reported in ppm versus the solvent signal as an internal standard [CD₃CN (¹H, δ = 1.94; ¹³C, δ = 1.24 ppm)] or versus external H₃PO₄ (85%) (³¹P: δ = 0 ppm); (s) = singlet, (d) = doublet, (t) = triplet, (m) = multiplet. ESI MS spectra were recorded on a Micromass Q-TOF-Ultima spectrometer. Elemental analyses were performed by the microanalytical laboratory of the department of chemistry of the University of Mainz using an Elementar vario EL Cube. IR spectra were recorded with a *Bruker ALPHA II FT-IR* spectrometer with a Platinum Di-ATR module. EPR spectra were recorded on a Miniscope MS 300 (Magnetech GmbH, Germany) with a frequency counter 5340A (HewlettPackard) (**1**³⁺) and a frequency counter FC 400 (Magnetech GmbH, Germany) (**1**⁺), respectively, at a microwave frequency of 9.39 GHz in frozen butyronitrile (77 K) (**1**³⁺) and frozen acetonitrile (77 K) (**1**⁺), respectively. Mn²⁺ in ZnS was used as external standard (g = 2.118, 2.066, 2.027, 1.986, 1.946, 1.906). Simulations were performed with the program package Easyspin for MatLab (R2015a).^[41] Electrochemical experiments were carried out on a *BioLogic SP-200* voltammetric analyzer using platinum wires as counter and working electrodes and 0.01 M Ag/AgNO₃ as the reference electrode. The measurements were carried out at a scan rate of 100 mV s⁻¹ for cyclic voltammetry experiments and at 50 mV s⁻¹ for square-wave voltammetry experiments using 0.1 M [ⁿBu₄][NPF₆] as the supporting electrolyte in CH₃CN. Potentials are referenced to the ferrocene/ferrocenium couple ($E_{1/2}$ = 95±5 mV under experimental conditions). UV/Vis/NIR spectroelectrochemical experiments were performed using a *BioLogic SP-50* voltammetric analyzer and a Specac omni-cell liquid transmission cell with CaF₂ windows equipped with a Pt-gauze working electrode, a Pt-gauze counter electrode and a Ag wire as pseudo reference electrode, melt-sealed in a polyethylene spacer (approximate path length 1 mm) in CH₃CN (0.3 mM and 0.9 mM for oxidation and reduction, respectively) containing 0.1 M [ⁿBu₄N][PF₆].^[42] IR spectroelectrochemical experiments were performed using a *BioLogic SP-200* voltammetric analyzer and using the same cell, electrodes and electrolyte as above (12 mm). UV/Vis/near-IR spectra were recorded on a *Varian Cary 5000* spectrometer using 1.0 cm cells (Hellma, Suprasil). Emission spectra were recorded on a *Varian Cary Eclipse* spectrometer. For low temperature photoluminescence measurements, a solution of the complex in freshly filtered butyronitrile was filled into a quartz cuvette in an argon filled glovebox and the cuvette was sealed and transferred to a Oxford cryostat (*Oxford instruments Optistat^{DN}*). Measurements were conducted at room temperature (295 K) and liquid nitrogen temperature (77 K).

Transient absorption spectra were recorded with a time resolution of ca. 100 fs by a pump-probe setup based on a Ti:sapphire laser system (CPA 2001, Clark MXR, Inc.) operating at a center wavelength of 775 nm with a repetition rate of 1 kHz. Applying a noncollinear optical parametric amplifier (NOPA), excitation pulses with a center wavelength of 620 nm were generated whose dispersion was controlled by a prism compressor. As probe, a white light continuum generated in a CaF₂ crystal was used. The polarizations of pump and probe were set to magic angle and the beams were focused into the sample to overlapping spots with diameters of 345 μ m for the pump and 150 μ m for the probe. After the sample, the probe was dispersed by a prism and the transmission changes were spectrally resolved recorded by a

7. Understanding Excited State Kinetics in Asymmetric Iron(II) Push-Pull Complexes

CCD array detector. The sample compound was dissolved in CH₃CN and the solution was filled into a 1 mm thick fused silica cuvette.

Ultrafast pump-probe IR-spectra were measured using a flow cell with a 8.6 mM acetonitrile solution at 295 K. A CPA amplification system (Spectra-Physics Spitfire Ace) with 100 fs-pulses of 800 nm wavelength was used as laser source. The pump laser with 610 nm wavelength was generated using a NOPA (Light Conversion TOPAS-White). Every second pump pulse was blocked using a chopper to generate the difference spectra from two sequent spectra. The probe laser was generated using a collinear OPA (Light Conversion TOPAS-Prime with DFG-extension) and detected using CPU^[43] and a CCD camera (Princeton Instruments PIXIS 2K) connected to a spectrometer (Princeton Instruments Acton SpectraPro SP-2500i). The lifetime was estimated from a Global Target Analysis with TIMP.^[44]

Intensity data for crystal structure determination were collected with a Bruker AXS Smart1000 CCD diffractometer with an APEX II detector and an Oxford cooling system and corrected for absorption and other effects using Mo KR radiation ($\lambda = 0.71073 \text{ \AA}$) at 173(2) K. The diffraction frames were integrated using the SAINT package, and most were corrected for absorption with MULABS.^[45,46] The structures were solved by direct methods and refined by the full-matrix method based on F^2 using the SHELXL-2014/7 software package.^[47,48] All nonhydrogen atoms were refined anisotropically, while the positions of all hydrogen atoms were generated with appropriate geometric constraints and allowed to ride on their respective parent carbon atoms with fixed isotropic thermal parameters.

DFT calculations were carried out using the ORCA program package (version 4.0.1).^[49] All calculations were performed using the B3LYP functional^[50–52] and employ the RIJCOSX approximation.^[53,54] Relativistic effects were calculated at the zeroth order regular approximation (ZORA) level.^[55] The ZORA keyword automatically invokes relativistically adjusted basis sets. To account for solvent effects, a conductor-like screening model (CPCM) modeling acetonitrile was used in all calculations.^[56,57] Geometry optimizations were performed using Ahlrichs polarized valence triple-zeta basis set (def2-TZVP)^[58,59]. Atom-pairwise dispersion correction was performed with the Becke-Johnson damping scheme (D3BJ).^[60,61] The energy of the electronic states and presence of energy minima were checked by numerical frequency calculations. Explicit counter ions and/or solvent molecules were not taken into account. The ³MC structures were found by using geometry constraints for certain Fe-N bonds and optimizing in a second step without geometry constraints. For the potential diagram all six Fe-N bonds were set to fixed values using geometry constraints. All optimized geometries were ascertained by numerical frequency analysis. The charge transfer number analyzes were done using TheoDORE 2.0.^[62]

For TDDFT calculations the optimally-tuned LC-BLYP functional has been chosen as the main theoretical approach which eliminates self-interaction error.^{[63][56]} This elimination leads to the more reliable predictions of the energies and properties of the charge-transfer electronic excited states.^[64–66] The details of the approach can be found, e.g., in^[67]. All range-separation parameter tuning calculations have been performed using the 6-31G(d) basis set. The optimal values of the (α ; ω) parameters are (0.0; 0.14) for **1**²⁺ and (0.0; 0.15) for **2**²⁺.

Further, the geometry optimizations with DFT and excited state linear-response TDDFT calculations have been conducted employing optimized α and ω range-separation parameters and the def2-TZVP basis set.^[68] Solvent effects have been included within the PCM approach.^[69] All tuning calculations were done with the Q-Chem 5.1 package^[70] whereas spectra have been computed with Gaussian16 suite.^[71] Excited state analysis has been done with the TheoDORE package^[62] which enables automatic wave function analysis and assignment of excitation localization at predefined molecular moieties.

For the LVC (linear vibronic coupling) surface hopping dynamics the geometry optimization was applied using ORCA 4.1. The ground state geometry was optimised using the B3LYP functional, def2-TZVP basis set, D3BJ dispersion correction, ZORA for relativistic effects with the SARC/J auxiliary basis set in gas phase. The TDDFT calculations included spin-orbit-

7. Understanding Excited State Kinetics in Asymmetric Iron(II) Push-Pull Complexes

coupling (SOC) calculation. An optimally tuned LC-BLYP functional ($\alpha = 0$; $\omega = 0.14$) was used for the excited state calculations. Initially 60 Singlet and 60 Triplet excited states were calculated for comparisons between methods and to choose the relevant excited states for the dynamics (see Surface Hopping). Wave function analysis was performed using TheoDORE 2.0. For the Surface Hopping (SH) molecular dynamics (MD) the SHARC MD suite^[72-74] was used. It includes an implementation of a linear vibronic coupling (LVC) model^[75] which allows efficient simulations of large molecules with many degrees freedom. 100 initial excited state coordinates were calculated from a Wigner distribution of the ground state PES.^[76,77] The dynamics started from 100 initial conditions from the energy range 1.5-2.5 eV around the 2 eV peak of the lowest energy absorption band. These were generated stochastically from the oscillator strength. The 137 propagated trajectories started from following excited states: S1 (4), S2 (14), S3 (30), S4 (28), S5 (40), S6 (20) and S7 (1). The trajectories were propagated for 1500 fs with a nuclear timestep of 0.5 fs and an electronic timestep of 0.02 fs. Non-adiabtic effects were described using a local diabaticization scheme.^[78] The kinetic energy was adjusted during surface hops to conserve total energy. The energy-based decoherence correction by Granucci, Persico and Zocante^[79] was used. For the hopping probabilities the standard SHARC scheme, based on wave function overlaps,^[80] was used. The LVC model was parametrised along 199 normal modes. 14 normal modes had to be excluded, because they could not be described well within the model, e.g. the torsion of the methyl group. The couplings related to the excluded normal modes were generally low, so their effect on the dynamics was expected to be low. 11 Singlet states, including the ground state, and 20 Triplet states were included. In addition, using exactly the same parameters and initial conditions, a second set of trajectories was calculated, with the difference that the nuclei were kept frozen in place.

HERFD-XANES (high energy resolution fluorescence detected X-ray absorption near edge structure) and CtC-XES (core-to-core X-ray emission spectroscopy) experiments were conducted at beamline ID26 of the ESRF (European Synchrotron Radiation Facility).^[81] During the experiments, the electron energy of the synchrotron was at 6.0 GeV, and its ring current varied between 180 and 200 mA. All measurements were carried out using the first harmonic of two u35 undulators. The incident photon energy was selected via the (311) reflection from a double Si crystal monochromator, leading to a photon flux of approximately 2×10^{13} photons·s⁻¹ on the sample position. The monochromator was calibrated using a Fe foil. All experiments were conducted with a Johann type spectrometer^[82,83] in a vertical Rowland geometry, using the (620) reflection of five spherically bent Ge crystal analyzers (with $R = 1$ m).^[84] The emission was monitored by a photodiode installed at about 90° scattering angle and at 45° to the sample surface. Fe K-edge HERFD-XANES were obtained by recording the intensity of the Fe CtC XES maximum as a function of the incident energy. During each HERFD-XANES scan, the undulator gap was kept at a fixed position and only the monochromator angle was changed. To minimize radiation damage, all measurements were carried out at 20 K using a He cryostat under vacuum conditions. Each HERFD-XANES measurement was carried out in 60 seconds. To achieve a satisfying signal to noise ratio four spectra were averaged, each measured at a different spot of the homogeneous sample. Each sample is tested for radiation damage in the beginning by ten fast HERFD-XANES scans over the pre-edge and whitenline with a scan time of 10 seconds on one spot, starting with a 100-times attenuated beam and ending with an unattenuated beam. Within these time frames, no radiation damage could be detected. CtC-XES spectra were recorded off resonance at an excitation energy of 7300 eV in the range of 7030-7080 eV, with a step width of 0.2 eV. To observe reasonable data, 3 spectra (60 second per scan) were recorded, utilizing a different sample spot for each scan. TDDFT (XANES)^[85,86] calculations were carried out using a modified TPSSh functional, with an adjusted Hartee-Fock exchange of 12.5 %, which has been applied in previous studies of our group on low-valent iron carbonyl / nitrosyl complexes,^[36] biomimetic copper complexes^[87] and iron poly-pyridyl complexes^[88,89] and has been shown to

7. Understanding Excited State Kinetics in Asymmetric Iron(II) Push-Pull Complexes

achieve a very good agreement between theory and experiment for these type of complexes concerning the splitting of metal-centered (MC) and metal-to-ligand charge transfer (MLCT) transitions in the near-edge to pre-edge region. The def2-TZVP^[68] basis set (with a special integration accuracy of 5) was applied on all atoms except Fe, for which the expanded CP(PPP) basis set^[90] is used (with a special integration accuracy of 7). All calculations were performed using the optimized structures (Orca 4.0: CPCM(acetonitrile)- RIJCOSX-B3LYP-D3BJ-ZORA/def2-TZVP, *vide supra*). Inclusion of polar crystal environment effects were included via the conductor-like polarizable continuum model (CPCM, $\epsilon = \text{infinity}$).^[57,91] All calculated XANES (TDDFT) transitions were broadened by 1.5 eV (fwhm). Calculated XANES were adjusted to experiment by shifting them by 151.3 eV. Kohn-Sham orbitals were visualized with the IboView program (version 20150427).^[92]

Synthesis of **1**[PF₆]₂ ([Fe(cpmp)₂][PF₆]₂)

A solution of 200 mg (0.700 mmol) cpmp in 4 mL acetonitrile was added to a solution of 116 mg Fe[BF₄]₂·6H₂O in 1 mL acetonitrile. The blue solution was stirred for 16 h at room temperature. Addition of 200 mL diethyl ether yielded in a blue precipitate that was washed with 200 mL diethyl ether to remove excess of ligand. The product was collected by filtration and dissolved in acetonitrile (1 mL). Addition of an aqueous solution of [NH₄][PF₆] (1 mg, 6 mmol, 40 eq. in 100 mL of H₂O) resulted in the precipitation of a blue solid, which was collected by filtration and purified by slow diffusion of diethyl ether into a solution of **1**[PF₆]₂ in acetonitrile to yield crystals suitable for single-crystal X-ray diffraction. The blue crystals were dried under reduced pressure. Yield: 131 mg (0.141 mmol, 47 %). ¹H NMR (CD₃CN, 300 K): δ /ppm = 8.26 (dd, ³J = 7.9 Hz, 2 H, H⁹), 8.07 (m, 4 H, H³, H⁴), 8.01 (d, ³J = 7.3 Hz, 2 H, H⁸), 7.87 (dd, ³J = 8.4, 8.4 Hz, 2 H, H¹⁶), 7.56 (d, ³J = 8.5 Hz, 2 H, H¹⁰), 7.45 (d, ³J = 5.9 Hz, 2 H, H¹), 7.21 (dd, ³J = 7.5, ³J = 4.0 Hz, 2 H, H²), 7.10 (d, ³J = 8.8 Hz, 2 H, H¹⁷), 6.83 (d, ³J = 5.8 Hz, 2 H, H¹⁴), 6.77 (d, ³J = 6.8 Hz, 2 H, H¹⁵), 2.91 (s, 6 H, H⁶). ¹³C{¹H} NMR (CD₃CN, 300 K): δ /ppm = 179.9 (C¹²), 159.3 (C⁷), 158.6 (C¹³), 158.2 (C⁵), 157.3 (C¹), 156.8 (C¹¹), 154.4 (C¹⁴), 140.0 (C¹⁶), 139.4 (C⁹), 138.4 (C⁴), 126.2 (C²), 126.1 (C³), 124.4 (C⁸), 120.2 (C¹⁵), 117.5 (C¹⁰), 112.0 (C¹⁷), 37.4 (C⁶). ³¹P NMR δ /ppm = -144.7 (sept, ¹J_{PF} = 707 Hz). MS (ESI⁺) *m/z* (%) = 318.05 (75.69, [Fe(cpmp)₂]²⁺), 365.05 (86.42, [Fe(cpmp)F]⁺), 655.16 ([Fe(cpmp)₂F]⁺), 781.8 (13.07, {[Fe(cpmp)₂][PF₆]}⁺), 1245.74 (22.61, {H[Fe(cpmp)₂]₃[PF₆]₄}²⁺), 1709.65 (25.39, {H₄[Fe(cpmp)₂]₄[PF₆]₆}²⁺). MS (HR-ESI⁺): calcd. for C₃₄H₂₈F₆FeN₈O₂P⁺: *m/z* = 781.1326 (100, [Fe(cpmp)₂][PF₆]⁺). Found: *m/z* = 781.1309 (100). Elem. anal. calcd. for C₃₄H₂₈F₁₂FeN₈O₂P₂ × 0.33 H₂O: C, 43.80; H, 3.10; N, 12.02. Found: C, 43.77; H, 3.22; N, 11.97. IR (ATR): $\tilde{\nu}$ /cm⁻¹ = 1669 (m, C=O), 1558(m), 1573 (m), 1482 (m), 1453 (m), 1435 (m), 1355 (m), 1320 (w), 1294 (vw), 1270 (w), 1244 (w), 1198 (vw), 1175 (w), 1154 (w), 1139 (w) 1122 (vw), 1090 (vw), 1067 (vw), 1020 (w), 972 (w), 833 (vs, PF), 793 (s), 754 (s), 713 (s), 673 (s), 649 (m), 633 (m), 578 (m), 559 (vs, PF₂, def.), 516 (m), 448 (w), 434 (w), 414 (w). CV (CH₃CN): *E*_{1/2} = -1.46 (rev.). -1.28 (rev.), +0.78 (rev.) V vs. FcH/FcH⁺. UV/VIS (CH₃CN): λ_{max} (ϵ) = 247 (20900, sh), 270 (28700), 300 (16500, sh), 350 (12200), 410 (5640, sh), 609 (3980 m⁻¹cm⁻¹).

Oxidation of **1**[PF₆]₂ ([Fe(cpmp)₂][NO₃]₃)

1[PF₆]₂ (100 mg, 0.108 mmol, 1.0 equiv.) was dissolved in a 5 mL CH₃CN and [NH₄]₂[Ce(NO₃)₆] (95 mg, 0.173 mmol, 1.6 equiv.) was added as a solid. After 5 minutes of stirring at room temperature the orange product was collected by filtration and dried under reduced pressure. EPR (frozen PrCN, 77 K): *g*_{1,1} = 2.74530, *g*_{2,1} = 2.66579, *g*_{1,2} = 2.23901, *g*_{2,2} = 2.23892, *g*_{3,1} = 1.67583, *g*_{3,2} = 1.60628; UV/Vis (CH₃CN): λ_{max} = 270, 314 (sh), 350, 962 nm, IR (ATR): $\tilde{\nu}$ /cm⁻¹ = 3235 (vw, br.), 3112 (vw, sh), 3087 (vw), 3030 (vw, sh), 1695 (w, C=O), 1649 (vw), 1595 (w), 1577 (vw), 1454 (s, sh), 1427 (vs, N-O), 1322 (vs), 1298 (vs), 1267 (vs), 1250 (vs, sh), 1204 (w), 1168 (w), 1159 (w), 1143 (w), 1102 (w), 1070 (vw), 1038 (m), 1019 (m), 971 (w), 892 (w), 816 (s, N-O), 788 (w), 780 (w), 761 (m), 734 (s, N-O), 706 (w), 679 (w), 658 (vw), 634 (vw), 615 (vw), 574 (w), 525 (vw), 512 (vw), 474 (vw), 456 (vw), 446 (vw), 432 (vw), 405 (w).

7. Understanding Excited State Kinetics in Asymmetric Iron(II) Push-Pull Complexes

Reduction of $1[\text{PF}_6]_2$ ($[\text{Fe}(\text{cpmp})_2]^+$)

$1[\text{PF}_6]_2$ (2.65 mg, 2.86 μmol , 1.0 equiv.) was dissolved in a 1.5 mL CH_3CN . Decamethylcobaltocene (0.63 mg, 1.91 μmol , 1.0 equiv.) was added to 1.0 mL of this solution as solid. EPR and IR spectra were measured after 5 minutes of stirring. EPR (frozen CH_3CN , 77 K): $g = 2.0075$.

Synthesis of $2[\text{PF}_6]_2$ ($[\text{Fe}(\text{cpmp})(\text{ddpd})][\text{PF}_6]_2$)

A solution of 100 mg (0.300 mmol) cpmp and 100 mg (0.300 mmol) ddpd in 2 mL dry acetonitrile was added to a suspension of 143 mg (0.400 mmol) $\text{Fe}(\text{OTf})_2$ in 5 mL dry acetonitrile under argon atmosphere. The yellow-green solution was stirred for 30 minutes at room temperature. Addition of 200 mL dry diethylether yielded in a green precipitate – containing both $[\text{Fe}(\text{ddpd})_2]^{2+}$ and $[\text{Fe}(\text{cpmp})(\text{ddpd})]^{2+}$. The product was purified by column chromatography using silica gel and a mixture of acetonitrile and saturated aqueous solution of potassium nitrate (8:1). The solvent was removed by freeze drying. The product was collected by filtration and dissolved in acetonitrile (1 mL). Addition of an aqueous solution of $[\text{NH}_4][\text{PF}_6]$ (1 mg, 6 mmol, 40 eq. in 100 mL of H_2O) resulted in the precipitation of a green solid, which was collected by filtration. The green crystals were dried under reduced pressure. Crystals suitable for single-crystal X-ray diffraction were yielded by slow diffusion of diethyl ether into a solution of $2[\text{PF}_6]_2$ in acetonitrile. Yield: 67.1 mg (0.072 mmol, 24 %).

^1H NMR (CD_3CN , 300 K): δ ppm = 8.17 (t, $^3J = 7.9$ Hz, 1 H), 8.04 (m, 3 H), 7.92 (d, $^3J = 7.4$ Hz, 1 H), 7.83 (m, 3 H), 7.44 (m, 2 H), 7.14 (m, 5 H), 7.03 (d, $^3J = 8.3$ Hz, 1 H), 6.98 (d, $^3J = 5.8$ Hz, 1 H), 6.78 (m, 2 H), 6.69 (m, 1 H), 6.63 (d, $^3J = 5.4$ Hz, 2 H), 3.04 (s, 3 H), 3.02 (s, 3 H), 2.83 (s, 3 H). $^{13}\text{C}\{^1\text{H}\}$ NMR (CD_3CN , 300 K): δ ppm = 181.5, 162.4, 161.6, 161.4, 161.1, 160.9, 159.5, 158.7, 158.3, 156.5, 156.0, 155.2, 141.6, 141.3, 140.9, 140.8, 140.4, 139.5, 127.8, 127.2, 126.1, 125.7, 121.4, 121.2, 121.1, 117.9, 113.7, 113.5, 113.1, 113.0, 112.4, 40.0, 39.9, 39.2. ^{31}P NMR δ ppm = -144.64 (sept, $^1J_{\text{PF}} = 706$ Hz). Although the number of ^1H and ^{13}C resonances, their intensity and multiplicity fit to the structure, the two ligand nuclei feature too similar chemical shifts to allow a detailed assignment. MS (ESI⁺) m/z (%) = 318.57 (96.01, $[\text{Fe}(\text{cpmp})(\text{ddpd})]^{2+}$), 366.08 (100, $[\text{Fe}(\text{ddpd})\text{F}]^{2+}$), 656.20 (56.92, $[\text{Fe}(\text{cpmp})(\text{ddpd})\text{F}]^{2+}$), 782.82 (13.31, $\{[\text{Fe}(\text{cpmp})(\text{ddpd})][\text{PF}_6]\}^+$), 1246.75 (26.02, $\{\text{H}[\text{Fe}(\text{cpmp})(\text{ddpd})]_3[\text{PF}_6]_4\}^+$), 1711.18 (33.09, $\{\text{H}_4[\text{Fe}(\text{cpmp})(\text{ddpd})]_4[\text{PF}_6]_6\}^{2+}$). MS (HR-ESI⁺): calcd. for $\text{C}_{34}\text{H}_{31}\text{F}_6\text{FeN}_9\text{OP}^+$: $m/z = 782.1643$ (100, $[\text{Fe}(\text{cpmp})(\text{ddpd})][\text{PF}_6]^+$). Found: 782.1642 (100). Elem. anal. calcd. for $\text{C}_{34}\text{H}_{31}\text{F}_{12}\text{FeN}_9\text{OP}_2 \times 1.25 \text{H}_2\text{O}$: C, 42.99; H, 3.55; N, 13.27. Found: C, 42.52; H, 3.04; N, 13.29. IR (ATR): $\tilde{\nu}/\text{cm}^{-1} = 1672$ (m, C=O), 1593 (m), 1580 (m), 1567 (m), 1493 (m), 1450 (s), 1432 (s), 1358 (m), 1340 (m), 1320 (w), 1304 (vw), 1290 (vw), 1270 (vw), 1278 (w), 1238 (w), 1196 (vw), 1171 (w), 1142 (m), 1134 (w), 1096 (w), 1065 (vw), 1020 (vw), 974 (vw), 949 (vw), 915 (vw), 875 (m), 831 (vs, PF), 978 (vs), 777 (s), 747 (vs), 717 (m), 672 (m), 647 (vw), 634 (vw), 589 (w), 583 (w), 555 (s, PF₂, def.), 516 (w), 446 (w), 414 (w). CV (CH_3CN): $E_{1/2} = -2.03$ (rev.), -1.36 (rev.), +0.55 (rev.) V vs. FcH/FcH⁺. UV/VIS (CH_3CN): $\lambda_{\text{max}}(\epsilon) = 244$ (21900), 276 (30100), 325 (15900), 365, (8630), 420 (5500, sh), 616 (2250 $\text{M}^{-1}\text{cm}^{-1}$).

Literature

- [1] B. Durham, J. V. Caspar, J. K. Nagle, T. J. Meyer, *J. Am. Chem. Soc.* **1982**, *104*, 4803–4810.
- [2] B. O'Regan, M. Grätzel, *Nature* **1991**, *353*, 737–740.
- [3] J.-F. Yin, M. Velayudham, D. Bhattacharya, H.-C. Lin, K.-L. Lu, *Coord. Chem. Rev.* **2012**, *256*, 3008–3035.
- [4] P. G. Bomben, K. C. D. Robson, B. D. Koivisto, C. P. Berlinguette, *Coord. Chem. Rev.* **2012**, *256*, 1438–1450.
- [5] R. D. Costa, E. Ortí, H. J. Bolink, F. Monti, G. Accorsi, N. Armaroli, *Angew. Chem. Int. Ed.* **2012**, *51*, 8178–8211.
- [6] P. Dreyse, B. Loeb, M. Soto-Arriaza, D. Tordera, E. Ortí, J. J. Serrano-Pérez, H. J. Bolink, *Dalton Trans.* **2013**, *42*, 15502–15513.
- [7] H. J. Bolink, L. Cappelli, E. Coronado, P. Gaviña, *Inorg. Chem.* **2005**, *44*, 5966–5968.
- [8] H. J. Bolink, E. Coronado, R. D. Costa, P. Gaviña, E. Ortí, S. Tatay, *Inorg. Chem.* **2009**, *48*, 3907–3909.
- [9] K. M. Maness, R. H. Terrill, T. J. Meyer, R. W. Murray, R. M. Wightman, *J. Am. Chem. Soc.* **1996**, *118*, 10609–10616.
- [10] A. Inagaki, M. Akita, *Coord. Chem. Rev.* **2010**, *254*, 1220–1239.
- [11] C. K. Prier, D. A. Rankic, D. W. C. MacMillan, *Chem. Rev.* **2013**, *113*, 5322–5363.
- [12] S. Campagna, F. Puntoriero, F. Nastasi, G. Bergamini, V. Balzani, *Top. Curr. Chem.* **2007**, *280*, 117–214.
- [13] W. Gawelda, A. Cannizzo, V.-T. Pham, F. van Mourik, C. Bressler, M. Chergui, *J. Am. Chem. Soc.* **2007**, *129*, 8199–8206.
- [14] M. C. Carey, S. L. Adelman, J. K. McCusker, *Chem. Sci.* **2019**, *10*, 134–144.
- [15] O. S. Wenger, *Chem. Eur. J.* **2019**, *25*, 6043–6052.
- [16] P. Chábera, K. S. Kjær, O. Prakash, A. Honarfar, Y. Liu, L. A. Fredin, T. C. B. Harlang, S. Lidin, J. Uhlig, V. Sundström, R. Lomoth, P. Persson, K. Wärnmark, *J. Phys. Chem. Lett.* **2018**, *9*, 459–463.
- [17] S. H. Wadman, M. Lutz, D. M. Tooke, A. L. Spek, F. Hartl, R. W. A. Havenith, G. P. M. van Klink, G. van Koten, *Inorg. Chem.* **2009**, *48*, 1887–1900.
- [18] C. Kreitner, E. Erdmann, W. W. Seidel, K. Heinze, *Inorg. Chem.* **2015**, *54*, 11088–11104.
- [19] M. Maestri, N. Armaroli, V. Balzani, E. C. Constable, Cargill Thompson, Alexander M. W., *Inorg. Chem.* **1995**, *34*, 2759–2767.
- [20] I. M. Dixon, F. Alary, M. Boggio-Pasqua, J.-L. Heully, *Dalton Trans.* **2015**, *44*, 13498–13503.
- [21] I. M. Dixon, S. Khan, F. Alary, M. Boggio-Pasqua, J.-L. Heully, *Dalton Trans.* **2014**, *43*, 15898–15905.
- [22] J. Steube, L. Burkhardt, A. Pöpcke, J. Moll, P. Zimmer, R. Schoch, C. Wölper, K. Heinze, S. Lochbrunner, M. Bauer, *Chem. Eur. J.* **2019**, *25*, 11826–11830.
- [23] H. Wolpher, O. Johansson, M. Abrahamsson, M. Kritikos, L. Sun, B. Åkermark, *Inorg. Chem. Commun.* **2004**, *7*, 337–340.
- [24] E. A. Medlycott, G. S. Hanan, *Chem. Soc. Rev.* **2005**, *34*, 133–142.
- [25] L. L. Jamula, A. M. Brown, D. Guo, J. K. McCusker, *Inorg. Chem.* **2014**, *53*, 15–17.
- [26] A. T. Baker, H. A. Goodwin, *Austr. J. Chem.* **1985**, *38*, 207–214.
- [27] C. Förster, M. Dorn, T. Reuter, S. Otto, G. Davarci, T. Reich, L. M. Carrella, E. Rentschler, K. Heinze, *Inorganics* **2018**, *6*, 86.
- [28] J. Moll, C. Wang, A. Pöpcke, C. Förster, U. Resch-Genger, S. Lochbrunner, K. Heinze, *Chem. Eur. J.* **2020**.
- [29] C. Kreitner, K. Heinze, *Dalton Trans.* **2016**, *45*, 13631–13647.
- [30] C. Kreitner, K. Heinze, *Dalton Trans.* **2016**, *45*, 5640–5658.

7. Understanding Excited State Kinetics in Asymmetric Iron(II) Push-Pull Complexes

- [31] A. K. C. Mengel, C. Bissinger, M. Dorn, O. Back, C. Förster, K. Heinze, *Chem. Eur. J.* **2017**, *23*, 7920–7931.
- [32] F. Schramm, V. Meded, H. Fliegl, K. Fink, O. Fuhr, Z. Qu, W. Klopper, S. Finn, T. E. Keyes, M. Ruben, *Inorg. Chem.* **2009**, *48*, 5677–5684.
- [33] A. K. C. Mengel, C. Förster, A. Breivogel, K. Mack, J. R. Ochsmann, F. Laquai, V. Ksenofontov, K. Heinze, *Chem. Eur. J.* **2015**, *21*, 704–714.
- [34] P. Alemany, D. Casanova, S. Alvarez, C. Dryzun, D. Avnir in *Reviews in Computational Chemistry* (Eds.: A. L. Parrill, K. B. Lipkowitz), John Wiley & Sons, Hoboken, NJ, USA, **2017**.
- [35] T. Devi, Y.-M. Lee, W. Nam, S. Fukuzumi, *J. Am. Chem. Soc.* **2018**, *140*, 8372–8375.
- [36] L. Burkhardt, M. Holzwarth, B. Plietker, M. Bauer, *Inorg. Chem.* **2017**, *56*, 13300–13310.
- [37] A. Britz, W. Gawelda, T. A. Assefa, L. L. Jamula, J. T. Yarranton, A. Galler, D. Khakhulin, M. Diez, M. Harder, G. Doumy, A. M. March, É. Bajnóczi, Z. Németh, M. Pápai, E. Rozsályi, D. Sárosiné Szemes, H. Cho, S. Mukherjee, C. Liu, T. K. Kim, R. W. Schoenlein, S. H. Southworth, L. Young, E. Jakubikova, N. Huse, G. Vankó, C. Bressler, J. K. McCusker, *Inorg. Chem.* **2019**, *58*, 9341–9350.
- [38] F. Plasser, S. Mai, M. Fumanal, E. Gindensperger, C. Daniel, L. González, *J. Chem. Theory Comput.* **2019**, *15*, 5031–5045.
- [39] S. Mai, M. F. S. J. Menger, M. Marazzi, D. L. Stolba, A. Monari, L. González, *Theor. Chem. Acc.* **2020**, *139*, 65.
- [40] A. Breivogel, C. Förster, K. Heinze, *Inorg. Chem.* **2010**, *49*, 7052–7056.
- [41] S. Stoll, A. Schweiger, *J. Magn. Reson.* **2006**, *178*, 42–55.
- [42] M. Krejčík, M. Daněk, F. Hartl, *J. Electroanal. Chem.* **1991**, *317*, 189–187.
- [43] A. Moore, N. Belabas, D. M. Jonas, *Opt. Lett.* **2005**, *30*, 1228–1230.
- [44] Katharine M. Mullen, Ivo H. M. van Stokkum, *J. Stat. Softw.* **2007**, *18*.
- [45] *SMART Data Collection and SAINT-Plus Data Processing, Inc.*, Bruker Analytical X-ray Instruments, Madison, WI, **2000**.
- [46] Stoe & Cie, X-Red. Stoe & Cie, **2002**, Darmstadt, Germany.
- [47] G. M. Sheldrick, *SHELXL-2014/7*, University of Göttingen, Göttingen, Germany, **2014**.
- [48] G. M. Sheldrick, *Acta Crystallogr. C Struct. Chem.* **2015**, *71*, 3–8.
- [49] F. Neese, *WIREs Comput. Mol. Sci.* **2018**, *8*, e1327.
- [50] A. D. Becke, *J. Chem. Phys.* **1993**, *98*, 5648–5652.
- [51] Chengteh Lee, Weitao Yang, R. G. Parr, *Phys. Rev. B* **1988**, *37*, 785–789.
- [52] B. Miehlich, A. Savin, H. Stoll, H. Preuss, *Chem. Phys. Lett.* **1989**, *157*, 200–206.
- [53] F. Neese, F. Wennmohs, A. Hansen, U. Becker, *Chem. Phys.* **2009**, *356*, 98–109.
- [54] R. Izsák, F. Neese, *J. Chem. Phys.* **2011**, *135*, 144105-1–11.
- [55] D. A. Pantazis, X.-Y. Chen, C. R. Landis, F. Neese, *J. Chem. Theory Comput.* **2008**, *4*, 908–919.
- [56] S. Miertus, E. Scrocco, J. Tomasi, *Chem. Phys.* **1981**, *55*, 117–129.
- [57] V. Barone, M. Cossi, *J. Phys. Chem. A* **1998**, *102*, 1995–2001.
- [58] A. Schäfer, H. Horn, R. Ahlrichs, *J. Chem. Phys.* **1992**, *97*, 2571–2577.
- [59] A. Schäfer, C. Huber, R. Ahlrichs, *J. Chem. Phys.* **1994**, *100*, 5829–5835.
- [60] S. Grimme, J. Antony, S. Ehrlich, H. Krieg, *J. Chem. Phys.* **2010**, *132*, 154104 1-19.
- [61] S. Grimme, S. Ehrlich, L. Goerigk, *J. Comput. Chem.* **2011**, *32*, 1456–1465.
- [62] F. Plasser, *TheoDORE. A package for theoretical density, orbital relaxation and exciton analysis*, at <http://theodore-qc.sourceforge.net>.
- [63] R. Baer, E. Livshits, U. Salzner, *Annu. Rev. Phys. Chem.* **2010**, *61*, 85–109.
- [64] S. I. Bokarev, O. S. Bokareva, O. Kühn, *Coord. Chem. Rev.* **2015**, *304-305*, 133–145.
- [65] O. S. Bokareva, G. Grell, S. I. Bokarev, O. Kühn, *J. Chem. Theory Comput.* **2015**, *11*, 1700–1709.
- [66] O. S. Bokareva, T. Möhle, A. Neubauer, S. I. Bokarev, S. Lochbrunner, O. Kühn, *Inorganics* **2017**, *5*, 23.

7. Understanding Excited State Kinetics in Asymmetric Iron(II) Push-Pull Complexes

- [67] T. Möhle, O. S. Bokareva, G. Grell, O. Kühn, S. I. Bokarev, *J. Chem. Theory Comput.* **2018**, *14*, 5870–5880.
- [68] F. Weigend, R. Ahlrichs, *Phys. Chem. Chem. Phys.* **2005**, *7*, 3297–3305.
- [69] J. Tomasi, B. Mennucci, R. Cammi, *Chem. Rev.* **2005**, *105*, 2999–3093.
- [70] Y. Shao, Z. Gan, E. Epifanovsky, A. T.B. Gilbert, M. Wormit, J. Kussmann, A. W. Lange, A. Behn, J. Deng, X. Feng, D. Ghosh, M. Goldey, P. R. Horn, L. D. Jacobson, I. Kaliman, R. Z. Khaliullin, T. Kuš, A. Landau, J. Liu, E. I. Proynov, Y. M. Rhee, R. M. Richard, M. A. Rohrdanz, R. P. Steele, E. J. Sundstrom, H. L. Woodcock, P. M. Zimmerman, D. Zuev, B. Albrecht, E. Alguire, B. Austin, G. J. O. Beran, Y. A. Bernard, E. Berquist, K. Brandhorst, K. B. Bravaya, S. T. Brown, D. Casanova, C.-M. Chang, Y. Chen, S. H. Chien, K. D. Closser, D. L. Crittenden, M. Diedenhofen, R. A. DiStasio, H. Do, A. D. Dutoi, R. G. Edgar, S. Fatehi, L. Fusti-Molnar, A. Ghysels, A. Golubeva-Zadorozhnaya, J. Gomes, M. W.D. Hanson-Heine, P. H.P. Harbach, A. W. Hauser, E. G. Hohenstein, Z. C. Holden, T.-C. Jagau, H. Ji, B. Kaduk, K. Khistyayev, J. Kim, J. Kim, R. A. King, P. Klunzinger, D. Kosenkov, T. Kowalczyk, C. M. Krauter, K. U. Lao, A. D. Laurent, K. V. Lawler, S. V. Levchenko, C. Y. Lin, F. Liu, E. Livshits, R. C. Lochan, A. Luenser, P. Manohar, S. F. Manzer, S.-P. Mao, N. Mardirossian, A. V. Marenich, S. A. Maurer, N. J. Mayhall, E. Neuscamman, C. M. Oana, R. Olivares-Amaya, D. P. O'Neill, J. A. Parkhill, T. M. Perrine, R. Peverati, A. Prociuk, D. R. Rehn, E. Rosta, N. J. Russ, S. M. Sharada, S. Sharma, D. W. Small, A. Sodt, T. Stein, D. Stück, Y.-C. Su, A. J.W. Thom, T. Tsuchimochi, V. Vanovschi, L. Vogt, O. Vydrov, T. Wang, M. A. Watson, J. Wenzel, A. White, C. F. Williams, J. Yang, S. Yeganeh, S. R. Yost, Z.-Q. You, I. Y. Zhang, X. Zhang, Y. Zhao, B. R. Brooks, G. K.L. Chan, D. M. Chipman, C. J. Cramer, W. A. Goddard, M. S. Gordon, W. J. Hehre, A. Klamt, H. F. Schaefer, M. W. Schmidt, C. D. Sherrill, D. G. Truhlar, A. Warshel, X. Xu, A. Aspuru-Guzik, R. Baer, A. T. Bell, N. A. Besley, J.-D. Chai, A. Dreuw, B. D. Dunietz, T. R. Furlani, S. R. Gwaltney, C.-P. Hsu, Y. Jung, J. Kong, D. S. Lambrecht, W. Liang, C. Ochsenfeld, V. A. Rassolov, L. V. Slipchenko, J. E. Subotnik, T. van Voorhis, J. M. Herbert, A. I. Krylov, P. M.W. Gill, M. Head-Gordon, *Mol. Phys.* **2015**, *113*, 184–215.
- [71] M. J. Frisch, G. W. Trucks, H. B. Schlegel, G. E. Scuseria, M. A. Robb, J. R. Cheeseman, G. Scalmani, V. Barone, G. A. Petersson, H. Nakatsuji, X. Li, M. Caricato, A. V. Marenich, J. Bloino, B. G. Janesko, R. Gomperts, B. Mennucci, H. P. Hratchian, J. V. Ortiz, A. F. Izmaylov, J. L. Sonnenberg, D. Williams-Young, F. Ding, F. Lipparini, F. Egidi, J. Goings, B. Peng, A. Petrone, T. Henderson, D. Ranasinghe, V. G. Zakrzewski, J. Gao, N. Rega, G. Zheng, W. Liang, M. Hada, M. Ehara, K. Toyota, R. Fukuda, J. Hasegawa, M. Ishida, T. Nakajima, Y. Honda, O. Kitao, H. Nakai, T. Vreven, K. Throssell, Montgomery, J. A., Jr., J. E. Peralta, F. Ogliaro, M. J. Bearpark, J. J. Heyd, E. N. Brothers, K. N. Kudin, V. N. Staroverov, T. A. Keith, R. Kobayashi, J. Normand, K. Raghavachari, A. P. Rendell, J. C. Burant, S. S. Iyengar, J. Tomasi, M. Cossi, J. M. Millam, M. Klene, C. Adamo, R. Cammi, J. W. Ochterski, R. L. Martin, K. Morokuma, O. Farkas, J. B. Foresman, D. J. Fox, *Gaussian 16, Revision A.03*, Gaussian, Inc., Wallingford CT, **2016**.
- [72] S. Mai, M. Richter, M. Heindl, M. F. S. J. Menger, A. J. Atkins, M. Ruckebauer, F. Plasser, L. M. Ibele, S. Kropf, M. Opiel, P. Marquetand, L. González, *SHARC2.1: Surface Hopping Including Arbitrary Couplings – Program Package for Non-Adiabatic Dynamics*, **2019**.
- [73] M. Richter, P. Marquetand, J. González-Vázquez, I. Sola, L. González, *J. Chem. Theory Comput.* **2011**, *7*, 1253–1258.
- [74] S. Mai, P. Marquetand, L. González, *WIREs Comput. Mol. Sci.* **2018**, *8*, e1370.
- [75] F. Plasser, S. Gómez, M. F. S. J. Menger, S. Mai, L. González, *Phys. Chem. Chem. Phys.* **2018**, *21*, 57–69.
- [76] M. Barbatti, R. Crespo-Otero, *Top. Curr. Chem.* **2016**, *368*, 415–444.
- [77] L. Sun, W. L. Hase, *J. Chem. Phys.* **2010**, *133*, 44313.

7. Understanding Excited State Kinetics in Asymmetric Iron(II) Push-Pull Complexes

- [78] G. Granucci, M. Persico, A. Toniolo, *J. Chem. Phys.* **2001**, *114*, 10608–10615.
- [79] G. Granucci, M. Persico, A. Zocante, *J. Chem. Phys.* **2010**, *133*, 134111.
- [80] F. Plasser, M. Ruckebauer, S. Mai, M. Oppel, P. Marquetand, L. González, *J. Chem. Theory Comput.* **2016**, *12*, 1207–1219.
- [81] C. Gauthier, V. A. Sole, R. Signorato, J. Goulon, E. Moguiline, *J. Synchrotron Rad.* **1999**, *6*, 164–166.
- [82] P. Carra, M. Fabrizio, B. T. Thole, *Phys. Rev. Lett.* **1995**, *74*, 3700–3703.
- [83] K. Hämäläinen, D. P. Siddons, J. B. Hastings, L. E. Berman, *Phys. Rev. Lett.* **1991**, *67*, 2850–2853.
- [84] P. Glatzel, U. Bergmann, *Coord. Chem. Rev.* **2005**, *249*, 65–95.
- [85] S. DeBeer George, T. Petrenko, F. Neese, *J. Phys. Chem. A* **2008**, *112*, 12936–12943.
- [86] S. DeBeer George, T. Petrenko, F. Neese, *Inorg. Chim. Act.* **2008**, *361*, 965–972.
- [87] N. J. Vollmers, P. Müller, A. Hoffmann, S. Herres-Pawlis, M. Rohrmüller, W. G. Schmidt, U. Gerstmann, M. Bauer, *Inorg. Chem.* **2016**, *55*, 11694–11706.
- [88] P. Zimmer, L. Burkhardt, R. Schepper, K. Zheng, D. Gosztola, A. Neuba, U. Flörke, C. Wölper, R. Schoch, W. Gawelda, S. E. Canton, M. Bauer, *Eur. J. Inorg. Chem.* **2018**, *2018*, 5203–5214.
- [89] P. Zimmer, L. Burkhardt, A. Friedrich, J. Steube, A. Neuba, R. Schepper, P. Müller, U. Flörke, M. Huber, S. Lochbrunner, M. Bauer, *Inorg. Chem.* **2018**, *57*, 360–373.
- [90] F. Neese, *Inorg. Chim. Act.* **202**, *337*, 181–192.
- [91] Y. Takano, K. N. Houk, *J. Chem. Theory Comput.* **2005**, *1*, 70–77.
- [92] G. Knizia, *IboView*, at <http://www.iboview.org>.

Supporting Information: Understanding Excited State Kinetics in Asymmetric Iron(II) Push-Pull Complexes

Johannes Moll,^[a] Lukas Sorge,^[a] Christoph Förster,^[a] Niklas Gessner,^[b] Patrick Nürnberger,^[b] XXXXXXXXXX,^[c] Matthias Bauer,^[c] Ayla Kruse,^[d] Stefan Lochbrunner,^[d] Olga Bokareva,^[d] Sergey Bokarev,^[d] Oliver Kühn,^[d] Omar Baig,^[e] Leticia González^[e] and Katja Heinze^{[a]}*

[a] Department of Chemistry, Johannes Gutenberg University, Mainz, Germany; [b] Department of Chemistry and Pharmacy, University of Regensburg, Germany; [c] Institute of Chemistry, University of Paderborn, Germany; [d] Institute for Physics and Department of Life, Light and Matter, University of Rostock, Germany; [e] Institute of theoretical chemistry, University of Vienna, Austria.

7. Understanding Excited State Kinetics in Asymmetric Iron(II) Push-Pull Complexes

NMR spectroscopy

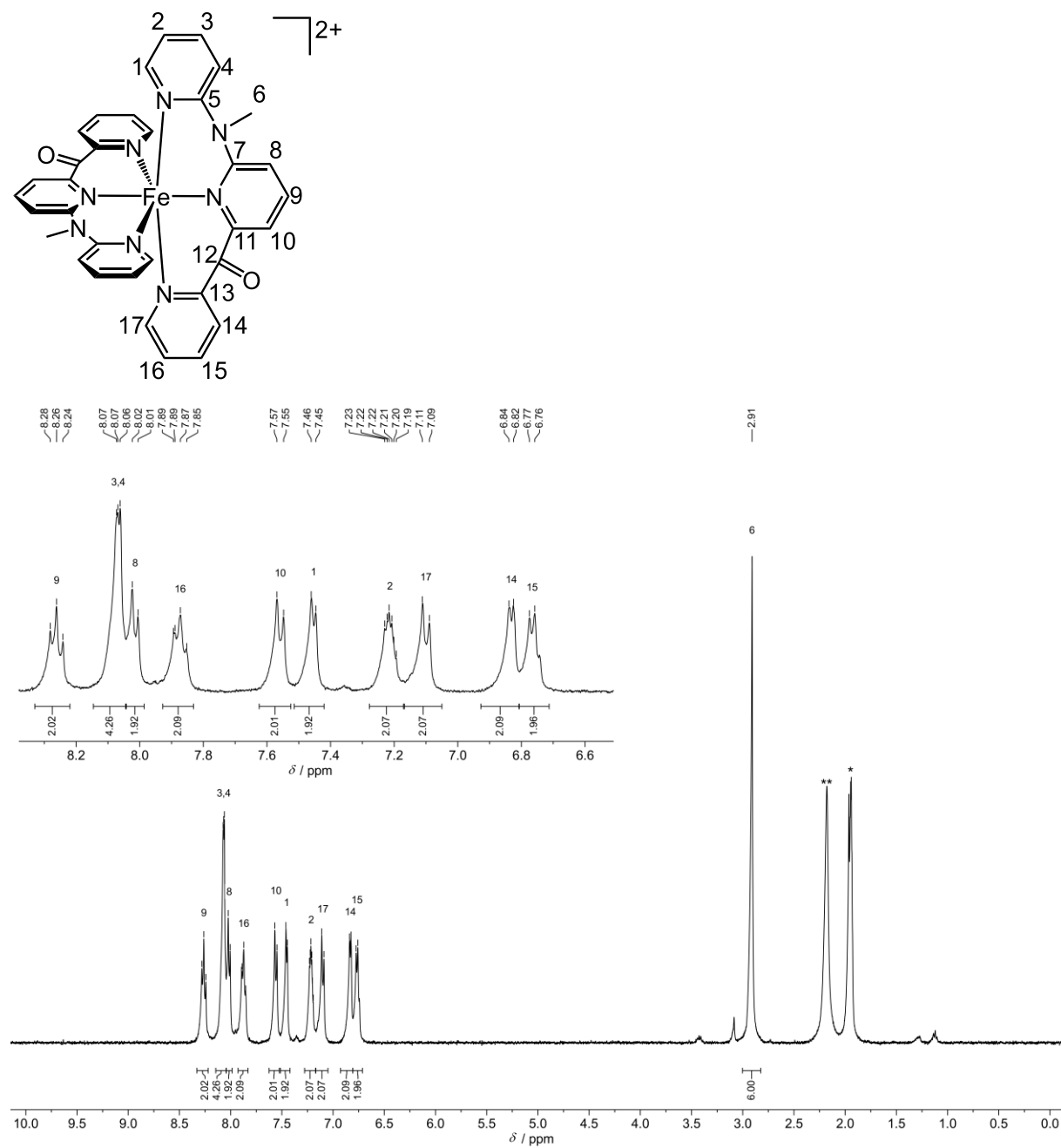


Figure S 1: 1H NMR spectrum of $1[PF_6]_2$ in CD_3CN at 293 K.

7. Understanding Excited State Kinetics in Asymmetric Iron(II) Push-Pull Complexes

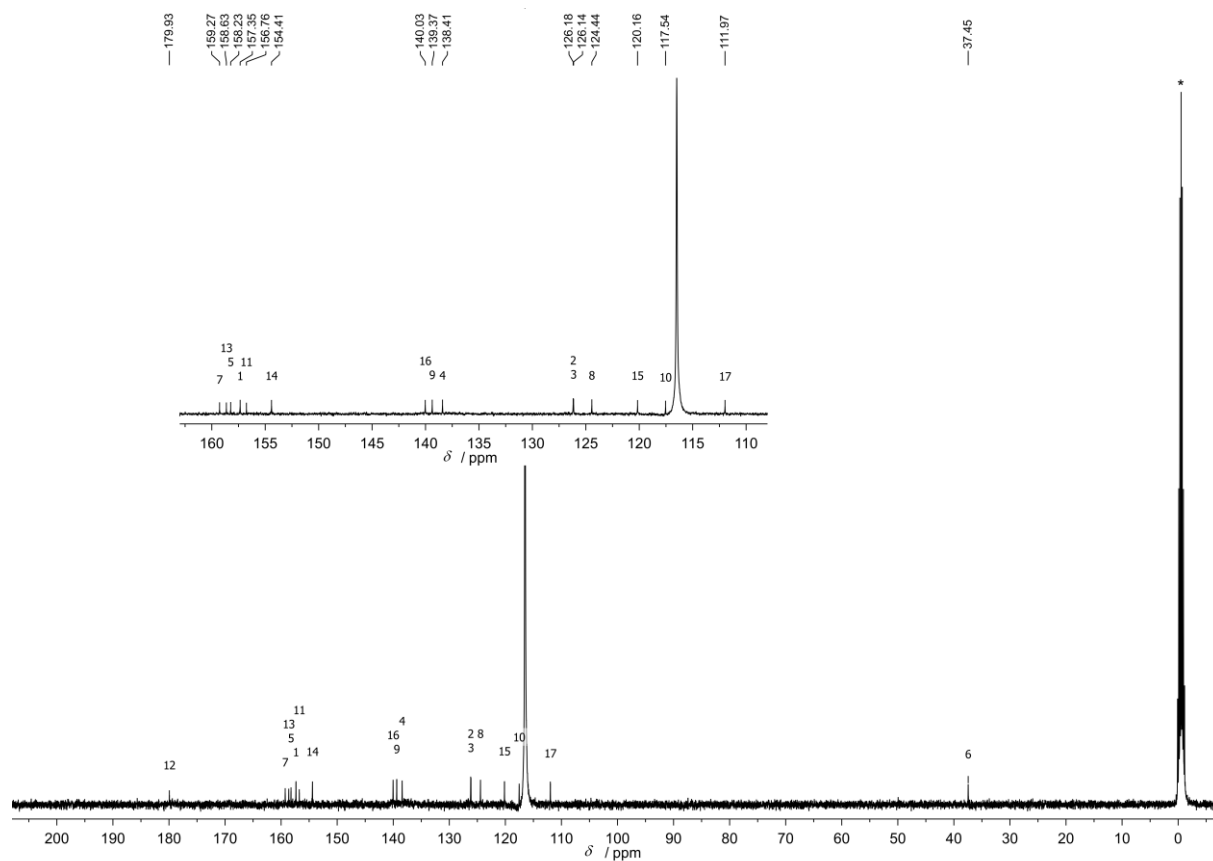


Figure S 2: $^{13}\text{C}\{^1\text{H}\}$ NMR spectrum of $1[\text{PF}_6]_2$ in CD_3CN at 293 K.

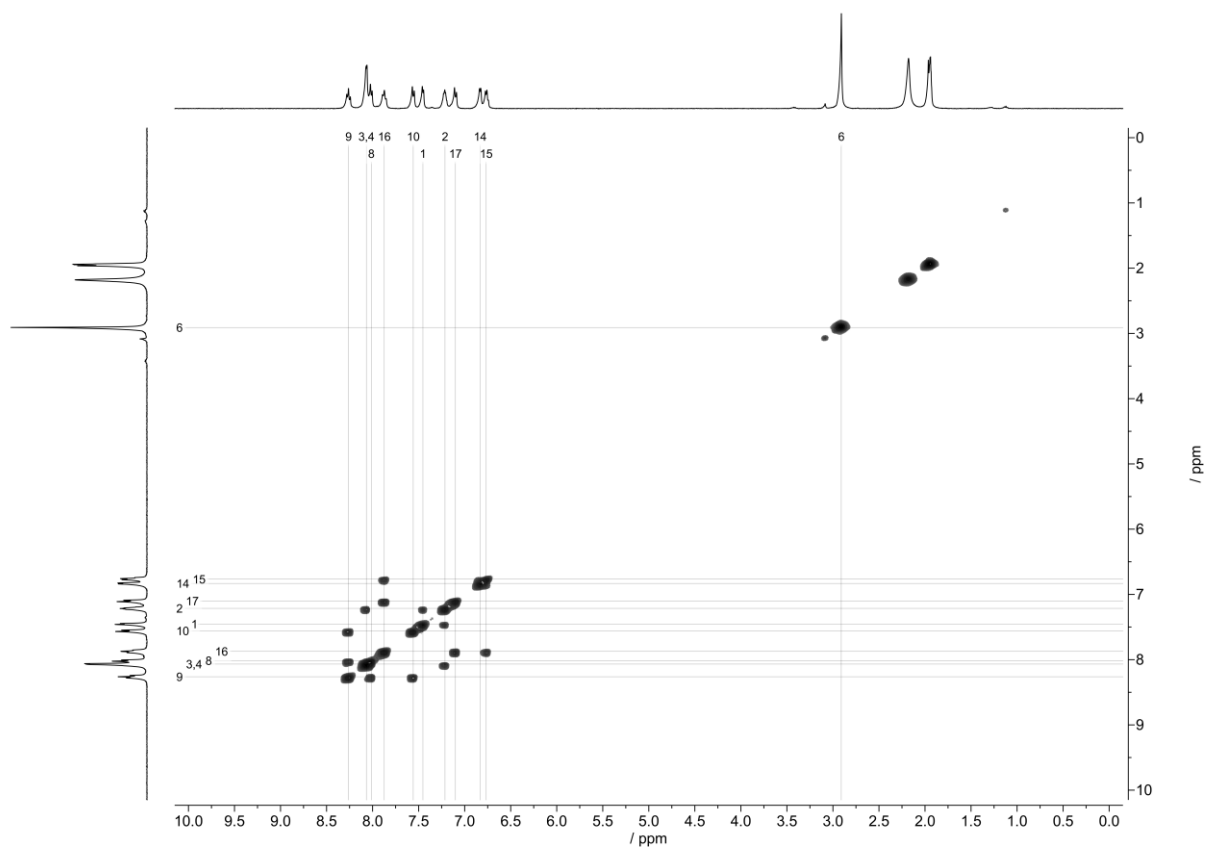


Figure S 3: $^1\text{H}\text{-}^1\text{H}$ COSY-NMR spectrum of $1[\text{PF}_6]_2$ in CD_3CN at 293 K.

7. Understanding Excited State Kinetics in Asymmetric Iron(II) Push-Pull Complexes

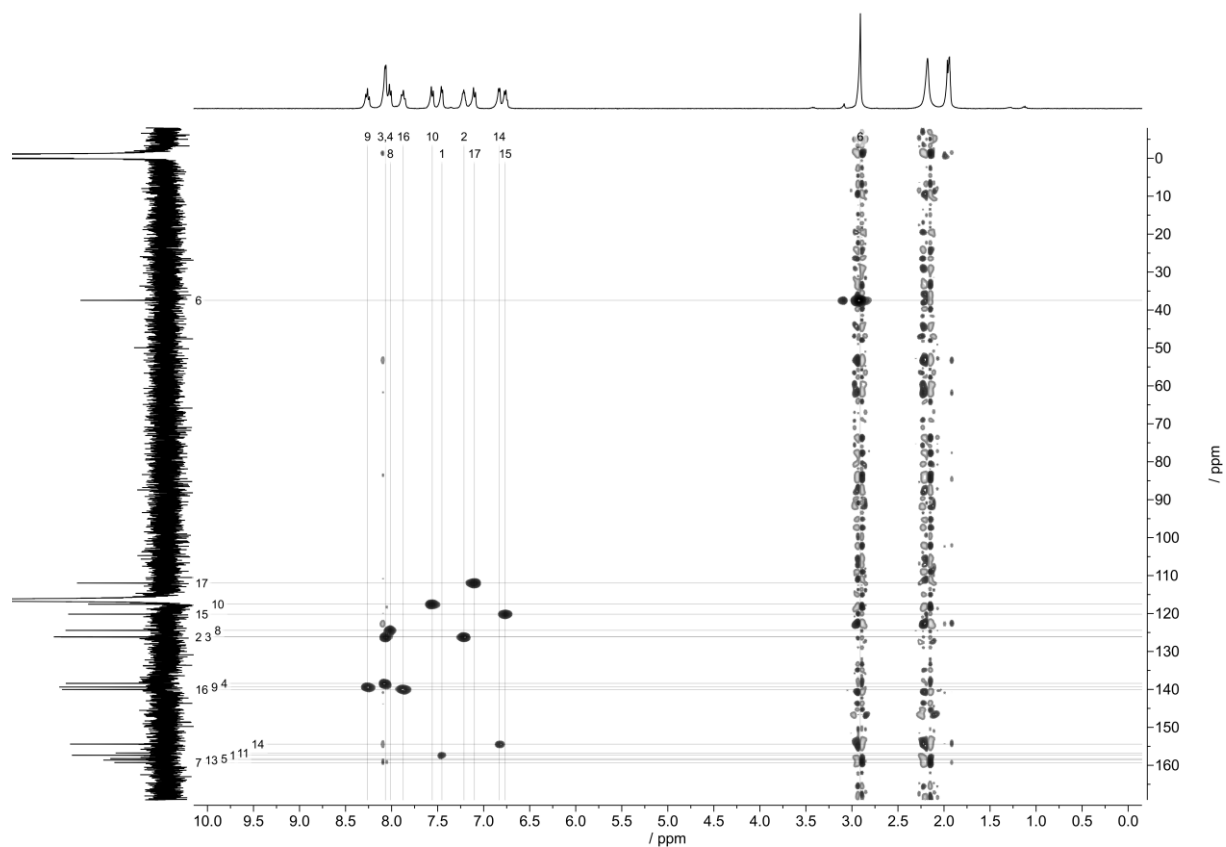


Figure S 4: ¹H-¹³C HMQC-NMR spectrum of **1**[PF₆]₂ in CD₃CN at 293 K.

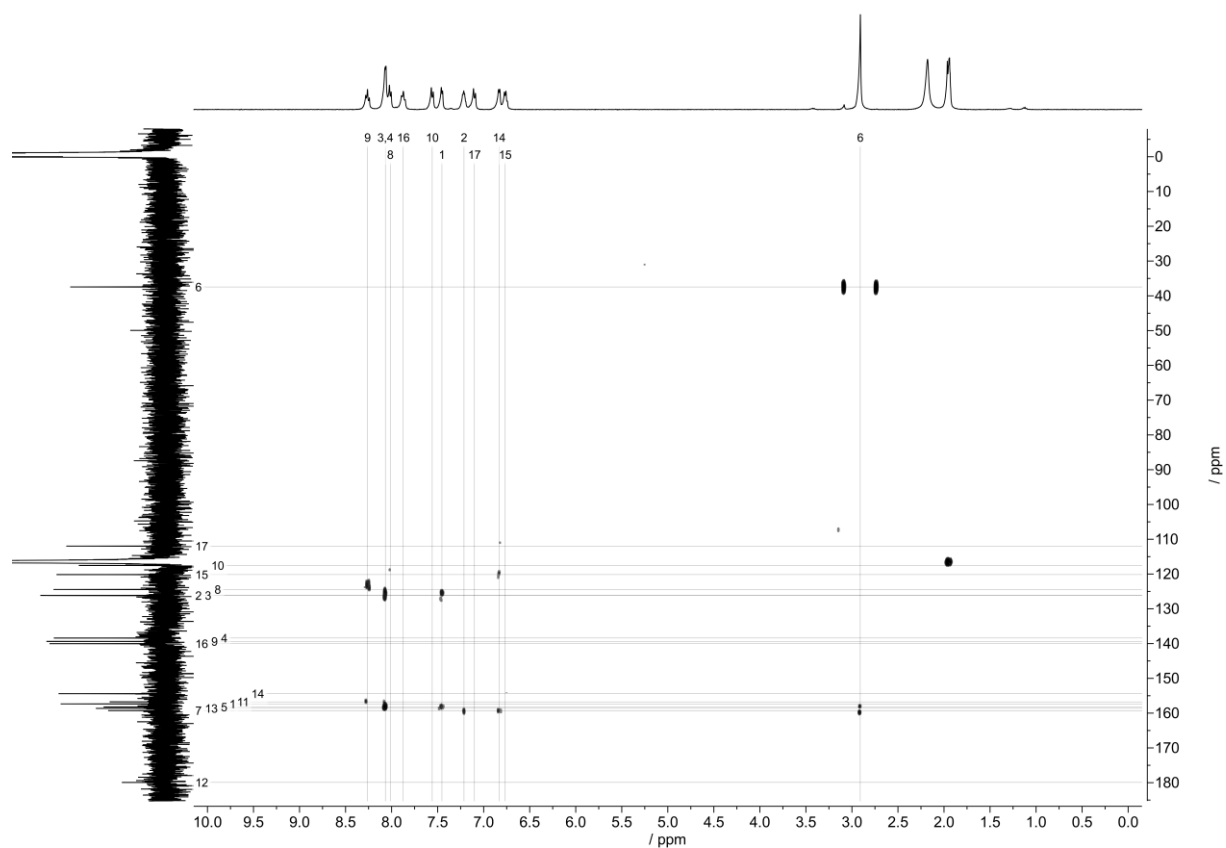


Figure S 5: ¹H-¹³C HMBC-NMR spectrum of **1**[PF₆]₂ in CD₃CN at 293 K.

7. Understanding Excited State Kinetics in Asymmetric Iron(II) Push-Pull Complexes

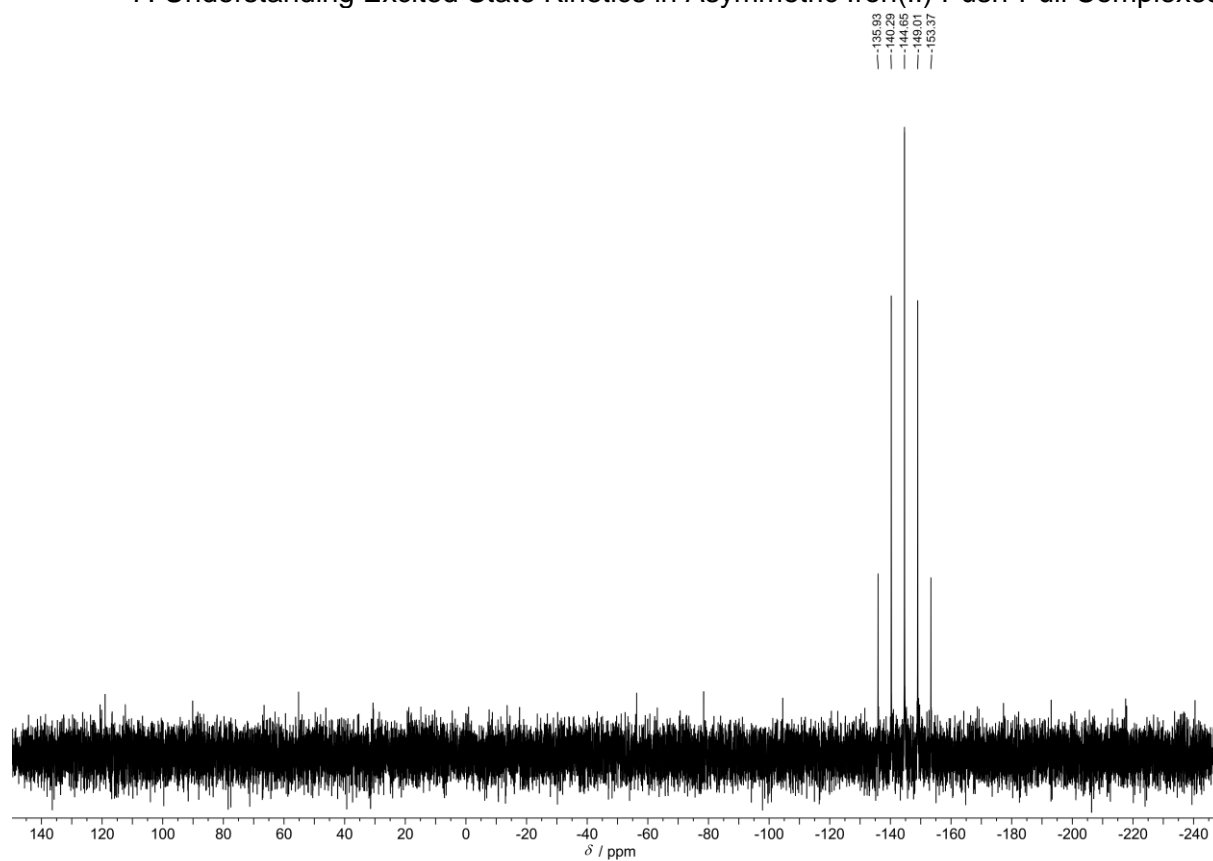


Figure S 6: ^{31}P NMR spectrum of **1**[PF₆]₂ in CD₃CN at 293 K.

7. Understanding Excited State Kinetics in Asymmetric Iron(II) Push-Pull Complexes

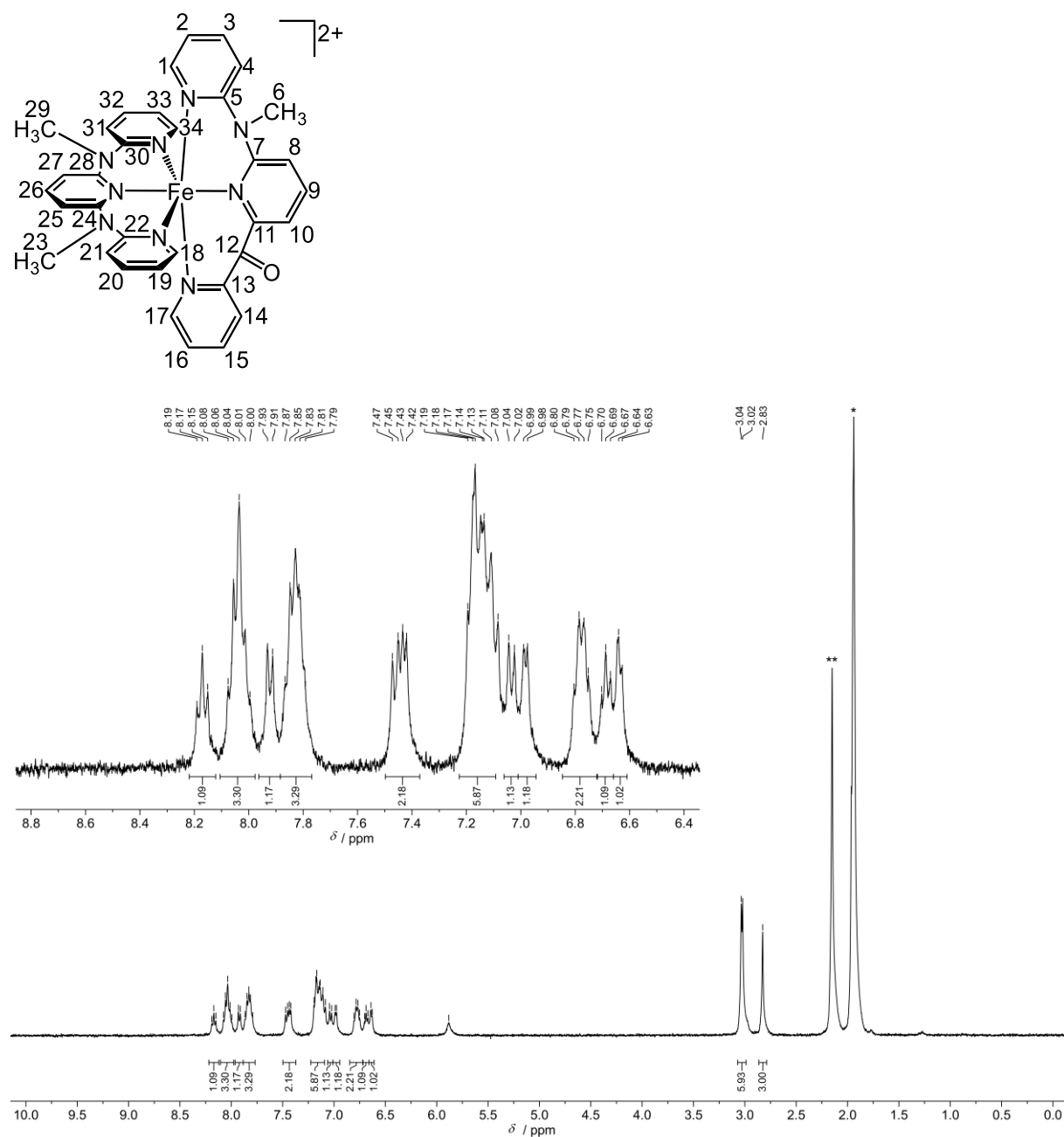


Figure S 7: ¹H NMR spectrum of **2**[PF₆]₂ in CD₃CN at 293 K.

7. Understanding Excited State Kinetics in Asymmetric Iron(II) Push-Pull Complexes

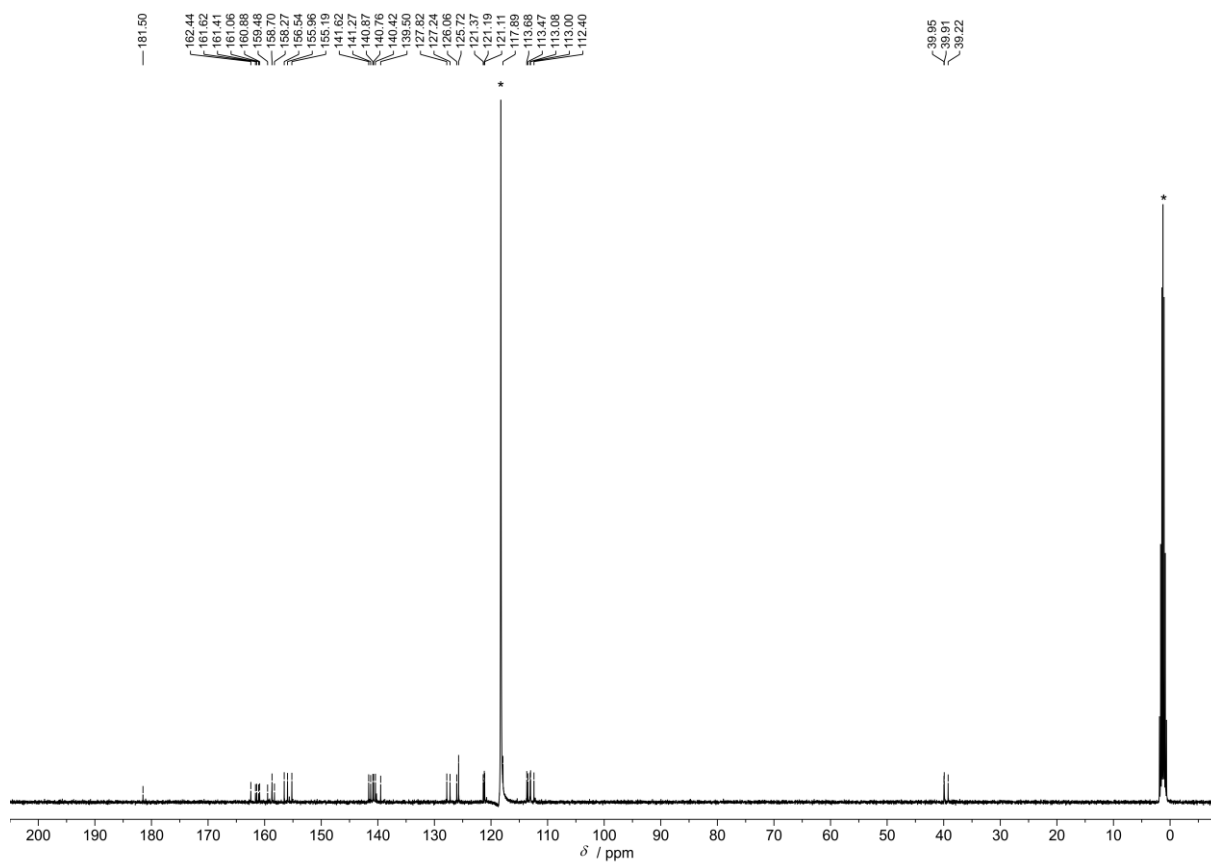


Figure S 8: $^{13}\text{C}\{^1\text{H}\}$ NMR of $2[\text{PF}_6]_2$ in CD_3CN at 293 K.

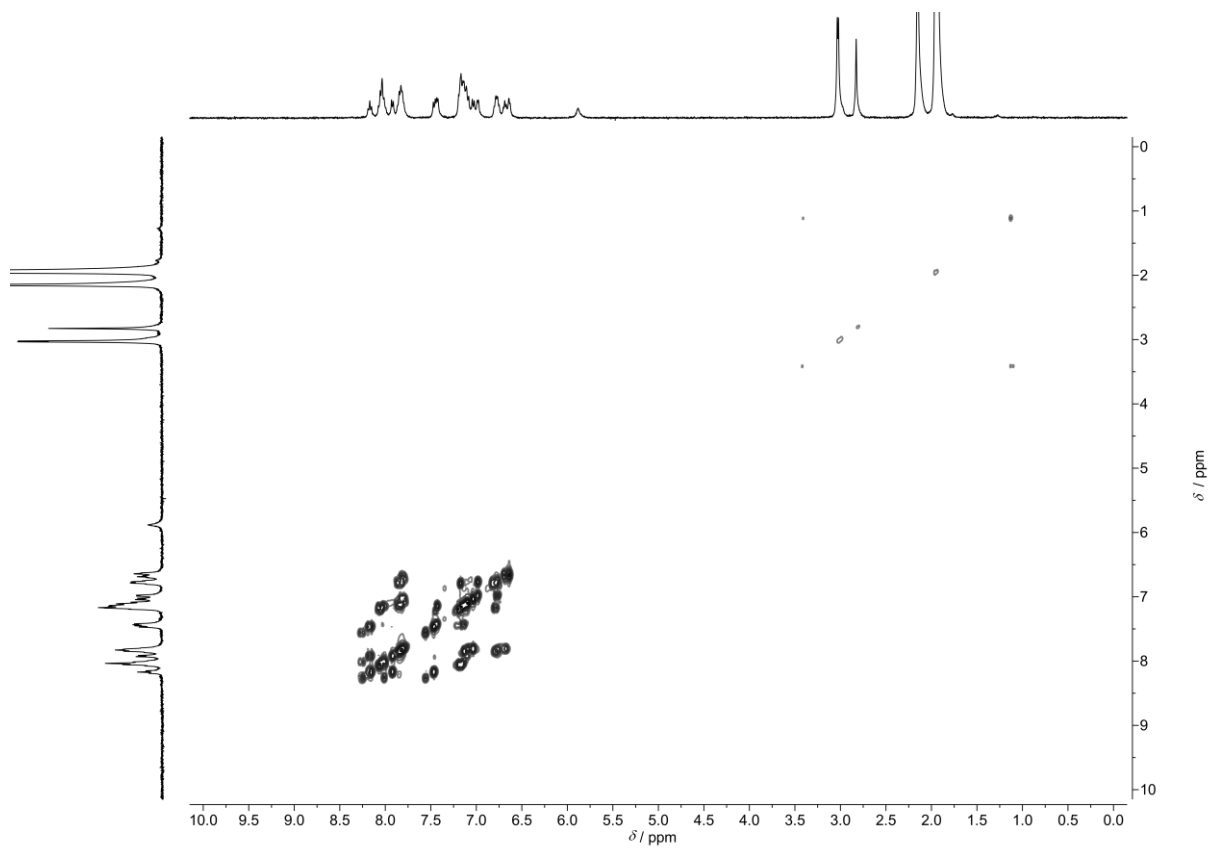


Figure S 9: ^1H - ^1H -COSY NMR spectrum of $2[\text{PF}_6]_2$ in CD_3CN at 293 K.

7. Understanding Excited State Kinetics in Asymmetric Iron(II) Push-Pull Complexes

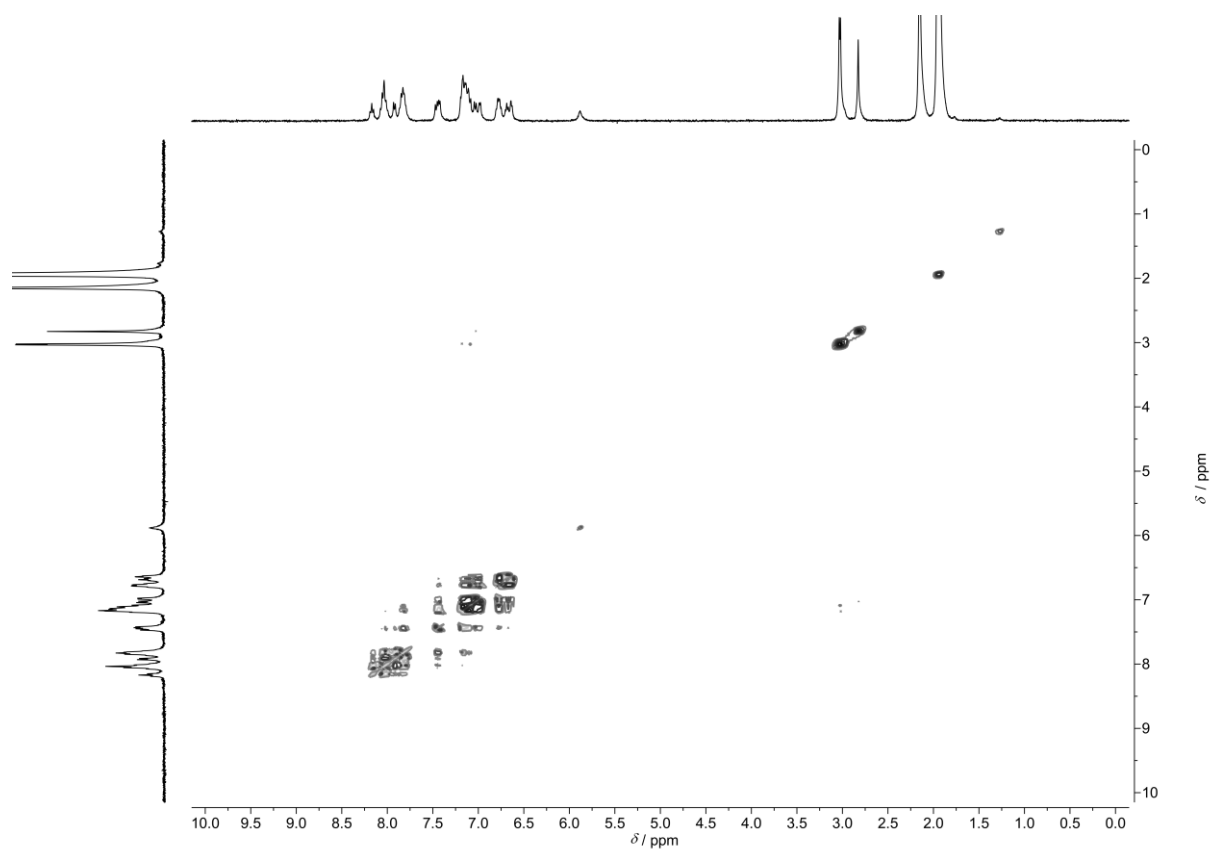


Figure S 10: ^1H - ^1H -NOESY NMR spectrum of $2[\text{PF}_6]_2$ in CD_3CN at 293 K ($t_{\text{mix}} = 1\text{s}$).

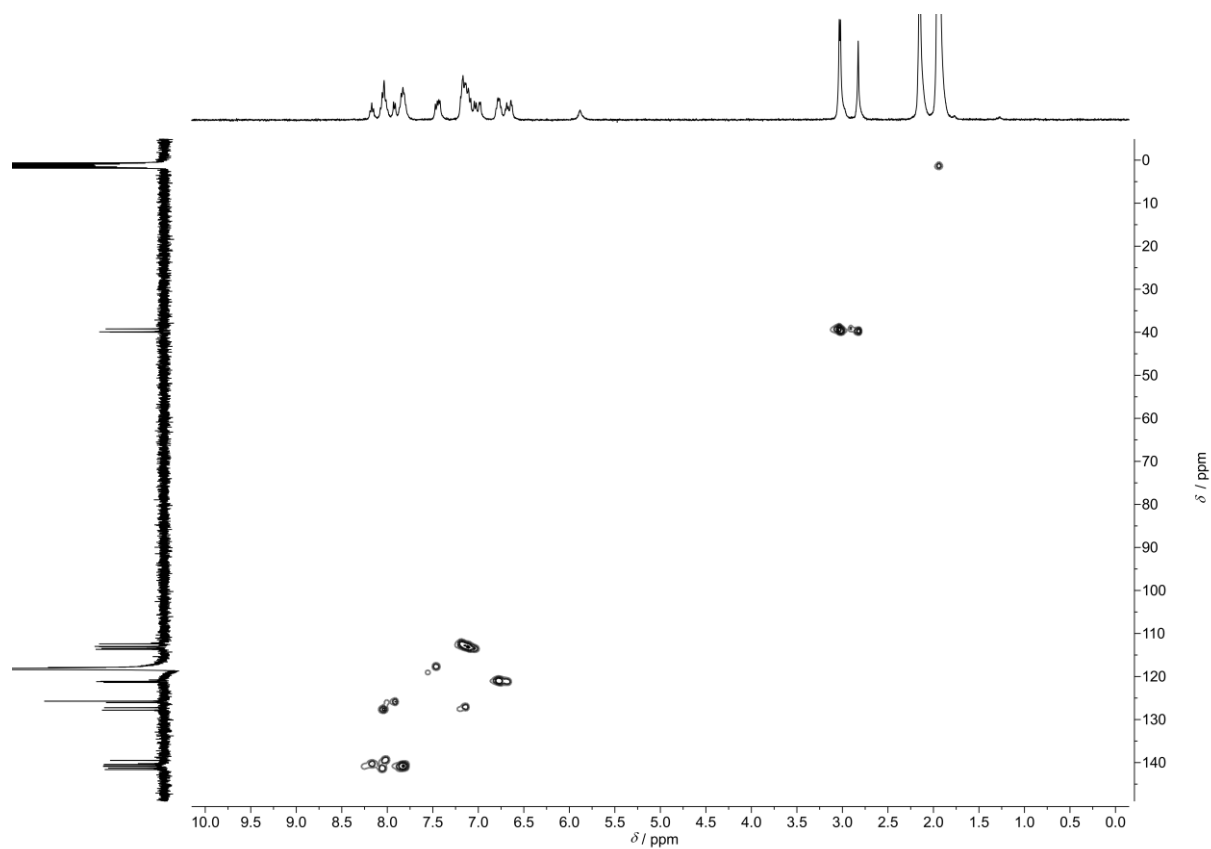


Figure S 11: ^1H - ^{13}C HSQC NMR spectrum of $2[\text{PF}_6]_2$ in CD_3CN at 293 K.

7. Understanding Excited State Kinetics in Asymmetric Iron(II) Push-Pull Complexes

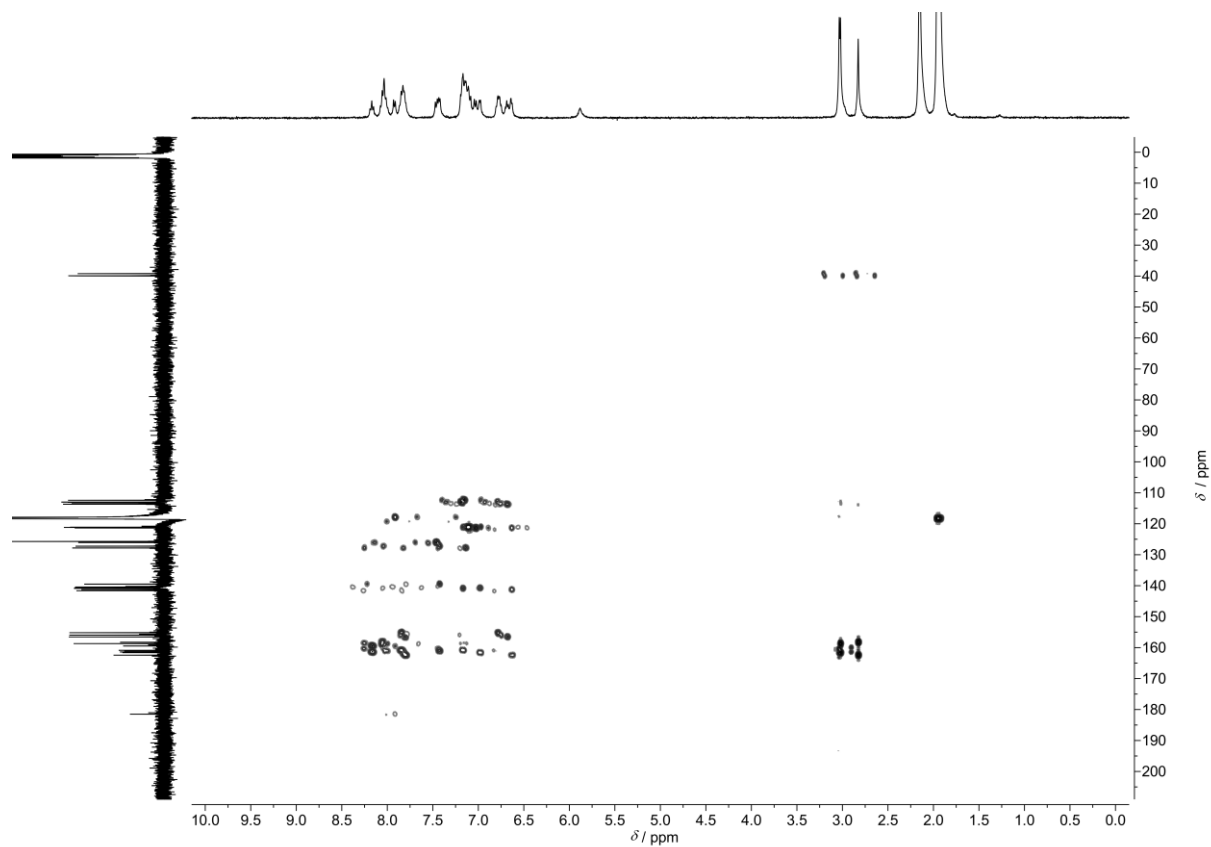


Figure S 12: ^1H - ^{13}C -HMBC NMR spectrum of $2[\text{PF}_6]_2$ in CD_3CN at 293 K.

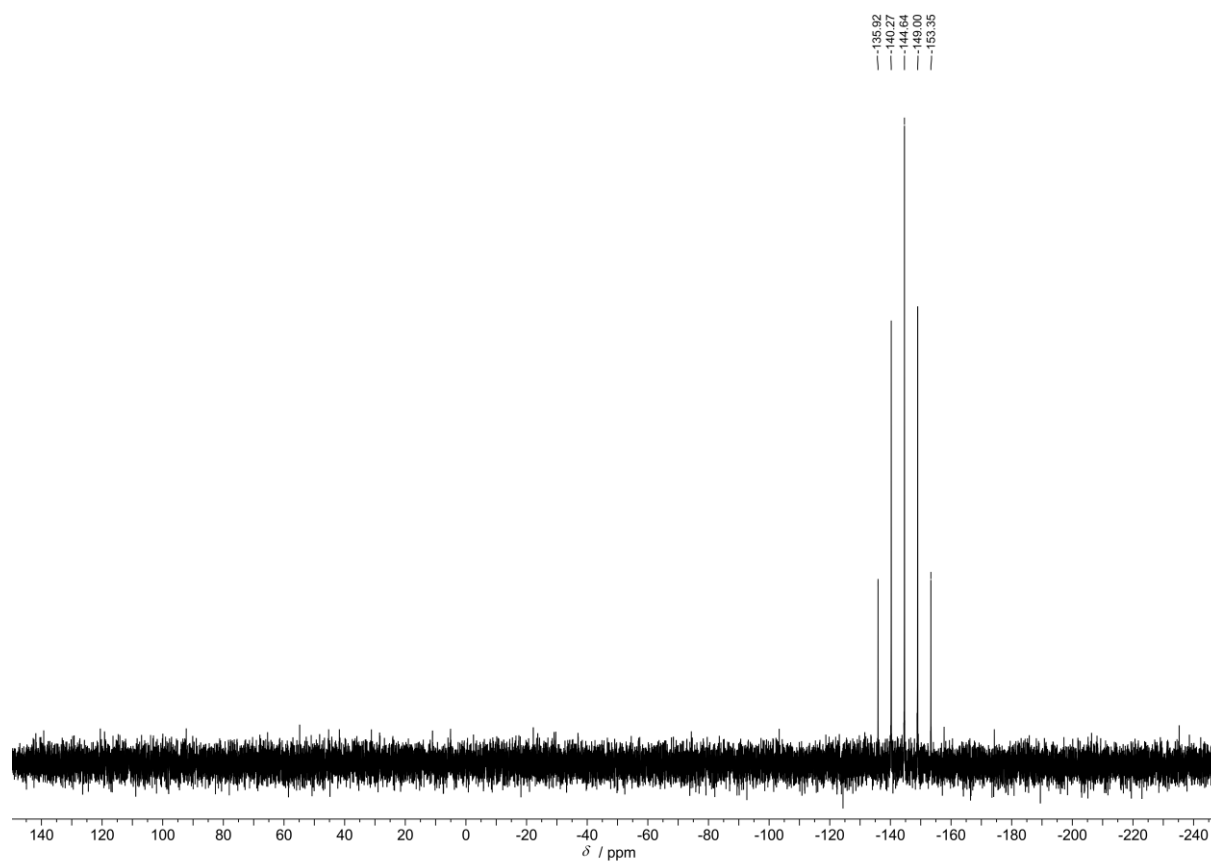


Figure S 13: ^{31}P NMR spectrum of $2[\text{PF}_6]_2$ in CD_3CN at 293 K.

7. Understanding Excited State Kinetics in Asymmetric Iron(II) Push-Pull Complexes

Mass spectrometry

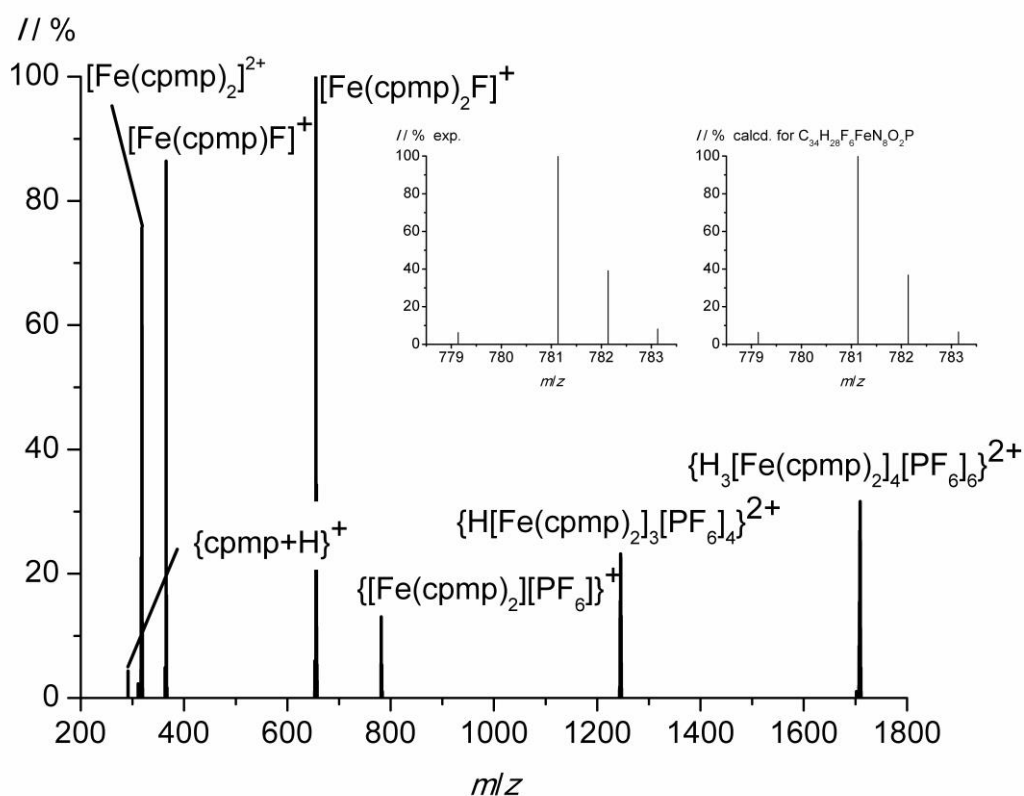


Figure S 14: ESI+ mass spectrum of $1[PF_6]_2$ in acetonitrile and calculated isotope pattern of $C_{34}H_{28}F_6FeN_8O_2P$.

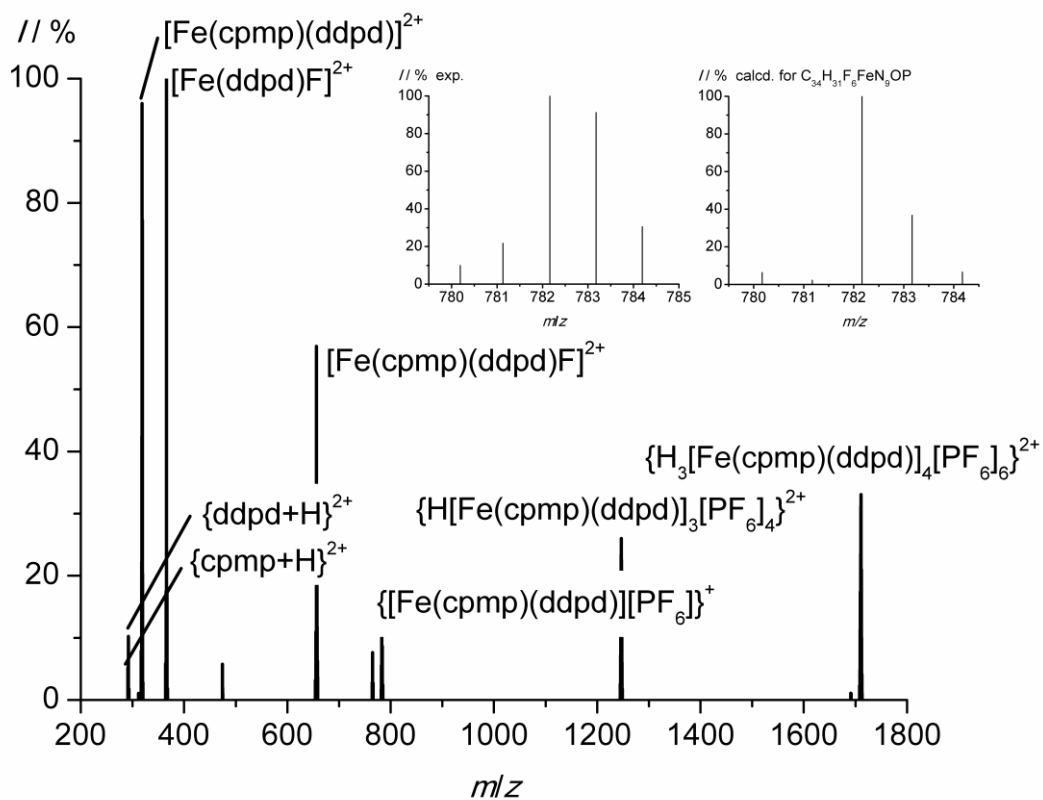


Figure S 15: ESI+ mass spectrum of $2[PF_6]_2$ in acetonitrile and calculated isotope pattern of $C_{34}H_{31}F_6FeN_9OP$.

7. Understanding Excited State Kinetics in Asymmetric Iron(II) Push-Pull Complexes

IR spectroscopy

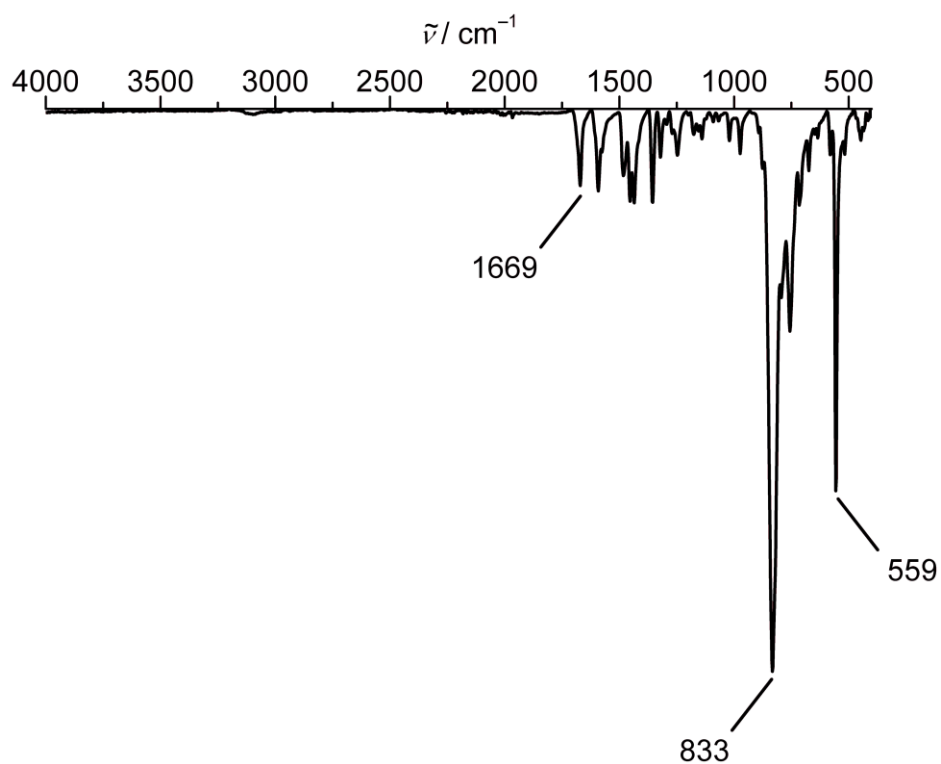


Figure S 16: IR spectrum of **1**[PF₆]₂.

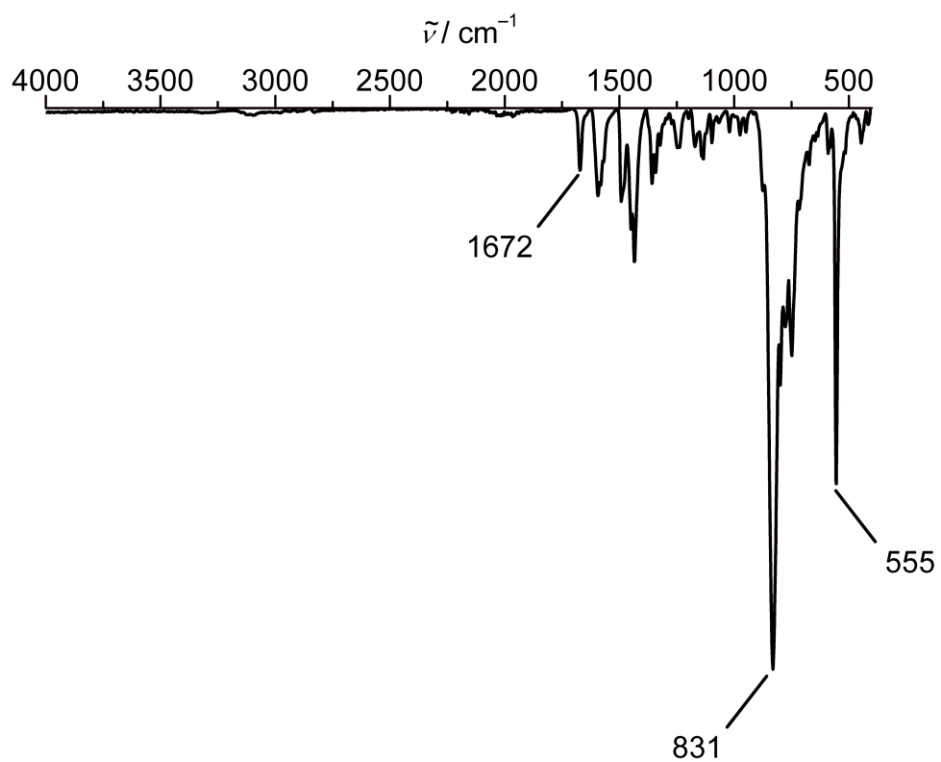


Figure S 17: IR spectrum of **2**[PF₆]₂.

7. Understanding Excited State Kinetics in Asymmetric Iron(II) Push-Pull Complexes

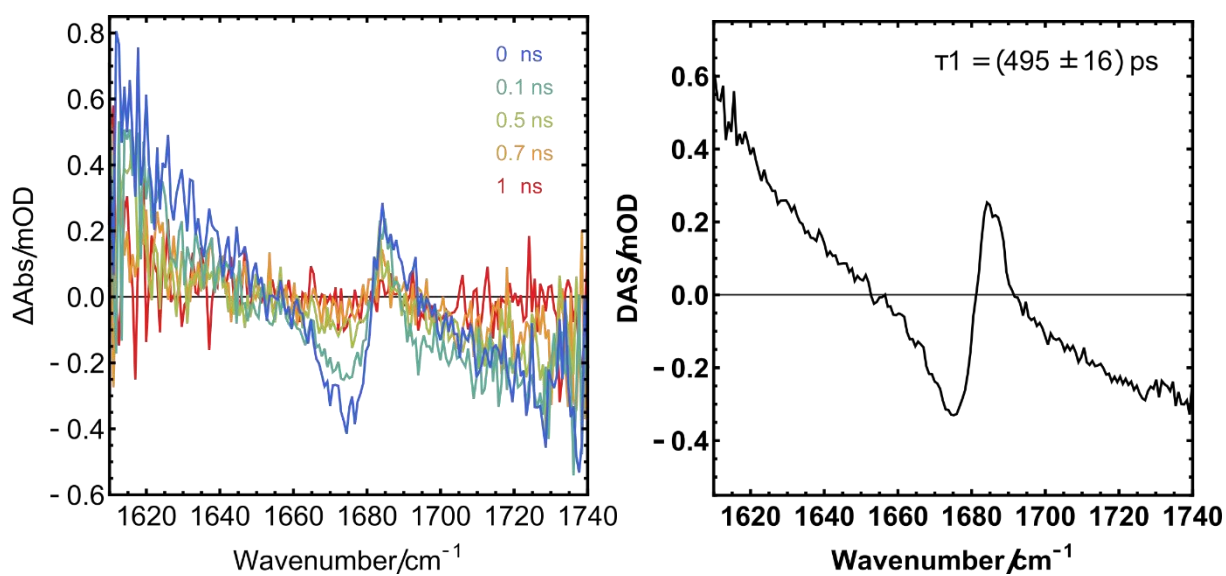


Figure S 18: IR transient absorption spectra (left) and amplitude spectrum (right) of 1[PF₆]₂ in CH₃CN after excitation at 610 nm.

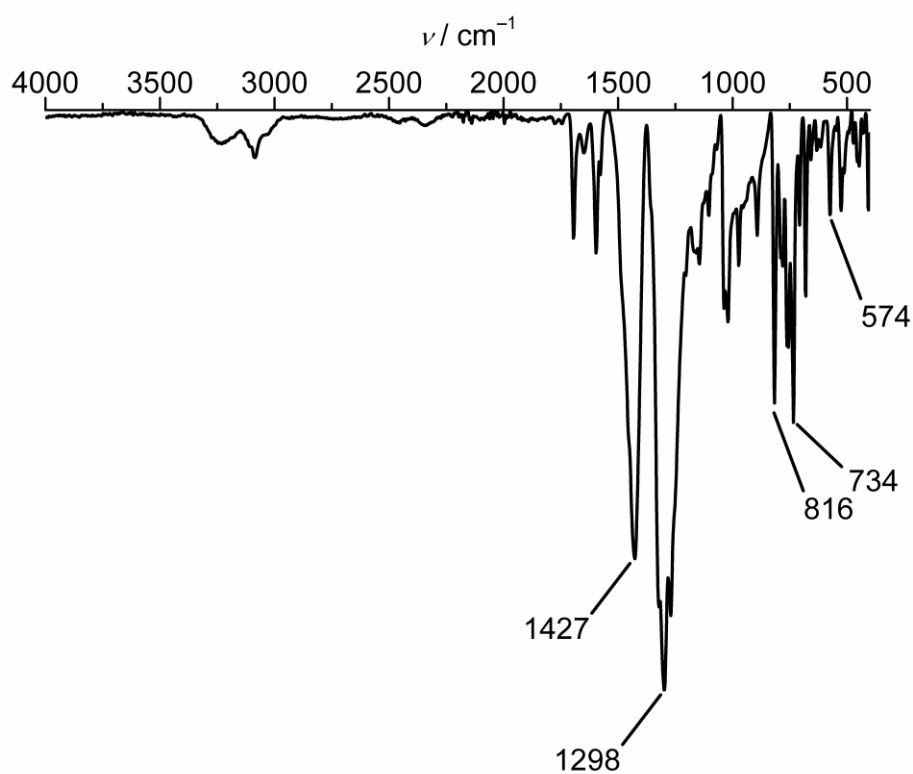


Figure S 19: ATR-IR spectrum of [Fe(cpmp)₂][NO₃]₃

7. Understanding Excited State Kinetics in Asymmetric Iron(II) Push-Pull Complexes

Absorption spectroscopy

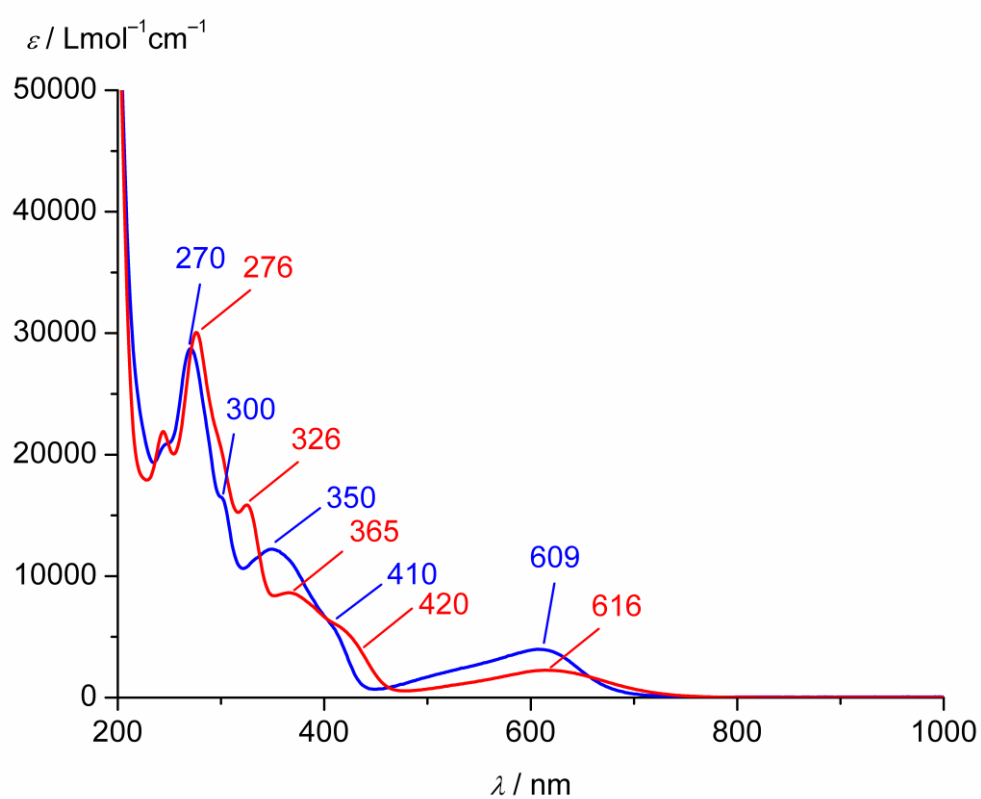


Figure S 20: UV/Vis spectrum of **1**[PF₆]₂ (blue) and **2**[PF₆]₂ (red) in acetonitrile at 298 K.

7. Understanding Excited State Kinetics in Asymmetric Iron(II) Push-Pull Complexes

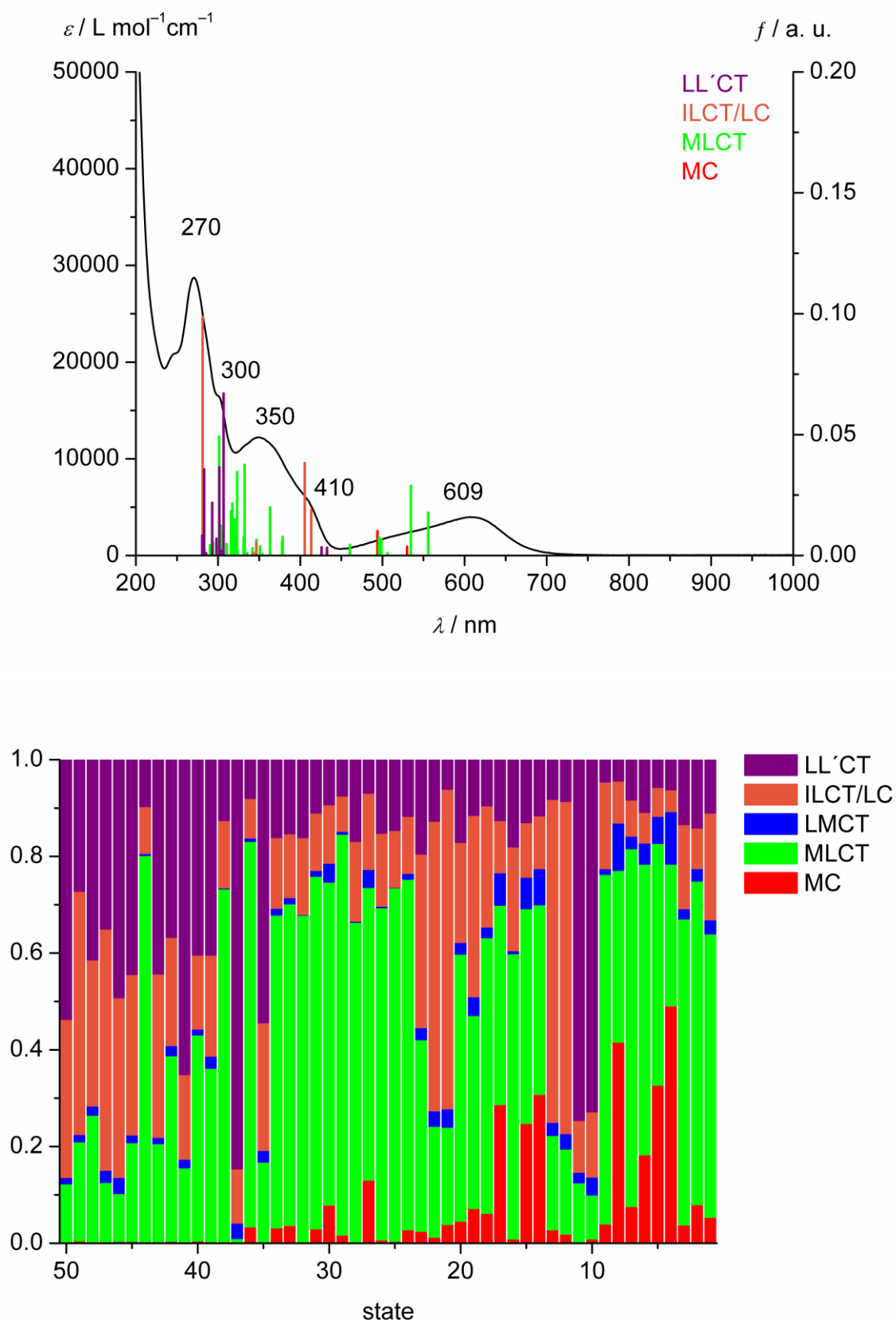


Figure S 21: a) UV/Vis spectrum (black) of $1[\text{PF}_6]_2$ in acetonitrile at 298 K and TDDFT calculated oscillator strength of 1^{2+} (colored tick spectrum, red: MC, green: MLCT, orange: ILCT/LC, purple: LL'CT as mean character, Orca 4.1: CPCM(acetonitrile)-RIJCOSX-B3LYP-D3BJ-ZORA/def2-TZVP). b) decomposition of the charge transfer number matrices into MC (red), MLCT (green), LMCT (blue), ILCT/LC (orange) and LL'CT (purple) using TheoDORE 2.0 for a three component system (metal, ligand 1 and ligand 2).

7. Understanding Excited State Kinetics in Asymmetric Iron(II) Push-Pull Complexes

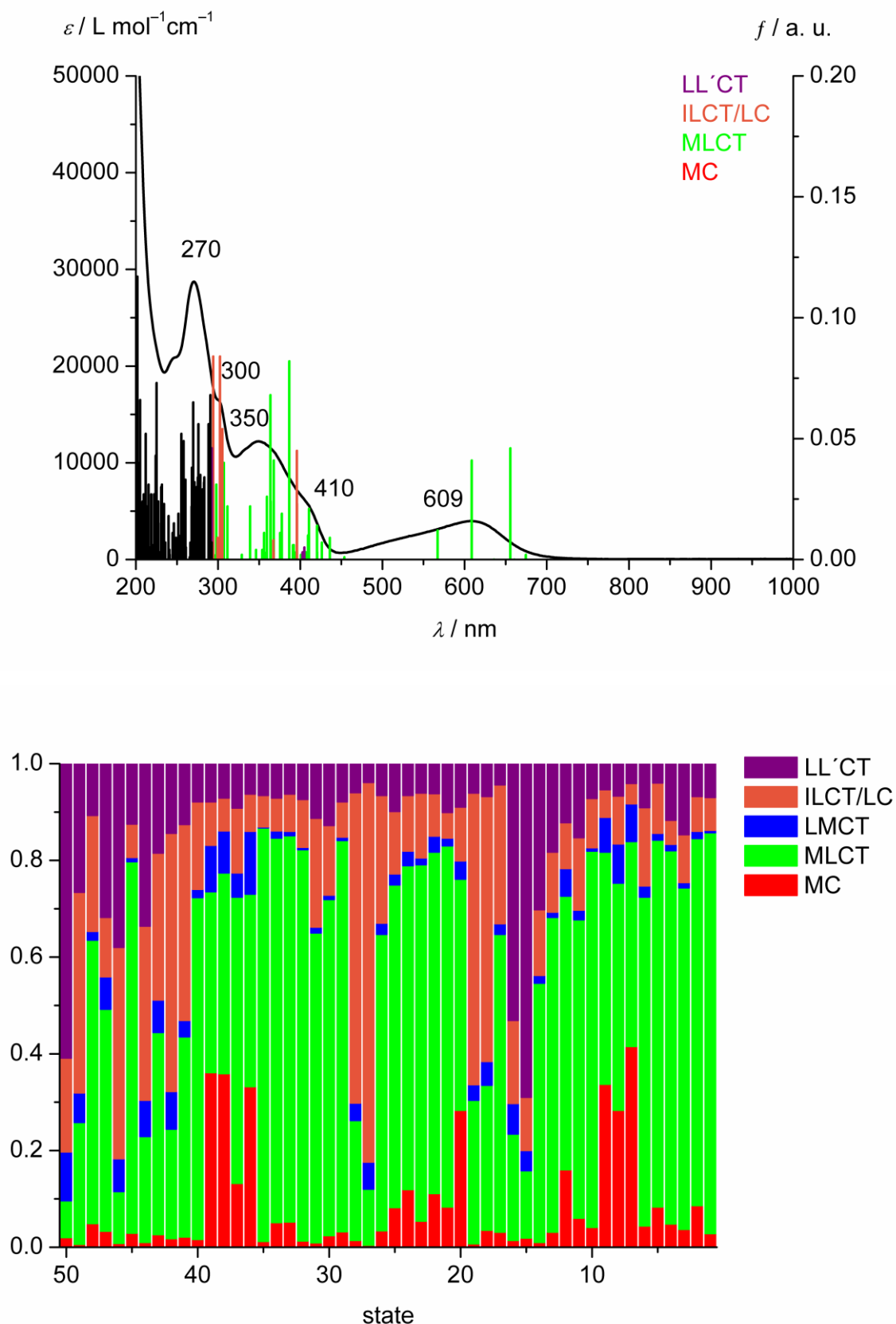


Figure S 22: a) UV/Vis spectrum (black) of **1**[PF₆]₂ in acetonitrile at 298 K and TDDFT calculated oscillator strength of **1**²⁺(colored tick spectrum, red: MC, green: MLCT, orange: ILCT/LC, purple: LL'CT as mean character, Gaussian 16: PCM-LC-BLYP-6-31G(d)- $\alpha = 0$, $\omega = 0.14$). b) decomposition of the charge transfer number matrices into MC (red), MLCT (green), LMCT (blue), ILCT/LC (orange) and LL'CT (purple) using TheoDRE 2.0 for a three component system (metal, ligand 1 and ligand 2).

7. Understanding Excited State Kinetics in Asymmetric Iron(II) Push-Pull Complexes

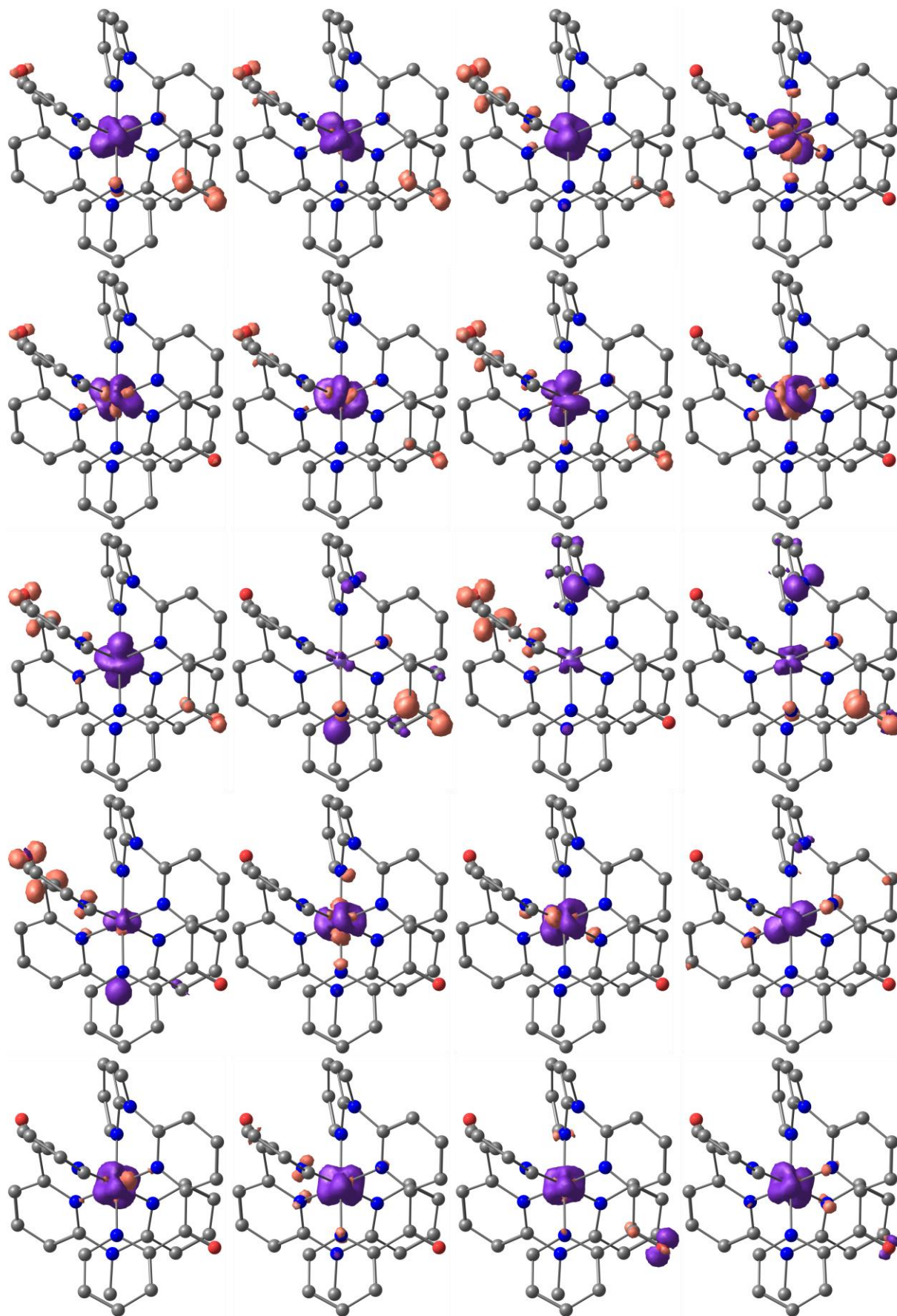


Figure S 23: Difference densities of 20 lowest energy transitions (TD-DFT, Orca 4.1: CPCM(acetonitrile)-RJCOSX-B3LYP-D3BJ-ZORA/def2-TZVP, contour value of 0.01; 3, 8 MC, 1 – 3, 5 – 7, 9, 14 – 20 MLCT; 12, 13 ILCT, 10, 11 LL'CT) of 1^{2+} .

7. Understanding Excited State Kinetics in Asymmetric Iron(II) Push-Pull Complexes

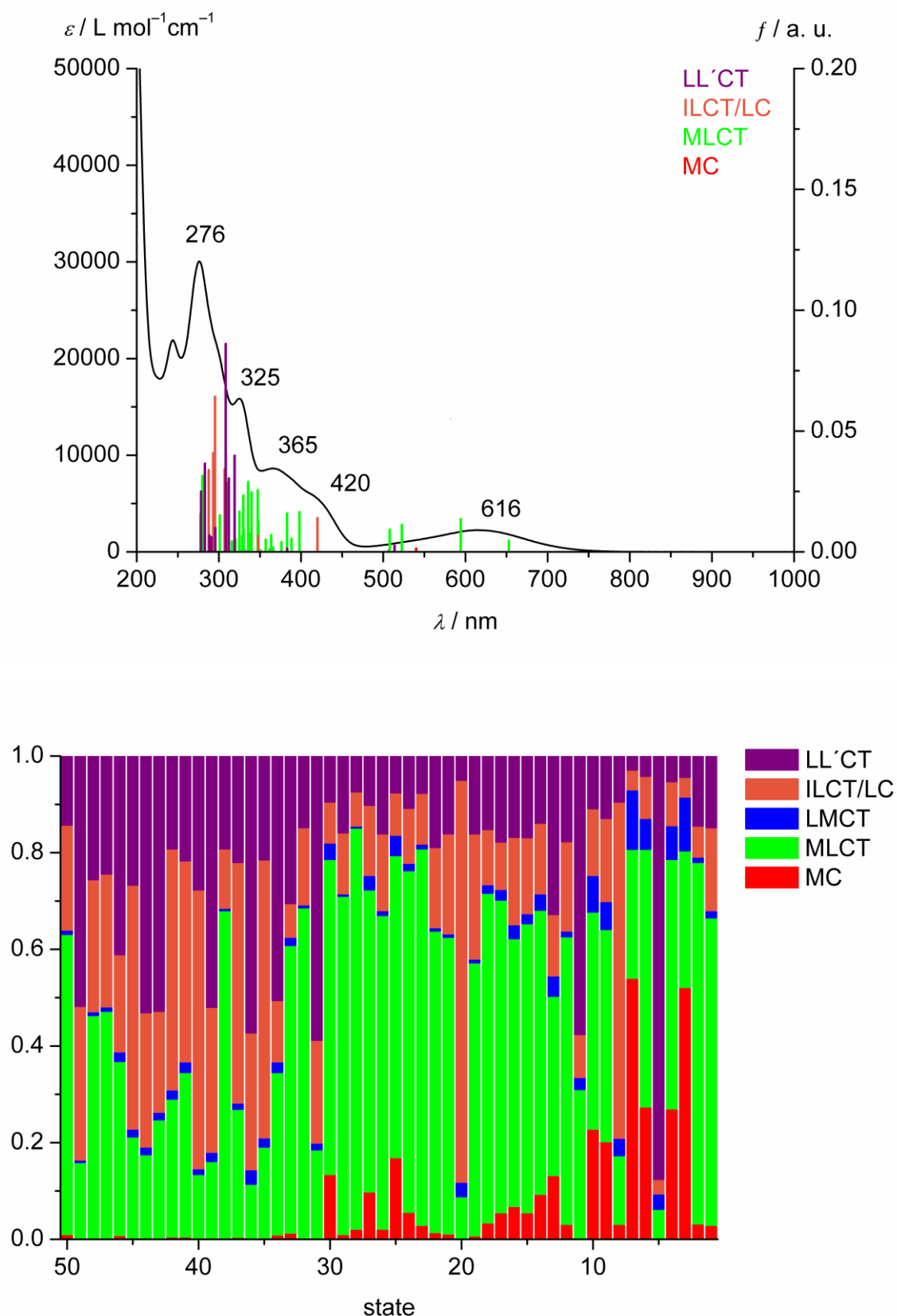


Figure S 24: a) UV/Vis spectrum (black) of $2[\text{PF}_6]_2$ in acetonitrile at 298 K and TDDFT calculated oscillator strength of 2^{2+} (colored tick spectrum, red: MC, green: MLCT, orange: ILCT/LC, purple: LL'CT as mean character, Orca 4.1: CPCM(acetonitrile)-RIJCOSX-B3LYP-D3BJ-ZORA/def2-TZVP). b) decomposition of the charge transfer number matrices into MC (red), MLCT (green), LMCT (blue), ILCT/LC (orange) and LL'CT (purple) using TheoDORE 2.0 for a three component system (metal, ligand 1 and ligand 2).

7. Understanding Excited State Kinetics in Asymmetric Iron(II) Push-Pull Complexes

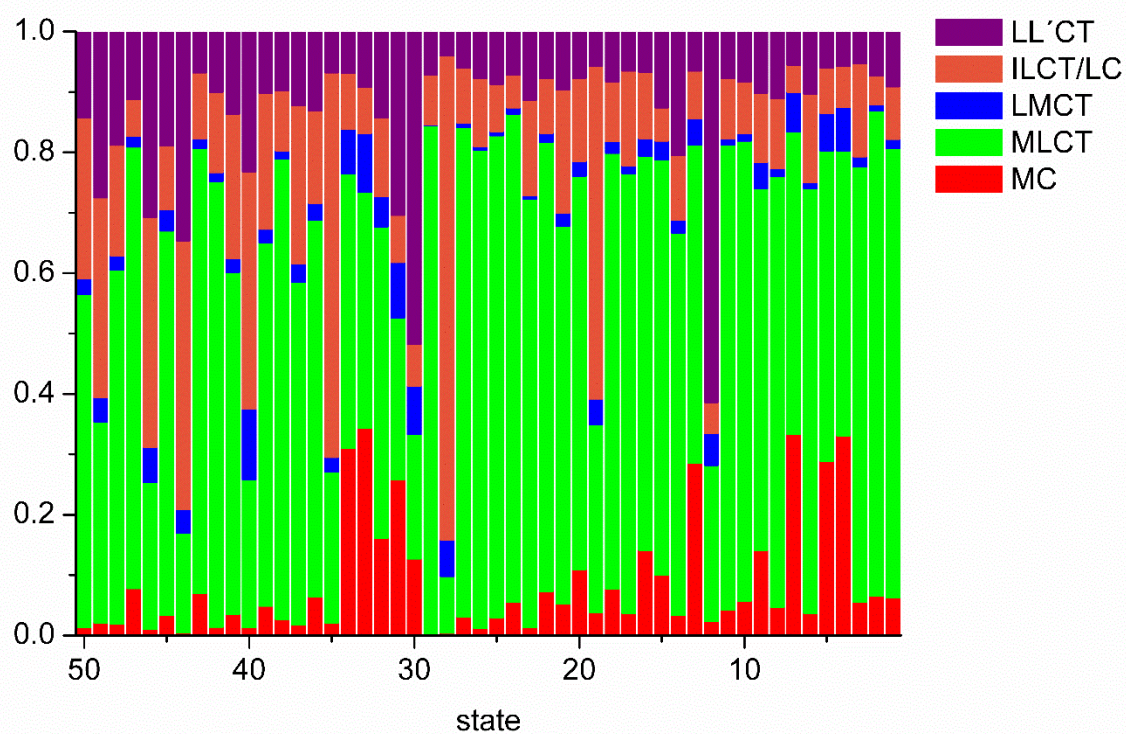
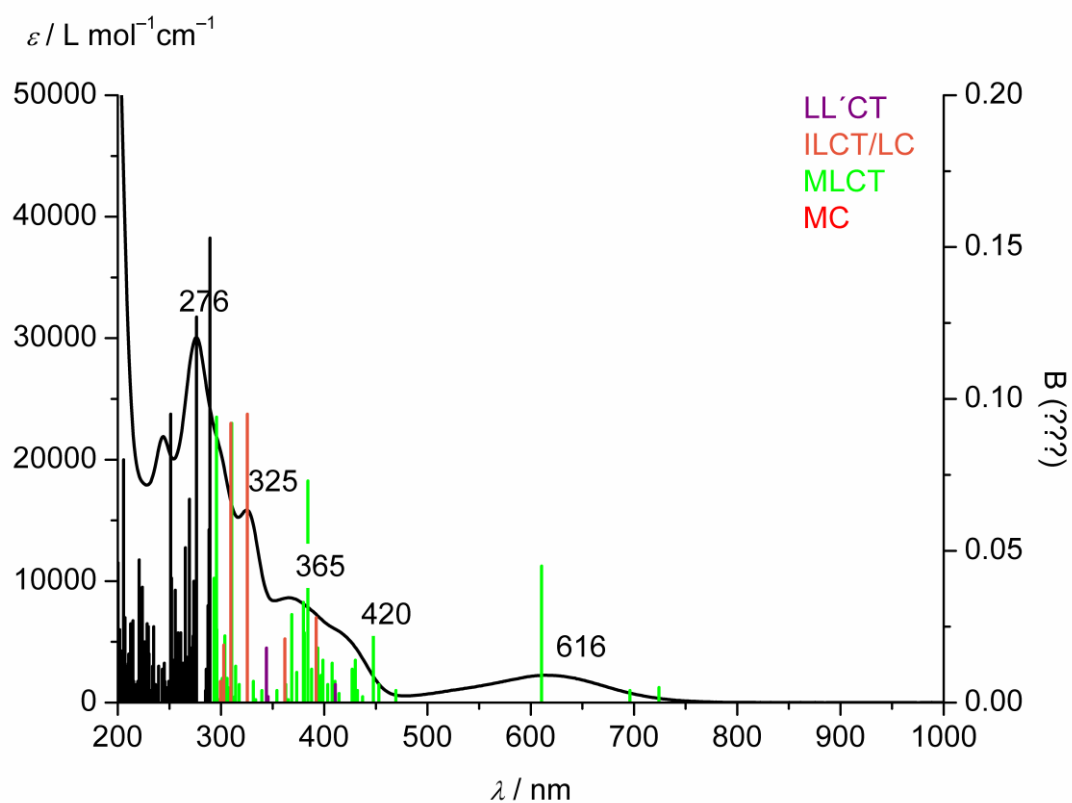


Figure S 25: a) UV/Vis spectrum (black) of $2[\text{PF}_6]_2$ in acetonitrile at 298 K and TDDFT calculated oscillator strength of 2^{2+} (colored tick spectrum, red: MC, green: MLCT, orange: ILCT, purple: LL'CT as mean character, Gaussian16: PCM-LC-BLYP-($\alpha = 0.0$; $\omega = 0.15$)-def2-TZVP. b) decomposition of the charge transfer number matrices into MC (red), MLCT (green), LMCT (blue), ILCT (orange) and LL'CT/LC (purple) using TheoDRE 2.0 for a three component system (metal, ligand 1 and ligand 2).

7. Understanding Excited State Kinetics in Asymmetric Iron(II) Push-Pull Complexes

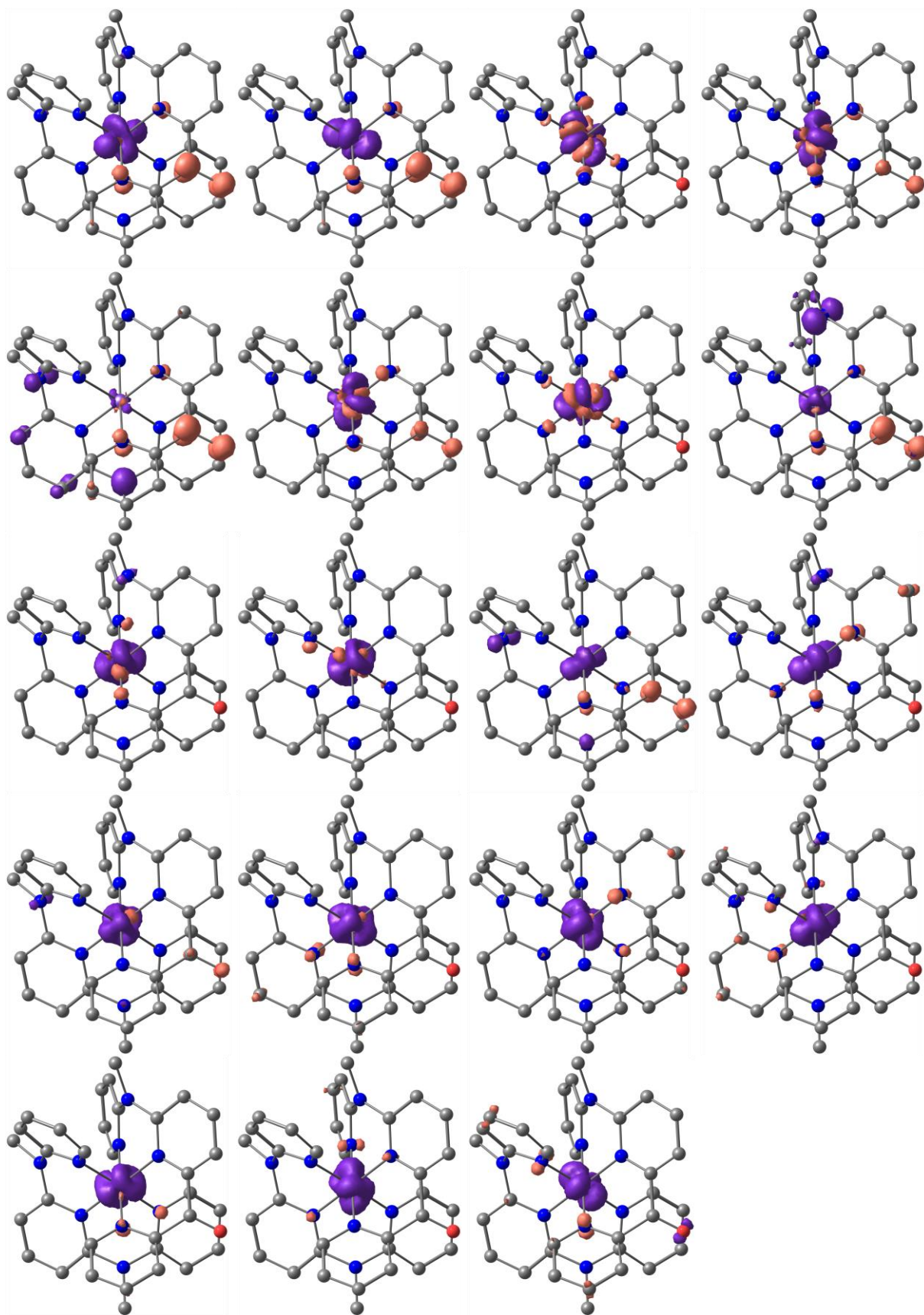


Figure S 26: Difference densities of 19 lowest energy transitions (TD-DFT, Orca 4.1: CPCM(acetonitrile)-RIJCOSX-B3LYP-D3BJ-ZORA/def2-TZVP, contour value of 0.01; 3, 7 MC, 1, 2, 4, 6, 9, 10, 12 – 19 MLCT; 8 ILCT/LC, 5, 11 LL^{CT}) of 2^{2+} .

7. Understanding Excited State Kinetics in Asymmetric Iron(II) Push-Pull Complexes

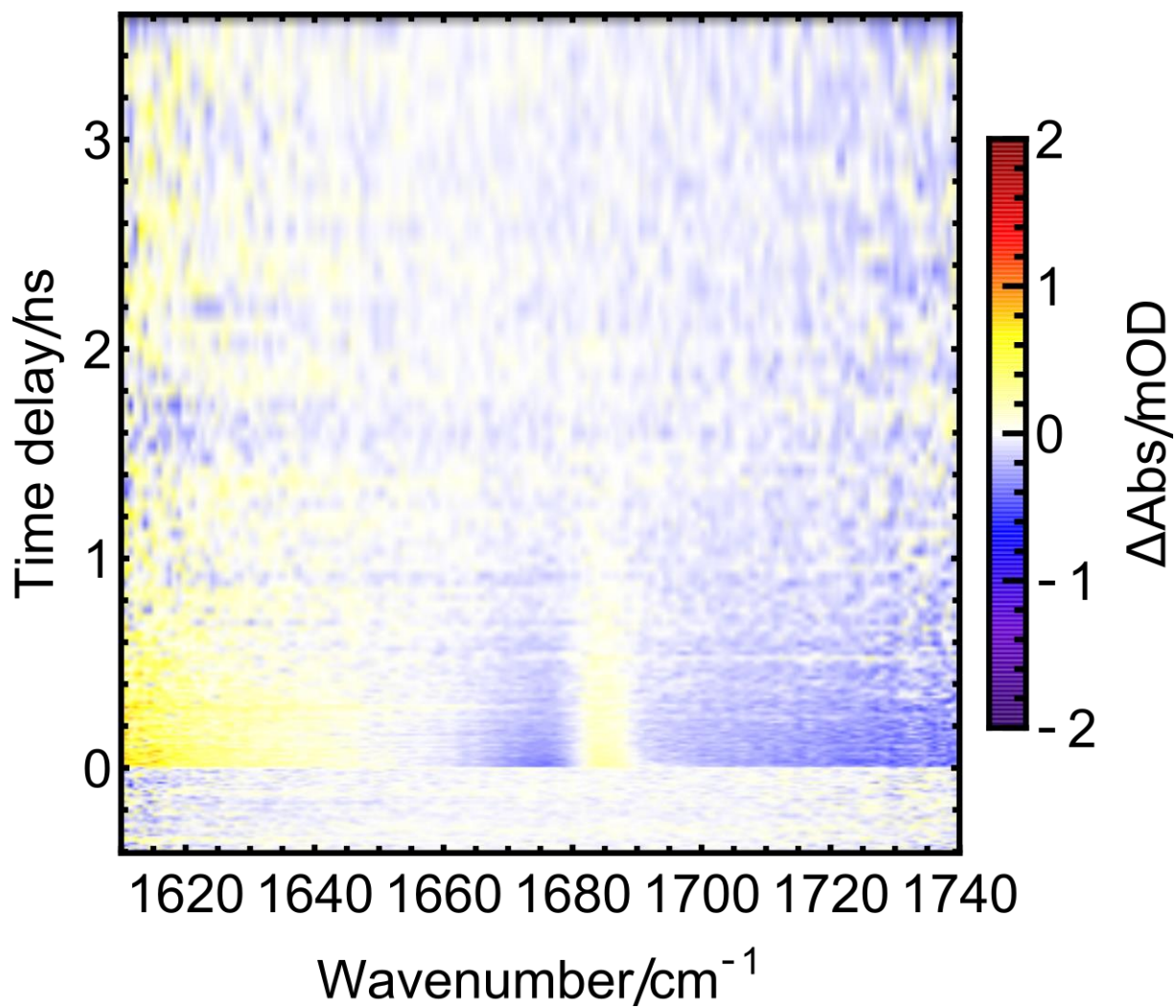


Figure S 27: TA-map for IR transient absorption $1[\text{PF}_6]_2$ in CH_3CN after excitation at 610 nm.

7. Understanding Excited State Kinetics in Asymmetric Iron(II) Push-Pull Complexes

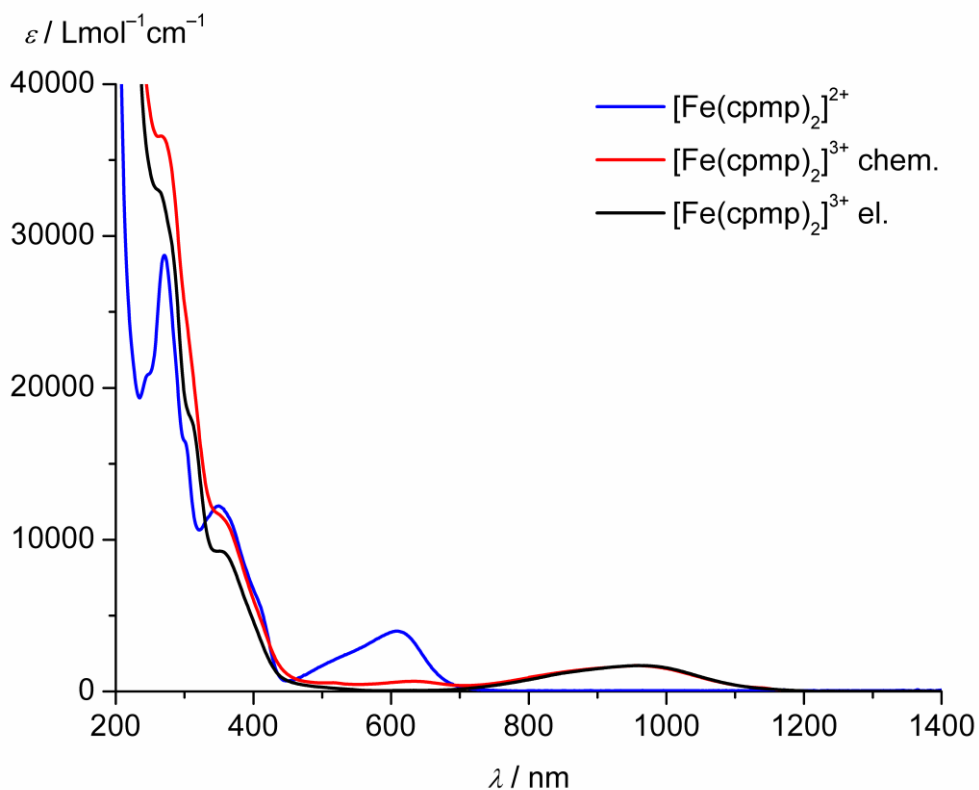


Figure S 28: UV/Vis absorption spectra of **1**[PF₆]₂ (blue), **1**²⁺ oxidized electrochemically to **1**³⁺ (black) and **1**[NO₃]₃ prepared by oxidation with (NH₄)₂[Ce(NO₃)₆] (red). Extinction coefficients of the oxidized species approximately estimated.

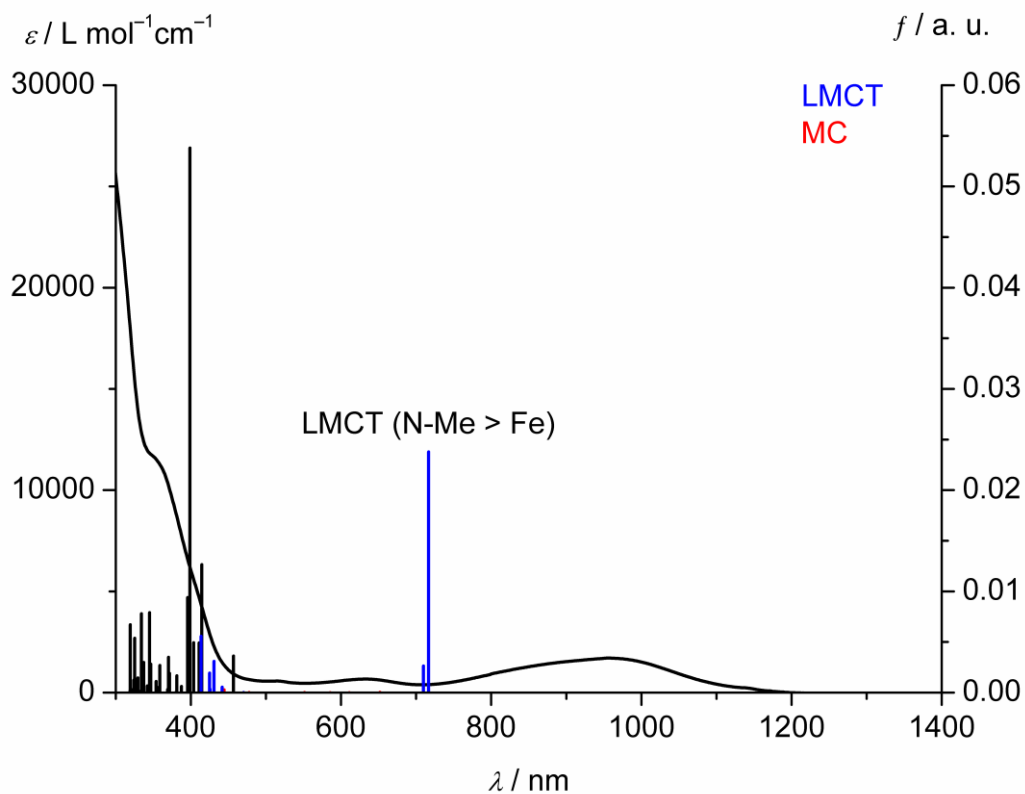


Figure S 29 UV/Vis spectrum (black) of **1**³⁺ in acetonitrile at 298 K and TDDFT calculated oscillator strength of **1**³⁺ (colored tick spectrum, red: MC, blue: LMCT, Orca 4.1: CPCM(acetonitrile)-RIJCOSX-B3LYP-D3BJ-ZORA/def2-TZVP).

7. Understanding Excited State Kinetics in Asymmetric Iron(II) Push-Pull Complexes

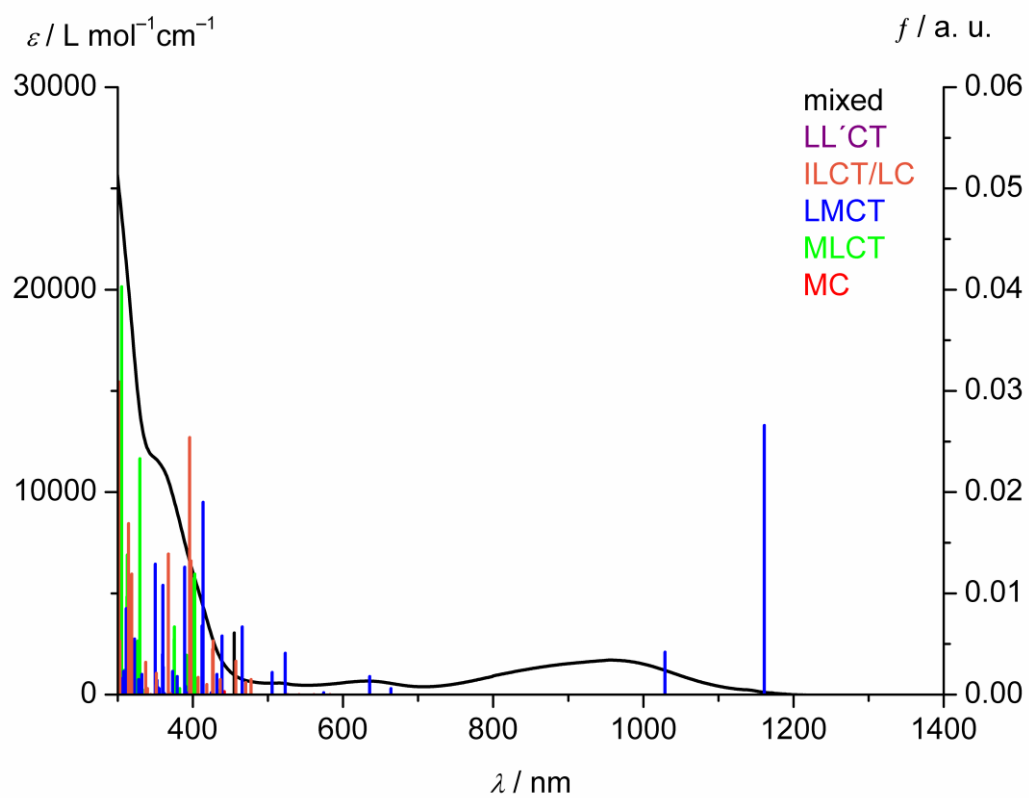


Figure S 30 UV/Vis spectrum (black) of 1^{3+} in acetonitrile at 298 K and TDDFT calculated oscillator strength of 1^{3+} (colored tick spectrum, red: MC, green: MLCT, blue: LMCT, orange: ILCT, purple: LL'CT as mean character, Gaussian16: PCM-LC-BLYP-($\alpha = 0.0$; $\omega = 0.15$)-def2-TZVP.

7. Understanding Excited State Kinetics in Asymmetric Iron(II) Push-Pull Complexes

Electrochemistry

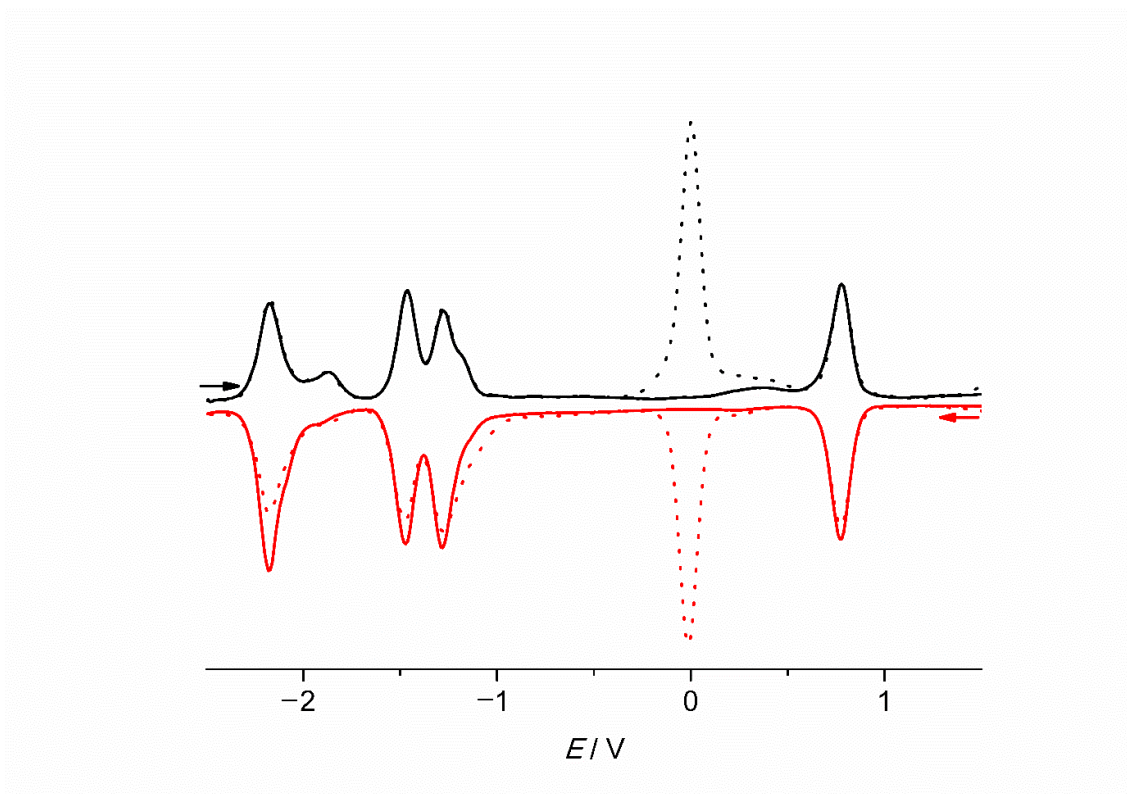


Figure S 31: Square wave voltammogram of $1[PF_6]_2$ with (solid) and without (dotted) Ferrocene, 1 mm in acetonitrile, 0.1 M $[nBu_4N][PF_6]$.

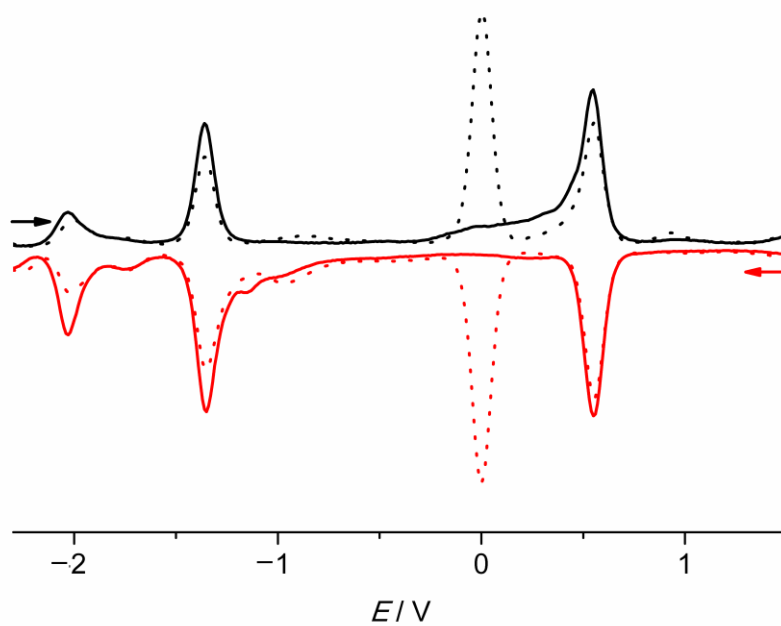


Figure S 32: Square wave voltammogram of $2[PF_6]_2$ with (solid) and without (dotted) Ferrocene, 1 mm in acetonitrile, 0.1 M $[nBu_4N][PF_6]$.

7. Understanding Excited State Kinetics in Asymmetric Iron(II) Push-Pull Complexes

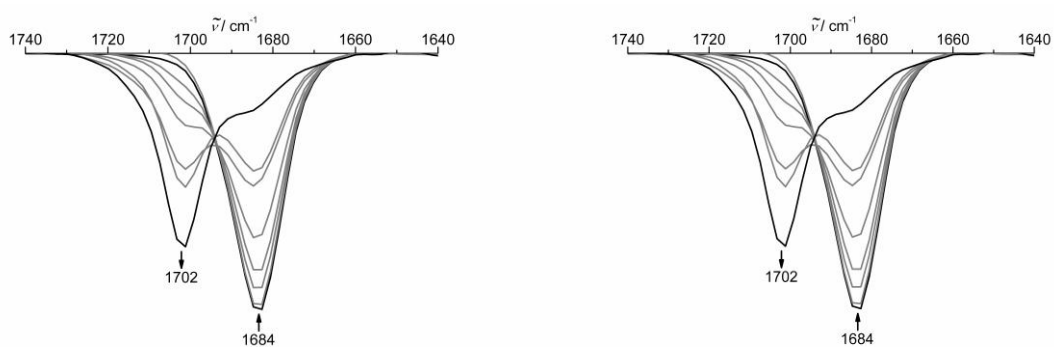


Figure S 33: a) IR spectra during electrochemical oxidation of 1^{2+} to 1^{3+} in acetonitrile with 0.1 M $[\text{tBu}_4\text{N}][\text{PF}_6]$ at 298 K. b) corresponding spectra during the re-reduction of 1^{3+} to 1^{2+} .

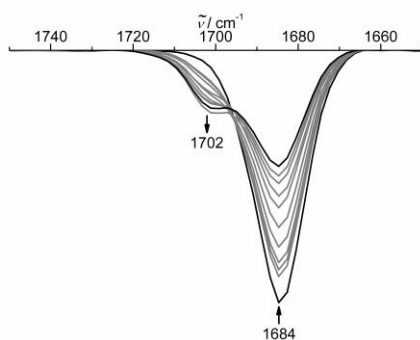


Figure S 34: IR spectra during electrochemical reduction of 1^{2+} to 1^+ in acetonitrile with 0.1 M $[\text{tBu}_4\text{N}][\text{PF}_6]$ at 298 K.

7. Understanding Excited State Kinetics in Asymmetric Iron(II) Push-Pull Complexes

Spin densities

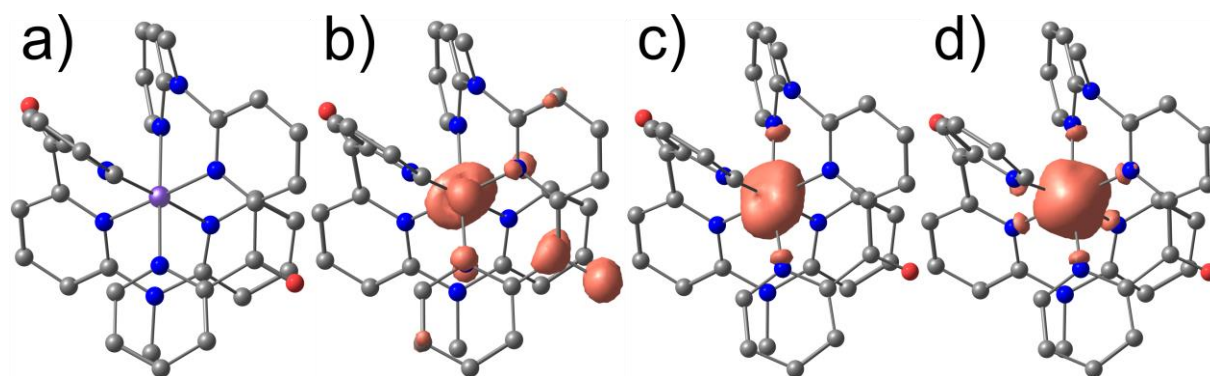


Figure S 35: a) Optimized geometry of ^1GS and spin density of b) $^3\text{MLCT}$ c) ^3MC and d) ^5MC states of 1^{2+} with contour values of 0.05.

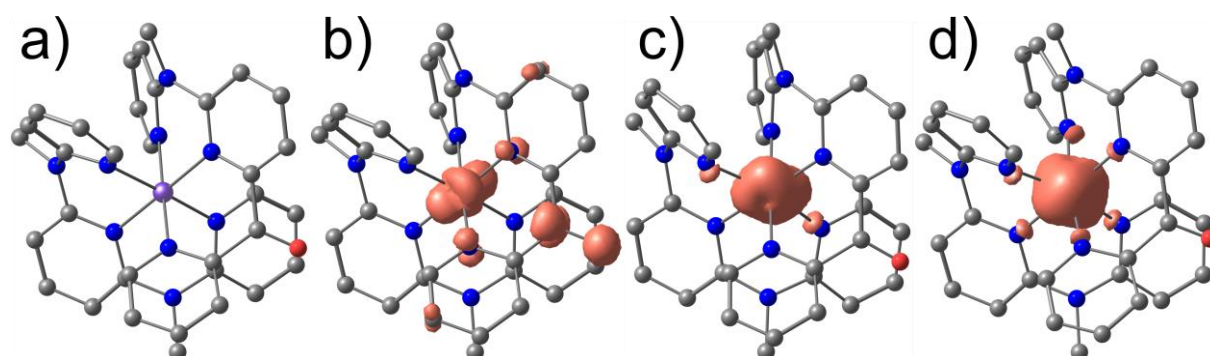


Figure S 36: a) Optimized geometry of ^1GS and spin density of b) $^3\text{MLCT}$ c) ^3MC and d) ^5MC states of 2^{2+} with contour values of 0.05.

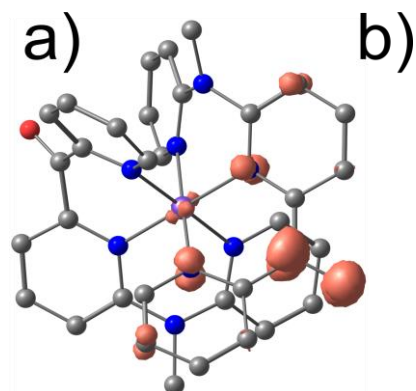


Figure S 37: Spin density of doublet states of a) 1^+ and b) 2^+ contour value of 0.01.

7. Understanding Excited State Kinetics in Asymmetric Iron(II) Push-Pull Complexes

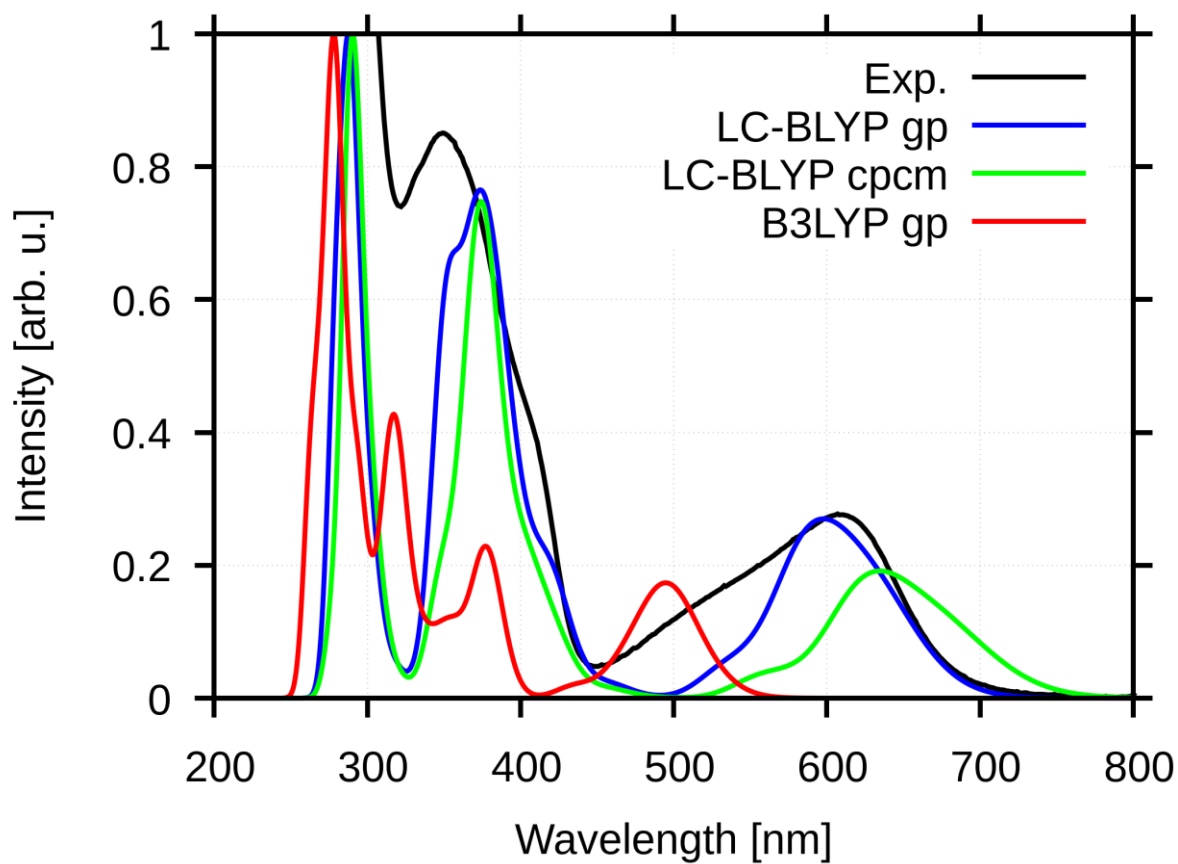


Figure S 38: UV/vis spectrum (black) of $1[PF_6]_2$ in acetonitrile at 298 K and convoluted spectra (FWHM 0.2 eV) from TDDFT ORCA 4.1 calculated oscillator strengths of 1^{2+} using RIJCOSX -LC-BLYP-D3BJ-Zora/def2-TZVP with $\alpha=0$, $\omega=0.14$ in gas phase (blue), RIJCOSX-LC-BLYP-D3BJ-Zora/def2-TZVP with $\alpha=0$, $\omega=0.14$ with CPCM(acetonitrile) solvation (green) and RIJCOSX-B3LYP-D3BJ-Zora/def2-TZVP (red).

7. Understanding Excited State Kinetics in Asymmetric Iron(II) Push-Pull Complexes

DFT-Structures

1^{2+} , 1^1GS

26	9.407642000	6.896781000	13.022421000
8	5.813006000	7.679861000	10.983532000
8	12.947271000	5.948838000	15.152174000
7	9.508700000	6.639473000	15.007761000
7	9.515677000	8.974961000	15.309422000
7	8.260224000	8.468250000	13.367348000
7	9.291587000	7.227859000	11.051880000
7	7.792005000	5.704046000	12.974778000
7	8.821024000	4.411290000	11.304998000
7	10.514217000	5.287246000	12.708952000
7	11.045906000	8.038217000	13.059798000
6	10.132967000	10.094343000	16.028004000
1	10.243120000	10.926308000	15.338019000
1	11.122200000	9.789457000	16.357360000
1	9.550822000	10.418275000	16.892775000
6	9.532801000	5.399975000	15.539702000
1	9.333541000	4.590314000	14.856601000
6	9.827087000	5.151359000	16.858489000
1	9.853519000	4.135100000	17.222802000
6	10.098245000	6.235725000	17.687615000
1	10.349908000	6.088611000	18.729197000
6	10.011931000	7.514204000	17.176234000
1	10.167108000	8.366535000	17.817124000
6	9.679039000	7.692716000	15.828858000
6	8.483619000	9.278689000	14.418758000
6	7.707891000	10.425964000	14.630515000
1	7.912026000	11.064931000	15.474181000
6	6.658855000	10.705738000	13.782072000
1	6.044713000	11.580002000	13.947269000
6	6.385693000	9.832782000	12.735925000
1	5.569911000	10.002507000	12.050134000
6	7.213790000	8.741366000	12.554322000
6	6.952937000	7.897047000	11.342508000
6	8.109739000	7.522364000	10.480045000
6	7.939312000	7.569371000	9.101934000
1	6.963751000	7.798619000	8.699441000
6	9.032998000	7.353628000	8.278523000
1	8.929902000	7.400521000	7.203044000
6	10.262244000	7.093469000	8.868281000
1	11.150922000	6.929491000	8.275882000
6	10.346421000	7.029653000	10.249221000
1	11.282968000	6.798656000	10.731817000
6	6.739126000	5.927464000	13.789712000
1	6.888987000	6.662417000	14.564626000
6	5.524353000	5.303004000	13.635658000
1	4.707781000	5.542994000	14.300587000
6	5.382795000	4.387798000	12.595241000
1	4.439206000	3.889735000	12.418698000
6	6.470861000	4.091773000	11.801012000

7. Understanding Excited State Kinetics in Asymmetric Iron(II) Push-Pull Complexes

1	6.394894000	3.344175000	11.028091000
6	7.685809000	4.742928000	12.037969000
6	10.065355000	4.285049000	11.931269000
6	8.640500000	3.719036000	10.025392000
1	9.555578000	3.824313000	9.449134000
1	7.834630000	4.206198000	9.482982000
1	8.407388000	2.658882000	10.140480000
6	10.817914000	3.123285000	11.728584000
1	10.428241000	2.333454000	11.107145000
6	12.032590000	2.976510000	12.363752000
1	12.615570000	2.076424000	12.226054000
6	12.480072000	3.992764000	13.197246000
1	13.419016000	3.924960000	13.723625000
6	11.700662000	5.126724000	13.338622000
6	12.261367000	6.225193000	14.188464000
6	12.142160000	7.640130000	13.730106000
6	13.216471000	8.488977000	13.969345000
1	14.061820000	8.118463000	14.529198000
6	13.185850000	9.777844000	13.462683000
1	14.011543000	10.455276000	13.631509000
6	12.077459000	10.171339000	12.726505000
1	12.007448000	11.158788000	12.293976000
6	11.034083000	9.279139000	12.552488000
1	10.149830000	9.571103000	12.008693000

7. Understanding Excited State Kinetics in Asymmetric Iron(II) Push-Pull Complexes

 1^{2+} , 1^1 GS (used for TDDFT, SHARC)

26	17.784841000	13.061008000	24.593067000
8	11.008508000	14.611629000	20.721921000
8	24.338354000	11.291023000	28.739391000
7	17.952718000	12.556507000	28.361857000
7	18.001806000	16.970089000	28.931899000
7	15.632683000	16.057783000	25.245909000
7	17.566905000	13.675115000	20.856573000
7	14.726004000	10.800051000	24.489336000
7	16.684373000	8.322322000	21.355944000
7	19.867294000	9.998632000	24.019221000
7	20.899200000	15.218649000	24.659455000
6	19.171819000	19.069953000	30.303993000
1	19.327290000	20.678667000	29.036161000
1	21.067692000	18.509198000	30.863328000
1	18.118350000	19.640224000	31.986397000
6	17.973874000	10.211396000	29.368859000
1	17.594210000	8.688529000	28.069867000
6	18.509613000	9.729310000	31.863469000
1	18.540344000	7.808040000	32.551433000
6	19.030909000	11.770130000	33.437207000
1	19.490161000	11.482505000	35.408200000
6	18.885409000	14.189353000	32.472301000
1	19.170926000	15.792727000	33.696037000
6	18.283756000	14.537907000	29.922647000
6	16.023927000	17.547623000	27.272864000
6	14.499440000	19.659247000	27.737294000
1	14.846845000	20.827990000	29.370879000
6	12.489494000	20.177540000	26.159728000
1	11.274865000	21.779622000	26.529664000
6	12.022475000	18.580502000	24.130207000
1	10.451852000	18.869010000	22.860020000
6	13.640623000	16.568761000	23.726766000
6	13.151348000	14.995520000	21.411833000
6	15.340594000	14.261560000	19.782081000
6	15.005388000	14.337704000	17.176310000
1	13.155671000	14.782908000	16.434223000
6	17.056993000	13.884808000	15.613439000
1	16.856122000	13.958972000	13.580422000
6	19.379482000	13.367231000	16.721823000
1	21.047932000	13.039283000	15.588981000
6	19.548574000	13.261500000	19.329132000
1	21.313940000	12.808964000	20.243741000
6	12.721202000	11.242752000	26.006024000
1	12.997590000	12.657311000	27.446034000
6	10.431211000	10.048474000	25.736411000
1	8.881172000	10.510507000	26.981244000
6	10.177063000	8.271165000	23.815637000
1	8.402734000	7.301979000	23.514727000
6	12.244808000	7.697705000	22.332147000
1	12.107649000	6.244269000	20.911220000
6	14.530128000	8.958045000	22.745981000

7. Understanding Excited State Kinetics in Asymmetric Iron(II) Push-Pull Complexes

6	19.043921000	8.102769000	22.532978000
6	16.330034000	7.008223000	18.945339000
1	18.049454000	7.194867000	17.836895000
1	14.802871000	7.924147000	17.920092000
1	15.884083000	5.003063000	19.158614000
6	20.504348000	5.931967000	22.144181000
1	19.807809000	4.437179000	20.945897000
6	22.783986000	5.665952000	23.381224000
1	23.903772000	3.974744000	23.127005000
6	23.585607000	7.575802000	24.992745000
1	25.333442000	7.452252000	26.038214000
6	22.094975000	9.708269000	25.239510000
6	23.123054000	11.793250000	26.872292000
6	22.955812000	14.457539000	25.942696000
6	25.023491000	16.025639000	26.358622000
1	26.600322000	15.308306000	27.439810000
6	25.018307000	18.439167000	25.343373000
1	26.612018000	19.689924000	25.616355000
6	22.931084000	19.198810000	23.944738000
1	22.847315000	21.049305000	23.082585000
6	20.919084000	17.551789000	23.664694000
1	19.248206000	18.108365000	22.636849000

7. Understanding Excited State Kinetics in Asymmetric Iron(II) Push-Pull Complexes

 1^{2+} , $3MLCT$

6	1.573889000	-2.510143000	-0.116770000
6	1.742317000	-3.901804000	-0.045049000
6	0.641854000	-4.714645000	0.081253000
6	-0.626833000	-4.141918000	0.155745000
6	-0.730590000	-2.769933000	0.140330000
7	0.350839000	-1.958308000	0.023885000
1	2.726371000	-4.328709000	-0.147782000
1	-1.517645000	-4.742805000	0.253614000
6	1.426604000	1.024056000	-2.316183000
6	2.446109000	1.288073000	-3.194980000
6	3.631302000	0.567149000	-3.066343000
6	3.724173000	-0.414790000	-2.103907000
6	2.634752000	-0.653936000	-1.259496000
7	1.524006000	0.098558000	-1.335162000
1	4.465756000	0.751918000	-3.729064000
1	0.501181000	1.571907000	-2.363835000
1	2.318535000	2.049088000	-3.950197000
1	4.612374000	-1.019587000	-2.029581000
6	-2.261068000	-1.108313000	1.362949000
6	-3.368281000	-1.126464000	2.199428000
6	-3.471283000	-0.171495000	3.200315000
6	-2.453864000	0.759728000	3.337430000
6	-1.386380000	0.729264000	2.456387000
7	-1.299064000	-0.177240000	1.473067000
1	-4.323334000	-0.163214000	3.865723000
1	-4.115763000	-1.894586000	2.068659000
1	-2.476534000	1.512458000	4.112093000
1	-0.591497000	1.454171000	2.527281000
6	1.002864000	2.761879000	0.231751000
6	0.864556000	4.150773000	0.132000000
6	-0.379981000	4.706042000	-0.056675000
6	-1.491491000	3.876768000	-0.179985000
6	-1.311048000	2.503289000	-0.147525000
7	-0.089972000	1.949694000	0.061364000
1	1.748142000	4.756428000	0.256045000
1	-2.468629000	4.290433000	-0.366435000
6	1.512478000	-0.807235000	2.466894000
6	2.575481000	-0.945355000	3.323287000
6	3.654529000	-0.058317000	3.195645000
6	3.583909000	0.948469000	2.265104000
6	2.447117000	1.079396000	1.441395000
7	1.456827000	0.147143000	1.512175000
1	4.522340000	-0.155819000	3.834353000
1	0.678607000	-1.489171000	2.519152000
1	2.568217000	-1.732313000	4.062915000
1	4.370433000	1.679915000	2.159038000
6	-2.377691000	0.659743000	-1.301833000
6	-3.459133000	0.420822000	-2.157862000
6	-3.339330000	-0.530451000	-3.147609000
6	-2.136981000	-1.220805000	-3.294509000
6	-1.129670000	-0.967490000	-2.398577000

7. Understanding Excited State Kinetics in Asymmetric Iron(II) Push-Pull Complexes

7	-1.256563000	-0.079880000	-1.385586000
1	-4.166423000	-0.714860000	-3.819651000
1	-4.361125000	1.003168000	-2.067575000
1	-1.988535000	-1.952064000	-4.074840000
1	-0.193632000	-1.497574000	-2.456714000
7	2.675536000	-1.700336000	-0.343582000
6	-2.104120000	-2.203742000	0.361179000
8	-3.071301000	-2.738771000	-0.134787000
1	0.760945000	-5.789167000	0.102173000
1	-0.500884000	5.779581000	-0.115843000
26	0.124829000	0.004871000	0.071287000
7	-2.419465000	1.664702000	-0.351400000
6	2.326384000	2.252606000	0.593877000
8	3.343305000	2.962869000	0.354631000
6	-3.737465000	2.168514000	0.050234000
1	-4.180266000	2.836011000	-0.690348000
1	-4.395679000	1.317189000	0.204675000
1	-3.630390000	2.698244000	0.992169000
6	3.997920000	-2.199458000	0.061623000
1	3.893165000	-2.726985000	1.004328000
1	4.441785000	-2.861291000	-0.682516000
1	4.646169000	-1.342714000	0.222287000

7. Understanding Excited State Kinetics in Asymmetric Iron(II) Push-Pull Complexes

 1^{2+} , 3MC

6	1.565160000	-2.647899000	-0.105927000
6	1.739423000	-4.038110000	-0.069604000
6	0.632625000	-4.854846000	0.027142000
6	-0.635996000	-4.288063000	0.103773000
6	-0.734242000	-2.910788000	0.125624000
7	0.344746000	-2.106447000	0.033298000
1	2.725099000	-4.464669000	-0.163953000
1	-1.527110000	-4.892343000	0.175249000
6	1.499650000	0.906809000	-2.318917000
6	2.551369000	1.162614000	-3.166616000
6	3.722485000	0.430033000	-3.000053000
6	3.770546000	-0.555366000	-2.034271000
6	2.654206000	-0.776267000	-1.221602000
7	1.551952000	-0.011051000	-1.329989000
1	4.582153000	0.608064000	-3.631827000
1	0.579329000	1.461971000	-2.395080000
1	2.458195000	1.926454000	-3.924413000
1	4.650962000	-1.167518000	-1.927733000
6	-2.266369000	-1.210810000	1.324853000
6	-3.392248000	-1.228463000	2.140504000
6	-3.524669000	-0.266739000	3.130083000
6	-2.515917000	0.673686000	3.276749000
6	-1.431873000	0.640605000	2.416141000
7	-1.311193000	-0.269186000	1.437956000
1	-4.389904000	-0.259227000	3.778494000
1	-4.132662000	-2.002026000	2.001498000
1	-2.560902000	1.433968000	4.043556000
1	-0.641751000	1.370200000	2.497319000
6	0.924332000	2.800172000	0.243151000
6	0.805520000	4.177121000	0.292854000
6	-0.456032000	4.740758000	0.135551000
6	-1.534888000	3.917206000	-0.094782000
6	-1.345390000	2.529878000	-0.167153000
7	-0.131939000	1.983206000	0.030998000
1	1.679149000	4.784707000	0.472956000
1	-2.514584000	4.337171000	-0.256798000
6	1.761796000	-0.682040000	2.604803000
6	2.899726000	-0.745551000	3.396464000
6	3.894613000	0.204017000	3.213406000
6	3.713698000	1.187326000	2.250334000
6	2.539391000	1.183055000	1.504808000
7	1.585937000	0.257972000	1.674610000
1	4.795645000	0.181432000	3.810979000
1	0.971408000	-1.413654000	2.710027000
1	2.996426000	-1.525455000	4.138624000
1	4.454199000	1.954875000	2.080930000
6	-2.462295000	0.736378000	-1.424828000
6	-3.574503000	0.580591000	-2.261177000
6	-3.527974000	-0.369365000	-3.263683000
6	-2.376497000	-1.133747000	-3.436113000
6	-1.331265000	-0.928447000	-2.562833000

7. Understanding Excited State Kinetics in Asymmetric Iron(II) Push-Pull Complexes

7	-1.381787000	-0.040451000	-1.556375000
1	-4.377618000	-0.498074000	-3.921043000
1	-4.442425000	1.210552000	-2.150598000
1	-2.295592000	-1.873078000	-4.219489000
1	-0.417435000	-1.501717000	-2.641665000
7	2.665435000	-1.805423000	-0.275381000
6	-2.100924000	-2.321996000	0.336991000
8	-3.070995000	-2.853916000	-0.162851000
1	0.753218000	-5.929712000	0.026283000
1	-0.588800000	5.813475000	0.175485000
26	0.108410000	-0.102124000	0.049544000
7	-2.455060000	1.711123000	-0.421099000
6	2.314177000	2.262889000	0.493195000
8	3.261012000	2.816104000	-0.028569000
6	-3.758094000	2.192531000	0.051030000
1	-4.226587000	2.905953000	-0.629032000
1	-4.413802000	1.334072000	0.173584000
1	-3.625102000	2.661602000	1.021859000
6	3.969513000	-2.296390000	0.181705000
1	3.830621000	-2.820215000	1.123387000
1	4.450014000	-2.964780000	-0.534784000
1	4.613731000	-1.439561000	0.360386000

7. Understanding Excited State Kinetics in Asymmetric Iron(II) Push-Pull Complexes

 1^{2+} , 5MC

6	1.604173000	-2.682507000	-0.157772000
6	1.799152000	-4.070196000	-0.099616000
6	0.711309000	-4.897198000	0.080503000
6	-0.558655000	-4.342256000	0.208951000
6	-0.673730000	-2.964650000	0.181083000
7	0.385761000	-2.150388000	0.010070000
1	2.784367000	-4.488081000	-0.230646000
1	-1.435023000	-4.956275000	0.349946000
6	1.651023000	0.866461000	-2.471061000
6	2.740717000	1.119882000	-3.271572000
6	3.890873000	0.363115000	-3.060668000
6	3.894083000	-0.625219000	-2.095772000
6	2.739863000	-0.833678000	-1.329252000
7	1.655263000	-0.064319000	-1.499778000
1	4.776981000	0.531450000	-3.657942000
1	0.735634000	1.432050000	-2.575253000
1	2.696711000	1.891978000	-4.025495000
1	4.765854000	-1.243634000	-1.958057000
6	-2.305403000	-1.307762000	1.390642000
6	-3.502281000	-1.319276000	2.098995000
6	-3.723649000	-0.339611000	3.057242000
6	-2.744989000	0.618875000	3.275857000
6	-1.585471000	0.571049000	2.516756000
7	-1.369558000	-0.368205000	1.592771000
1	-4.644428000	-0.327313000	3.624118000
1	-4.231183000	-2.091737000	1.904842000
1	-2.873531000	1.396565000	4.015346000
1	-0.807899000	1.312908000	2.640051000
6	0.924849000	2.916273000	0.242388000
6	0.818996000	4.294517000	0.277711000
6	-0.444234000	4.859606000	0.127594000
6	-1.534142000	4.041658000	-0.079558000
6	-1.347789000	2.653152000	-0.142212000
7	-0.136714000	2.110944000	0.044682000
1	1.696580000	4.901222000	0.441219000
1	-2.513608000	4.467635000	-0.228194000
6	1.764604000	-0.657575000	2.552795000
6	2.893823000	-0.706008000	3.355835000
6	3.871898000	0.263683000	3.189520000
6	3.681347000	1.252192000	2.233978000
6	2.514005000	1.238564000	1.477264000
7	1.578355000	0.290027000	1.630511000
1	4.768293000	0.253080000	3.794410000
1	0.988028000	-1.405524000	2.639835000
1	2.998988000	-1.491709000	4.090540000
1	4.410053000	2.033802000	2.079774000
6	-2.475081000	0.831629000	-1.361207000
6	-3.612356000	0.654761000	-2.159912000
6	-3.598982000	-0.314152000	-3.144345000
6	-2.454914000	-1.083701000	-3.340438000
6	-1.382277000	-0.861694000	-2.507752000

7. Understanding Excited State Kinetics in Asymmetric Iron(II) Push-Pull Complexes

7	-1.397084000	0.050455000	-1.519459000
1	-4.471536000	-0.456613000	-3.767853000
1	-4.478360000	1.283695000	-2.033049000
1	-2.402069000	-1.841612000	-4.108083000
1	-0.472669000	-1.438542000	-2.600866000
7	2.709156000	-1.840909000	-0.358211000
6	-2.057731000	-2.402449000	0.392699000
8	-2.999964000	-2.943220000	-0.150280000
1	0.845484000	-5.970287000	0.106592000
1	-0.571238000	5.933439000	0.158061000
26	0.120820000	-0.020462000	0.021135000
7	-2.454464000	1.819848000	-0.369730000
6	2.299437000	2.340613000	0.479307000
8	3.258638000	2.874897000	-0.039789000
6	-3.750577000	2.301274000	0.122162000
1	-4.235316000	3.004086000	-0.557648000
1	-4.400716000	1.443146000	0.272929000
1	-3.597421000	2.785012000	1.082791000
6	3.999502000	-2.315351000	0.155802000
1	3.829689000	-2.817765000	1.103966000
1	4.508874000	-2.999012000	-0.525596000
1	4.635250000	-1.452296000	0.337040000

7. Understanding Excited State Kinetics in Asymmetric Iron(II) Push-Pull Complexes

 1^{3+} , $2^{1}MC$

6	1.543690000	-2.529956000	-0.164428000
6	1.706064000	-3.921088000	-0.161297000
6	0.604630000	-4.738243000	-0.017402000
6	-0.649768000	-4.160354000	0.129279000
6	-0.740648000	-2.779871000	0.161121000
7	0.333965000	-1.969138000	0.032768000
1	2.683593000	-4.348731000	-0.316429000
1	-1.542879000	-4.755583000	0.241091000
6	1.453606000	1.057794000	-2.294646000
6	2.470969000	1.317822000	-3.184459000
6	3.636377000	0.564080000	-3.086950000
6	3.710599000	-0.439949000	-2.142324000
6	2.624537000	-0.659239000	-1.286275000
7	1.530867000	0.117490000	-1.332909000
1	4.467942000	0.738765000	-3.756430000
1	0.539427000	1.628013000	-2.321325000
1	2.354522000	2.096953000	-3.923297000
1	4.583002000	-1.070510000	-2.088394000
6	-2.239158000	-1.101940000	1.423697000
6	-3.339099000	-1.117839000	2.276940000
6	-3.435491000	-0.157202000	3.270072000
6	-2.418475000	0.781237000	3.381669000
6	-1.364300000	0.745290000	2.486160000
7	-1.279305000	-0.164251000	1.502762000
1	-4.277499000	-0.147096000	3.948164000
1	-4.085497000	-1.889421000	2.160868000
1	-2.436414000	1.541738000	4.149249000
1	-0.571280000	1.473979000	2.534738000
6	0.975326000	2.782981000	0.276993000
6	0.839492000	4.173842000	0.118582000
6	-0.394964000	4.718644000	-0.141329000
6	-1.498465000	3.878136000	-0.276172000
6	-1.306226000	2.506325000	-0.176676000
7	-0.103603000	1.959649000	0.091863000
1	1.717947000	4.785619000	0.249024000
1	-2.471871000	4.278149000	-0.509715000
6	1.567315000	-0.842354000	2.473878000
6	2.621580000	-0.961762000	3.352891000
6	3.654739000	-0.020363000	3.276242000
6	3.549509000	1.007008000	2.369676000
6	2.422359000	1.102324000	1.522795000
7	1.474837000	0.126826000	1.546301000
1	4.513917000	-0.090757000	3.930722000
1	0.767519000	-1.567196000	2.486719000
1	2.641127000	-1.774472000	4.064414000
1	4.301424000	1.777683000	2.298072000
6	-2.366972000	0.646418000	-1.325784000
6	-3.439883000	0.422163000	-2.198945000
6	-3.322222000	-0.536430000	-3.184002000
6	-2.129074000	-1.244682000	-3.306081000
6	-1.131422000	-0.995353000	-2.392856000

7. Understanding Excited State Kinetics in Asymmetric Iron(II) Push-Pull Complexes

7	-1.251292000	-0.104845000	-1.386298000
1	-4.141566000	-0.710690000	-3.868511000
1	-4.334245000	1.019341000	-2.126577000
1	-1.978816000	-1.982846000	-4.079961000
1	-0.199800000	-1.536473000	-2.435063000
7	2.654669000	-1.710684000	-0.370011000
6	-2.102398000	-2.207003000	0.430448000
8	-3.089040000	-2.753659000	-0.024791000
1	0.718565000	-5.813341000	-0.037523000
1	-0.515385000	5.789012000	-0.247773000
26	0.115623000	-0.006465000	0.090190000
7	-2.415846000	1.651221000	-0.371986000
6	2.287536000	2.289221000	0.688920000
8	3.302046000	3.033875000	0.507906000
6	-3.732384000	2.152380000	0.019340000
1	-4.185853000	2.809403000	-0.726647000
1	-4.389580000	1.301715000	0.186244000
1	-3.630258000	2.697071000	0.953922000
6	3.965276000	-2.218367000	0.039606000
1	3.850654000	-2.757232000	0.975985000
1	4.422740000	-2.876798000	-0.702036000
1	4.619482000	-1.368212000	0.215819000

7. Understanding Excited State Kinetics in Asymmetric Iron(II) Push-Pull Complexes

 $2^{2+}, 1GS$

6	1.423123000	-2.500659000	-0.251653000
6	1.589922000	-3.880525000	-0.298565000
6	0.480097000	-4.690965000	-0.145131000
6	-0.760670000	-4.121636000	0.074925000
6	-0.862056000	-2.734210000	0.144404000
7	0.214104000	-1.935417000	-0.033692000
1	2.561032000	-4.305416000	-0.492651000
1	-1.627264000	-4.741198000	0.234739000
6	1.352623000	1.077813000	-2.402233000
6	2.363893000	1.310205000	-3.304383000
6	3.524517000	0.547792000	-3.202500000
6	3.598278000	-0.441066000	-2.242774000
6	2.517661000	-0.637726000	-1.374813000
7	1.431415000	0.154213000	-1.420682000
1	4.351599000	0.704396000	-3.882015000
1	0.443628000	1.656201000	-2.434540000
1	2.248035000	2.076578000	-4.056676000
1	4.466582000	-1.076880000	-2.183137000
6	-2.275558000	-1.150379000	1.359576000
6	-3.382166000	-1.173476000	2.219823000
6	-3.520948000	-0.184086000	3.172088000
6	-2.539475000	0.796596000	3.280623000
6	-1.479926000	0.754978000	2.403711000
7	-1.365351000	-0.166015000	1.426837000
1	-4.372463000	-0.192943000	3.839164000
1	-4.104115000	-1.971633000	2.161363000
1	-2.594046000	1.577399000	4.025212000
1	-0.697372000	1.496023000	2.451454000
6	0.895679000	2.800113000	0.190011000
6	0.809114000	4.180865000	0.186425000
6	-0.439669000	4.766457000	0.019611000
6	-1.539564000	3.956583000	-0.168108000
6	-1.381778000	2.565712000	-0.189273000
7	-0.178422000	1.996803000	0.018885000
1	1.700220000	4.771025000	0.335353000
1	-2.512518000	4.389208000	-0.339051000
6	1.456589000	-0.792558000	2.430181000
6	2.493295000	-0.858321000	3.344517000
6	3.517552000	0.075314000	3.274378000
6	3.442491000	1.062650000	2.305507000
6	2.359564000	1.074276000	1.431654000
7	1.393154000	0.140019000	1.467519000
1	4.348389000	0.042282000	3.965754000
1	0.658805000	-1.517663000	2.453135000
1	2.490502000	-1.637763000	4.093256000
1	4.192477000	1.835528000	2.225976000
6	-2.463276000	0.729108000	-1.365827000
6	-3.568137000	0.489753000	-2.192346000
6	-3.487296000	-0.489653000	-3.161945000
6	-2.298386000	-1.196334000	-3.316744000
6	-1.265577000	-0.924897000	-2.448291000

7. Understanding Excited State Kinetics in Asymmetric Iron(II) Push-Pull Complexes

7	-1.350518000	-0.016884000	-1.457625000
1	-4.336641000	-0.685616000	-3.802568000
1	-4.462068000	1.083941000	-2.095969000
1	-2.177426000	-1.951820000	-4.079155000
1	-0.335063000	-1.465585000	-2.514448000
7	2.537417000	-1.668679000	-0.439586000
7	-2.109202000	-2.147969000	0.397939000
6	3.845131000	-2.189805000	-0.034200000
1	4.289484000	-2.861375000	-0.771822000
1	4.513423000	-1.347313000	0.127463000
1	3.728074000	-2.720974000	0.906547000
6	-3.301114000	-2.899486000	-0.000740000
1	-3.593710000	-3.658532000	0.727818000
1	-4.120178000	-2.196508000	-0.132825000
1	-3.103273000	-3.379525000	-0.955055000
1	0.581460000	-5.766568000	-0.202914000
1	-0.549560000	5.842336000	0.018079000
26	0.029428000	0.035523000	0.005365000
7	-2.494938000	1.754072000	-0.423031000
6	2.247913000	2.212045000	0.472062000
8	3.247302000	2.764977000	0.055957000
6	-3.804273000	2.251959000	0.004318000
1	-4.269337000	2.915880000	-0.726765000
1	-4.455072000	1.398517000	0.179961000
1	-3.682639000	2.784313000	0.943294000

7. Understanding Excited State Kinetics in Asymmetric Iron(II) Push-Pull Complexes

 2^{2+} , 3^{3MLCT}

6	1.411919000	-2.499934000	-0.227815000
6	1.553738000	-3.881619000	-0.253269000
6	0.428781000	-4.674318000	-0.123584000
6	-0.809615000	-4.091322000	0.069194000
6	-0.897116000	-2.706134000	0.137568000
7	0.198323000	-1.920710000	-0.030002000
1	2.519512000	-4.323484000	-0.432351000
1	-1.685483000	-4.699822000	0.217707000
6	1.364496000	1.078254000	-2.355316000
6	2.397541000	1.342017000	-3.219957000
6	3.566954000	0.595866000	-3.095640000
6	3.631692000	-0.409008000	-2.153824000
6	2.530208000	-0.642080000	-1.322039000
7	1.436386000	0.132749000	-1.393588000
1	4.411739000	0.780127000	-3.745456000
1	0.448658000	1.643109000	-2.400634000
1	2.292005000	2.121503000	-3.959656000
1	4.508459000	-1.030851000	-2.081780000
6	-2.288430000	-1.111200000	1.343529000
6	-3.402077000	-1.095255000	2.193728000
6	-3.498992000	-0.116008000	3.159210000
6	-2.476120000	0.821034000	3.291730000
6	-1.417676000	0.756729000	2.420772000
7	-1.345253000	-0.159518000	1.429915000
1	-4.352035000	-0.098920000	3.823846000
1	-4.156237000	-1.861104000	2.119855000
1	-2.500623000	1.587281000	4.052245000
1	-0.605807000	1.462820000	2.478197000
6	0.896384000	2.802757000	0.194492000
6	0.747227000	4.192382000	0.101644000
6	-0.501084000	4.740753000	-0.077127000
6	-1.608588000	3.905276000	-0.199163000
6	-1.418315000	2.532336000	-0.174490000
7	-0.193422000	1.983665000	0.025912000
1	1.627772000	4.802960000	0.222444000
1	-2.588959000	4.313203000	-0.381670000
6	1.475357000	-0.789322000	2.381691000
6	2.545610000	-0.919208000	3.232892000
6	3.605119000	-0.010322000	3.114643000
6	3.509780000	1.006090000	2.196465000
6	2.367577000	1.123158000	1.377349000
7	1.395740000	0.175196000	1.441915000
1	4.477334000	-0.098455000	3.748800000
1	0.657498000	-1.490489000	2.427497000
1	2.556846000	-1.718230000	3.959644000
1	4.280386000	1.755099000	2.096536000
6	-2.480416000	0.680277000	-1.322243000
6	-3.583752000	0.395604000	-2.138952000
6	-3.466416000	-0.562153000	-3.122165000
6	-2.247523000	-1.215664000	-3.302997000
6	-1.219813000	-0.918057000	-2.444293000

7. Understanding Excited State Kinetics in Asymmetric Iron(II) Push-Pull Complexes

7	-1.340045000	-0.023251000	-1.439247000
1	-4.310159000	-0.782119000	-3.762069000
1	-4.501743000	0.947171000	-2.024444000
1	-2.102828000	-1.951367000	-4.079854000
1	-0.269684000	-1.418910000	-2.526374000
7	2.534977000	-1.694291000	-0.414737000
7	-2.135903000	-2.110669000	0.389246000
6	3.837865000	-2.244794000	-0.021347000
1	4.267015000	-2.899371000	-0.781385000
1	4.514287000	-1.415359000	0.166896000
1	3.710686000	-2.798635000	0.903774000
6	-3.337889000	-2.857440000	-0.002609000
1	-3.627386000	-3.606789000	0.735046000
1	-4.150699000	-2.148474000	-0.135429000
1	-3.144845000	-3.342962000	-0.954438000
1	0.518737000	-5.751315000	-0.166427000
1	-0.628711000	5.813888000	-0.130923000
26	0.023693000	0.038606000	0.015267000
7	-2.524726000	1.692863000	-0.383403000
6	2.225707000	2.303988000	0.540789000
8	3.233067000	3.031201000	0.306216000
6	-3.842513000	2.186615000	0.029737000
1	-4.302513000	2.837293000	-0.715484000
1	-4.488910000	1.330982000	0.209418000
1	-3.728210000	2.731106000	0.961782000

7. Understanding Excited State Kinetics in Asymmetric Iron(II) Push-Pull Complexes

 $2^{2+}, {}^3MC$

6	-1.529828000	-2.527937000	0.175751000
6	-1.753938000	-3.902183000	0.157513000
6	-0.677995000	-4.752987000	-0.013828000
6	0.591646000	-4.228188000	-0.169594000
6	0.756163000	-2.845401000	-0.152222000
7	-0.291609000	-2.009954000	0.019799000
1	-2.746195000	-4.295741000	0.306235000
1	1.437950000	-4.875260000	-0.334232000
6	-1.574905000	0.990839000	2.485072000
6	-2.662130000	1.239593000	3.293568000
6	-3.818457000	0.494352000	3.074894000
6	-3.830189000	-0.479177000	2.093966000
6	-2.677398000	-0.677937000	1.322928000
7	-1.589827000	0.080592000	1.498200000
1	-4.700497000	0.658085000	3.679611000
1	-0.654517000	1.547216000	2.600719000
1	-2.609843000	1.996876000	4.062177000
1	-4.704072000	-1.093586000	1.948705000
6	2.400521000	-1.341948000	-1.214464000
6	3.693414000	-1.270740000	-1.757326000
6	3.975158000	-0.285076000	-2.684124000
6	2.978239000	0.601795000	-3.084553000
6	1.740989000	0.474596000	-2.492591000
7	1.466093000	-0.448100000	-1.558767000
1	4.969700000	-0.217100000	-3.104551000
1	4.455545000	-1.980902000	-1.482951000
1	3.161969000	1.372651000	-3.818640000
1	0.931572000	1.149438000	-2.739395000
6	-0.817692000	2.895116000	-0.216046000
6	-0.702866000	4.271459000	-0.200411000
6	0.567840000	4.823109000	-0.066132000
6	1.656543000	3.992373000	0.089217000
6	1.462743000	2.604441000	0.130987000
7	0.243071000	2.076047000	-0.061822000
1	-1.581635000	4.885913000	-0.321172000
1	2.641286000	4.407314000	0.231336000
6	-1.455428000	-0.696450000	-2.470308000
6	-2.474692000	-0.711035000	-3.406653000
6	-3.458802000	0.265127000	-3.351142000
6	-3.367618000	1.237897000	-2.368356000
6	-2.303851000	1.199445000	-1.473293000
7	-1.371255000	0.230107000	-1.503096000
1	-4.272818000	0.275784000	-4.062922000
1	-0.684417000	-1.449739000	-2.479233000
1	-2.488759000	-1.484142000	-4.161802000
1	-4.090545000	2.036654000	-2.295042000
6	2.464582000	0.744867000	1.341079000
6	3.542841000	0.513660000	2.203390000
6	3.433802000	-0.453843000	3.181683000
6	2.242024000	-1.160872000	3.308409000
6	1.231268000	-0.893327000	2.414575000

7. Understanding Excited State Kinetics in Asymmetric Iron(II) Push-Pull Complexes

7	1.341481000	0.010475000	1.420521000
1	4.262847000	-0.639209000	3.851444000
1	4.441117000	1.103177000	2.124360000
1	2.101455000	-1.913257000	4.070477000
1	0.297501000	-1.429046000	2.458846000
7	-2.632644000	-1.667838000	0.338065000
7	2.057981000	-2.326260000	-0.292135000
6	-3.914061000	-2.126329000	-0.206292000
1	-4.446492000	-2.810121000	0.457784000
1	-4.539061000	-1.255626000	-0.391634000
1	-3.728661000	-2.624472000	-1.153785000
6	3.149377000	-3.122772000	0.277245000
1	3.555384000	-3.850183000	-0.429853000
1	3.944002000	-2.450446000	0.593446000
1	2.777211000	-3.644451000	1.152922000
1	-0.828989000	-5.824248000	-0.027529000
1	0.702920000	5.896282000	-0.065436000
26	-0.026534000	0.072422000	-0.036973000
7	2.542014000	1.754655000	0.376571000
6	-2.178331000	2.321985000	-0.494444000
8	-3.169125000	2.873684000	-0.060353000
6	3.878074000	2.232278000	0.004791000
1	4.314815000	2.899375000	0.750215000
1	4.523596000	1.368631000	-0.127045000
1	3.808989000	2.749964000	-0.947222000

7. Understanding Excited State Kinetics in Asymmetric Iron(II) Push-Pull Complexes

 2^{2+} , 5MC

6	1.456755000	-2.634735000	-0.283506000
6	1.642065000	-4.011644000	-0.349704000
6	0.544995000	-4.835802000	-0.167813000
6	-0.699119000	-4.286909000	0.086275000
6	-0.816393000	-2.899017000	0.151967000
7	0.246578000	-2.096029000	-0.041879000
1	2.612613000	-4.426976000	-0.568089000
1	-1.550766000	-4.922382000	0.264669000
6	1.534884000	0.931111000	-2.539142000
6	2.661678000	1.267503000	-3.251958000
6	3.833028000	0.563053000	-2.980894000
6	3.822915000	-0.459870000	-2.053675000
6	2.630128000	-0.753589000	-1.374805000
7	1.523974000	-0.027231000	-1.595228000
1	4.749568000	0.800643000	-3.504104000
1	0.598845000	1.451703000	-2.686101000
1	2.630510000	2.062586000	-3.982174000
1	4.716283000	-1.035521000	-1.877959000
6	-2.309149000	-1.337337000	1.361845000
6	-3.486622000	-1.344287000	2.128607000
6	-3.693456000	-0.343344000	3.056394000
6	-2.727931000	0.645157000	3.235426000
6	-1.597803000	0.583208000	2.453036000
7	-1.401988000	-0.364422000	1.519879000
1	-4.597773000	-0.343622000	3.650260000
1	-4.212463000	-2.133293000	2.022645000
1	-2.853316000	1.438980000	3.957288000
1	-0.816087000	1.325864000	2.539730000
6	0.826087000	2.979209000	0.121471000
6	0.719484000	4.358398000	0.098738000
6	-0.543620000	4.916339000	-0.074375000
6	-1.633736000	4.089763000	-0.242078000
6	-1.449140000	2.699233000	-0.239439000
7	-0.236604000	2.166458000	-0.036276000
1	1.597642000	4.971543000	0.231496000
1	-2.614083000	4.507885000	-0.407735000
6	1.738000000	-0.592343000	2.439893000
6	2.871929000	-0.619661000	3.236566000
6	3.829775000	0.370241000	3.067481000
6	3.613866000	1.356004000	2.115274000
6	2.441219000	1.321303000	1.365569000
7	1.526064000	0.354476000	1.522248000
1	4.729601000	0.376281000	3.667286000
1	0.977996000	-1.357050000	2.524601000
1	2.997909000	-1.406197000	3.967272000
1	4.326749000	2.151119000	1.957002000
6	-2.620648000	0.804442000	-1.315191000
6	-3.837610000	0.452419000	-1.920924000
6	-3.861352000	-0.597249000	-2.817381000
6	-2.682383000	-1.270483000	-3.129959000
6	-1.531111000	-0.868910000	-2.492894000

7. Understanding Excited State Kinetics in Asymmetric Iron(II) Push-Pull Complexes

7	-1.501007000	0.119870000	-1.583806000
1	-4.795852000	-0.881510000	-3.282213000
1	-4.740975000	1.000602000	-1.713736000
1	-2.662290000	-2.088512000	-3.834828000
1	-0.586753000	-1.361906000	-2.677064000
7	2.575545000	-1.787605000	-0.442892000
7	-2.079949000	-2.330125000	0.405938000
6	3.852276000	-2.296712000	0.068431000
1	4.377916000	-2.931440000	-0.647769000
1	4.485818000	-1.451331000	0.326485000
1	3.658905000	-2.866392000	0.972501000
6	-3.247072000	-3.106227000	-0.027165000
1	-3.549541000	-3.862967000	0.699733000
1	-4.073527000	-2.420635000	-0.194922000
1	-3.009269000	-3.590653000	-0.969251000
1	0.660462000	-5.910286000	-0.222222000
1	-0.670177000	5.990530000	-0.093431000
26	0.023458000	0.031979000	-0.046195000
7	-2.565354000	1.864759000	-0.409870000
6	2.206169000	2.418258000	0.366630000
8	3.159084000	2.962676000	-0.154653000
6	-3.837560000	2.355003000	0.132192000
1	-4.396840000	2.962641000	-0.581514000
1	-4.442121000	1.500718000	0.426985000
1	-3.632324000	2.943366000	1.021160000

Literature

- [1] F. Plasser, TheoDORE. *A package for theoretical density, orbital relaxation and exciton analysis*, at <http://theodore-qc.sourceforge.net>.

8. Excited-State Kinetics of an Air-Stable Cyclometalated Iron(II) Complex

Jakob Steube, [REDACTED], Ayla Pöpcke, Johannes Moll, Peter Zimmer, Roland Schoch, Christoph Wölper, Katja Heinze, Stefan Lochbrunner and Matthias Bauer



Chem. Eur. J. **2019**, *25*, 11826–11830.

The first cyclometalated iron(II) complex $[\text{Fe}(\text{pbpy})(\text{tpy})]^+$ (pbpy: 6-phenyl-2,2'-bipyridine, tpy: 2:2',6':2"-terpyridine) was synthesized and compared to $[\text{Fe}(\text{tpy})_2]^{2+}$ as well as the theoretical predictions on this complex. As a result of the cyclometalation the $^1\text{MLCT}$ absorption is significantly red-shifted and the $^3\text{MLCT}$ lifetime is increased by a factor of 5.5 to 800 fs.

Author Contributions

Jakob Steube from the University of Paderborn carried out the synthesis of the title molecule, provided and analyzed NMR, MS, Cyclic and Square Wave Voltammetry, optical absorption spectroscopy and wrote the manuscript. [REDACTED] from the University of Paderborn analyzed the X-Ray spectroscopic measurements, performed (TD) DFT calculations and wrote the manuscript. Ayla Kruse (geb. Pöpcke) and Prof. Stefan Lochbrunner from the University of Rostock conducted and analyzed transient absorption spectroscopy and wrote the manuscript. Johannes Moll and Prof. Katja Heinze performed and analyzed spectroelectrochemical measurements and wrote the manuscript. Dr. Peter Zimmer from the University of Paderborn contributed by important and fruitful discussions and comments. Dr. Roland Schoch and Dr. Christoph Wölper from the University of Paderborn performed single crystal structure X-Ray diffraction, solved the structures and wrote the manuscript. Principal investigator Prof. Matthias Bauer from the University of Paderborn planned the research, contributed to the design of the title molecule and wrote the manuscript.

Supporting Information for this article is found at pp. 189.

“Steube, J.; [REDACTED]; Pöpcke, A.; Moll, J.; Zimmer, P.; Schoch, R.; Wölper, C.; Heinze, K.; Lochbrunner, S.; Bauer, M. *Chem. Eur. J.* **2019**, *25*, 11826–11830. Copyright Wiley-VCH Verlag GmbH & Co. KGaA. Reproduced with permission.”

8. Excited-State Kinetics of an Air-Stable Cyclometalated Iron(II) Complex

Photochemistry

Excited-State Kinetics of an Air-Stable Cyclometalated Iron(II) Complex

 Jakob Steube,^[a] ██████████,^[a] Ayla Pöpcke,^[b] Johannes Moll,^[c] Peter Zimmer,^[a] Roland Schoch,^[a] Christoph Wölper,^[d] Katja Heinze,^[c] Stefan Lochbrunner,^[b] and Matthias Bauer^{*[a]}

Abstract: The complex class $[\text{Fe}(\text{N}^{\wedge}\text{N}^{\wedge}\text{C})(\text{N}^{\wedge}\text{N}^{\wedge}\text{N})]^+$ with an Earth-abundant metal ion has been repeatedly suggested as a chromophore and potential photosensitizer on the basis of quantum chemical calculations. Synthesis and photophysical properties of the parent complex $[\text{Fe}(\text{pbpy})(\text{tpy})]^+$ (Hpbpy = 6-phenyl-2,2'-bipyridine and tpy = 2,2':6',2''-terpyridine) of this new chromophore class are now reported. Ground-state characterization by X-ray diffraction, electrochemistry, spectroelectrochemistry, UV/Vis, and X-ray spectroscopy in combination with DFT calculations proves the high impact of the cyclometalating ligand on the electronic structure. The photophysical properties are significantly improved compared to the prototypical $[\text{Fe}(\text{tpy})_2]^{2+}$ complex. In particular, the metal-to-ligand absorption extends into the near-IR and the $^3\text{MLCT}$ lifetime increases by 5.5, whereas the metal-centered excited triplet state is very short-lived.

The long-standing quest for iron complexes that substitute noble metals in photochemical applications as photosensitizers in photocatalytic reactions and as luminescence emitters, is currently carried out with great effort. To this end, long-lived metal-to-ligand charge transfer (MLCT) states have to be achieved in Fe^{II} complexes. Ruthenium(II) provides this essential property more or less intrinsically with suited ligands, whereas

this is not the case in iron(II) complexes. Because of the much smaller $t_{2g}-e_g^*$ ligand field splitting in iron(II) complexes, the metal e_g^* levels are usually lower in energy, which favors a very fast deactivation of the MLCT states into nonemissive and catalytically inactive metal-centered (MC) states.^[1,2]

Approaches to establish iron(II) complexes as emissive or photocatalytically active materials follow two fundamental strategies to prolong MLCT lifetimes: the stabilization of MLCT states and the destabilization of the MC states. From an application point of view, bis(tridentate) ligand-iron(II) combinations are superior to tris(bidentate) iron(II) complexes, as the former ones are typically more inert toward substitution.^[3] Since recorded $^3\text{MLCT}$ lifetimes are so far reported for bidentate complexes,^[4] further lifetime engineering in tridentate-coordinated Fe^{II} complexes^[5,6] and derivatives thereof are thus highly important.

An overview of the conceptual approaches to increase the $^3\text{MLCT}$ lifetime of Fe^{II} complexes was recently given by Wenger.^[7] Optimized octahedral symmetry in combination with π -accepting ligands to lower the t_{2g} -levels, or a push-pull ligand combination to stabilize MLCT states while destabilizing the MC states, are successful concepts established by McCusker^[8] and Heinze^[9] for $[\text{Fe}(\text{N}^{\wedge}\text{N}^{\wedge}\text{N})_2]^{2+}$ chromophores. Exchange of pyridyl units by N-heterocyclic carbene (NHC) ligands by Wärnmark, Gros, and Bauer lead to $[\text{Fe}(\text{C}_{\text{NHC}}^{\wedge}\text{N}^{\wedge}\text{C}_{\text{NHC}})_2]^{2+}$ and related complexes.^[10,11,12] NHCs are stronger σ -donors, destabilizing the MC states and thus extending MLCT lifetimes. In combination with polypyridine ligands in heteroleptic complexes the undesired properties of bis(NHC) ligands to raise the $^3\text{MLCT}$ energy can be partially compensated.^[11] For all these compounds of the type $[\text{Fe}(\text{N}^{\wedge}\text{N}^{\wedge}\text{N})_2]^{2+}$ and $[\text{Fe}(\text{C}_{\text{NHC}}^{\wedge}\text{N}^{\wedge}\text{C}_{\text{NHC}})_2]^{2+}$ experimental and theoretical studies complement and support each other.^[6,13]

In contrast, quantum chemical predictions provided by Jakubikova et al. and Dixon et al.^[14,15,16] for the effects of exchanging an N-donor by a cyclometalating ligand could not be confirmed experimentally so far. Although aryl carbanion ligands in the form of 2-phenylpyridine, 1,3-di(2-pyridinyl)benzene, and 6-phenyl-2,2'-bipyridine (Hpbpy already found applications in the context of noble metal complexes,^[17,18] air- and water-stable cyclometalated Fe^{II} compounds, allowing for photochemical applications, are lacking up to date.^[19] With this work we will fill this gap and present a) a synthetic access to heteroleptic, cyclometalated $[\text{Fe}(\text{N}^{\wedge}\text{N}^{\wedge}\text{N})(\text{N}^{\wedge}\text{N}^{\wedge}\text{C}_{\text{cm}})]^+$ complexes, here in the form of $[\text{Fe}(\text{pbpy})(\text{tpy})]^+$ (tpy = 2,2':6',2''-terpyri-

[a] J. Steube, Dipl.-Chem. ██████████, Dr. P. Zimmer, Dr. R. Schoch, Prof. Dr. M. Bauer
Institute of Inorganic Chemistry and Center for Sustainable Systems Design (CSSD), University of Paderborn, Warburger Straße 100
33098 Paderborn (Germany)
E-mail: matthias.bauer@upb.de

[b] A. Pöpcke, Prof. Dr. S. Lochbrunner
Institute of Physics and Department of Life, Light and Matter
University of Rostock, 18051 Rostock (Germany)

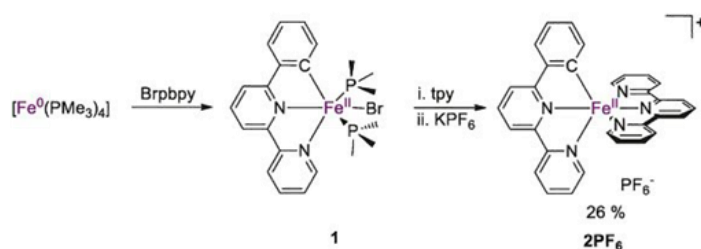
[c] J. Moll, Prof. Dr. K. Heinze
Institute of Inorganic Chemistry and Analytical Chemistry
Johannes Gutenberg University
Duesbergweg 10-14, 55128 Mainz (Germany)

[d] Dr. C. Wölper
Institute for Inorganic Chemistry and Center for Nanointegration
Duisburg-Essen (Cenide), University of Duisburg-Essen
Universitätsstraße 5-745117 Essen (Germany)

Supporting information and the ORCID identification number(s) for the author(s) of this article can be found under:
<https://doi.org/10.1002/chem.201902488>.

dine) and b) thoroughly investigate the ground- and excited-state characteristics in comparison to the prototypical complex $[\text{Fe}(\text{tpy})_2]^{2+}$ to prove the high potential of cyclometalating ligands for increasing MLCT lifetimes.

The established synthesis of cyclometalated complexes by C–H-activation,^[20,21] as with ruthenium(II) and other 4d/5d transition metals, could not be transferred to iron(II) complexes. Instead, an oxidative addition involving the low valent $[\text{Fe}(\text{PMe}_3)_4]$ precursor has been developed (Scheme 1). This approach is similar to that developed by Klein et al. for cyclome-



Scheme 1. Synthesis of cyclometalated complex 2PF_6 .

talated nickel(II) complexes.^[22] The phosphane iron(0) complex is treated with the ligand precursor 6-(2-bromophenyl)-2,2'-bipyridine (Brpbpy).^[23] This results in the octahedral cyclometalated phosphane bromido iron(II) intermediate *trans*- $\text{FeBr}(\text{pbpy})(\text{PMe}_3)_2$ (**1**), which can be isolated under inert conditions. Addition of a stoichiometric amount of terpyridine substitutes the phosphanes and the halide yielding the air- and water-stable complex $[\text{Fe}(\text{pbpy})(\text{tpy})](\text{PF}_6)_2$ (**2PF₆**) after anion exchange (Scheme 1).

Single crystals suitable for X-ray diffraction could be obtained with BPh_4 as the counterion (Figure 1). As the phenyl ring is disordered over the two ligands in a one to one ratio, the Fe–C distance is the mean value of a Fe–N1 and a Fe–C1 bond length. Also, the Fe–N3 distances are the average of the

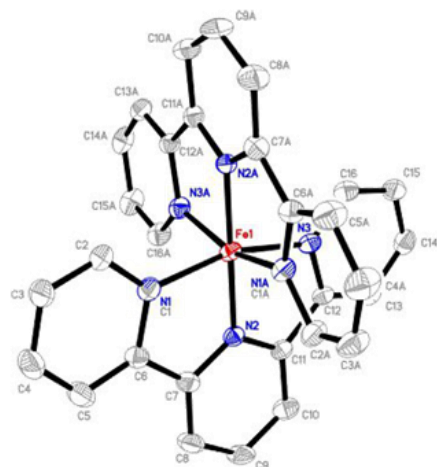


Figure 1. Single-crystal structure of $[\text{Fe}(\text{tpy})(\text{pbpy})](\text{BPh}_4)$ (**2BPh₄**) drawn with anisotropic displacement ellipsoids at a 50% probability level. Hydrogen atoms and the counterion are not displayed for reasons of clarity.

tpy–Fe–N and pbpy–Fe–N values. Still, a shorter Fe–C1/N1 bond of 1.944 Å and a slightly elongated Fe–N3 bond of 1.981 Å *trans* to the Fe–C bond compared to the outer Fe–N bond lengths in $[\text{Fe}(\text{tpy})_2]^{2+}$ are observed due to the *trans* effect of the strong Fe–C bond.^[24] These structural results are in good accordance with the structure calculated by DFT.

The ground-state of **2** is characterized by optical spectroscopy, electrochemistry, and spectroelectrochemistry, combined with advanced hard X-ray spectroscopic techniques. The latter is less established for photochemical research yet offers a multitude of information about core-excited states. This in turn allows to calibrate and validate the selected theoretical approach for the ground state.^[25,26]

A low-spin (LS) configuration of **2** is confirmed by NMR and core-to-core X-ray emission spectroscopy (CtC-XES)^[26] at the iron K-edge, similar to the reference complex $[\text{Fe}(\text{tpy})_2]^{2+}$ (**3**). The LUMO and HOMO levels are probed in detail by HERFD-XANES (high energy resolution fluorescence detected XANES)^[27] and VtC-XES (valence-to-core X-ray emission spectroscopy) in combination with TD-DFT calculations.^[25,26,28] From the HERFD-XANES prepeak analysis of **2** and **3** it can be deduced that the core-excited

MC states, formed by the metal-centered e_g^* acceptor orbitals, are destabilized significantly in the cyclometalated complex. This result nicely confirms the chosen approach of using cyclometalating ligands to destabilize MC excited states of iron(II) as has been found in the homologous ruthenium(II) complex $[\text{Ru}(\text{tpy})(\text{pbpy})]^+$.^[21,29,30] In contrast, no significant effect on the t_{2g} levels by cyclometalation is observed with VtC-XES. With VtC-XES, the occupied levels of lower energy are probed that prove the σ -bonding interaction of the pbpy[−] ligand and the Fe $3d_z^2$ orbital, as well as the stabilization of the phenyl/polypyridyl σ and π fragment orbitals in **2** as compared to **3**.

Consequently, the Kohn–Sham molecular orbital diagrams (Figure 2) obtained by DFT calculations with MeCN as the solvent using the SMD solvation model^[31] show a significant destabilization of the HOMO- t_{2g} levels of reduced degeneracy,^[15] in agreement with the strong π -donor properties of the cyclometalating ligand. The LUMO is located at the tpy ligand in **2**, whereas the pbpy[−] ligand only contributes to molecular orbitals of higher energy,^[29] similar to the Ru^{II} congener.^[30] Since the LUMO is less destabilized than the HOMO, the HOMO–LUMO gap is decreased by 0.44 eV in **2** compared to **3**. The unoccupied metal-centered e_g^* orbitals of **2** are destabilized, the d_z^2 orbital to a larger extent than the $d_{x^2-y^2}$ orbital due to the covalent Fe–C bond located on the *z*-axis.^[32]

According to the MO diagrams, the HOMO and LUMO levels of **2** are significantly affected by the cyclometalating ligand (Figure 2). This is furthermore reflected in the electrochemical properties of **2**. The redox potential is significantly lowered by -0.83 V for the reversible $\text{Fe}^{\text{II/III}}$ redox wave compared to **3** (-0.11 and 0.72 V vs. FcH/FcH^+ , respectively) as a result of the larger π -donor strength of the cyclometalating moiety.^[15,16,32] This agrees with the theoretically predicted destabilization of the t_{2g} -orbitals by 0.76 eV (Figure 2). A similar value for the

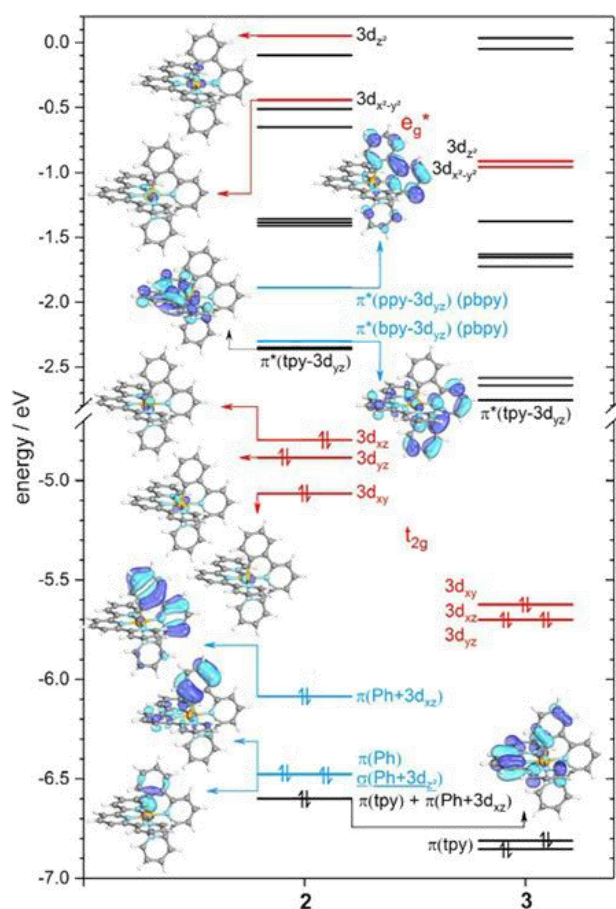


Figure 2. DFT-calculated molecular orbital diagrams of **2** and **3** (def2-TZVPP, TPSSh, SMD). Levels with significant Fe 3d contribution are shown in red, levels with significant pbpy contributions in blue.

cathodic shift of 0.74 V is known for the $[\text{Ru}(\text{pbpy})(\text{tpy})]^{2+/2+}$ and $[\text{Ru}(\text{tpy})_2]^{2+/3+}$ redox couples.^[29] The ligand-centered reduction waves of **2** are also cathodically shifted (−1.97 and −2.25 V) in comparison to **3**, but to a smaller extent. This is due to a weaker influence of the cyclometalating ligand on the LUMO levels, which are dominated by the tpy ligand. Consequently, the HOMO–LUMO gap in **2** is smaller than that in **3**.

In the electronic absorption spectra, **2** shows a strong panchromatic absorption up into the NIR region (Figure 3) with broadened peaks due to the lower symmetry^[18,21,33] and concomitant larger t_{2g} splitting in comparison to **3**.^[15] The MLCT maximum of **2** at $\lambda_{\text{max}}=618$ nm ($\epsilon_{\text{max}}=0.92 \times 10^4 \text{ M}^{-1} \text{ cm}^{-1}$) is redshifted compared to that of **3** ($\lambda_{\text{max}}=552$ nm, $\epsilon_{\text{max}}=1.12 \times 10^4 \text{ M}^{-1} \text{ cm}^{-1}$) due to the destabilized t_{2g} orbitals (Figure 2).

The MLCT absorption bands were assigned using TD-DFT calculations. The high energy shoulder A (Figure 3b) at around 550 nm is mainly characterized by a transition to a π^* -type orbital delocalized on the pbpy[−] ligand, whereas the final state of B is dominated by a π^* -type acceptor orbital located on the bpy fragment of the pbpy[−] ligand. Complementary, C results from a transition to a tpy π^* -type acceptor orbital. Finally, the low energy shoulder D is composed of three acceptor orbitals,

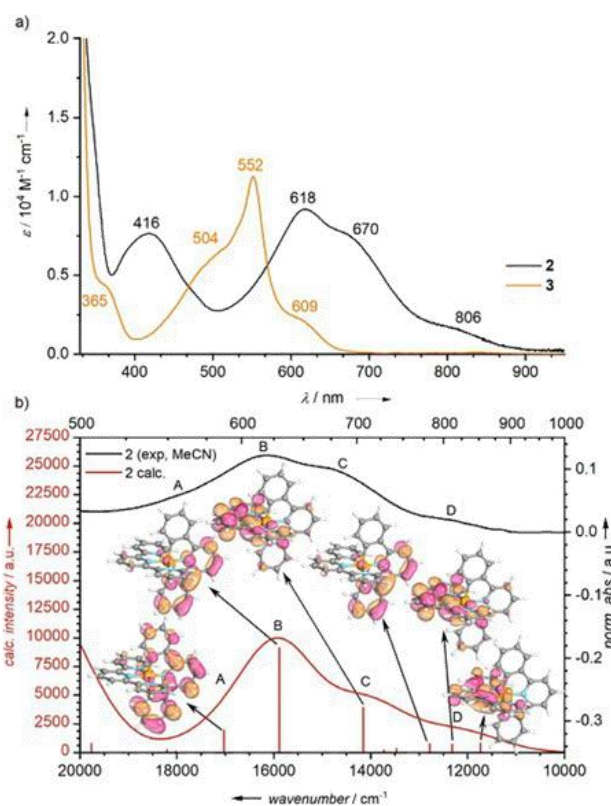


Figure 3. a) Electronic absorption spectra of **2** and **3** (10^{-5} M in MeCN) b) Comparison of the normalized experimental spectrum of **2** with the TDDFT calculated spectrum. Dominant acceptor orbitals are shown.

two with mainly tpy π^* - and one with bpy π^* -character at pbpy[−]. Solvatochromic shifts in different solvents (MeCN, MeOH, EtOH, acetone, DCM, and DMSO) confirm the asymmetric charge distribution in these MLCT states.

In luminescence measurements of **2** at 293 K in MeCN, no emission could be detected. This either points to low-lying MC states^[11] or highly distorted MLCT states,^[30] which cause an efficient nonradiative decay. Excited-state dynamics were thus probed by ultrafast pump–probe spectroscopy.^[11,34,35] Transient absorption spectra of **2** in MeCN with a time resolution of about 50 fs and excitation pulses centered at 615 nm are shown for selected delay times in the Supporting Information. Decay associated amplitude spectra (DAS) obtained by a global fit are depicted in Figure 4.

After optical excitation, the transient absorption spectra of complex **2** exhibit a maximum at 500 nm and two negative bands with minima at 425 and 620 nm. The transient signals decay completely within less than 20 ps. The dynamics were analyzed by globally fitting a double exponential decay to the data. The fit reproduces the measurement very well, resulting in time constants of $\tau_1=0.8$ and $\tau_2=12$ ps. The corresponding DAS are compared to the difference spectrum between the oxidized **2**⁺ and **2** obtained from spectroelectrochemical measurements (Figure 4). For *N*-heterocyclic carbene iron(II) complexes MLCT states have been identified by comparison with the combination of difference spectra between oxidized

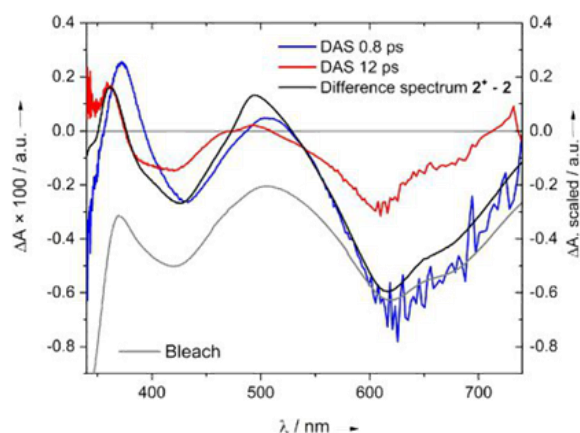


Figure 4. Decay associated amplitude spectra (DAS) of the two exponential components with time constants of 0.8 and 12 ps resulting from a double-exponential global fit (left scale) to the ultrafast absorption measurements. The DAS are compared to the scaled bleach and scaled difference spectrum obtained from spectroelectrochemical oxidation measurements (right scale) of complex **2**.

and reduced species and the ground-state spectrum, respectively.^[11,35,36] Unfortunately, this procedure cannot be directly transferred to the cyclometalated complex **2** due to the irreversibility of the reduction process in spectroelectrochemical experiments and the fact, that no characteristic intense, low-energy LMCT transition is found for the electrochemically generated Fe^{III} species but merely a rather weak absorption around 500 nm (Supporting Information, Figure S17; difference spectrum “2⁺–2[–]” in Figure 4).

The short-lived component (τ_1) exhibits indeed a weak excited-state absorption (ESA) signal around 500 nm (Figure 4). The difference spectrum “2⁺–2[–]” reasonably matches the DAS (τ_1) and consequently, we assign this lifetime to a MLCT state (Figure 4). Together with the very short lifetime of 0.8 ps, this component is, therefore, assigned to a ³MLCT state with high confidence. This triplet state is populated after excitation into a ¹MLCT state, followed by ultrafast intersystem crossing.^[1,11,37] With this assignment, the [Fe(N^{^N}^N)(N^{^N}^N^C_{cm})]⁺ complex [Fe(pbpy)(tpy)]⁺ (**2**), therefore, shows an MLCT lifetime of 0.8 ps increased by a factor of 5.5 compared to its [Fe(N^{^N}^N)]²⁺ counterpart [Fe(tpy)]²⁺ **3** exhibiting a MLCT lifetime of 145 fs.^[35]

The longer-lived component is assigned to a ³MC state due to its similarity to the ground-state bleach. Wärnmark^[10,35] and Gros^[38] pointed out for NHC complexes that such behavior indicates a missing population of the ⁵MC state. For a ⁵MC state typically a nanosecond lifetime is expected due to the double spin state change required in the relaxation. Thus, the very short lifetime of 12 ps for **2** makes a contribution of a quintet ⁵MC state unlikely^[8,9] as it would additionally require an elongation of all iron–ligand bonds, which is unlikely due to the presence of the Fe–C_{cm} bond.

A conceivable alternative interpretation of the longer-lived component assigns a second ³MLCT state to the τ_2 lifetime, resulting from an independent excitation of the tpy[–] and pbpy[–] ligands. The excitation wavelength of 615 nm is indeed excit-

ing transitions involving different acceptor ligands (Figure 3). After relaxation and ISC of the individual MLCT states, internal conversion between ³MLCT(tpy) and ³MLCT(pbpy) states might be hindered due to the orthogonal arrangement of the tpy and pbpy[–] ligands. Although the DAS of the two components resemble each other (apart from the ESA at 500 nm), we consider the scenario of parallel ¹MLCT(tpy)→³MLCT(tpy)→¹A₁ and ¹MLCT(pbpy)→³MLCT(pbpy)→¹A₁ relaxation pathways as rather unlikely. This possibility would require direct relaxation pathways from both ³MLCT states into the ¹A₁ ground state bypassing the typically involved ³MC state. This is very much at odds with theoretical predictions for such complexes.^[16,32]

Consequently, the effects of the terminal cyclometalation in **2** are as follows. First, we observe a ¹MLCT→³MLCT→³MC→¹A₁ deactivation cascade, which differs significantly from **3** featuring a long-lived ⁵MC state as the finally populated excited state.^[35] Second, the ³MLCT lifetime in **2** ($\tau_1=0.8$ ps) increases by a factor of 5.5 compared to that of **3** ($\tau_1=145$ fs).^[35,38] This effect is significant, as complexes with even two NHC ligands [Fe(C^{^N}^N)(tpy)]²⁺ or [Fe(N^{^N}^N)]²⁺ merely yield ³MLCT lifetimes below 100 fs.^[11] In principle, the ⁵MC state could still be lower in energy than the ³MLCT state, but would remain unpopulated due to a high activation barrier caused by strong distortions. Still, our time-resolved measurements confirm the theoretical calculations of Dixon et al.^[16] and Jakubikova et al.^[15] predicting a ³MC<³MLCT<⁵MC ordering of states in **2**, which is our third conclusion.

In summary, an oxidative addition synthetic access to cyclometalated iron(II) complexes was developed. This allowed the ground state, and, in particular, the excited state characterization of such chromophores with an Earth-abundant metal ion filling the so-far existing theory–experiment knowledge gap. The ³MLCT stabilization of 0.95 eV with respect to the reference bis(terpyridine) iron(II) complex predicted by theoretical calculations^[16] resulted in an increased ³MLCT lifetime by a factor of 5.5 accompanied by a bathochromic shift of the absorption bands into the NIR. Both beneficial effects are mandatory for future photochemical applications of iron(II) complexes. To this end, ³MLCT distortion needs to be further probed and finally controlled to increase the ³MLCT lifetime of iron(II) complexes with tridentate ligands.

Acknowledgements

This work was supported by Deutsche Forschungsgemeinschaft [DFG, Priority Program SPP 2102 “Light-controlled reactivity of metal complexes” (BA 4467/7-1, LO 714/11-1, HE2778/14-1)]. The European Synchrotron Radiation Facility is acknowledged for provision of beamtime at beamline ID26. J. S. thanks the Deutsche Bundesstiftung Umwelt (DBU) for a PhD scholarship.

Conflict of interest

The authors declare no conflict of interest.

Keywords: iron · photochemistry · excited-state kinetics · transient absorption spectroscopy · DFT calculations

- [1] E. A. Juban, A. L. Smeigh, J. E. Monat, J. K. McCusker, *Coord. Chem. Rev.* **2006**, *250*, 1783.
- [2] A. Cannizzo, C. J. Milne, C. Consani, W. Gawelda, C. Bressler, F. van Mourik, M. Chergui, *Coord. Chem. Rev.* **2010**, *254*, 2677.
- [3] a) P. Zimmer, P. Müller, L. Burkhardt, R. Schepper, A. Neuba, J. Steube, F. Dietrich, U. Flörke, S. Mangold, M. Gerhards, M. Bauer, *Eur. J. Inorg. Chem.* **2017**, *11*, 1504; b) T. Duchanois, L. Liu, M. Pastore, A. Monari, C. Cebrián, Y. Trolez, M. Darari, K. Magra, A. Francés-Monerris, E. Domenichini, M. Beley, X. Assfeld, S. Haacke, P. C. Gros, *Inorganics* **2018**, *6*, 63.
- [4] a) P. Chabera, K. S. Kjaer, O. Prakash, A. Honarfar, Y. Liu, L. A. Fredin, T. B. Harlang, S. Lidin, J. Uhlig, V. Sundstrom, et al., *J. Phys. Chem. Lett.* **2018**, *9*, 459; b) Y. Liu, K. S. Kjaer, L. A. Fredin, P. Chábera, T. Harlang, S. E. Canton, S. Lidin, J. Zhang, R. Lomoth, K.-E. Bergquist et al., *Chem. Eur. J.* **2015**, *21*, 3628.
- [5] a) S. M. Fatur, S. G. Shepard, R. F. Higgins, M. P. Shores, N. H. Damrauer, *J. Am. Chem. Soc.* **2017**, *139*, 4493; b) S. Mukherjee, D. E. Torres, E. Jakubikova, *Chem. Sci.* **2017**, *8*, 8115.
- [6] M. Pápai, G. Vankó, T. Rozgonyi, T. J. Penfold, *J. Phys. Chem. Lett.* **2016**, *7*, 2009.
- [7] O. S. Wenger, *Chem. Eur. J.* **2019**, *25*, 6043.
- [8] L. L. Jamula, A. M. Brown, D. Guo, J. K. McCusker, *Inorg. Chem.* **2014**, *53*, 15.
- [9] A. K. C. Mengel, C. Förster, A. Breivogel, K. Mack, J. R. Ochsmann, F. Laquai, V. Ksenofontov, K. Heinze, *Chem. Eur. J.* **2015**, *21*, 704.
- [10] L. A. Fredin, M. Pápai, E. Rozsályi, G. Vankó, K. Wärnmark, V. Sundström, P. Persson, *J. Phys. Chem. Lett.* **2014**, *5*, 2066.
- [11] P. Zimmer, L. Burkhardt, A. Friedrich, J. Steube, A. Neuba, R. Schepper, P. Müller, U. Flörke, M. Huber, S. Lochbrunner, M. Bauer, *Inorg. Chem.* **2018**, *57*, 360.
- [12] a) Y. Liu, P. Persson, V. Sundstrom, K. Wärnmark, *Acc. Chem. Res.* **2016**, *49*, 1477; b) D. Leshchev, T. C. B. Harlang, L. A. Fredin, D. Khakhulin, Y. Liu, E. Biasin, M. G. Laursen, G. E. Newby, K. Haldrup, M. M. Nielsen, K. Wärnmark, V. Sundström, P. Persson, K. S. Kjaer, M. Wulff, *Chem. Sci.* **2018**, *9*, 405; c) M. Pastore, T. Duchanois, L. Liu, A. Monari, X. Assfeld, S. Haacke, P. C. Gros, *Phys. Chem. Chem. Phys.* **2016**, *18*, 28069.
- [13] D. C. Ashley, E. Jakubikova, *Inorg. Chem.* **2018**, *57*, 9907.
- [14] a) S. Mukherjee, C. Liu, E. Jakubikova, *J. Phys. Chem. A* **2018**, *122*, 1822; b) I. M. Dixon, G. Boissard, H. Whyte, F. Alary, J.-L. Heully, *Inorg. Chem.* **2016**, *55*, 5089.
- [15] S. Mukherjee, D. N. Bowman, E. Jakubikova, *Inorg. Chem.* **2015**, *54*, 560.
- [16] I. M. Dixon, F. Alary, M. Boggio-Pasqua, J.-L. Heully, *Dalton Trans.* **2015**, *44*, 13498.
- [17] a) H. Kisserwan, A. Kamar, T. Shoker, T. H. Ghaddar, *Dalton Trans.* **2012**, *41*, 10643; b) R. Kaneko, G. Wu, K. Sugawa, J. Otsuki, A. Islam, L. Han, I. Bedja, R. K. Gupta, *J. Organomet. Chem.* **2017**, *833*, 61; c) L. L. Tinker, S. Bernhard, *Inorg. Chem.* **2009**, *48*, 10507; d) P. Coppo, E. A. Plummer, L. de Cola, *Chem. Commun.* **2004**, 1774; e) M. S. Lowry, S. Bernhard, *Chem. Eur. J.* **2006**, *12*, 7970; f) T. Tsuzuki, N. Shirasawa, T. Suzuki, S. Tokito, *Adv. Mater.* **2003**, *15*, 1455.
- [18] P. G. Bomben, K. C. D. Robson, B. D. Koivisto, C. P. Berlinguette, *Coord. Chem. Rev.* **2012**, *256*, 1438.
- [19] A. S. Estrada-Montaño, A. D. Ryabov, A. Gries, C. Gaiddon, R. Le Lagadec, *Eur. J. Inorg. Chem.* **2017**, *12*, 1673.
- [20] a) M. Albrecht, *Chem. Rev.* **2010**, *110*, 576; b) S. Fernandez, M. Pfeiffer, V. Ritleng, C. Sirlin, *Organometallics* **1999**, *18*, 2390; c) E. C. Constable, J. M. Holmes, *J. Organomet. Chem.* **1986**, *301*, 203.
- [21] P. G. Bomben, K. C. D. Robson, P. A. Sedach, C. P. Berlinguette, *Inorg. Chem.* **2009**, *48*, 9631.
- [22] D. L. Jameson, L. E. Guise, *Tetrahedron Lett.* **1991**, *32*, 1999.
- [23] L. A. Barrios, C. Bartual-Murgui, E. Peyrecave-Lleixà, B. Le Guennic, S. J. Teat, O. Roubeau, G. Aromí, *Inorg. Chem.* **2016**, *55*, 4110.
- [24] M. Bauer, *Phys. Chem. Chem. Phys.* **2014**, *16*, 13827.
- [25] P. Glatzel, U. Bergmann, *Coord. Chem. Rev.* **2005**, *249*, 65.
- [26] a) M. Agote-Arán, I. Lezcano-González, A. G. Greenaway, S. Hayama, S. Díaz-Moreno, A. B. Kroner, A. M. Beale, *Appl. Catal. A* **2019**, *570*, 283; b) P. Eisenberger, P. M. Platzman, H. Winick, *Phys. Rev. Lett.* **1976**, *36*, 623; c) O. V. Safonova, M. Tromp, J. A. van Bokhoven, F. M. F. de Groot, J. Evans, P. Glatzel, *J. Phys. Chem. B* **2006**, *110*, 16162; d) A. J. Atkins, M. Bauer, C. R. Jacob, *Phys. Chem. Chem. Phys.* **2015**, *17*, 13937.
- [27] a) M. U. Delgado-Jaime, S. DeBeer, M. Bauer, *Chem. Eur. J.* **2013**, *19*, 15888; b) A. J. Atkins, M. Bauer, C. R. Jacob, *Phys. Chem. Chem. Phys.* **2013**, *15*, 8095; c) K. M. Lancaster, K. D. Finkelstein, S. DeBeer, *Inorg. Chem.* **2011**, *50*, 6767; d) B. Lassalle-Kaiser, T. T. Boron, V. Krewald, J. Kern, M. A. Beckwith, M. U. Delgado-Jaime, H. Schroeder, R. Alonso-Mori, D. Nordlund, T.-C. Wenig, D. Sokaras, F. Neese, U. Bergmann, V. K. Yachandra, S. DeBeer, V. L. Pecoraro, J. Yano, *Inorg. Chem.* **2013**, *52*, 12915; e) C. J. Pollock, S. DeBeer, *J. Am. Chem. Soc.* **2011**, *133*, 5594.
- [28] S. H. Wadman, M. Lutz, D. M. Tooke, A. L. Spek, F. Hartl, R. W. A. Havenith, G. P. M. van Klink, G. van Koten, *Inorg. Chem.* **2009**, *48*, 1887.
- [29] C. Kreitner, K. Heinze, *Dalton Trans.* **2016**, *45*, 13631.
- [30] A. V. Marenich, C. J. Cramer, D. G. Truhlar, *J. Phys. Chem. B* **2009**, *113*, 6378.
- [31] I. M. Dixon, S. Khan, F. Alary, M. Boggio-Pasqua, J.-L. Heully, *Dalton Trans.* **2014**, *43*, 15898.
- [32] T. C. Motley, L. Troian-Gautier, M. K. Brennaman, G. J. Meyer, *Inorg. Chem.* **2017**, *56*, 13579.
- [33] P. Zimmer, L. Burkhardt, R. Schepper, K. Zheng, D. Gosztola, A. Neuba, U. Flörke, C. Wölper, R. Schoch, W. Gawelda, S. E. Canton, M. Bauer, *Eur. J. Inorg. Chem.* **2018**, *48*, 5203.
- [34] Y. Liu, T. Harlang, S. E. Canton, P. Chábera, K. Suárez-Alcántara, A. Fleckhaus, D. A. Vithanage, E. Göransson, A. Corani, R. Lomoth, V. Sundström, Kenneth Wärnmark, *Chem. Commun.* **2013**, *49*, 6412.
- [35] A. M. Brown, C. E. McCusker, J. K. McCusker, *Dalton Trans.* **2014**, *43*, 17635.
- [36] W. Gawelda, A. Cannizzo, V.-T. Pham, F. van Mourik, C. Bressler, M. Chergui, *J. Am. Chem. Soc.* **2007**, *129*, 8199.
- [37] T. Duchanois, T. Etienne, C. Cebrián, L. Liu, A. Monari, M. Beley, X. Assfeld, S. Haacke, P. C. Gros, *Eur. J. Inorg. Chem.* **2015**, *14*, 2469.
- [38] J. E. Monat, J. K. McCusker, *J. Am. Chem. Soc.* **2000**, *122*, 4092.

Manuscript received: May 29, 2019

Accepted manuscript online: June 1, 2019

Version of record online: June 26, 2019

8. Excited-State Kinetics of an Air-Stable Cyclometalated Iron(II) Complex

CHEMISTRY

A European Journal

Supporting Information

Excited-State Kinetics of an Air-Stable Cyclometalated Iron(II) Complex

Jakob Steube,^[a] [REDACTED]^[a] Ayla Pöpcke,^[b] Johannes Moll,^[c] Peter Zimmer,^[a]
Roland Schoch,^[a] Christoph Wölper,^[d] Katja Heinze,^[c] Stefan Lochbrunner,^[b] and
Matthias Bauer^{*[a]}

chem_201902488_sm_miscellaneous_information.pdf

Supporting Information

Content

Experimental Section	2
Synthesis.....	3
Quantum chemical calculations.....	8
X-Ray spectroscopy	8
Electrochemistry.....	11
UV-Vis Spectroscopy.....	18
Spectroelectrochemistry	29
Ultrafast Pump-Probe Spectroscopy.....	34
NMR Spectra.....	37
References	40

Experimental Section

The reactions were carried out under argon atmosphere using standard Schlenk techniques. Dry THF was obtained from reflux and subsequent distillation over potassium. Solvents were degassed prior to use. Chemicals were purchased from Sigma Aldrich, TCI or ACROS and used without purification. NMR spectra were recorded using a Bruker Avance 500 spectrometer. ESI-MS spectra were measured with a Waters Synapt G2 quadrupole – Time of flight spectrometer.

Spectroelectrochemical measurements were carried out on a BioLogic SP-50 and SP-200 voltammetric analyzer, respectively in a Specac omni-cell liquid transmission cell with CaF₂ windows equipped with a Pt gauze working electrode, a Pt counter electrode and a Ag pseudoreference electrode, melt-sealed in a polyethylene spacer (path length 1 mm for oxidation and 0.5 mm for reduction experiments) using 0.1 M [*n*-Bu₄N][PF₆] as the supporting electrolyte in MeCN. UV/Vis/NIR spectro-electrochemical absorption spectra were measured on a Jasco V-770 spectrometer for oxidation measurements and on a Varian Cary 5000 spectrometer for reduction experiments.

Cyclic and square-wave voltammograms were carried out at room-temperature using a compactstat potentiostat from Ivium with an analyte concentration of 10⁻³ M in a MeCN/0.1 M [*n*-Bu₄N][PF₆] electrolyte. In a three-electrode configuration, a Pt working electrode (1 mm diameter), Ag/0.01 M AgNO₃, 0.1 M [*n*-Bu₄N][PF₆] in MeCN as reference and a Pt plate (~1 cm² surface area) as a counter electrode were used. Ferrocene was used as an internal standard and added after the measurements to reference them to the respective Fe^{0/+} couple. The resulting spectra were analyzed using the Iviumsoft software (v. 2.794). The redox transitions were checked for reversibility using the diagnostic criteria from Nicholson^[1] and the Randles-Sevcik equation.^[2]

Standard UV-Vis absorption spectra were recorded on a Varian Cary 50 spectrometer at a concentration of 10⁻⁵ M.

The crystallographic data of [Fe(tpy)(pbpy)]BPh₄ **2 BPh4** were recorded using a Bruker SMART CCD area detector diffractometer working with graphite monochromated MoK_α radiation ($\lambda = 0.71073 \text{ \AA}$) at T = 130(2) K. The measurement of [Fe(pbpy)(PMe₃)₂Cl]PF₆ **1a Cl** was carried out using a Bruker D8 Kappa II applied with an APEX II detector and monochromated MoK_α radiation ($\lambda = 0.71073 \text{ \AA}$) at T = 100(2) K. Structure solutions were carried out by direct methods,^[3] full matrix least squares refinement based on F².^[3] All not-hydrogen atoms were refined anisotropically, hydrogen positions were derived from geometrical reasons and afterwards refined at idealized positions riding on the carbon atoms with isotropic displacement parameters U_{iso}(H) = 1.2U_{eq}(C) and d(C-H) = 0.96 Å. The methyl groups are idealized with tetrahedral angles in a combined rotating and rigid group refinement with the 1.5 fold isotropic displacement parameters of the equivalent U_{ij} of the corresponding carbon atom.

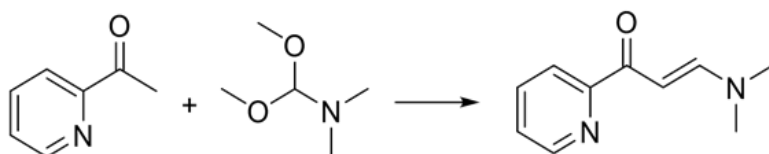
8. Excited-State Kinetics of an Air-Stable Cyclometalated Iron(II) Complex

Transient absorption spectra of complex **2** were obtained by a pump-probe setup with a time resolution of 50 fs using a non-collinear optical parametric amplifier (NOPA) tuned to a center wavelength of 615 nm for pumping and a white light continuum for probing. Both the white light generation and the NOPA were pumped by a regenerative Ti:sapphire laser system operating at 775 nm and a repetition rate of 1 kHz. The polarizations of the pump and probe pulses were set to magic angle with respect to each other to avoid effects due to orientational relaxation. Pump and probe beam were focused onto the sample to overlapping spots with diameters of approximately 460 μm and 140 μm , respectively. The sample solution was measured in a fused silica cuvette with a thickness of 100 μm .

Synthesis

Tetrakis(trimethylphosphine)iron(0) and 2,2':6',2''-terpyridine were prepared according to the literature.^[4]

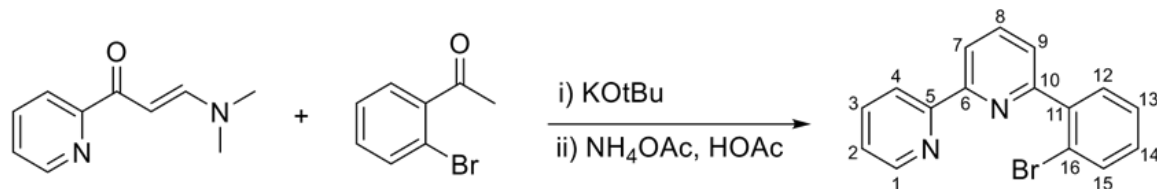
3-(Dimethylamino)-1-(2-pyridinyl)-2-propenone



2-Acetylpyridine (9.0 mL, 80 mmol) and *N,N*-dimethylformamide dimethyl acetal (11.2 mL, 80 mmol) were heated under air under reflux for 6 h. After cooling to room temperature, the dark suspension was filtered. The solids were washed with pentane (50 mL) and a mixture of pentane and diethylether (2:1, 80 mL) and dried in vacuo. The product was isolated as a light green powder (**70 %**, 9.87 g, 56 mmol).

¹H NMR (500 MHz, CDCl₃) δ (ppm) = 8.55 (ddd, $J=4.8, 1.8, 0.9$, 1H), 8.06 (dt, $J=7.9, 1.1$, 1H), 7.83 (d, $J=12.7$, 1H), 7.71 (td, $J=7.7, 1.8$, 1H), 7.28 (ddd, $J=7.5, 4.7, 1.3$, 1H), 6.38 (d, $J=12.7$, 1H), 3.08 (s, 3H), 2.90 (s, 3H).

¹³C NMR (126 MHz, CDCl₃) δ (ppm) = 186.82, 156.24, 154.65, 148.22, 136.63, 125.32, 121.95, 91.21, 45.03, 37.40.

6-(2-Bromophenyl)-2,2'-bipyridine

Under argon, a flask was charged with potassium tert-butoxide (8.98 g, 80 mmol) and dry THF (140 mL). Subsequently 2'-bromoacetophenone (7.96 g, 40 mmol) was added. The mixture was stirred for 2 h and 3-(dimethylamino)-1-(2-pyridyl)-2-propenone (7.05 g, 40 mmol) was added in counterstream. The reaction mixture was stirred for further 14 h. Afterwards, ammonium acetate (30.8 g, 400 mmol) and acetic acid (50 mL) were added under air. The mixture was heated and the THF was distilled over in 2 h. The Acetic Acid was removed via rotary evaporator. The black oil was diluted with water (100 mL) and neutralized with sodium carbonate. The suspension was extracted with DCM (3 x 40 mL) and the solvent of the organic phase was removed. To the dark oil toluene (40 mL) was added and was filtered over celite and was washed with a small amount of toluene. The black solution was passed over a small column of silica and washed further with toluene. The resulting red solution was adsorbed on silica gel and purified using column chromatography (7 % ethyl acetate in hexane). A yellow oil could be obtained, which was recrystallized from hexane. The product was isolated as colorless needles (**25 %**, 3.59 g 11.5 mmol).

¹H NMR (500 MHz, CDCl₃) δ (ppm) = 8.69 (ddd, *J* = 4.8, 1.8, 0.9 Hz, 1H, **1**), 8.52 (dt, *J* = 8.0, 1.1 Hz, 1H, **4**), 8.42 (dd, *J* = 7.9, 1.0 Hz, 1H, **7**), 7.90 (t, *J* = 7.8 Hz, 1H, **8**), 7.80 (ddd, *J* = 8.0, 7.5, 1.8 Hz, 1H, **3**), 7.74 – 7.69 (m, 1H, **12**), 7.64 (dd, *J* = 7.7, 1.9 Hz, 1H, **15**), 7.62 (dd, *J* = 7.7, 1.0 Hz, 1H, **9**), 7.43 (td, *J* = 7.5, 1.2 Hz, 1H, **14**), 7.34 – 7.29 (m, 1H, **2**), 7.30 – 7.24 (m, 1H, **13**).

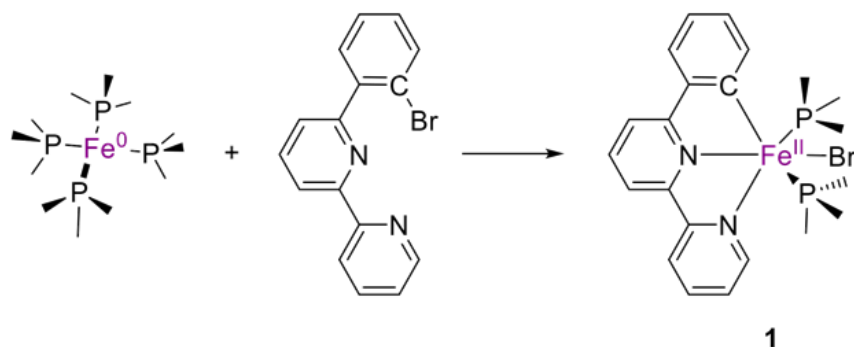
¹³C NMR (126 MHz, CDCl₃) δ (ppm) = 157.99 (**10**), 156.62 (**5**), 156.17 (**6**), 149.50 (**1**), 141.73 (**11**), 137.27 (**3**), 137.22 (**8**), 133.90 (**12**), 132.09 (**15**), 130.08 (**13**), 127.90 (**14**), 124.93 (**9**), 124.14 (**2**), 122.39 (**16**), 121.93 (**4**), 120.05 (**7**).

Calculated for C₁₆H₁₁BrN₂: C = 61.76, H = 3.56 N = 9.00

Found: C = 61.76, H = 3.58, N = 9.08

8. Excited-State Kinetics of an Air-Stable Cyclometalated Iron(II) Complex

[Fe(pbpy)(PMe₃)₂Br] (**1**)



A flask was charged with tetrakis(trimethylphosphine)iron(0) (360 mg, 1 mmol) and dry THF (10 mL) and cooled to -80 °C in a N₂/EtOH bath. 6-(2-Bromophenyl)-2,2'-bipyridine (311 mg, 1 mmol) in THF (8 mL) was added to the yellow solution and stirred for 2 h.

For isolation of this intermediate, the solution was stirred for further 16 h, while allowing to warm to room temperature. Subsequently the solvent was removed in vacuo and the resulting brown orange solid was dried thoroughly to remove residual PMe₃. The raw product was dissolved in dry toluene (25 mL) and filtered. The solvent was removed from the filtrate to yield **1** as a dark brown solid (190 mg, 0.37 mmol, **21** %).

¹H NMR (500 MHz, Benzene-*d*₆) δ (ppm) = 10.09 (d, *J* = 5.7 Hz, 1H), 8.65 (d, *J* = 7.6 Hz, 1H), 7.76 (d, *J* = 7.6 Hz, 1H), 7.42 – 7.18 (m, 4H), 7.01 (d, *J* = 8.0 Hz, 2H), 6.88 (dd, *J* = 16.4, 7.7 Hz, 2H), 0.51 (t, *J* = 3.8 Hz, 18H).

³¹P NMR (202 MHz, C₆D₆) δ (ppm) = -43.00.

Due to the reactivity towards oxygen, this intermediate readily oxidizes but is stable towards water. Most of the residue obtained from the filtration is the oxidized complex of **1** (Fe^{III} instead of Fe^{II}), **1a** with an unknown anion, which was later converted into the PF₆ salt (yield not determined).

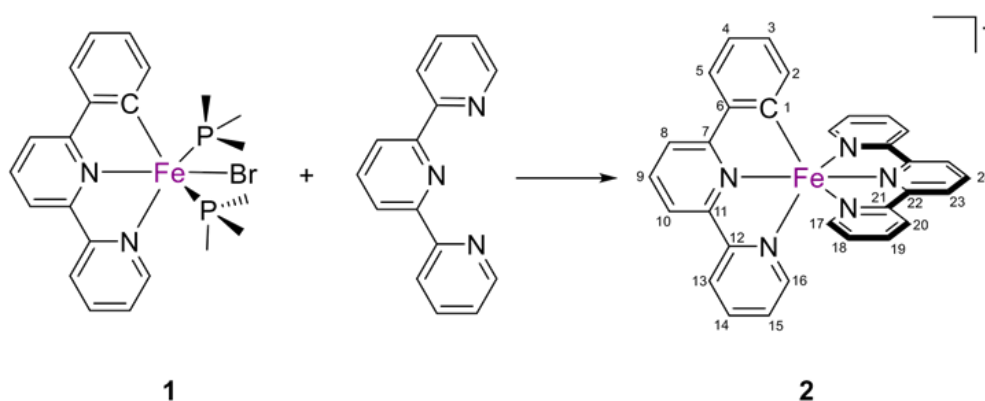
The ¹H-NMR spectrum shows only minor impurities, mostly residual solvent. One characteristic triplet of the methyl groups at 0.51 ppm and only a single resonance in the ³¹P-NMR spectrum indicates that the two PMe₃ ligands are in *trans*-position.

It is yet unclear if there is any reactivity of **1** towards C-Cl bonds, but after work up of the first reaction using chloroform and dichloromethane following the further reaction with terpyridine (see synthesis of **2**), compound **1a-Cl** was obtained, where a chlorido ligand is coordinated to iron instead of a bromido ligand (**1a**). Crystals of the chlorido complex suitable for X-ray diffraction were obtained by slowly

8. Excited-State Kinetics of an Air-Stable Cyclometalated Iron(II) Complex

diffusing pentane into a solution containing both **1a-Cl** and **2** (cf. fig. S1). The crystal structure confirms the *trans* position of the trimethyl phosphane ligands.

[Fe(pbpy)(tpy)]PF₆ (**2**)



To the reaction mixture of [FeBr(pbpy)(PMe₃)₂] (**1**), terpyridine (233 mg, 1 mmol) was added and the solution was stirred overnight and allowed to warm to room temperature. The solvent was removed and the dark residue was redissolved in a minimal amount of methanol (15 mL) under air. The dark solution was added dropwise to a large excess of diethylether (200 mL). The suspension was stirred for 20 minutes and filtered.

The purple residue was washed with water to remove the bis(terpyridine) complex **3**, until the filtrate acquired a pale blue color. This indicated that only **2** Br was left which has a low solubility in water. For yield maximation it is possible to extract the aqueous phase with DCM. The residue was dissolved in methanol (20 mL) and stirred with KPF₆ (2 eq. 368 mg) for 30 minutes, after which 80 mL water were added. The green precipitate was purified using reversed phase column chromatography (C18 Silica, 17 % C) with methanol as eluent. The eluting green band was collected. This chromatographic procedure was repeated two times. The green raw product was crystallized from acetone/pentane to yield dark green crystals of **2** (**26 %**, 171 mg, 0.26 mmol) based on [Fe(PMe₃)₄].

¹H NMR (500 MHz, Acetone-*d*₆) δ (ppm) = 8.89 (d, *J* = 7.9 Hz, 2H, **23**), 8.67 (d, *J* = 2.9 Hz, 1H, **10**), 8.66 (d, *J* = 3.1 Hz, 1H, **13**), 8.52 (d, *J* = 8.0 Hz, 2H, **17**), 8.46 (d, *J* = 8.0 Hz, 1H, **8**), 8.38 – 8.34 (m, 1H, **9**), 8.34 – 8.31 (m, 1H, **24**), 7.98 – 7.93 (m, 1H, **14**), 7.93 – 7.90 (m, 1H, **5**), 7.73 (td, *J* = 7.7, 1.5 Hz, 2H, **18**), 7.64 (d, *J* = 5.4 Hz, 1H, **16**), 7.18 (ddd, *J* = 7.1, 5.5, 1.2 Hz, 1H, **15**), 7.09 (d, *J* = 5.7 Hz, 2H, **20**), 7.00 (ddd, *J* = 7.2, 5.7, 1.3 Hz, 2H, **19**), 6.75 (td, *J* = 7.4, 1.2 Hz, 1H, **4**), 6.47 (td, *J* = 7.3, 1.3 Hz, 1H, **3**), 5.70 (dd, *J* = 7.5, 1.1 Hz, 1H, **2**).

8. Excited-State Kinetics of an Air-Stable Cyclometalated Iron(II) Complex

^{13}C NMR (126 MHz, Acetone- d_6) δ (ppm) = 196.84 (**1**), 168.69 (**7**), 158.53 (**21**), 158.51 (**11**), 158.05 (**12**), 157.53 (**22**), 151.89 (**16**), 151.00 (**20**), 147.80 (**6**), 138.29 (**14**), 137.05 (**9**), 136.06 (**2**), 135.48 (**18**), 130.29 (**24**), 128.94 (**3**), 126.99 (**15**), 126.13 (**19**), 124.84 (**5**), 123.71 (**13**), 123.12 (**4**), 122.83 (**17**), 121.96 (**23**), 119.64 (**10**), 118.73 (**8**).

HRMS (ESI): m/z [$M\text{-PF}_6$] $^+$ calculated for $\text{C}_{31}\text{H}_{22}\text{FeN}_5$: 520.1225, found: 520.1283 m/z

Elemental analysis calculated for $\text{C}_{31}\text{H}_{22}\text{F}_6\text{FeN}_5\text{P}$: C = 55.96, H = 3.33, N = 10.59

Found: C = 55.71, H = 3.47, N = 10.51

UV-Vis (MeCN): λ (ϵ) = 416 nm ($0.77 \cdot 10^4 \text{ M}^{-1} \text{ cm}^{-1}$), 618 nm, ($0.92 \cdot 10^4 \text{ M}^{-1} \text{ cm}^{-1}$), 670 nm ($0.76 \cdot 10^4 \text{ M}^{-1} \text{ cm}^{-1}$), 806 nm ($0.17 \cdot 10^4 \text{ M}^{-1} \text{ cm}^{-1}$)

[Fe(pbpy)(tpy)](BPh₄) (2 BPh₄)

[Fe(pbpy)(tpy)](PF₆) (0.006 mmol, 3.6 mg) was dissolved in MeOH (2 mL) and NaBPh₄ (4 eq., 0.024 mmol, 8.2 mg) was added. The green precipitate was filtered off and washed thoroughly with water. The product was dissolved in a miniscule amount of DCM and layered with n-hexane. Single crystals of **2BPh₄** were obtained after a few days (3.8 mg, 0.0045 mmol, 75 %).

Quantum chemical calculations

All calculations presented here were performed using the ORCA program system (version 4.0.1).^[7] Unconstrained geometry optimizations were conducted via the PBEh-3c method of the Grimme group.^[8] All presented optimized structures are confirmed to be minima structures by numerical frequency calculations and the absence of negative frequencies. Correction for dispersion interaction was included by DFT-D3 with Becke-Johnson damping (D3BJ)^[9] for all calculations presented here.

TD-DFT XANES^[10] and DFT VtC-XES^[11] calculations were accomplished using a modified TPSSh^[12] functional, with an adjusted Hartree-Fock exchange of 12.5 %^[13–16] in conjunction with the RIJCOSX approximation and the def2-TZVP^[17] basis set, combined with the def2-TZVP/J^[18] auxiliary basis set (with a special integration accuracy of 5) on all atoms except Fe, for which the expanded CP(PPP) basis set^[19] (with a special integration accuracy of 7) was used.

TD-DFT UV/VIS calculations were accomplished using a modified TPSSh functional, with an adjusted Hartree-Fock exchange of 5 % in conjunction with the RIJCOSX approximation and the def2-TZVP basis set,^[17] combined with the def2-TZVP/J^[18] auxiliary basis set (with a special integration accuracy of 5) on all atoms. It has been shown in a previous computational study of complexes **2** and **3** that the non-hybrid functional TPSS^[12] outperforms the hybrid functional TPSSh (10 % Hartree-Fock exchange).^[20] Nevertheless, we observed a benefit of a slight inclusion of only 5 % Hartree-Fock exchange in respect to the overall accuracy of modelling the whole UV/VIS spectra (see figure S15), especially concerning the splitting between MLCT features and ligand localized features for both complexes (**2** and **3**).

TD-DFT UV/VIS transitions were broadened by a 1750 cm⁻¹ Gaussian (fwhm) and shifted by -1900 cm⁻¹. Kohn-Sham orbitals were visualized with the IboView program (version 20150427).^[21] Orbital populations were extracted via Löwdin Reduced Orbital Population Analysis using MOAnalyzer (version 1.2).^[22]

DFT levels shown in the manuscript were calculated using the TPSSh functional in conjunction with the def2-TZVPP basis set using very tight SCF convergence criteria (energy change of 10⁻⁹ au). Solvation by acetonitrile is covered by the SMD solvation model.^[23]

X-Ray spectroscopy

CtC-XES

Core-to-core X-ray emission spectroscopy (CtC-XES, K $\beta_{1,3}$ emission),^[24,25–27] valence-to-core X-ray emission spectroscopy (VtC-XES, K $\beta_{2,5}$ emission)^[28a–c,11,28d] and high energy resolution fluorescence

8. Excited-State Kinetics of an Air-Stable Cyclometalated Iron(II) Complex

detected XANES (HERFD-XANES)^[29] were performed in the solid state and the results compared to the reference complex **3**.

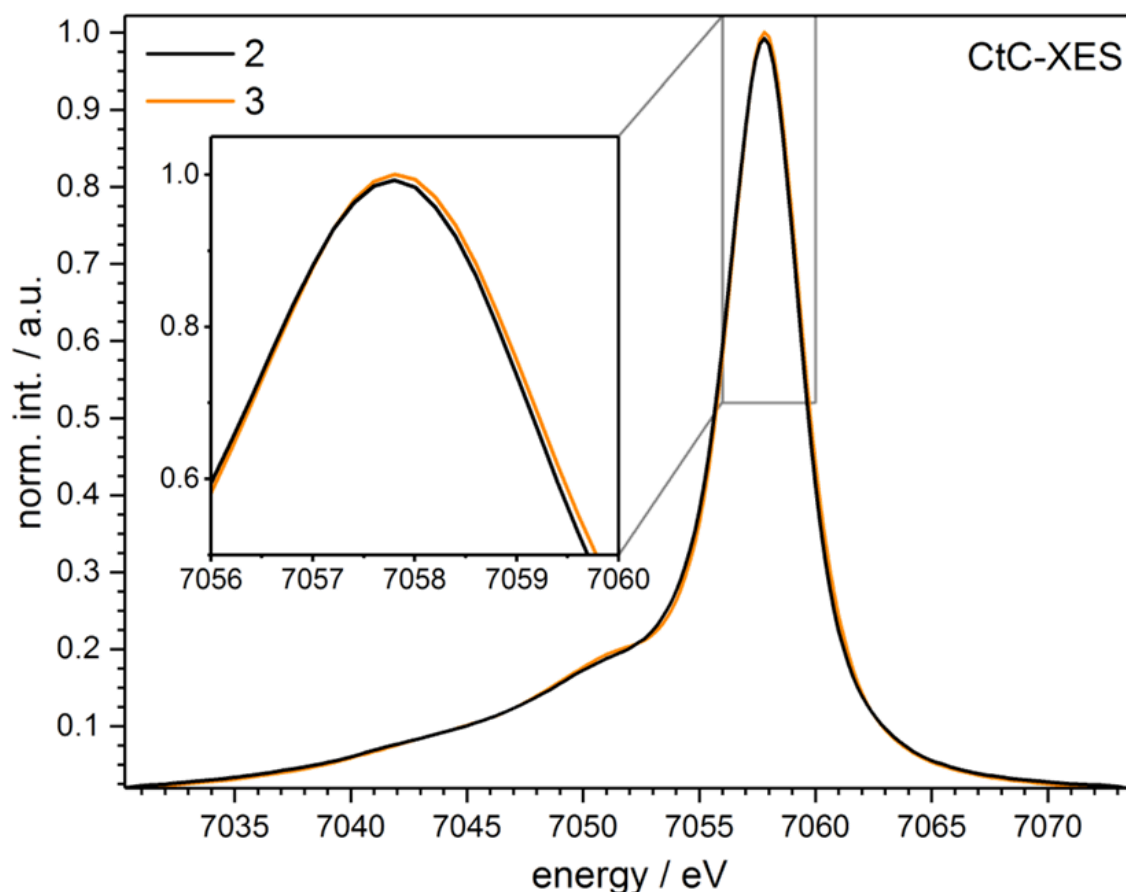


Figure S1: Experimental CtC-XES spectra of complexes **2** and **3**

The obtained CtC-XES spectrum of **2** is compared to the spectrum of the reference complex **3** in figure S3. Both complexes (**2**, **3**) are clearly in a low-spin configuration (LS, $S = 0$), since the satellite ($K\beta'$) is not separated from the mainline ($K\beta_{1,3}$) and the intensity ratio between both signals ($K\beta'/K\beta_{1,3}$) is small.^[27]

Nevertheless, the mainline is slightly red shifted for complex **2** in relation to **3**. Since both complexes are in a Fe $3d^6$ LS configuration, this shift is interpreted as an increased covalency between the central Fe atom and the pbpy ligand (**2**) compared to tpy (**3**).^[25–27]

HERFD-XANES

In general, a well-resolved, asymmetrical pre-edge feature A at around 7114 eV and three near-edge features B (at around 7118 eV), C (at around 7123 eV) and D (at around 7125 eV), are observed (see figure S4, top). Since near-edge features are caused by transition to higher LUMO levels, we will focus on the pre-edge feature A. A slightly increased pre-edge energy is observed for **2** (7113.8 eV), in comparison to **3** (7113.6 eV). To understand the quantum mechanical origin of the observed HERFD-

XANES features, TD-DFT XANES calculations applying the TPSSh functional with an adjusted Hartree-Fock exchange of 12.5 % were performed (Figure S4, bottom).^[13–16] Since an excellent agreement between experiment and theory is obtained, further information of the underlying transitions can be extracted. For both **2** and **3** the pre-edge feature A consists mainly of Fe 1s → e_g* transitions, superimposed by contributions of tpy π* dominated acceptor orbitals (predominant acceptor orbitals of predominant core-excited states S1 to S5 are shown in figure S4). Therefore, the experimentally observed blue shift of pre-edge feature A of complex **2** in relation to **3** is attributed to a destabilization of the e_g* and / or tpy π* energies.

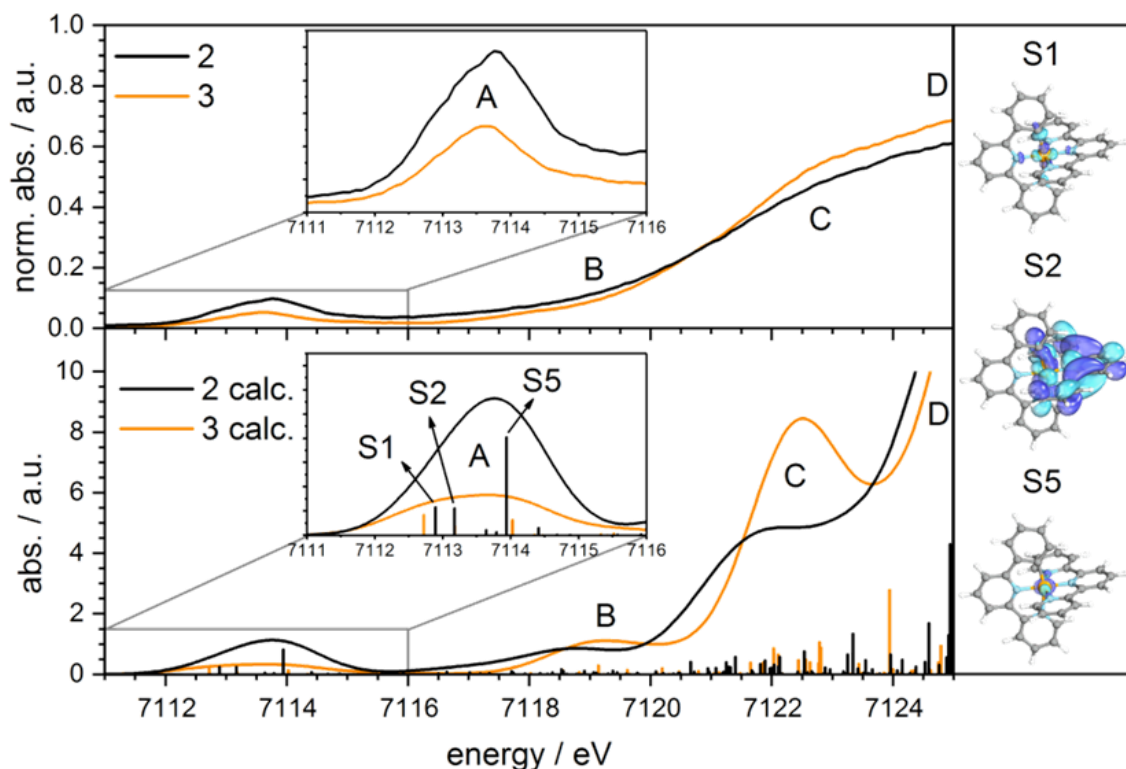


Figure S2: Experimental Fe K-edge HERFD-XANES spectra of complexes **2** and **3** (top) in comparison to theoretical Fe K-edge XANES spectra (bottom).

VtC-XES

Complementary to HERFD-XANES, VtC-XES was applied to characterize the HOMO states of **2**. Experimental spectra are shown in figure S5 (top). The VtC-XES spectrum is dominated by a strong band, which can be divided into four spectral regions: low-energy shoulder A, main feature B, shoulder C and high-energy feature D. The low-energy shoulder A and the main feature B of **2** are decreased in intensity and red shifted in relation to **3**. The high-energy shoulder C is only observed for the

8. Excited-State Kinetics of an Air-Stable Cyclometalated Iron(II) Complex

cyclometalated complex **2** and is not expected to appear in Fe^{II} polypyridyl/NHC complexes,^[16] since it is connected to the interaction of the pbpy ligand and the Fe center (cf. figure S5, bottom).

The VtC-XES spectra were simulated by DFT calculations using an adjusted TPSSh functional (for details see quantum-chemical calculations section). Theory and experiment agree very well (see Figure S5). The low-energy shoulder A is caused by phenyl/polypyridyl σ donor orbitals, while the main feature B originates from a superposition phenyl/polypyridyl σ/π donor orbitals (donor orbitals of the predominant transitions of VtC-XES features A - D are shown in Figure S5), in line with previous studies on similar compounds.^[16] Therefore, the observed redshift of feature A and B of complex **2** is led back to a stabilization of the phenyl/polypyridyl σ and π levels in relation to **3**. The additional feature C is caused by a single transition of a donor orbital which reflects the σ bonding interaction of the pbpy ligand and the Fe $3d_{z^2}$ orbital.

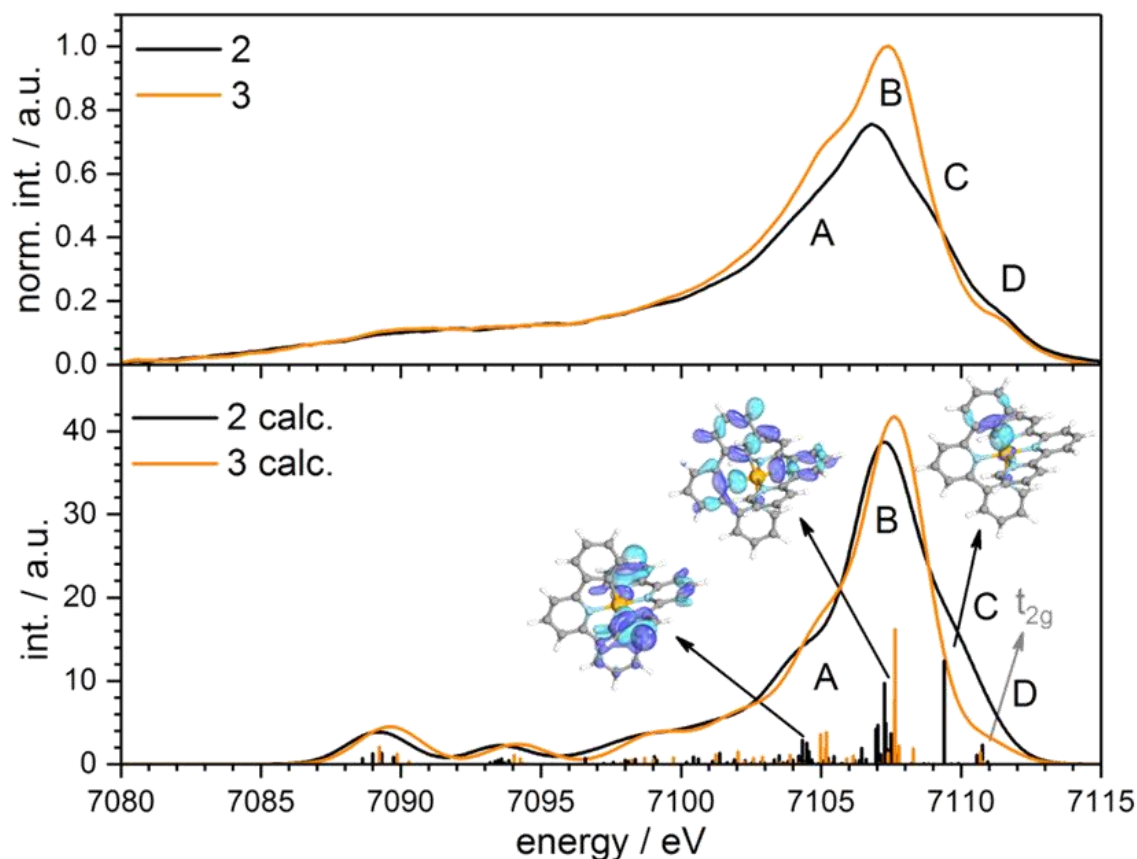


Figure S3: Experimental Fe K-edge VtC-XES spectra of complexes **2** and **3** (top) in comparison to theoretical Fe K-edge VtC-XES spectra (bottom).

Electrochemistry

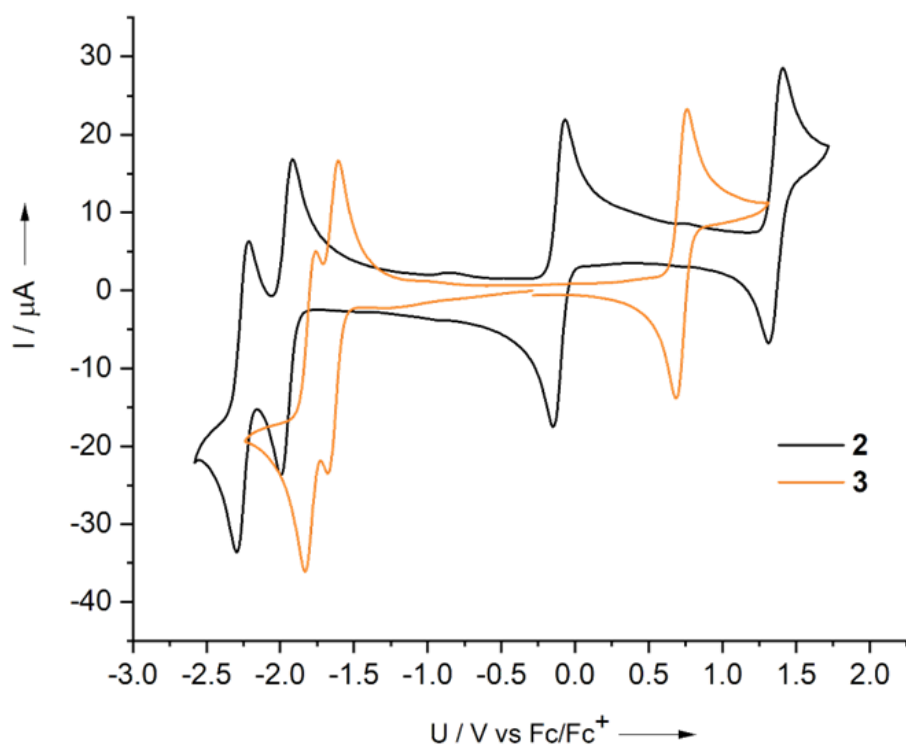


Figure S4: Cyclic voltammogram of **2** and **3** (scan rate 100 mV/s, MeCN).

The data for the $[\text{Fe}(\text{tpy})_2](\text{PF}_6)_2$ complex **3** was already published.^[30]

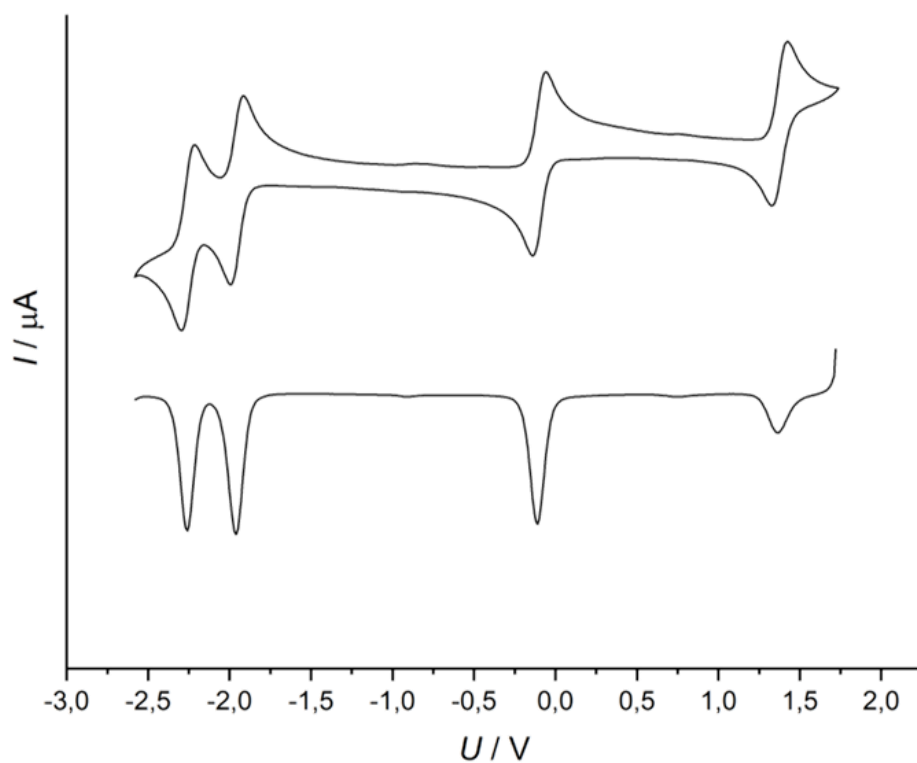


Figure S5: Cyclic voltammogram (scan rate 100 mV/s) and square-wave voltammogram (25 Hz) of $[\text{Fe}(\text{pbpy})(\text{tpy})]\text{PF}_6$ **2** in MeCN.

8. Excited-State Kinetics of an Air-Stable Cyclometalated Iron(II) Complex

Table S 1: Electrochemical data for the reversible oxidation at $E_{1/2}^0 = -0.11$ V vs. $\text{Fc}^{0/+}$ of complex **2**.

ν / mV/s	50	100	200	400	600	800	1000
E_{pc} / V	-0.15	-0.15	-0.15	-0.15	-0.15	-0.15	-0.16
E_{pa} / V	-0.07	-0.07	-0.07	-0.07	-0.07	-0.06	-0.06
$E_{1/2}$ / V	-0.11	-0.11	-0.11	-0.11	-0.11	-0.11	-0.11
I_{pc} / μA	-1.23	-1.71	-2.49	-3.60	-4.42	-5.14	-5.68
I_{pa} / μA	1.22	1.73	2.57	3.75	4.47	5.19	5.85
ΔE / mV	85	-80	-75	-75	-85	-90	-95
$ I_c/I_a $	1.01	0.99	0.97	0.96	0.99	0.99	0.97
$ I_{pc}/\nu^{1/2} $	0.17	0.17	0.18	0.18	0.18	0.18	0.18
$ I_{pa}/\nu^{1/2} $	0.17	0.17	0.18	0.19	0.18	0.18	0.18

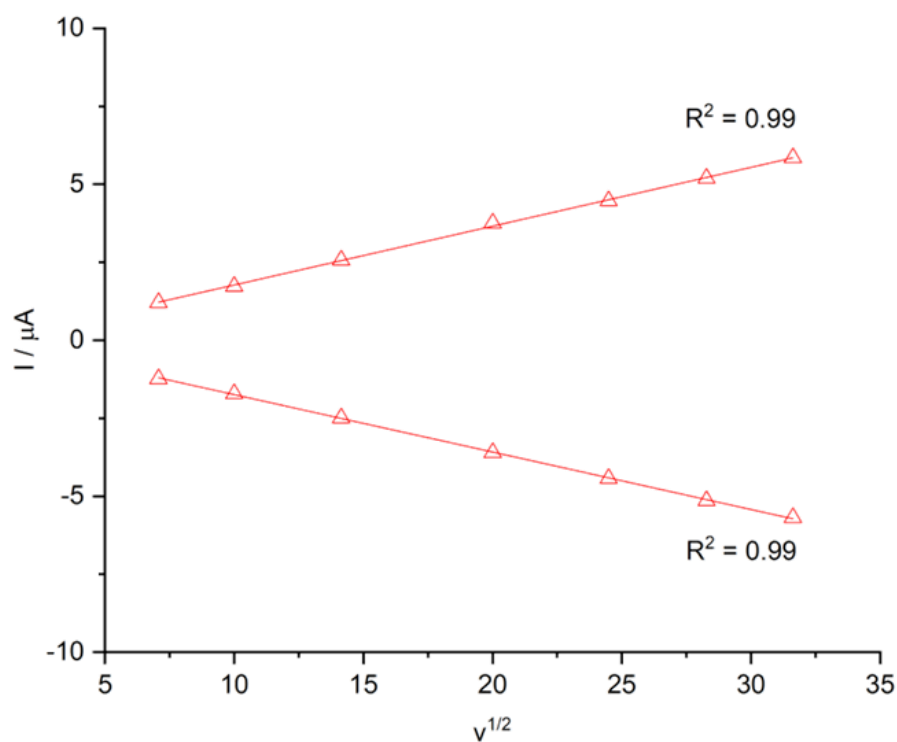


Figure S6: Linear dependence of forward current peaks I_{pc} and I_{pa} versus the square root of the scan rate ν for the reversible oxidation at $E_{1/2}^0 = -0.11$ V vs. $\text{Fc}^{0/+}$ of complex **2**.

8. Excited-State Kinetics of an Air-Stable Cyclometalated Iron(II) Complex

Table S2: Electrochemical data for the irreversible oxidation at $E_{1/2}^0 = 1.37$ V vs. $\text{Fc}^{0/+}$ of complex **2**.

v / mV/s	50	100	200	400	600	800	1000
E_{pc} / V	1.31	1.31	1.30	1.30	1.29	1.28	1.27
E_{pa} / V	1.42	1.42	1.43	1.44	1.45	1.46	1.47
$E_{1/2}$ / V	1.37	1.37	1.37	1.37	1.37	1.37	1.37
I_{pc} / μA	-1.03	-1.39	-1.89	-2.43	-2.72	-3.00	-3.12
I_{pa} / μA	1.06	1.46	1.96	2.55	2.92	3.17	3.33
ΔE / mV	110	110	130	140	160	180	200
$ I_c/I_a $	0.97	0.96	0.96	0.95	0.93	0.95	0.94
$ I_{pc}/v^{1/2} $	0.15	0.14	0.13	0.12	0.11	0.11	0.10
$ I_{pa}/v^{1/2} $	0.15	0.15	0.14	0.13	0.12	0.11	0.11

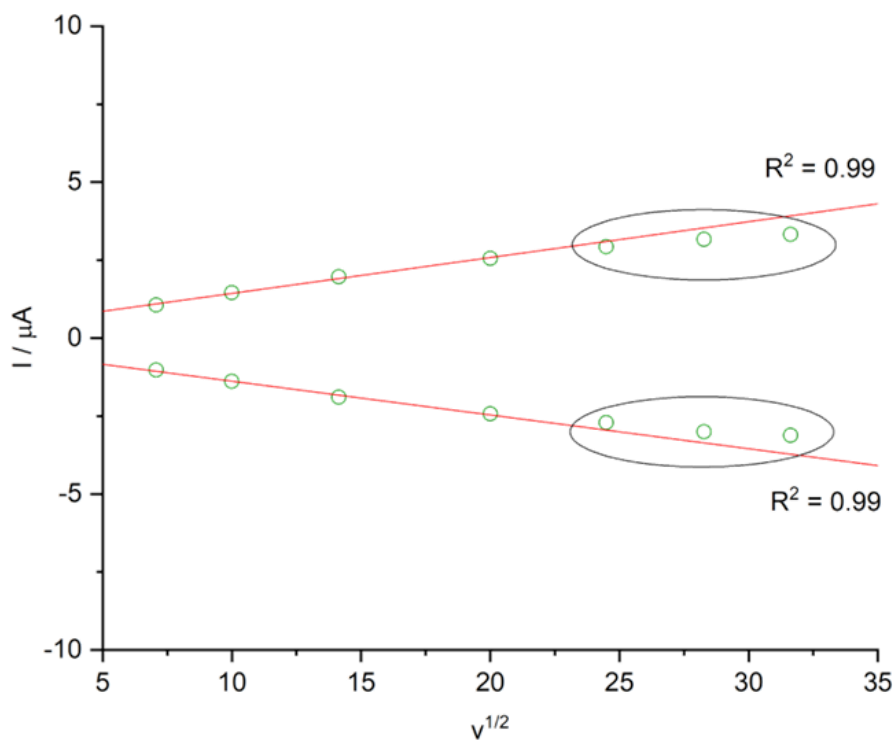


Figure S7: Linear dependence of forward current peaks I_{pc} and I_{pa} versus the square root of the scan rate v for the irreversible oxidation at $E_{1/2}^0 = 1.37$ V vs. $\text{Fc}^{0/+}$ of complex **2**. Encircled data points ($v = 600, 800, 1000$ mV/s) are excluded from the linear fit. This means that the Randles-Sevcik equation is only valid for the 50-400 mV/s scan rates.

8. Excited-State Kinetics of an Air-Stable Cyclometalated Iron(II) Complex

Table S3: Electrochemical data for the quasireversible reduction at $E_{1/2}^0 = -1.96$ V vs. $\text{Fc}^{0/+}$ of complex **2**.

v / mV/s	50	100	200	400	600	800	1000
E_{pc} / V	-2.00	-2.00	-2.00	-2.00	-2.00	-2.01	-2.01
E_{pa} / V	-1.91	-1.92	-1.92	-1.92	-1.92	-1.92	-1.91
$E_{1/2}$ / V	-1.96	-1.96	-1.96	-1.96	-1.96	-1.96	-1.96
I_{pc} / μA	-1.04	-1.50	-2.39	-3.46	-4.00	-4.64	-4.81
I_{pa} / μA	1.08	1.58	2.25	3.29	3.89	4.32	4.81
ΔE / mV	90	80	75	80	80	90	100
$ I_{\text{c}}/I_{\text{a}} $	1.04	1.05	0.94	0.95	0.97	0.93	1.00
$ I_{\text{pc}}/v^{1/2} $	0.15	0.15	0.17	0.17	0.16	0.16	0.15
$ I_{\text{pa}}/v^{1/2} $	0.15	0.16	0.16	0.16	0.16	0.15	0.15

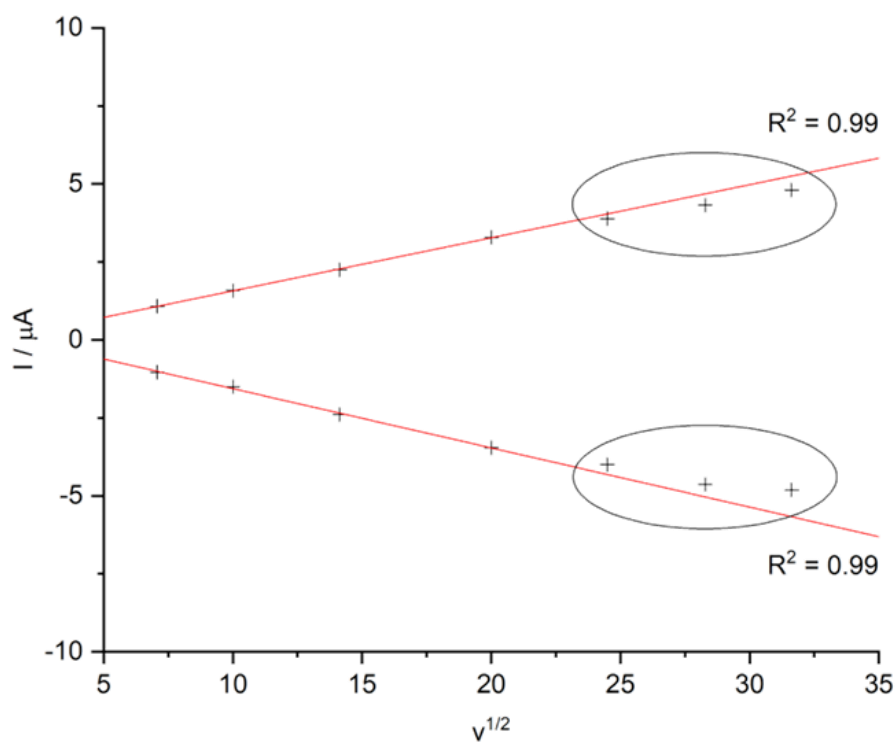


Figure S8: Linear dependence of forward current peaks I_{pc} and I_{pa} versus the square root of the scan rate v for the quasireversible reduction at $E_{1/2}^0 = -1.96$ V vs. $\text{Fc}^{0/+}$ of complex **2**. Encircled data points ($v = 600, 800, 1000$ mV/s) are excluded from the linear fit. This means that the Randles-Sevcik equation is only valid for the 50-400 mV/s scan rates.

8. Excited-State Kinetics of an Air-Stable Cyclometalated Iron(II) Complex

8. Excited-State Kinetics of an Air-Stable Cyclometalated Iron(II) Complex

Table S4: Electrochemical data for the quasireversible reduction at $E_{1/2}^0 = -2.25$ V vs. $\text{Fc}^{0/+}$ of complex **2**.

v / mV/s	50	100	200	400	600	800	1000
E_{pc} / V	-2.30	-2.30	-2.29	-2.29	-2.30	-2.30	-2.31
E_{pa} / V	-2.21	-2.22	-2.22	-2.22	-2.22	-2.21	-2.21
$E_{1/2}$ / V	-2.25	-2.26	-2.25	-2.26	-2.26	-2.26	-2.26
I_{pc} / μA	-1.14	-1.41	-2.16	-3.24	-3.89	-4.56	-4.89
I_{pa} / μA	1.05	1.43	2.24	3.34	3.91	4.50	4.96
ΔE / mV	85	80	75	70	80	90	100
$ I_c/I_a $	0.92	1.01	1.04	1.03	1.01	0.99	1.01
$ I_{pc}/v^{1/2} $	0.16	0.14	0.15	0.16	0.16	0.16	0.15
$ I_{pa}/v^{1/2} $	0.15	0.14	0.16	0.17	0.16	0.16	0.16

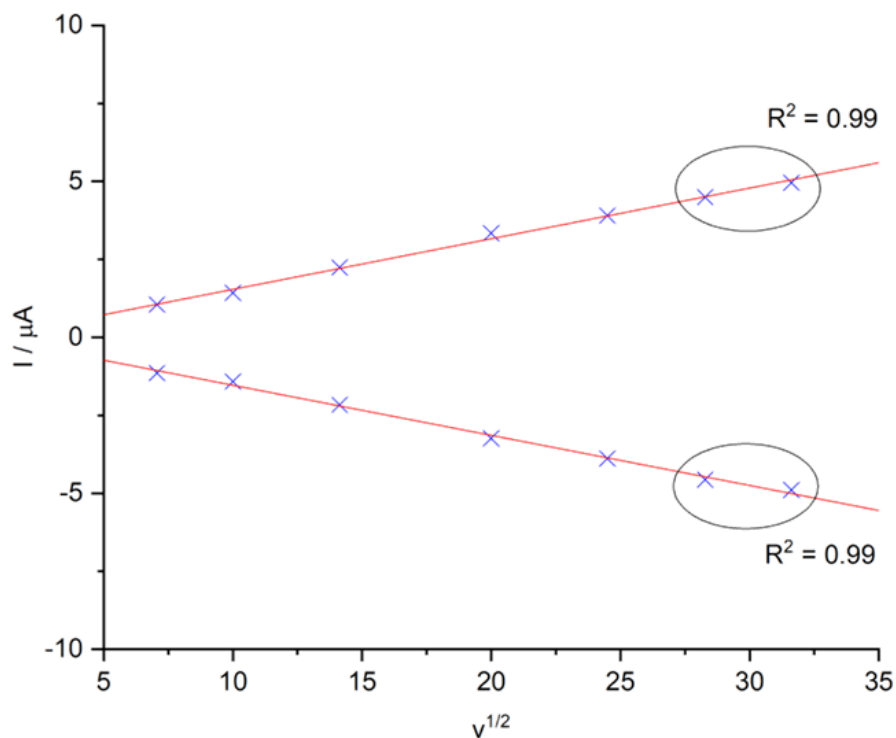


Figure S9: Linear dependence of forward current peaks I_{pc} and I_{pa} versus the square root of the scan rate v for the quasireversible reduction at $E_{1/2}^0 = -2.25$ V vs. $\text{Fc}^{0/+}$ of complex **2**. Encircled data points ($v = 800, 1000$ mV/s) are excluded from the linear fit. This means that the Randles-Sevcik equation is only valid for the 50-600 mV/s scan rates.

UV-Vis Spectroscopy

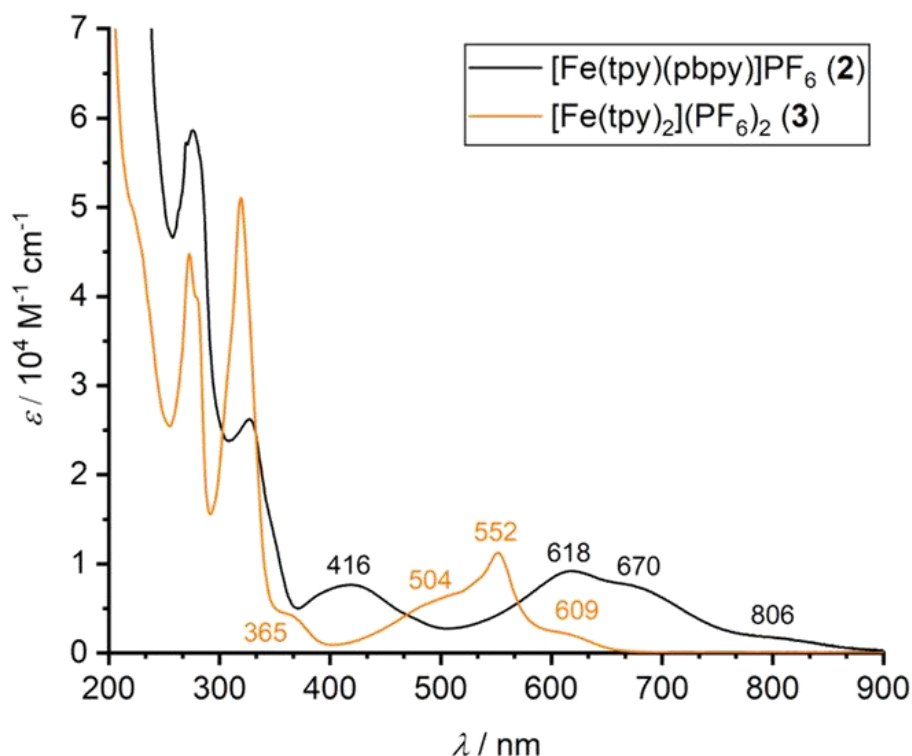


Figure S10: Electronic absorption spectra of **2** and **3** in MeCN

The data for the [Fe(tpy)₂](PF₆)₂ complex **3** was already published.^[30]

The absorption properties of **2** and **3** are quite different. While the absorption maximum in **3** is located at 552 nm, the absorption maximum in **2** is bathochromically shifted to 618 nm. The absorption itself reaches up into the NIR with shoulders at 670 and 806 nm.

The bands below 375 nm are caused by ligand localized transitions. The bands above 375 nm are expected to be MLCT-based transitions. The exact assignment was done via TD-DFT calculations and is further discussed in the “quantum chemical calculations” paragraph. Table S5 summarizes the main donor and acceptor orbitals from the transitions in the 500-900 nm region.

The complex was also examined for solvatochromism, as shown in figure S13. UV-Vis absorption spectra were recorded in methanol, ethanol, acetonitrile (MeCN), dichloromethane (DCM), dimethylsulfoxide (DMSO), and acetone at a respective concentration of 10⁻⁵ M and normalized to the MLCT-absorption maximum. Beside of DMSO, the spectral position of the absorption maximum correlates linearly with the permittivity ϵ of the solvents and increasing the permittivity by going from

8. Excited-State Kinetics of an Air-Stable Cyclometalated Iron(II) Complex

DCM to MeCN results in a small hypsochromic shift ($\Delta\lambda = -9$ nm; $+232$ cm^{-1} difference) (figure S14).

Using ET(30) values^[31] no such correlation with shifts of the absorption band is found.

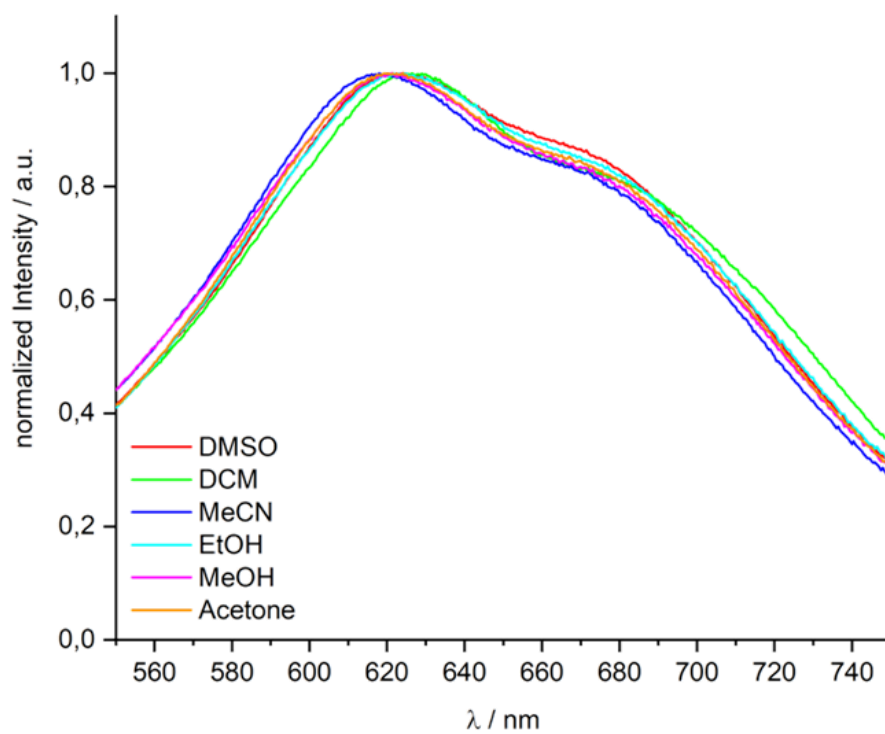


Figure S11: MLCT-absorption maxima normalized to 1 of (2) in different solvents (10^{-5} mol L^{-1}).

8. Excited-State Kinetics of an Air-Stable Cyclometalated Iron(II) Complex

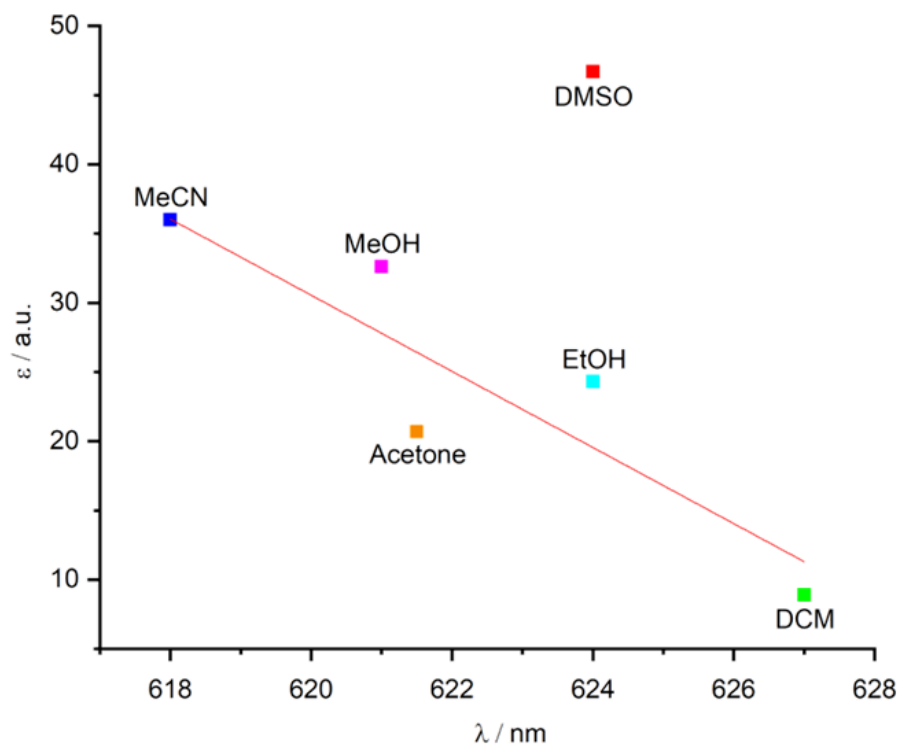


Figure S12: Wavelength of the MLCT absorption maxima of (**2**) in different solvents plotted versus the relative permittivity of the respective solvent. The linear fit excludes the data point of DMSO since it severely deviates from the overall trend.

8. Excited-State Kinetics of an Air-Stable Cyclometalated Iron(II) Complex

Calculated UV/VIS spectra

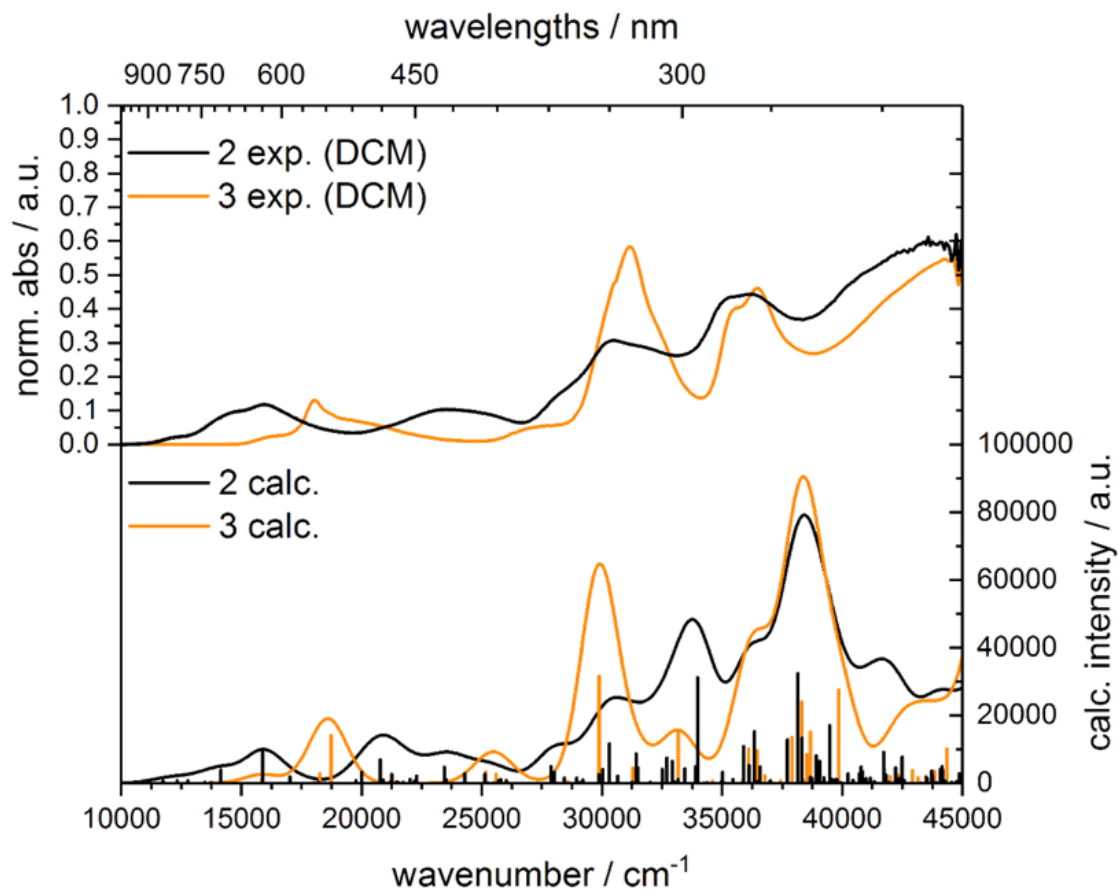


Figure S13: Experimental UV/VIS/NIR spectra of **2** and **3** in DCM (top) in comparison to theoretical UV/VIS/NIR spectra (bottom).

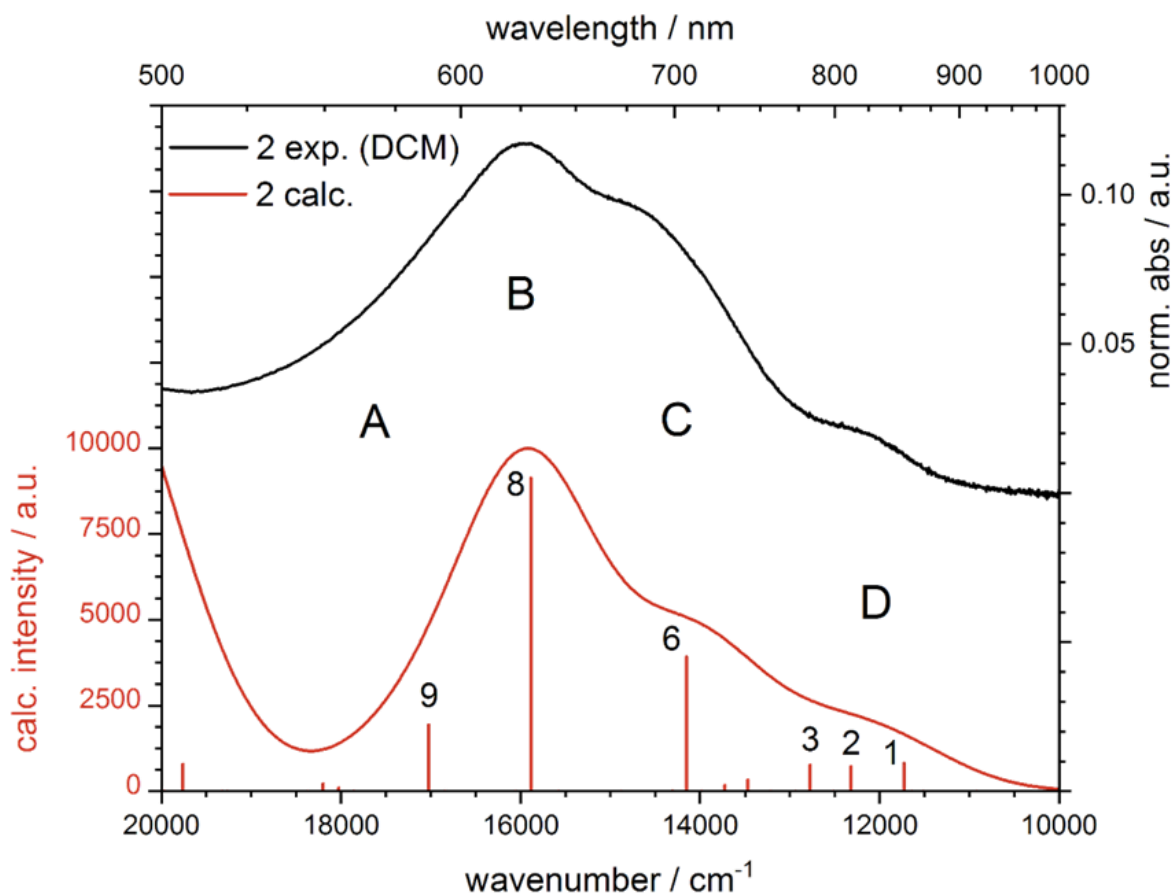


Figure S14: Experimental UV/VIS of **2** in DCM (top) in comparison to theoretical UV/VIS spectrum (bottom). Predominant transitions are labeled by their singlet excited state order, with 1 being the transition to singlet excited state of lowest energy.

The theoretical UV/VIS spectra of **2** and **3** were calculated by TDDFT using the TPSSh functional with an adjusted Hartree-Fock exchange to 5 %. An overall impressive agreement could be achieved (as shown in figure S15), especially in the low-energy region from 500 – 900 nm (figure S16, which allows an extraction of detailed information about the involved molecular levels and their chemical nature. Since our main interest here is the MLCT region, we will focus on the low-energy signal of complex **2** for clarity, located between 500 and 900 nm.

In general, four spectral features are observed in the MLCT region, starting with the high-energy shoulder A, followed by main feature B and low-energy shoulders C and D. All underlying predominant transitions (figure S16, labeled transitions 1 – 9) are caused by Fe localized donor orbitals, which reflect the Fe t_{2g} orbitals (HOMO-2, HOMO-1, HOMO; detailed information about the excited state composition is given in table S5; acceptor and donor orbital compositions are given in table S5). High-energy shoulder A is solely caused by a transition to singlet excited state 9, whose predominant acceptor orbital is the LUMO+3, reflecting a pbpy π^* orbital. Only minor proportions of the LUMO+1 reflecting

8. Excited-State Kinetics of an Air-Stable Cyclometalated Iron(II) Complex

the antibonding Fe $3d_{xz/yz} - \text{tpy } \pi^*$ and the LUMO+2, reflecting the Fe $3d_{xy} - \text{bpy } \pi^*$ interaction are contributing to excited state 9 (see supporting information table S6). Main feature B is evoked by transition 8, which is composed of the LUMO+2 (Fe $3d_{xy} - \text{bpy } \pi^*$) as the predominant acceptor and the LUMO+1 (Fe $3d_{xz/yz} - \text{tpy } \pi^*$) as the minor acceptor. Transition 6 is causing shoulder C, with the LUMO as the main acceptor, which reflects a tpy π^* orbital and the LUMO+2 (Fe $3d_{xy} - \text{bpy } \pi^*$) as secondary acceptor. Low-energy shoulder D is caused by three transitions, 1, 2 and 3 (see table S5), with the predominant acceptors LUMO+1 (Fe $3d_{xz/yz} - \text{tpy } \pi^*$), LUMO (tpy π^*) and LUMO+2 (Fe $3d_{xy} - \text{bpy } \pi^*$). No additional significant secondary contributions to the excited states 1, 2 and 3 are observed.

8. Excited-State Kinetics of an Air-Stable Cyclometalated Iron(II) Complex

Table S5: Detailed information about the excited state composition of predominant transition causing low-energy UV/VIS/NIR features A – D of complex **2** (Figure S21). Only transitions occupying at least 10 % of the excited state composition are taken into account for clarity.

Feature	Order	Excited state composition	Donor	Acceptor
A	9	HOMO → LUMO+3 (0.55)		
		HOMO-1 → LUMO+1 (0.16)		
		HOMO-2 → LUMO+2 (0.10)		
B	8	HOMO-2 → LUMO+2 (0.55)		
		HOMO-1 → LUMO+1 (0.28)		
C	6	HOMO-1 → LUMO (0.61)		
		HOMO-1 → LUMO+2 (0.23)		
D	3	HOMO → LUMO+2 (0.90)		
		2 HOMO → LUMO (0.92)		
		1 HOMO → LUMO+1 (0.92)		

Table S6: AO populations of predominant acceptor and donor orbitals of the MLCT transitions in the UV/VIS/NIR spectrum.

Element / ligand / fragment	Population ^[a] / %						
	H-2 ^[b]	H-1 ^[b]	H ^[b]	L ^[c]	L+1 ^[c]	L+2 ^[c]	L+3 ^[c]
Fe 3d	78.7	71.7	65.7	1.4	12.9	6.3	2.1
tpy	2.1	14.7	6.6	62.2	59.8	7.1	7.6
bpy (pbpy)	8.6	1.1	5	7.7	1.5	59.4	52.5
ph (pbpy)	2.5	2.1	13.1	0.3	0.7	0.4	10.2

^[a] Population of the given element via Löwdin reduced orbital population analysis. All given values are the sum over all AOs of a given element or fragment.

^[b] H : HOMO, ^[c] L : LUMO

8. Excited-State Kinetics of an Air-Stable Cyclometalated Iron(II) Complex

XYZ coordinates of all optimized structures:

Optimized structure of **3**:

59

C	5.04873391857648	2.90881959139104	-4.30698938987414
C	6.11165793721858	2.05310485324152	-4.05703785731485
C	6.37638753986199	1.62060597526765	-2.76576830958664
C	5.55423294314135	2.06569013456251	-1.74039936975324
N	4.53995155575388	2.88753012196515	-2.00566617263250
C	4.26538233180264	3.31640980298293	-3.23662562706555
C	3.09854604370143	4.21264589894118	-3.28206158452367
C	5.65776972209847	1.72889107217986	-0.31121747425080
C	6.63212162070624	0.89816469702652	0.21484310183638
C	6.63956788666347	0.64474492549012	1.57738126971416
C	5.67009158734726	1.23169848673194	2.36997752188489
C	4.72834646630151	2.05179370867612	1.77051935150979
N	4.71590081425521	2.29899028287865	0.46627775644637
C	1.51107374898522	5.62302784741817	-4.37610888844452
C	2.61860210795344	4.79258639307887	-4.44376420379448
N	2.51768985671111	4.43376436455490	-2.08605652948038
C	1.45721553620322	5.23021204324965	-2.02817834537639
C	0.91928423947501	5.84617513215441	-3.14621258378318
Fe	3.42648682850047	3.46403047061360	-0.56441880189273
C	2.63431401913328	5.14835137543843	1.53378968280025
N	2.31052411143759	4.03555153194229	0.87702286744759
C	1.24105756118405	3.30390500043642	1.18624584166730
C	0.41079295662243	3.69026326855477	2.22878643938646
C	0.72631019847266	4.84582592311539	2.92853074722173
C	1.84616933610325	5.58989788504347	2.58696215893623
C	1.08947475261901	2.12077080228129	0.32369167878132
C	3.85563766368586	5.78378698451933	1.01306410842467
N	2.04810593489426	1.98689166131232	-0.61423673752151
C	1.99421935341340	0.94808107241297	-1.43903920121182
C	0.99320132457794	-0.00745785197328	-1.37830368197635
C	0.00681464045214	0.12475768944686	-0.41795743910423
C	0.05696551216582	1.20692286159302	0.44644919358886
C	6.12908824158791	6.79652352055865	-0.10094629038933

8. Excited-State Kinetics of an Air-Stable Cyclometalated Iron(II) Complex

C	5.53028737619034	5.63484279666717	-0.56007394155931
N	4.42367972287162	5.13541456825054	-0.02308400013848
C	4.39536343024871	6.95006953873171	1.52750167419909
C	5.55084531963741	7.46586493075097	0.96221248871001
H	6.73727317085112	1.72057764736325	-4.87395474784508
H	4.84690706876410	3.24142972941077	-5.31492169664719
H	7.20489650141915	0.95321106684960	-2.57746869844870
H	7.38084562966121	0.44968585551355	-0.42253008002359
H	7.39184852239768	-0.00100140815501	2.00886912034962
H	5.63643762771616	1.06264112091537	3.43652897290001
H	3.95877476451813	2.52417109538803	2.36569772795763
H	3.09647295731823	4.60496087471390	-5.39475461352339
H	1.11998080491300	6.08622193485259	-5.27142504923848
H	0.05446923124751	6.48581654897691	-3.04521730340792
H	1.01499352183180	5.38640641805557	-1.05367147207593
H	5.96060432320803	5.09072124597273	-1.38978530031311
H	7.02969857256080	7.16131913098172	-0.57324430486679
H	5.98907830047317	8.37569174260503	1.34855526055099
H	3.92710004246005	7.45738226817046	2.35895324536066
H	2.08705940414004	6.48876477325191	3.13587608983056
H	0.09544646007580	5.16843382013609	3.74538811160930
H	-0.46262636926466	3.11495989635580	2.49990820339273
H	-0.70358167420050	1.32950247603287	1.20435336324951
H	-0.79095008377397	-0.60083936023412	-0.33939277496416
H	0.99506326864025	-0.83451621889679	-2.07344650283500
H	2.77832881448821	0.86968898025268	-2.17972900389262

Optimized structure of **2**:

59

C	-3.46611127795230	0.02295240893246	2.65466417803603
C	-3.54683337654611	-1.23072056929200	2.06805770749277
C	-2.90391529377373	-1.43701544686603	0.85608411214570
N	-2.22116012104150	-0.44882707888722	0.27760001747021
C	-2.14279089461917	0.76767533827102	0.81710932017977
C	-2.76289467725263	1.04024519420368	2.02788805212421
C	-2.89240802668868	-2.66838095646685	0.05710234657080
C	-3.53575133970865	-3.83916459575320	0.42660388052777

8. Excited-State Kinetics of an Air-Stable Cyclometalated Iron(II) Complex

C	-3.48016625485121	-4.93337104723917	-0.41834323901660
C	-2.78377210733400	-4.81998125340261	-1.60908622538935
C	-2.16620423032035	-3.61804566962395	-1.90783828500214
N	-2.21162348456606	-2.56627517152483	-1.09907080657092
C	-1.38279076174888	1.70401440000740	-0.01969104729382
N	-0.92341248724693	1.16805943821642	-1.16528623391734
C	-0.24774790641287	1.94210413832280	-2.00595955231725
C	0.01189590770076	3.27732186632204	-1.75086830384102
C	-0.45172429087026	3.83262197894586	-0.57087914731887
C	-1.16111349849053	3.03262294711889	0.30721981976305
N	-0.66213714306044	-1.04696355356477	-3.14801295599806
C	0.59444973144660	-1.48110268096433	-3.24887910696832
C	1.17460488969588	-1.70373301600302	-4.48545762369182
C	0.40146823520324	-1.45869355731285	-5.61595315799163
C	-0.89836151974957	-1.00873067931405	-5.49208222421214
C	-1.43156746908281	-0.80139363494114	-4.21682084324274
C	-2.76513485231464	-0.33507700673651	-3.85937568977690
C	-3.73521141577559	-0.01746526867074	-4.81113941915589
C	-4.97895788405946	0.41904593816163	-4.39803971546044
C	-5.24081155298557	0.53383325945675	-3.03720800286054
C	-4.26700545718864	0.21476327045372	-2.09941729021028
C	-2.99818125990160	-0.22965524135005	-2.46930329236614
C	1.23513417899573	-1.67642430162355	-1.93688523090944
N	0.45039838068293	-1.38865591584573	-0.88393150422584
C	0.93988555688867	-1.53361697416463	0.34140834965741
C	2.22973354374692	-1.96987005179162	0.58861325802782
C	3.04398836320798	-2.26756425533391	-0.49083298114465
C	2.53937867281019	-2.11858830673732	-1.77072918871564
Fe	-1.42629679440046	-0.75269014290155	-1.40557089460140
H	-3.96009139067870	0.21016547422581	3.59785498715730
H	-4.10654660115763	-2.02035746319583	2.54832640020207
H	-2.71122846037305	2.02175796194621	2.47665849814632
H	-4.07911141470793	-3.89852902086070	1.35892582433464
H	-3.97694341938523	-5.85608120277780	-0.15244681371976
H	-2.71901839925349	-5.64467001320198	-2.30391804027905
H	-1.62312629826953	-3.49509359681515	-2.83453602644506
H	0.09296899271918	1.48193433265281	-2.92298101587970

8. Excited-State Kinetics of an Air-Stable Cyclometalated Iron(II) Complex

H	0.56378773442380	3.86450261457521	-2.47040530332293
H	-0.26946610965814	4.87265517155604	-0.33850977872452
H	-1.54032401762769	3.44330958715241	1.23219061572283
H	2.19115202147110	-2.05579040978836	-4.58293426997288
H	0.82286470054241	-1.62221996590752	-6.59864702304583
H	-1.49498501204473	-0.81981946205211	-6.37275725776805
H	-3.53231226695483	-0.10637630672708	-5.87223266800146
H	-5.73949642550313	0.66833348938425	-5.12534538704842
H	-6.21491724419055	0.87573304916170	-2.70915360902219
H	-4.52497320832202	0.32238527572942	-1.04981659246546
H	0.27563411073166	-1.29160237915295	1.16080297544997
H	2.58117351961393	-2.07140121788109	1.60515150388080
H	4.05821615336400	-2.61104227070333	-0.34038923684520
H	3.15700095282430	-2.34492744942096	-2.62803686214980

Spectroelectrochemistry

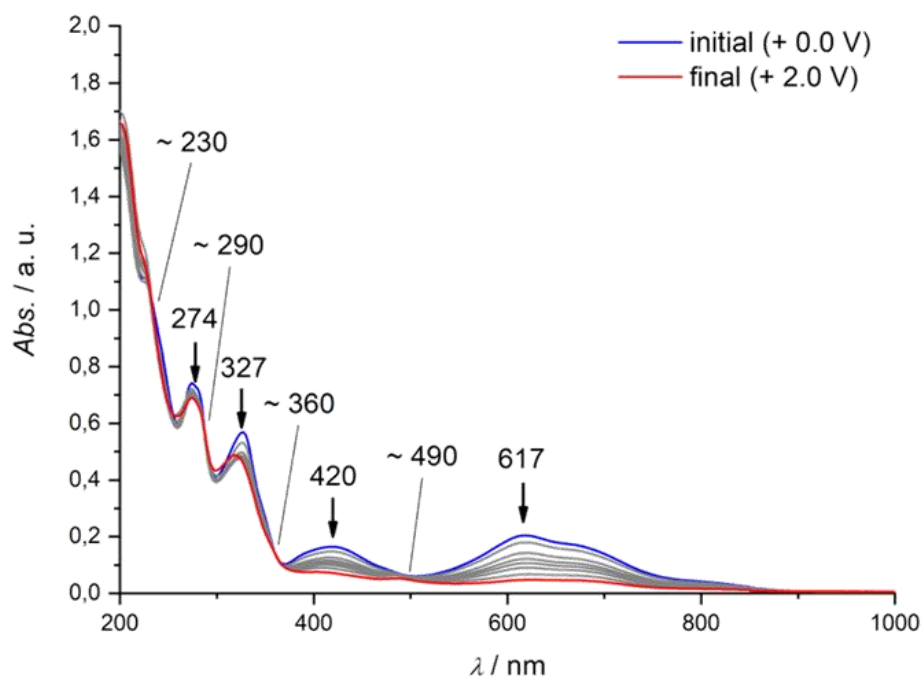


Figure S15: Changes in the UV/vis/NIR spectra during the oxidation of **2** to **2⁺** (0.0 V \rightarrow 2.0 V) in MeCN/[*n*-Bu₄N][PF₆] during OTTLE spectroelectrochemistry. Maxima and isosbestic points indicated.

8. Excited-State Kinetics of an Air-Stable Cyclometalated Iron(II) Complex

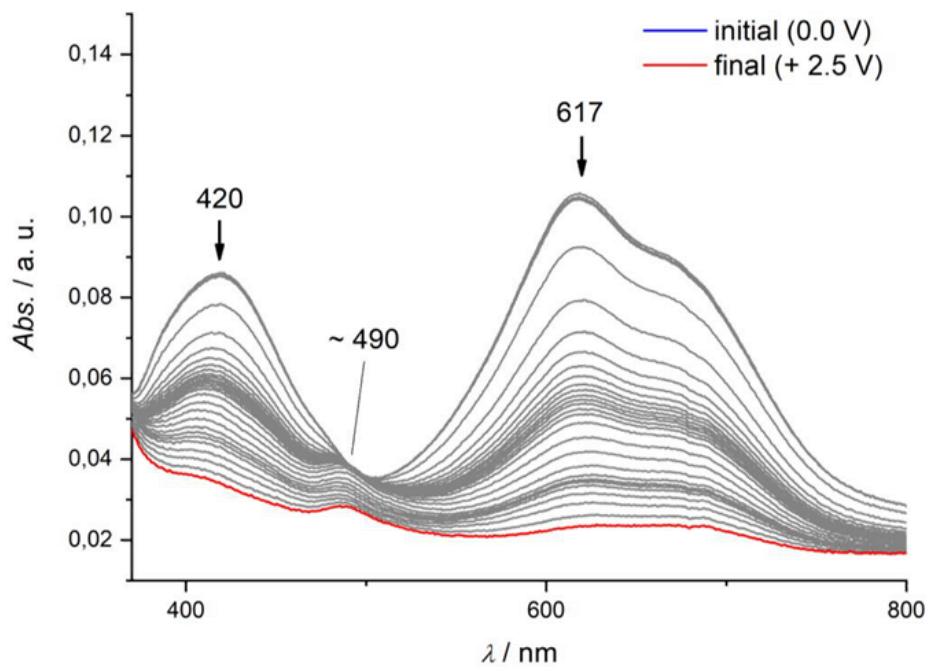


Figure S16: Changes in the UV/vis/NIR spectra during the oxidation of **2** to **2⁺** (0.0 V \rightarrow 2.5 V) in MeCN/[*n*-Bu₄N][PF₆] during OTTLE spectroelectrochemistry (zoom in the CT region). Maxima and isosbestic points indicated.

8. Excited-State Kinetics of an Air-Stable Cyclometalated Iron(II) Complex

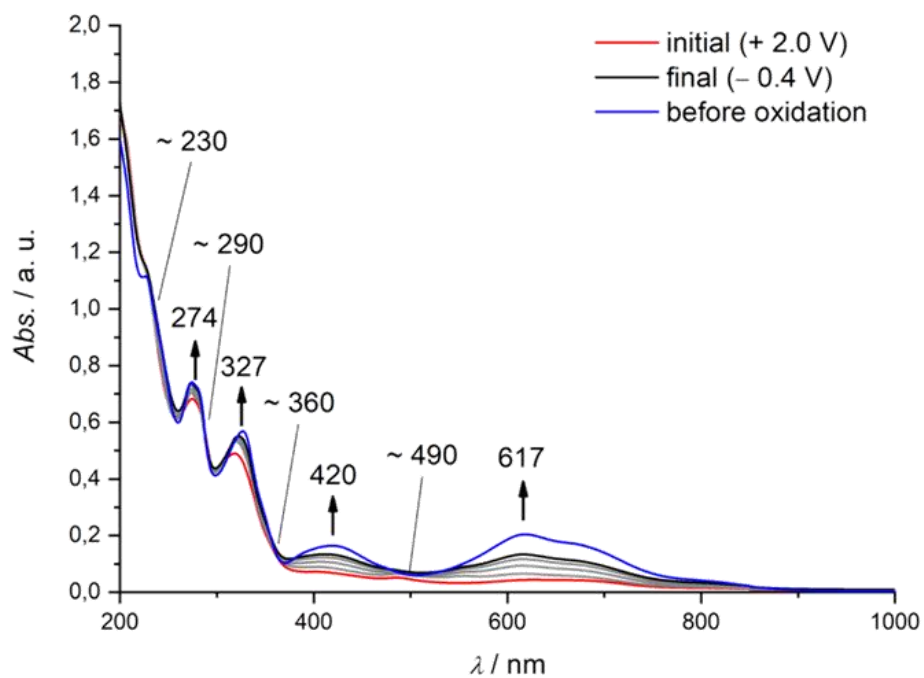


Figure S17: Changes in the UV/vis/NIR spectra during the re-reduction of 2^+ to 2 ($2.0 \text{ V} \rightarrow -0.4 \text{ V}$) in $\text{MeCN}/[n\text{-Bu}_4\text{N}][\text{PF}_6]$ during OTTLE spectroelectrochemistry. Maxima and isosbestic points indicated.

8. Excited-State Kinetics of an Air-Stable Cyclometalated Iron(II) Complex

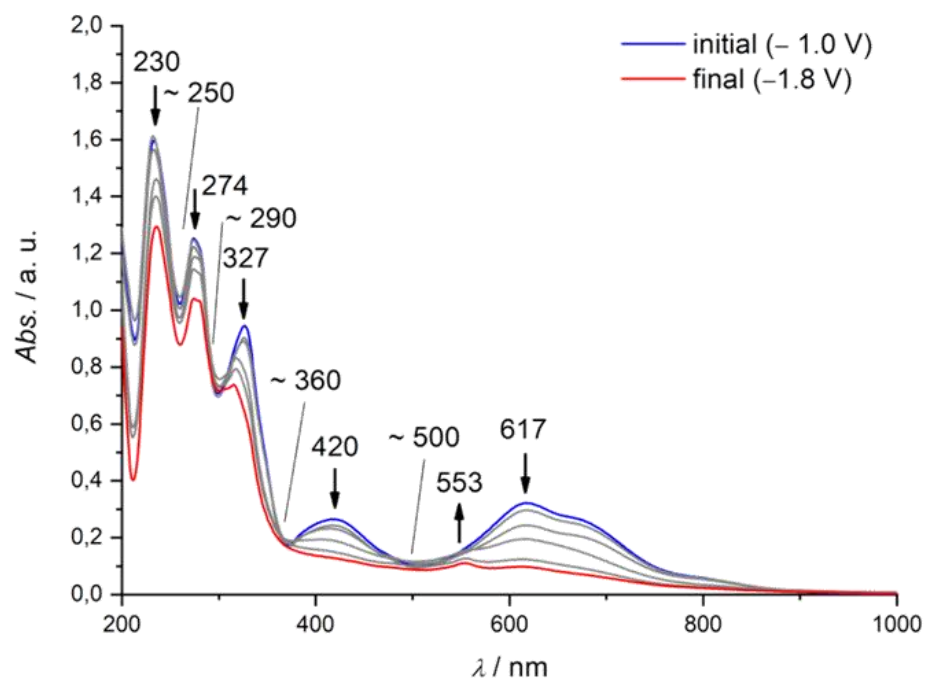


Figure S18: Changes in the UV/vis/NIR spectra during the reduction of **2** to **2⁻** (-1.0 V \rightarrow -1.8 V) in MeCN/[*n*-Bu₄N][PF₆] during OTTLE spectroelectrochemistry. Maxima and isosbestic points indicated.

8. Excited-State Kinetics of an Air-Stable Cyclometalated Iron(II) Complex

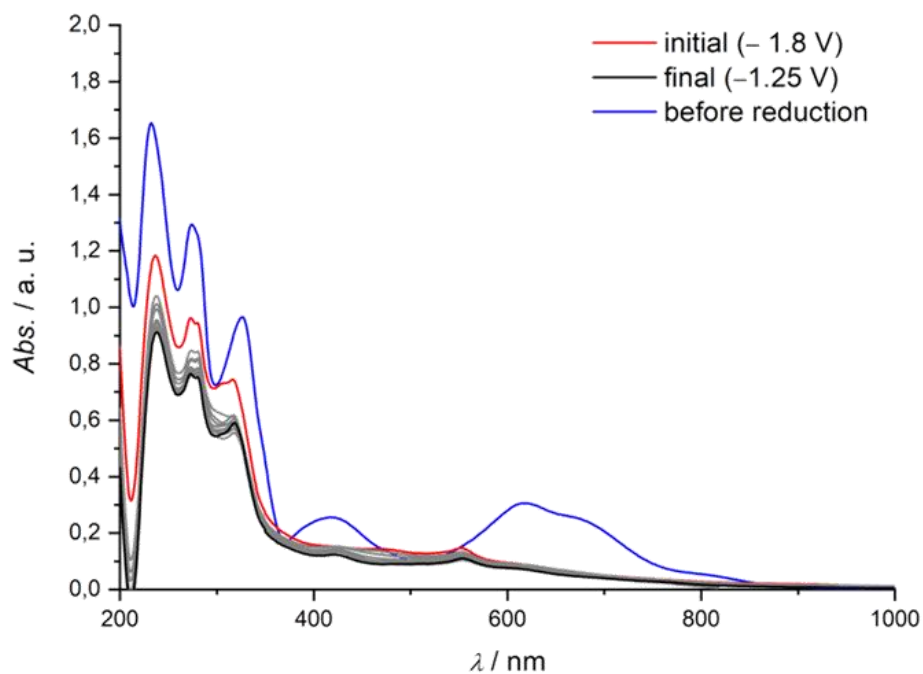


Figure S19: Changes in the UV/vis/NIR spectra during the attempted re-oxidation of $\mathbf{2}^-$ to $\mathbf{2}$ (-1.8 V \rightarrow -1.25 V) in MeCN/[*n*-Bu₄N][PF₆] during OTTLE spectroelectrochemistry. Clearly, the reduction is irreversible on the timescale of the spectroelectrochemical experiment.

Ultrafast Pump-Probe Spectroscopy

Ultrafast pump-probe measurements were performed on **2** dissolved in acetonitrile applying excitation pulses centered at 615 nm. Figure S22 a) shows recorded transient spectra for the specified delay times between probe and pump. The data were analyzed by a global double exponential fit. The resulting decay associated amplitude spectra (DAS) are depicted in Figure S22 b) and labelled with the obtained decay times.

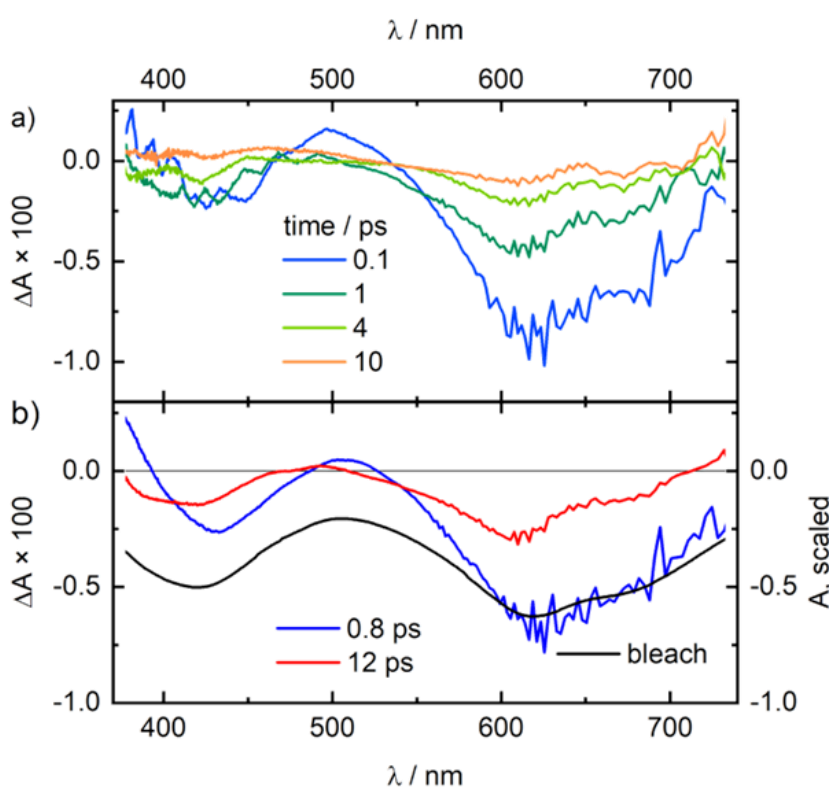


Figure S20: (a) Transient absorption spectra of **2** in acetonitrile at the specified delay times after optical excitation at 615 nm. (b) DAS of two exponential components with time constants of 0.8 ps and 12 ps obtained by a double exponential global fit (left scale). The DAS are compared to the scaled bleach (right scale) of complex **2**.

The graph shows for comparison also the scaled bleach, i.e. the inverted ground state absorption spectrum. Both DAS are similar to the bleach with dominating negative signals which means that most of the observed absorption change is due depopulation of the electronic ground state. The DAS of the shorter time constant exhibits at 500 nm and below 400 nm positive contributions demonstrating that also excited state absorption (ESA) is present. The observation of two steps in the excited state dynamics points to the following relaxation scenario. The $^1\text{MLCT}$ singlet state excited. However, iron(II) complexes exhibit typically an extremely fast intersystem crossing^[16,32] and the $^3\text{MLCT}$ triplet state is

8. Excited-State Kinetics of an Air-Stable Cyclometalated Iron(II) Complex

most probably populated within the time resolution of our pump-probe measurements. This notion is supported by the absence of any fluorescence. The short time constant of 0.8 ps reflects the depopulation of the $^3\text{MLCT}$ state into the ^3MC state. The latter decays with a lifetime of 12 ps back to the electronic ground state resulting thereafter in a completely recovered ground state absorption.

To check for solvent effects, additional transient absorption measurements were performed with **2** dissolved in dichloromethane and methanol. There, a very similar behavior as for MeCN was observed, although with somewhat different time constants. The results are shown in Figure S23. Since the solubility of **2** is lower in methanol, the measurement was in this case performed with a lower concentration. The concentrations read as follows:

2 in acetonitrile: $c = 0.62$ mol/L; in dichloromethane: $c = 0.78$ mol/L; in methanol: $c = 0.18$ mol/L

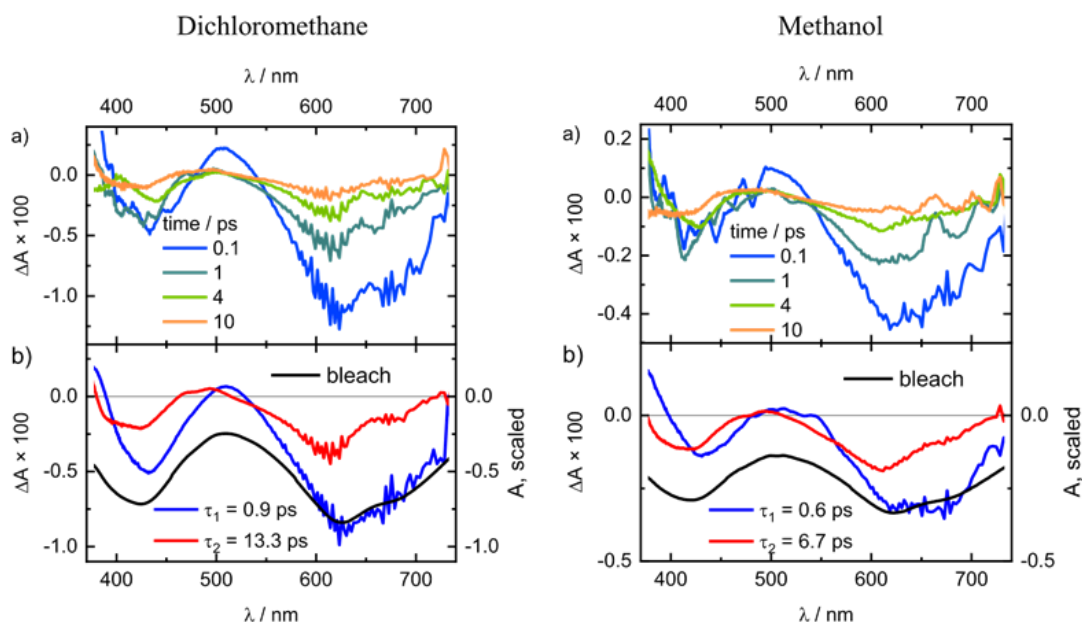


Figure S21: Transient absorption spectra of **2** in dichloromethane (left) and methanol (right) at different times after excitation with pulses at 615 nm (top, part a)) and the corresponding decay associated amplitude spectra of the exponential decay components labelled with the respective time constants (bottom, part b)). While the decay times in acetonitrile (*cf.* Figure S22) and dichloromethane are quite similar, they are significantly shorter in methanol.

In general, the transient absorption measurements were carried out with magic angle (55°) between the polarizations of the pump and probe pulses to avoid effects due to rotational diffusion of the molecules. In acetonitrile the sample was in addition also investigated with parallel and perpendicular polarizations. But no significant differences to the magic angle configuration were observed, see Figure S24.

8. Excited-State Kinetics of an Air-Stable Cyclometalated Iron(II) Complex

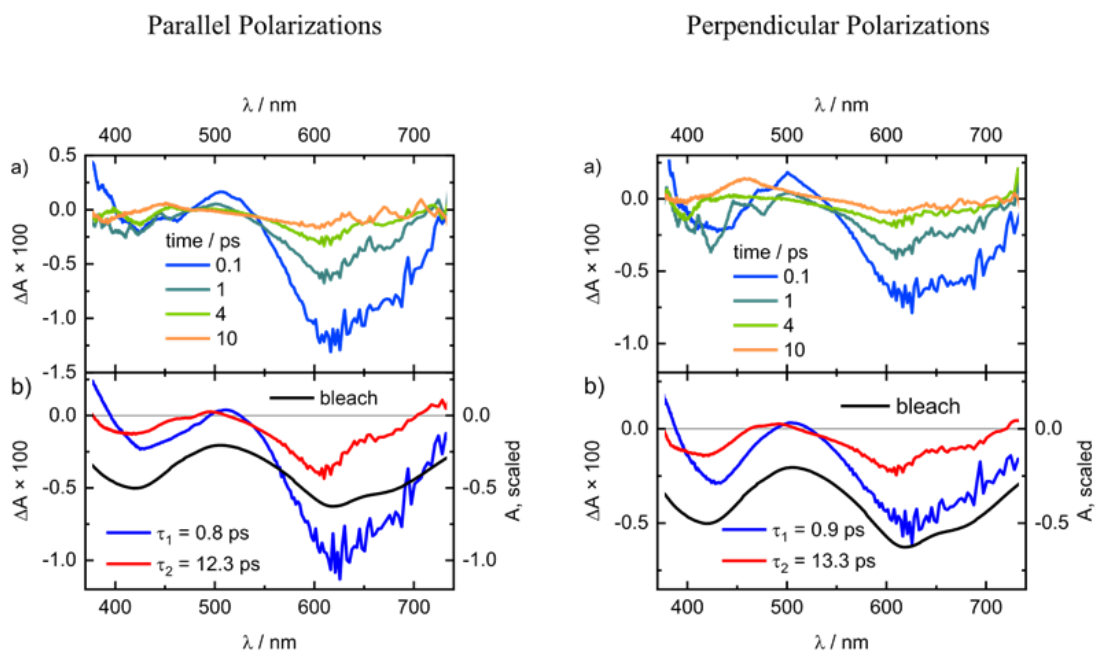


Figure S22: fs-Transient absorption measurements of **2** in MeCN with different polarizations: parallel (left) and perpendicular (right). Top, part a) Transient spectra at different times after excitation with pulses at 615 nm. Bottom, part b) DASs of the decay components labelled with the respective time constants.

8. Excited-State Kinetics of an Air-Stable Cyclometalated Iron(II) Complex

NMR Spectra

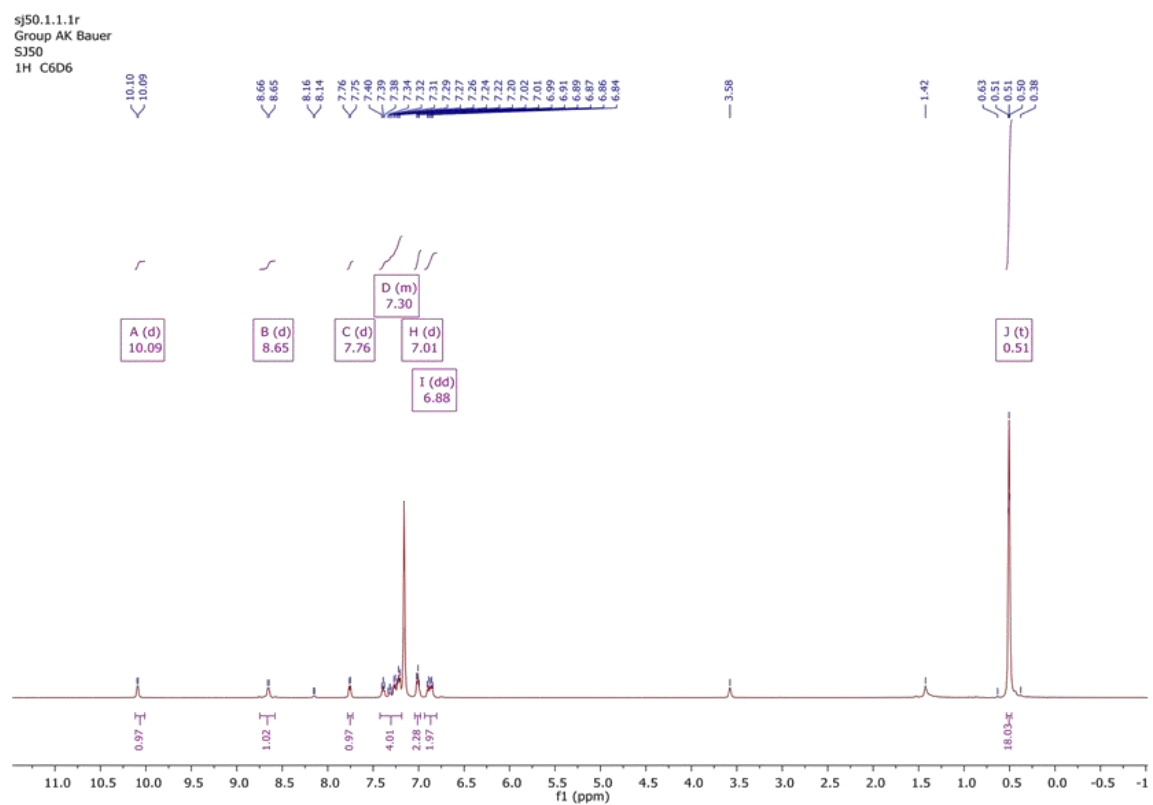


Figure S23: ^1H -NMR spectrum of $[\text{Fe}(\text{pbpy})(\text{PMe}_3)_2\text{Br}]$ **1** in C_6D_6

8. Excited-State Kinetics of an Air-Stable Cyclometalated Iron(II) Complex

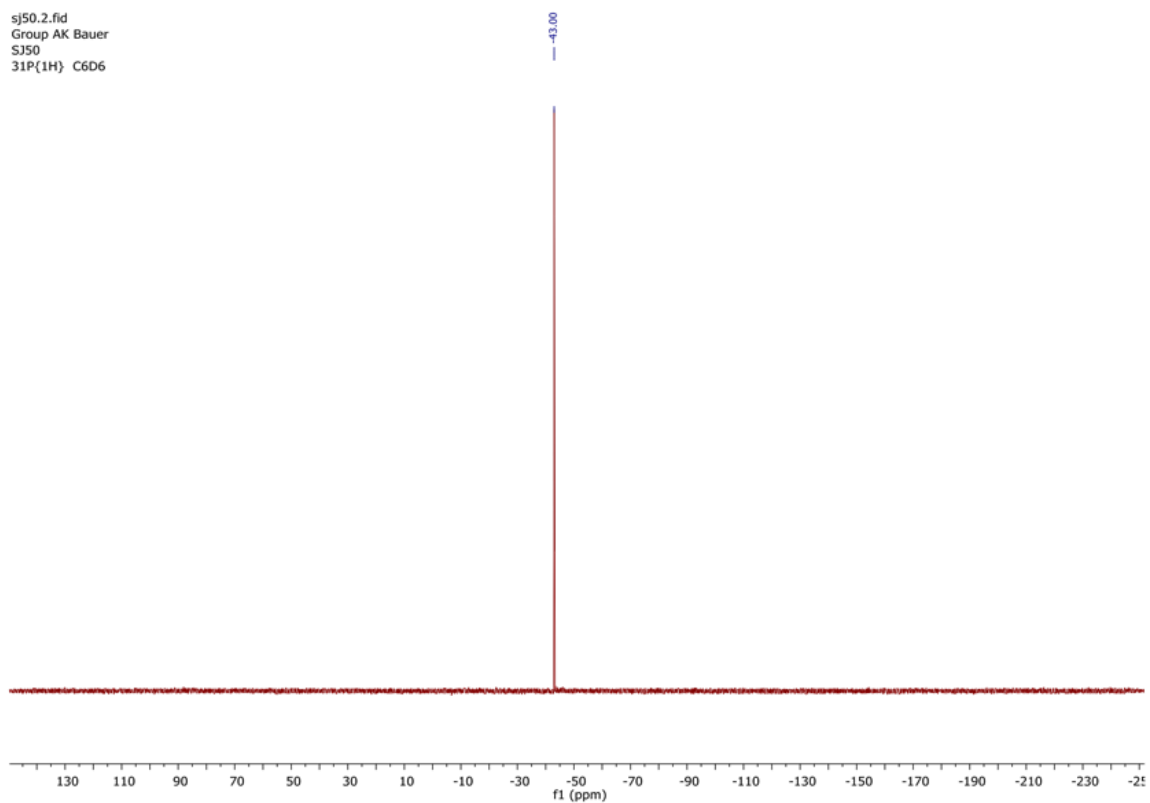


Figure S24: ^{31}P -NMR spectrum of $[\text{Fe}(\text{pbpy})(\text{PMe}_3)_2\text{Br}]$ **1** in C_6D_6

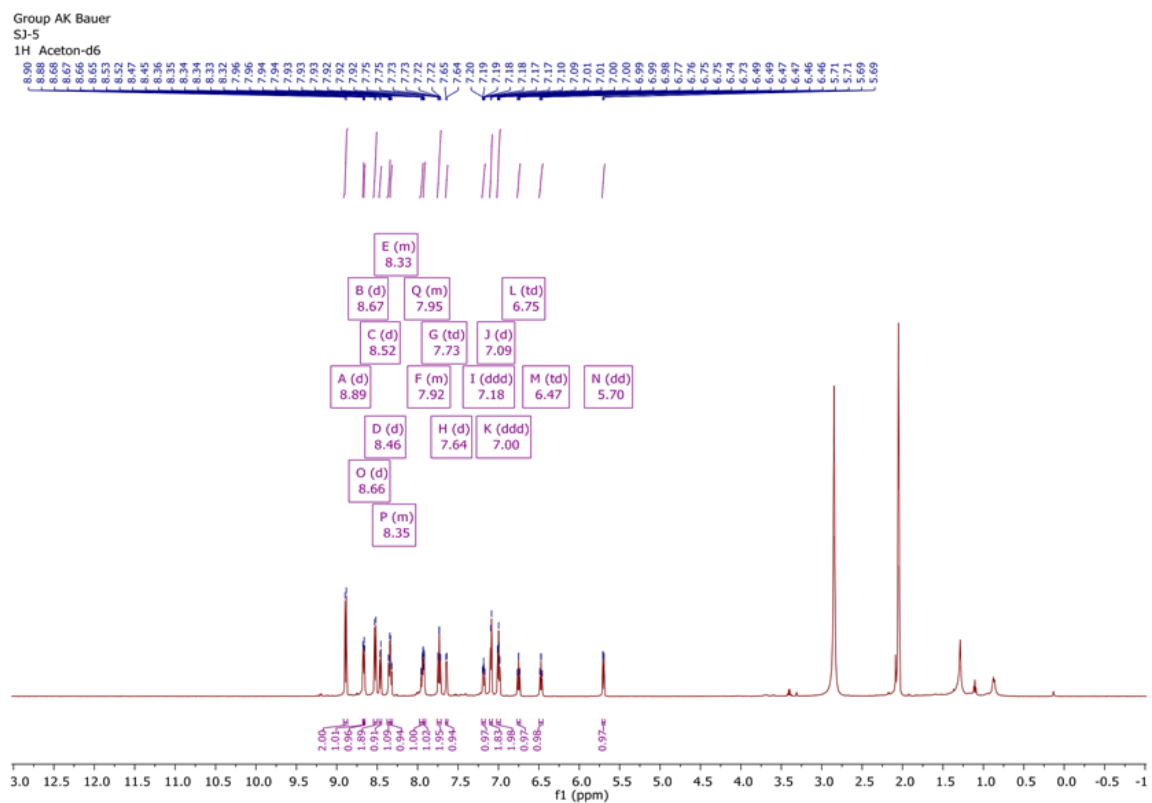


Figure S25: ^1H -NMR spectrum of $[\text{Fe}(\text{pbpy})(\text{tpy})]\text{PF}_6$ **2** in Aceton- d_6

8. Excited-State Kinetics of an Air-Stable Cyclometalated Iron(II) Complex

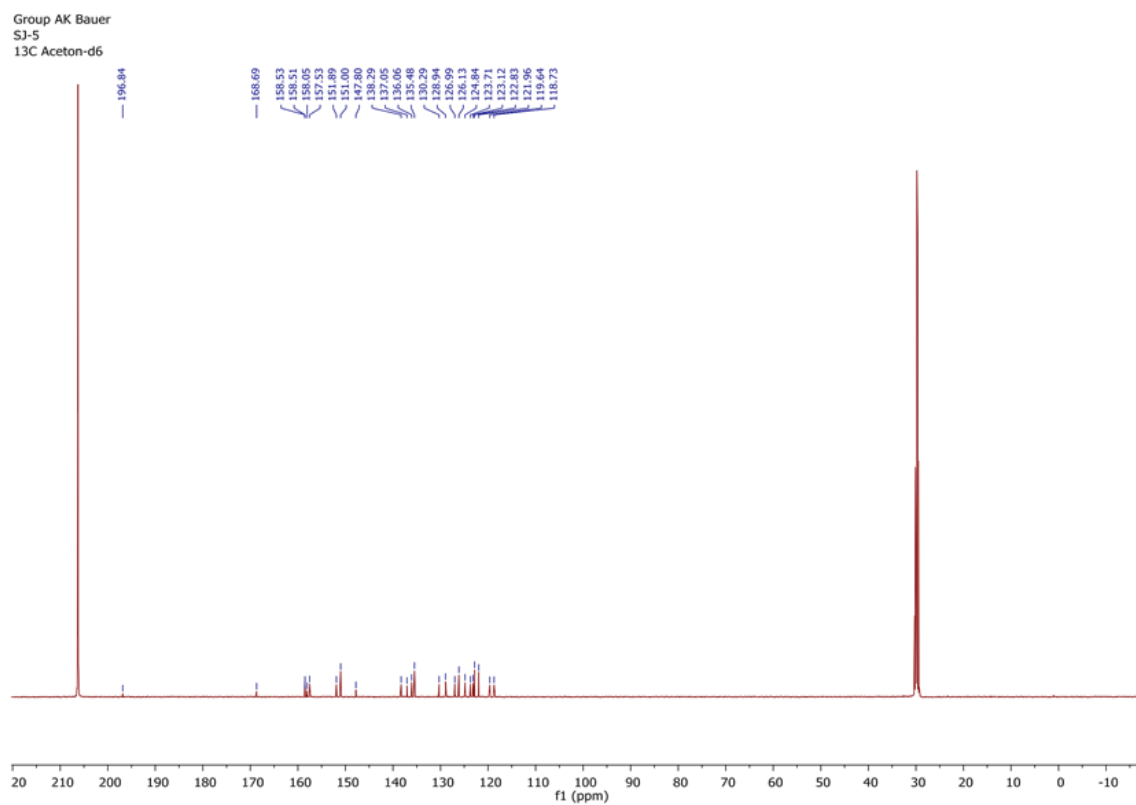


Figure S26: ^{13}C -NMR spectrum of $[\text{Fe}(\text{pbpy})(\text{tpy})]\text{PF}_6$ **2** in Acetone- d_6

References

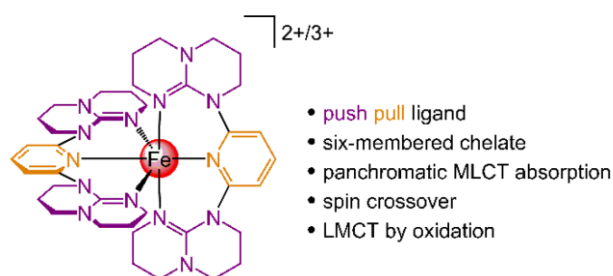
- [1] a) R. S. Nicholson, I. Shain, *Anal. Chem.* **1964**, *36*, 706; b) J. Heinze, *Angew. Chem.* **1984**, *96*, 823.
- [2] a) J. E. B. Randles, *Trans. Faraday Soc.* **1948**, *44*, 327; b) F. Scholz, A. M. Bond, R. G. Compton, D. A. Fiedler, G. Inzelt, H. Kahlert, Š. Komorsky-Lovrić, H. Lohse, M. Lovrić, F. Marken et al., *Electroanalytical Methods*, Springer Berlin Heidelberg, Berlin, Heidelberg, **2010**.
- [3] G. M. Sheldrick, *Acta Crystallogr., Sect. A: Found. Crystallogr.* **2008**, *64*, 112.
- [4] a) P. Bhattacharya, J. A. Krause, H. Guan, *Organometallics* **2011**, *30*, 4720; b) D. L. Jameson, L. E. Guise, *Tetrahedron Lett.* **1991**, *32*, 1999.
- [5] D. Kratzert, J. J. Holstein, I. Krossing, *Journal of applied crystallography* **2015**, *48*, 933.
- [6] a) A. L. Spek, *Acta crystallographica. Section D, Biological crystallography* **2009**, *65*, 148; b) A. L. Spek, *Acta crystallographica. Section C, Structural chemistry* **2015**, *71*, 9.
- [7] F. Neese, *WIREs Comput Mol Sci* **2017**, *2*, e1327.
- [8] S. Grimme, J. G. Brandenburg, C. Bannwarth, A. Hansen, *The Journal of chemical physics* **2015**, *143*, 54107.
- [9] a) L. Goerigk, S. Grimme, *Physical chemistry chemical physics : PCCP* **2011**, *13*, 6670; b) S. Grimme, S. Ehrlich, L. Goerigk, *Journal of computational chemistry* **2011**, *32*, 1456; c) S. Grimme, J. Antony, S. Ehrlich, H. Krieg, *The Journal of chemical physics* **2010**, *132*, 154104.
- [10] a) S. DeBeer George, T. Petrenko, F. Neese, *J. Phys. Chem. A* **2008**, *112*, 12936; b) S. DeBeer George, T. Petrenko, F. Neese, *Inorganica Chimica Acta* **2008**, *361*, 965.
- [11] N. Lee, T. Petrenko, U. Bergmann, F. Neese, S. DeBeer, *J. Am. Chem. Soc.* **2010**, *132*, 9715.
- [12] J. Tao, J. P. Perdew, V. N. Staroverov, G. E. Scuseria, *Physical review letters* **2003**, *91*, 146401.
- [13] L. Burkhardt, M. Holzwarth, B. Plietker, M. Bauer, *Inorg. Chem.* **2017**, *56*, 13300.
- [14] P. Zimmer, L. Burkhardt, R. Schepper, K. Zheng, D. Gosztola, A. Neuba, U. Flörke, C. Wölper, R. Schoch, W. Gawelda et al., *Eur. J. Inorg. Chem.* **2018**, *2018*, 5203.
- [15] N. J. Vollmers, P. Müller, A. Hoffmann, S. Herres-Pawlis, M. Rohrmüller, W. G. Schmidt, U. Gerstmann, M. Bauer, *Inorganic chemistry* **2016**, *55*, 11694.
- [16] P. Zimmer, L. Burkhardt, A. Friedrich, J. Steube, A. Neuba, R. Schepper, P. Müller, U. Flörke, M. Huber, S. Lochbrunner et al., *Inorg. Chem.* **2018**, *57*, 360.
- [17] F. Weigend, R. Ahlrichs, *Phys. Chem. Chem. Phys.* **2005**, *7*, 3297.
- [18] F. Weigend, *Phys. Chem. Chem. Phys.* **2006**, *8*, 1057.
- [19] F. Neese, *Inorganica Chimica Acta* **2002**, *337*, 181.
- [20] I. M. Dixon, S. Khan, F. Alary, M. Boggio-Pasqua, J.-L. Heully, *Dalton Trans.* **2014**, *43*, 15898.
- [21] G. Knizia, *iboview*.

8. Excited-State Kinetics of an Air-Stable Cyclometalated Iron(II) Complex

- [22] M. U. Delgado-Jaime, S. DeBeer, *Journal of computational chemistry* **2012**, *33*, 2180.
- [23] A. V. Marenich, C. J. Cramer, D. G. Truhlar, *J. Phys. Chem. B* **2009**, *113*, 6378.
- [24] a) G. Vankó, T. Neisius, G. Molnar, F. Renz, S. Karpati, A. Shukla, F. M. F. de Groot, *J. Phys. Chem. B* **2006**, *110*, 11647; b) U. Bergmann, P. Glatzel, *Photosynthesis research* **2009**, *102*, 255.
- [25] C. J. Pollock, M. U. Delgado-Jaime, M. Atanasov, F. Neese, S. DeBeer, *J. Am. Chem. Soc.* **2014**, *136*, 9453.
- [26] S. D. Gamblin, D. S. Urch, *Journal of Electron Spectroscopy and Related Phenomena* **2001**, *113*, 179.
- [27] P. Glatzel, U. Bergmann, *Coord. Chem. Rev.* **2005**, *249*, 65.
- [28] P. Zimmer, P. Müller, L. Burkhardt, R. Schepper, A. Neuba, J. Steube, F. Dietrich, U. Flörke, S. Mangold, M. Gerhards et al., *Eur. J. Inorg. Chem.* **2017**, *2017*, 1504.
- [29] a) G. Smolentsev, A. V. Soldatov, J. Messinger, K. Merz, T. Weyhermüller, U. Bergmann, Y. Pushkar, J. Yano, V. K. Yachandra, P. Glatzel, *J. Am. Chem. Soc.* **2009**, *131*, 13161; b) C. J. Pollock, S. DeBeer, *Acc. Chem. Res.* **2015**, *48*, 2967; c) C. J. Pollock, S. DeBeer, *J. Am. Chem. Soc.* **2011**, *133*, 5594; d) M. U. Delgado-Jaime, S. DeBeer, M. Bauer, *Chem. Eur. J.* **2013**, *19*, 15888.
- [30] a) M. Bauer, *Phys. Chem. Chem. Phys.* **2014**, *16*, 13827; b) A. J. Atkins, M. Bauer, C. R. Jacob, *Phys. Chem. Chem. Phys.* **2013**, *15*, 8095; c) T. E. Westre, P. Kennepohl, J. G. DeWitt, B. Hedman, K. O. Hodgson, E. I. Solomon, *J. Am. Chem. Soc.* **1997**, *119*, 6297.
- [31] a) Y. Liu, T. Harlang, S. E. Canton, P. Chábera, K. Suárez-Alcántara, A. Fleckhaus, D. A. Vithanage, E. Göransson, A. Corani, R. Lomoth et al., *Chem. Comm.* **2013**, *49*, 6412; b) Y. Liu, P. Persson, V. Sundstrom, K. Wärnmark, *Acc. Chem. Res.* **2016**, *49*, 1477; c) T. Duchanois, T. Etienne, C. Cebrián, L. Liu, A. Monari, M. Beley, X. Assfeld, S. Haacke, P. C. Gros, *Eur. J. Inorg. Chem.* **2015**, *2015*, 2469; d) L. Liu, T. Duchanois, T. Etienne, A. Monari, M. Beley, X. Assfeld, S. Haacke, P. C. Gros, *Phys. Chem. Chem. Phys.* **2016**, *18*, 12550.

9. Panchromatic Absorption and Oxidation of an Iron(II) Spin Crossover Complex

Johannes Moll, Christoph Förster, Alexandra König, Luca M. Carrella, Manfred Wagner, [REDACTED], [REDACTED], Eva Rentschler and Katja Heinze



The iron(II) complex $[\text{Fe}(\text{dgpy})_2]^{2+}$ (dgpy: 2,6-diguandylpyridine) performs thermal spin crossover (SCO) in the *meridional* fashion. Besides this temperature dependent equilibrium between high and low-spin form of the *meridional* complex a asymmetric iron(II) high-spin compound – most likely *cis-fac*- $[\text{Fe}(\text{dgpy})_2]^{2+}$ – is formed during the synthesis that does not undergo

spin transition or isomerization. The occurrence of SCO demonstrates the weak ligand field strength of the dgpy ligand due to its low π -accepting ability and the high flexibility of this ligand.

Author Contributions

Johannes Moll and Alexandra König from the Johannes Gutenberg University in Mainz synthesized and characterized the iron complexes presented in this manuscript, conducted UV-VIS and IR spectroscopic experiments and all DFT calculations as well. Johannes Moll carried out the electrochemical, spectroelectrochemical and EPR experiments. Dr. Luca Carrella and Prof. Eva Rentschler from the Johannes Gutenberg University in Mainz performed SQUID experiments, [REDACTED] and [REDACTED] from the Johannes Gutenberg University in Mainz performed Mößbauer experiments. Room temperature NMR spectroscopy was conducted by Johannes Moll, temperature dependent NMR spectroscopy by Dr. Manfred Wagner from the Max Planck Institute for Polymer Research in Mainz. The crystal structures were solved and refined by Dr. Christoph Förster from the Johannes Gutenberg University in Mainz. The manuscript was written by Johannes Moll and Katja Heinze.

Supporting Information for this article is found at pp. 271.

“Moll, J.; Förster, C.; König, A.; Carrella, L.; Wagner, M.; [REDACTED]; [REDACTED]; Rentschler, E.; Heinze, K. Manuscript submitted to Inorganic Chemistry.

9. Panchromatic Absorption and Oxidation of an Iron(II) Spin Crossover Complex

9. Panchromatic Absorption and Oxidation of an Iron(II) Spin Crossover Complex

Submitted to Inorganic Chemistry

This document is confidential and is proprietary to the American Chemical Society and its authors. Do not copy or disclose without written permission. If you have received this item in error, notify the sender and delete all copies.

Panchromatic Absorption and Oxidation of an Iron(II) Spin Crossover Complex

Journal:	<i>Inorganic Chemistry</i>
Manuscript ID	Draft
Manuscript Type:	Article
Date Submitted by the Author:	n/a
Complete List of Authors:	Moll, Johannes; Johannes Gutenberg Universitat Mainz, Department of Chemistry Förster, Christoph; Johannes Gutenberg Universitat Mainz, Department of Chemistry König, Alexandra; Johannes Gutenberg Universitat Mainz, Department of Chemistry Carrella, Luca; Universitat Mainz, Duesbergweg 10-14, D-55128 Mainz, Department of Chemistry Wagner, Manfred; Max-Planck-Institut für Polymerforschung, [REDACTED]; Johannes Gutenberg Universitat Mainz, Department of Chemistry [REDACTED]; Johannes Gutenberg Universitat Mainz, Department of Chemistry Rentschler, Eva; Johannes Gutenberg Universitat Mainz, Department of Chemistry Heinze, Katja; Johannes Gutenberg Universitat Mainz, Department of Chemistry

SCHOLARONE™
Manuscripts

Panchromatic Absorption and Oxidation of an Iron(II) Spin Crossover Complex

Johannes Moll,[†] Christoph Förster,[†] Alexandra König,[†] Luca M. Carrella,[†] Manfred Wagner,[‡]

■■■■■■■■■■, [†]■■■■■■■■■■, [†]Eva Rentschler,[†] and Katja Heinze*[†]

[†] Department of Chemistry, Johannes Gutenberg University, Duesbergweg 10-14, 55128 Mainz, Germany

[‡] Max Planck Institute for Polymer Research, Ackermannweg 10, 55128 Mainz, Germany.

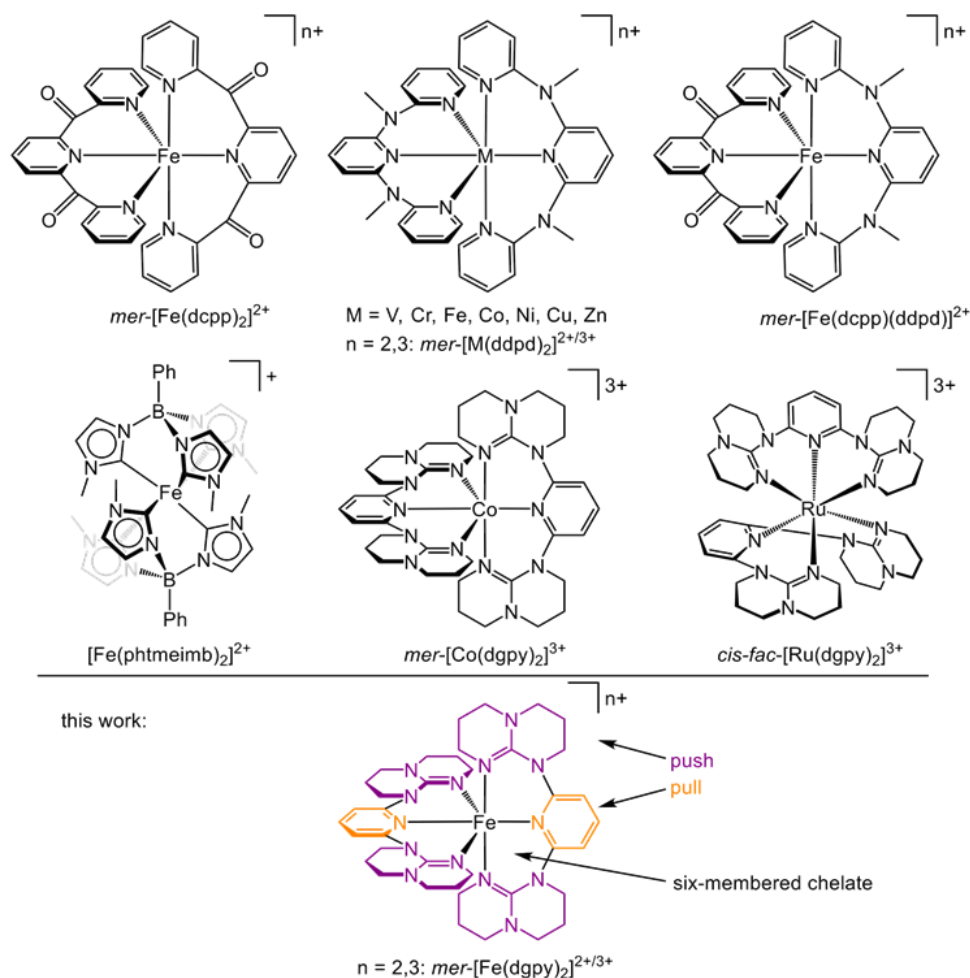
ABSTRACT: In order to expand and exploit the useful properties of d⁶-iron(II) and d⁵-iron(III) complexes in potential magnetic, photophysical or magneto-optical applications, crucial ligand-controlled parameters are the ligand field strength in a given coordination mode and the availability of suitable metal and ligand frontier orbitals for charge transfer processes. The push-pull ligand 2,6-diguanyldipyridine (dgpy) features low-energy π^* orbitals at the pyridine site and strongly electron-donating guanidynyl donors combined with the ability to form six-membered chelate rings for optimal metal-ligand orbital overlap. The electronic ground states of the pseudo-octahedral d⁶- and d⁵-complexes *mer*-[Fe(dgpy)₂]²⁺, *cis-fac*-[Fe(dgpy)₂]²⁺ and *mer*-[Fe(dgpy)₂]³⁺ as well as their charge-transfer (CT) and metal-centered (MC) excited states are probed by variable temperature UV/Vis absorption, NMR, EPR and Mössbauer spectroscopy, magnetic susceptibility measurements at variable temperature as well as quantum chemical calculations.

1
2
3 INTRODUCTION
4
5

6 The coordination chemistry of pseudo-octahedral iron(II) and iron(III) complexes is dominated by
7 variable spin states that can be realized and the resulting well-explored spin-crossover (SCO)
8 phenomenon.¹⁻⁴ Temperature, pressure and light stimuli can switch between the low- and high-
9 spin states (d⁶-iron(II): ¹A_{1g}, ⁵T_{2g} in O_h symmetry).^{1-3,5,6} The optical switching process has been
10 termed light-induced excited spin state trapping (LIESST). Excitation of the prototypical complex
11 [Fe(ptz)₆]²⁺ (ptz = 1-propyl tetrazole) in its low-spin state (¹A_{1g}) with green light at low-temperature
12 populates the ligand field (or metal-centered) states (¹T_{1g} and ¹T_{2g}). Fast and efficient double
13 intersystem crossing (ISC) via the ligand field triplet states (³T_{1g}/³T_{2g}) states either leads to
14 relaxation back to the low-spin state or to population of the metastable high-spin state.^{7,8} Prolonged
15 irradiation at sufficiently low temperature can fully populate the metastable high-spin state.
16 Iron(II) complexes with suitable chromophoric ligands can be initially excited into singlet metal-
17 to-ligand charge transfer (¹MLCT) states and subsequently undergo ISC processes to the
18 metastable high-spin ligand field state.⁹⁻¹¹ Selective excitation of the low-temperature trapped
19 metastable high-spin state of [Fe(ptz)₆]²⁺ with 820 nm light, re-populates the low-spin ground state
20 (reverse-LIESST effect). The lifetime of the metastable high-spin state depends on the conditions,
21 especially the available thermal energy. At room temperature, relaxation of photoexcited iron(II)
22 complexes with nearly octahedral [FeN₆] coordination, e.g. [Fe(dcpp)₂]²⁺ and [Fe(dcpp)(ddpd)]²⁺
23 (Chart 1), to the low-spin ground state occurs on the pico- to nanosecond timescale (dcpp = 2,6-
24 bis(2-carboxypyridyl)pyridine; ddpd = *N,N'*-dimethyl-*N,N'*-dipyridin-2-ylpyridine-2,6-
25 diamine).¹⁰⁻¹²

26
27
28
29
30
31
32
33
34
35
36
37
38
39
40
41
42
43
44
45
46
47
48
49
50
51
52
53 **Chart 1.** Pseudo-octahedral transition metal complexes with six-membered chelate rings relevant
54 to this study.
55
56
57
58
59
60

9. Panchromatic Absorption and Oxidation of an Iron(II) Spin Crossover Complex



Beyond the thermal and light-switchable SCO, attempts to install low-energy 3MLCT states as lowest excited states in iron(II) complexes have become a vivid, yet challenging research focus.¹³ This is inspired by the useful photophysics of homologous ruthenium(II) complexes, especially with $[RuN_6]$ coordination sphere, such as $[Ru(bpy)_3]^{2+}$ derivatives and analogues (bpy = 2,2'-bipyridine). The aim is to increase the lifetime of the 3MLCT state of iron(II) complexes by hindering the fast relaxation to the high-spin state to allow for 3MLCT phosphorescence and bimolecular reactivity of the 3MLCT excited state (photoredox catalysis).¹³⁻¹⁵ Current attempts focus on increasing the intrinsically weak ligand field splitting of iron(II) by using strong field ligands such as carbene donors and by improving metal-ligand orbital overlap (high energy 3T and

1
2
3
4
5
6
7
8
9
10
11
12
13
14
15
16
17
18
19
20
21
22
23
24
25
26
27
28
29
30
31
32
33
34
35
36
37
38
39
40
41
42
43
44
45
46
47
48
49
50
51
52
53
54
55
56
57
58
59
60

5T states) and on decreasing the $^1/3MLCT$ energies by push-pull effects, e.g. in $[Fe(dcpp)(ddpd)]^{2+}$ (Chart 1).^{12,16} The latter strategy additionally improves the absorption across the visible and near-infrared spectral region (panchromatic absorption) which is desirable to harvest a higher portion of the sunlight.^{17,14} The highest reported 3MLCT lifetimes of iron(II) complexes and bimolecular reactivity were achieved using carbene, cyclometalating or (phenanthridin-4-yl)(quinolin-8-yl)amido ligands.^{18–26} Iron(II) complexes of *N*-heterocyclic carbene ligands with appended anthracenyl or pyrenyl chromophores display ligand based fluorescence with nanosecond lifetimes,²⁷ while appended zinc porphyrins enable a weak emission with 3MLCT character and a 3MLCT lifetime of 160 ps.²⁸

Oxidation of iron(II) complexes to their d^5 -iron(III) congeners in a strong field environment can also yield luminescent complexes, yet with an inverted charge transfer direction. The low-spin iron(III) complex $[Fe(btz)_3]^{3+}$ ($btz = 3,3'$ -dimethyl-1,1'-bis(*p*-tolyl)-4,4'-bis(1,2,3-triazol-5-ylidene)) is luminescent at room temperature with a 2LMCT fluorescence lifetime of 100 ps.²⁹ This has been increased in the hexacarbene iron(III) complex $[Fe(phtmeimb)_2]^+$ to a lifetime of 2 ns ($phtmeimb = phenyl[tris(3-methylimidazol-1-ylidene)$, Chart 1).³⁰ The d^6 -low-spin cobalt(III) complex $[Co(dgpy)_2]^{3+}$ ($dgpy = 2,6$ -diguanidylpyridine, Chart 1) with a tridentate pyridine/guanidine ligand takes advantage of LMCT states as well. In this case a blue emissive 3LMCT state with 5.07 ns lifetime is realized.³¹ The low-spin ruthenium(III) complex $[Ru(dgpy)_2]^{3+}$ has been reported as well. Yet enabled by the flexibility of six-membered chelate rings, the $dgpy$ ligand coordinates in a facial manner. Luminescence properties of *cis-fac*- $[Ru(dgpy)_2]^{3+}$ were not reported (Chart 1).³² With $ddpd$ as ligand, *cis-fac* isomers have been reported occasionally as well, yet the thermodynamically preferred coordination mode for $ddpd$ is meridional (Chart 1).^{33,34}

1
2
3 The exceptionally successful complexes with LMCT luminescence, $[\text{Fe}(\text{phtmeimb})_2]^+$ and
4 $[\text{Co}(\text{dgpy})_2]^{3+}$, possess six-membered chelate rings with the metal center. This geometrical feature
5
6 is also shared by most successful spin-flip emitters based on chromium(III) and vanadium(III)
7
8 using for example the ddpd ligand (Chart 1; $[\text{M}(\text{ddpd})_2]^{3+}$, $\text{M} = \text{Cr}, \text{V}$).^{34,35,36,37} With the versatile
9
10 properties of iron(II) and iron(III) complexes combined with medium-to-strong field ligands
11
12 forming six-membered chelates and possessing push-pull character in mind, we set out to explore
13
14 the magnetic and absorptive properties of the d^6 -iron(II) and d^5 -iron(III) complexes $[\text{Fe}(\text{dgpy})_2]^{2+}$
15
16 and $[\text{Fe}(\text{dgpy})_2]^{3+}$ (Chart 1 bottom), especially focusing on SCO behavior and MLCT/LMCT
17
18 absorption properties.
19
20
21
22
23

24 25 EXPERIMENTAL SECTION

26
27
28 **General procedures.** All reagents were used as received from commercial suppliers (Acros
29
30 Organics, Alfa Aesar, Fischer and Sigma-Aldrich). CH_3CN and CD_3CN were distilled from CaH_2 .
31
32 Diethylether and THF were distilled from sodium and potassium, respectively. d_6 -Acetone was
33
34 degassed by purging with argon and dried over molecular sieve 4 Å. The ligand dgpy was
35
36 synthesized according to a literature procedure.³² ^1H NMR spectra were recorded on a Bruker
37
38 Avance DRX 400 spectrometer (400.31 MHz), on a Bruker Avance III HD 400 spectrometer
39
40 (400.13 MHz) or on a Bruker Avance III 600 spectrometer (600.13 MHz) with 5 mm TCI-
41
42 CryoProbe with z-gradient ant ATM. Temperature-dependent ^1H NMR spectra were recorded on
43
44 a Bruker Avance III HD 500 spectrometer (500.15 MHz) with a BBFO 5 mm $^1\text{H}/\text{X}/^{19}\text{F}$ probe head
45
46 (z-gradient, sweep width of 250 ppm, 90° pulse angle for 14.7 μs) using a dewar- N_2 cooling unit.
47
48 A methanol standard was used for temperature calibration. All resonances are reported in ppm
49
50 versus the solvent signal as an internal standard (CD_3CN , $\delta = 1.940$; d_6 -acetone, $\delta = 2.050$ ppm).³⁸
51
52
53
54
55
56
57
58
59
60
ESI mass spectra were recorded on an Agilent 6545 QTOF-MS spectrometer. ATR IR spectra

1
2
3 were recorded with a Bruker ALPHA II FT-IR spectrometer with a Platinum Di-ATR module
4
5 inside an argon filled glovebox. Elemental analyses were performed by the microanalytical
6
7 laboratory of the department of chemistry of the University of Mainz using an Elementar vario EL
8
9 Cube. X-band EPR spectra were recorded on a Miniscope MS 300 (Magnettech GmbH, Germany)
10
11 with a frequency counter FC 400 (Magnettech GmbH, Germany) at a microwave frequency of
12
13 9.39 GHz in frozen butyronitrile (77 K). Mn^{2+} in ZnS was used as external standard ($g = 2.118,$
14
15 2.066, 2.027, 1.986, 1.946, 1.906). Simulations were performed with the program package
16
17 Easyspin for MatLab (R2016b).³⁹ Electrochemical experiments were carried out on a BioLogic
18
19 SP-200 voltammetric analyzer using platinum wires as counter and working electrodes and 0.01
20
21 M Ag/AgNO₃ as the reference electrode. The measurements were carried out at a scan rate of 100
22
23 mV s⁻¹ for cyclic voltammetry experiments and at 50 mV s⁻¹ for square-wave voltammetry
24
25 experiments using 0.1 M [ⁿBu₄N][PF₆] as the supporting electrolyte in CH₃CN. Potentials are
26
27 referenced to the ferrocene/ferrocenium couple ($E_{1/2} = 110 \pm 5$ mV under the experimental
28
29 conditions). UV/Vis spectroelectrochemical experiments were performed using a BioLogic SP-50
30
31 voltammetric analyzer and a Specac omni-cell liquid transmission cell with CaF₂ windows
32
33 equipped with a Pt-gauze working electrode, a Pt-gauze counter electrode and a Ag wire as pseudo
34
35 reference electrode, melt-sealed in a polyethylene spacer (approximate path length 1 mm) 2 mM
36
37 in CH₃CN containing 0.1 M [ⁿBu₄N][PF₆].⁴⁰ UV/Vis spectra were recorded on a Varian Cary 5000
38
39 spectrometer using 1.0 cm cells with a Schott valve. Emission spectra were recorded on a Varian
40
41 Cary Eclipse spectrometer. For temperature dependent optical spectroscopy, a freshly prepared
42
43 butyronitrile⁴¹ solution of the complex was filled into a quartz cuvette in an argon filled glovebox
44
45 and the cuvette was sealed and transferred to an Oxford cryostat (Oxford instruments OptistatDN)
46
47 or Varian Cary Peltier element, respectively. DC magnetic studies were performed with a Quantum
48
49
50
51
52
53
54
55
56
57
58
59
60

1
2
3 Design MPMS-XL-7 SQUID magnetometer on a powdered microcrystalline sample. Variable
4
5 temperature susceptibility data were collected in a temperature range of 150–350 K under an
6
7 applied field of 0.1 Tesla. Experimental susceptibility data were corrected for the underlying
8
9 diamagnetism using Pascal's constants. The temperature dependent magnetic contribution of the
10
11 holder was experimentally determined and subtracted from the measured susceptibility data. ⁵⁷Fe
12
13 Mössbauer spectra were collected using a custom-built set-up adapted with a Montana C2 closed-
14
15 cycle cryostat at temperatures of 100, 200, 250, 275 and 300 K using approx. 180 mg sample in a
16
17 2 cm² PE vessel. Original spectra were folded according to a calibration with α -Fe (ambient
18
19 conditions). Spectra were fitted using the Voigt-based-fitting (VBF) approach⁴² as implemented in
20
21 the software package Recoil.⁴³
22
23
24
25
26

27 Intensity data for crystal structure determination were collected with a STOE IPDS-2T
28
29 diffractometer from STOE & CIE GmbH for the PF₆⁻ salts and with a STADIVARI diffractometer
30
31 from STOE & CIE GmbH for the OTf⁻ salt, respectively, using Mo-K α radiation ($\lambda = 0.71073 \text{ \AA}$).
32
33 The diffraction frames were integrated using the STOE X-Area software package⁴⁴ and were
34
35 corrected for absorption with MULABS⁴⁵ of the PLATON software package⁴⁶ for the PF₆⁻ salts
36
37 and with STOE LANA⁴⁷ for the OTf⁻ salt, respectively.
38
39
40
41

42 The structures were solved and refined by the full-matrix method based on F^2 using the SHELXL
43
44 2018/3 software package^{48,49} for the PF₆⁻ salts and using the SHELXL 2016/6 software package^{48,50}
45
46 for the OTf⁻ salt, respectively and the ShelXle graphical interface.⁵¹ All non-hydrogen atoms were
47
48 refined anisotropically while the positions of all hydrogen atoms were generated with appropriate
49
50 geometric constraints and allowed to ride on their respective parent atoms with fixed isotropic
51
52 thermal parameters. Crystallographic data (excluding structure factors) for the structures reported
53
54 in this paper have been deposited with the Cambridge Crystallographic Data Centre as
55
56
57
58
59
60

1
2
3 supplementary publication no. CCDC-2062797, CCDC-2062796 and CCDC-2059034 for
4
5 **1[OTf]₂×0.5CH₃CN**, **1[PF₆]₂×CH₃CN** and **1[PF₆]₃×1.5CH₃CN**, respectively.
6
7

8
9 **Crystallographic Data of 1[OTf]₂×CH₃CN.** C₄₀H₅₄F₆FeN₁₄O₆S₂×0.5CH₃CN (1081.47);
10
11 orthorhombic; *Pna*2₁; *a* = 23.8225(6) Å, *b* = 14.0082(3) Å, *c* = 14.0621(4) Å; *V* = 4692.7(2) Å³; *Z*
12 = 4; density, calcd. = 1.531 g cm⁻³, *T* = 173(2) K, *μ* = 0.499 mm⁻¹; *F*(000) = 2252.0; crystal size
13 0.480 × 0.223 × 0.080 mm; *θ* = 2.052 to 25.995 deg.; -29 ≤ *h* ≤ 28, -17 ≤ *k* ≤ 17, -17 ≤ *l* ≤ 17; rfln
14 collected = 56186; rfln unique = 9195 [*R*(int) = 0.0609]; completeness to *θ* = 25.995 deg. = 100.0
15 %; semi empirical absorption correction from equivalents; max. and min. transmission 0.9816 and
16 0.1681; data 9195; restraints 188, parameters 779; goodness-of-fit on *F*² = 1.034; final indices [*I*
17 > 2σ(*I*)] *R*₁ = 0.0658, *wR*₂ = 0.1718; *R* indices (all data) *R*₁ = 0.0806, *wR*₂ = 0.1867; largest diff.
18 peak and hole 0.662 and -0.528 e Å⁻³, absolute structure parameter = -0.01(2).
19
20
21
22
23
24
25
26
27
28
29
30

31 **Crystallographic Data of 1[PF₆]₂×CH₃CN.** C₃₈H₅₄F₁₂FeN₁₄P₂×CH₃CN (1093.79); orthorhombic;
32
33 *Pna*2₁; *a* = 23.548(5) Å, *b* = 13.868(3) Å, *c* = 13.904(3) Å; *V* = 4540.5(16) Å³; *Z* = 4; density,
34 calcd. = 1.600 g cm⁻³, *T* = 120(2) K, *μ* = 0.504 mm⁻¹; *F*(000) = 2264.0; crystal size 0.730 × 0.500
35 × 0.300 mm; *θ* = 2.701 to 27.938 deg.; -31 ≤ *h* ≤ 30, -15 ≤ *k* ≤ 18, -18 ≤ *l* ≤ 18; rfln collected = 38787;
36
37 rfln unique = 10803 [*R*(int) = 0.0339]; completeness to *θ* = 25.242 deg. = 99.9 %; semi empirical
38 absorption correction from equivalents; max. and min. transmission 1.12683 and 0.91783; data
39 10803; restraints 13, parameters 670; goodness-of-fit on *F*² = 1.053; final indices [*I* > 2σ(*I*)] *R*₁ =
40 0.0293, *wR*₂ = 0.0724; *R* indices (all data) *R*₁ = 0.0311, *wR*₂ = 0.0737; largest diff. peak and hole
41 0.402 and -0.233 e Å⁻³, absolute structure parameter = -0.006(2).
42
43
44
45
46
47
48
49
50
51
52

53 **Crystallographic Data of 1[PF₆]₃×1.5CH₃CN.** C₃₈H₅₄F₁₈FeN₁₄P₃×1.5CH₃CN (1259.29);
54
55 monoclinic; *Ia*; *a* = 16.368(3) Å, *b* = 36.078(7) Å, *c* = 17.311(4) Å, *β* = 92.05°; *V* = 10216(4) Å³;
56
57
58
59
60

1
2
3
4 $Z = 8$; density, calcd. = 1.638 g cm^{-3} , $T = 120(2) \text{ K}$, $\mu = 0.506 \text{ mm}^{-1}$; $F(000) = 5168.0$; crystal size
5
6 $0.240 \times 0.147 \times 0.040 \text{ mm}$; $\theta = 2.611$ to 26.000 deg. ; $-20 \leq h \leq 20$, $-44 \leq k \leq 44$, $-21 \leq l \leq 20$; rfln
7
8 collected = 32744; rfln unique = 18600 [$R(\text{int}) = 0.0905$]; completeness to $\theta = 25.242 \text{ deg.} = 99.9$
9
10 %; semi empirical absorption correction from equivalents; max. and min. transmission 1.16201
11
12 and 0.84225; data 18600; restraints 1139, parameters 1609; goodness-of-fit on $F^2 = 1.128$; final
13
14 indices [$I > 2\sigma(I)$] $R_1 = 0.0805$, $wR_2 = 0.1536$; R indices (all data) $R_1 = 0.1335$, $wR_2 = 0.1864$;
15
16 largest diff. peak and hole 0.577 and $-0.603 \text{ e \AA}^{-3}$, absolute structure parameter = $-0.01(2)$.
17
18

19
20
21 Density Functional Theory (DFT) calculations were carried out using the ORCA program package
22
23 (version 4.1.1).⁵² All calculations were performed using the B3LYP functional⁵³⁻⁵⁵ employing the
24
25 RIJCOSX approximation.^{56,57} Relativistic effects were calculated at the zeroth order regular
26
27 approximation (ZORA) level.⁵⁸ The ZORA keyword automatically invokes relativistically
28
29 adjusted basis sets. To account for solvent effects, a conductor-like screening model (CPCM)
30
31 modeling acetonitrile was used in all calculations.^{59,60} Geometry optimizations were performed
32
33 using Ahlrichs' polarized valence triple-zeta basis set (def2-TZVP).^{61,62} Atom-pairwise dispersion
34
35 correction was performed with the Becke-Johnson damping scheme (D3BJ).^{63,64} The energy of the
36
37 electronic states and presence of energy minima were checked by numerical frequency
38
39 calculations. Explicit counter ions and/or solvent molecules were not taken into account. The
40
41 charge transfer number analyses of the time-dependent DFT (TDDFT) calculated transitions were
42
43 done using TheoDORÉ 2.2.^{65,66}
44
45
46
47
48

49
50 Synthesis of **1[OTf]₂**. A solution of 108 mg (0.306 mmol, 2.2 eq) dgpy in dry THF (13 mL) was
51
52 added to a suspension of 70 mg (0.14 mmol, 1.0 eq) Fe[OTf]₂ in dry THF (50 mL). The solution
53
54 turned red. Dark red crystals precipitated after stirring at ambient temperature for 24 h. The product
55
56
57
58
59
60

1
2
3
4 was collected by filtration under inert conditions and purified by crystallization via slow diffusion
5
6 of dry diethylether into a concentrated solution in acetonitrile to yield 65 mg (0.06 mmol, 44 %)
7
8 of **1[OTf]₂**. Elem. anal. calcd. for C₄₀H₅₄F₆FeN₁₄O₆S₂: C, 45.29; H, 5.13; N, 18.48. Found: C, 45.26;
9
10 H, 5.33; N, 18.88. ¹H NMR (400 MHz, CD₃CN, 293 K): δ / ppm = 29.3 (s, 4 H), 14.8 (s, 8 H),
11
12 12.6 (s, 4 H), 11.6 (s, 3.63 H), 9.3 (s, 4 H), 8.0 (s, 2 H), 6.9 (s, 4 H), 4.8 (s, 4 H), -0.1 (s, 4 H), -
13
14 4.4 (s, 4.69 H). ¹H NMR (400 MHz, d₆-acetone, 293 K): δ / ppm = 31.8 (s, 4 H), 16.2 (s, 4 H), 16.0
15
16 (4 H), 14.0 (s, 4 H), 12.1 (s, 2.30 H), 10.2 (s, 4 H), 8.3 (s, 2 H), 7.5 (s, 4 H), 5.0 (s, 4 H), 0.1 (s, 4
17
18 H), -4.5 (s, 4 H). ¹H NMR (500 MHz, d₆-acetone, 193 K; **mer-1²⁺**): δ / ppm = 8.71 (s, 3 H), 8.16
19
20 (s, 2 H), 4.37 (m, 8 H), 3.85 (s, 4 H), 3.73 (m, 12 H), 2.42 (m, 8 H), 1.78 (s, 4 H). ¹H NMR (500
21
22 MHz, d₆-acetone, 193 K; **cis-fac-1²⁺**): δ / ppm = 98.6 (s), 96.2 (s), 65.9 (s), 61.6 (s), 55.2 (s), 37.9
23
24 (s), 34.2 (s), 33.3 (s), 30.2 (s), 22.7 (s), 17.2 (s), 11.4 (s), -9.9 (s), -14.3 (s), -15.0 (s), -26.2 (s), -
25
26 37.8 (s), -48.3 (s), -66.1 (s). MS (ESI⁺): m/z (%) = 354.240 (100, [dgpy+H]⁺), 381.199 (19,
27
28 [Fe(dgpy)₂]²⁺), 504.199 (33, {[dgpy+2H][OTf]}⁺), 911.351 (20, {[Fe(dgpy)₂][OTf]}⁺). MS (HR-
29
30 ESI⁺): calcd. for C₃₉H₅₄F₃FeN₁₄O₃S⁺: m/z = 911.3520. Found: 911.3510. IR (ATR): $\tilde{\nu}$ / cm⁻¹ = 3104
31
32 (vw), 2944 (vw), 2861 (vw), 1606 (m), 1590 (m), 1502 (w), 1453 (w, sh), 1430 (m), 1374 (w),
33
34 1325 (w), 1301 (vw), 1263 (s), 1219 (w), 1198 (m), 1140 (s), 1110 (w, sh), 1062 (vw), 1028 (s),
35
36 994 (vw, sh), 911 (vw), 885 (vw, sh), 850 (vw), 806 (w), 752 (vw), 731 (vw), 706 (vw, sh), 634
37
38 (vs), 610 (vw, sh), 571 (w), 557 (w), 516 (m). UV/Vis (CH₃CN, 295 K): λ_{max} / nm (ϵ / M⁻¹ cm⁻¹) =
39
40 222 (41900), 255 (26700), 302 (15200), 466 (961), 530 (996), 582 nm (957). CV (CH₃CN, 0.1 M
41
42 [nBu₄N][PF₆], vs. ferrocene, 295 K): $E_{1/2}$ / V = -0.65 (rev., **mer-1^{2+/3+}**), -0.37 (rev., **cis-fac-1^{2+/3+}**),
43
44 +0.97 V (qrev., coordinated dgpy⁰⁺).

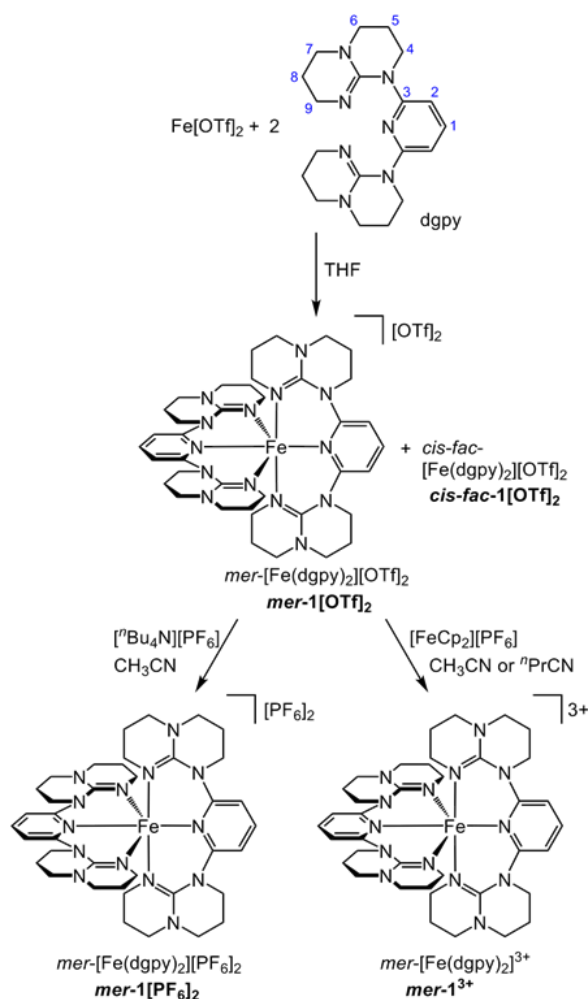
1
2
3 Synthesis of **1**[PF₆]₂. **1**[OTf]₂ (16 mg, 0.015 mmol, 1.0 eq) and [ⁿBu₄N][PF₆] (310 mg, 0.800
4 mmol, 53 eq) were dissolved in dry acetonitrile (2 mL). Slow diffusion of diethylether into this
5 solution yielded crystals suitable for XRD analysis.
6
7

8
9
10 Oxidation of **1**[OTf]₂ to **1**³⁺. **1**[OTf]₂ (34 mg, 0.032 mmol, 1.0 eq) and [FeCp₂][PF₆] (11 mg, 0.032
11 mmol, 1.0 eq) were dissolved in dry solvent (2 mL). CD₃CN, butyronitrile and CH₃CN were used
12 for ¹H NMR, EPR and optical spectroscopy, respectively. Slow diffusion of diethylether into a
13 CH₃CN solution yielded crystals suitable for XRD analysis. ¹H NMR (400 MHz, CD₃CN, 293 K):
14 δ / ppm = 54.0 (s, 4 H), 46.3 (s, 2 H), 31.0 (5 H), 25.9 (s, 4 H), 24.6 (s, 3 H), 20.8 (s, 3 H), 9.2 (s,
15 2 H), 5.2 (s, 4 H), 0.2 (s, 3 H), -1.3 (s, 4 H), -10.6 (s, 4 H). EPR (PrCN, 77 K): $g_{1,2,3}$ = 2.617, 2.197,
16 1.768; Δg = 0.849. UV/Vis (CH₃CN, 295 K): λ_{\max} / nm (ϵ / M⁻¹ cm⁻¹) = 310 (11500), 395 (2140),
17 462 (3410), 486 (sh, 3330).
18
19
20
21
22
23
24
25
26
27
28

29 RESULTS AND DISCUSSION

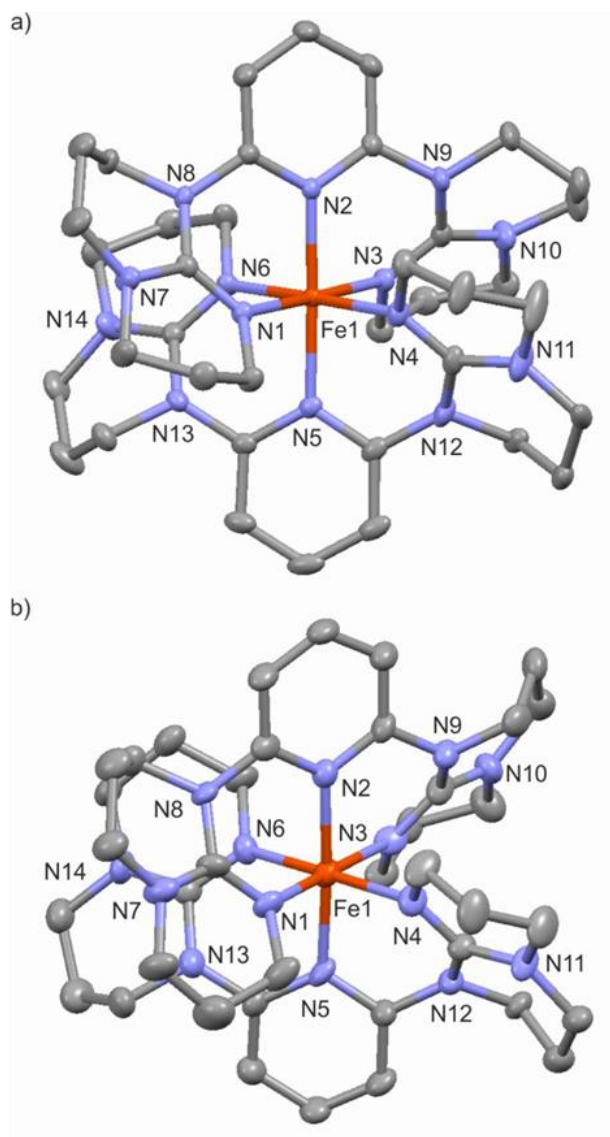
30
31
32
33 **Synthesis.** The homoleptic iron(II) target complex [Fe(dgpy)₂][OTf]₂ (**1**[OTf]₂) precipitated as
34 dark red solid from a solution of iron(II) triflate and 2.2 equivalents of the ligand dgpy³² under
35 inert conditions in THF at room temperature (Scheme 1). Its composition was confirmed by
36 elemental analysis, IR and ¹H NMR spectroscopy as well as ESI⁺ mass spectrometry (Supporting
37 Information, Figures S1–S4). Anion metathesis with [ⁿBu₄N][PF₆] formed the corresponding
38 hexafluorophosphate salt **1**[PF₆]₂ (Scheme 1).
39
40
41
42
43
44
45
46
47

48 **Scheme 1.** Synthesis of iron(II/III) complexes with the ligand dgpy. Atom numbering used for
49 NMR assignments shown in blue.
50
51
52
53
54
55
56
57
58
59
60



38
39
40
41
42
43
44
45
46
47
48
49
50
51
52
53
54
55
56
57
58
59
60

Diffusion of diethyl ether into CH_3CN solutions yielded crystals suitable for single crystal X-ray diffraction analyses. Similar to $[\text{Co}(\text{dgpy})_2]^{3+}$,³¹ yet in contrast to the reported cis-facially coordinated $[\text{Ru}(\text{dgpy})_2]^{3+}$ complex (Chart 1),³² the dgpy ligand coordinates in a meridional fashion in the iron(II) complex *mer-1*²⁺ as confirmed by X-ray diffraction analyses of single crystals of $1[\text{OTf}]_2 \times 0.5\text{CH}_3\text{CN}$ (*Pna*2₁; severely disordered guanidine rings in the cation; 173 K) and $1[\text{PF}_6]_2 \times \text{CH}_3\text{CN}$ (isopointal; *Pna*2₁; 120 K; Figure 1). In the latter salt, the disorder of the heterocyclohexyl rings of the coordinated dgpy ligands is less severe and consequently only the metrical data of this analysis will be discussed in the following.



43 **Figure 1.** Molecular structures of the cations of a) $1[\text{PF}_6]_2 \times \text{CH}_3\text{CN}$ (120 K) and b)
44 $1[\text{PF}_6]_3 \times 1.5\text{CH}_3\text{CN}$ (120 K, only one of the two independent cations A/B in the asymmetric unit
45 shown) determined by XRD. Thermal ellipsoids are displayed at 50 % probability. Hydrogen
46 atoms are omitted for clarity.
47
48
49
50
51
52
53
54
55
56
57
58
59
60

Table 1. Selected bond lengths / Å and angles / deg of the cations of **1**[PF₆]₂×CH₃CN (120 K) and **1**[PF₆]₃×1.5CH₃CN (120 K, two independent cations A/B in the asymmetric unit) obtained by XRD and of *mer-1*²⁺ (low-spin), *mer-1*²⁺ (high-spin), *cis-fac-1*²⁺ and *mer-1*³⁺ (low-spin) obtained by DFT calculations.

	1 [PF ₆] ₂	1 [PF ₆] ₃ (A)	1 [PF ₆] ₃ (B)	low-spin <i>mer-1</i> ²⁺	high-spin <i>mer-1</i> ²⁺	high-spin <i>cis-fac-1</i> ²⁺	low-spin <i>mer-1</i> ³⁺
	XRD			DFT			
M1–N1	2.001(2)	1.93(1)	1.95(1)	2.010	2.145	2.151	1.952
M1–N2	1.959(2)	1.96(1)	1.96(1)	1.981	2.176	2.240	1.975
M1–N3	1.996(2)	1.98(1)	1.97(1)	2.008	2.151	2.145	1.993
M1–N4	1.999(2)	1.97(1)	1.94(1)	2.025	2.167	2.151	1.947
M1–N5	1.946(2)	1.95(1)	1.95(1)	1.982	2.173	2.272	1.969
M1–N6	2.007(2)	1.93(1)	1.96(1)	2.011	2.157	2.174	1.997
N1–Fe1–N2	89.23(8)	88.7(4)	89.0(4)	87.8	82.0	78.3	88.8
N2–Fe1–N3	89.25(9)	90.1(4)	90.5(4)	88.5	82.8	80.1	88.3
N4–Fe1–N5	89.04(8)	90.3(4)	88.8(4)	87.5	81.1	79.4	88.3
N5–Fe1–N6	88.53(8)	87.6(4)	90.9(4)	88.1	81.4	78.4	87.9
S(OC-6)	0.08	0.15	0.08	0.13	1.51	1.25	0.12

The Fe–N distances between 1.946–2.007 Å in *mer-1*²⁺ clearly suggest a low-spin state of iron(II).^{67–69} Compared to the isoelectronic low-spin cobalt(III) complex [Co(dgpy)₂]³⁺, the metal–ligand bond lengths are slightly larger due to the lower charge of the central ion. This has also been observed for the [Fe(ddpd)₂]²⁺ / [Co(ddpd)₂]³⁺ pair.^{12,34} Fe–N distances of the central pyridine units are smaller than the Fe–N distances of the terminal guanidine moieties (Table 1), similar to the cobalt(III) complex.³¹ This M–N distance difference between terminal and central donor atoms is similar to [M(ddpd)₂]ⁿ⁺ complexes featuring six-membered chelate rings, yet much less pronounced than in [M(tpy)₂]ⁿ⁺ complexes with five-membered chelate rings (tpy = 2,2':6',2''-terpyridine).³⁴ Consequently, the [FeN₆] local symmetry of *mer-1*²⁺ is much closer to an ideal octahedron with a shape parameter *S*(OC-6)⁷⁰ of 0.08 than [Fe(tpy)₂]²⁺ with a much larger shape parameter of *S*(OC-6) = 1.81.³⁴ Although the XRD analyses of single crystals at 120 and 173 K

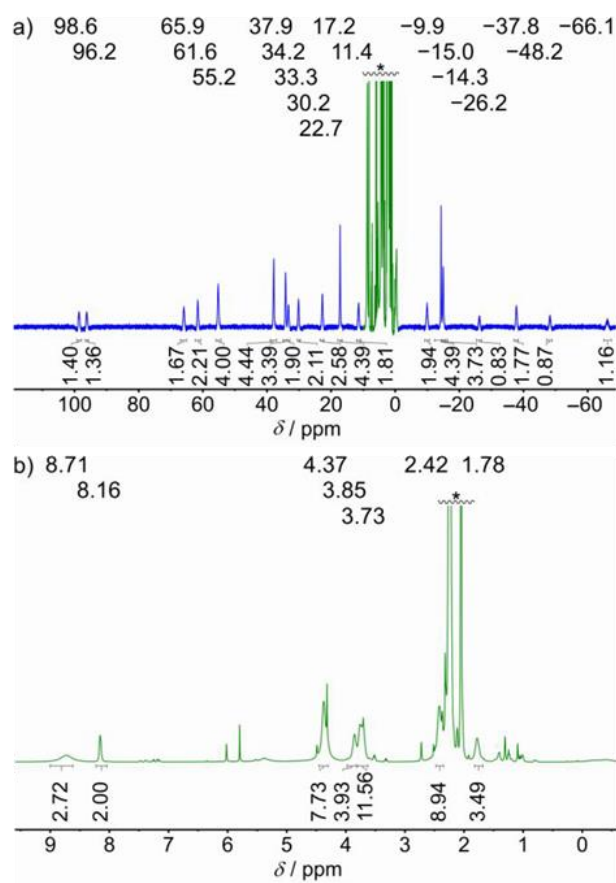


Figure 3. a) ¹H NMR spectrum of **1**[OTf]₂ in d₆-acetone at 193 K. Resonances of the *cis-fac* isomer are colored blue. b) Zoom into the diamagnetic region of the ¹H NMR spectrum at 193 K showing the resonances of low-spin *mer-1*²⁺ in green.

The appearance of averaged signals instead of separated signals for the high- and low-spin isomers indicates a fast exchange between both spin states as typically observed for iron(II) and cobalt(III) SCO complexes.^{71–77} From the line widths of the proton resonances at 31.78, 16.21 and 15.95 ppm (298 K), a high-spin/low-spin exchange constant k_{hl} was estimated around $(7.2–30) \times 10^5 \text{ s}^{-1}$, a range typically observed for SCO complexes (Supporting Information, Table S1).⁶⁷ Yet, other dynamics such as chair-twist boat ring flipping might affect the NMR line widths as well, especially the resonances of the aliphatic protons.

1
2
3
4
5
6
7
8
9
10
11
12
13
14
15
16
17
18
19
20
21
22
23
24
25
26
27
28
29
30
31
32
33
34
35
36
37
38
39
40
41
42
43
44
45
46
47
48
49
50
51
52
53
54
55
56
57
58
59
60

Unexpectedly, a set of 19 clearly discernible, paramagnetically shifted ^1H NMR resonances were additionally present ($\delta = +99$ to -66 ppm at 193 K; Figures 2 and 3). These resonances shift almost linearly with temperature (Figure 2; Supporting Information, Figures S5 and S6). With respect to the iron(II) SCO complex *mer-1*²⁺, they integrate to less than 20 %. The observed large paramagnetic shift confirms a high-spin species and the number of resonances suggests a much less symmetric structure of this species. A conceivable paramagnetic iron(III) impurity is excluded on the basis of the intended preparation and ^1H NMR spectroscopic characterization of the iron(III) complex *mer-1*³⁺ showing very different ^1H NMR resonances (vide infra). As a conceivable trans-facial isomer possesses C_2 symmetry and consequently only a single set of ligand proton resonances, we tentatively assign these broad and shifted resonances to the cis-facial isomer *cis-fac-1*²⁺ with C_1 symmetry. This complex possesses a high-spin electronic ground state down to 183 K. In the temperature range 247–193 K the ^1H NMR resonances of *cis-fac-1*²⁺ are clearly visible and integrable (Figure 2). The relative integrals of resonances of *mer-1*²⁺ and *cis-fac-1*²⁺ are temperature-independent suggesting that the relative amounts do not significantly change with temperature and hence, equilibration of the isomers is unlikely.

For both isomers, some integrals of ^1H resonances are lower than expected for dgpy ligands. Furthermore, traces of uncoordinated ligand (detected in the 600 MHz ^1H NMR spectrum), presumably formed by dissociation from the complex, show integrals lower than expected for the aliphatic protons of dgpy (Scheme 1, Experimental Section, Supporting Information, Figure S7). We suspect that the dgpy ligand coordinated to iron(II) undergoes partial H/D exchange at these positions with the deuterated solvent, which reduces the integrals for these proton resonances.

The *mer* and *cis-fac* isomers of **1**²⁺ reproducibly formed during the synthetic procedure. Yet, attempts to separate *cis-fac* and *mer* isomers by crystallization of the bulk material failed.

Consequently, we take into account a constant amount of high-spin *cis-fac-1*²⁺ being present in the bulk material of *mer-1*²⁺ in the following discussion – in addition to the temperature-dependent SCO behavior of *mer-1*²⁺.

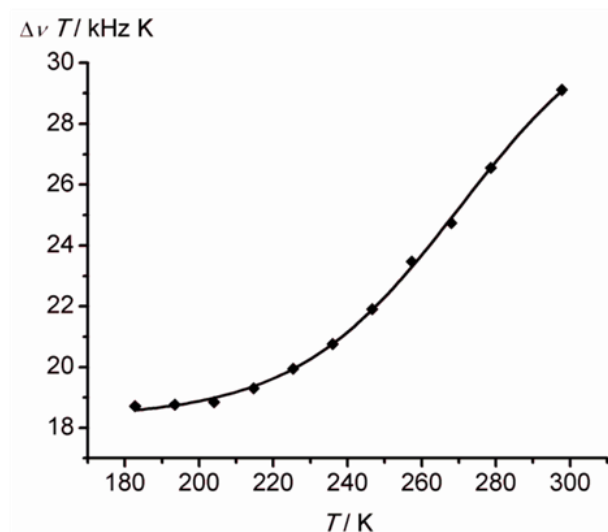
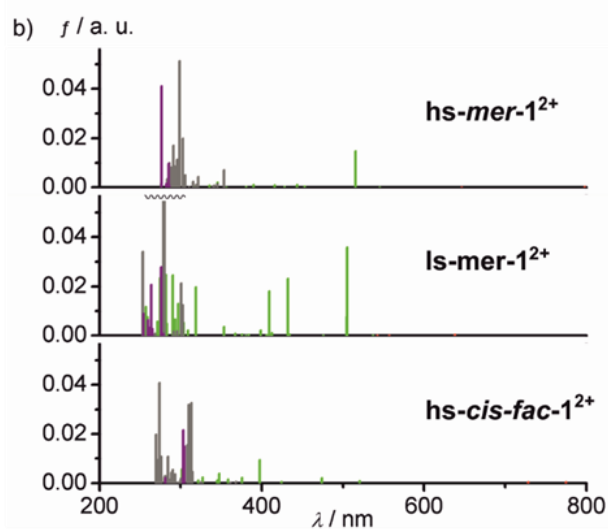
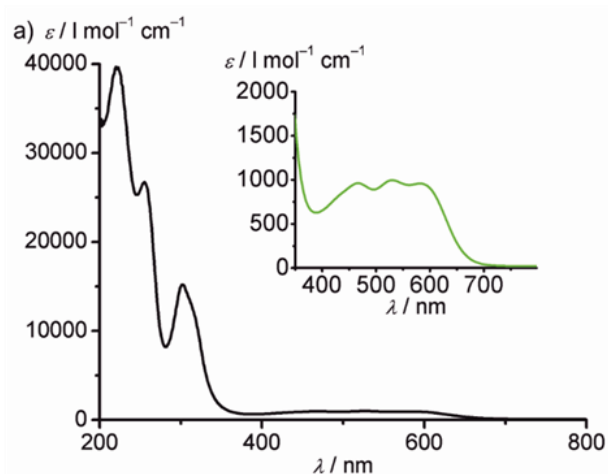


Figure 4. $\Delta\nu T$ vs. T data obtained from ¹H NMR measurements of **1**[OTf]₂ using Evans' method in d₆-acetone and fit according to $R \ln K = -\Delta H/T + \Delta S$ using $\Delta H = 29.6(8)$ kJ mol⁻¹ and $\Delta S = 110(3)$ J mol⁻¹ K⁻¹.

Applying Evans' method^{78–80} in deuterated acetone at variable temperature to determine the magnetic properties in solution and accounting for the presence of high-spin *cis-fac-1*²⁺ yields the $\Delta\delta T$ vs. T plot of *mer-1*²⁺ depicted in Figure 4 (Supporting Information, Figures S8–S9). The thus obtained experimental magnetic data were fit to a distribution between the low-spin and high-spin complexes without taking into account any cooperativity giving $\Delta H = 29.6(8)$ kJ mol⁻¹ and $\Delta S = 110(3)$ J mol⁻¹ K⁻¹. The spin-transition temperature $T_{1/2} = 269$ K with 50 % low- and 50 % high-spin fractions is close to room temperature. At room temperature (293 K), 75 % of the *mer-1*²⁺ complexes are in the high spin state. From the higher degeneracy of the high-spin state (⁵T₂; 15

1
2
3 microstates) compared to the low-spin state (1A_1 ; 1 microstate), the theoretical entropic gain
4
5 amounts to $\Delta S_{el} = R \ln(\Omega_{high-spin}/\Omega_{low-spin}) = R \ln(15/1) = 22.5 \text{ J mol}^{-1} \text{ K}^{-1}$. If the orbital degeneracy
6
7 of the high-spin state is significantly lifted, the electronic contribution to the entropy amounts to
8
9 only $\Delta S_{el} = R \ln(\Omega_{high-spin}/\Omega_{low-spin}) = R \ln(5/1) = 13.4 \text{ J mol}^{-1} \text{ K}^{-1}$.⁸¹ Consequently, the major entropy
10
11 gain ΔS_{vib} (80–88 %) results from higher vibrational degrees of freedom of the high-spin state. The
12
13 larger DFT calculated bond lengths of the high-spin state (high-spin *mer-1*²⁺) as compared to low-
14
15 spin *mer-1*²⁺ reflect this structural and vibrational contribution (Table 1).
16
17
18
19
20



1
2
3 **Figure 5.** a) UV/Vis spectrum of **1[OTf]₂** in acetonitrile at 293 K. The inset shows a zoom into
4 the MLCT region. b) TDDFT calculated transitions of high-spin **mer-1²⁺**, low-spin **mer-1²⁺** and
5 high-spin **cis-fac-1²⁺**, respectively, with the color code indicating the character of the transition
6 according to charge transfer number analyses (green: MLCT, gray: ILCT/LC, purple: LL'CT; The
7 oscillator strengths of the MC states are too small to be visible on this scale; Supporting
8 Information, Figures S10–S12).
9
10
11
12
13
14
15
16

17 The bulk material of **1[OTf]₂** at 293 K is thus composed of approximately 61 % high-spin **mer-**
18 **1²⁺**, 20 % low-spin **mer-1²⁺** and 19 % high-spin **cis-fac-1²⁺**. The absorption spectrum of **1[OTf]₂**
19 dissolved in CH₃CN at 293 K (Figure 5) showed absorption bands at 222, 255, and 302 nm
20 assigned to mainly ligand-based transitions and three maxima in the visible spectral region at 466,
21 530 and 582 nm assigned to MLCT transitions. Time-dependent DFT calculations
22 ((CPCM(acetonitrile)-RIJCOSX-B3LYP-D3BJ-ZORA/def2-TZVP)) on high-spin **mer-1²⁺**, low-
23 spin **mer-1²⁺** and high-spin **cis-fac-1²⁺** cations predicted MLCT transitions in the correct energy
24 region at 515, 505 and 474 nm, respectively (Figure 5). Weak spin-allowed metal-centered
25 transitions for the low- and high-spin complexes (¹MC of low-spin **mer-1²⁺**: 542, 557, 638 nm;
26 ⁵MC of high-spin **mer-1²⁺**: 545, 646 nm; ⁵MC of high-spin **cis-fac-1²⁺**: 728, 775 nm) have been
27 identified at even lower energy in all cases by the quantum chemical calculations and the
28 corresponding analysis of the charge transfer numbers (Supporting Information, Figures S10–
29 S12).
30
31
32
33
34
35
36
37
38
39
40
41
42
43
44
45
46
47
48
49
50
51
52
53
54
55
56
57
58
59
60

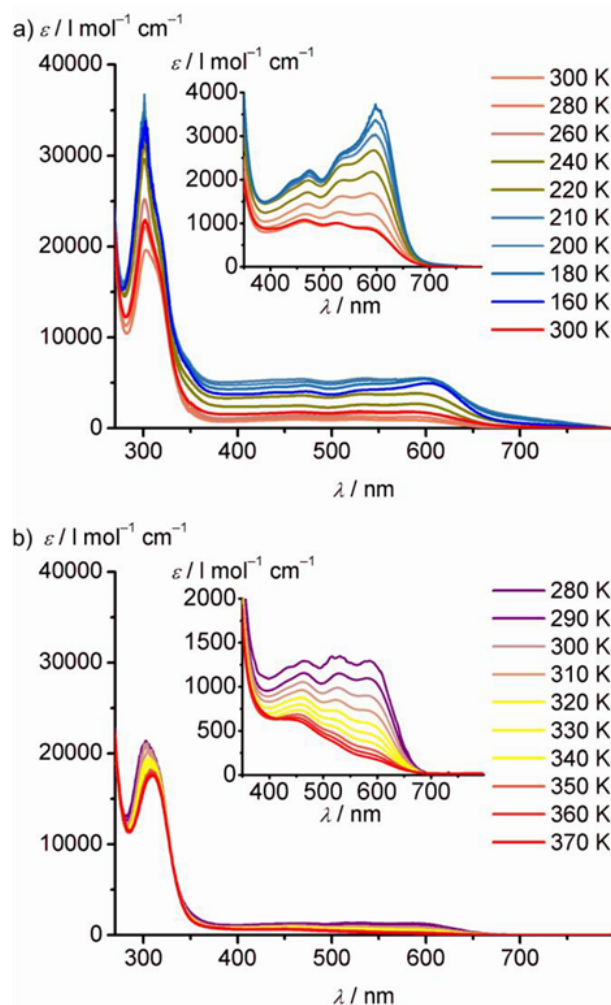
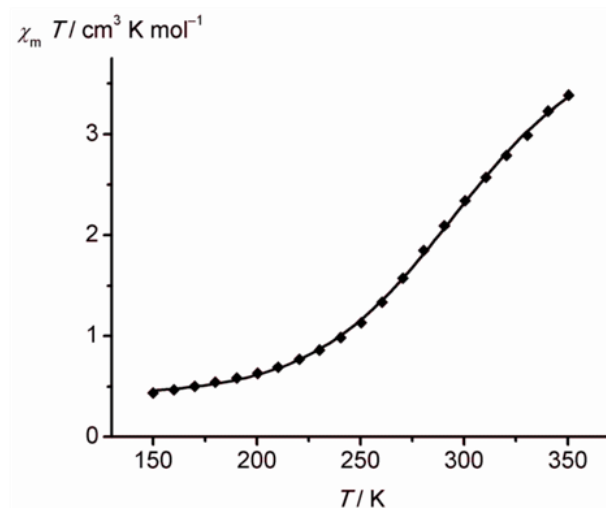


Figure 6. Variable temperature UV/Vis spectra of $1[\text{OTf}]_2$ in butyronitrile, a) during cooling from 300 K to 160 K and re-warming to 300 K and b) during warming from 280 K to 370 K.

Upon cooling to 160 K in butyronitrile, the intensity of the ligand-centered UV bands and the low-energy MLCT bands increased (Figure 6a). Re-warming to 300 K restores the spectrum confirming reversibility (Figure 6a). Furthermore, the pattern of the MLCT bands changed as the low-energy MLCT band increased much stronger at low temperature (Figure 6a). Upon heating to 370 K, the lowest energy MLCT band almost bleached (Figure 6b). The observed band pattern at low temperature resembles the TDDFT calculated pattern of low-spin mer-1^{2+} (Figure 5b, 6a). Fitting

1
2
3 the absorbance at 540 nm vs. temperature (in butyronitrile) with a distribution between the low-
4
5 and high-spin complexes without taking into account any cooperativity gives $\Delta H = 30(1) \text{ kJ mol}^{-1}$
6
7
8
9
10
11
12
13
14
15
16
17
18
19
20
21
22
23
24
25
26
27
28
29
30
31
32
33
34
35
36
37
38
39
40
41
42
43
44
45
46
47
48
49
50
51
52
53
54
55
56
57
58
59
60

the absorbance at 540 nm vs. temperature (in butyronitrile) with a distribution between the low- and high-spin complexes without taking into account any cooperativity gives $\Delta H = 30(1) \text{ kJ mol}^{-1}$ and $\Delta S = 107(3) \text{ J mol}^{-1} \text{ K}^{-1}$ (Supporting Information, Figure S13) in very good agreement with the thermodynamic parameters obtained from the paramagnetically shifted ^1H NMR solvent resonances in acetone (Supporting Information, Figures S8 and S9). The temperature-dependent optical characteristics of $\mathbf{1}^{2+}$ in acetone indeed match those measured in butyronitrile (Supporting Information, Figure S14), confirming that the solvent plays no significant role for the relative stability of high- and low-spin states of *mer-1* $^{2+}$.



41
42
43
44
45
46
47
48
49
50
51
52
53
54
55
56
57
58
59
60

Figure 7. χT vs. T data obtained from magnetic susceptibility measurements of *mer-1*[OTf] $_2$ using a SQUID magnetometer and fit according to $R \ln K = -\Delta H/T + \Delta S$ using $\Delta H = 25.2(9) \text{ kJ mol}^{-1}$ and $\Delta S = 88(3) \text{ J mol}^{-1} \text{ K}^{-1}$. The residual magnetic susceptibility at low temperature arises from the presence of high-spin [*cis-fac-1*][OTf] $_2$.

1
2
3 In order to probe for potential cooperative effects in the solid state, the χT product of solid **1**[OTf]₂
4 was measured using a SQUID magnetometer. Cooling the sample to 150 K and re-warming to 350
5 K revealed a gradual SCO without any hysteresis (Supporting Information, Figure S13). Taking
6
7
8 K revealed a gradual SCO without any hysteresis (Supporting Information, Figure S13). Taking
9
10 into account the presence of the high-spin *cis-fac-1*²⁺ isomer, gave a fit of the χT vs. T curve with
11
12 $\Delta H = 25.2(9)$ kJ mol⁻¹ and $\Delta S = 88(3)$ J mol⁻¹ K⁻¹ (Figure 7). These values compare well to the
13
14 data obtained from NMR and optical spectroscopy in solution. They also document that
15
16 cooperativity between the *mer-1*²⁺ cations is absent both in solution and in the solid state and that
17
18 the environment has no significant impact on the relative stability of high- and low-spin *mer-1*²⁺.
19
20
21
22

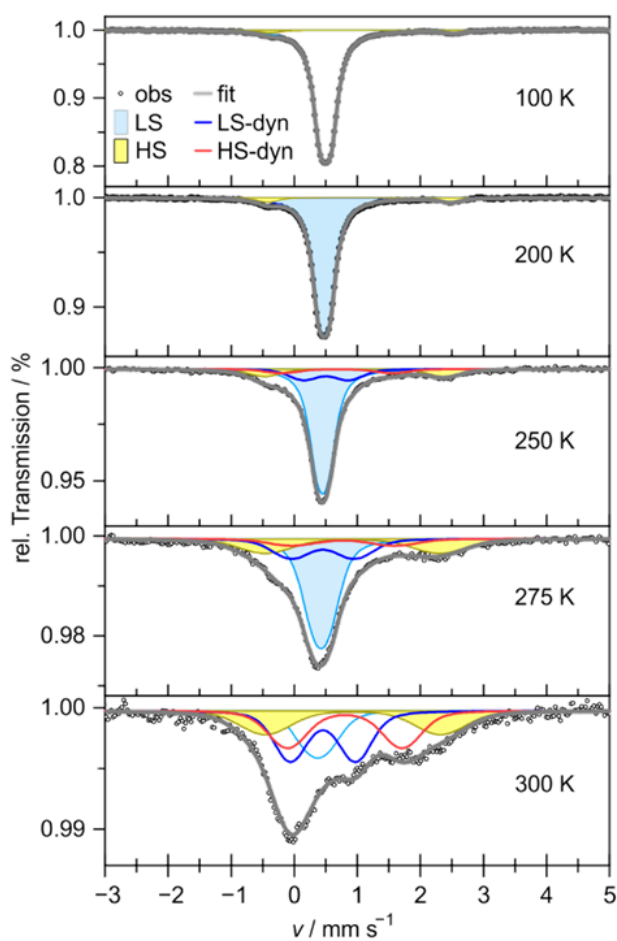


Figure 8. ^{57}Fe Mössbauer spectra of $\mathbf{1}[\text{OTf}]_2$ taken at the indicated temperatures. Deconvoluted subspectra are indicated.

Table 2. ^{57}Fe Mössbauer hyperfine parameters (center shift (CS), quadrupole splitting (QS), Gaussian width of the quadrupole splitting distribution (σ_{QS}) and site populations of $\mathbf{1}[\text{OTf}]_2$ at selected temperatures.

T / K	site	$CS / \text{mm s}^{-1}$	$QS / \text{mm s}^{-1}$	$\sigma_{QS} / \text{mm s}^{-1}$	site populations / %
300	ls	0.37(1)	0.3(1)	0.4(2)	18(1)
	ls-dyn	0.46(1)	1.03(5)	0.40(5)	32(1)
	hs	0.93(1)	2.8(1)	0.7(1)	23(1)
	hs-dyn	0.80(1)	1.82(6)	0.50(6)	27(1)
275	ls	0.43(1)	0.25(3)	0.26(5)	50(1)
	ls-dyn	0.45(1)	1.01(5)	0.49(8)	20(1)
	hs	0.92(1)	2.76(9)	0.72(9)	21(1)
	hs-dyn	0.77(1)	1.6(2)	0.6(2)	9(1)
250	ls	0.45(1)	0.17(1)	0.13(2)	68(1)
	ls-dyn	0.51(1)	0.72(3)	0.34(6)	12(1)
	hs	0.95(1)	2.84(6)	0.41(6)	14(1)
	hs-dyn	0.68(1)	1.8(1)	0.4(1)	6(1)
200	ls	0.47(1)	0.16(1)	0.04(1)	93.9(5)
	hs	1.03(1)	2.89(4)	0.21(5)	6.1(5)
100	ls	0.50(1)	0.17(1)	0.06(1)	96.1(3)
	hs	1.08(2)	2.92(4)	0.19(6)	3.9(3)

^{57}Fe Mössbauer spectra of $\mathbf{1}[\text{OTf}]_2$ at selected temperatures are shown in Figure 8 and individual hyperfine parameters are given in Table 2. The low temperature spectra were well fitted by two principle subspectra referring to each spin configuration (low-spin and high-spin), providing the center shift (CS), quadrupole splitting (QS) and the Gaussian width of the quadrupole splitting distribution (σ_{QS}). At approximately 250 K, the linewidths of each subspectrum broadened and additional contributions appeared at the foothills of the respective absorption lines, as typically found in dynamic scenarios. These additional subspectra represent the species arising from the low-spin and high-spin states, respectively. The modelling followed the two center shifts

1
2
3 resembling the main high-spin and low-spin contributions. Importantly, strongly diverging
4 quadrupole splittings were evident with increasing temperature. We assign these developing
5 features to the dynamic part of the transformation (high-spin-dyn and low-spin-dyn).
6
7

8
9
10 Having established the SCO behavior of $\mathbf{1}^{2+}$ in solution and in the solid state, we probed potential
11 luminescence properties of the high- and low-spin complexes at room temperature and at 77 K in
12 butyronitrile, respectively. However, no emission could be detected after excitation at wavelengths
13 between 190 nm and 605 nm with our equipment. This finding agrees with the presence of low-
14 energy MC states, which enable efficient non-radiative decay (Supporting Information, Figures
15 S10–S12).
16
17

18
19
20 **Redox Chemistry.** The bulk material $\mathbf{1}[\text{OTf}]_2$ dissolved in CH_3CN with $[\text{tBu}_4\text{N}][\text{PF}_6]$ as
21 supporting electrolyte showed a quasi-reversible oxidation wave at +0.97 V vs. ferrocene (Figure
22 9; Supporting Information, Figure S16) assigned to the oxidation of the coordinated dgpy ligand.
23 A reversible oxidation was observed at –0.65 V vs. ferrocene and was assigned to the $\text{Fe}^{\text{II/III}}$ redox
24 couple of *mer*- $\mathbf{1}^{2+}/\textit{mer}$ - $\mathbf{1}^{3+}$. For comparison, the $[\text{M}(\text{dgpy})_2]^{2+/3+}$ couple appeared at –0.69 V vs.
25 ferrocene (M = Ru; *cis-fac* isomer)^{32,82} and at –0.98 V (M = Co; *mer* isomer).^{31,82} A reversible
26 smaller wave is visible in the cyclic and square wave voltammograms at –0.37 V vs. ferrocene.
27 Uncoordinated dgpy is irreversibly oxidized at +0.37 V under the same conditions thus excluding
28 ligand dissociation under the oxidative conditions. The ratio of the peak currents of the waves at –
29 0.37 V and –0.65 V amounts to approximately 20 % (Figure 9). As we have already assigned an
30 approximately 19 % amount of the sample to the high-spin *cis-fac*- $\mathbf{1}^{2+}$ isomer, we attribute this
31 wave to the $\text{Fe}^{\text{II/III}}$ redox couple of the high-spin *cis-fac*- $\mathbf{1}^{2+}$ isomer.
32
33
34
35
36
37
38
39
40
41
42
43
44
45
46
47
48
49
50
51
52
53
54
55
56
57
58
59
60

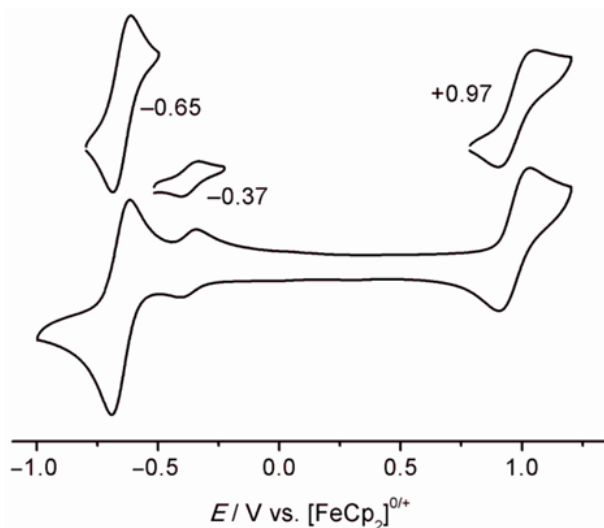


Figure 9. Cyclic voltammogram of **1[OTf]₂**, 1 mM in acetonitrile containing 0.1 M [ⁿBu₄N][PF₆] as supporting electrolyte.

The negative Fe^{II/III} redox potentials enable oxidation of both isomers to the respective iron(III) complexes by dioxygen or by ferrocenium salts. Addition of one equivalent [FeCp₂][PF₆] to a solution of **1[OTf]₂** yielded **1³⁺** (Scheme 1). Structure analysis of a single crystal of **1[PF₆]₃·1.5CH₃CN** by XRD confirmed the meridional coordination of the dgpy ligands and the low-spin state based on the short Fe–N distances (Table 1, Figure 1). The Fe–N bond lengths are further confirmed by DFT calculations on low-spin *mer-1³⁺* (Table 1). The ¹H NMR spectrum of **1³⁺** shows resonances strongly shifted to lower or higher fields ($\delta = +54$ to -11 ppm; Figure 10a; Supporting Information, Figure S17). The number of observed resonances fits to a C₂-symmetric complex *mer-1³⁺*. Using only 0.5 equivalents of the oxidant [FeCp₂][PF₆] instead of 1.0 equivalents resulted in separate signal sets for the iron(III) complex *mer-1³⁺* and the (mainly high-spin) iron(II) complex *mer-1²⁺* (Figure 10a). This indicates a rather slow electron exchange between *mer-1²⁺* and *mer-1³⁺* on the ¹H NMR timescale (400 MHz) at room temperature.

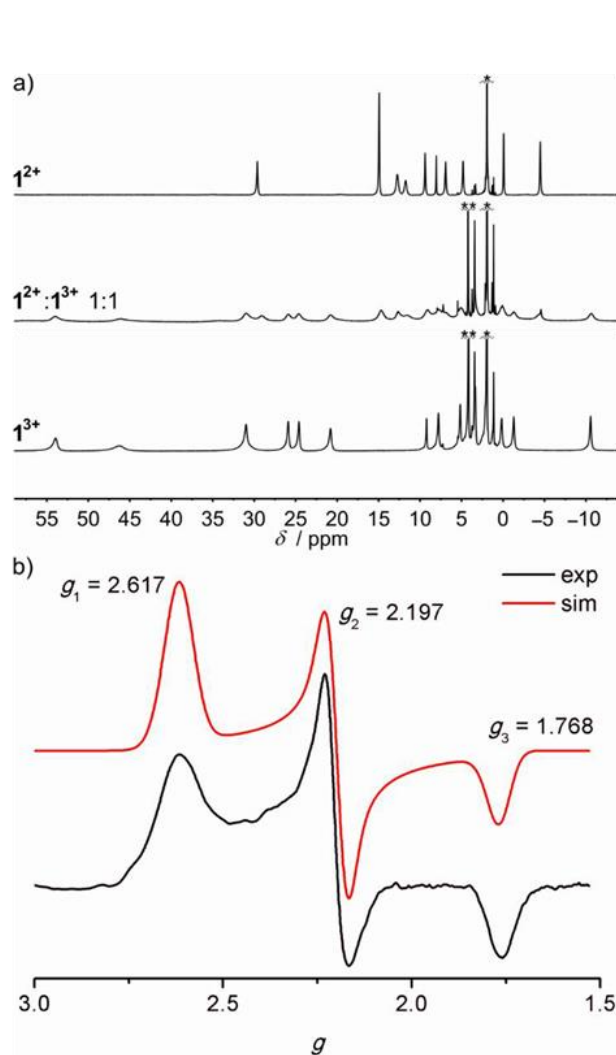
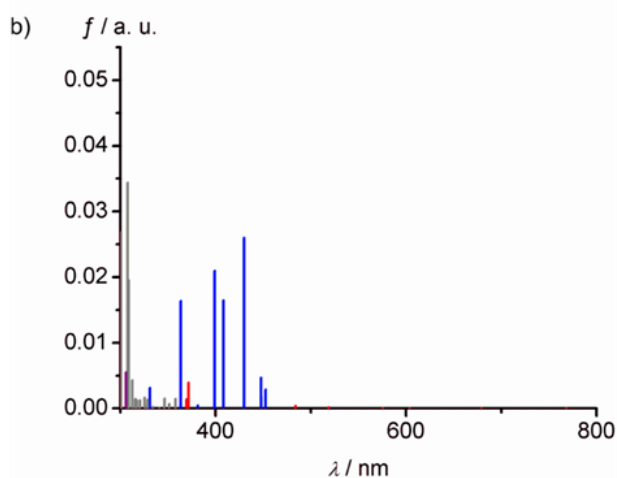
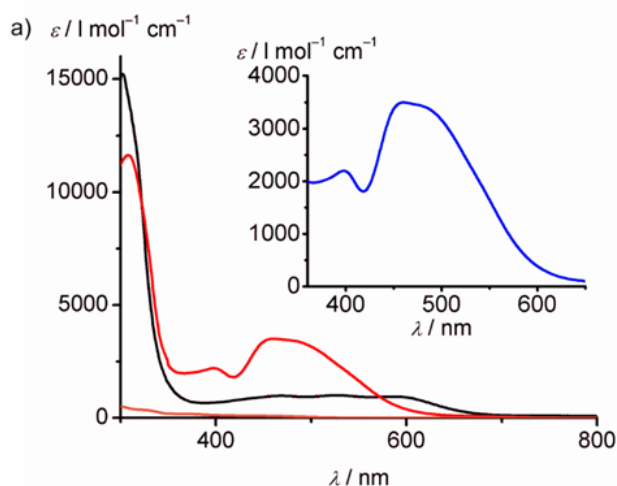


Figure 10. a) ^1H NMR spectra of $\mathbf{1}[\text{OTf}]_2$ in CD_3CN at room temperature without and with 0.5 and 1 eq of $[\text{FeCp}_2][\text{PF}_6]$ added, * denotes acetonitrile, ** denotes ferrocene, b) baseline-corrected X-band EPR spectrum (black) of $\mathbf{1}[\text{OTf}]_2$ with 1 eq of $[\text{FeCp}_2][\text{PF}_6]$ added in butyronitrile at 77 K and simulated spectrum (red).

In the X-band EPR spectrum of $\mathbf{1}[\text{OTf}]_2$ and one equivalent $[\text{FeCp}_2][\text{PF}_6]$ in frozen butyronitrile solution, a rhombic EPR resonance appeared with $g_{1,2,3} = 2.617, 2.197, 1.768$ (77 K; Figure 10b; Supporting Information, Figure S18). This pattern is characteristic for pseudo-octahedral low-spin iron(III) complexes, e.g. with $g_{1,2,3} = 2.490, 2.296, 1.815$ and $g_{1,2,3} = 2.821, 2.247, 1.561$ reported

1
2
3
4 for low-spin $[\text{Fe}(\text{ddpd})_2]^{3+}$ and $[\text{Fe}(\text{dcpp})(\text{ddpd})]^{3+}$, respectively.¹² The g -anisotropy of $\mathbf{1}^{3+}$ with Δg
5
6 $= g_1 - g_3 = 0.849$ is in between that of the homoleptic complex $[\text{Fe}(\text{ddpd})_2]^{3+}$ ($\Delta g = 0.675$) and the
7
8 heteroleptic complex $[\text{Fe}(\text{dcpp})(\text{ddpd})]^{3+}$ ($\Delta g = 1.26$).¹² Contributions of a conceivable minor Fe^{III}
9
10 species *cis-fac-1*³⁺ are not discernible. Several reasons might account for this absence. The amount
11
12 of *cis-fac-1*³⁺ could be too small to be detectable, the g -tensor of *cis-fac-1*³⁺ could be similar to
13
14 that of *mer-1*³⁺, *cis-fac-1*³⁺ could have isomerized to *mer-1*³⁺ or *cis-fac-1*³⁺ could be an EPR-silent
15
16 high-spin complex due to the weaker ligand field strength of facially coordinated dgpy. With the
17
18 data at hand, this cannot be decided.
19
20
21
22



1
2
3 **Figure 11.** a) UV/Vis spectrum of **1[OTf]₂** before (black) and after (red) oxidation with 1 eq of
4 [FeCp₂][PF₆]; UV/Vis spectrum of [FeCp₂] in orange at 300 K for comparison. b) TDDFT
5 calculated transitions of low-spin **mer-1³⁺** with the color code indicating the character of the
6 transition according to charge transfer analyses (red: MC, blue: LMCT, gray: ILCT/LC, purple:
7 LL'CT. The oscillator strengths of the MC states in red are hardly visible on this scale; Supporting
8 Information, Figure S19).
9

10
11
12
13
14
15
16
17
18 Electrochemical or chemical oxidation of **1[OTf]₂** bleaches the MLCT band at 582 nm and gives
19 rise to a 462 nm band with a shoulder around 500 nm (Supporting Information, Figure S20, Figure
20 11a). TDDFT calculations and charge transfer number analysis^{65,66} assign ²LMCT character from
21 the electron-rich guanidine moieties to the electron deficient iron(III) center to the these absorption
22 bands (Fig. 11b). Several less intense MC transitions are located at even lower energy (Supporting
23 Information, Figure S19). In contrast to the fluorescent hexacarbene iron(III) complexes
24 [Fe(btz)₃]³⁺ and [Fe(phtmeimb)₂]⁺,^{29,30} excitation of **mer-1³⁺** at wavelengths between 398 nm and
25 485 nm in dry butyronitrile did not result in observable ²LMCT fluorescence, neither at room
26 temperature in fluid solution nor at 77 K in frozen solution. This is likely due to the presence of
27 these low-energy ²MC states, which enable non-radiate deactivation of the excited states.⁸³
28
29
30
31

32
33
34
35
36
37
38
39
40
41
42 Although we are aware that the relative energy of low- and high-spin states calculated by DFT
43 methods critically depend on the exact exchange,^{84,85} and that the B3LYP functional artificially
44 favors the high-spin state,⁸⁶ we note that the Gibbs free enthalpy difference at 298 K between low-
45 and high spin **mer-1²⁺** calculated by DFT (B3LYP) ($\Delta G_{298,mer,DFT} = -36$ kJ mol⁻¹ favoring the high-
46 spin at this temperature) is much smaller than that for low- and high-spin **cis-fac-1²⁺** ($\Delta G_{298,cis-fac} =$
47 -67 kJ mol⁻¹) in agreement with the SCO behavior of **mer-1²⁺** ($\Delta G_{298,mer,exp} = -3$ kJ mol⁻¹ from the
48 thermodynamic data in solution) and the high-spin character of **cis-fac-1²⁺**. Conceivable low- and
49
50
51
52
53
54
55
56
57
58
59
60

1
2
3 high-spin *trans-fac-1*²⁺ isomers are unfavorable compared to low-spin *mer-1*²⁺ by 52 kJ mol⁻¹ and
4
5 to high-spin *cis-fac-1*²⁺ by 39 kJ mol⁻¹, respectively. We also note that the calculated difference in
6
7 electronic energies favors the high-spin state of *mer-1*²⁺ by only -10 kJ mol⁻¹. Consequently, the
8
9 DFT calculations correctly predict SCO behavior, high-spin character and a high energy for the
10
11 *mer-1*²⁺, *cis-fac-1*²⁺ and *trans-fac-1*²⁺ isomers, respectively. TDDFT calculations describe the CT
12
13 properties of *1*²⁺ and *1*³⁺ (spin-allowed MLCT, LL'CT/ILCT, LMCT; Supporting Information,
14
15 Figure S10–S12, S19) qualitatively correct. Furthermore, MC excited states (with the same
16
17 multiplicity as the ground state) are lower in energy than the charge transfer states in all cases.
18
19 This MC < CT ordering likely applies to states of different multiplicity than the ground state as
20
21 well, namely the triplet (and quintet) MC excited states of low-spin *1*²⁺ and the quartet MC states
22
23 of low-spin *1*³⁺, explaining the absence of CT luminescence.
24
25
26
27
28

29 CONCLUSION

30
31
32 The donor-acceptor ligand dgpy preferably coordinates to iron(II) in a meridional fashion giving
33
34 *mer*-[Fe(dgpy)₂]²⁺ (*mer-1*²⁺), while a cis-facial isomer *cis-fac-1*²⁺ is present in lower amounts. The
35
36 ligand field strength in the meridional coordination mode is higher than in the cis-facial
37
38 coordination mode, resulting in SCO behavior of *mer-1*²⁺ and a high-spin state of *cis-fac-1*²⁺. Low-
39
40 spin *mer-1*²⁺, high-spin *mer-1*²⁺ and high-spin *cis-fac-1*²⁺ exhibit ¹MLCT/⁵MLCT absorption bands
41
42 in the visible spectral region. The room temperature composition of a solution of *1*²⁺ yields a nearly
43
44 constant panchromatic absorption from 400 to 600 nm. In spite of the low-energy MLCT states
45
46 and the comparably high ligand field strength in the meridional coordination mode, MC excited
47
48 states are lower in energy than the ^{1/3}MLCT states and consequently luminescence is not observed.
49
50 Oxidation of *mer-1*²⁺ gives the low-spin complex *mer-1*³⁺ with ²LMCT absorption bands around
51
52 460–500 nm. In spite of the high ligand field strength of the iron(III) complex, MC excited states
53
54
55
56
57
58
59
60

1
2
3 of *mer-1*³⁺ are still lower in energy than the CT states preventing fluorescence from the ²LMCT
4 states.
5
6

7
8
9 ASSOCIATED CONTENT

10
11
12 **Supporting Information.** The Supporting Information is available free of charge at
13 <https://pubs.acs.org/doi/10.1021/acs.inorgchemxxx>.
14
15

16
17 Detailed NMR, IR, ESI⁺, EPR, UV/Vis, SQUID, and electrochemical data, fitting procedures,
18 information on computational studies including charge transfer number analyses, difference
19 densities and Cartesian coordinates of optimized geometries (PDF).
20
21
22

23
24
25 AUTHOR INFORMATION

26
27
28 **Corresponding Author.** Katja Heinze – Department of Chemistry, Johannes Gutenberg
29 University, Duesbergweg 10-14, 55128 Mainz, Germany; E-mail: katja.heinze@uni-mainz.de;
30
31
32 ORCID 0000-0003-1483-4156
33

34
35
36 **Authors**

37
38 Johannes Moll – Department of Chemistry, Johannes Gutenberg University, Duesbergweg 10-14,
39 55128 Mainz
40

41
42
43 Christoph Förster – Department of Chemistry, Johannes Gutenberg University, Duesbergweg 10-
44 14, 55128 Mainz; ORCID 0000-0003-4971-5368
45
46

47
48
49 Alexandra König – Department of Chemistry, Johannes Gutenberg University, Duesbergweg 10-
50 14, 55128 Mainz
51
52

1
2
3 Luca M. Carrella – Department of Chemistry, Johannes Gutenberg University, Duesbergweg 10-
4
5 14, 55128 Mainz
6
7

8
9 Manfred Wagner – Max Planck Institute for Polymer Research, Ackermannweg 10, 55128 Mainz,
10
11 Germany
12
13

14 [REDACTED] – Department of Chemistry, Johannes Gutenberg University, Duesbergweg 10-
15
16 14, 55128 Mainz; [REDACTED]
17
18

19 [REDACTED] – Department of Chemistry, Johannes Gutenberg University, Duesbergweg 10-14,
20
21 55128 Mainz; [REDACTED]
22
23

24
25 Eva Rentschler – Department of Chemistry, Johannes Gutenberg University, Duesbergweg 10-14,
26
27 55128 Mainz; ORCID 0000-0003-1431-3641
28
29

30 31 **Author Contributions**

32
33 The manuscript was written through contributions of all authors. All authors have given approval
34
35 to the final version of the manuscript.
36
37

38 39 **Notes**

40
41 The authors declare no competing financial interest.
42
43
44

45 46 **ACKNOWLEDGMENT**

47
48 Financial support from the Deutsche Forschungsgemeinschaft [Priority Program SPP 2102 “Light-
49
50 controlled reactivity of metal complexes” (HE 2778/14-1)] is gratefully acknowledged (K.H.).
51
52 A.M. acknowledges support from the Carl-Zeiss Foundation. We thank Prof. Tanja Weil (Max
53
54 Planck Institute for Polymer Research, Mainz, Germany) for NMR support.
55
56
57
58
59
60

REFERENCES

1. *Spin crossover in transition metal compounds I*; Gütllich, P., Goodwin, H. A., Eds.; Topics in Current Chemistry 233; Springer: Berlin/Heidelberg, 2004.
2. *Spin Crossover in Transition Metal Compounds II*; Gütllich, P., Goodwin, H. A., Eds.; Topics in Current Chemistry 234; Springer: Berlin/Heidelberg, 2004.
3. *Spin Crossover in Transition Metal Compounds III*; Gütllich, P., Goodwin, H. A., Eds.; Topics in Current Chemistry 235; Springer: Berlin/Heidelberg, 2004.
4. Weber, B. *Coord. Chem. Rev.* **2009**, *253*, 2432–2449.
5. Halcrow, M. A. *Polyhedron* **2007**, *26*, 3523–3576.
6. Halcrow, M. A. *Coord. Chem. Rev.* **2009**, *253*, 2493–2514.
7. Decurtins, S.; Gütllich, P.; Hasselbach, K. M.; Hauser, A. W.; Spiering, H. *Inorg. Chem.* **1985**, *24*, 2174–2178.
8. Decurtins, S.; Gütllich, P.; Köhler, C. P.; Spiering, H.; Hauser, A. W. *Chem. Phys. Lett.* **1984**, *105*, 1–4.
9. McCusker, J. K.; Walda, K. N.; Dunn, R. C.; Simon, J. D.; Magde, D.; Hendrickson, D. N. *J. Am. Chem. Soc.* **1993**, *115*, 298–307.
10. Jamula, L. L.; Brown, A. M.; Guo, D.; McCusker, J. K. *Inorg. Chem.* **2014**, *53*, 15–17.
11. Britz, A.; Gawelda, W.; Assefa, T. A.; Jamula, L. L.; Yarranton, J. T.; Galler, A.; Khakhulin, D.; Diez, M.; Harder, M.; Doumy, G.; March, A. M.; Bajnóczi, É.; Németh, Z.; Pápai, M.; Rozsályi, E.; Sárosiné Szemes, D.; Cho, H.; Mukherjee, S.; Liu, C.; Kim, T. K.; Schoenlein, R. W.; Southworth, S. H.; Young, L.; Jakubikova, E.; Huse, N.; Vankó, G.; Bressler, C.; McCusker, J. K. *Inorg. Chem.* **2019**, *58*, 9341–9350.
12. Mengel, A. K. C.; Förster, C.; Breivogel, A.; Mack, K.; Ochsmann, J. R.; Laquai, F.; Ksenofontov, V.; Heinze, K. *Chem. Eur. J.* **2015**, *21*, 704–714.
13. Wenger, O. S. *Chem. Eur. J.* **2019**, *25*, 6043–6052.
14. Hockin, B. M.; Li, C.; Robertson, N.; Zysman-Colman, E. *Catal. Sci. Technol.* **2019**, *9*, 889–915.
15. Lindh, L.; Chábera, P.; Rosemann, N. W.; Uhlig, J.; Wärnmark, K.; Yartsev, A.; Sundström, V.; Persson, P. *Catalysts* **2020**, *10*, 315.
16. Duchanois, T.; Liu, L.; Pastore, M.; Monari, A.; Cebrián, C.; Trolez, Y.; Darari, M.; Magra, K.; Francés-Monerris, A.; Domenichini, E.; Beley, M.; Assfeld, X.; Haacke, S.; Gros, P. C. *Inorganics* **2018**, *6*, 63.
17. Arias-Rotondo, D. M.; McCusker, J. K. *Chem. Soc. Rev.* **2016**, *45*, 5803–5820.

- 1
2
3
4
5
6
7
8
9
10
11
12
13
14
15
16
17
18
19
20
21
22
23
24
25
26
27
28
29
30
31
32
33
34
35
36
37
38
39
40
41
42
43
44
45
46
47
48
49
50
51
52
53
54
55
56
57
58
59
60
18. Chábera, P.; Kjær, K. S.; Prakash, O.; Honarfar, A.; Liu, Y.; Fredin, L. A.; Harlang, T. C. B.; Lidin, S.; Uhlig, J.; Sundström, V.; Lomoth, R.; Persson, P.; Wärnmark, K. *J. Phys. Chem. Lett.* **2018**, *9*, 459–463.
 19. Fredin, L. A.; Pápai, M.; Rozsályi, E.; Vankó, G.; Wärnmark, K.; Sundström, V.; Persson, P. *J. Phys. Chem. Lett.* **2014**, *5*, 2066–2071.
 20. Harlang, T. C. B.; Liu, Y.; Gordivska, O.; Fredin, L. A.; Ponceca, C. S., JR; Huang, P.; Chábera, P.; Kjær, K. S.; Mateos, H.; Uhlig, J.; Lomoth, R.; Wallenberg, R.; Styring, S.; Persson, P.; Sundström, V.; Wärnmark, K. *Nat. Chem.* **2015**, *7*, 883–889.
 21. Liu, Y.; Harlang, T. C. B.; Canton, S. E.; Chábera, P.; Suarez-Alcantara, K.; Fleckhaus, A.; Vithanage, D. A.; Goransson, E.; Corani, A.; Lomoth, R.; Sundström, V.; Wärnmark, K. *Chem. Commun.* **2013**, *49*, 6412–6414.
 22. Liu, Y.; Persson, P.; Sundström, V.; Wärnmark, K. *Acc. Chem. Res.* **2016**, *49*, 1477–1485.
 23. Zimmer, P.; Müller, P.; Burkhardt, L.; Schepper, R.; Neuba, A.; Steube, J.; Dietrich, F.; Flörke, U.; Mangold, S.; Gerhards, M.; Bauer, M. *Eur. J. Inorg. Chem.* **2017**, *2017*, 1504–1509.
 24. Steube, J.; Burkhardt, L.; Pöpcke, A.; Moll, J.; Zimmer, P.; Schoch, R.; Wölper, C.; Heinze, K.; Lochbrunner, S.; Bauer, M. *Chem. Eur. J.* **2019**, *25*, 11826–11830.
 25. Dixon, I. M.; Alary, F.; Boggio-Pasqua, M.; Heully, J.-L. *Dalton Trans.* **2015**, *44*, 13498–13503.
 26. Braun, J. D.; Lozada, I. B.; Kolodziej, C.; Burda, C.; Newman, K. M. E.; van Lierop, J.; Davis, R. L.; Herbert, D. E. *Nat. Chem.* **2019**, *11*, 1144–1150.
 27. Dierks, P.; Pöpcke, A.; Bokareva, O. S.; Altenburger, B.; Reuter, T.; Heinze, K.; Kühn, O.; Lochbrunner, S.; Bauer, M. *Inorg. Chem.* **2020**, *59*, 14746–14761.
 28. Jiang, T.; Bai, Y.; Zhang, P.; Han, Q.; Mitzi, D. B.; Therien, M. J. *Proc. Natl. Acad. Sci. U.S.A.* **2020**, *117*, 20430–20437.
 29. Chábera, P.; Liu, Y.; Prakash, O.; Thyrhaug, E.; Nahhas, A. E.; Honarfar, A.; Essen, S.; Fredin, L. A.; Harlang, T. C. B.; Kjær, K. S.; Handrup, K.; Ericson, F.; Tatsuno, H.; Morgan, K.; Schnadt, J.; Haggstrom, L.; Ericsson, T.; Sobkowiak, A.; Lidin, S.; Huang, P.; Styring, S.; Uhlig, J.; Bendix, J.; Lomoth, R.; Sundström, V.; Persson, P.; Wärnmark, K. *Nature* **2017**, *543*, 695–699.
 30. Kjær, K. S.; Kaul, N.; Prakash, O.; Chábera, P.; Rosemann, N. W.; Honarfar, A.; Gordivska, O.; Fredin, L. A.; Bergquist, K.-E.; Häggström, L.; Ericsson, T.; Lindh, L.; Yartsev, A.; Styring, S.; Huang, P.; Uhlig, J.; Bendix, J.; Strand, D.; Sundström, V.; Persson, P.; Lomoth, R.; Wärnmark, K. *Science* **2019**, *363*, 249–253.
 31. Pal, A. K.; Li, C.; Hanan, G. S.; Zysman-Colman, E. *Angew. Chem. Int. Ed.* **2018**, *57*, 8027–8031.

- 1
2
3
4
5
6
7
8
9
10
11
12
13
14
15
16
17
18
19
20
21
22
23
24
25
26
27
28
29
30
31
32
33
34
35
36
37
38
39
40
41
42
43
44
45
46
47
48
49
50
51
52
53
54
55
56
57
58
59
60
32. Pal, A. K.; Zaccheroni, N.; Campagna, S.; Hanan, G. S. *Chem. Commun.* **2014**, *50*, 6846–6849.
33. Förster, C.; Gorelik, T. E.; Kolb, U.; Ksenofontov, V.; Heinze, K. *Eur. J. Inorg. Chem.* **2015**, *2015*, 920–924.
34. Förster, C.; Dorn, M.; Reuter, T.; Otto, S.; Davarci, G.; Reich, T.; Carrella, L. M.; Rentschler, E.; Heinze, K. *Inorganics* **2018**, *6*, 86.
35. Otto, S.; Grabolle, M.; Förster, C.; Kreitner, C.; Resch-Genger, U.; Heinze, K. *Angew. Chem. Int. Ed.* **2015**, *54*, 11572–11576.
36. Dorn, M.; Kalmbach, J.; Boden, P.; Pöpcke, A.; Gómez, S.; Förster, C.; Kuczelinis, F.; Carrella, L. M.; Büldt, L. A.; Bings, N. H.; Rentschler, E.; Lochbrunner, S.; González, L.; Gerhards, M.; Seitz, M.; Heinze, K. *J. Am. Chem. Soc.* **2020**, *142*, 7947–7955.
37. Wang, C.; Otto, S.; Dorn, M.; Kreidt, E.; Lebon, J.; Sršan, L.; Di Martino-Fumo, P.; Gerhards, M.; Resch-Genger, U.; Seitz, M.; Heinze, K. *Angew. Chem. Int. Ed.* **2018**, *57*, 1112–1116.
38. Fulmer, G. R.; Miller, A. J. M.; Sherden, N. H.; Gottlieb, H. E.; Nudelman, A.; Stoltz, B. M.; Bercaw, J. E.; Goldberg, K. I. *Organometallics* **2010**, *29*, 2176–2179.
39. Stoll, S.; Schweiger, A. *J. Magn. Reson.* **2006**, *178*, 42–55.
40. Krejčík, M.; Daněk, M.; Hartl, F. *J. Electroanal. Chem.* **1991**, *317*, 189–187.
41. Schoeller, W. W.; Niemann, J. *J. Am. Chem. Soc.* **1986**, *108*, 22–26.
42. Rancourt, D. G.; Ping, J. Y. *Nucl. Instr. Meth. B* **1991**, *58*, 85–97.
43. Lagarec, K.; Rancourt, D. G. *Recoil (1998); Software package v1.05 (2002)*, 1998.
44. *STOE & Cie, X-Area*; STOE & Cie GmbH: Darmstadt, Germany
45. Blessing, R. H. *Acta Crystallogr. A* **1995**, *51*, 33–38.
46. Spek, A. L. *Acta Crystallogr. D Biol. Crystallogr.* **2009**, *65*, 148–155.
47. Koziskova, J.; Hahn, F.; Richter, J.; Kožíšek, J. *Acta Chim. Slovaca* **2016**, *9*, 136–140.
48. Sheldrick, G. M. *Acta Crystallogr. A* **2015**, *71*, 3–8.
49. Sheldrick, G. M. *SHELXL-2018/3*; University of Göttingen: Göttingen, Germany, 2018.
50. Sheldrick, G. M. *SHELXL-2016/6*; University of Göttingen: Göttingen, Germany, 2016.
51. Hübschle, C. B.; Sheldrick, G. M.; Dittrich, B. *J. Appl. Crystallogr.* **2011**, *44*, 1281–1284.
52. Neese, F. *WIREs Comput. Mol. Sci.* **2018**, *8*, e1327.
53. Becke, A. D. *J. Chem. Phys.* **1993**, *98*, 5648–5652.

- 1
2
3
4
5
6
7
8
9
10
11
12
13
14
15
16
17
18
19
20
21
22
23
24
25
26
27
28
29
30
31
32
33
34
35
36
37
38
39
40
41
42
43
44
45
46
47
48
49
50
51
52
53
54
55
56
57
58
59
60
54. Chengteh Lee; Weitao Yang; Parr, R. G. *Phys. Rev. B* **1988**, *37*, 785–789.
 55. Miehlich, B.; Savin, A.; Stoll, H.; Preuss, H. *Chem. Phys. Lett.* **1989**, *157*, 200–206.
 56. Neese, F.; Wennmohs, F.; Hansen, A.; Becker, U. *Chem. Phys.* **2009**, *356*, 98–109.
 57. Izsák, R.; Neese, F. *J. Chem. Phys.* **2011**, *135*, 144105-1–11.
 58. Pantazis, D. A.; Chen, X.-Y.; Landis, C. R.; Neese, F. *J. Chem. Theory Comput.* **2008**, *4*, 908–919.
 59. Miertus, S.; Scrocco, E.; Tomasi, J. *Chem. Phys.* **1981**, *55*, 117–129.
 60. Barone, V.; Cossi, M. *J. Phys. Chem. A* **1998**, *102*, 1995–2001.
 61. Schäfer, A.; Horn, H.; Ahlrichs, R. *J. Chem. Phys.* **1992**, *97*, 2571–2577.
 62. Schäfer, A.; Huber, C.; Ahlrichs, R. *J. Chem. Phys.* **1994**, *100*, 5829–5835.
 63. Grimme, S.; Antony, J.; Ehrlich, S.; Krieg, H. *J. Chem. Phys.* **2010**, *132*, 154104-1–19.
 64. Grimme, S.; Ehrlich, S.; Goerigk, L. *J. Comput. Chem.* **2011**, *32*, 1456–1465.
 65. Plasser, F. *TheoDORE*: at <http://theodore-qc.sourceforge.net>
 66. Plasser, F. *J. Chem. Phys.* **2020**, *152*, 84108-1–14.
 67. Gütllich, P.; Hauser, A. W.; Spiering, H. *Angew. Chem. Int. Ed. Engl.* **1994**, *33*, 2024–2054.
 68. Phan, H.; Hrudka, J. J.; Igimbayeva, D.; Lawson Daku, L. M.; Shatruk, M. *J. Am. Chem. Soc.* **2017**, *139*, 6437–6447.
 69. Guionneau, P.; Marchivie, M.; Bravic, G.; Létard, J.-F.; Chasseau, D. Structural Aspects of Spin Crossover. Example of the [Fe^{II}L_n(NCS)₂] Complexes In *Topics in Current Chemistry*, 234, Springer, Berlin/Heidelberg, 2004, pp 97–128.
 70. Alemany, P.; Casanova, D.; Alvarez, S.; Dryzun, C.; Avnir, D. Continuous Symmetry Measures: A New Tool in Quantum Chemistry In *Reviews in Computational Chemistry*, John Wiley & Sons, Hoboken, NJ, USA, 2017, pp 289–352.
 71. De, S.; Tewary, S.; Garnier, D.; Li, Y.; Gontard, G.; Lisnard, L.; Flambard, A.; Breher, F.; Boillot, M.-L.; Rajaraman, G.; Lescouëzec, R. *Eur. J. Inorg. Chem.* **2018**, *2018*, 414–428.
 72. Gütllich, P.; McGarvey, B. R.; Kläui, W. *Inorg. Chem.* **1980**, *19*, 3704–3706.
 73. Eberspach, W.; El Murr, N.; Kläui, W. *Angew. Chem. Int. Ed. Engl.* **1982**, *21*, 915–916.
 74. Navon, G.; Kläui, W. *Inorg. Chem.* **1984**, *23*, 2722–2725.
 75. Kläui, W.; Eberspach, W.; Gütllich, P. *Inorg. Chem.* **1987**, *26*, 3977–3982.

- 1
2
3
4
5
6
7
8
9
10
11
12
13
14
15
16
17
18
19
20
21
22
23
24
25
26
27
28
29
30
31
32
33
34
35
36
37
38
39
40
41
42
43
44
45
46
47
48
49
50
51
52
53
54
55
56
57
58
59
60
76. Petzold, H.; Djomgoue, P.; Hörner, G.; Heider, S.; Lochenie, C.; Weber, B.; Ruffer, T.; Schaarschmidt, D. *Dalton Trans.* **2017**, *46*, 6218–6229.
77. Petzold, H.; Djomgoue, P.; Hörner, G.; Lochenie, C.; Weber, B.; Ruffer, T. *Dalton Trans.* **2018**, *47*, 491–506.
78. Evans, D. J. *J. Chem. Soc.* **1959**, 2003–2005.
79. Schubert, E. M. *J. Chem. Educ.* **1992**, *69*, 62.
80. Piguet, C. *J. Chem. Educ.* **1997**, *74*, 815–816.
81. Hauser, A. W. Ligand Field Theoretical Considerations In *Topics in Current Chemistry*, 233, Springer, Berlin/Heidelberg, 2004, pp 49–58.
82. Connelly, N. G.; Geiger, W. E. *Chem. Rev.* **1996**, *96*, 877–910.
83. Förster, C.; Heinze, K. *Chem. Soc. Rev.* **2020**, *49*, 1057–1070.
84. Reiher, M.; Salomon, O.; Artur Hess, B. *Theor. Chem. Acc.* **2001**, *107*, 48–55.
85. Rudavskiy, A.; Sousa, C.; Graaf, C. de; Havenith, R. W. A.; Broer, R. *J. Chem. Phys.* **2014**, *140*, 184318.
86. Bowman, D. N.; Jakubikova, E. *Inorg. Chem.* **2012**, *51*, 6011–6019.

Panchromatic Absorption and Oxidation of an Iron(II) Spin Crossover Complex

Johannes Moll,[†] Christoph Förster,[†] Alexandra König,[†] Luca M. Carrella,[†] Manfred Wagner,[‡]
██████████,[†] ██████████,[†] Eva Rentschler,[†] and Katja Heinze*[†]

[†] Department of Chemistry, Johannes Gutenberg University, Duesbergweg 10-14, 55128 Mainz, Germany

[‡] Max Planck Institute for Polymer Research, Ackermannweg 10, 55128 Mainz, Germany.

Iron(II) complexes

Characterization of 1 [OTf] ₂ (IR, ¹ H NMR, ESI ⁺) [Figures S1–S4]	S2
Variable temperature NMR spectroscopic studies of 1 [OTf] ₂ [Figures S5–S9]	S4
TDDFT and charge transfer analyses of 1 ²⁺ [Figures S10–S12]	S8
Variable temperature UV/Vis spectroscopic studies of 1 [OTf] ₂ [Figures S13–S14]	S11
Variable temperature magnetic susceptibility measurement of 1 [OTf] ₂ [Figure S15]	S12
Square-wave voltammograms of 1 [OTf] ₂ [Figure S16]	S12

Iron(III) complex

Characterization of 1 ³⁺ (¹ H NMR, EPR) [Figures S17–S18]	S13
TDDFT and charge transfer analysis of 1 ³⁺ [Figure S19]	S14
UV/Vis spectra of 1 [OTf] ₂ during electrochemical oxidation [Figure S20]	S15

Cartesian coordinates of DFT optimized geometries	S16
--	-----

9. Panchromatic Absorption and Oxidation of an Iron(II) Spin Crossover Complex

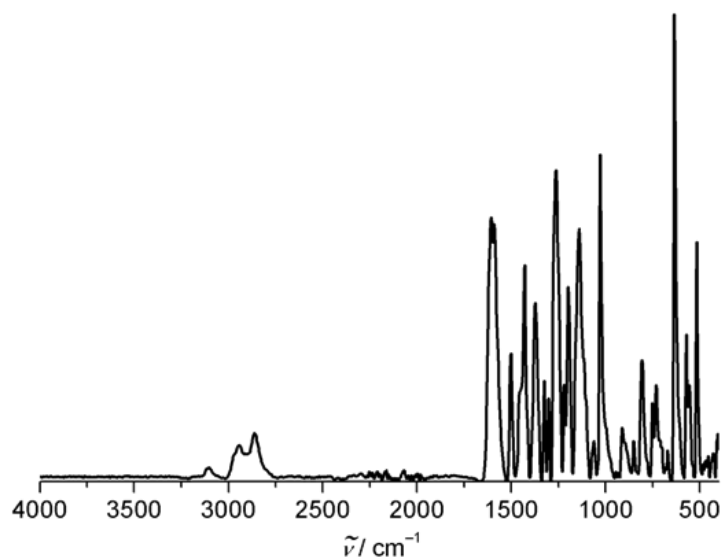


Figure S1. ATR IR spectrum of **1[OTf]₂**.

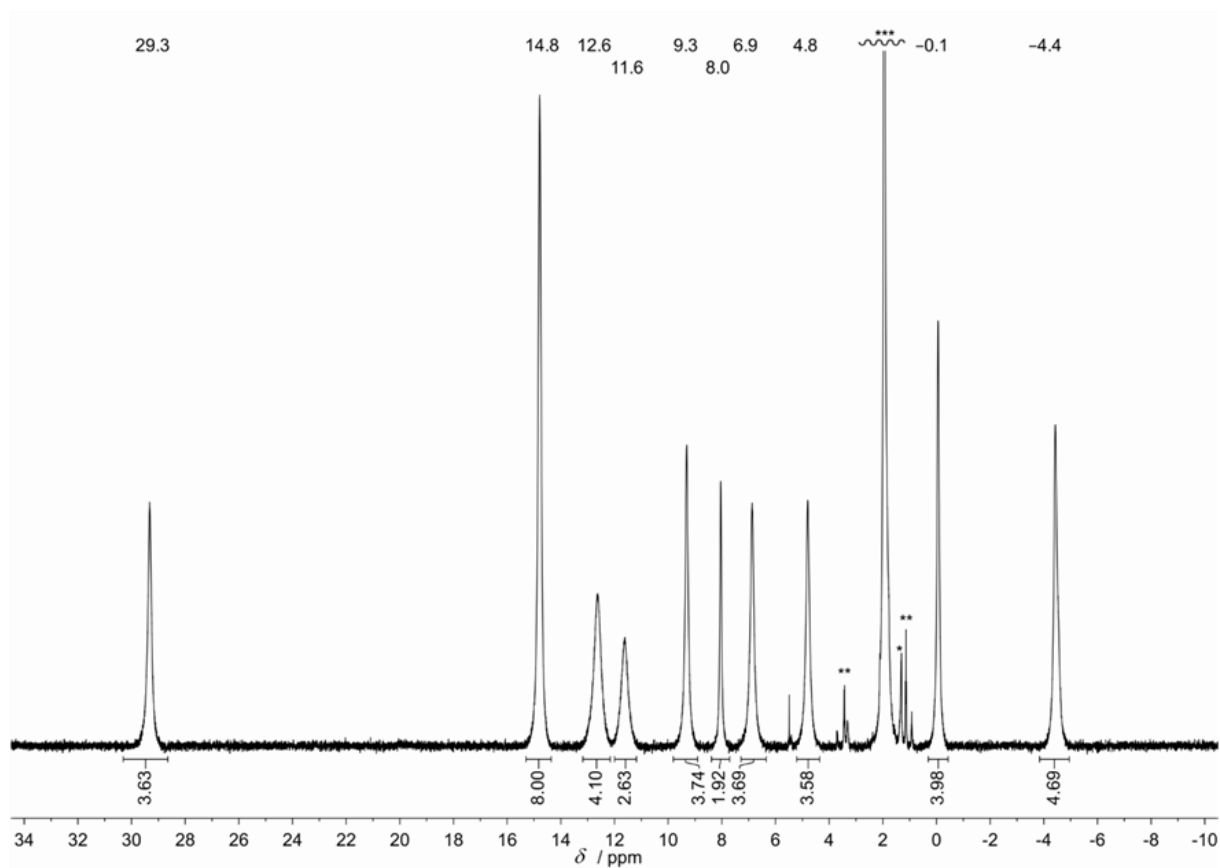


Figure S2. ¹H NMR spectrum of **1[OTf]₂** in dry, deaerated CD₃CN at 293 K (* residual grease; ** residual diethylether; *** acetonitrile).

9. Panchromatic Absorption and Oxidation of an Iron(II) Spin Crossover Complex

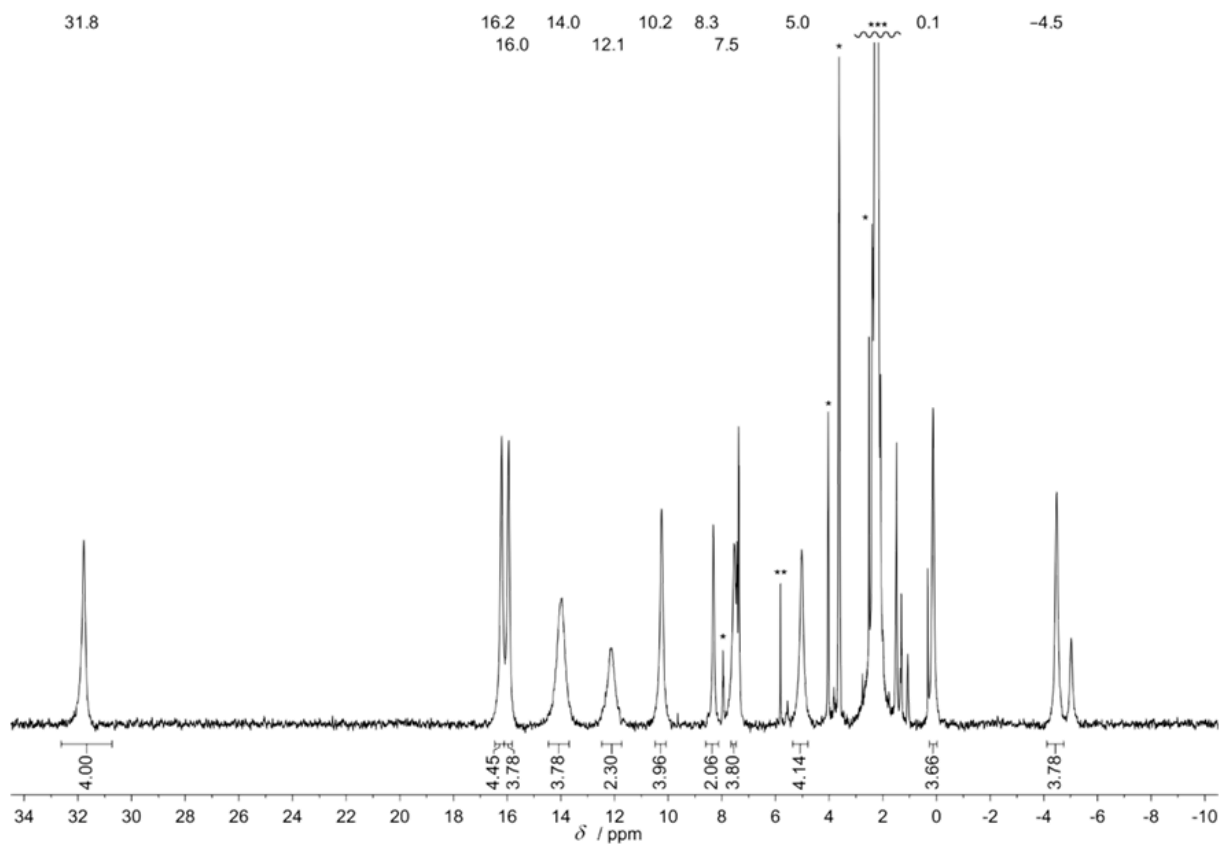


Figure S3. ^1H NMR spectrum of $1[\text{OTf}]_2$ in dry, deaerated d_6 -acetone at 293 K (* residual $[\text{dgyH}]^+$; ** residual dichloromethane; *** acetone), chemical shifts referenced to the acetone resonance stemming from the capillary insert of the Evans' NMR measurement.

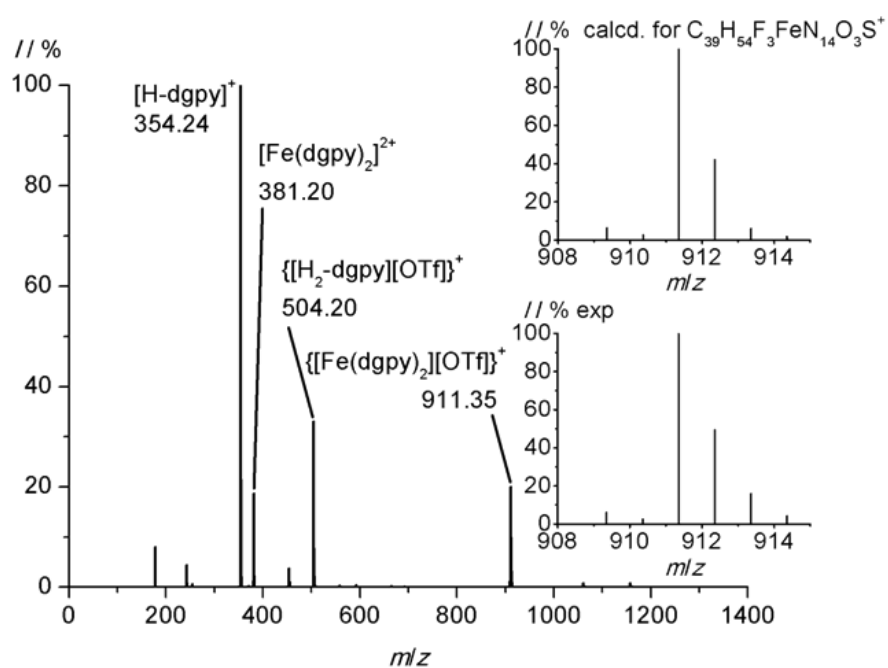


Figure S4. ESI^+ mass spectrum of $1[\text{OTf}]_2$ in dry, deaerated acetonitrile.

9. Panchromatic Absorption and Oxidation of an Iron(II) Spin Crossover Complex

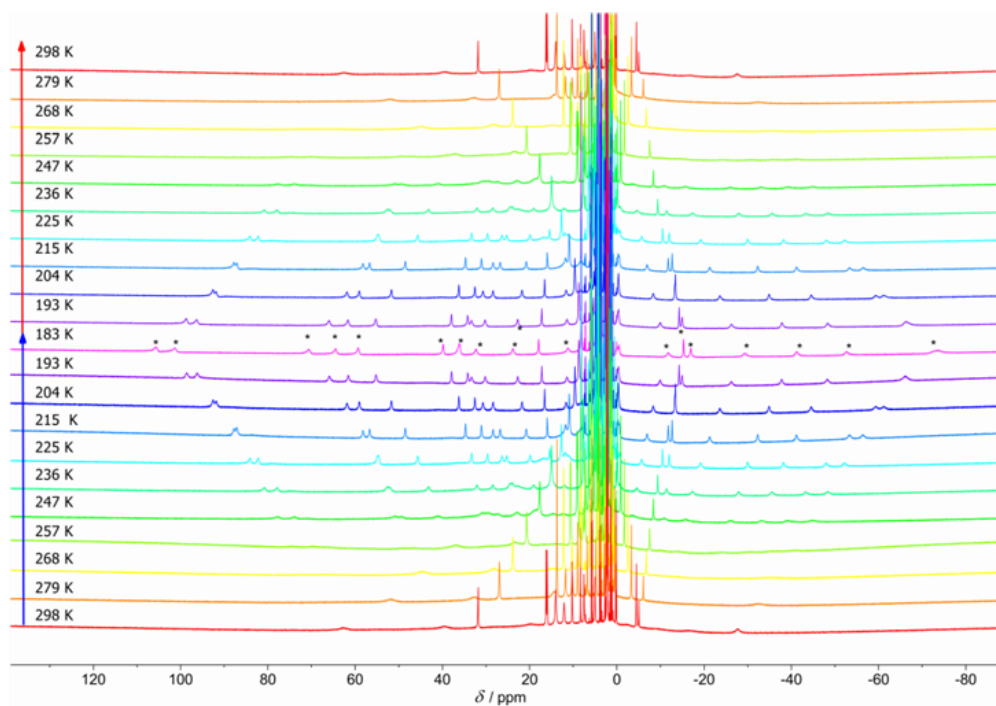


Figure S5. Variable temperature ^1H NMR spectra of $1[\text{OTf}]_2$ in d_6 -acetone (cooling and re-warming).

Resonances of the *cis-fac* isomer are marked with asterisks in the spectrum at 183 K.

Table S1. $k_{\text{hs}} / \text{s}^{-1}$ calculated from temperature dependent ^1H NMR experiments using the following equation:

$$k_{\text{hl}}(T) = \frac{\pi}{2} \left(\frac{(\delta_{\text{hs}} - \delta_{\text{ls}})^2}{\Delta(T)} \right)$$

with δ_{hs} and δ_{ls} denoting the chemical shifts of the same resonance for the high-spin and low-spin state, respectively, and $\Delta(T)$ is the line width of the respective resonance.

T / K	resonance at $\delta = 31.8 \text{ ppm}$	resonance at $\delta = 16.2 \text{ ppm}$	resonance at $\delta = 16.0 \text{ ppm}$
298	3.14×10^6	1.57×10^6	1.49×10^6
279	2.58×10^6	1.16×10^6	1.10×10^6
268	2.07×10^6		
257	1.81×10^6	8.29×10^5	7.89×10^5
247	1.52×10^6	7.54×10^5	7.17×10^5
236	1.31×10^6	7.74×10^5	7.36×10^5
225	1.49×10^6	8.29×10^5	7.89×10^5
215	1.52×10^6	9.68×10^5	9.21×10^5
204	1.69×10^6	1.16×10^6	1.10×10^6
193	2.00×10^6	1.61×10^6	1.53×10^6

9. Panchromatic Absorption and Oxidation of an Iron(II) Spin Crossover Complex

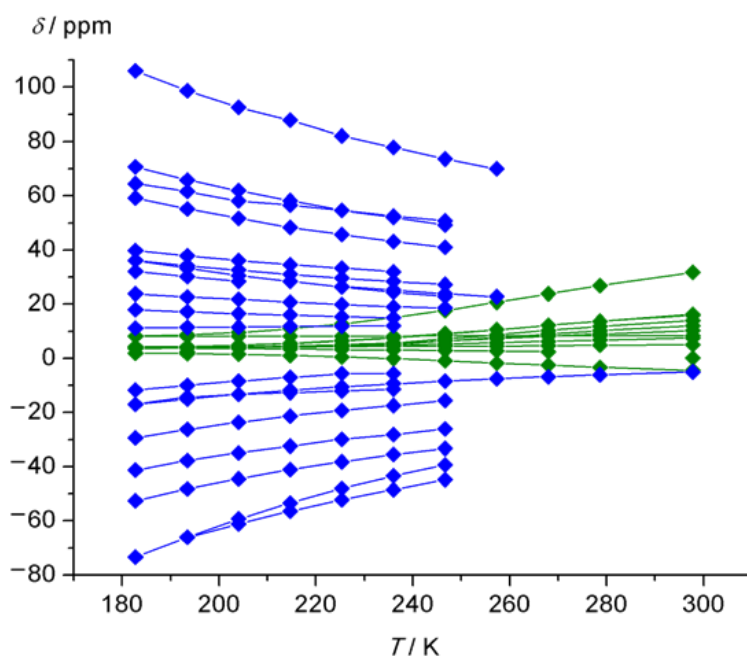


Figure S6. Chemical shifts of ^1H NMR resonances of $1[\text{OTf}]_2$ vs. temperature derived from variable temperature ^1H NMR experiments in dry, deaerated d_6 -acetone, green: *mer*- 1^{2+} , blue: *cis-fac*- 1^{2+} .

9. Panchromatic Absorption and Oxidation of an Iron(II) Spin Crossover Complex

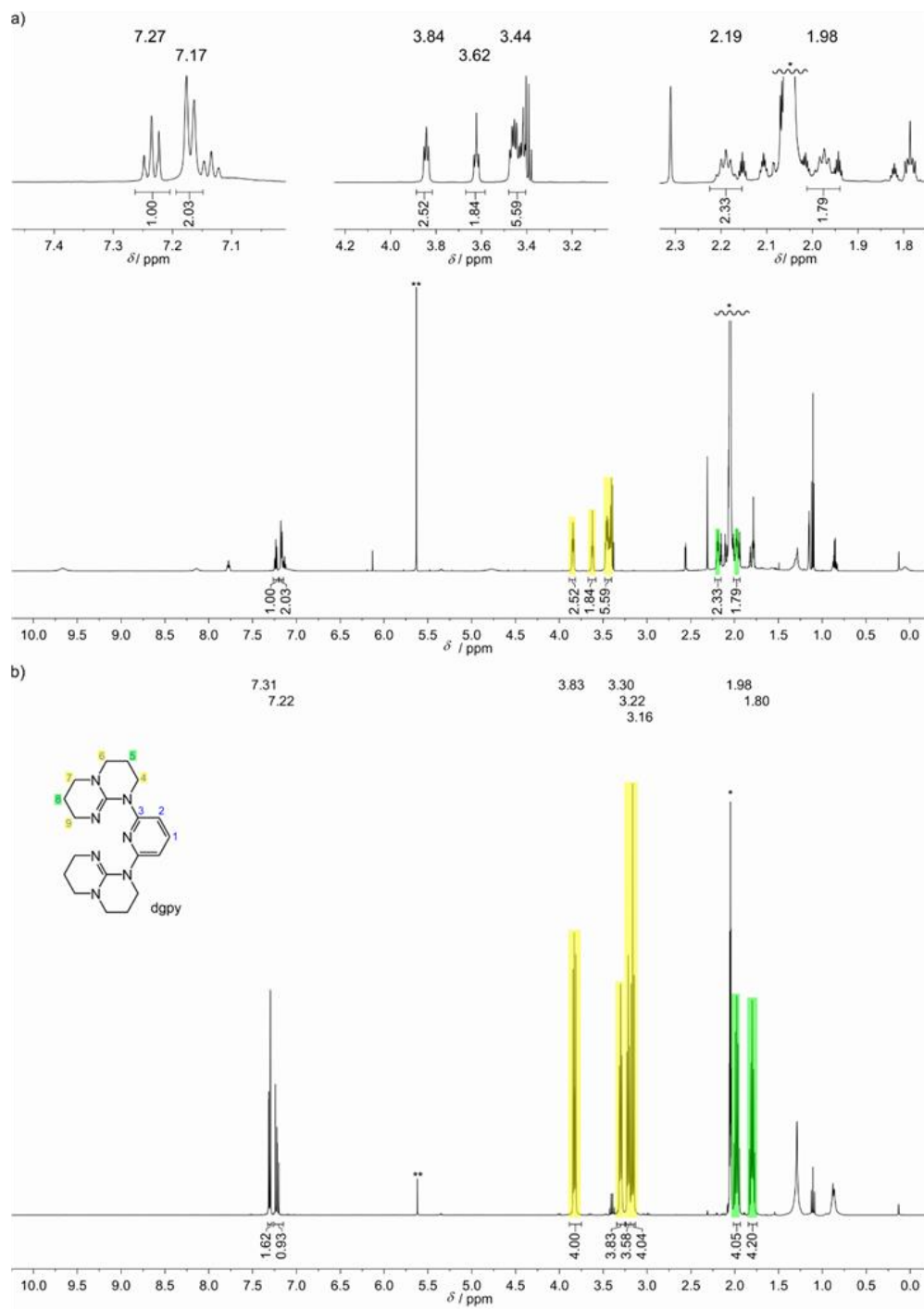


Figure S7. ^1H NMR spectra of a) $1[\text{OTf}]_2$ after 7 days in d_6 -acetone at 293 K showing resonances of the free ligand with reduced integrals for H^4 – H^9 resulting from H/D exchange and b) dgpy in in dry, deaerated d_6 -acetone at 293 K for comparison (* acetone; ** residual dichloromethane).

9. Panchromatic Absorption and Oxidation of an Iron(II) Spin Crossover Complex

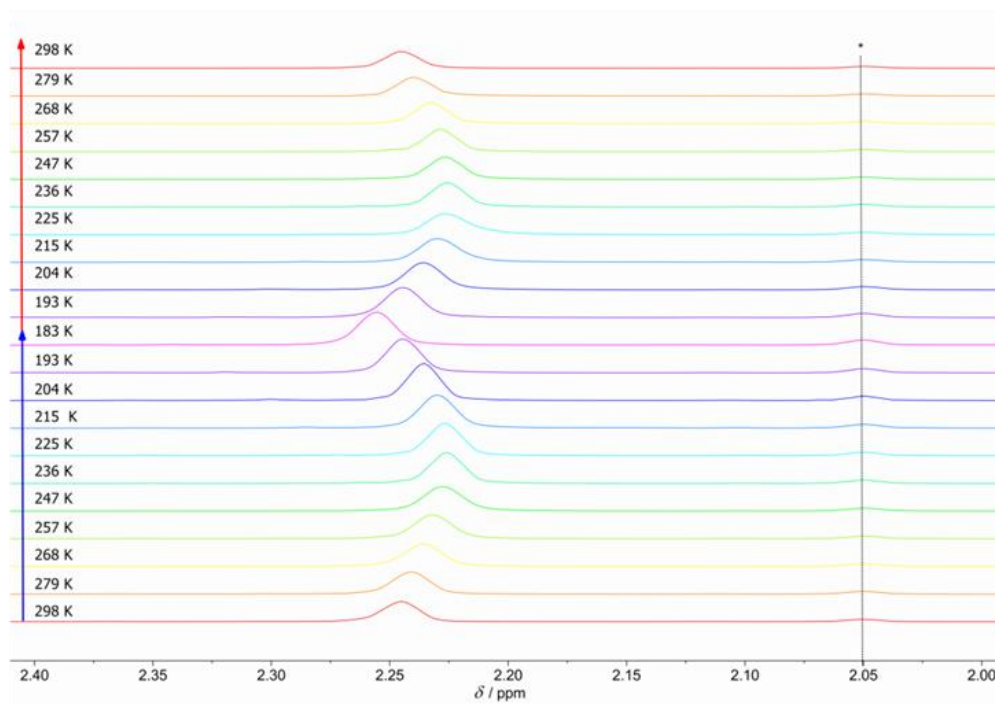


Figure S8. Excerpt of ^1H NMR spectra of $\mathbf{1}[\text{OTf}]_2$ in dry, deaerated d_6 -acetone at different temperatures showing the temperature dependent shift of the acetone resonance referenced to the acetone standard in the inside capillary (Evans' method).

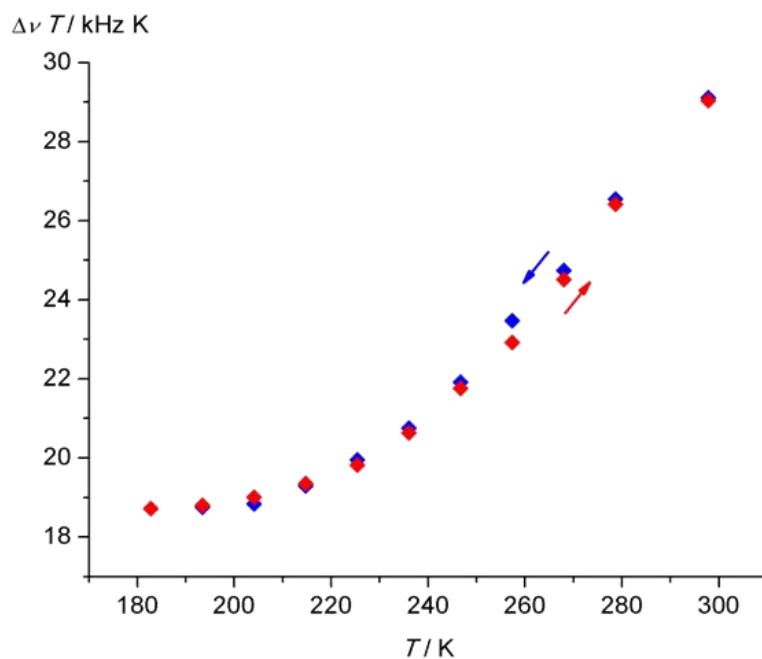


Figure S9. $\Delta\nu T$ vs. T data obtained from ^1H NMR measurements of $\mathbf{1}[\text{OTf}]_2$ using Evans' method in d_6 -acetone (blue: cooling; red: re-warming).

9. Panchromatic Absorption and Oxidation of an Iron(II) Spin Crossover Complex

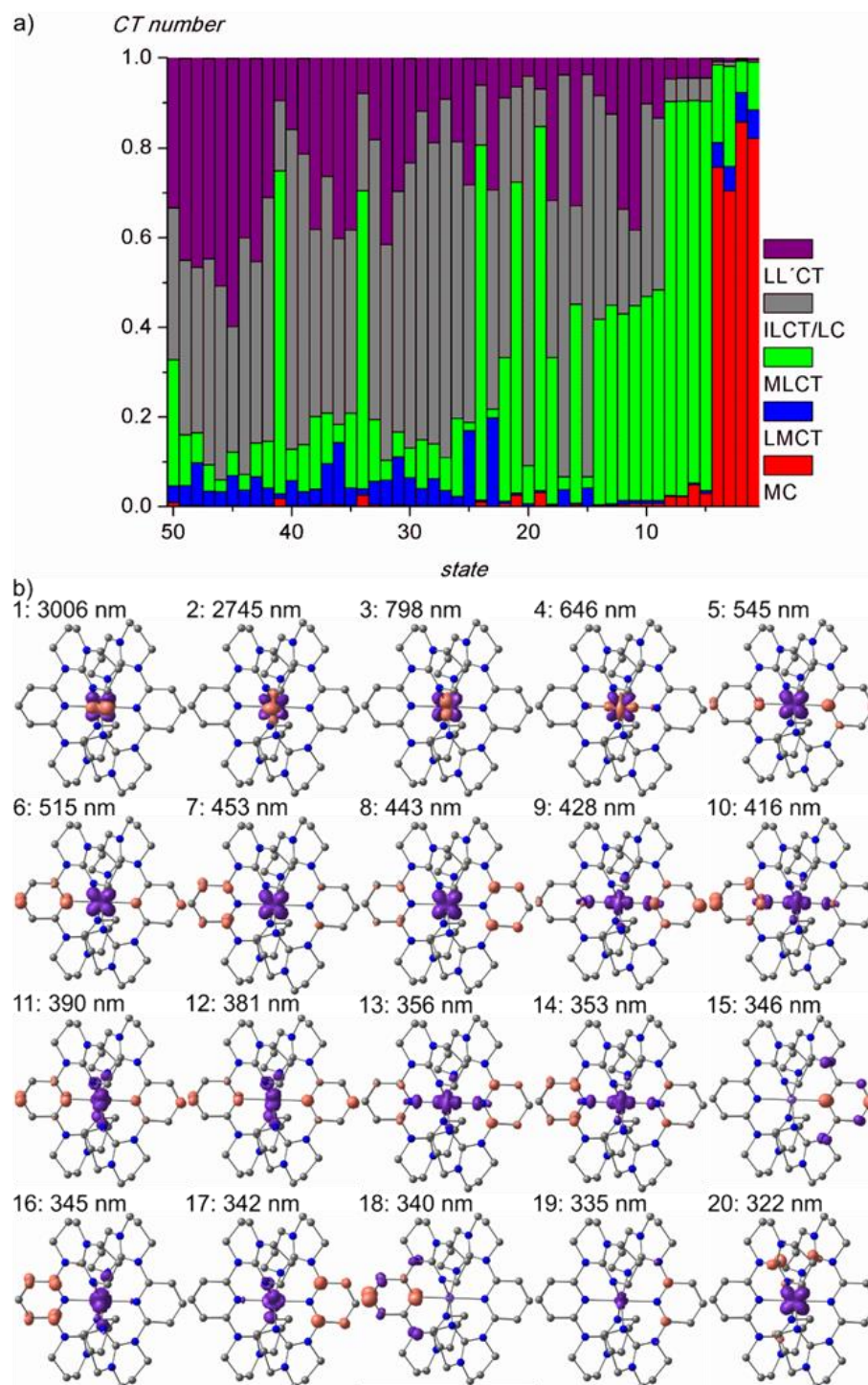


Figure S10. a) Charge transfer analysis of the 50 lowest spin-allowed transitions of high-spin *mer-1*²⁺ (red: MC, blue: LMCT, green: MLCT, gray: ILCT/LC, purple: LL'CT) and b) difference densities of the 20 lowest spin-allowed transitions of high-spin *mer-1*²⁺ with the respective wavelength (purple = electron loss; orange = electron gain). The two lowest transitions reflect the split ⁵T ground state.

9. Panchromatic Absorption and Oxidation of an Iron(II) Spin Crossover Complex

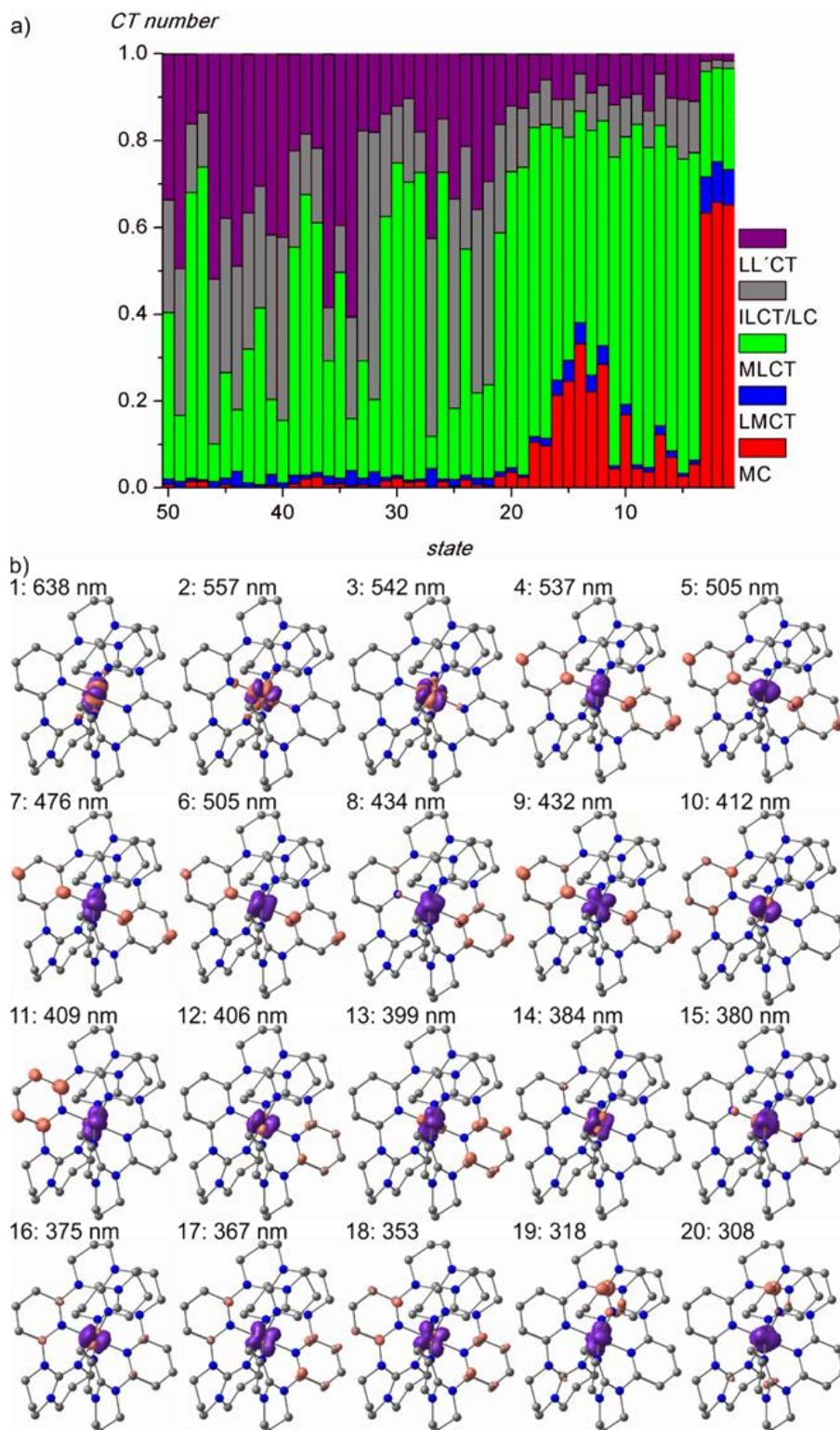


Figure S11. a) Charge transfer analysis of the 50 lowest spin-allowed transitions of low-spin *mer-1*²⁺ (red: MC, blue: LMCT, green: MLCT, gray: ILCT/LC, purple: LL'CT) and b) difference densities of the 20 lowest spin-allowed transitions of low-spin *mer-1*²⁺ with the respective wavelength (purple = electron loss; orange = electron gain).

9. Panchromatic Absorption and Oxidation of an Iron(II) Spin Crossover Complex

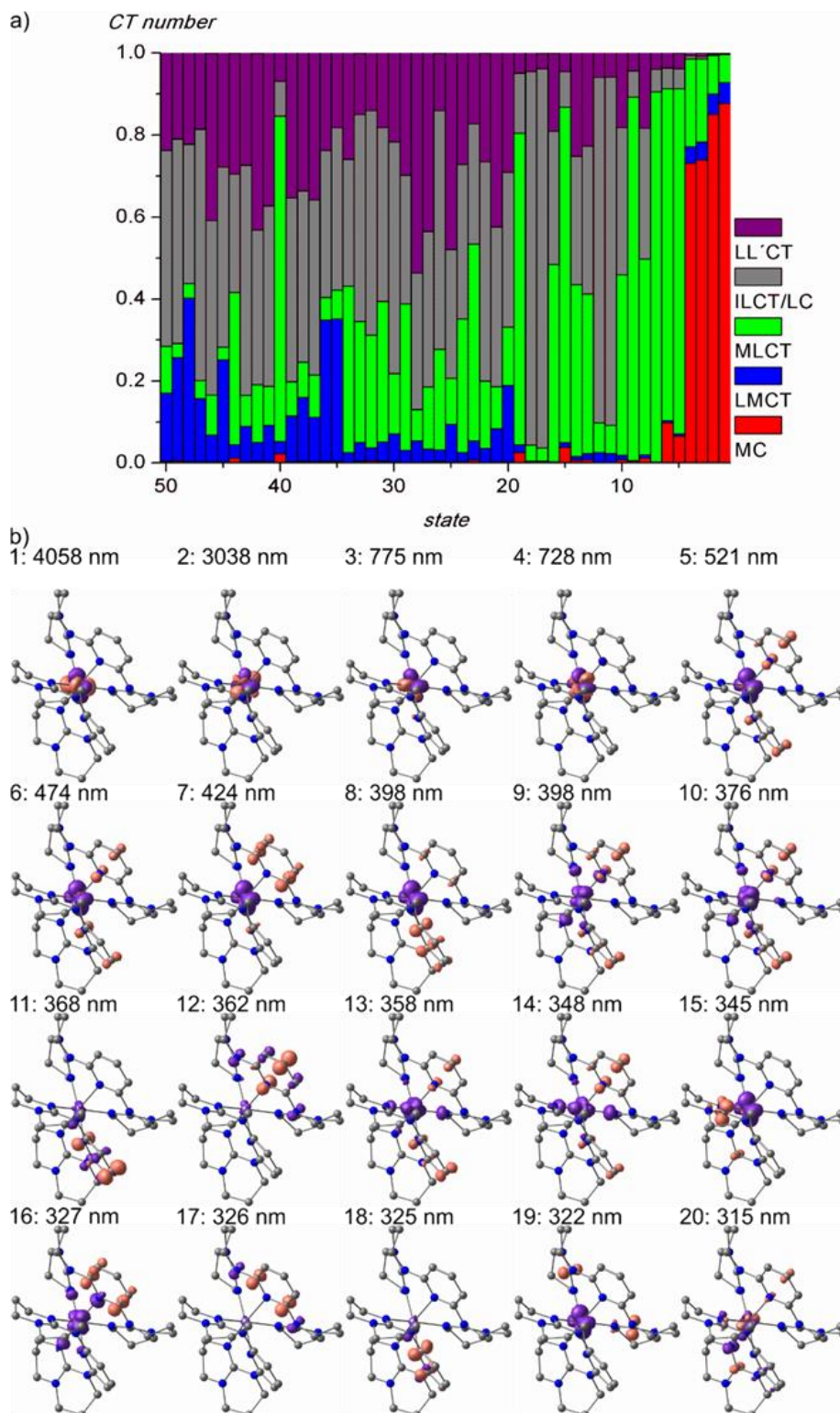


Figure S12. a) Charge transfer analysis of the 50 lowest spin-allowed transitions of high-spin *cis-fac-1*²⁺ (red: MC, blue: LMCT, green: MLCT, gray: ILCT/LC, purple: LL'CT) and b) difference densities of the 20 lowest spin-allowed transitions of high-spin *cis-fac-1*²⁺ with the respective wavelength (purple = electron loss; orange = electron gain). The two lowest transitions reflect the split ⁵T ground state.

9. Panchromatic Absorption and Oxidation of an Iron(II) Spin Crossover Complex

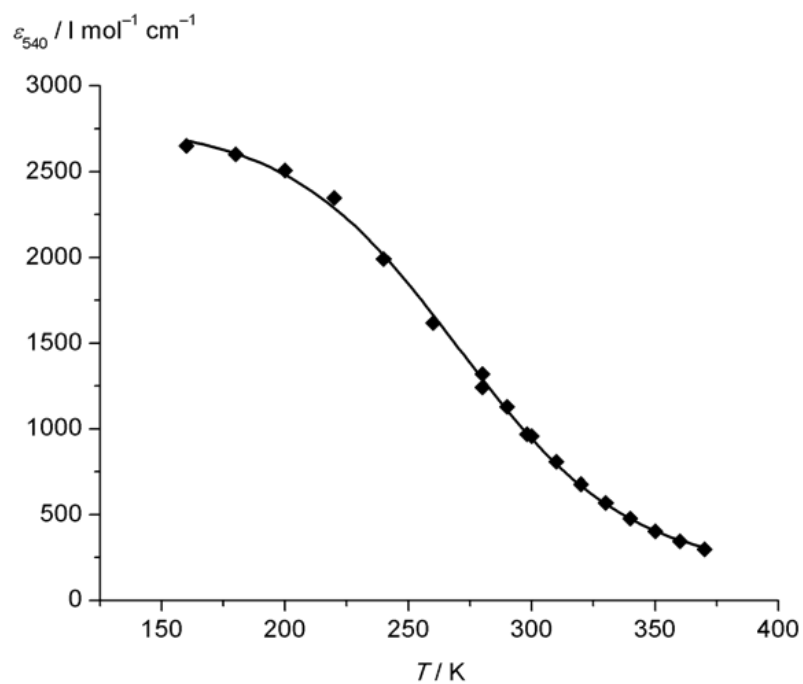


Figure S13. ϵ_{540} vs. T data obtained from optical measurements of $\mathbf{1}[\text{OTf}]_2$ in butyronitrile and according to $R \ln K = -\Delta H/T + \Delta S$ using $\Delta H = 30(1) \text{ kJ mol}^{-1}$ and $\Delta S = 107(3) \text{ J mol}^{-1} \text{ K}^{-1}$.

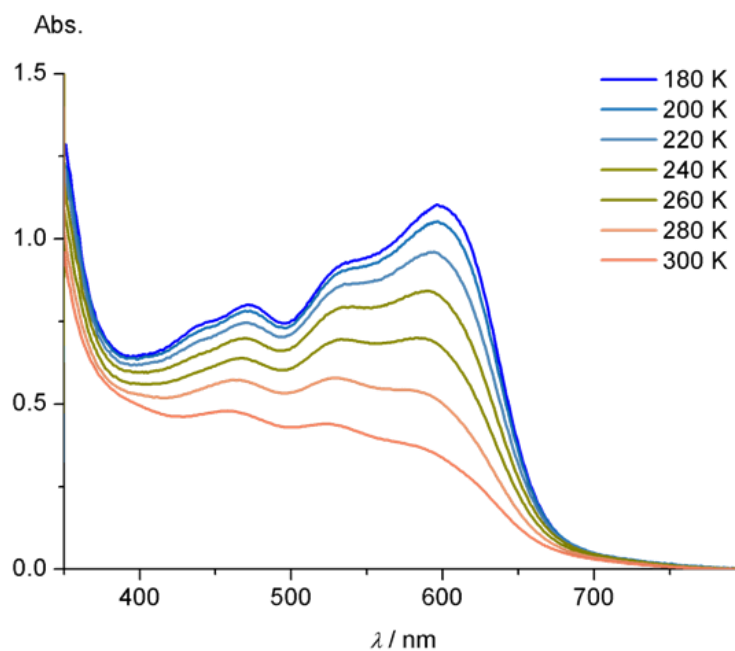


Figure S14. Variable temperature UV/Vis spectra of $\mathbf{1}[\text{OTf}]_2$ in acetone during cooling to 180 K (cryostat).

9. Panchromatic Absorption and Oxidation of an Iron(II) Spin Crossover Complex

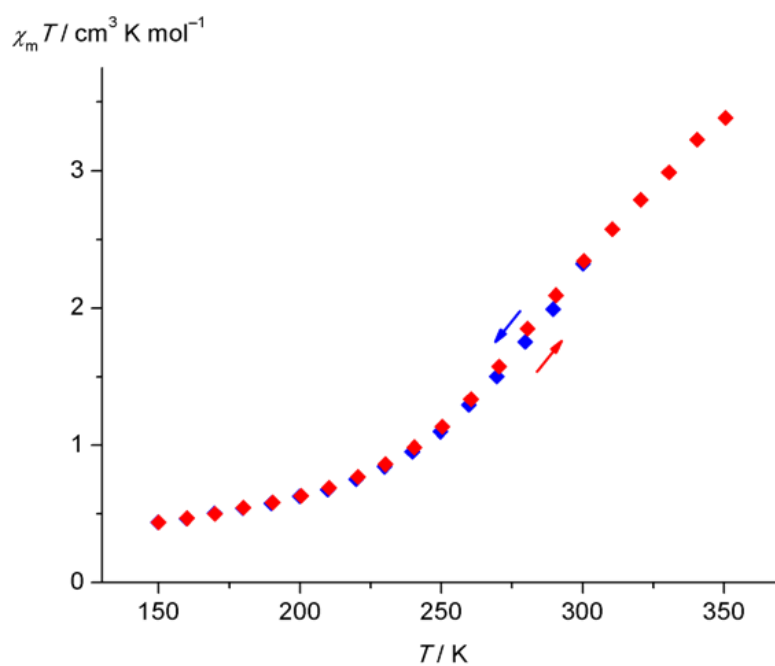


Figure S15. χT vs. T data obtained from magnetic susceptibility measurements of **1**[OTf]₂ using a SQUID magnetometer during cooling (blue) and re-warming (red).

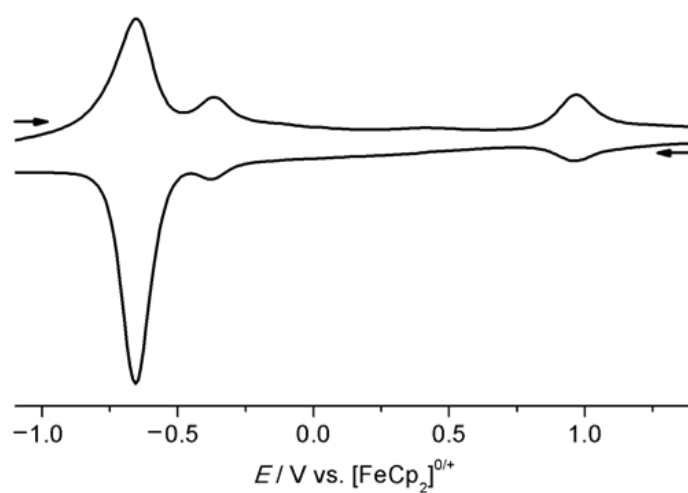


Figure S16. Square-wave voltammograms of **1**[OTf]₂, 1 mM in acetonitrile containing 0.1 M [nBu₄N][PF₆] as supporting electrolyte.

9. Panchromatic Absorption and Oxidation of an Iron(II) Spin Crossover Complex

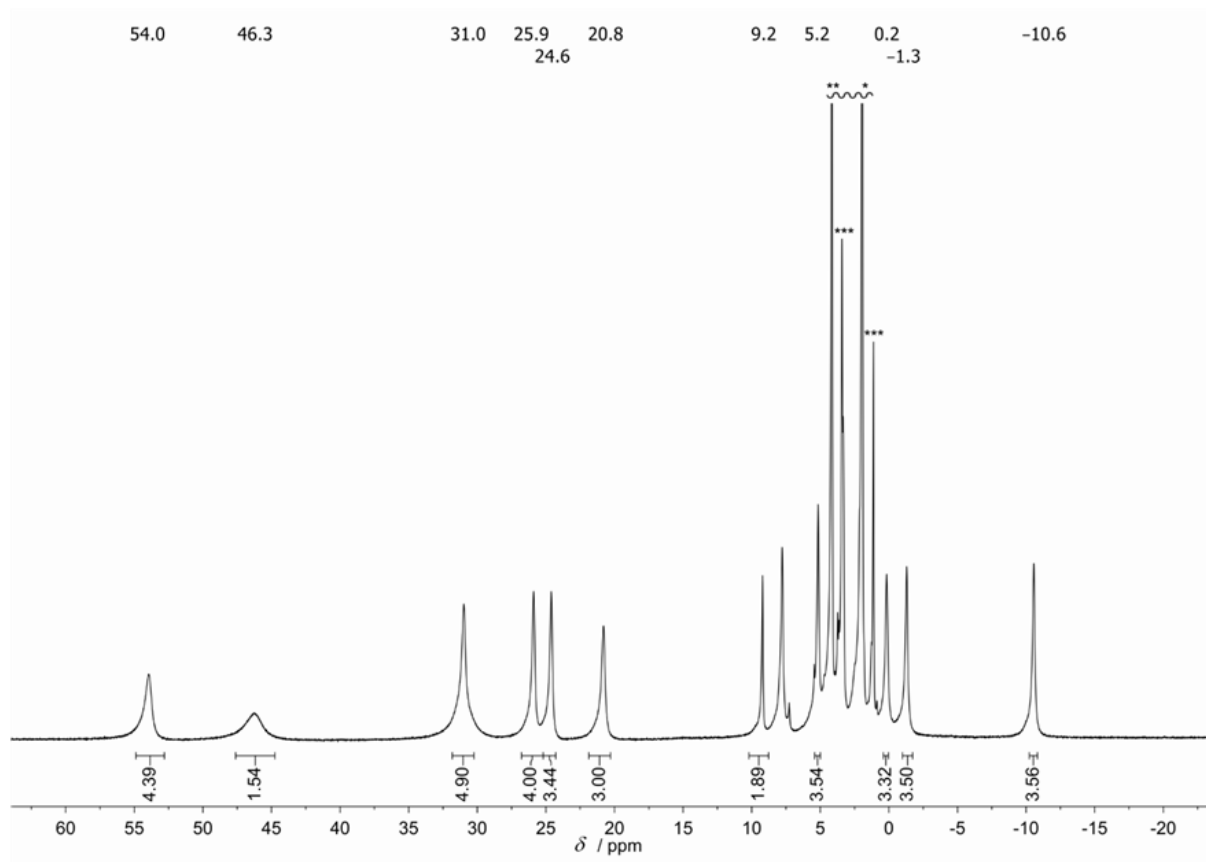


Figure S17. ^1H NMR spectrum of $1[\text{OTf}]_2$ after addition of equivalent $[\text{FeCp}_2][\text{PF}_6]$ in dry, deaerated CD_3CN at 293 K (* acetonitrile, ** ferrocene, *** unknown decomposition products).

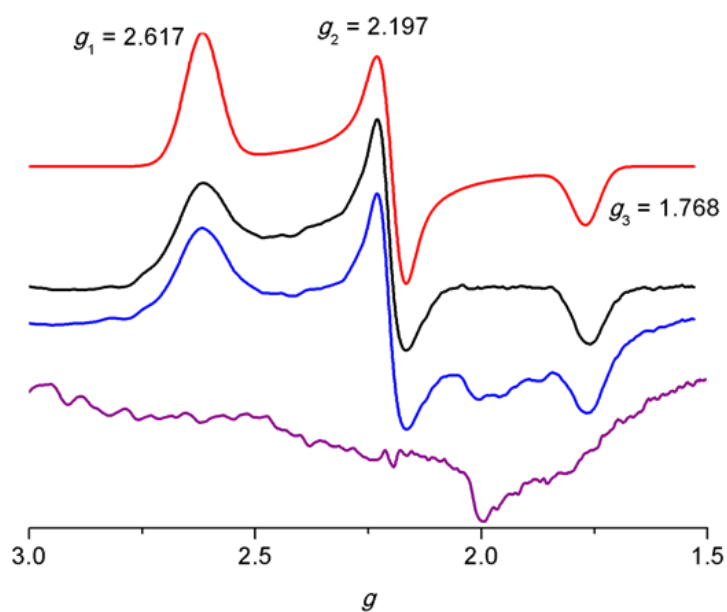


Figure S18. X-band EPR spectrum of $1[\text{OTf}]_2$ with 1 eq of $[\text{FeCp}_2][\text{PF}_6]$ added in butyronitrile at 77 K before (blue) and after baseline (purple) correction (black) and simulated spectrum (red).

9. Panchromatic Absorption and Oxidation of an Iron(II) Spin Crossover Complex

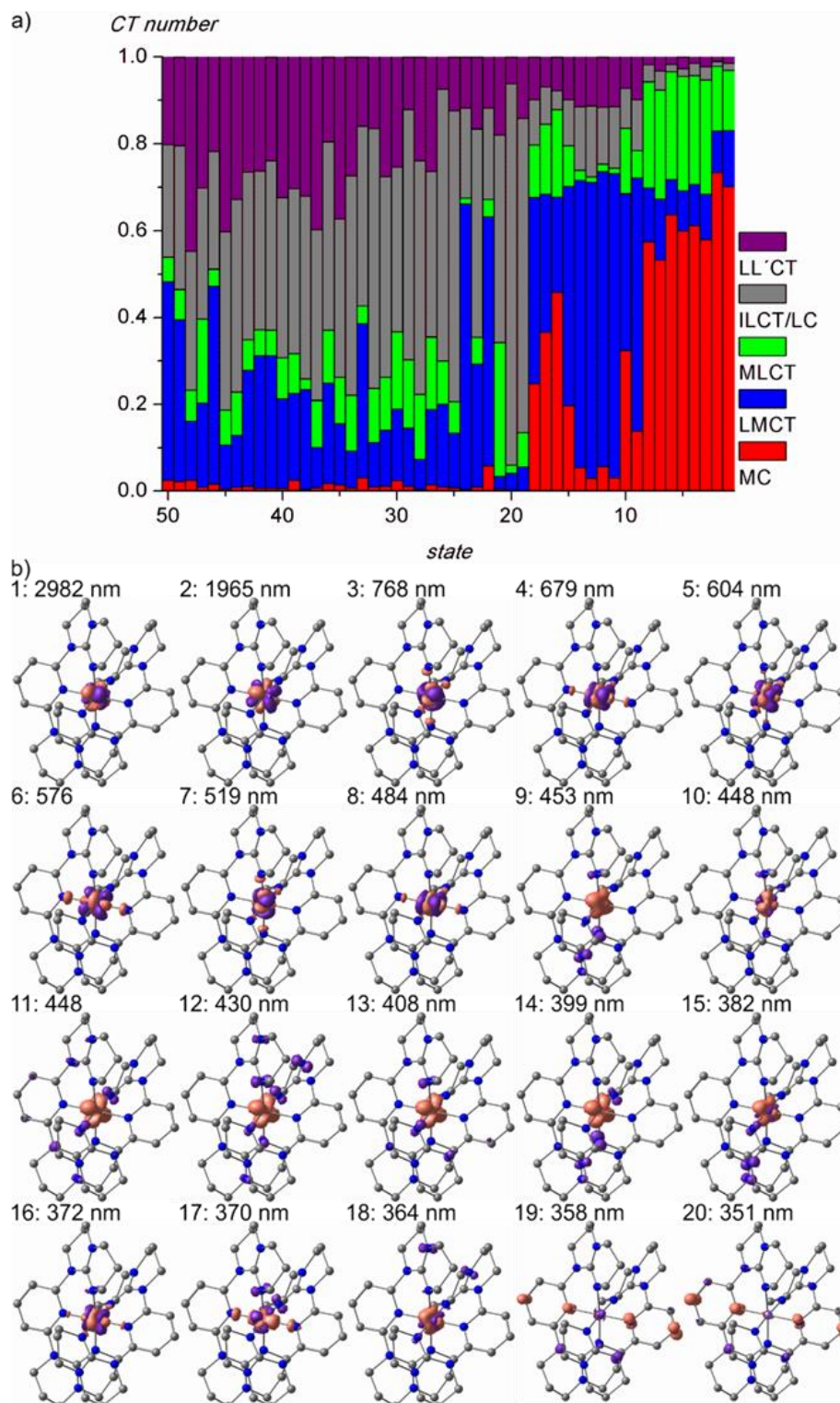


Figure S19. a) Charge transfer analysis of the 50 lowest spin-allowed transitions of low-spin *mer-1*³⁺ (red: MC, blue: LMCT, green: MLCT, gray: ILCT/LC, purple: LL'CT) and b) difference densities of the 20 lowest spin-allowed transitions of low-spin *mer-1*³⁺ with the respective wavelength (purple = electron loss; orange = electron gain). The two lowest transitions reflect the split ²T ground state.

9. Panchromatic Absorption and Oxidation of an Iron(II) Spin Crossover Complex

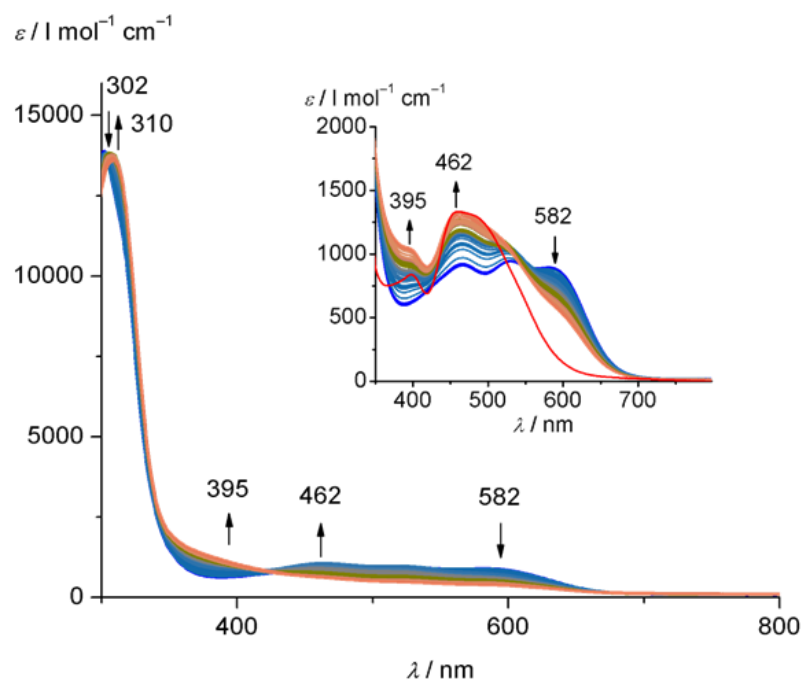


Figure S20. UV/Vis spectra of **1**[OTf]₂ during electrochemical oxidation in acetonitrile containing 0.1 M [^tBu₄N][PF₆] at 300 K.

9. Panchromatic Absorption and Oxidation of an Iron(II) Spin Crossover Complex

Cartesian coordinates of DFT optimized geometries (atomic number, x, y, z coordinates)

*mer-1*²⁺, low-spin

6	1.697611000	-2.801685000	0.111101000
6	1.822343000	-4.191657000	0.132690000
6	0.746398000	-4.956896000	0.528903000
6	-0.438637000	-4.335937000	0.865622000
6	-0.525854000	-2.945712000	0.791052000
7	0.534203000	-2.187877000	0.428475000
1	2.736640000	-4.670318000	-0.169633000
1	-1.272376000	-4.927071000	1.198893000
6	1.635715000	0.798382000	-2.164863000
6	2.341055000	0.350751000	-3.430711000
6	3.790134000	0.082471000	-3.083933000
7	3.883384000	-0.732131000	-1.871388000
6	2.787313000	-0.950419000	-1.084020000
7	1.717001000	-0.222297000	-1.122965000
1	4.299199000	-0.464902000	-3.882422000
1	2.089914000	1.729380000	-1.812680000
1	2.276081000	1.116564000	-4.203735000
6	-1.894681000	-1.228199000	1.893628000
7	-3.044793000	-1.108063000	2.625468000
6	-3.097448000	-0.183737000	3.754976000
6	-2.264100000	1.044560000	3.468767000
6	-0.886409000	0.612157000	3.008826000
7	-0.918049000	-0.375720000	1.927359000
1	-2.739741000	-0.689636000	4.658590000
1	-0.337083000	0.185552000	3.854037000
6	1.342435000	2.530491000	0.554663000
6	1.270574000	3.924607000	0.518990000
6	0.065022000	4.529038000	0.231436000
6	-1.046266000	3.745909000	0.003413000
6	-0.931579000	2.356996000	0.081005000
7	0.253587000	1.754858000	0.340531000
1	2.132459000	4.530176000	0.733561000
1	-1.980126000	4.211989000	-0.253412000
6	2.014117000	-1.039820000	2.803172000
6	2.671247000	-0.442107000	4.034560000
6	4.037895000	0.062911000	3.623917000
7	3.938646000	0.841231000	2.387812000
6	2.778248000	0.867014000	1.661651000
7	1.850501000	-0.029692000	1.760325000
1	4.474681000	0.713317000	4.387442000
1	2.629934000	-1.865082000	2.431825000
1	2.766920000	-1.183757000	4.827258000
6	-2.124543000	0.453080000	-0.907843000
7	-3.279238000	0.205395000	-1.597774000
6	-3.281629000	-0.686428000	-2.757227000
6	-1.865448000	-0.965129000	-3.212893000
6	-1.053142000	-1.347227000	-1.992298000
7	-1.062209000	-0.281284000	-0.993287000
1	-3.868388000	-0.199148000	-3.540561000
1	-1.861092000	-1.768481000	-3.949648000
1	-0.016263000	-1.548837000	-2.249907000
7	2.839267000	-2.048346000	-0.213191000
7	-1.776697000	-2.350004000	1.058914000

9. Panchromatic Absorption and Oxidation of an Iron(II) Spin Crossover Complex

6	-2.941753000	-3.218603000	0.808136000
1	-2.949212000	-4.067048000	1.495778000
1	-2.851332000	-3.608896000	-0.204809000
1	0.830436000	-6.034760000	0.572226000
1	-0.008339000	5.607467000	0.182869000
26	0.393354000	-0.221002000	0.391576000
7	-2.102687000	1.594944000	-0.091789000
7	2.603366000	1.948208000	0.782466000
6	3.758908000	2.812168000	0.486076000
6	-3.366394000	2.319014000	0.125010000
1	-3.542218000	3.048274000	-0.671405000
1	-3.279714000	2.863251000	1.062424000
6	5.225811000	-1.208036000	-1.557261000
6	5.265078000	-1.748288000	-0.147020000
6	4.128417000	-2.729067000	-0.004121000
1	4.107638000	-3.173098000	0.989462000
1	5.165444000	-0.946791000	0.586288000
1	5.526030000	-1.982956000	-2.270959000
1	5.914525000	-0.367876000	-1.682195000
6	-4.224585000	-1.940585000	2.423125000
6	-4.229426000	-2.461472000	1.006362000
1	-5.070148000	-3.135098000	0.843928000
1	-4.312692000	-1.636941000	0.296680000
1	-4.249477000	-2.774109000	3.135236000
1	-5.095568000	-1.314751000	2.621485000
1	-4.141193000	0.082842000	3.918602000
1	4.331132000	1.023435000	-2.934067000
1	1.868077000	-0.556037000	-3.816485000
1	0.583621000	1.005837000	-2.344513000
1	4.271818000	-3.532037000	-0.732919000
1	6.210574000	-2.257198000	0.037437000
1	-0.310633000	1.466294000	2.669514000
1	-2.188323000	1.659460000	4.366321000
1	-2.749672000	1.642375000	2.697405000
1	1.033720000	-1.448644000	3.030539000
1	2.059938000	0.381078000	4.412988000
1	4.728404000	-0.773440000	3.472081000
6	5.041756000	2.022545000	0.571423000
6	5.168627000	1.515074000	1.988980000
1	5.988297000	0.796882000	2.085312000
1	5.882454000	2.668812000	0.321797000
1	5.029673000	1.198162000	-0.142700000
1	3.822866000	3.643342000	1.194712000
1	3.609954000	3.226389000	-0.509734000
1	5.380706000	2.345290000	2.671373000
6	-4.524806000	1.353200000	0.148295000
6	-4.595765000	0.700936000	-1.212328000
1	-5.446757000	1.894245000	0.358292000
1	-4.384318000	0.608130000	0.933393000
1	-5.286946000	-0.147204000	-1.213729000
1	-4.957113000	1.415900000	-1.958878000
1	-3.790635000	-1.621613000	-2.497331000
1	-1.433188000	-0.076074000	-3.679770000
1	-1.459939000	-2.266551000	-1.562760000

9. Panchromatic Absorption and Oxidation of an Iron(II) Spin Crossover Complex

*mer-1*²⁺, high-spin

6	1.744217000	-2.972882000	0.201627000
6	1.903949000	-4.358592000	0.305076000
6	0.830056000	-5.123626000	0.712963000
6	-0.383340000	-4.519815000	0.985187000
6	-0.489080000	-3.138724000	0.833421000
7	0.561106000	-2.389211000	0.458618000
1	2.835380000	-4.836293000	0.056806000
1	-1.217325000	-5.111656000	1.321380000
6	1.740973000	0.588986000	-2.226578000
6	2.496643000	0.121767000	-3.455829000
6	3.927384000	-0.148852000	-3.039045000
7	3.976537000	-0.887164000	-1.771279000
6	2.839018000	-1.130476000	-1.052862000
7	1.752777000	-0.437204000	-1.190575000
1	4.454650000	-0.750884000	-3.784912000
1	2.199895000	1.507988000	-1.845529000
1	2.474724000	0.873268000	-4.245226000
6	-1.942138000	-1.449553000	1.892242000
7	-3.188355000	-1.259166000	2.416047000
6	-3.364725000	-0.345636000	3.546073000
6	-2.407645000	0.823126000	3.452045000
6	-1.006546000	0.290471000	3.229196000
7	-0.925823000	-0.677747000	2.138599000
1	-3.212761000	-0.895251000	4.481442000
1	-0.648819000	-0.189091000	4.147748000
6	1.299993000	2.697387000	0.603028000
6	1.230396000	4.091736000	0.613181000
6	0.012622000	4.696433000	0.374397000
6	-1.104961000	3.921597000	0.141355000
6	-0.981274000	2.529061000	0.169345000
7	0.207705000	1.938376000	0.395485000
1	2.097504000	4.694175000	0.819363000
1	-2.042178000	4.399073000	-0.081245000
6	2.182364000	-0.825617000	2.924995000
6	3.019878000	-0.251715000	4.053500000
6	4.317624000	0.242127000	3.450119000
7	4.075640000	0.976255000	2.203221000
6	2.825097000	1.048678000	1.656868000
7	1.883490000	0.199707000	1.930427000
1	4.843911000	0.918114000	4.130305000
1	2.731500000	-1.650395000	2.456932000
1	3.232070000	-1.003054000	4.814143000
6	-2.208903000	0.640278000	-0.871009000
7	-3.396670000	0.393695000	-1.502226000
6	-3.446319000	-0.407790000	-2.730248000
6	-2.052566000	-0.734962000	-3.223582000
6	-1.229683000	-1.163794000	-2.025030000
7	-1.153481000	-0.091036000	-1.039899000
1	-4.008704000	0.169219000	-3.470226000
1	-2.100211000	-1.523799000	-3.974430000
1	-0.212737000	-1.430496000	-2.304938000
7	2.873187000	-2.198773000	-0.139199000
7	-1.758491000	-2.540304000	1.030984000
6	-2.898263000	-3.413011000	0.692891000
1	-3.004828000	-4.217927000	1.425358000

9. Panchromatic Absorption and Oxidation of an Iron(II) Spin Crossover Complex

1	-2.687473000	-3.865443000	-0.274567000
1	0.939210000	-6.195288000	0.817038000
1	-0.065842000	5.775794000	0.365240000
26	0.375977000	-0.229765000	0.456941000
7	-2.152428000	1.760474000	-0.019586000
7	2.573891000	2.104975000	0.765105000
6	3.704785000	2.951256000	0.336812000
6	-3.412050000	2.476824000	0.260014000
1	-3.612851000	3.227615000	-0.509297000
1	-3.291732000	2.993722000	1.209256000
6	5.308929000	-1.341452000	-1.392475000
6	5.289234000	-1.825524000	0.036598000
6	4.172184000	-2.831400000	0.158133000
1	4.114117000	-3.236126000	1.166673000
1	5.124786000	-0.992923000	0.721392000
1	5.641570000	-2.139602000	-2.065124000
1	5.995477000	-0.500698000	-1.520295000
6	-4.371374000	-2.028726000	2.043926000
6	-4.181694000	-2.622090000	0.668983000
1	-5.010530000	-3.284761000	0.421771000
1	-4.136016000	-1.833927000	-0.084215000
1	-4.565735000	-2.817470000	2.779340000
1	-5.222524000	-1.346144000	2.066137000
1	-4.399448000	-0.003060000	3.532862000
1	4.479089000	0.789688000	-2.927213000
1	2.032658000	-0.787964000	-3.844424000
1	0.702513000	0.823880000	-2.450319000
1	4.370074000	-3.657549000	-0.530066000
1	6.236251000	-2.298175000	0.294586000
1	-0.312804000	1.098624000	3.006867000
1	-2.455744000	1.415564000	4.366678000
1	-2.694625000	1.464738000	2.620675000
1	1.239348000	-1.234244000	3.278157000
1	2.480023000	0.570548000	4.529242000
1	4.987931000	-0.597740000	3.242724000
6	4.973024000	2.135782000	0.269784000
6	5.256911000	1.644292000	1.668544000
1	6.080153000	0.925276000	1.684145000
1	5.790846000	2.757779000	-0.091751000
1	4.850244000	1.298422000	-0.418290000
1	3.863009000	3.778771000	1.034551000
1	3.446645000	3.370908000	-0.633522000
1	5.543120000	2.479173000	2.317334000
6	-4.570516000	1.511870000	0.302224000
6	-4.694552000	0.896832000	-1.069771000
1	-5.482250000	2.046083000	0.567086000
1	-4.396930000	0.741103000	1.053470000
1	-5.396953000	0.058528000	-1.073493000
1	-5.064872000	1.635812000	-1.788194000
1	-4.010116000	-1.325363000	-2.533908000
1	-1.593510000	0.142588000	-3.685433000
1	-1.679371000	-2.053894000	-1.573555000

9. Panchromatic Absorption and Oxidation of an Iron(II) Spin Crossover Complex

cis-fac-1²⁺, low-spin

26	4.375608000	2.957099000	12.369363000
7	5.950385000	2.226160000	13.471914000
7	6.887734000	0.474884000	14.758019000
7	4.702536000	0.309116000	13.928725000
7	3.251122000	2.154832000	13.850053000
7	2.017883000	4.154014000	14.025908000
7	2.912867000	6.205168000	14.684705000
7	4.239294000	4.668317000	13.481060000
7	2.691682000	3.436039000	11.283808000
7	0.653598000	2.667715000	10.314655000
7	2.054516000	1.182511000	11.379269000
7	4.380884000	1.275197000	11.219627000
7	6.632306000	1.602772000	10.645534000
7	7.350257000	3.394665000	9.356812000
7	5.593703000	3.696931000	10.906776000
6	7.184139000	2.991453000	13.643296000
1	7.281237000	3.644459000	12.782503000
1	7.099958000	3.627842000	14.528751000
6	8.410289000	2.107876000	13.773551000
1	9.294440000	2.714618000	13.971147000
1	8.578450000	1.557377000	12.847919000
6	8.190119000	1.125807000	14.898565000
1	8.238183000	1.627476000	15.870673000
1	8.953348000	0.345311000	14.894175000
6	5.886951000	1.063388000	14.042350000
6	6.832322000	-0.833505000	15.420496000
1	7.532252000	-1.491550000	14.892865000
6	5.452343000	-1.454905000	15.405734000
1	5.532095000	-2.528000000	15.581110000
1	4.822087000	-1.028316000	16.187845000
6	4.860808000	-1.141714000	14.045370000
1	3.904427000	-1.616694000	13.859908000
1	5.535461000	-1.466727000	13.251813000
6	3.474913000	0.884157000	14.247930000
6	2.508649000	0.147929000	14.935125000
1	2.683668000	-0.870394000	15.233905000
6	1.326815000	0.773943000	15.278235000
1	0.563729000	0.229682000	15.818599000
6	1.147285000	2.113891000	14.996519000
1	0.264642000	2.615961000	15.349982000
6	2.148681000	2.791176000	14.296275000
6	0.722066000	4.794291000	14.271195000
1	0.582656000	5.571093000	13.519641000
1	-0.068450000	4.068706000	14.126122000
6	0.754675000	5.424456000	15.648228000
1	1.033215000	4.674113000	16.389978000
6	1.785939000	6.532734000	15.565726000
1	2.184324000	6.793544000	16.549676000
1	1.318042000	7.431142000	15.152300000
6	3.126126000	5.013648000	14.059171000
6	3.871771000	7.306454000	14.599122000
1	3.311299000	8.218276000	14.380295000
1	4.340349000	7.435209000	15.579995000
6	4.918802000	7.037059000	13.546385000
1	4.503967000	7.214223000	12.550976000

9. Panchromatic Absorption and Oxidation of an Iron(II) Spin Crossover Complex

1	5.762189000	7.713978000	13.683846000
6	5.360137000	5.589409000	13.678020000
1	5.797947000	5.436673000	14.670287000
1	6.128079000	5.349360000	12.954517000
6	2.399911000	4.794062000	10.805445000
1	2.828265000	5.488968000	11.521731000
1	2.908774000	4.959753000	9.854458000
6	0.915275000	5.062803000	10.627311000
1	0.766039000	6.035712000	10.157152000
1	0.411310000	5.081091000	11.591972000
6	1.843523000	2.512697000	10.979792000
6	-0.025648000	0.268835000	10.407693000
1	0.272297000	-0.609842000	9.834859000
6	0.828329000	0.430120000	11.661811000
1	1.095500000	-0.518440000	12.115860000
1	0.281382000	1.003300000	12.409417000
6	3.254642000	0.540213000	11.124270000
6	3.279327000	-0.814623000	10.791078000
1	2.372293000	-1.391958000	10.723533000
6	4.502642000	-1.387232000	10.501635000
1	4.560631000	-2.436123000	10.242828000
6	5.645640000	-0.608400000	10.460807000
1	6.574335000	-1.047563000	10.142822000
6	5.541087000	0.748804000	10.777570000
6	7.940637000	1.047530000	10.277976000
1	8.705915000	1.681923000	10.724185000
1	8.051229000	0.058289000	10.706361000
6	8.055376000	1.070825000	8.767075000
1	8.998043000	0.639531000	8.430819000
1	7.246741000	0.478537000	8.337695000
6	7.955559000	2.532872000	8.331505000
1	7.385745000	2.633822000	7.403120000
1	8.952705000	2.935738000	8.148559000
6	6.470662000	2.955485000	10.301589000
6	7.559074000	4.820449000	9.107774000
1	8.636236000	4.999974000	9.062141000
1	7.144493000	5.072157000	8.126407000
6	6.894007000	5.652959000	10.180936000
1	7.470901000	5.621942000	11.107425000
1	6.836225000	6.692128000	9.855697000
6	5.508024000	5.075279000	10.415958000
1	4.947467000	5.109950000	9.477110000
1	4.952690000	5.654985000	11.140597000
6	0.150430000	1.521393000	9.538979000
6	0.316342000	3.976740000	9.763130000
1	-1.065768000	0.131018000	10.705141000
1	-0.795357000	1.830710000	9.099873000
1	0.841564000	1.317716000	8.714419000
1	-0.770654000	4.053862000	9.715991000
1	0.702507000	4.052693000	8.739255000
1	-0.210796000	5.842973000	15.932033000
1	7.203848000	-0.711899000	16.440376000

9. Panchromatic Absorption and Oxidation of an Iron(II) Spin Crossover Complex

cis-fac-1²⁺, high-spin

26	4.452861000	3.089533000	12.386462000
7	5.970892000	2.166675000	13.599507000
7	6.813358000	0.321116000	14.794507000
7	4.597291000	0.326417000	14.022758000
7	3.237507000	2.244448000	14.068150000
7	2.038667000	4.274290000	14.164467000
7	2.918695000	6.326000000	14.852181000
7	4.253028000	4.837514000	13.612724000
7	2.626997000	3.411287000	11.250659000
7	0.669006000	2.526556000	10.251975000
7	2.150006000	1.112762000	11.311711000
7	4.453456000	1.289947000	10.999045000
7	6.714385000	1.680786000	10.517367000
7	7.344881000	3.443665000	9.134701000
7	5.732178000	3.803259000	10.811871000
6	7.237385000	2.867426000	13.790088000
1	7.340050000	3.587018000	12.979543000
1	7.207850000	3.435250000	14.726505000
6	8.411589000	1.906293000	13.802909000
1	9.343716000	2.434783000	14.005646000
1	8.500686000	1.423954000	12.829346000
6	8.177195000	0.855366000	14.864782000
1	8.341609000	1.269652000	15.864835000
1	8.865357000	0.017139000	14.739330000
6	5.833777000	0.994309000	14.134516000
6	6.676418000	-0.976145000	15.468414000
1	7.332962000	-1.678074000	14.943287000
6	5.257857000	-1.508306000	15.453343000
1	5.269744000	-2.586786000	15.612555000
1	4.658045000	-1.056035000	16.244730000
6	4.680980000	-1.134637000	14.101610000
1	3.704079000	-1.559067000	13.905456000
1	5.338099000	-1.471942000	13.298804000
6	3.390101000	0.947039000	14.371157000
6	2.370790000	0.218156000	14.990096000
1	2.482361000	-0.820050000	15.248619000
6	1.205819000	0.885217000	15.319157000
1	0.405980000	0.351476000	15.815743000
6	1.071105000	2.237871000	15.068397000
1	0.182141000	2.748813000	15.392713000
6	2.130611000	2.902323000	14.440040000
6	0.738489000	4.929055000	14.346417000
1	0.642164000	5.701056000	13.581737000
1	-0.052428000	4.210902000	14.172123000
6	0.712121000	5.564164000	15.721629000
1	0.942582000	4.810469000	16.476228000
6	1.761471000	6.659228000	15.691267000
1	2.123618000	6.907153000	16.692198000
1	1.322146000	7.566630000	15.266847000
6	3.139749000	5.148849000	14.208771000
6	3.877765000	7.431510000	14.780650000
1	3.310991000	8.345972000	14.593465000
1	4.357974000	7.536466000	15.758405000
6	4.914076000	7.200727000	13.704790000
1	4.479549000	7.388194000	12.719238000

9. Panchromatic Absorption and Oxidation of an Iron(II) Spin Crossover Complex

1	5.746195000	7.891082000	13.844999000
6	5.374464000	5.756367000	13.795362000
1	5.847257000	5.581012000	14.768716000
1	6.121484000	5.530372000	13.039107000
6	2.280171000	4.752137000	10.771657000
1	2.686420000	5.468888000	11.482515000
1	2.776559000	4.936338000	9.815073000
6	0.780234000	4.938713000	10.614889000
1	0.560768000	5.903301000	10.155219000
1	0.297487000	4.919471000	11.592133000
6	1.853706000	2.433510000	10.922495000
6	0.106642000	0.096770000	10.371899000
1	0.460248000	-0.761691000	9.800167000
6	0.958964000	0.313375000	11.618148000
1	1.265134000	-0.616662000	12.085024000
1	0.394859000	0.875532000	12.361642000
6	3.368298000	0.505371000	11.025546000
6	3.447159000	-0.869502000	10.787411000
1	2.574263000	-1.500628000	10.782594000
6	4.697067000	-1.398094000	10.522101000
1	4.799144000	-2.458866000	10.332146000
6	5.815989000	-0.585112000	10.443881000
1	6.764880000	-1.017733000	10.180875000
6	5.646358000	0.788419000	10.653760000
6	8.037774000	1.151848000	10.163712000
1	8.784485000	1.825168000	10.584761000
1	8.182134000	0.182657000	10.626177000
6	8.140428000	1.118321000	8.651991000
1	9.094574000	0.707180000	8.322587000
1	7.349608000	0.480603000	8.255510000
6	7.986997000	2.555889000	8.154722000
1	7.420348000	2.595768000	7.220422000
1	8.970340000	2.985415000	7.957644000
6	6.542875000	3.032625000	10.151483000
6	7.524905000	4.866444000	8.833197000
1	8.593332000	5.042420000	8.687644000
1	7.027475000	5.091305000	7.884823000
6	6.962559000	5.733282000	9.940697000
1	7.618755000	5.715160000	10.814202000
1	6.889528000	6.764657000	9.594430000
6	5.602808000	5.175252000	10.319803000
1	4.939706000	5.206194000	9.448489000
1	5.129213000	5.768719000	11.096392000
6	0.194203000	1.356719000	9.496463000
6	0.227463000	3.825089000	9.748861000
1	-0.920274000	-0.108972000	10.675681000
1	-0.778789000	1.619615000	9.087697000
1	0.867180000	1.183765000	8.650984000
1	-0.863349000	3.829106000	9.742084000
1	0.569856000	3.945935000	8.714457000
1	-0.260154000	5.996688000	15.957621000
1	7.056683000	-0.872804000	16.487153000

9. Panchromatic Absorption and Oxidation of an Iron(II) Spin Crossover Complex

*trans-fac-1*²⁺, low-spin

6	1.643488000	-2.532894000	-0.922980000
6	1.639530000	-3.908310000	-1.167316000
6	0.431380000	-4.572252000	-1.263777000
6	-0.750062000	-3.863368000	-1.190941000
6	-0.688482000	-2.489531000	-0.955679000
7	0.486611000	-1.859443000	-0.719999000
1	2.554971000	-4.451433000	-1.317954000
1	-1.689222000	-4.359512000	-1.367762000
6	2.302363000	1.376567000	-2.438069000
6	3.483365000	1.255984000	-3.383295000
6	4.701424000	0.853388000	-2.586722000
7	4.402609000	-0.314085000	-1.756971000
6	3.110440000	-0.614025000	-1.425299000
7	2.107010000	0.179237000	-1.633220000
1	5.526414000	0.577773000	-3.245795000
1	2.427181000	2.249626000	-1.788787000
1	3.664273000	2.198818000	-3.900431000
6	-1.921604000	-0.489337000	-1.605003000
7	-2.934499000	-0.337743000	-2.507691000
6	-3.084999000	0.929696000	-3.224028000
6	-1.736514000	1.597807000	-3.383177000
6	-1.111371000	1.700967000	-2.008652000
7	-1.026566000	0.405901000	-1.332585000
1	-3.782438000	1.582915000	-2.687852000
1	-1.716769000	2.377926000	-1.403594000
6	1.635576000	2.676878000	0.803599000
6	1.631856000	4.072853000	0.719309000
6	0.415606000	4.733423000	0.784262000
6	-0.757602000	4.026197000	0.962889000
6	-0.688593000	2.631848000	0.963556000
7	0.477140000	1.981766000	0.776197000
1	2.542453000	4.640174000	0.653758000
1	-1.692423000	4.538373000	1.122415000
6	2.216152000	-1.389436000	2.202455000
6	2.515567000	-1.046247000	3.652530000
6	3.838963000	-0.306758000	3.653145000
7	3.936773000	0.591473000	2.496563000
6	2.899819000	0.749028000	1.619801000
7	2.008928000	-0.170175000	1.425503000
1	3.969938000	0.292995000	4.558807000
1	3.071660000	-1.934236000	1.796708000
1	2.591597000	-1.942436000	4.267878000
6	-1.844839000	0.633331000	1.799428000
7	-2.899669000	0.526584000	2.663486000
6	-3.069417000	-0.683326000	3.462066000
6	-2.475853000	-1.866977000	2.730539000
6	-1.053792000	-1.528401000	2.311389000
7	-0.970875000	-0.280703000	1.538678000
1	-4.135881000	-0.821624000	3.645477000
1	-2.480376000	-2.743727000	3.378526000
1	-0.645070000	-2.326256000	1.695181000
7	2.882954000	-1.874074000	-0.837299000
7	-1.863455000	-1.733618000	-0.944855000
6	-3.154150000	-2.403139000	-0.755237000
1	-3.773444000	-1.750855000	-0.134685000

9. Panchromatic Absorption and Oxidation of an Iron(II) Spin Crossover Complex

1	-2.996133000	-3.320596000	-0.198699000
1	0.414308000	-5.635062000	-1.465866000
1	0.394899000	5.815159000	0.756671000
26	0.462198000	0.042703000	0.070366000
7	-1.832925000	1.870587000	1.137520000
7	2.835698000	1.977556000	0.920176000
6	4.070514000	2.763003000	0.743310000
6	-3.171580000	2.413388000	0.871905000
1	-3.711832000	1.643917000	0.318461000
1	-3.082054000	3.276571000	0.221218000
6	5.580744000	-1.065590000	-1.338951000
6	5.241722000	-1.927894000	-0.150702000
6	4.027981000	-2.745135000	-0.517772000
1	3.727912000	-3.395575000	0.300524000
1	5.043985000	-1.310483000	0.727662000
1	5.954832000	-1.677228000	-2.166958000
1	6.359476000	-0.340629000	-1.093152000
6	-4.063222000	-1.252996000	-2.701600000
6	-3.828339000	-2.619317000	-2.093719000
1	-4.782108000	-3.134144000	-1.977514000
1	-3.190062000	-3.225407000	-2.738415000
1	-4.951793000	-0.795081000	-2.251777000
1	-4.247280000	-1.329389000	-3.774249000
1	-3.529895000	0.701140000	-4.192499000
1	5.050911000	1.680754000	-1.959000000
1	3.271102000	0.492564000	-4.136415000
1	1.397789000	1.546147000	-3.018330000
1	4.281305000	-3.378361000	-1.373380000
1	6.067281000	-2.598527000	0.085270000
1	-0.118755000	2.133969000	-2.045816000
1	-1.858449000	2.588112000	-3.822312000
1	-1.104701000	1.004404000	-4.048635000
1	1.350974000	-2.027830000	2.094373000
1	1.714198000	-0.422557000	4.054760000
1	4.668847000	-1.018508000	3.604329000
6	5.296145000	1.927127000	1.021138000
6	5.167323000	1.364110000	2.417227000
1	5.992393000	0.688292000	2.654636000
1	6.181853000	2.554665000	0.932776000
1	5.387722000	1.112144000	0.303222000
1	4.075151000	3.611934000	1.430672000
1	4.076382000	3.154310000	-0.274148000
1	5.173830000	2.168940000	3.161677000
6	-3.913254000	2.731257000	2.167734000
6	-3.428896000	1.763095000	3.251692000
1	-4.985113000	2.626338000	1.993958000
1	-3.725434000	3.755750000	2.491818000
1	-2.652508000	2.233926000	3.863139000
1	-4.241022000	1.479074000	3.916466000
1	-2.578046000	-0.553306000	4.433171000
1	-3.078466000	-2.104056000	1.855066000
1	-0.422518000	-1.448650000	3.199662000

9. Panchromatic Absorption and Oxidation of an Iron(II) Spin Crossover Complex

*trans-fac-1*²⁺, high-spin

6	1.671062000	-2.609604000	-1.045968000
6	1.673979000	-3.991629000	-1.255974000
6	0.458492000	-4.644831000	-1.360954000
6	-0.727273000	-3.936779000	-1.308463000
6	-0.660299000	-2.556495000	-1.104921000
7	0.515708000	-1.936718000	-0.905861000
1	2.588500000	-4.546108000	-1.370543000
1	-1.664949000	-4.441107000	-1.472435000
6	2.314480000	1.390394000	-2.380536000
6	3.518036000	1.322732000	-3.299970000
6	4.717886000	0.905115000	-2.485821000
7	4.413383000	-0.307327000	-1.724389000
6	3.119409000	-0.639948000	-1.439797000
7	2.108890000	0.155928000	-1.626732000
1	5.569817000	0.677013000	-3.128123000
1	2.416802000	2.236887000	-1.692779000
1	3.699525000	2.288146000	-3.773144000
6	-1.941579000	-0.543609000	-1.730747000
7	-3.038180000	-0.397733000	-2.527056000
6	-3.279370000	0.872850000	-3.216194000
6	-1.969077000	1.576943000	-3.488618000
6	-1.214758000	1.669573000	-2.179375000
7	-1.041838000	0.369154000	-1.533089000
1	-3.944383000	1.501625000	-2.614563000
1	-1.760750000	2.330478000	-1.501926000
6	1.670622000	2.713867000	0.872957000
6	1.671276000	4.106279000	0.719699000
6	0.449285000	4.760461000	0.715474000
6	-0.734452000	4.063622000	0.877693000
6	-0.658312000	2.670256000	0.958154000
7	0.515989000	2.025648000	0.875202000
1	2.578921000	4.677703000	0.647555000
1	-1.672107000	4.587650000	0.963794000
6	2.244158000	-1.396559000	2.192308000
6	2.570742000	-1.112139000	3.648902000
6	3.897718000	-0.379725000	3.664212000
7	3.972409000	0.598324000	2.572724000
6	2.942851000	0.767681000	1.690945000
7	2.063881000	-0.151174000	1.454954000
1	4.050100000	0.158297000	4.604348000
1	3.069367000	-1.965761000	1.757361000
1	2.649548000	-2.031348000	4.228934000
6	-1.827008000	0.665783000	1.802713000
7	-2.845128000	0.615081000	2.712114000
6	-3.035058000	-0.583939000	3.523416000
6	-2.545010000	-1.798196000	2.762443000
6	-1.126603000	-1.534278000	2.278701000
7	-1.010646000	-0.287836000	1.512268000
1	-4.096331000	-0.666710000	3.761432000
1	-2.572982000	-2.677056000	3.407251000
1	-0.785524000	-2.348063000	1.639415000
7	2.897039000	-1.931850000	-0.926831000
7	-1.830029000	-1.790018000	-1.077207000
6	-3.105048000	-2.453412000	-0.787547000
1	-3.686998000	-1.783970000	-0.149633000

9. Panchromatic Absorption and Oxidation of an Iron(II) Spin Crossover Complex

1	-2.909755000	-3.354433000	-0.215931000
1	0.439001000	-5.711490000	-1.542882000
1	0.427763000	5.839640000	0.633110000
26	0.518456000	0.045033000	-0.061862000
7	-1.799741000	1.898609000	1.116490000
7	2.872342000	2.019007000	1.032479000
6	4.104385000	2.813813000	0.870117000
6	-3.138816000	2.454146000	0.878766000
1	-3.709342000	1.675147000	0.372368000
1	-3.061606000	3.292704000	0.194681000
6	5.590315000	-1.054202000	-1.292627000
6	5.224331000	-1.950479000	-0.138471000
6	4.044250000	-2.785315000	-0.569250000
1	3.722139000	-3.449633000	0.229588000
1	4.976364000	-1.352694000	0.740917000
1	5.996197000	-1.639278000	-2.124581000
1	6.350950000	-0.325715000	-1.004815000
6	-4.133208000	-1.358598000	-2.703582000
6	-3.854931000	-2.708765000	-2.076604000
1	-4.796798000	-3.225746000	-1.892395000
1	-3.250037000	-3.328980000	-2.739628000
1	-5.029750000	-0.918837000	-2.253563000
1	-4.323581000	-1.455303000	-3.773876000
1	-3.800968000	0.640986000	-4.144490000
1	5.027646000	1.706387000	-1.806804000
1	3.336547000	0.587562000	-4.088432000
1	1.419409000	1.572432000	-2.970790000
1	4.340039000	-3.404434000	-1.421416000
1	6.054133000	-2.607232000	0.119758000
1	-0.238476000	2.122887000	-2.319179000
1	-2.156827000	2.569975000	-3.897862000
1	-1.388613000	1.009420000	-4.220522000
1	1.352047000	-2.001410000	2.080737000
1	1.780723000	-0.498327000	4.087479000
1	4.723914000	-1.089047000	3.553314000
6	5.336142000	1.991356000	1.159708000
6	5.186895000	1.399715000	2.541907000
1	6.020601000	0.737819000	2.786230000
1	6.213303000	2.634279000	1.100035000
1	5.457352000	1.189917000	0.429786000
1	4.089788000	3.662786000	1.557387000
1	4.120392000	3.206794000	-0.146879000
1	5.156848000	2.189287000	3.301793000
6	-3.829080000	2.827026000	2.188567000
6	-3.329993000	1.876845000	3.283094000
1	-4.908570000	2.743576000	2.054632000
1	-3.605954000	3.855033000	2.476596000
1	-2.525243000	2.346860000	3.856613000
1	-4.125928000	1.628811000	3.981097000
1	-2.488810000	-0.479780000	4.467644000
1	-3.203051000	-1.991081000	1.915427000
1	-0.453592000	-1.500941000	3.139587000

9. Panchromatic Absorption and Oxidation of an Iron(II) Spin Crossover Complex

*mer-1*³⁺, low-spin

6	1.677145000	-2.796588000	0.079878000
6	1.788497000	-4.184564000	0.075818000
6	0.702856000	-4.947650000	0.446276000
6	-0.478341000	-4.329328000	0.797750000
6	-0.554738000	-2.939738000	0.760822000
7	0.511380000	-2.188564000	0.404432000
1	2.700764000	-4.663165000	-0.231611000
1	-1.313902000	-4.924044000	1.116752000
6	1.603233000	0.829576000	-2.134511000
6	2.358767000	0.422488000	-3.382455000
6	3.801405000	0.192328000	-2.993232000
7	3.877623000	-0.669560000	-1.808200000
6	2.780200000	-0.935488000	-1.063156000
7	1.690967000	-0.215943000	-1.109613000
1	4.356449000	-0.311328000	-3.787141000
1	2.020399000	1.765871000	-1.757060000
1	2.293502000	1.205568000	-4.136683000
6	-1.874881000	-1.201455000	1.871065000
7	-3.001203000	-1.011316000	2.588038000
6	-3.091844000	0.018570000	3.631884000
6	-2.135780000	1.156971000	3.374655000
6	-0.781557000	0.588652000	3.011910000
7	-0.859475000	-0.360088000	1.891968000
1	-2.880146000	-0.455733000	4.594203000
1	-0.359478000	0.069296000	3.876611000
6	1.322585000	2.518500000	0.573928000
6	1.238306000	3.908750000	0.549683000
6	0.025817000	4.506150000	0.280110000
6	-1.083187000	3.722904000	0.047835000
6	-0.959687000	2.336212000	0.102064000
7	0.230290000	1.744803000	0.359329000
1	2.097678000	4.518540000	0.758825000
1	-2.018920000	4.187942000	-0.201954000
6	1.990732000	-1.087733000	2.752583000
6	2.666671000	-0.517117000	3.983490000
6	4.031786000	-0.022134000	3.563847000
7	3.922847000	0.785542000	2.342077000
6	2.766091000	0.851588000	1.639895000
7	1.824845000	-0.047581000	1.732070000
1	4.484493000	0.614054000	4.327428000
1	2.599280000	-1.905560000	2.359372000
1	2.764187000	-1.280959000	4.753527000
6	-2.117099000	0.423106000	-0.897662000
7	-3.255197000	0.108745000	-1.553160000
6	-3.246071000	-0.800275000	-2.706174000
6	-1.831886000	-1.021607000	-3.187860000
6	-0.989033000	-1.375810000	-1.983035000
7	-1.020380000	-0.298452000	-0.986309000
1	-3.866537000	-0.336109000	-3.474846000
1	-1.806972000	-1.829330000	-3.917920000
1	0.047770000	-1.544737000	-2.256486000
7	2.822555000	-2.045158000	-0.219679000
7	-1.789243000	-2.332218000	1.065926000
6	-2.973186000	-3.195167000	0.833648000
1	-2.942273000	-4.053685000	1.503241000

9. Panchromatic Absorption and Oxidation of an Iron(II) Spin Crossover Complex

1	-2.914604000	-3.556467000	-0.191696000
1	0.776965000	-6.026265000	0.461015000
1	-0.053801000	5.583954000	0.244794000
26	0.367015000	-0.225173000	0.385342000
7	-2.117830000	1.566823000	-0.104093000
7	2.585236000	1.941585000	0.784792000
6	3.737734000	2.818901000	0.487163000
6	-3.394299000	2.291007000	0.087387000
1	-3.550675000	3.001646000	-0.726876000
1	-3.318111000	2.849133000	1.016137000
6	5.211995000	-1.197727000	-1.524083000
6	5.254048000	-1.760296000	-0.124632000
6	4.110994000	-2.734722000	0.004817000
1	4.072432000	-3.180383000	0.996872000
1	5.170726000	-0.966481000	0.618749000
1	5.471551000	-1.966158000	-2.258083000
1	5.917040000	-0.372994000	-1.646759000
6	-4.161358000	-1.901572000	2.504712000
6	-4.254079000	-2.452584000	1.102947000
1	-5.087710000	-3.147168000	1.011444000
1	-4.409131000	-1.646737000	0.385956000
1	-4.078264000	-2.708920000	3.238415000
1	-5.034790000	-1.305564000	2.761536000
1	-4.122018000	0.371046000	3.654663000
1	4.304513000	1.140880000	-2.782861000
1	1.925445000	-0.488469000	-3.802192000
1	0.552465000	1.007003000	-2.346094000
1	4.251558000	-3.532413000	-0.727224000
1	6.193398000	-2.283281000	0.046564000
1	-0.089875000	1.376694000	2.745290000
1	-2.057792000	1.774533000	4.269088000
1	-2.507662000	1.788240000	2.570615000
1	1.013950000	-1.496089000	2.987813000
1	2.070982000	0.302204000	4.390887000
1	4.712874000	-0.858325000	3.382117000
6	5.025131000	2.039712000	0.575414000
6	5.138976000	1.515151000	1.985893000
1	5.973633000	0.818852000	2.091251000
1	5.860039000	2.699798000	0.346085000
1	5.035752000	1.224672000	-0.148703000
1	3.787511000	3.643838000	1.201074000
1	3.582226000	3.231656000	-0.507746000
1	5.301300000	2.336056000	2.690703000
6	-4.546689000	1.320768000	0.117151000
6	-4.582706000	0.630590000	-1.222455000
1	-5.473237000	1.865320000	0.289790000
1	-4.422613000	0.601129000	0.927245000
1	-5.269941000	-0.217925000	-1.223898000
1	-4.907832000	1.321082000	-2.005116000
1	-3.715925000	-1.746168000	-2.421312000
1	-1.443987000	-0.119157000	-3.666197000
1	-1.364130000	-2.304608000	-1.548606000

10. Curriculum Vitae

Personal data

date and place of birth: [REDACTED]

Experiences

- 02/2021 – present **Scientist**
 in the Department of chemistry
 at the Johannes Gutenberg University in Mainz
- Scientific support for the DFG priority program “Light Controlled Reactivity of Metal Complexes“
 - Scientific support for spectrometers and laboratory equipment
- 03/2017 – 11/2020 **Scientist**
 in the Department of chemistry
 at the Johannes Gutenberg University in Mainz
- Research during PhD studies including scientific publications:
Eur. J. Inorg. Chem. **2017**, 5033–5040.
Chem. Eur. J. **2019**, 25, 11826–1830.
Chem. Eur. J. **2020**, 26, 6820–6832.
 - Supervision of students in lab courses and research
- 01/2012 – 12/2015 **Student employee for product development**
 Filtermedia at BRITA GmbH, Taunusstein
- experiments and evaluation for market analysis for supply chain
 - Quality control of intern production

Studies and school

- 03/2017 – present **PhD in inorganic photochemistry**
 “Ligand Controlled Electronic Structure of Iron and Ruthenium Complexes”
- 10/2013 – 12/2016 Master studies of chemistry
 Master thesis: “Symmetrie-erlaubte Intraligand- und Charge-Transfer-Zustände in Fe(II)- und Ru(II)-Komplexen“ in the group of Prof. Katja Heinze, Johannes Gutenberg University in Mainz
- 10/2010 – 12/2013 Bachelor studies of chemistry
 Bachelor thesis: “Kleine Moleküle mit asymmetrisch substituiertem Diketopyrrolopyrrol für Anwendungen in Hybrid-Solarzellen” in the group of Prof. Rudolf Zentel, Johannes Gutenberg University in Mainz
- 07/2010 Dilthey-Gymnasium, Wiesbaden
 Allgemeine Hochschulreife (grade 1,6)

10. Curriculum Vitae

Skills

Languages	English: EU-Level C1 Latin: Latinum
EDP	MS-Word, Excel & PowerPoint (daily use), Origin
Driver license	Class B
Honorary post	2007 – present Member of volunteer fire brigade
Hobby	Standard dance, hiking